THE UNIVERSITY
of EDINBURGH

Structural Design and the use of Reinforced Concrete for Wave Energy Converters

Leah Barker Ewart

Industrial Doctoral Centre for Offshore Renewable Energy

A thesis submitted in partial fulfilment of the requirements for the award of an Engineering Doctorate

Industrial Doctoral Centre for Offshore Renewable Energy

2019

Abstract

Structural design aspects and material selection choices for Wave Energy Converters (WECs) have a large impact on capital expenditure and life-cycle operating costs. The aim of this thesis is to consider the governing design issues and material selection choices in the early design stages in order to improve lifecycle cost. The work was carried out in close collaboration with Albatern and the thesis will draw on the WaveNET array as a case study. The WaveNET array is a novel multi-body floating array system, harnessing power through the relative motion of buoyant Node elements, and rigid Link elements, which are connected via an articulated Joint Module.

The thesis reviews the concept design process and develops methods for assessing the trade-off between maximising power production, and minimising structural loading over the lifetime of the structure to optimise LCoE. Concept assessment methods are developed with the aid of structural load data from physical and numerical models. Developing these methods at an early stage in the design process ensures that potential structural issues are highlighted when it is still easy to make design changes.

This work also investigates the potential for reinforced concrete materials to reduce construction costs for floating WECs, by carrying out design tasks related to the Node structure within the array. A techno-economic feasibility study shows that reinforced concrete provides excellent mechanical properties at a low unit cost. It highlights potential benefits of advanced concrete mixes, particularly for devices with weight and buoyancy restrictions which push conventional concrete design to its limits. The behaviour of critical steel-concrete connections, which need to transmit highly dynamic loads about multiple axes, is also assessed. High-level analysis work of commonly used connections is carried out using FEA models, with particular emphasis on the fatigue behaviour, in order to identify appropriate connection techniques.

The main contributions of this thesis are:

- a comparison of fatigue analysis methods for floating WECs;
- the advancement of knowledge regarding the application of conventional and advanced concrete materials for floating WECs;
- the advancement of knowledge regarding the behaviour of steel-concrete connections for floating WECs.

Acknowledgements

The work in this thesis would not have been possible without the support of many people.

First I would like to thank my academic supervisors Prof Nigel Barltrop, Prof Tim Stratford and Dr Philipp Thies for their ongoing support, advice, guidance and feedback. Their wide ranging research interests have been invaluable in helping to pull together a cohesive thesis.

Thanks also go to my industrial supervisors, David Findlay at Albatern, and Jon Benzie at Pelamis and Quoceant who have been instrumental in shaping my research. David's creative vision drove the 12S development work, and I am indebted to Jon's in depth analysis knowledge and patience in explaining FEA problems, without which I would still be staring at Abaqus models of steel-concrete connections, wondering why they weren't working.

Working across multiple companies has given me the opportunity to work with many people who have had a positive influence on this thesis. Early research carried out at Pelamis would not have been possible without the input of Vincent O'Donoghue and Noushin Khosravi, together with the Concrete Technology Unit at the University of Dundee. Investigations at Albatern built on the efforts of the whole of the Albatern internal design team; particular thanks go to Anthony McDonald who took time to run additional numerical models so that I could use the results here.

Additionally I am ever grateful for the endless support of my husband Martin, who was willing to move to a city he had never visited in order to allow me to pursue this doctorate, and our two year old son Jonah, whose toddler enthusiasm for life has provided a welcome respite from thesis writing.

Finally I would like to thank IDCORE, which is funded by the Energy Technologies Institute and RCUK Energy programme (grant no. EP/J500847/1, and Wave Energy Scotland who provided funding to Albatern and Quoceant through the Novel Wave Energy Converter, and Structural Materials and Manufacturing Processes research programmes.

Declaration

I declare that this thesis was composed by myself, that the work contained herein is my own except where explicitly stated otherwise in the text, and that this work has not been submitted for any other degree or professional qualification except as specified.

Leah Barker Ewart

Contents

Abstract iii

Acknowledgements v

Declaration vii

Contents ix

List of Figures xi

List of Tables xiii

Nomenclature xv

I Introduction and Literature Review 1

1 Introduction 3

1.1 Thesis background . . . 3

1.2 Albatern development progress . . . 5

1.3 Thesis structure . . . 9

1.4 Contributions to knowledge . . . 10

2 Literature review I: Structural design process 13

2.1 Structural design of wave energy converters . . . 13

2.2 Fatigue design methods . . . 15

3 Literature review II: Material selection 19

3.1 Materials in the renewable industry . . . 19

3.2 Advanced concrete materials . . . 24

3.3 Summary . . . 36

4 Literature review III: Steel- Concrete Connections 39

4.1 Concrete steel joints . . . 39

4.2 Concrete behaviour . . . 46

4.3 Summary . . . 51

II Conceptual design **53**

5 Initial concept selection **57**
5.1 Context . . . 57
5.2 Concept assessment and selection methodology . . . 59
5.3 Power output and force assessment results . . . 68
5.4 Decision matrix results . . . 74
5.5 Summary and discussion . . . 79

6 Concept modelling activities for load definition **81**
6.1 Modelling Context . . . 82
6.2 Tank testing methodology . . . 82
6.3 Numerical modelling methodology . . . 95
6.4 Modelling activities - results . . . 98
6.5 Summary and conclusions . . . 118

7 PTO torque limitation **123**
7.1 PTO torque limitation methodology . . . 124
7.2 PTO Torque limitation: Optimisation results . . . 128
7.3 PTO Torque limit - discussion and conclusion . . . 132

8 Summary of final load cases **135**
8.1 PTO articulation loads for design . . . 135
8.2 Design sea states and limit state load cases . . . 138
8.3 Final comments . . . 139

III Use of reinforced concrete for Wave Energy Converters **141**

9 Node material selection **145**
9.1 High level material selection . . . 146
9.2 Preliminary node design and costing . . . 152
9.3 Summary . . . 155

10 Advanced concrete materials **157**
10.1 Design and analysis process . . . 158
10.2 Material properties . . . 165
10.3 Conventional reinforced concrete design . . . 170
10.4 Design modifications . . . 180
10.5 Option comparison . . . 187
10.6 Scale Effect . . . 192
10.7 Discussion and conclusions . . . 196

11 Connection design **201**
11.1 Background and context 202
11.2 Connection assessment methodology 203
11.3 Results of preliminary options assessment 210
11.4 Results of detailed connection assessment 219
11.5 Discussion and conclusions 228

IV Final remarks **233**

12 Concluding remarks **235**
12.1 Discussion of research outcomes in relation to objectives 236
12.2 Key conclusions 241
12.3 Further work 242

Appendices

A Publications **245**

B FRC material properties from the literature **283**

C Unit costs for LCoE calculation **287**

D Material selection **291**

E Rates and cost build ups **303**

F Node design appendix **307**

G Connection design calculations **333**

References **349**

List of Figures

1.1 6S module components . . . 6
1.2 WaveNET development scales . . . 6
1.3 Array configurations . . . 6
1.4 6S deployment images . . . 8
1.5 12S design concept . . . 9

2.1 Qualification process . . . 15

3.1 Concrete for the wind industry . . . 21
3.2 Floating wave energy converters . . . 22
3.3 Limpet wave energy converter . . . 22
3.4 Wavestar wave energy converter . . . 23
3.5 SFRC load deflection curves . . . 28
3.6 Uniaxial tensile behaviour of FRC . . . 29
3.7 Cracking of SHCC . . . 30
3.8 S-N curves for concrete . . . 32
3.9 SLS stress-strain relations for FRC . . . 34
3.10 ULS simplified stress-strain relations for FRC . . . 35
3.11 FRC idealised stress-strain response . . . 36

4.1 Composite steel/concrete beam . . . 40
4.2 Offshore embedment plate . . . 40
4.3 Shear stud load transfer . . . 41
4.4 Perfobond . . . 42
4.5 Steel rib profiles . . . 42
4.6 Different types of shear connectors . . . 43
4.7 Proprietary cast in anchors . . . 43
4.8 Wind turbine foundation anchor system . . . 44
4.9 Vici Venus steel to concrete connection . . . 45
4.10 Post-installed anchors . . . 45
4.11 3D behaviour of concrete . . . 47
4.12 Wholer-curves for steel-concrete fasteners . . . 48
4.13 Evolution of concrete cracks in fatigue loading . . . 49

5.1 Concept option assessment flowchart . . . 60
5.2 Base Case . . . 61

5.3 Modular Concept . . . 61
5.4 AEP vs PTO torque, 1st stage . . . 69
5.5 Link arm utilisation vs PTO damping, 1st stage . . . 70
5.6 Power output vs PTO torque, variable buoyancy . . . 71
5.7 Node comparison, $\%AEP$ vs PTO damping . . . 73
5.8 Node comparison, link arm utilisation vs PTO damping . . . 74
5.9 12S preferred design concept . . . 79

6.1 Squid configuration on tank floor at Flowave . . . 83
6.2 Node and link configuration . . . 83
6.3 1 Hex model naming conventions . . . 84
6.4 Mooring grid schematic . . . 84
6.5 Wire drive mechanisms for tank testing model . . . 85
6.6 West Harris site location . . . 86
6.7 West Haris occurence matrix . . . 87
6.8 Link arm end torque measurement . . . 89
6.9 Sensor location . . . 91
6.10 Snapshots of the 1Hex model with mooring system . . . 95
6.11 Numerical model articulation axis . . . 96
6.12 Velocity vs mechanical torque at pitch articulation . . . 97
6.13 Intermediate load reversal as part of a larger range . . . 104
6.14 Successive rainflow counts . . . 105
6.15 Local maxima and minima in time history . . . 106
6.16 Torque cycle count histogram . . . 106
6.17 Test sea states . . . 107
6.18 Test sea states . . . 107
6.19 Articulation pitch torque RAOs, obtained from numerical model runs . . . 110
6.20 Calculation of $S_R(f)$ . . . 110
6.21 Loading range histograms . . . 112
6.22 Comparison of fatigue cycles, tank testing & numerical model . . . 113
6.23 Comparison of torque histograms for spectral and time domain methods . . . 115
6.24 Reponse spectrum for LA5S . . . 116
6.25 Upcrossing spectrum compared with Gaussian response . . . 117

7.1 Extract from torque limited time history for LA5 . . . 124
7.2 PTO mechanism schematic . . . 125
7.3 Extrapolate mechanical power matrix, unlimited torque . . . 129
7.4 Extrapolate mechanical power matrix, torque limit = 600kNm . . . 129
7.5 PTO torque limit vs AEP . . . 129
7.6 PTO torque limit vs cost . . . 131

7.7 Torque limit vs Costs, AEP and LCoE . . . 131

8.1 West Harris Occurence Matrix with design sea states . . . 139

9.1 Overview of Node structure . . . 145
9.2 Typical loads experienced by node structure . . . 147
9.3 Material selection charts . . . 150
9.4 Preliminary design options . . . 154

10.1 Locations for calculation of dynamic wave pressure . . . 160
10.2 Section of node model in Abaqus . . . 163
10.3 Design sections . . . 164
10.4 σ-CMOD values for concrete . . . 166
10.5 Generic Node Dimensions . . . 170
10.6 Conceptual reinforcement schematic . . . 171
10.7 Node buoyancy schematic . . . 172
10.8 SLS stress distribution - linear elastic concrete compressive stress . . . 174
10.9 ULS and ALS stress distribution . . . 174
10.10 ULS(c) max stress - no post-tensioning . . . 175
10.11 ULS(c) max stress - with 1.5MPa post-tensioning . . . 175
10.12 Reference design Cross section dimensions . . . 177
10.13 Outline rebar layout . . . 178
10.14 Reinforcement requirements at junction between base column and cone section 180
10.15 UHPFRC cross section requirements (dimensions in mm) . . . 183
10.16 Max principal tensile stress ULS(c) . . . 185
10.17 SHCC cross section requirements (dimensions in mm) . . . 185
10.18 Carbon fibre wrap schematic . . . 187
10.19 Option costs presented as a multiplier of the reference design baseline cost . . . 190
10.20 GFRP sandwich construction schematic . . . 193
10.21 Schematics for different options for 6S scale node . . . 195
10.22 Option costs as a multiplier of the steel baseline cost . . . 195

11.1 Joint overview . . . 202
11.2 Connection loads . . . 202
11.3 Connection schematics . . . 204
11.4 Local connection loads . . . 205
11.5 Articulation load RAOs . . . 207
11.6 Section through FEA model for dowel connection . . . 208
11.7 Connection option schematics (a) and (b) . . . 211
11.8 Connection option schematics (c) and (d) . . . 212
11.9 Shear stud failure modes . . . 213

11.10 Dowel connector failure modes 214
11.11 Cast in anchor failure modes 215
11.12 Post-tensioned bar failure modes 216
11.13 Abaqus model schematics 220
11.14 Finite element results - Stud static loads 222
11.15 Finite element results - Dowel static loads 223
11.16 Finite element results - Post-tensioned bar static loads 224
11.17 Fatigue damage in the stud connection 226
11.18 Fatigue damage in the composite dowel connection 227
11.19 Fatigue damage in the post-tensioned bar 227
11.20 Pelamis connection schematics 231

F.1 Location of convergence study 307
F.2 Variation in principle stress with no. of through thickness elements) 308
F.3 Derivation of design moments and axial force from through section stresses . . 309
F.4 Cross sectional stress values (s11) for the top slab, section B, for ULS1(a) . . 309
F.5 SLS stress-strain relationship for UHPFRC sections 317
F.6 ULS stress-strain relationship for UHPFRC sections 317
F.7 Maximum principle stress in UHPFRC Node Structure 318

List of Tables

1.1 Albatern planned development stages 7

3.1 FRC classifications 27
3.2 Flexural strength outputs from standard bending test 33

5.1 “Modular” concept variations 63
5.2 Second stage concept variations 64
5.3 Tube design resistances 67
5.4 Comparison table for 1st stage assessment concepts 75
5.5 Comparison table for 1st stage assessment variants 76
5.6 Comparison table for 2nd stage assessment 77
5.7 Decision matrices, 1st stage assessments 78
5.8 Decision matrices, 2nd stage assessments 78

6.1 Regular test sea states 86
6.2 Irregular sea states (Jonswap, gamma = 1) 86
6.3 Options for end articulation torque measurements 90
6.4 Link arm for measurement options 91
6.5 Details of instrumentation used for load measurement 92
6.6 Optimum damping values 93
6.7 Summary of load data from tank tests 94
6.8 Numerical models vs tank test results, regular waves 99
6.9 Tank test vs numerical model results, irregular waves, average torque 101
6.10 Tank test vs numerical model results, irregular waves, peak torque 102
6.11 Calculation of weighting factors 108
6.12 Annual fatigue damage based on numerical model and tank testing results . . 112
6.13 Annual fatigue damage using spectral methods 114
6.14 Bandwidth comparison of structural reponse with incoming wave 116

7.1 Systems, subsystems and components for the Albatern 12S array 126
7.2 Categories and contribution to whole life cost 127
7.3 Systems, subsystems and components of array for cost purposes 128
7.4 Hydraulic cylinder estimated size and costs 130
7.5 Required link arm cross sectional area (CSA) 130
7.6 Normalised LCoE values for different cost assumptions 132

8.1 Peak articulation actions from numerical model - SLS loadcase 136

8.2 Peal articulation actions from numerical Model - ULS loadcase 137
8.3 PTO articulation load cases for ongoing design work 137
8.4 Articulation loads for spectral fatigue analysis 138
8.5 Limit state load case combinations 138

9.1 Qualitative design constraints for the node 147
9.2 Materials that perform better than steel when considering minimum weight . . 151
9.3 Materials that perform better than steel when considering minimum cost 151
9.4 Summary of potential node materials 152
9.5 Preliminary design concrete option; quantities and costs 154
9.6 Preliminary design steelwork option; quantities and costs 154
9.7 Summary of material parameters Node structure made from steel or concrete 156

10.1 Global PTO loads (Environmental load Q) 159
10.2 Applied pressure forces (Environmental Load E) 161
10.3 Applied operational loads for fatigue analysis 162
10.4 Load cases for design 162
10.5 Partial load factors 162
10.6 Linear elastic concrete properties for model 163
10.7 stress-CMOD values for preliminary design (UHPFRC) 167
10.8 Equations for characteristic uniaxial tensile stress-strain values for design . . . 168
10.9 Residual flexural strength values for preliminary design (MPa) 169
10.10 Uniaxial tensile strength values for preliminary design (MPa) 169
10.11 Material properties for structural carbon fibre wrapping material 169
10.12 Node buoyancy and mass properties 171
10.13 Design actions for the Innerwall Base location 173
10.14 Reinforcement requirements for reference design 174
10.15 Reference conventional RC design section requirements 177
10.16 Final node buoyancy and mass properties 178
10.17 Maximum principal stress for different limits for UHPFRC option 181
10.18 UHPFRC section thickness requirements 183
10.19 UHPFRC section mass and buoyancy properties 183
10.20 SHCC section mass and buoyancy properties 186
10.21 Final node buoyancy and mass properties 187
10.22 Option comparison 188
10.23 Material quantities for different design options 189
10.24 Reference RC option 190
10.25 Option 1: UHPFRC 191
10.26 Option 2: SHCC & UHPFRC 191
10.27 Option 3: Carbon fibre 191

10.28 Characteristic parameters of different WaveNET array scales 192
10.29 Scaled design actions for 6S design 193
10.30 6S options cost comparison 196

11.1 PTO articulation load cases for ongoing design work 205
11.2 Connection loads 205
11.3 S-N data for connection details 207
11.4 Fatigue damage calculation for different options 216
11.5 Option design parameters 217
11.6 Connection advantages and disadvantage discussion 218
11.7 Percentage of concrete elements with tensile damage >0.8 225

B.1 Mechanical properties of FRC 284

C.1 Assumed unit costs for LCoE calculation, for a torque limit of $1\,\mathrm{MNm}$ 288

D.1 Summary of material parameters 294

E.1 Unit rates for cost estimates - baseline 304
E.2 Unit rates for cost estimates - optimistic 305
E.3 Unit rates for cost estimates - pessimistic 306

F.1 Convergence study values 308
F.2 Top slab design section through section stresses 309
F.3 Top slab design section bending and axial force derivation 309
F.4 SLS design actions 310
F.5 ULS and ALS design actions for slab sections 310
F.6 S-N curve constants 315
F.7 Fatigue checks 316
F.8 Reference option 320
F.9 Option 1: UHPFRC 321
F.10 Option 1: SHCC & UHPFRC 322
F.11 Option 3: Carbon fibre 323
F.12 Scaled design actions for 6S design 324
F.13 6S options cost comparison 331

Nomenclature

Acronyms

AEP	Annual energy yield
ALS	Accidental limit state
CFRP	Carbon fibre reinforced polymer
CMOD	Crack mouth opening displacement
DoF	Degree of freedom
F	Force
FLS	Fatigue limit state
FRC	Fibre reinforced concrete
FRP	Fibre reinforced polymer
GFRP	Glass fibre reinforced polymer
GTA	German technical approval
LCoE	Levelised cost of energy
M	Moment
NM	Numerical model
pdf	Probability density function
PSD	Power spectral density
PTO	Power take off
RAO	Response amplitude operator
RC	Reinforced concrete
SFRC	Steel fibre reinforced concrete
SHCC	Strain hardening cement composites
SLS	Serviceability limit state
TL	Torque limit
TT	Tank testing
UF	Utilisation factor
UHPC	Ultra high performance concrete
UHPFRC	Ultra high performance fibre reinforced concrete
ULS	Ultimate limit state
WEC	Wave energy converter
WES	Wave Energy Scotland

Symbols

ε	Strain
ε_{ct}	cracking strain for FRC
ε_{Ftu}	ultimate tensile strain for FRC
ε_{pc}	strain at peak tensile stress of UHPFRC
γ	partial safety factor
ω	Angular velocity
Ω	Bandwidth parameter
σ	Stress
$_d$	subscript denoting design values
$_k$	subscript denoting characteristic value
D	accumulated fatigue damage
d_f	Fibre diameter
f_{cck}	Characteristic compressive cube strength of concrete
f_{ct}	Tensile cracking strength of FRC
f_{Fts}	SLS residual tensile strength of FRC
f_{Ftu}	ULS residual tensile strength of FRC
f_{pk}	Peak tensile strength of UHPFRC
f_{Ri}	Residual stress relating to point on s-CMOD curve
f_{tk}	Characteristic tensile strength
f_L	Stress at first crack (limit of proportionality)
f_y	Yield strength
H	Regular wave height
H_{max}	Statistical maximum wave height in storm event
H_s	Significant wave height
I	Current

l_f	Fibre length	T	Regular wave period
n_i	number of stress cycles in stress block i	T_p	Peak wave period
		v_f	fibre volume fraction
N_i	number of cycles to failure at constant stress range	x	Fibre factor = $V_f.l_f/d_f$

Descriptions

WaveNET	Multi-body array system developed by Albatern
Squid	Unit of WaveNET array system, consisting of three link arms, one central node, and three outer nodes (or Anti-Nodes)
1-Hex	Array configuration, consisting of 9 link arms and 9 nodes
3-Hex	Array configuration, consisting of 18 link arms, and 16 nodes
Singler node	Node with only one link arm attached
Central node	Node with three link arms attached
Doubler node	Node with two link arms attached

PART I

Introduction and Literature Review

Chapter 1

Introduction

1.1 Thesis background

Renewable energy technologies have a vital role to play in combating climate change and helping the UK government reach their carbon emission reduction commitments. Marine renewable technologies could provide a significant proportion of the overall energy mix, especially in the UK, but considerable research is still needed in order to extract the energy from these sources in a cost effective manner. Wave power is one of the least developed of these technologies but has one of the highest potential resources. Actual resource estimates vary greatly, but the global annual theoretical resource is thought to be in the region of 30,000TWhr, compared to a global annual electricity supply of 16,800 TWhr (IPCC, 2012) with the extractable percentage estimated between 5 % to 25 % (see Barstow et al., 2008; Gunn and Stock-Williams, 2012)

A significant amount of research has been carried out into wave energy generation, but as an industry there are still many challenges to overcome. A majority of research focusses on proof of concept and the development of the energy capture technology, with structural design issues and material selection being a secondary concern. However there need to be reductions in the levelised cost of energy (LCoE) to make wave power technologies competitive within the overall energy market, and structural design and material choices can have a significant impact on capital expenditure and life-cycle operating costs. One particular area for potential cost reduction is the use of low cost materials that are suitable for use in the harsh marine environment such as reinforced concrete, which gives good corrosion and fatigue properties while providing excellent strength and stiffness at low unit cost.

1.1.1 Research objectives

This thesis focusses on the conceptual design of a floating wave energy converter (WEC), with the aim of helping to take steps towards a reduction in LCoE by considering structural design and material selection choices at an early stage in the design process. The objectives of this research are as follows:

1. To assess the trade off between power production and structural loading at an early stage in the design process, when the outcome can have the most influence on decision making, using LCoE as an assessment metric;
2. To determine best practice methods for using physical and numerical model output for preliminary structural design, with particular emphasis on fatigue loading, which is often the design driver for dynamic WEC structures;
3. To investigate the use of reinforced concrete as a low cost material for WECs, highlighting potential issues with the material, and reducing associated risks and uncertainties;
4. To advance the knowledge of dynamic connections between concrete and steel components; these connections are often critical to the overall function of a floating WEC.

1.1.2 Thesis context

This Engineering Doctorate has been carried out under the industrial supervision of the following companies:

- The project started at **Pelamis Wave Power (PWP)**, investigating the use of post-tensioned concrete for the tubes of the Pelamis WEC (June - December 2014).
- Following the closure of PWP, the project moved to **Albatern Ltd**, covering development tasks related to scaling up the Albatern WaveNET array from the 6S system (in sea trials at the time of writing), to the 12S system, alongside work on the applicability of using concrete for certain array elements (January 2015 - February 2017).
- In March 2017, financial difficulties forced Albatern to reassess its priorities, and the company paused development of the 12S array. At this point, the project moved to **Quoceant**, working alongside their ACE-WEC project (Advanced Concrete Materials for Wave Energy Converters), funded by Wave Energy Scotland (WES), investigating the potential for advanced fibre reinforced concretes to offer benefits over conventional materials.

The bulk of this work has been carried out alongside Albatern's internal development projects, therefore uses the Albatern 12S WaveNET array as a case study. However, the time spent at other companies highlights the wider implications of the research, as many of the themes are very relevant to other developers and devices. The parallels between the work at Albatern, and in the wider industry are highlighted throughout this Thesis. An overview of the development

of the Albatern WaveNET array system is provided in Section 1.2 for further background and context.

The work reported in this thesis was carried out in parallel with the Albatern's internal research projects, and as such builds on the efforts of the Albatern design team, which consisted of the following members:

- David Findlay (Albatern CTO)
- Johann Praeffe (Mechanical Engineer)
- Graham Terry (Mechanical Engineer)
- Vivien Mavel (Hydrodynamic Modeller)
- Yan Gunawardena (Operations Manager)
- Hector Fleck (Workshop Manager)
- Alex McMillan (MSc Student)
- Bin Li (Electrical Engineer)
- Ciaran Frost (IDCORE student)
- Calum Kenny (IDCORE student)
- Anthony McDonald (IDCORE student)

Where this research makes direct use of work carried out by these people this is acknowledged as required throughout the text.

1.2 Albatern development progress

Albatern seeks to create a reliable and ultimately marketable wave energy device; the work carried out in this thesis contributes to this aim by ensuring that structural design issues are captured in the WEC development process at an early stage, and minimising capital and operating costs through the use of cost effective materials such as reinforced concrete where appropriate.

The Albatern device is the WaveNET array, made up of interconnected modules called 'Squids', as shown in the schematic in Figure 1.1. Passing waves induce relative motion at each of the joints within the Squid unit, which is converted to electrical power via a hydraulic power take-off system.

Albatern planned to develop WaveNET at different scales, so that each deployed array could be configured to match site conditions and project power requirements. The original development plans are detailed in Table 1.1, which gives the minimum required water depth, maximum design significant wave height (H_s, relating to the 1 in 100 year storm event), and the estimated upper limit of potential array power, dependent on the exact array configuration.

The different device scales are shown in Figure 1.2, with proposed array configurations shown in Figure 1.3 (Albatern, 2017*b*). These figures are based on a simple scaling up of the 6S

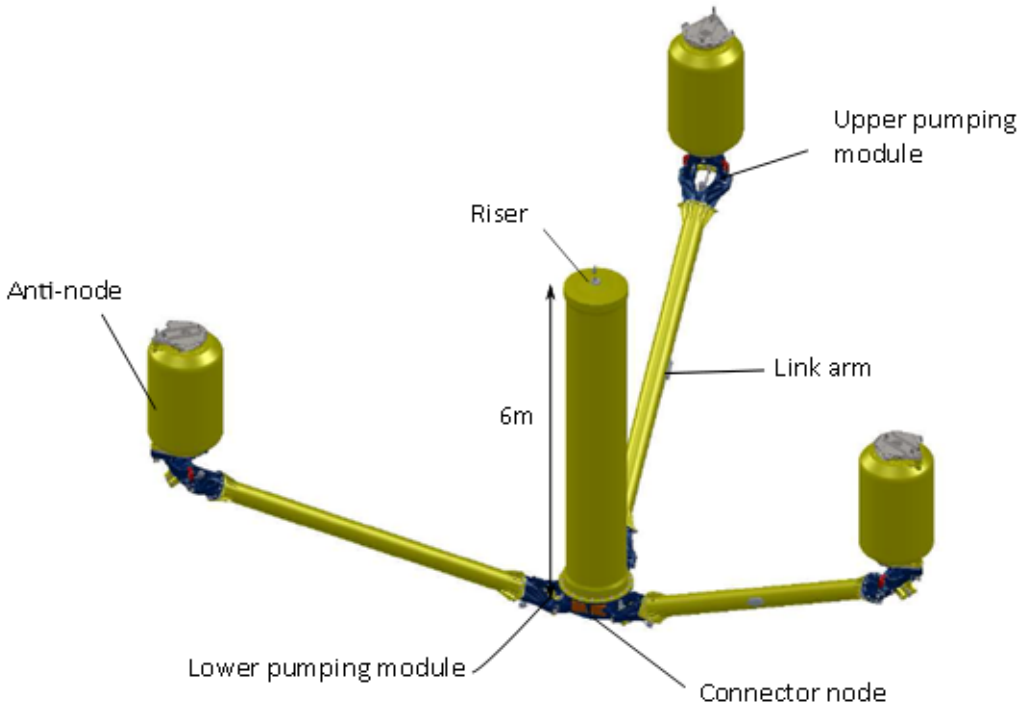

Figure 1.1: 6S Squid module - *Background drawing credit Graham Terry*

concept; however larger devices will have different configurations as discussed in more detail later. The 6S devices have a dual purpose; they have commercial potential in markets such as aquaculture and remote communities, where traditional power generation methods are expensive, while testing and deployment provides useful data for larger grid scale development.

Table 1.1: Albatern planned development stages

Array name	Development stage	Water depth m	H_s m	Potential array power
Series 6 [6S]	In testing	> 20	< 6	up to 150 kW
Series 12 [12S]	In development and the focus of this thesis	> 30	< 14	up to 900 kW
Series 24 [24S]	Potential future development - but not discussed within this report	-	-	up to 100 MW

Albatern has carried out various sea trials with up to six fully built 6S Squid units. Testing of 3 connected devices (a 1-Hex array) was carried out between 2012 and 2014 to demonstrate installation and deployment procedures, and provide proof of concept for the electrical and hydraulic systems. All six modules were connected together into a '3-Hex' array in late 2015 in Kishorn Loch to gather data on power output and device response in a sheltered location. The devices were then moved to Mingary Bay as part of a pre-commercialisation project to

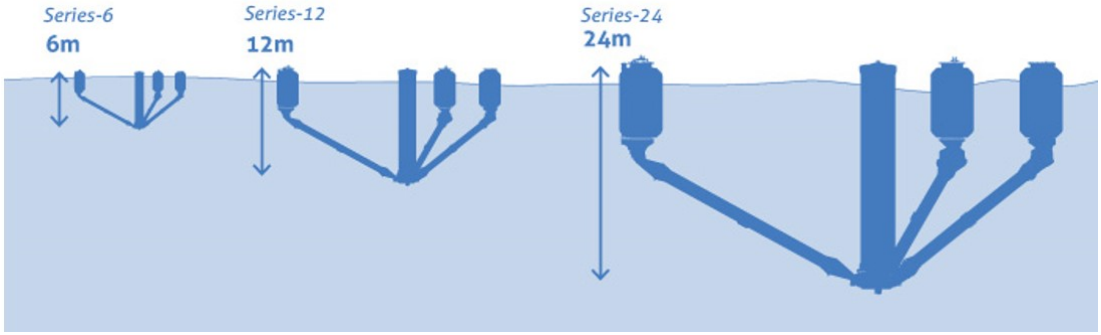

Figure 1.2: WaveNET development scales (Albatern, 2017*b*)

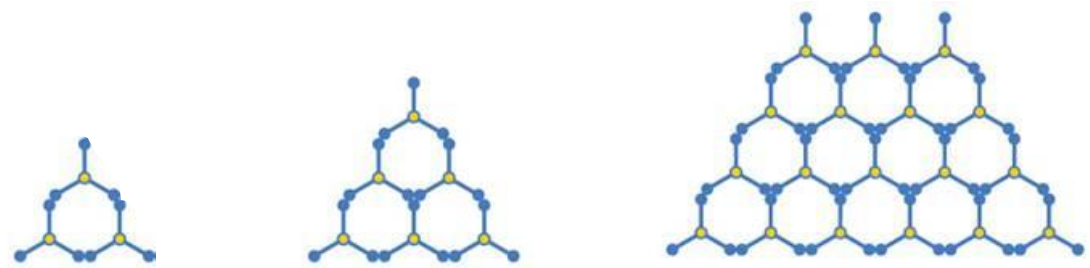

(a) '1-Hex' array (3 no. Squids)

(b) '3-Hex' array (6 no. Squids)

(c) Infinite larger arrays

Figure 1.3: Proposed array configurations (Albatern, 2017*a*)

gather information on performance and behaviour while outputting any generated electricity to the grid. Mingary bay is still a relatively sheltered, limited fetch location (1 in 100 yr H_s of around 2.5 m), but is representative of a typical aquaculture site. Various deployment photos are shown in Figure 1.4.

Alongside the 6S testing, Albatern were also developing the 12S device; this research project has, for the main part, been carried out in parallel with that work. The original intention was to simply double the physical scale of the 6S array, however initial design work highlighted a number of concerns with this which led the company to consider alternatives. These included issues with connection of the individual "Squids" into the larger array (currently the most complex part of the deployment process and only likely to get more difficult at a larger scale), the capability of the power take off (PTO) joint modules to generated the required amount of torque, and the unreasonably large forces generated in the riser and the link arms as the scale increases. Concept development work is the subject of Part II, and the final preferred design option for the 12S array is shown in Figure 1.5. This configuration was the focus of a tank testing programme funded under the Wave Energy Scotland (WES) Novel Wave Energy Converter (NWEC I) competition, discussed further in Chapter 6.

In March 2017 Albatern decided to pause development of the 12S device and focus on commercialising the 6S system. Therefore there are aspects of this concept shown in Figure 1.5 which are not fully finalised; in particular the exact configuration of the PTO system. The

(a) Single squid, lifted with small telehandler

(b) Squid launch from slipway at Mingary

(c) Squids on crane barge for transportation

(d) Aerial view of 3-Hex array at Kishorn

(e) 3-Hex array at Kishorn

Figure 1.4: 6S deployment images - *photo credit, Yan Gunawardena and Calum Kenny*

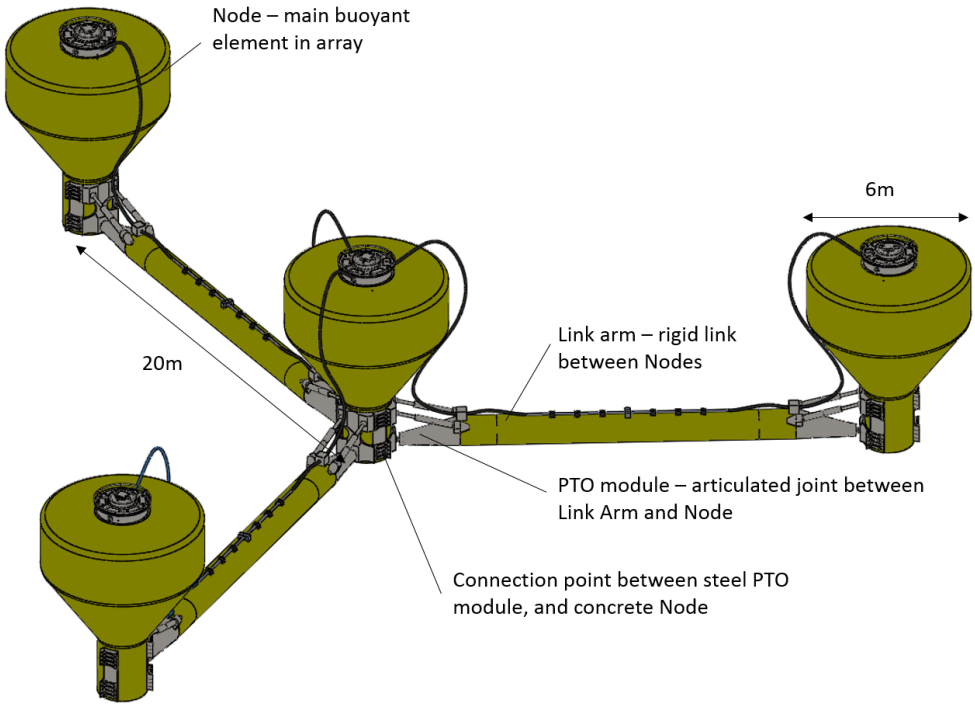

Figure 1.5: 12S current design concept - “Squid” arrangement

development of the PTO is outside the scope of this thesis, and therefore the structural design and development has progressed on the assumption that the layout of this component is as shown in Figure 1.5.

1.3 Thesis structure

This thesis is structured in four parts. Technical content is included in Parts II and III.

Part II covers the concept design process, focussing on the trade off between power production and structural loading to optimise overall LCoE. This part consists of the following chapters:

- Initial concept development work to identify the preferred design configuration of the 12S WaveNET array is covered in Chapter 5, using both power production and structural loading as assessment criteria.
- Structural loads have been evaluated with the aid of physical and numerical models. The process for extracting the relevant load data from these models is discussed in Chapter 6, with particular emphasis on fatigue loading.
- The compromise between power production and structural loading is investigated further in Chapter 7, which investigates the optimum PTO torque limit which gives the lowest overall LCoE.

Part III covers design tasks that focus on the potential use of reinforced concrete materials in order to reduce construction costs. This part consists of the following chapters:

- A techno-feasibility study into different materials for the Node is included in Chapter 9, which highlights reinforced concrete as the preferred option, with good technical qualities when considering low cost construction in the offshore environment.
- A study comparing advanced concrete technologies with more conventional materials is included in Chapter 10.
- The connection between the PTO module and Node is one of the most critical structural elements within the array as it is crucial to the overall device function, and is subject to a unique set of design conditions that are beyond scope of other steel-concrete connection applications. High level design work on this element is included within in Chapter 11

A literature review is presented in **Part I** (following this introduction); this has been split into three chapters covering design issues in Chapter 2, the material selection process in Chapter 3, and steel-concrete connections in Chapter 4.

The outcomes of the whole thesis are brought together in **Part IV**, which includes a discussion of results in the context of the research objectives set out above, draws general conclusions, and sets out further potential work that has been highlighted through the course of the thesis.

1.4 Contributions to knowledge

While the project focusses on the Albatern 12S array system, there are many parallels to other wave energy devices, therefore much of the work carried out for this project is relevant to the wider industry. In particular, the main learning outcomes and contributions are as follows:

- Development of assessment methods to investigate the trade off between structural loading and power production at an early stage in the design process.
  - Structural design choices can have a significant impact on the LCoE, and therefore it is important to consider these early on, when it is possible to influence the decision process, rather than later when it can become prohibitively difficult to make design changes. The assessment tools developed in this thesis could be modified to suit a wide range of devices, and applied as part of the qualification process for novel technology.
- Increased understanding of the structural behaviour of complex multi-body array systems, and methods for modelling such systems to provide relevant load data.
  - Analysis of the physical and numerical models to develop load cases for design provides insights into modelling procedures and the overall behaviour of a novel multi-body array, and could be useful to others looking to develop similar systems.

Particular emphasis is given to fatigue loading, including a comparison of different time and frequency domain fatigue analysis methods.

- Advancement of knowledge regarding application of conventional and advanced concrete materials for wave energy converters
  - While reinforced concrete is commonly used in the marine environment, it has yet to be utilised for a floating wave energy converter. This thesis shows that concrete can be the preferred material for certain structural components, providing good technical properties at a lower cost than conventional materials such as steel. The work also shows that there is a place for the use of more advanced concrete mixes for applications where conventional concretes are not suitable, such as devices with weight and buoyancy restrictions.
- Advancement of knowledge regarding steel-concrete connections for floating wave energy converters.
  - One of the barriers to the use of concrete materials for wave energy converters is the behaviour of the critical connections between concrete structural elements and mechanical steel components such at the PTO system. These connections provide a set of complex design conditions as they need to transmit large, dynamic loads about multiple degrees of freedom. This thesis provides a review of current connection techniques and carries out analysis work to identify the most appropriate connection methods for this purpose.

While the analysis and findings reported in this thesis can be solely contributed to the author, on occasion it builds on work carried out by other members of the Albatern design team. Where this occurs, this is explicitly stated in the text.

Chapter 2

Literature review I: Structural design process

As noted by Tom et al. (2016), while a significant amount of research has been carried out into optimum control of wave energy converters to maximise power absorption, such research often neglects the impact that this has on peak loads and fatigue damage. However the structural components of a WEC account for approximately 30% of the overall Cost of Energy (see De Andres et al., 2017; Low Carbon Innovation Coordination Group, 2012); therefore optimising structural design is an important step on the path to commercialisation.

The research work carried out in Part II investigates the trade off between power absorption and structural loading during the conceptual design phase, at a point where consideration of structural design issues can have the most influence on the overall design process. This chapter of the literature review provides background and context to the work carried out in that section. Section 2.1 provides an overview of currently available research into structural design of WECs, and Section 2.2 provides more details on fatigue design and analysis processes.

2.1 Structural design of wave energy converters

As previously noted, initial research into wave energy focussed predominantly on optimising power production, however this has started to change in recent years, with an increasing emphasis on structural loading issues. Bodies such as Wave Energy Scotland (WES) acknowledge the impact of structural loading on the success of a device, and WES funded projects are required to find a balance between the following key metrics (Arup and Cruz Atcheson Consulting, 2016):

- Affordability: are the capital expenditure and operating costs at an acceptable level?
- Reliability: can the device function throughout the design life, in all expected operational sea states?
- Survivability: can the device survive the most extreme sea states expected during the design life?

- Performance: will the device produce enough power over its lifetime to justify the required expenditure?

Robust structural designs can have a significant impact on all four of these aspects.

One of the issues with encompassing structural design questions at the concept development phase is the lack of available design guidance. The failure to create a solid design basis at the conceptual design stage is noted as one of the barriers to implementing wave energy technologies on a large scale, and 94% of surveyed WEC developers agree that clearer design methodologies are required (Arup and Cruz Atcheson Consulting, 2016).

Structural design is typically carried out to internationally recognised codes of practice such as the DNV GL Offshore standards to ensure that a structure meets a specified target reliability through its design life. WECs however are novel devices which fall outside of the scope of the such codes, which were developed for large static offshore oil and gas infrastructure, with very different characteristics to dynamic WECs. To overcome the issues surrounding a lack of industry specific guidance, a number of documents have been produced by different bodies to provide best practice guidelines for WEC design, including:

- **Guidelines on design and operation of wave energy converters (DNV, 2005)**: This document brings together the recommendations from applicable DNV offshore codes for steel, concrete and composite structures.
- **Generic WEC Systems Breakdown (Hamedni et al., 2014) and Generic WEC Risk ranking and failure mode analysis (Hamedni and Ferreira, 2014)**: These documents were published as part of the Structural Design of Wave Energy Devices project (SDWED) (Aalborg University, 2014) led by Aalborg University between 2010 to 2014. The aim of the project was to develop a common design basis for WECs, with optimised structural processes which can drive down cost, while increasing reliability
- **Structural forces and stresses for wave energy devices (Arup and Cruz Atcheson Consulting, 2016)** This report publishes the results of a Wave Energy Scotland (WES) landscaping study looking at structural forces and stresses for WEC, and provides the most current review of design guidance for the industry

In addition to these documents, the design of novel technology is covered in DNV-RP-A203: Recommended practice for Technology Qualification (DNV, 2013). A systematic qualification process is important in order to identify and manage risks and uncertainties to produce a safe and economical design. The process set out in DNV-RP-A203 is related specifically to wave and tidal energy converters in the Offshore Service Specification DNV-OSS-312 Certification of Tidal and Wave Energy Converters (DNV, 2008), as shown in Figure 2.1.

It is noted that this process includes a phase for selecting Qualification Methods; these are focussed activities designed to reduce some of the risks associated with the design and behaviour of novel technologies. Typical qualification activities include technical analyses,

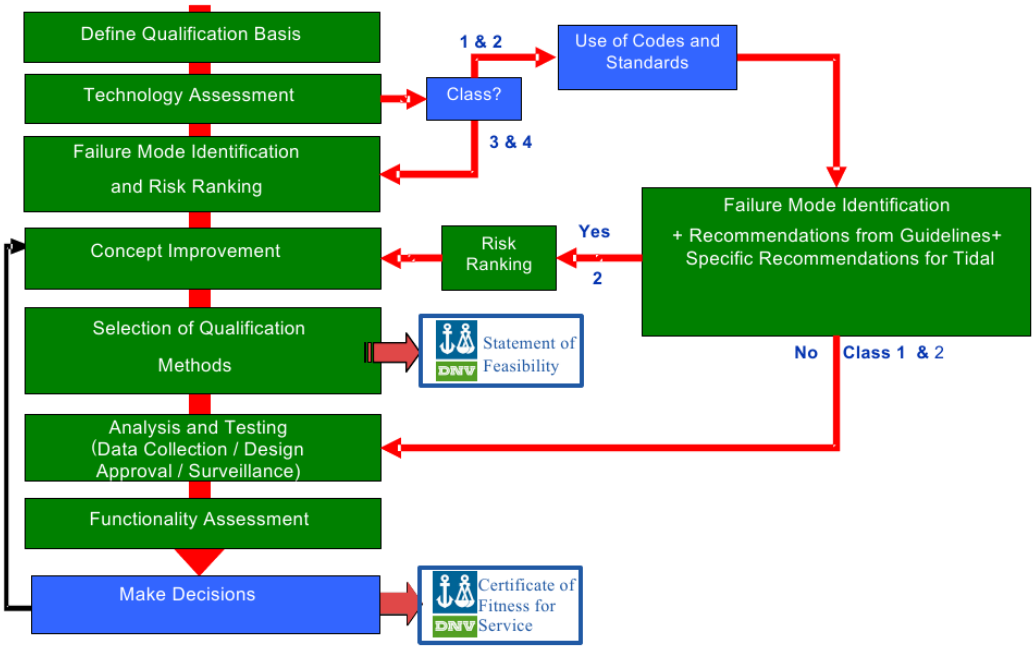

Figure 2.1: Qualification process set out in DNV-OSS-312, Figure 4.2 (DNV, 2008)

component lab testing, and tank testing. For the Albatern 12S device, important qualification activities included physical and numerical modelling of the device; both were carried out during the concept development phase, and are discussed in detail in Chapter 6.

2.2 Fatigue design methods

Fatigue is an important design driver for WECs and as such needs careful consideration when considering the structural reliability. However, fatigue loading is complex, and can be difficult to assess at a conceptual design phase. Section 6.4.3 uses load data from numerical and physical modelling to compare different fatigue analysis methods, with the aim of identifying the most appropriate for the concept design for the 12S device. This section of the literature review discusses typical methods available for fatigue assessment in order to support that work.

In general the design codes follow the linear damage hypothesis for fatigue analysis, meaning that cumulative fatigue damage can be calculated in accordance with the Palmgren-Miner summation as shown below (DNV GL, 2014).

$$D = \sum_{i=1}^{k} \frac{n_i}{N_i} = \frac{1}{a} \sum_{i=1}^{k} n_i (\Delta\sigma_i)^m \leq \eta \tag{2.1}$$

Where:

D = accumulated fatigue damage,
$\Delta\sigma$ = stress range,
k = number of stress blocks,
n_i = number of stress cycles in stress block i
N_i = number of cycles to failure at constant stress range
a = intercept of the S-N curve with the log N axis
m = negative inverse slope of the S-N curve
η = usage factor

Classical fatigue analysis is carried out in the time domain. In this process rainflow counting methods are used to determine n_i based on stress time histories for a location of interest (Schijve, 2001).

While fatigue assessment carried out in the time domain using rainflow cycle counting methods is considered the "gold standard" for estimating fatigue damage from variable amplitude loading (Larsen and Irvine, 2015), this is only possible when there is a full set of stress time history data. This is not always available or easily obtainable, as determining a full set of appropriate stress time histories requires intensive computational effort; in addition the stochastic nature of the combined wave and PTO loads make it impossible to exactly simulate the loading history over the life span of the WEC structure. Therefore it is often more appropriate to apply fatigue methods based in the frequency domain (so called "Spectral Methods"), particularly at the preliminary design stage.

Rapid spectral fatigue analysis methods based in the frequency domain were widely adopted in the 1980's for the offshore oil industry (Halfpenny, 1999), which allow the stress range histogram to be predicted for each sea state included in the wave scatter diagram for a particular deployment site. The resulting stress range histogram can then be used to calculate fatigue damage in accordance with the Palmgrem Miner linear accumulation method in the same manner as the output from a rainflow count.

Spectral methods model the random nature of the loading as a stationary Gaussian stochastic process characterised by a particular probability density function (pdf); and predict the stress cycle histogram based on the properties of the power spectral density (PSD) of the structural response (see for example Halfpenny, 1999; Benasciutti and Tovo, 2006; Herve et al., 2015). The accuracy of the resulting stress histogram is therefore very dependant on the accuracy of the applied pdf.

The original spectral method developed by Bendat (1964) was based on the Rayleigh distribution which is a narrowband approximation; however it is well documented that the narrowband assumption is conservative when the response is more broadband in nature (see for example Zurkinden et al., 2013; Halfpenny, 1999), as is the case with offshore wave loading. To account for this, a number of methods have been developed that give more

accurate predictions for wideband loading, as discussed by Benasciutti and Tovo (2006) and Larsen and Irvine (2015) amongst others. These include the Wirsching-Light correction formula (as used in ABS, 2005), which applies a correction factor to the narrowband solution; the Zhao-Baker method, which assumes that the pdf is a combination of one Weibull and one Rayleigh density (Zhao and Baker, 1992); and the Dirlik formulation, which is an empirically derived pdf (Dirlik, 1985) shown to have good correlation with the rainflow counting method.

Of these, the Dirlik method is possibly the most famous (Benasciutti and Tovo, 2006), and is commonly used for the analysis of for offshore wind turbine structures, (see for example Yeter et al., 2013; Kleineidam et al., 2005; Halfpenny, 1999).

In order to determine the most appropriate method for use during the concept design phase, three different methods for calculating the stress range histogram are used for comparison in the analysis work described in Section 6.4.3. These include:

- Rainflow counting methods using load time histories output from the numerical and physical models (time domain);
- Spectral fatigue using the Rayleigh pdf (frequency domain method for narrowband loading);
- Spectral fatigue using the Dirlik pdf (frequency domain method for wideband loading).

Chapter 3

Literature review II: Material selection

Design work in Part III, (specifically Chapters 9 and 10) investigates material choices for the design of the Node structure within the WaveNET array, specifically focussing on concrete materials. This chapter of the literature review provides background information to support that work. A high level discussion of material issues for marine renewables, and a review of applications of offshore concrete are covered in the Section 3.1. Section 3.2 reviews the behaviour of advanced concrete, to help identify the properties used for design in Chapter 10.

3.1 Materials in the renewable industry

Appropriate material selection plays an important role in ensuring that a safe, reliable and cost effective structural design can be achieved, particularly in the harsh offshore environment.

The need for optimum material selection in the marine renewable industry has been recognised since the development of the first WECs in the late 1970's. Hudson et al. (1980) emphasised the benefit of focussed research effort in this area to reduce WEC development costs, highlighting the main material risks as corrosion, fatigue, marine fouling, impact loading and fracture. Similar themes were discussed by Gooch (2000) in his evaluation of material issues in renewable applications; he also noted that such issues are generally not seen as critical within the industry despite having an influence on efficiency and cost - a sentiment echoed by Salter (2003) who highlighted a lack of specific material investigations in his review of industry wide research requirements.

While it may not always have been a priority, a number of individual developers have acknowledged the need for efficient material selection to reduce costs. For example, Pelamis carried out a materials study in 2003, looking at concrete and glass fibre reinforced plastic (GFRP) as alternatives to steel, (Anderson, 2003), SEEWEC carried out research into the use of filament wound GRP for their point absorber buoys (Paepegem et al., 2011), and the FLOAT project investigated the use of high performance concrete for the Wavestar and DexaWave devices (Hi-Con A/S, 2012, 2016). Materials research has also been brought to the attention of the wider industry through the Wave Energy Scotland (WES) "Structural

materials and manufacturing processes" project programme (Wave Energy Scotland, 2017), funding a wide range of materials research, covering rotational moulded plastics, advanced composites, elastomeric materials and concrete amongst others.

However, while there are a number of different materials that could (and should) be explored further for offshore renewables, the focus of this thesis is the use of reinforced concrete (RC) materials, which can be shown to offer excellent properties at a low cost (see the material selection process in Chapter 9). The next section of the literature review therefore focusses on the use of concrete materials for offshore and renewable applications.

3.1.1 History of concrete in the offshore environment

Concrete has a long history of use in the offshore environment for many different applications, including nearshore and offshore floating and fixed structures. It has excellent durability properties, and there are many examples of concrete structures surviving virtually maintenance free in the ocean for many years.

The first known use of floating concrete was in 1848, when Joseph Louis Lambot built a boat using a sand-cement mortar over a framework of iron bars and mesh (Hoff, 2008). Over half a century later, in 1917, the first self-propelled RC vessel was constructed in Norway, and during the 1st and 2nd World Wars an increased demand for shipping and a shortage of plate steel resulted in the construction of a number of concrete ships. While most modern ships use steel to minimise weight and increase fuel efficiency and speed, concrete vessels have minimal maintenance requirements and have been shown to be very cost effective. For example, a number of barges constructed in the Philippines between 1964 and 1966 were 16% cheaper to fabricate, and 67% cheaper to maintain than similar steel vessels (Sandvik et al., 2004).

Outside of these examples, the primary user of offshore concrete is the oil and gas industry. The Ekofisk Tank was the first major offshore concrete structure to be used for hydrocarbon exploitation, and paved the way for more than 40 such structures around the world. It was installed in the North Sea in 1973, and survived maintenance free until decommissioning began in 2006 (Pérez Fernández and Lamas Pardo, 2013).

One of the critical concerns for offshore concrete structures is corrosion of the internal steel reinforcing bars, but offshore platforms have proved to be very resilient in this regard. A Norwegian study looked at chloride penetration and reinforcement corrosion for six such platforms and found that all were in excellent condition, and at no risk of chloride concentrations reaching critical limits required for corrosion within their lifespan, (Sandvik et al., 2004).

Although the examples discussed in this section show that concrete structures in the offshore environment can survive virtually maintenance free, it should be noted that good workmanship and quality assurance of the manufacturing process are essential. Failures of

concrete structures can be attributed to factors such as improper cover, misplaced reinforcement, improper handling, poor quality concrete, and insufficient concrete compaction (Sandvik et al., 2004). Therefore, the sensitivity of structures to reinforcement corrosion needs to be considered during the design process, and correct quality control procedures are needed during construction, to ensure that concrete structures act effectively throughout their design lives.

3.1.2 Use of concrete in renewable industry

An early adopter of concrete for renewable applications was the wind industry, both on and offshore. As wind turbines get larger, the forces on the foundation and towers increases, resulting in the need for increased structural strength and stiffness. A study into the potential use of concrete turbine towers (Tricklebank et al., 2007) highlights significant advantages of the material including; durability in the marine environment, with low maintenance requirements; improved dynamic properties compared to materials such as steel; and cost competitiveness, especially for volume production of large diameter structures. It also offers design and construction flexibility due to ability to have different material mixes for different situations. Additionally the study stated that concrete has a low environmental impact with lower embodied CO_2 when compared to steel. Concrete towers have been used successfully onshore in Europe, particularly in Germany, and the towers can be constructed using pre-cast sections (see Figure 3.1 (a)), or can be slip-formed on location.

Offshore, the focus is on the use of concrete gravity bases (see Figure 3.1 (b)) due to the previously discussed advantages such as cost-effectiveness, durability in the offshore environment, and good fatigue properties (The Concrete Centre, 2014). With larger turbines, the use of concrete towers could also offer benefits, although increased weight, and difficulties associated with offshore construction makes the benefit less attractive than for their onshore counterparts.

(a) Enercon precast tower sections (ENERCO, 2013)

(b) Offshore gravity base foundations (The Concrete Centre, 2014)

Figure 3.1: Concrete for the wind industry

The advantages of concrete have also been recognised by the wave energy industry, and while the material has not yet been utilized for a floating WEC, it has been considered by a number of developers, including DexaWave (DexaWave, 2013), who considered using concrete for the pontoons of their hinged barge, and Pelamis, who were investigating using post-tensioned concrete for the tubes of their line attenuator device (see Figure 3.2 (b) and Khosravi et al., 2015). In addition, the CREATE project (Arup, 2018), funded as part of the WES Structural Materials and Manufacturing Processes call (Wave Energy Scotland, 2017), aimed to confirm that the use of concrete technologies could make a step change in LCoE in the wave energy sector.

(a) DexaWave schematic of full scale device (DexaWave, 2013)

(b) Pelamis P2 prototype testing at EMEC *photo credit: Pelamis*

Figure 3.2: Floating wave energy converters

The actual use of concrete within the wave industry has to date been restricted to fixed bottom, shore-line converters such as the Limpet Oscillating Water Column (OWC) as shown in Figure 3.3. The physical scale of these types of devices make concrete the ideal choice of material, as it can be used economically in mass volumes to construct large robust structures to house the energy generating turbines.

Figure 3.3: Limpet WEC on Islay (Fernandes, 2013)

3.1.3 Novel concrete concepts

Looking beyond conventional RC, there are also a number of applications where more advanced concrete materials have been investigated. For example the GICON-TLP (a tension leg platform substructure for a 6MW offshore wind turbine) utilises fibre reinforced lightweight concrete in order to meet the stringent weight requirements of the foundation. Adam et al. (2016) state that the material used for this structure must be durable in the harsh environmental condition, and be able to resist the cyclic and dynamic loads; very similar requirements to floating wave energy converters. The inclusion of fibres within the light weight concrete mix increases the flexural tensile and compressive strength of the materials.

In the wave energy industry, the ForskEL FLOAT research and development programme has funded research into the possible use of Ultra High Performance Fibre Reinforced Concrete (UHPC) for the DexaWave pontoons and Wavestar floats (Hi-Con A/S, 2012, 2016). The Wavestar device consists of a number of semi-submerged floats attached to a fixed structure, currently manufacture from GFRP. The device generates energy from the motion of the floats as they raise and lower with the passing waves. The DexaWave device consists of two rigid pontoons connected together with a single hinge.

The research was conducted in conjunction with the pre-cast manufacture Hi-Con, who are one of the leading producers of the concrete product CRC (Compact Reinforced Composite); a type of UHPFRC using a 2.5% volume fraction of short (13 mm), stiff and strong steel fibres, combined with high strength concrete (150-400MPa), to create a material with bending strengths in excess of 20MPa (Hi-Con A/S, 2016). This was used to design the Wavestar floats and allowed for thin wall sections (≤ 50 mm) to be constructed without conventional reinforcement, to meet the specified weight restrictions. This is a particular issue for the Wavestar machine, which relies on the ability to lift the floats clear of the water to ensure survivability in storm conditions, meaning conventional concrete sections could not be utilised in this case.

Wavestar prototypes were originally manufactured from glass fibre composites, but the FLOAT project showed that CRC concrete would be significantly cheaper, with a potential saving up to 77% per float compared to the GFRP option. These were very complex to manufacture which was a major issue for volume production and overall (Morton Kramer and Frigaard, 2011). They also experienced durability issues, with float damage occurring on the half scale device in 2010, and it was hoped that the use of CRC would overcome these types of problems. A single CRC float was installed on the $1/10^{th}$ scale prototype at Nissum Bredning in 2007 (see Figure 3.4), where it has been operating successfully ever since (Hi-Con A/S, 2012).

Although CRC has potential for use on the Wavestar device, the study concluded that it would not be appropriate for use on the DexaWave as it is not economical compared to conventional

(a) Damaged CFRP float on 1/2 scale prototype (Morton Kramer and Frigaard, 2011)

(b) CRC float on 1/10 scale prototype (Hi-Con A/S, 2012)

Figure 3.4: Wavestar wave energy converter

concrete. These examples show that while UHPFRC materials appear to be well suited for use in the offshore environment, and in particular to resist dynamic loads associated with floating WECs, they may only prove to be economical when there are particular constraints such as weight or buoyancy requirements. If it is possible to make a conventional concrete design work, then it is likely that this would be the more cost-effective solution.

3.2 Advanced concrete materials

The previous section carried out a review of the application of concrete materials to offshore renewable energy devices, including advanced concrete mixes, and the study carried out in Chapter 10 investigates the potential benefits of these more advanced materials. This section reviews the literature available on this topic to support that work. A summary of alternative materials for internal reinforcing bars (rebar) is included in Section 3.2.1, a brief discussion of the application of external fabric reinforcement is included in Section 3.2.2, and an in-depth review of fibre reinforced concrete is given in Section 3.2.3, covering typical material properties, and suitable methods of deriving design values, together with a summary of applicable design codes.

3.2.1 Alternative materials for reinforcement bars

The predominant cause of structural deterioration in conventional RC is corrosion of the steel rebar, which is a particular risk in the offshore structures. While corrosion is preventable by selecting the correct concrete mix, using appropriate cover to the reinforcement, and ensuring good quality control during construction, in certain circumstances it is advantageous to use non-corrosive reinforcing materials to improve structural durability.

The use of non-corrosive alternatives is relatively common, particularly in the USA where coated and stainless steel rebar are used for bridge construction (Walsh and Henderson, 2016). The practice is less evident in Europe, but is recognised as providing benefits over conventional reinforcing materials (Markeset et al., 2006).

Conventional steel rebar embedded in good quality concrete will not corrode, due to the formation of a protective iron-oxide film which, combined with the alkaline conditions of the surrounding concrete creates a passive environment. Corrosion occurs when the ingress of chlorides and carbonation into the protective concrete breaks down this passive coating. These processes occur over time, and depend on the nature of the surrounding environment (as well as the exact concrete mix); for example high temperatures and relative humidity increases chloride diffusion rates, leading to increased corrosion damage (Walsh and Henderson, 2016). Therefore non-corrosive reinforcing materials offer the most advantage for structures with a long service life, and in harsh environmental conditions such as bridges. In these circumstances there are significant life-cycle cost benefits associated with lower maintenance and repair requirements, which offset the increased capital costs of the materials.

The typical design life of most wave energy devices is 20 years; considerably lower than bridge structures where specified service lives are in excess of 100 years. Therefore there are unlikely to be cost advantages to using alternative rebar materials for WEC structures. Markeset et al. (2006) states that for environments with moderate temperature and relative humidities, with low design service life (10-30 years), carbon steels are most appropriate, and therefore alternative rebar materials for internal reinforcement are not considered further in this thesis.

3.2.2 External wraps and fabrics

Composite materials such as fibre reinforced plastics (FRP) are emerging as effective and reliable materials for repair, strengthening and retrofitting of existing structures and as such are the subject of a significant amount of academic research, some of which has been encapsulated in standard design codes and recommendations (Arya et al., 2002). There is very little evidence of this type of reinforcement being used for the construction of new structures, but there is the potential for utilising the technique to reduce the internal reinforcement requirements. While it is unlikely to be cost effective to use this as a global reinforcement

solution, there may be potential for localised strengthening applications, or as stay-in-place formwork, as has been used in marine piles for many years. Fam et al. (2003) describe a number of applications for CFPR tubes filled with concrete for marine applications, and list the advantages as being non-corrosive, eliminating the need for internal rebar, and cost reductions associated with combining reinforcement and formwork.

One of the concerns with this type of system is the durability of epoxy bond in the marine environment, which is raised by a number of authors (e.g. Newlands et al., 2018; Frigione and Lettieri, 2018) . One of the issues is lack of evidence of use of such materials in these conditions; however tests carried out by Long et al. (2012) on the bond between CFRP and concrete in the tidal environment show an early reduction of shear strength on specimens compared to those applied in the dry. This would be an aspect that would need careful consideration if using external wraps as strengthening for wave energy converters.

3.2.3 Fibre reinforced concrete

The set of advanced materials that appear to offer the most potential advantages over conventional RC are Fibre Reinforced Concretes (FRC). These materials include discrete fibres within the concrete mix to improve the material behaviour, particularly in the post-cracking phase under tensile loads. FRC has increased ductility compared to conventional concrete due to the capacity of the fibres to bridge crack faces.

FRCs have been in development for a number of years, with the first studies published in the 1960s (Romualdi and Batson, 1963). They are primarily used for non-structural purposes, with fibres added to improve early age properties and reduce cracking due to plastic or drying shrinkage; however it is becoming more and more common to use the material for structural applications (Mindess, 2007). As well as improved durability and strength properties compared to plain concrete, the use of fibres also offers advantages in construction time and cost when the requirement for internal reinforcing bars is reduced or eliminated.

There is a vast body of research on the material properties of FRCs, which is reviewed in a number of references, (e.g. Naaman, 2008; Eide and Hisdal, 2012; Buttignol et al., 2017; Newlands and Jones, 2017). A majority of the commercial development mixes use carbon steel fibres. In recent years there has been an increased focus on alternative fibre materials such as basalt, glass and carbon fibres (Wang et al., 2017) with enhanced strength and durability properties; however these materials are much more costly than steel fibres, and the behaviour is less studied, and therefore they are not considered further in this thesis. Much of the discussion would however be relevant to these materials, and there would be scope for carrying out further investigations if FRC is shown to have a significant advantage over conventional RC for the manufacture of wave energy structures.

(a) Mechanical properties overview

There are many factors which influence the behaviour of FRC, including (amongst others) fibre type, shape, length, and aspect ratio, as well as the exact nature of the underlying concrete mix. Buttignol et al. (2017) note that the optimum mix design would give a material with tensile strain hardening behaviour, low permeability, high tensile and compressive strength and self-compacting properties, however it is very difficult to fulfil all of these conditions in a single mix.

FRCs are characterised by their post-cracking tensile behaviour, and can be described as either "strain-softening", where the residual tensile strength decreases after the first crack appears, or "strain-hardening" where residual strength increases in the post-crack phase.

The literature describes many different types of FRC however there does not appear to be a common naming convention. For the purpose of this thesis, three different classes have been defined; steel fibre reinforced concrete (SFRC); strain hardening cement composites SHCC; and ultra-high performance fibre reinforced concrete (UHPFRC). The properties of each are summarised in Table 3.1, together with the typical fibre volume fraction (v_f) (as a % of overall concrete volume).

Table 3.1: Classifications of fibre reinforced concrete mixes

Type	v_f	Description
SFRC	$\leq 2\%$	Mix characterised by post-cracking strain softening behaviour, with peak tensile strengths the same as plain concrete. Typical compressive strengths ≤ 50 MPa.
SHCC	1.5 - 2.5%	Mix characterised by post-cracking strain hardening behaviour, with moderate residual tensile strengths up to 2x that of normal strength concrete. Peak strength achieved at large strains (4-5%). Typical compressive strengths 50 - 100 MPa
UHPFRC	up to 5%	Mix characterised by immediate post-cracking strain hardening behaviour, with high residual tensile strengths up to 10x that of normal strength concrete. Peak strength achieved at small strains (0.5-1%). Typical compressive strengths $\geq$ 100MPa.

(i) Compressive strength

The inclusion of fibres at low volumes ($\leq 1\%$) only has an effect on the cracked behaviour of concrete, and therefore the compressive strength of normal strength concrete remains virtually unchanged (di Prisco et al., 2013). High performance concretes (UHPCs) use fine aggregates with a low water-cement ratio to create a very hard mix, with increased compressive strength. Plain UHPCs are very brittle, with explosive compressive failure mechanisms (Eide and Hisdal, 2012), therefore fibres are often included to increases the ductility, as they have a restraining and confining effect, which also increases the compressive strength of the

concrete. Various experimental studies show that compressive strength increases with increasing fibre volume (see Yu et al., 2014; Eldin et al., 2014).

(ii) Tensile behaviour

The addition of fibres has the greatest impact on the post-cracking tensile strength of concrete. Plain concrete is a brittle material, with good compressive properties, but very low tensile strength (≤ 4 MPa). Conventional concrete design makes use of internal steel reinforcement bars to resist the tension forces once the concrete has cracked. The use of fibres can provide an alternative to these steel bars, and (depending on the exact material properties) can reduce, or even eliminate the need for internal reinforcement.

The exact post-cracking tensile behaviour of FRC is dependent on a large number of factors, and material properties for design are typically determined on a case-by-case basis. Most currently available commercial FRC mixes use low fibre dosages which result in strain softening behaviour; they do not increase the flexural strength of the material, but do improve toughness and ductility. Typical post-cracking behaviour for a range strain softening cement mixes (SFRCs) are shown in Figure 3.5.

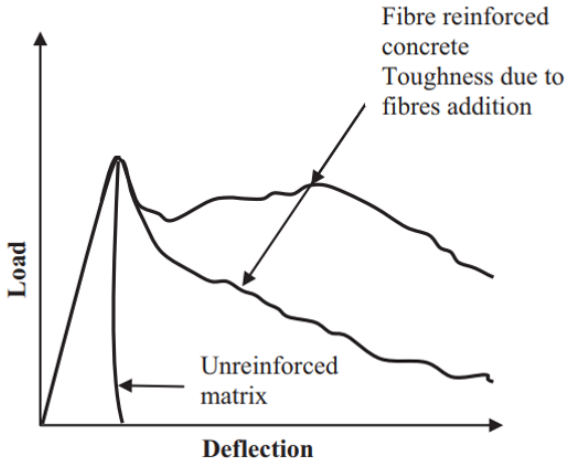

Figure 3.5: Typical load deflection curves for strain softening SFRCs (ACI, 1996)

Strain-hardening materials are characterised by an increase in tensile strength after initial cracks occur; with the formation of multiple "micro-cracks" up to the peak strength of the concrete. These types of mixes are often classified as high-performance composite materials due to the increased peak tensile strength (Naaman, 2008). Experimental studies show that it is possible obtain UHPFRC mixes with flexural tensile strengths in excess of 20MPa (e.g. Yu et al., 2014; Eldin et al., 2014). However, while UHPFRCs technically exhibit strain hardening behaviour immediately after initial cracks occur, peak strengths are reached at low strains (less than 1% depending on the exact mix properties, see Pyo, 2014, López et al., 2015, and Park et al., 2012). After the peak strength is exceeded, crack localisation occurs, and the

residual strength of the material drops off as the strain increases. In comparison, mixes that exhibit lower tensile strengths can reach peak strength at much higher (4-5%). This longer period of continuous strain hardening leads to the classification of Strain Hardening Cement Composites (SHCC), although other names such as High Performance Fibre Reinforced Concretes (HPFRC), or Engineered Cement Composites (ECC) are also found in the literature. The difference between the behaviour of UHPFRC and SHCC mixes are shown in Figure 3.6, which shows the uniaxial tensile behaviour for different classes of concrete. van Zijl and Boshoff (2008) suggest that this strain-hardening type of behaviour can be achieved with moderate fibre volumes of between 1.5-2.5%.

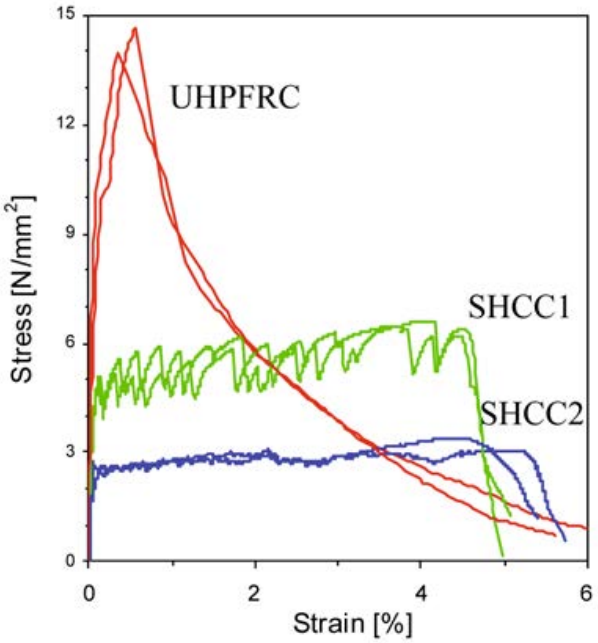

Figure 3.6: Uniaxial tensile behaviour of classes of fibre reinforced concrete (van Zijl and Boshoff, 2008)

The experimental evidence shows that when all other factors are kept the same, peak tensile strengths increase with increasing fibre volume fractions (see Kang et al., 2010; Eldin et al., 2014) however volume fraction is only one of a number of factors that affect the tensile strength. Fibre length and aspect ratio (length / diameter) also have an impact, with tensile strengths increasing with greater values of each of these factors (see Yazıcı et al., 2007; Thomas and Ramaswamy, 2007). There is also an increasing amount of research into mixes with combinations of fibres, as a combination of short, fine fibres (which activate when micro-cracks occur) and longer fibres (which activate when macro-cracks form) can improve flexural and fatigue behaviour when compared with a single fibre type mix (Walraven, 2009).

As a final point, most literature shows that the flexural bending strength of FRC materials is greater than the uniaxial tensile strength (which is usually the parameter used in design).

(iii) Crack control, durability and permeability

Providing adequate crack control is one of the driving criteria in the design of concrete structures. While RC materials are designed to crack in tension to utilise the composite properties of the concrete matrix and the steel reinforcement, the development of cracks is the main cause of steel bar corrosion. In addition, the development of through thickness cracks can lead to leakage, which causes problems in watertight structures such as floating WECs.

One of the major advantages of fibre reinforced concrete is the improved cracking behaviour across all types of FRC mixes. As steel fibres transfer tensile stresses across cracks, this leads to a reduction in crack widths when compared to plain or conventionally reinforced concrete. In addition, for SHCC materials, strain hardening behaviour is characterized by the formation of micro-cracks before crack localisation (Figure 3.7), keeping material permeability low, even at the post-cracking phase (Buttignol et al., 2017). Increasing strain results in an increase in the number of cracks, while the width of an individual crack remains the same throughout the strain hardening phase.

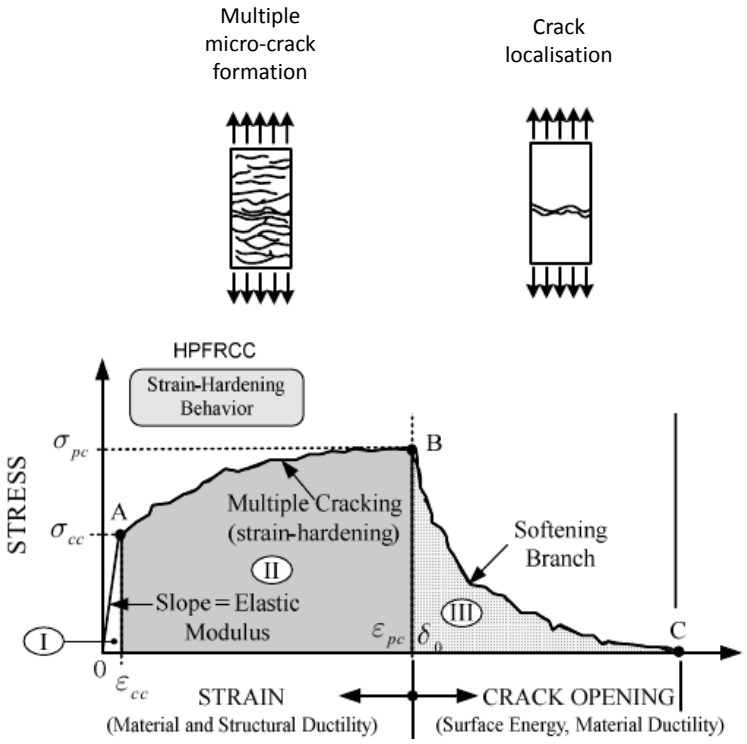

Figure 3.7: Micro cracking and crack localisation in SHCC (Naaman, 2008)

The permeability of SHCCs and other cementitious materials has been investigated by a number of authors (see Lepech and Li, 2009; Aldea et al., 1999) with the general conclusion being that provided the widths of micro-cracks remain below a critical value (approx 60μm) then the permeability of the cracked material does not significantly increase compared to the

uncracked material (van Zijl, 2011). This remains true up to the point of crack localisation, which can occur between 2 to 5% strain or even higher. While UHPFRC materials also exhibit strain hardening behaviour immediately following initial cracking, peak tensile strengths are achieved at low strain levels, after which crack localisation occurs. To ensure adequately low permeability in UHPFRC structures is it recommended that strain levels are kept below 0.15% (Charron et al., 2007).

The benefits of using SHCC as a method of seepage control has been recognised by various authors for structures such as tunnels (Maidl and Dietrich, 1992), dams (Liu et al., 2016), and buildings (Yu et al., 2017), either on its own, or used as a waterproofing layer. There is limited research relating to the use of SHCC for watertight offshore structures, but low permeability in the cracked state is a particularly useful property and could provide significant benefits for floating wave energy converters as well as other offshore structures.

It is noted that the type of structures mentioned above are not typically subject to dynamic loadings. Indeed Denarié and Bruhwiler (2011) note that while the permeability of concrete decreases with decreasing crack width, finer micro-cracks lead to higher capillary absorption, which can be amplified under cyclic loading. While capillary absorption can increase the potential for corrosion of internal reinforcement, this is less of an issue for FRC structures than for conventional RC. While internal fibres can corrode, the corrosion product deposited around the fibre is not sufficient to build up enough pressure to cause spalling of the concrete (Eide and Hisdal, 2012), therefore corrosion of individual fibres does not significantly affect the overall strength. The contribution of capillary absorption on through section seepage and leakage in watertight structures is less certain, however Denarié and Bruhwiler (2011) notes that the inclusion of a water repellent additive in the fresh concrete mix reduces capillary action in micro-cracked SHCC, indicating that there are solutions to the problem. Therefore the use of SHCC in watertight dynamic structures is an area which warrants further research.

In addition to the inherent crack control associated with the formation of micro-cracks, high performance FRCs also exhibit self-healing behaviour. While this occurs in all cementitious materials, it is particularly evident in high performance concretes with low water-cement ratios. This results in a large portion of un-hydrated cement particles after initial curing, which are then available for hydration when water permeates into the structural cracks (Buttignol et al., 2017). The limiting crack width for self healing is reported as being between 30μm (Hover et al., 2015) and 100μm (Ma et al., 2014), which is in the range of the micro-crack width opening in SHCC, therefore this phenomenon could also prove beneficial for WECs manufactured using such a material. There are questions regarding the applicability of this behaviour to cylic loading, as the self-healing capabilities will naturally decrease over time as cement particles are hydrated in ongoing loading cycles. It may be that this behaviour is only beneficial for cracks formed under infrequent ULS loads.

(iv) Fatigue

An increasing use of FRCs has led to an increase in the study in the fatigue behaviour, particularly as many of the common uses of FRCs (e.g. bridge decks and industrial floors) are subject to cyclic loads. However, there is a great variety in the fatigue behaviour for different mixes and Lee and Barr (2004) note that there are many gaps in knowledge, due to the complexities in testing, and the many different influencing factors.

Despite this, there is general agreement that FRC has better fatigue behaviour than plain concrete under tensile and flexural loading where the action of fibre bridging and pull-out dissipates energy in the wake of the crack tip, inhibiting crack growth (Lee and Barr, 2004). The relationship between stress ranges and number of cycles to failure depends primarily on the fibre volume, with increasing volumes appearing to increase the fatigue life (Johnston and Zemp, 1991). While fibres appear to improve the behaviour under flexural loading, the same is not the case for compressive loading, where the addition of fibres could potentially have a negative effect. Fibre crack bridging does not provide a benefit for compressive loads, and it possible that the inclusion of fibres results in more flaws in the structural member. Figure 3.8 shows a set of S-N curves derived from the results of a number of experimental studies (Lee and Barr, 2004); Figure (a) shows the results for compression loading tests where there is very little difference between the different mixes, and Figure (b) shows the results of the flexural tests, where the beneficial effects of the inclusion of the fibres can be clearly seen.

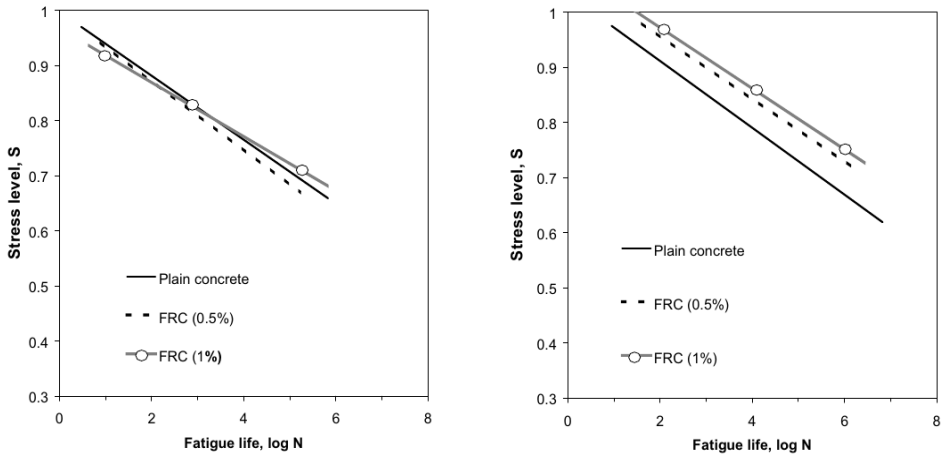

(a) S-N curves compressive loading (b) S-N curves flexural loading

Figure 3.8: Comparison of S-N curves for plain and FR concrete (Lee and Barr, 2004)

Despite the uncertainties and difference shown in the body of research available on the topic, there is generally a common consensus that the inclusion of fibres acts to improve the flexural fatigue behaviour of concrete materials, or at least does not make it worse, and this is a valid conclusion that can be taken forward to the design stage of this report.

(v) Workability and manufacture

Fibres decrease the workability of concrete, and this initially limited the development of UHPFRC (Walraven, 2009). However the implementation of super-plasticisers, water-reducing admixtures and fillers improve the behaviour, allowing the development of high strength mixes with increasing fibre volume fractions (see di Prisco et al., 2013; Yu et al., 2014). DNV (2012) recommends a maximum v_f of much of 2%, however the literature emphasises the importance of aspect ratio as well as volume fraction on workability, and give limits on fibre factor ($x_f = V_f.l_f/d_f$) rather than volume fraction. Buttignol et al. (2017) suggests an upper bound fibre factor limit of 2.5, which gives a much greater scope for increased volume fractions with an appropriate aspect ratio, and there are published results of experimental studies on UHPFRC mixes with volume fractions up to 5% without any adverse effects on workability (Kang et al., 2010).

(b) Design methods and standards

There are a lack of international design standards relating to the use of fibre reinforced concretes, particularly UHPRFRC, and this a significant barrier to the use of the material in structural situations (see Buttignol et al., 2017; Pilakoutas et al., 2009). This section provides a review of two of the codes that do exist and discusses their applicability to floating WECs.

(i) DNVGL-ST-C502 Offshore Concrete Structures (DNV GL, 2018)

This code covers the design of offshore concrete structures, and predominantly deals with conventional concrete mixes up to a compressive strength of 90MPa. However it does allow for the inclusion of fibres, in combination with conventional rebar. The code provides a method of estimating a tensile strength value (f_{tk}) based on the fibre volume fraction (v_f) and the characteristic compressive strength of the concrete (f_{cck}) (see Equation 3.1) which can be used for ULS calculations. However SLS checks are to be carried out using the design values for plain concrete.

$$f_{tk} = (0.48 + 0.1v_f)\sqrt{f_{cck}} \tag{3.1}$$

There is no reference to members without internal rebar, and the standard only covers concrete material properties up to 90MPa and volume fractions up to 2%, therefore does not adequately cover UHPFRC.

(ii) *fib* Model Code for Concrete Structures 2010 (fib, 2013)

The *fib* Model code differs from existing operational codes (which are legal documents based on mature industry knowledge), as it aims to encompass new developments in concrete structures and materials with the same level of safety and serviceability as more established technology. While it is not directly applicable to offshore structures, it follows the same design philosophy as both the Eurocodes and the DNV offshore codes, therefore its design methods are considered to be appropriate for design of floating WECs.

This document provides a detailed discussion of design methods for FRCs covering all types of mix. It specifies that material properties should be determined by a standard notched beam bending test in accordance with EN 14651, which gives the values of residual flexural strengths for different crack mouth opening displacements (CMOD) as shown in 3.2.

Table 3.2: Flexural strength outputs from standard bending test

ID	CMOD (mm)	stress	Comment
L	0	f_L	Limit of proportionality (first crack)
1	0.5	f_{R1}	SLS residual strength
2	1.5	f_{R2}	
3	2.5	f_{R3}	ULS residual strength
4	3.5	f_{R4}	

These values can then be used to derive uniaxial tensile properties using the simplified equations included below. The residual tensile strengths can be used for both SLS and ULS analysis, unlike the DNV code, which does not allow for an increase in strength at SLS.

Residual tensile strength (SLS) $f_{Fts} = 0.45 f_{R1}$

Residual tensile strength (ULS) $f_{Ftu} = f_{Fts} - \frac{w_u}{CMOD_3}(f_{Fts} - 0.5 f_{R3} + 0.2 f_{R1} \geq 0)$

The code also provides material constitutive laws (as shown in Figures 3.9 (SLS) and 3.10 (ULS)) relating stress (σ) and strain (ε), allowing moment and axial forces to be calculated for section design, in the same manner as for conventional RC.

These figures cover both strain hardening and strain softening materials; however it is assumed either the material reaches a peak strength at the SLS residual strength value and then reduces, (for strain softening materials with an initially increased peak strength) or that the residual strength continues to increase up to ULS value (for strain hardening materials). While these relationships cover standard SFRC and SHCC materials, they do not capture the behaviour of UHPFRC which reaches a peak strength above the SLS strength. Therefore some modifications to these laws would need to be made in order to proceed with a UHPFRC design.

The code can be used for sections both with and without additional conventional reinforcement. While the design methods presented in the code allow for any FRC mix to be used, the rules are developed on the experience of standard SFRC with predominantly strain softening behaviour and it is noted that additional rules may apply for UHPFRC materials.

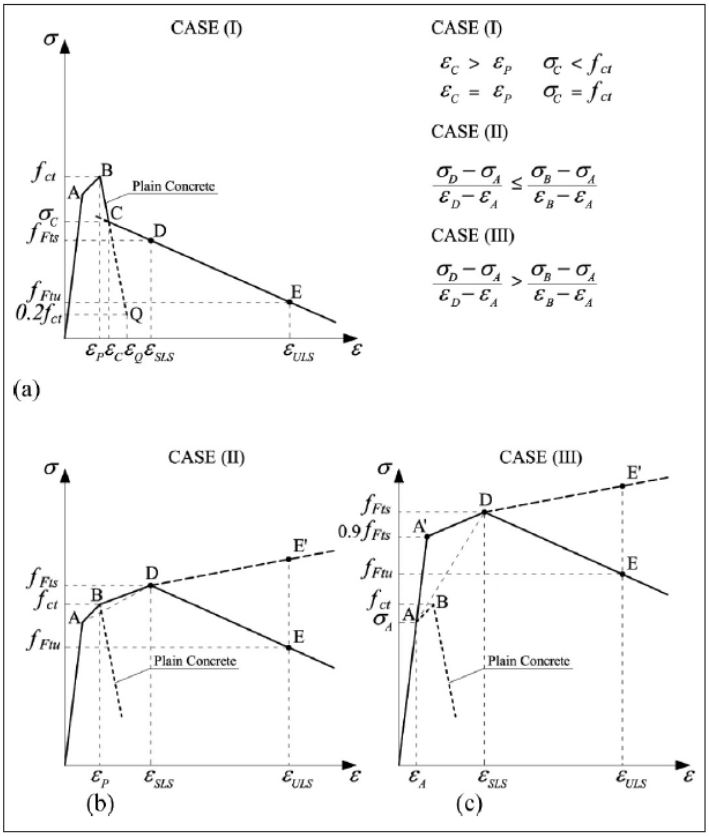

Figure 3.9: Stress-strain relations at SLS for softening (a) and softening or hardening (b,c) behaviour of FRC (fib, 2013)

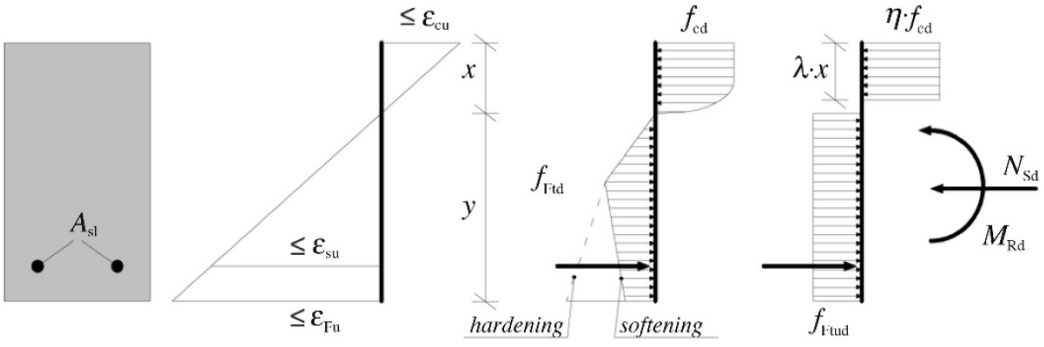

Figure 3.10: Simplified stress-strain relationships for ULS design (fib, 2013)

(c) Material property derivation

The difficulty in estimating a characteristic tensile property of an FRC material is one of the obstacles holding back implementation of SFRC as a structural material (de Montaignac et al., 2012). While there are a number of standard test methods to determine the relevant strength

properties for a specific mix, for initial design it is more useful to be able to use preliminary properties that can be easily altered during an ongoing design development process.

This is recognised by a number of authors, who have attempted to derive theoretical relationships from experimental results, (e.g. Kang et al., 2010; Yazıcı et al., 2007; Eldin et al., 2014). However the empirical equations that are presented in these papers are only valid within the limits of the experimental data used for the regression analysis. This is shown in Table B.1 included in Appendix B which summarises some of the strength parameters presented in the literature (taken from Yazıcı et al., 2007; Thomas and Ramaswamy, 2007; Bencardino, 2013; Eldin et al., 2014; Yu et al., 2014; Kang et al., 2010), alongside values calculated using some of the suggested empirical equations.

Theoretical equations for the tensile behaviour of strain hardening FRC materials are also presented by Naaman (2008), who proposes the idealised relationship shown in Figure 3.11.

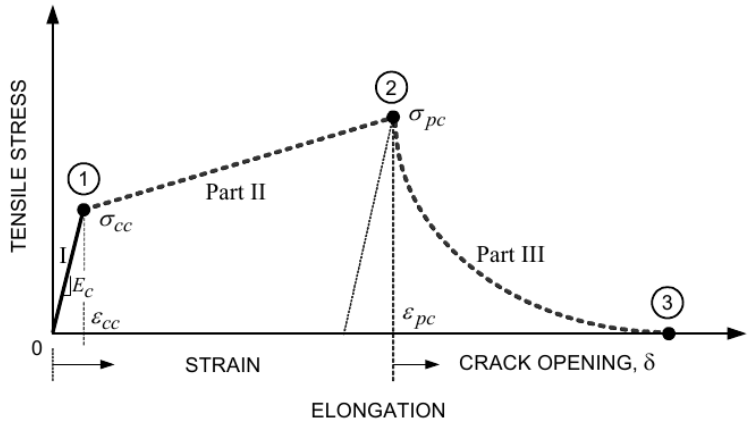

Figure 3.11: Idealised stress-elongation response in tension of a strain-hardening FRC composite for modelling

These equations attempt to encompass all potential design situations, however only reinforce how difficult it is to predict the behaviour of an FRC material using theoretical relationships, due to the number of factors which have to be included. For example the equation for deriving the peak strength is given in Equation 3.2.

$$\sigma_{pc} = \lambda \tau \frac{L}{d} V_f \tag{3.2}$$

Which appears simple enough; however λ is the product of several coefficients:

$$\lambda = \lambda_1 \lambda_2 \lambda_3 \lambda_5 \qquad \lambda_2 = 4\alpha_2 \lambda_4 \tag{3.3}$$

which cover factors ranging from the embedded length of the fibres from the face of the crack, the orientation of the fibres, grouping effect of fibres, and reduction factors due to the fibre

alignment, amongst others (for further details see Naaman, 2008). For this reason, any design work carried out using theoretically derived mechanical properties, should always be backed up with appropriate material testing during the detailed design phase.

3.3 Summary

This chapter has reviewed material selection choices for floating WECs, with particular emphasis on conventional and advanced reinforced concrete mixes, highlighting the advantages of using such materials in the offshore environment.

A review of mechanical properties of FRC materials has highlighted the great variation in available mixes, and the difficulties with predicting theoretical properties for design, indicating that material is a necessity to derive properties for detailed design. However, there are number of empirical relationships that have been derived in the literature that can be used for preliminary design work. In particular, the analysis work carried out in Chapter 10 will make use of the following findings:

- Two different mixes will be considered: UHPFRC with high peak tensile strength ($\approx$ 10x conventional RC) at low strain, and SHCC with medium residual tensile strength ($\approx$ 2x conventional RC) at higher strain (4-5%).
- Theoretical values of peak strengths will be calculated using equation given by Thomas and Ramaswamy (2007), which was based on FRC materials with base compressive strength between 35 MPa and 85 MPa. While this equation is only truly valid within these limits, it under-predicts peak strengths for higher strength concrete, and therefore is acceptable for preliminary design. Other points on the strength curve will be derived using information Bencardino (2013), and Naaman (2008).
- Constitutive stress-strain relationships for design will be based on information given in the Model Code (fib, 2013).
- SHCC materials have been shown to have improved permeability characteristics compared to conventional RC in structures such as dams and tunnels. This thesis assumes that this is also applicable to dynamic offshore structures.
- While there are questions regarding fatigue behaviour of FRC, in general is appears that this is improved compared to conventional RC. The assumption of this thesis is that this is indeed the case.

In addition to FRC materials, the benefits of using external wraps as a replacement for internal reinforcement will also be considered.

Chapter 4

Literature review III: Steel-Concrete Connections

Design work in Chapter 11 investigates connections between concrete and steel components in floating WECs. This chapter provides background information to support that work. Section 4.1 provides an overview of current connection methods, and discusses their applicability to floating WECs. Section 4.2 summarises the different constitutive models for concrete, and published methods for carrying out fatigue analysis, which provides the background for the connection analysis methods developed in Chapter 11.

4.1 Concrete steel joints

The materials landscaping study carried out by Wave Energy Scotland (2016*a*) highlights the long term durability of connections between steel and concrete components in WECs as an area of risk associated with the adoption of concrete materials in the industry. These connections are often critical to the function of the device, requiring the transmission of large, dynamic loads about multiple axes of freedom while remaining watertight, as noted by Khosravi et al. (2015), who considered the use of concrete for the primary construction material for the Pelamis line attenuator.

Sharma and Hofmann (2017) note that connections between steel and concrete have existed since the beginning of reinforced concrete construction, however the parameters are forever changing, with new products constantly in development for increasingly novel applications with every changing loading regimes. Over the years many different connection methods have been developed, which can generally be categorised as follows:

- Cast-in fully composite solutions;
- Cast-in removable solutions;
- Post-installed anchors; and
- Adhesive connections.

These are discussed in more detail in the following sections, with the emphasis on reviewing the suitability of each for the application of floating wave energy converters.

4.1.1 Cast-in fully composite solutions

(a) Welded shear connectors

One of the most common uses for mechanical shear connectors is for composite bridge structures, where welded headed shear studs are often used to transfer longitudinal shear between steel support beams and concrete decks (see Figure 4.1).

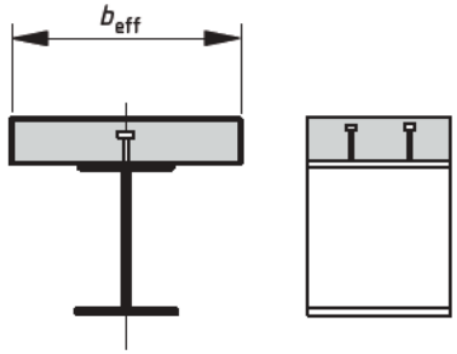

Figure 4.1: Composite steel/concrete beam (BSI, 2004*b*)

These shear studs are commonly used as they are very easy to install, providing the contractor has access to a specifically designed stud welding machine (Valente, 2007). Because of this, the behaviour of these shear studs is well understood, and design can be carried out in accordance with standard design codes (e.g BSI, 2004*b*).

In composite bridge construction, shear between the concrete and the beam flange is the primary loading, which is not the case for floating WECs. However, there is a history of groups of these types of anchors being used in the offshore environment to resist multi-axial loading. For example Sandvik et al. (2004) reports on the use of embedment plates being used in the oil and gas industry for connecting topside infrastructure (generally concrete) to floating hulls (generally steel), and attachment of various ancillary members (riser, fairleads, towing and mooring brackets etc) to the main structure (see Figure 4.2)

The main disadvantage of this connection is the amount of slippage that has to occur before the full shear capacity is mobilised resulting in stress concentrations and crushing of the surrounding concrete, and poor fatigue behaviour if subject to high cyclic loading (see Figure 4.3). Also the individual shear capacity is quite low, and therefore many connectors are required to provide a full shear connection, which can be labour intensive (Shariati et al., 2012).

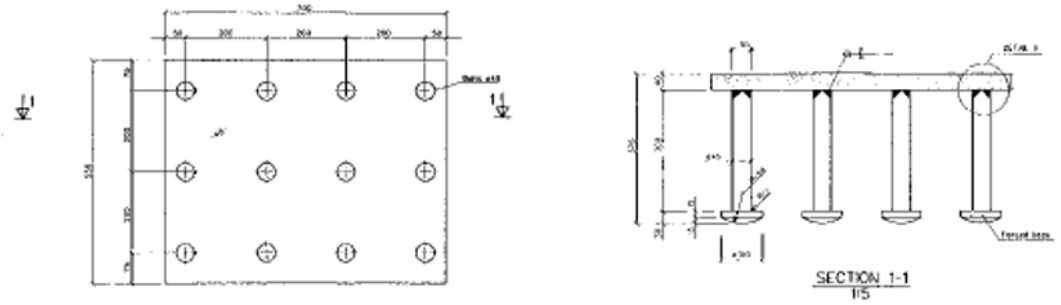

Figure 4.2: Typical embedment plate used in the offshore industry (Sandvik et al., 2004)

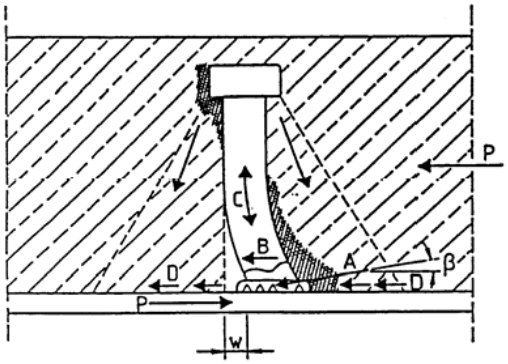

Figure 4.3: Load transfer from welded shear stud (Valente, 2007)

(b) Composite dowel connectors

The bridge designers Leonhardt, Andra and Partners developed the Perfobond shear connectors in the 1970s as an alternative for shear connection in composite bridges (see Shariati et al., 2012). The connector itself has a high shear capacity, and the composite shear resistance is developed through concrete compression dowels that form in the holes of shear connector (see Figure 4.4). Reinforcing bars can be placed through the holes to improve the overall ductility of the connection and increase the overall shear resistance. Fatigue behaviour is improved, as less slip is required to mobilise the shear connection, resulting in more elastic behaviour than for shear heads.

The disadvantage of this connection is the difficulty in placing the required rebar; to overcome this further research was carried out into strips with open cut-outs as part of the PreCoBeam project (see Lorenc et al., 2014). This led to the development of puzzle and clothoidal shaped ribs; the design of which has been encompassed in a recently published German Technical Approval (GTA) (see Feldmann et al., 2016, for more details), which have been shown to have superior shear strength when compared to shear studs. The Puzzle and Clothoidal rib shapes are shown in Figure 4.5; in general the clothoidal shape is recommended due to the improved fatigue properties for the shape (Berthellemy, 2013).

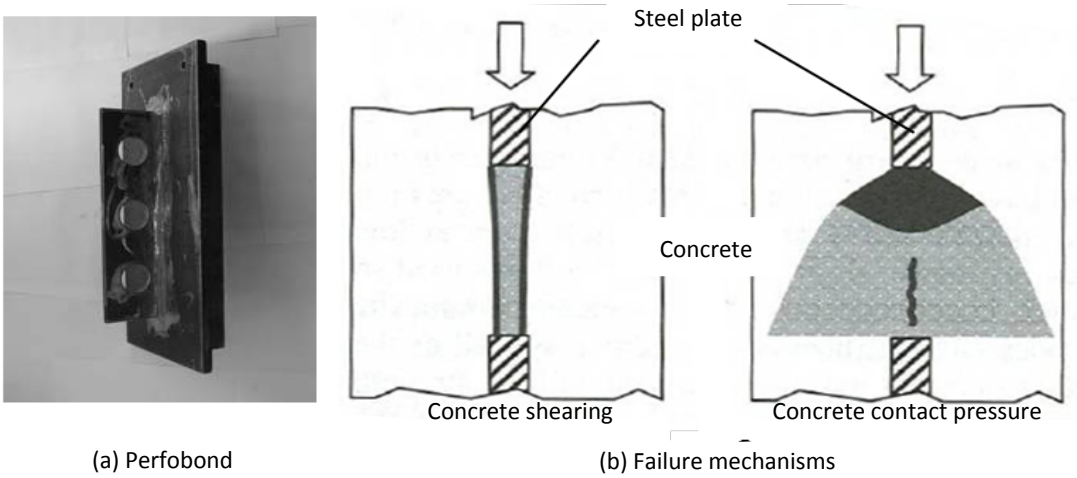

Figure 4.4: Perfobond - schematic and failure mechanisms (Valente, 2007)

Figure 4.5: Steel rib profiles

It is noted that the GTA only covers connectors subject to shear loading as this is application of most of the current research. It does not cover tensile loading, although this is addressed separately by Classen and Hegger (2016). In terms of fatigue, Feldmann et al. (2016) states that tensile loading perpendicular to the dowel in fatigue is not currently allowed by the code, to avoid unacceptable deterioration of the shear connector. It is therefore possible that this connector is not suitable to use in multi-axial dynamic regimes, however Classen and Gallwoszus (2016) notes in his dicussion on concrete fatigue that the code imposed fatigue limits are conservative; it may be that this limit is relaxed over time. The Classen and Gallwoszus (2016) paper discusses the reduction in the stiffness of the connection due to concrete degradation under fatigue loads, and outlines a method for including for this in design.

(c) Alternative mechanical connectors

With mechanical shear connectors, there are many possibilities for the shape of the cast in section, as discussed in reviews on shear connection options by Shariati et al. (2012) and Xie and Valente (2011). Examples of some alternatives are shown in Figure 4.6. These have mostly been developed to overcome issues with shear studs, such as labour intensive welding procedures, and low individual shear strength, but have not been widely adopted and therefore will not be considered further in this thesis.

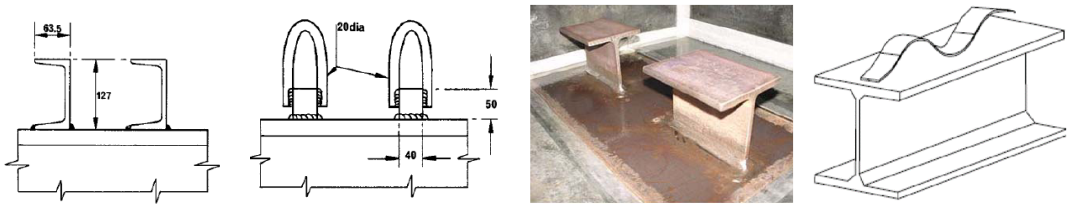

(a) channel **(b)** hoop **(c)** T connector **(d)** Waveform-strip

Figure 4.6: Different types of shear connectors (Xie and Valente, 2011; Shariati et al., 2012)

4.1.2 Cast-in removable solutions

(a) Cast-in anchors

The connection solutions discussed above are fully composite solutions, with the embedded steel connection component cast into the concrete, and permanently attached to the external steelwork requiring that it is incorporated into the concrete formwork. However this may not always be feasible, or indeed advantageous. The alternative to fully composite solutions are cast-in anchors with separate fastening systems that allow removal of the external steel component.

There are a wide variety of proprietary products that have been developed for this purpose as shown in Figure 4.7; a majority of which consist of a headed anchor cast into the concrete, with a socket which allows the external steelwork to be attached separately using fastening bolts.

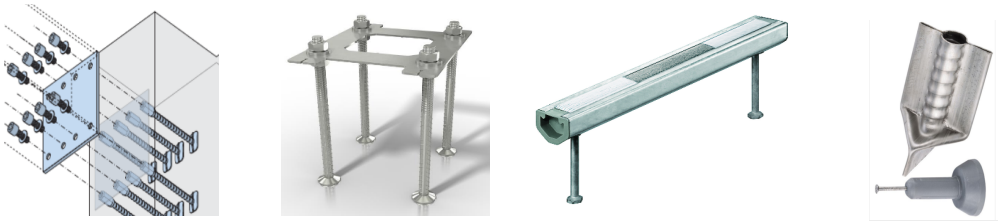

(a) Halfen HSC-B Steel-Concrete connection **(b)** Peikko PPM anchor bolt **(c)** Halfen HAC channel connector **(d)** Tierod Anchor

Figure 4.7: Proprietary cast in anchors

A majority of these solutions consist of a single headed anchor, which can be used in groups to resist loads about multiple axes. However, channel connectors (Figure 4.7 (c)) are also very common, having been used since 1916 (Eligehausen, 2017); the advantages of these are stated by Mahrenholtz and Sharma (2017) as flexible construction tolerances, robust connection taking loads about multiple axes, with no onsite welding or driling required. While it is possible that these could have applications for WECs, it is considered that the single anchor solutions give greater flexibility, and therefore will be the focus of analysis work carried out in Chapter 11.

The design of headed anchors is covered in the draft version of BS-EN 1992 (BSI, 2013), which gives the failure mechanisms of cast-in anchor systems as failure of the steel connector in tension or shear, pull out of the fastener (caused by crushing of the concrete under the fastener head), concrete cone failure in tension, or edge failure in shear (governed by the concrete shear strength). Providing that these different failure modes are addressed, these types of connections are well suited to resisting loading around multiple axis.

The fastening bolts can also be pre-loaded, which improves fatigue resistance in tension as the pre-load reduces the stress fluctuations in the bolt due to cyclic loading. Pre-loading also improves behaviour in shear, as providing the frictional resistance is greater than the applied shear force, this results in a non-slip connection and the shear force is transmitted directly into the concrete, rather than taken by the steel fastener.

It is required practice in offshore engineering to use preloaded bolts in steel-steel connections to reduce fatigue damage (DNV GL, 2014), but is less commonly specified in steel-concrete connections, as often the driver for design of such connections in civil engineering applications is the ultimate static resistance. However, even in these applications preloaded bolts are recommended for connections where fatigue load is likely to be significant (see Hilti AG, 2010).

(b) Post-tensioned bars

An extension of pre-loaded bolts is the use of pre-tensioned reinforcing bars, which are commonly used in onshore wind turbine foundations to connect steel towers to concrete gravity bases (see Göransson and Nordenmark, 2011; Macalloy, 2012), as shown in Figure 4.8.

Post-tensioned solutions have also been proposed for offshore wind turbines by Vici Ventus (Ventus, 2011) as shown in Figure 4.9; this connection has a steel transition ring connected to the concrete foundation using post-tensioning, with the steel tower bolted to the transition piece.

A disadvantage of this type of connection is that they could provide a path for water ingress into the concrete leading to durability issues, especially if the bolts are cast all the way

Figure 4.8: Foundation anchor system for onshore wind turbine (Macalloy, 2012)

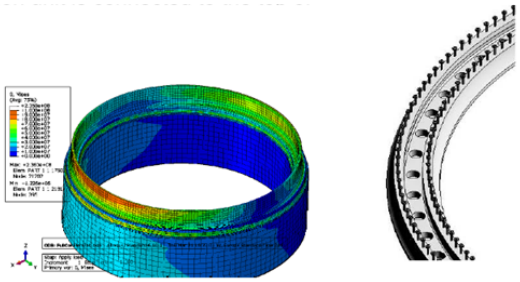

Figure 4.9: Vici Ventus steel to concrete connection (Ventus, 2011)

through a section. This is possible to overcome through provision of protective coatings for bolt ends, and any problems with corrosion will also be evident during inspections.

4.1.3 Post-installed anchors

Post-installed anchors are generally used for retrofitting applications to develop composite action in non-composite floor or bridge systems (Xie and Valente, 2011), or for in-situ installations where accurate placing of cast in connections is not possible.

Post-installed anchors include chemically bonded anchors (which are placed into pre-drilled holes and then adhered into place using epoxy or similar adhesive), or anchors with mechanical interlock, which are dropped into predrilled holes, and the tightened to connect with the concrete substrate as shown in Figure 4.10 (see Eligehausen, 2017, for further discussion).

While post-installed anchors have been shown to have superior fatigue strength compared to welded shear studs (Xie and Valente, 2011), it is considered that cast-in solutions are preferable for pre-cast construction, as they can be fully tied into the concrete, and integrated with the internal reinforcement. In particular there would be concerns with using chemically bonded anchors, as adverse environmental conditions (as occur offshore) are likely to negatively affect the behaviour of the adhesive, and very little research has been carried out on the behaviour of submerged bonded anchors (Blanchette, 2012).

(a) Bonded anchors **(b)** Expansion Anchors **(c)** Undercut Anchors

Figure 4.10: Examples of post-installed anchors (Eligehausen, 2017)

4.1.4 Flat faced adhesive connections

The final connection type considered in this review is flat-faced adhesive connections, where external plates (either steel or FRP) are bonded to the flat concrete surface. These types of connections have been used successfully for a number of years to upgrade ageing concrete bridges in order to improve bending and shear resistance. Shear forces are transferred through the adhesive bond between the plate and the concrete, and do not rely on any mechanical connection. This practice has resulted in an extensive amount of research carried out into the bond strength of these types of connections, and different methods for numerically and analytically analysing these joints have been developed (see Barnes and Mays, 2001; Chen and Tao, 2011; Lu et al., 2005).

It is noted by Si Larbi et al. (2007) that these types of connection also have the potential to replace traditional mechanical shear connections in composite construction. This would overcome some of the issues associated with mechanical shear connection including fatigue and high stress concentrations. However as for adhesive anchors, there very little investigation to date into the durability of such connections in the marine environment.

Newlands et al. (2018) recognise the potential benefit of flat faced adhesive connections for the offshore renewable industry, and as such are conducting research into the adhesive concrete joints exposed to seawater, however there is little published literature relating to steel-concrete joints, particularly with regards to fatigue loading. Therefore, while these types of joints could have potential, particularly if combined with post-tensioning as was being considered for the Pelamis device (see Khosravi et al., 2015; Anderson, 2003), it is considered that the amount of research and analysis work required for this type of connection is beyond the scope of this study.

4.2 Concrete behaviour

Section 11.4 carries out analysis of different connection options, focussing on the behaviour of the concrete under cyclic loads. This section of the literature review provides background and context to the work by describing the failure models for concrete, and how these can be related to fatigue damage prediction for uni-axial and multi-axial stress states.

4.2.1 Concrete failure models

The composite nature of concrete (strength carrying aggregates, bound by a cement based matrix) results in a non-homogeneous, anisotropic material, which acts differently under different load conditions (uniaxial, biaxial or multiaxial); as such, accurate models describing the triaxial material behaviour are complex in nature. Understanding of concrete failure modes is an important step in understanding the fatigue damage process and possible assessment methods, and this section provides an overview of the different models that have been developed. These are described in a multitude of different text books and references, including Wittel (2016) and Grünberg and Göhlmann (2013).

The three dimensional behaviour of concrete is most commonly described in terms of the principal stress, with the failure plane given in terms of the compressive and tensile meridians and the shape of the deviatoric plane as shown in Figure 4.11.

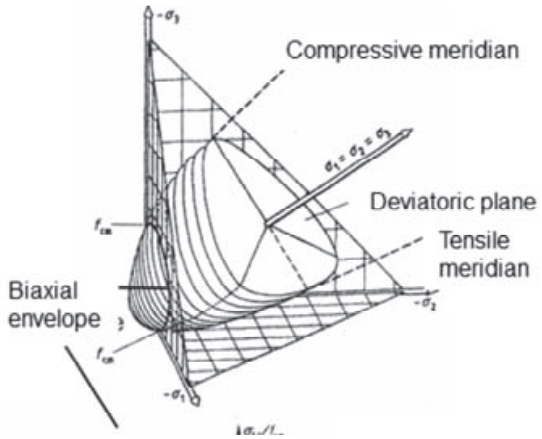

Figure 4.11: Three dimensional behaviour of concrete (Wittel, 2016)

Many different models have been developed to described the shape of the meridians and deviatoric planes. The simplest are the one-parameter models: the most well known are the Rankine criteria for brittle materials where failure is determined by the maximum tensile principal stress; and the Tresca or Von Mises criteria which describe ductile behaviour, but are independent of the hydrostatic stress, therefore have limited validity for concrete.

The increase in strength with respect to increasing hydrostatic stresses can be taken into account with 2 parameter models such as the Mohr-Coulomb (which gives a hexagonal failure pyramid in the principal stress state) or Drucker-Prager failure conditions (which describes a conical shaped failure plane). The one and two parameter failure criteria can also be combined to give a three parameter model, for example the ductile and brittle failure modes are both captured by combining the Drucker-Prager and Rankine criteria. However criteria combinations result in discontinuous edges in the failure surfaces which are difficult to deal with in numerical models (Grünberg and Göhlmann, 2013). To overcome this issue, higher-parameter models were developed that describe a continuously evolving failure surface. The most common of these are the Willam-Warnke three and five parameter models (William and Warnke, 1975), which describe a failure surface with different angles for the tensile and compressive meridians, and a deviatoric failure plane which varies elliptically between the meridians. The five parameter model has curved meridian lines, which is an improvement over the three parameter model, where the meridians are straight and therefore deviate from the actual concrete behaviour at high pressures.

4.2.2 Concrete fatigue behaviour and prediction

While metal fatigue has been under investigation for more than a century, concrete fatigue is considerably less advanced and less understood, as it is not generally a critical failure mode in traditional concrete construction. However, with the advance of structures subject to dynamic wind and wave loads (such as wind turbine structures) and advancement of high-performance lightweight structures, the subject has been receiving increasing attention (Ahsan, 2016). In particular the impact of concrete fatigue on connection points should not be overlooked, as it can be the dominant fatigue failure mode, particularly in the low cycle, or very high cycle load regimes (as concrete does not experience a fatigue endurance limit), as shown in Figure 4.12. The exact boundaries between concrete and steel fatigue failure are very dependant on the exact configuration of a particular configuration, which adds further complications to the fatigue life prediction.

The evolution of fatigue damage in concrete is characterised by the initial formation of micro-cracks, followed by a period of stable-crack propagation. Failure occurs when crack propagation becomes unstable, resulting in a significant increase in strain as shown in Figure 4.13. As fatigue damage increases, the concrete stiffness degrades, resulting in non-linear behaviour, which does not follow the linear damage accumulation as predicted using the common Palmgren-Miner hypothesis. It is noted that this is still typically used in practice, and is included in design codes (e.g. in DNV-OS-C502, DNV, 2012), potentially as there are no other practical alternatives (RILEM Technical Committee 36-RDL, 1994).

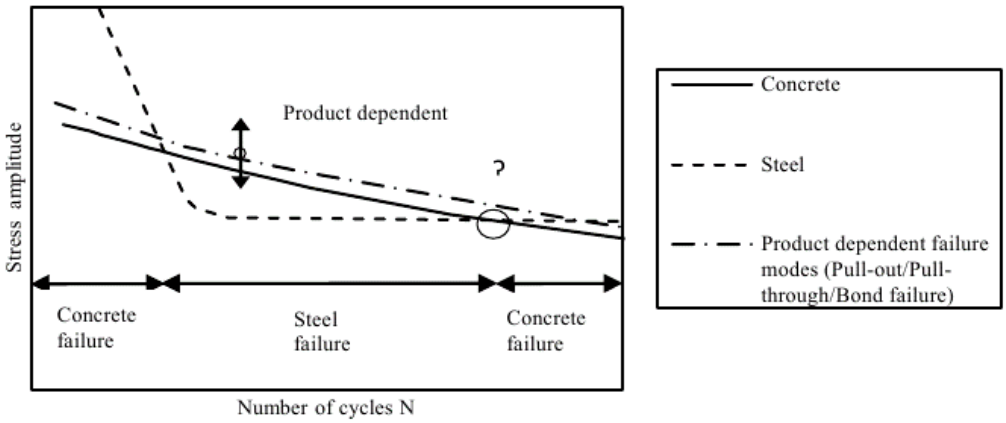

Figure 4.12: Wholer-curve for different fastener failure modes under fatigue loading, (Toth et al., 2016)

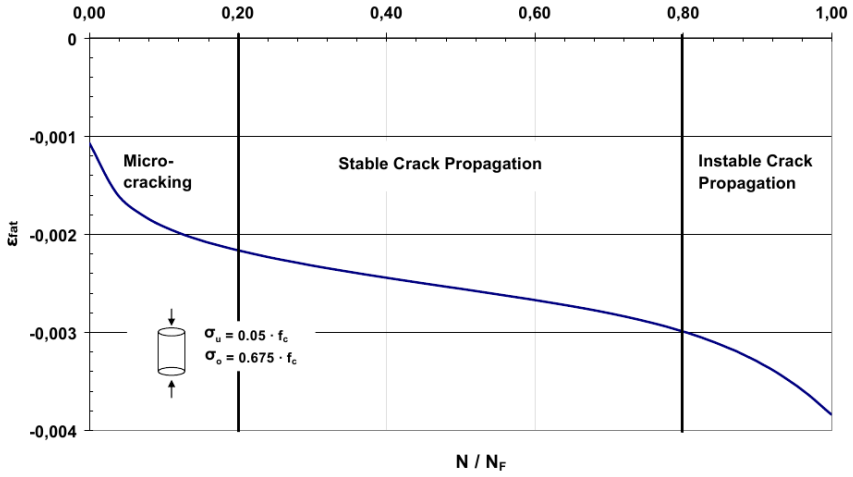

Figure 4.13: Evolution of concrete cracks in fatigue loading (N = number of cycles, N_F = number of cycles to failure (Grünberg et al., 2005)

The PM hypothesis does not take into account the order of fatigue loads, and can either under or over-predict the fatigue life of concrete, depending on the exact load-cycle history, as shown by Grünberg et al. (2005) in their work on concrete fatigue for wind turbine foundations.

In addition to the complexities regarding the non-linear evolution of fatigue damage in concrete, fatigue behaviour is further complicated by the sensitivity of concrete failure strength to the tri-axial stress state. With reference to the concrete damage models described earlier, confining compressive pressure significantly increases concrete strength, and increases fatigue life. Conversely lateral tension reduces the overall strength, with a corresponding impact on fatigue damage. This is particularly relevant for connection points between steel and concrete components which are subjected to highly concentrated loads, with complex, multi-axial stress states (see Grünberg et al., 2005; Toth et al., 2016), even under single degree

of freedom loads. The problem gets even more complicated for multi degree of freedom loading regimes.

The fatigue behaviour of concrete in uni-axial compression is well understood, but to date there has been little research into the impact of biaxial and triaxial fatigue loading. Current design codes present S-N curves which are generally based on the uniaxial behaviour of plain concrete, and therefore do not fully capture the complex multi-axial stress states that occur in steel-concrete connections. A number of recent papers have focussed on this deficiency and provide alternative methods for calculating the fatigue life of concrete under multi-axial load regimes.

Toth et al. (2016) notes that S-N curves for different fastener types developed from experimental data differs from the S-N curves for plain concrete under uni-axial loads (which are the basis for the curves presented in the design codes), and therefore proposes a fatigue damage calculation method based on dissipated energy of a particular connection (obtained experimentally) combined with a fracture mechanics approach using the Paris law. However this requires a detailed connection design to be available for testing, and therefore is not relevant for high level option analysis.

Grünberg et al. (2005) proposes a non-linear approach for multi-stage loading using an energy based fracture mechanics approach, taking into account the stiffness degradation of the concrete over time. This is extended in Grünberg and Göhlmann (2013) to take account of multi-axial stress states by using concrete failure models to predict material specific damage values that lead to altered failure envelopes depending on the number of load cycles that have occurred and the tri-axial stress state. However, the reference notes that this method involves iterative calculation of the dissipated energy, and material specific parameters (such as the volume-specific crushing energy), and therefore is not really suitable for high level preliminary design. An alternative method using the Palmgren-Miner hypothesis is therefore presented, which takes account of multi-axial stresses by including a modification to the S-N curve of concrete for uniaxial loading, as shown in Equation 4.1 (DNV GL, 2018).

$$log_{10}N = C_1 . \frac{1 - \sigma_{max}/f_c}{1 - \sigma_{min}/f_c} \tag{4.1}$$

where f_c is the uniaxial concrete compressive strength. The modified S-N curve replaces f_c with $f_c(\sigma_1, \sigma_2, \sigma_3)$ which is the compressive strength based on the triaxial loading state, calculated from the concrete failure model (the 5 parameter Willam-Warnke model is used in the reference). Modified S-N curves depending on different loading conditions (uniaxial, biaxial and triaxial stress states) are also presented in Song et al. (2006), and while these are based on a small amount of experimental data (and therefore the application is limited to the conditions of the test cases), this does lend weight to the fact that using modified S-N curves is an appropriate way to account for multi-axial stress states in concrete fatigue analysis.

4.2.3 Fatigue analysis methods

In order to take account of the full effect of multi-stage and multi-axial loading on the concrete fatigue, a full time-domain analysis would need to be carried out, taking into account loading histories over the full design life for all the details of relevance. This would be very calculation intensive, and require a level of knowledge about the load regime that is not available at this preliminary level of design. It is therefore useful to identify spectral methods of analysis that can be carried out in the frequency domain.

Standard spectral methods (as discussed in Section 2.2) were originally developed for uniaxial loading states and therefore are based on a single stress component. In order to take into account multi-axial stresses, an "equivalent-stress" concept is often employed, whereby the full stress tensor is reduced to a single value using a failure criteria that is relevant to the material in question. Much of the literature refers to equivalent stress states based on the Von Mises criteria (Benasciutti et al., 2015), as modified by Pitoiset and Preumont (Pitoiset et al., 1998). However the use of the Von Mises criteria has known limitations as it can only be related to materials which have the same S-N curve for tension, compression and torsion (Niesłony et al., 2012), which is not the case for concrete. There appears to be limited research on multi-axial spectral fatigue analysis using concrete failure models, and while the development of this would be an interesting area of research, it is well beyond the scope of this study. Halfpenny (1999) suggests using the maximum absolute principal stress as an input into the uni-axial spectral method, and therefore this will be the approach adopted in this study. The effect of multi-axial loading will be considered by applying a single correction to the S-N curve, following the method suggested in Grünberg and Göhlmann (2013). It is noted that there are many limitations with this method, and it would not be appropriate for a detailed design analysis, however will allow a comparative analysis of different connection options to be carried out.

4.3 Summary

This chapter has reviewed different steel-connection types, and provided an overview of concrete failure models and fatigue behaviour that supports the design of such connections. The main points from this review that will be taken forward to the design work in Chapter 11 are as follows:

- There are many different types of steel-concrete connections which have been developed for a multitude of applications. The set of connections which appears to be the most suitable for floating WECS are those with steel components cast into the concrete to provide a mechanical resistance to loading.

- It is often assumed that the steel components are the most critical when it comes to fatigue life of composite connections. However, in very dynamic connections with multi-axial loads, concrete fatigue should not be overlooked.
- Fatigue behaviour of concrete is very dependant on the multi-axial stress state within the concrete. In order to make an assessment of the fatigue life of the concrete it important to be able to predict the triaxial strength (which can be significantly more, or less than the uniaxial strength). Concrete is a composite, non-homogenous, anisotropic material, which behaves in a complex manner under different loading conditions. As such accurate models describing the material behaviour are complex in nature, with multiple parameters. The William-Warnke model predicts the behaviour well in most loading conditions, and therefore will be used in this thesis.
- Fatigue in concrete is non-linear, and dependant on the order of applied loading cycles. It is therefore not well described by the linear damage accumulation hypothesis. However, this is commonly used in design (and is recommended in the DNV offshore codes), due to a lack of simple alternatives. It is therefore considered to be acceptable for the purpose of the preliminary design work carried out in this thesis.
- Spectral fatigue methods will be utilised for design, and the effect of multi-axial stress states on fatigue damage will be taken into account by adjusting the concrete S-N curve to take account of the triaxial concrete strength.

PART II

Conceptual design

Part II - Conceptual Design Introduction

This part of the thesis covers work on developing the overall 12S WaveNET concept, focussing on optimising power output and structural loading alongside other assessment metrics.

Maximising power production across all sea states can increase the overall opportunities for revenue generation. However, greater power production results in larger loads applied to the structure and the power take off (PTO) system, which in turn increases the cost of the device components. It is therefore important to consider the trade-off between maximising power production and minimising structural loading at an early developmental stage to ensure that it is possible to design a reliable and robust WEC structure, while achieving an acceptable Levelised Cost of Energy (LCoE).

The aim of the work described within this part is to develop methods that allow these factors to be incorporated into all the early stages of the overall design process, from initial conceptual option selection through to the definition of the loads for ongoing design work.

This work is of benefit to Albatern as a company[1] as it provides the mechanism for carrying out a structured design development process, taking into account factors that might otherwise have been ignored in the early concept assessment phase. The methods developed in this section could also be beneficial to the wider industry, as they can be adapted and applied to other wave energy devices and systems.

Concept development and assessment work has been carried out with the aid of results from physical and numerical models, and these are also described within this part. The Albatern WaveNET array system is a novel system, with multiple interacting floating bodies, which create interesting challenges for modelling work. The work carried out to extract loading results from the models, and compare and contrast the results from the two different modelling methods has given a greater insight into the structural behaviour of the device and the appropriateness of the different modelling techniques. The knowledge gained from this process could offer benefits to others attempting to carry out similar activities in the future.

The structure of this part is as follows:

- Work carried out at the beginning of the concept development stage to identify the preferred configuration for the 12S WaveNET array, using power production and structural loading as assessment metrics is included in **Chapter 5**.
- Preliminary modelling activities carried out using the preferred configuration identified in Chapter 5 is covered in **Chapter 6**. Both physical models and numerical models were

1. Or would have been, if the 12S development work had been continued

developed (by others); this chapter extracts the relevant results from the tests, and compares and contrasts the two different modelling methods. The aim of this chapter is to identify the relevant structural loads for the device, in order to set out load cases for ongoing detailed design work.

- The theme of investigating the compromise between power production and structural loading is continued in **Chapter 7**, which builds on the modelling work in Chapter 6 to identify the optimum PTO torque limit which results in a minimum LCoE.
- A summary that brings together all the work covered within this Part is included in **Chapter 8** to set out the appropriate load cases to be taken forward to the more detailed design activities relating to the Node structure, which are covered in Part III.

Chapter 5

Initial concept selection

This chapter details work carried out to develop a methodology for assessing different concept options for the 12S WaveNET array. The aim of this work is to select the preferred option to be taken forward for further design development, taking account of both power production and structural loading as assessment criteria.

The structure of this chapter is as follows:

- **Section 5.1** sets out the context for the research, discussing limitations of 6S WaveNET array.
- The assessment method is set out in **Section 5.2**, starting with an overview of the different concepts that have been considered. The section includes a brief discussion on the numerical modelling that has been carried out (by others in the Albatern design team) in order to produce power matrices and design loads, and then sets out the different assessment criteria and the Decision Matrix logic.
- Power and force assessment results are presented in **Section 5.3**, with the results of the Decision matrix analysis shown in **Section 5.4**.
- A summary and final discussion is included in S**ection 5.5.**

While the assessment procedures developed here are the work of the author, the process has been carried out with input from other members of the Albatern team, which is noted as required throughout the chapter.

5.1 Context

Albatern have a well developed concept for the 6S WaveNET array, consisting of modular Squid units that can fit onto a lorry for easy transportation (as can be seen in Figure 1.4 in the Introduction), which are then joined together in the water. The Squid unit consists of three link arms connected at a central node to a surface piercing“riser" and at three outer “anti-nodes" which float at the surface as seen in Figure 1.1 . Each connection point consists of an articulated joint which move with the waves. Hydraulic rams at each joint then pump fluid through a generator in order to convert the incoming wave energy to electrical power.

Albatern's original development plan had been to scale up the 6S Squid concept for the 12S array, building directly on the knowledge gained from the 6S testing programme. However, initial investigations raised a number of concerns associated with scaling up this concept, as discussed below:

Deployment and connection of the devices: The 6S Squid modules are deployed horizontally, then flooded with water to rotate into the vertical position. The anti-nodes of adjacent Squids are then connected together manually, whilst on the water, using a small boat for access. This process is currently the most complex part of the deployment process, and would get even more difficult at a larger scale.

Capability of the power take off (PTO) module: The 6S Squid includes an innovative power take off module, consisting of a single hydraulic ram housed within an articulated joint which allows for large rotations without reaching an end stop. While this works well at 7.5kW, it is very difficult to scale up the concept to 75kW as required for the 12S array.

Force generation in riser: The 12S array is twice the physical size of the 6S device, designed to be deployed in waves with more than twice as high (H). This results in bending moments (BM) at the base of the 12S riser that could be in the region of 16 x the magnitude of the 6S riser, as illustrated below:

$$BM = force(F).eccentricity(e)$$
$$F \propto Area(A).H \propto Length(L).Diameter(D).H$$
$e \propto L$, therefore $BM \propto L^2DH$ and:
$$BM_{12S} \propto (2L_{6S})^2(2D_{6S})(2H_{6S}) = 16BM_{6S}.$$

This magnitude of bending moment is difficult to deal with in the current configuration.

Link arm torsion forces: The nature of the motion of the 6S array results in significant torsion forces in the link arm, which again will increase for the 12S array, potentially to unmanageable levels.

For these reasons, Albatern took the decision to revisit the 12S design, and to undertake an extended period of concept development to try and overcome some of the issues. At the start of this process, a number of alternative concepts were proposed by the wider Albatern team; this chapter sets out a structured method for assessing the different concepts, and ultimately selecting the preferred option. A Decision Matrix Analysis methodology has been applied, using power production capability and structural loading metrics as assessment criteria.

As discussed in the introduction to this part, maximising power generation increases overall opportunities for revenue generation, and is often used as the headline figure for evaluating different concepts (which was historically the case at Albatern.) However, increased power production often results in larger structural loads, and increasing device cost; the structured assessment methodology set out in this chapter allows the impact of structural loading to be easily included alongside power generation capabilities at the early conceptual design phase.

While the method has been developed specifically for the Albatern 12S array, it could also be modified and applied elsewhere.

5.2 Concept assessment and selection methodology

5.2.1 Concept overview

Concept assessment has been carried out in two stages. The first stage compares the original scaled up version of the 6S (the “Base case”) against an improved “Modular” concept, developed to overcome some of the issues highlighted in Section 5.1. The second stage carries out analysis on further options that build on the learning outcomes from the 1st analysis stage. An overview of the assessment process is shown in Figure 5.1, and the different concepts are discussed in more detail below. Decisions regarding concepts to be included in the assessment were carried out with input from the whole Albatern team.

A. Base case

The base case is defined as a scaled version of the current 6S prototype devices (physical scale factor of 2, to give a riser length of 12m). This concept consists of a system of link arms, surface floating anti-nodes, and sunken nodes with a surface piercing riser, as seen in Figure 5.2(a). Link arms are connected to the nodes and anit-nodes via articulated “joint modules”. Each articulation is damped about the pitch axis; the yaw axis has an associated stiffness, and the torsion axis is fixed. The definition of the articulation axes are shown in Figure 5.2 (b)

B. Modular concept

The "Modular Concept" (shown in Figure 5.3), is so named as it consists of separate Node and Link Arm modules, which are deployed individually and then connected together once floating, to simplify the deployment installation and maintenance procedures. A single Node module replaces the node and anti-nodes of the base case, with one Node providing attachment point for three Link Arms. The Node and Link elements are connected via a hitching mechanism, and some degree of movement is allowed around each of the axis of rotation at the connection to try and minimise the build up of forces that do not contribute to the overall power output. Node elements are 6.6m in diameter.

The first assessment stage considers different variations of the Modular concept, looking at the following parameters:

- The effect of different power take off mechanisms, categorised by the characteristics of each the articulation axis as shown in Figure 5.2 (b).

Figure 5.1: Concept option assessment flowchart

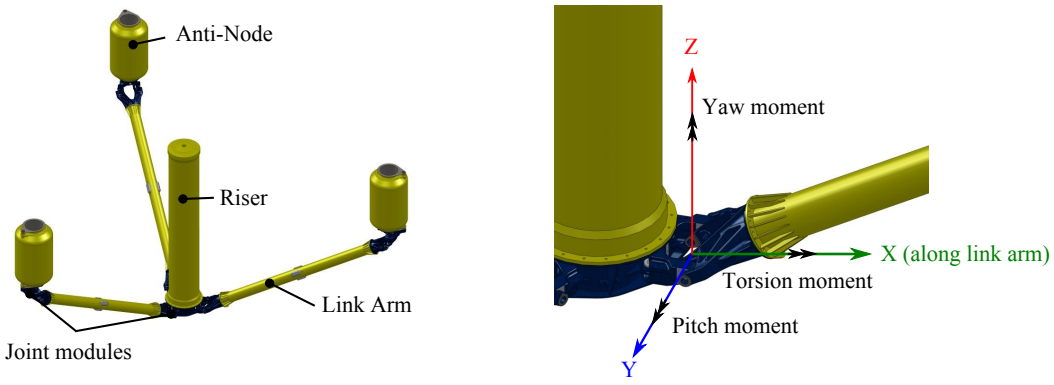

(a) Squid module (b) Articulation axes definition

Figure 5.2: Base Case *background drawing credit: Graham Terry*

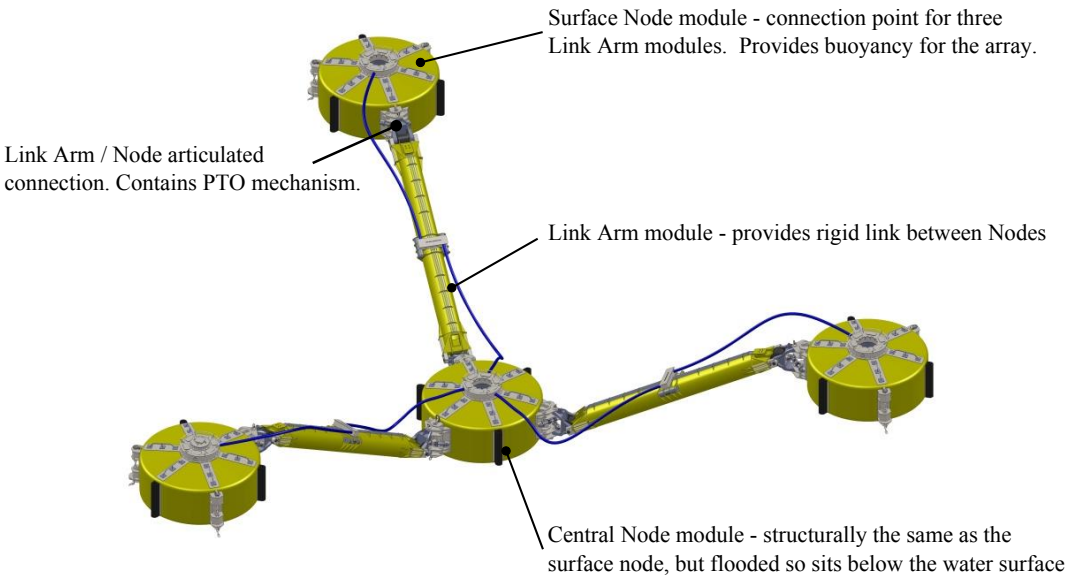

Figure 5.3: Modular Concept

  - Power take off about a single axis (pitch), with a stiff yaw axis, referred to as a "Single PTO". The torsion axis is locked (no rotation is allowed) - this replicates the conditions used for the Base Case.
  - Power take off about two axis (the pitch and yaw axes), with a locked torsion axis, referred to as a "Secondary PTO" configuration.
  - Power take off about three axis, (pitch, yaw and torsion), is referred to as a Ball Joint.

- Effect of ability to vary level of central node
- Benefits / disadvantages of a surface piercing element. A surface piercing element is defined as a component which is attached below the surface, but has some proportion of its volume above the surface, as is the case with the riser in the Base Case.

The different concepts are discussed in more detail in Table 5.1.

C. 2nd stage concepts - different node options

Results from the first assessment stage are discussed in greater detail in Section 5.3, but most importantly the analysis showed that concepts which exploit the pitching response of the node (e.g. concept B.1.b(i) with an 'Active Hammer') improved power generation without significantly increasing the loads in the structure. This result was explored further in the second stage of analysis, which looks in more detail at different node options, investigating shapes of surface piercing risers, and the looking at the benefits of a planar array system compared to the original concepts which include a surface and sunken node element. The concepts included in the second stage are shown in Table 5.2.

Table 5.1: "Modular" concept variations

Concept name	Concept description
B.1 Single PTO, High stiffness	Linear damping applied about pitch axis, High stiffness applied about yaw axis (15MNm/rad), Locked torsion axis.
B.1.a Variable buoyancy 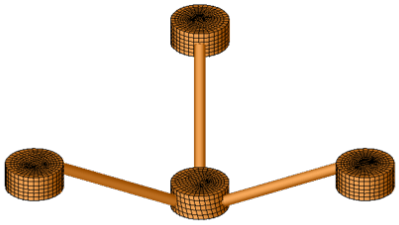	Concept to investigate the effect of a variable buoyancy central node, achieved by flooding the central node or emptying internal chamber, and by changing mooring pre-tension.
B.1.b Hammer 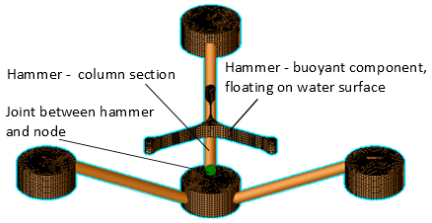	This concept includes a "hammer" element attached to the central node. The hammer is an element with a slender column attached to the sunken node, with a larger buoyant volume which floats on the water surface. Two different variations have been considered: (i) Power take off at the joint between the hammer and the node ('Active Hammer'); (ii) A rigid joint between hammer and node.
B.1.c Riser 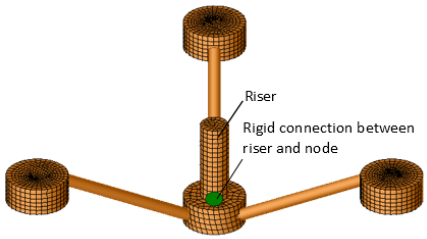	In this concept a 3m diameter surface piercing riser is included, rigidly connected to the node.
B.2 Single PTO, Low stiffness	This concept is similar to B.1, but with the lower level of stiffness about the yaw axis, in an attempt to reduce the loading throughout the array. (0.7MNm/rad)
B.3 Secondary PTO	This concept has a secondary power take off mechanism (linear damper) applied around the yaw axis, to increase power output.
B.4 Ball joints	In this concept, power take off occurs about each of the three rotational degrees of freedom; the purpose of this model is to try and reduce some of the loads by freeing the torsional degree of freedom (DoF), while also increasing power output.

Table 5.2: Second stage concept variations

Concept name	Concept description
C.1 Conical / surface node 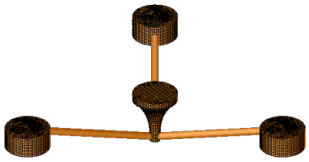	This concept aims to exploit the apparent power generation improvements for concepts where the node pitching response is exploited; the central node is replaced by a surface piercing conical node of the same weight and diameter, with the connection point 6m below the water surface.
C.2 Planar conical node 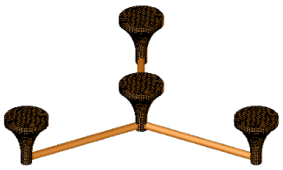	This concept uses the conical node in all locations, taking advantages of the pitch response at all node locations, and improving constructability as all the nodes are the same.
C.3 Planar riser 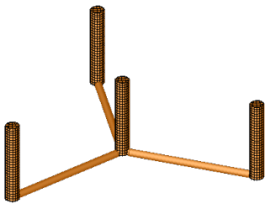	This concept looks at the effect of using lighter, simpler riser structure (2m diameter and 12m length), to investigate what effect this has on the overall power output.

5.2.2 Concept modelling

Note: Concept modelling activities and results post-processing were carried out by Vivien Mavel (Hydrodynamic modeller), and Johann Praeffe (Mechanical Engineer) at Albatern. An overview of the process is included here for completeness.

The power output and structural loads for the different concepts have been quantified through the use of hydrodynamic models, using Ansys AQWA (2013), set up and run by others at Albatern. The models have been run in regular sea states, with 1m wave amplitude at a range of frequencies, in order to determine the Response Amplitude Operator (RAO) which gives the magnitude of the structural response to a sinusoidal wave of unit amplitude. The RAOs have then been used in order to generate a power matrix (which shows the performance of the device across all operational sea states), and set of extreme articulation loads for each concept.

The methodology employed assumes that the structural response in linear, and can therefore be extrapolated for increasing wave heights. This is not strictly correct as it ignores non-linear effects such as viscous damping, and non-linear wave characteristics in more extreme sea states. However is it considered appropriate for concept development due to the fast speed of analysis and processing that is required.

To investigate the impact of increasing array size, models have been run for three different array size: with a single 'Squid' (3no. link arms, 4no. nodes, 1no. 75kW generator), a '1 Hex' array (9no. link arms, 9no. nodes, 3no. 75kW generators) and a '3Hex' array (18no. link arms, 16no. nodes, 6no. 75kW generators) as defined in Figure 1.3 in the Introduction. Models have been run with different levels of PTO damping to investigate the impact on power output and loads.

The modelling work and results post-processing was carried out by others within the Albatern team, with the results used by the author in this concept assessment and selection process.

5.2.3 Concept assessment criteria

Note: Concept assessment criteria were developed by the author, but in discussion with other Albatern team members.

The concepts detailed in Section 5.2.1 have been assessed using a number of quantitative and qualitative metrics as discussed below. These have been selected as the metrics that have the most influence on the LCoE.

- Quantitative metrics related to power generation:
  - Overall power output for array;
  - Required PTO torque magnitude to achieve desired device performance;
  - Evidence of power output improvement with increasing array size.
- Quantitative force assessment.
- Qualitative methods relating to:
  - Constructibility;
  - Installation;
  - Operations and maintenance;

(a) Power generation metrics

(i) Overall power output

Note: Power generation metrics were calculated by Johan Praeffe as part of the post-processing of the modelling results. An overview of the process is included here for completeness.

The performance characteristics required for the device as specified by Albatern are:

- Rated capacity of PTO generator = 75kW
- Capacity factor = 0.3
- Availability = 0.95
- Electro-mechanical efficiency = 0.85.

Using these parameters gives the following required yearly mechanical energy yield (AEP_{req}) for the different array sizes:

- Squid (with 3 PTO generators) = 244MWh/yr
- 1Hex (with 6 PTO generators) = 732MWh/yr
- 3Hex (with 9 PTO generators) = 1464MWh/yr.

For concept assessment the achievable power output is represented as percentage of this AEP_{req} (% AEP_{req}), to give a single metric which allows a comparison of different concepts, and also different array sizes in a way that using the absolute power output would not.

(ii) Required PTO torque magnitude

In the full scale device, the maximum power output will be limited by the maximum torque that the primary PTO mechanism can generate. The results of the numerical modelling shows the articulation torque magnitude required in order to generate the AEP_{req} as specified above. Increasing the PTO torque increases overall costs and structural loading, so the lower the torque required to achieve the required mechanical energy yield, the better the concept.

(iii) Evidence of power output improvement with array size

Testing of the 6S array has shown that increasing the array size gives power performance improvements, in terms of the amount of power produced per PTO generator; Albatern hopes to replicate this behaviour with the 12S array. Array improvements are indicated with an increase in the % AEP_{req} metric with increasing array size.

(b) Force assessment

Note: The force assessment process has been developed by the author as part of this research process, using results from the numerical models developed by others

At this stage it would not be appropriate to try and carry out a design for each component of the array for each concept; therefore the link arm has been taken to be representative of the design of the whole array. A simple design check has been carried out, comparing the resistance of a representative link arm cross section to the applied design loads (taken from the extreme articulation loads, as calculated from the numerical modelling). This gives a Link Arm Utilisation Factor (UF_{LA}) that is used as a concept comparison metric.

The representative link arm section is taken as a standard steel tube with the following dimensions: Length = 11 m, outer diameter = 1.219 m, wall thickness = 12 mm, steel yield strength = 355 MPa. The design resistances have been calculated using the Norsok N-004 code for offshore structural steel. The 6 degree of freedom (DOF) forces (F_X, F_Y, and F_Z) and moments (M_X, M_Y, and M_Z) as given at each of the articulation points have been combined with the design resistances to calculate the UF_{LA} for each concept. The calculated design resistances, together with the UF_{LA} equations are shown in Table 5.3.

Table 5.3: Tube design resistances

Force component	Symbol	Resistance	UF_{LA}
Axial (compression)	$N_{c,Rd}$	15.1 MN	$F_{XD}/N_{c,RD}$
Shear	V_{Rd}	4.7 MN	$\sqrt{(F_{YD}^2 + F_{ZD}^2)}/V_{RD} \leq 1$
Bending	M_{Rd}	5.0 MNm	$\sqrt{(M_{YD}^2 + M_{ZD}^2)}/M_{RD} \leq 1$
Torsion	$M_{T,Rd}$	5.6 MNm	$M_{XD}/M_{T,RD} \leq 1$

If the calculated $UF_{LA} < 1$, then the link arm is deemed to be acceptable for the particular failure mode in question. If it is ≥ 1, then the link arm could potentially fail and therefore the link arm cross section would have to increase. The analysis shows that the axial and shear failure modes are not critical - it is the combined bending and torsion failure modes that drive the design, and therefore it is these failure modes that are shown on Figures 5.5 and 5.8.

(c) Constructibility, installation, and operations and maintenance

Note: Qualitative assessment of these issues has been carried out in discussion with the wider Albatern team

Power assessment and structural loading have a significant impact on the LCoE of a device, and provide quantitative metrics for comparison. However, how easy it is to manufacture, install and maintain a device can also affect the device costs, and it is relevant to include these factors in the decision making process at an early stage. It is difficult to quantify the effects of these parameters at this stage, so a qualitative assessment for each concept has been carried out.

5.2.4 Decision matrices

Note: Decision matrix criteria have been developed by the author.
The final concept selection has been carried out with the aid of Decision matricies, which provide a quantitative assessment of the various metrics discussed above. Each metric is given a score, with the total score for a concept given as the sum of the metric scores, multiplied by a weighting factor which indicates which metrics have the most influence on the LCoE. The higher the score the better a concept performs. The scores for different metrics have been assigned on the following basis:

$\%\ AEP_{req}$

1. Achieves less than 80% for all array configurations (array configuration defined as either a Squid, 1Hex or 3Hex array)
2. Achieves up to 80% for at least 1 configuration
3. Achieves 100% for at least 1 configuration

4. Achieves 100% for at least 2 configuration
5. Achieves > 100% for at least 2 configurations

Torque level:

1. Does not reach 100%AEP_{req} at any reasonable torque level
2. 100% performance efficiency at >500kNm torque
3. 100% performance efficiency at <500kNm torque

Evidence of array improvement:

1. None
2. Slight
3. Strong

Force assessment:

1. $UF_{LA} > 1$ for most levels of damping for bending AND torsion
2. $UF_{LA} > 1$ for most levels of damping for bending OR torsion
3. $UF_{LA} < 1$ for some levels of damping for bending AND torsion
4. $UF_{LA} < 1$ for damping levels less than 6000kNm/rad/s for bending AND torsion
5. $UF_{LA} < 1$ for most levels of damping for bending AND torsion

Constructability / Installation / O&M:

Assessed on a scale of 1 to 5, with 1 being the hardest (most issues, or highest level of uncertainty) and 5 being the easiest (least issues, or highest level of uncertainty)

5.3 Power output and force assessment results

5.3.1 1st stage concept comparisons

The following graphs show example comparisons of power output and force generation for the different concepts.

(a) Effect of different PTO configurations

Figure 5.4 shows a plot of maximum PTO torque vs $\%AEP_{req}$ for the 1st stage options. Figure 5.4 (a) shows the B.1 concepts with different PTO mechanisms alongside the Base Case, all in a 1Hex array configuration. The plot shows that the $\%AEP_{req}$ increases with increasing PTO torque (as would be expected), and the Base Case performs worse than all the other options; only achieving a maximum of 60%AEP_{req}. The best performing concept in terms of power generation is Option B1 - (Single PTO, with a high stiffness applied about the yaw axis), which achieves 100%AEP_{req} at a torque level of approximately 625 kNm. Figure 5.4 (b)

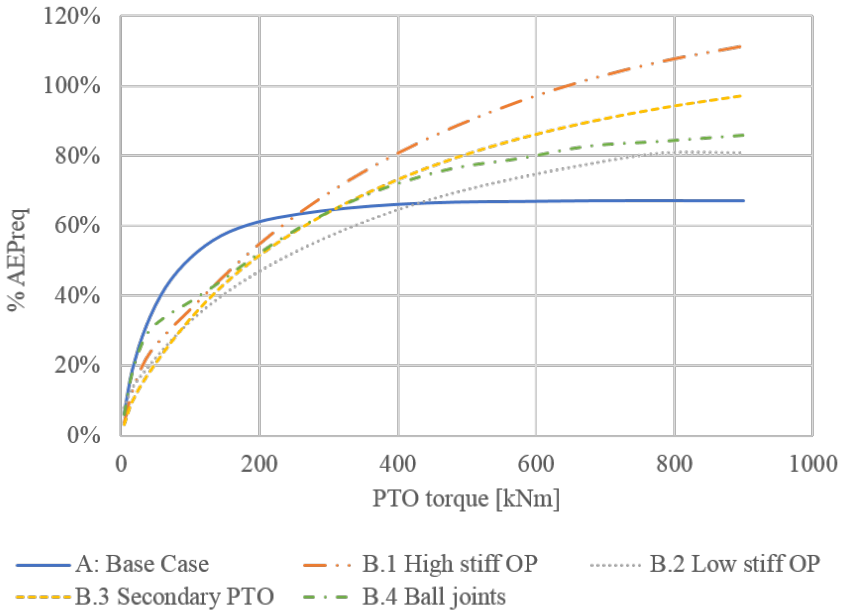

(a) Comparison of different options – modelled with a 1 Hex array

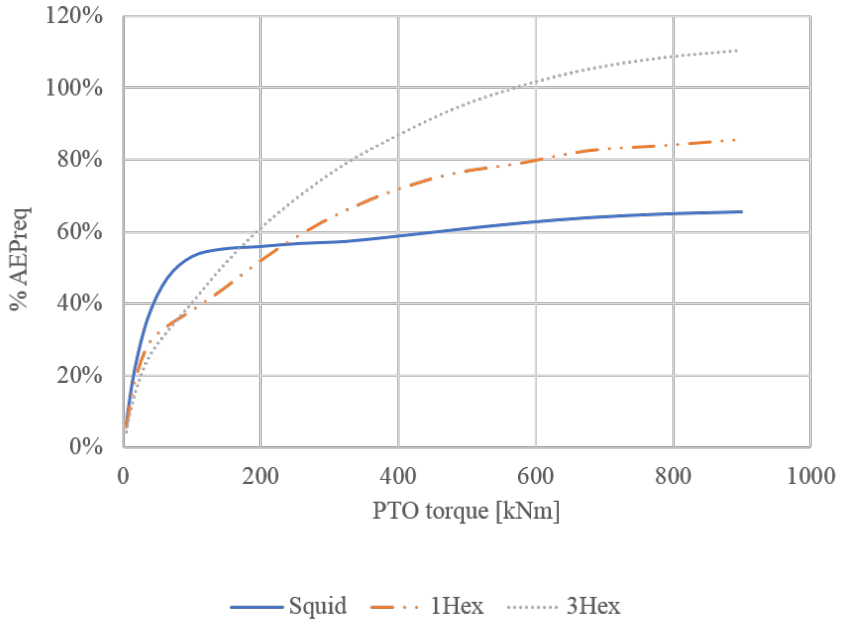

(b) Comparison of option B.4, modelled at different array scales

Figure 5.4: 1st stage concept comparison - graphs of $\%AEP_{req}$ vs PTO torque

shows the B4 option (Ball Joint) at different array scales, clearly showing the improvement in power performance with increasing array size.

Figure 5.5 shows the UF_{LA} for the initial concept options varying with applied PTO damping, with (a) showing the UF_{LA} for the biaxial bending moments and (b) showing the UF_{LA} for the torsion moments. All results in these graphs are for the 1Hex array configuration. These figures show that option B.4 (Ball joint) has the lowest link arm loads, while B.1 (Single PTO with high stiffness about the yaw axis) has the highest loads, particularly at higher damping levels.

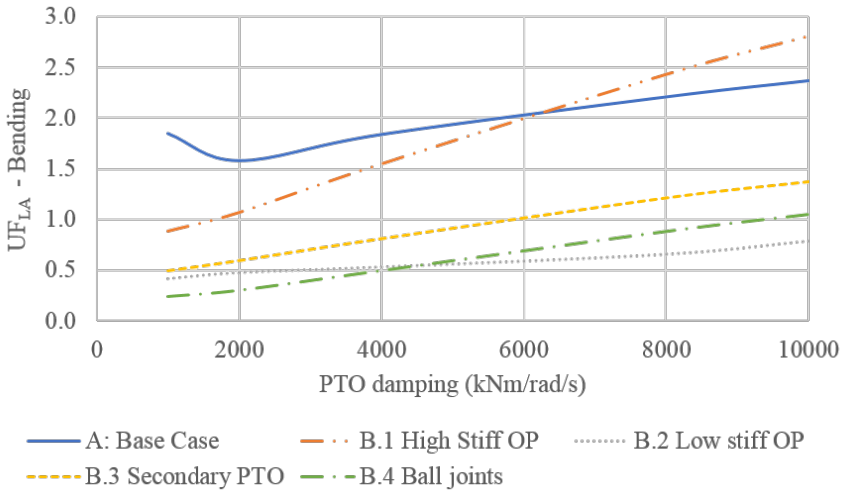

(a) Bi-axial bending moment

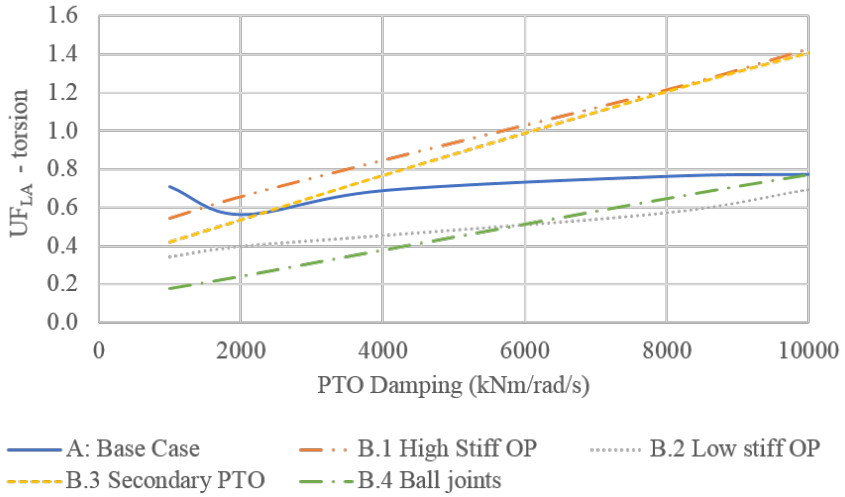

(b) Torsion moment

Figure 5.5: 1st stage concept comparison - link arm utilisation factors vs PTO damping. If $UF_{LA} \geq 1$ link arm could fail, and link arm cross section should be increased.

(b) Effect of variable buoyancy control and surface piercing riser

Figure 5.6, provide comparisons for the different variants of the B.1 12S node concept, looking at the effect of variable buoyancy of the central node (a), and the provision of a surface piercing riser (b).

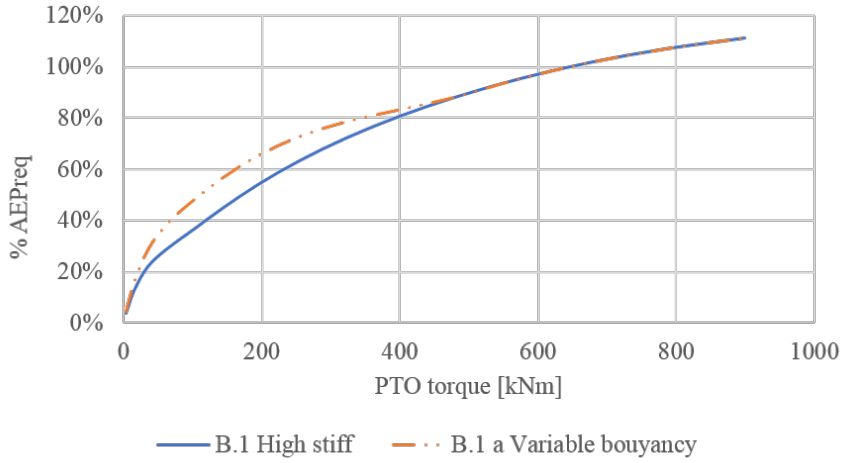

(a) Effect of variable buoyancy (for 1 Hex array)

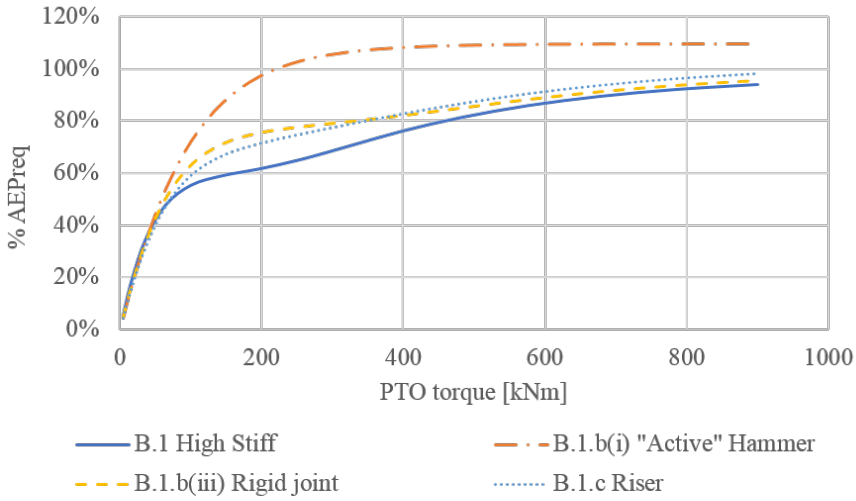

(b) Effect of surface piercing riser (for Squid)

Figure 5.6: B.1 concept variation comparison - $\%AEP_{req}$ vs PTO torque

Figure 5.6 (a) compares the power output for concept B.1 (Single PTO with high stiffness), where the link arms are maintained at an angle of 30°, with B.1.a where the link arm angle can be varied between 5 and 30°, and the optimal angle is selected for each sea state. It can be seen from this graph that for lower torque levels, there are improvements in performance of approximately 25 to 30% but this improvement tails off with increasing torque levels.

It is thought that the reason for this is that at lower PTO torque levels the individual nodes have an increased pitch response, and this response is enhanced at shallower link arm angles. When the maximum torque level is increased, the individual pitch response of the node decreases, and power is generated more from the relative motion of adjacent nodes; this effect is more pronounced at steeper link arm angles.

Figure 5.6 (b) compares the effect of different surface piercing members with the general B.1 concept. This shows that a surface piercing 'Active Hammer' seems to have a significant beneficial improvement on performance (B.1.b.(i)), as additional power is available from the pitch response of the hammer moving relative to the node. However there does not appear to be any significant change for the concepts where the surface piercing member is rigidly connected to the node (B.1.b.(ii), or B.1.c), which indicates that the presence of the surface piercing component is not increasing the response of the node itself, only adding an additional axis for extracting power.

Analysis for these options was only carried out on a Squid array in order to give an initial impression of any potential benefit. The only option that showed significant improvement was for the Active Hammer (B.1.b.(i)), but as this concept requires additional pumping modules and increases the overall complexity of the device, it was not explored further. However it did highlight that an increased node pitch response has a beneficial impact on performance; this result has been explored further in the 2nd stage analysis.

5.3.2 2nd stage concept analysis

Figures 5.7 and 5.8 provide comparisons of the power output and the force generation for the 2nd stage analysis concepts, comparing options C.1 (Conical/surface node), C.2 (Planar conical node) and C.3 (Planar riser) against the B.4 (Ball Joint concept), as this was highlighted as the preferred option from the 1st stage of analysis (giving good power output, with low structural forces, and evidence of improvement in array size).

Figure 5.7 (a) shows the $\%AEP_{req}$ against PTO torque for all the 2nd stage options for a 1Hex array configuration, and shows that there appears to be significant improvement in performance for the planar conical node concept (C.2), with the required performance being achieved at low torque limits. There is a slight increased benefit to replacing the sunken node with a conical surface piercing node, but the lightweight riser concept does not give the required levels of performance for any array or torque level. Figure 5.7 (a) shows the $\%AEP_{req}$ for option C.2 for the three different array configurations, showing a slight performance improvement with array size.

Figure 5.8 shows the link arm utilisation factors for concepts B.4, C.1 and C.2 and show that while there is a slight increase in bending utilisation factors for concepts C.1 and C.2, these

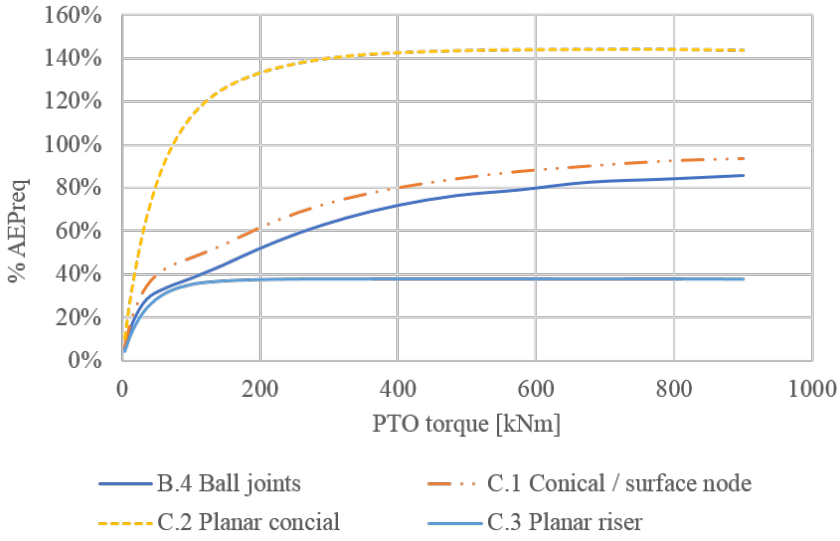

(a) Comparison of different options – modelled with a 1 Hex array

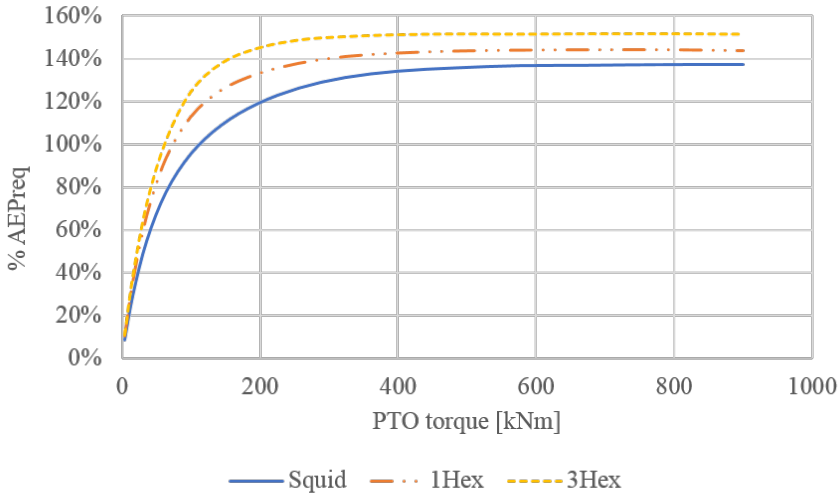

(a) Comparison of option C.2, modelled at different array scales

Figure 5.7: Node comparison, $\%AEP$ vs PTO damping

are not a great cause for concern, as the UF_{LA} is still less than 1 up to damping levels of around 6000kNm.

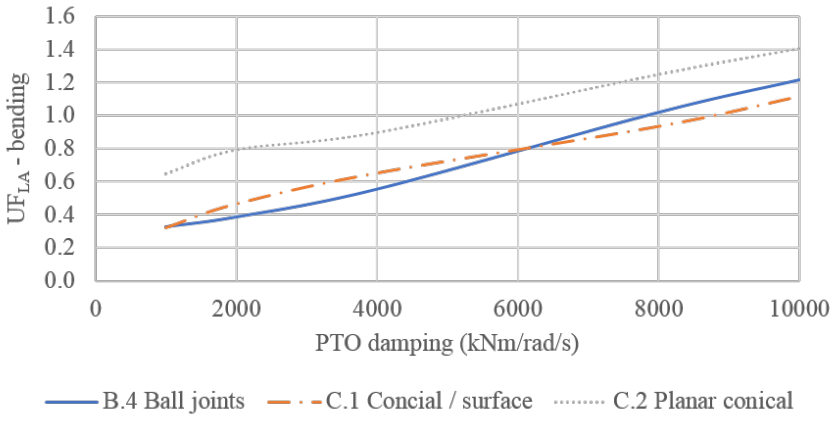

(a) Bi-axial bending moment

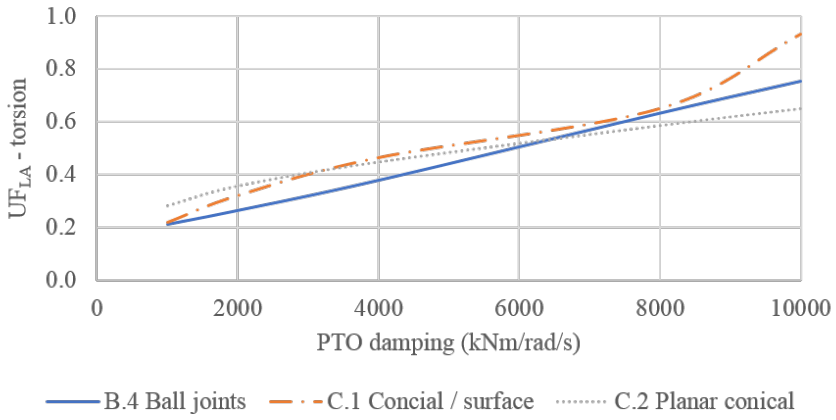

(b) Torsion moment

Figure 5.8: Node comparison, link arm utilisation vs PTO damping. If $UF_{LA} \geq 1$ link arm could fail, and link arm cross section should be increased.

5.4 Decision matrix results

Note: Decision matrices have been developed by the author, using input from the wider Albatern team as highlighted in previous sections.

Tables 5.4 to 5.6 summarise the different concepts as discussed in the previous sections based on the assessment criteria set out in Section 5.2.

Tables 5.7 and 5.8 and show the final Decision Matrices.

Table 5.4: Comparison table for 1st stage assessment concepts

Top level concept	A.1 Base Case (2x 6s)	B Concrete base case			
Variant		**B.1 Single PTO High Stiffness OP**	**B.2 Single PTO Low stiffness OP**	**B.3 Secondary PTO**	**B.4a Ball joints**
% of required performance achieved	SQ: 27% 1Hex: 65% 3Hex: 80%	SQ: 95% 1He: 110% 3Hex: 110%	SQ: 50% 1Hex: 80% 3Hex: 75%	1Hex: 95%	SQ: 67% 1Hex: 85% 3Hex: 110%
Torque level related to 100% performance*	SQ: 400kNm 1Hex: 400kNm 3Hex: 600kNm	SQ: 900kNm 1Hex: 900kNm 3Hex: 640kNm	SQ: 200kNm 1Hex: 900kNm 3Hex: 900kNm	SQ: 1Hex: 900kNm 3Hex:	SQ: 900kNm 1Hex: 900kNm 3Hex: 600kNm
Evidence of array improvement?	Yes – strong	Yes - slight	V. slight, as arrays perform better than squid	Only 1Hex considered	Yes - strong
Force assessment	**Bending UF> 1.5** for 1 and 3 Hex for most damping levels	**Bending UF between 1 and 3** for most damping levels. Torsion forces increase with array size, **Torsion UF> 1** for most damping levels for 3Hex	Generally lower forces than A and B.12. **Bending and torsion UF > 1** above damping of 6000kNm for 1 and 3 Hex	Similar to low stiffness case (B.2)	Lowest UF of all initial concepts. **Torsion UF always <1, bending UF < 1** for damping lower than 8000kNm for 1 and 3Hex
Constructability issues	Well understood – similar to 6S	High stiffness difficult to achieve in reality		More complex joint module required for 2 DoF PTO	More complex joint module required for 3 DoF PTO
Installation	Difficulties with raising squid from horizontal towing to vertical	Relatively simple with links and nodes that connect at surface level	Relatively simple with links and nodes that connect at surface level	Relatively simple with links and nodes that connect at surface level	Relatively simple with links and nodes that connect at surface level
O & M	Similar issues to installation if squid module needs to be removed	Increased modularity improves O&M procedures	Increased modularity improves O&M procedures	Increased modularity improves O&M procedures	Increased modularity improves O&M procedures

* Where 100% of required performance is not achieved for a particular array, torque level present relates to the torque level for the maximum performance level achieved

Table 5.5: Comparison table for 1st stage assessment variants

Top level concept	B. 1 Concrete base case (high stiff)		
Variant	B.1.b(i) Hammer, active PTO	B.1.b(ii) Hammer, rigid joint	B.1.c Riser
% of required perf. achieved	SQ: 110%	SQ: 95%	SQ: 98%
Torque level related to 100% performance*	SQ: 400%	SQ: 900kNm	SQ 900kNm
Evidence of array improvement?	Only squid considered	Only squid considered	Only squid considered
Force assessment	Similar to B.1	Similar to B.1	Similar to B.1
Constructability issues	Increased complexity for construction due to additional component	Increased complexity for construction due to additional component	Increased complexity for construction due to additional component
Installation	Increased complexity for installation due to additional component	Increased complexity for installation due to additional component	Increased complexity for installation due to additional component
O & M	Increased complexity for O&M due to additional component	Increased complexity for O&M due to additional component	Increased complexity for O&M due to additional component

Table 5.6: Comparison table for 2nd stage assessment

Top level concept	C. Node comparisons		
Variant	C.1(i) Conical / surface node	C2 (i) Planar Conical node	C3 Planar riser
% of required perf. achieved	SQ: 80% 1Hex: 92% 3Hex: 120%	SQ: 138% 1Hex: 144% 3Hex: 151%	1Hex: 38% 3Hex: 37%
Torque level related to 100% performance*	SQ: 900kNm 1Hex: 900kNm 3Hex: 500kNm	SQ: 100kNm 1Hex: 100kNm 3Hex: 100kNm	SQ: 1Hex: 200 3Hex: 200
Evidence of array improvement?	Yes - strong	Yes – mild improvement	No
Force assessment	Slight increase in bending UF compared to B.4, but still < 1 for most damping levels	Increase in bending UF compared to B.4, but still < 1 for damping levels up to 6000kNm	Not assessed directly due to low power, but utilisation factors are assumed to low
Constructability issues	More complex node shape, and using different node shapes increases construction complexity	More complex node shape, but all nodes are the same	Simpler node shape to construct
Installation	Underwater connection for link arm / ode, and connections on different levels	Underwater connection for link arm / node	Underwater connection for link arm / node. Uncertainty about method for towing and installing riser.
O & M	More difficult to navigate through array due to shallow link arm angle	Planar link arm allows boat navigation through array	Planar link arm allows boat navigation through array

Table 5.7: Decision matrices, 1st stage assessments

Criteria	Weighting	A1 Base Case	B Concrete base case			
			B1 Single PTO High Stiffness	B2 Single PTO Low stiffness	B3 Secondary PTO	B4 Ball joints
% of required perf. achieved	5	2	4	2	2	3
Torque level related to 100% performance*	4	1	2	1	1	2
Evidence of array improvement?	2	3	2	1	2	3
Force assessment	3	2	1	3	4	5
Constructability issues	1	4	4	5	4	3
Installation	2	1	5	5	4	4
O & M	2	1	5	5	4	4
	Total	**34**	**59**	**50**	**50**	**63**

Table 5.8: Decision matrices, 2nd stage assessments

Criteria	Weighting	C Node comparison options		
		C.1(i) Conical / surface node	C2 (i) Planar Conical node	C3 Planar riser
% of required perf. achieved	5	3	5	1
Torque level related to 100% performance*	4	2	3	1
Evidence of array improvement?	2	3	2	3
Force assessment	3	4	4	5
Constructability issues	1	1	2	3
Installation	2	2	3	2
O & M	2	2	3	2
	Total	**50**	**67**	**41**

5.5 Summary and discussion

The concept development work described in the previous sections has highlighted that the following options have achieved the highest scores.

- B4 Modular concept with ball joints: **Decision Matrix Score = 63**
- C2 Planar conical node concept: **Decision Matrix Score = 67**

Due to the limitations of the simplified concept design process, and the uncertainties in the modelling process, it would be preferable to take both options forward for detailed design. However, time and budgetary constraints meant that Albatern needed to focus ongoing design work on just one option; therefore Option C2 was chosen as the preferred option. This option is the focus of the rest of the work detailed in this thesis; a schematic of the option is shown in Figure 5.9 (note this figure was included in the Introduction, and for clarity has been reproduced here).

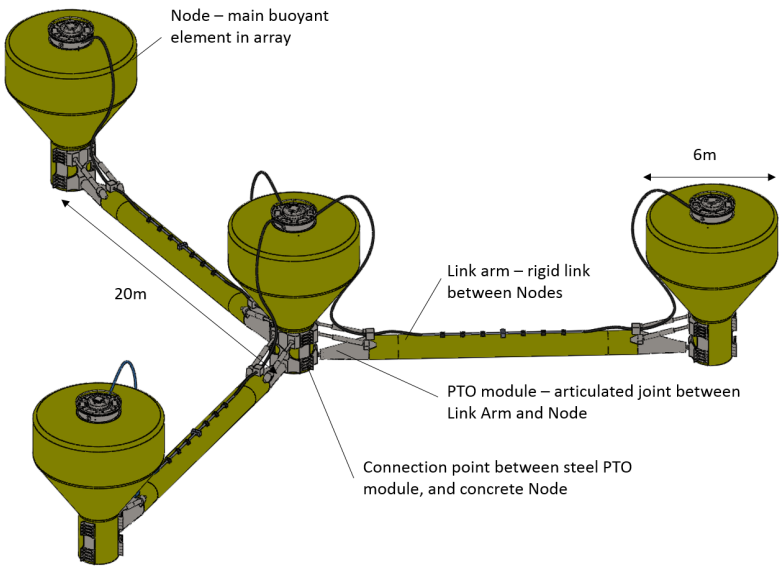

Figure 5.9: 12S preferred design concept

The main features of this option are as follows:

- Conical shaped nodes, each with connection points for three link arms.
- “Planar" array system - i.e. all link arm connection points are at the same level, beneath the water surface, in contrast to the 6S array, which had surface and subsurface connection points at the nodes and anti-nodes.
- Node dimensions: Max diameter = 6.5 m, Depth to link arm connection point 7 m, Node to node distance = 21 m
- PTO system capable of taking power out of each of the three axis of rotation (referred to as the “Ball Joint” connection.)

Chapter 6

Concept modelling activities for load definition

Chapter 5 concluded that a planar array system, with conical Nodes, and a Ball Joint Power Take Off (PTO) system (capable of extracting power about three axes of rotation) gave the best compromise between power generation capability, low structural loading, and acceptable construction, installation and operation and maintenance (O&M) methods.

The next step in the concept development process is to define a set of design loads for the device. This chapter describes the modelling activities carried out to determine the PTO loads, which feed into the design activities for the Node structure covered in Part III. The aim of this section is to extract and compare the relevant data from the different models, in order to derive preliminary design loads for the 12S WaveNET array.

The WaveNET array is a novel multi-body system, with complex behaviour due to the interactions between the inter-connected bodies, and the attempt to capture power about multiple degrees of freedom, at multiple locations throughout the array. While the modelling described in this chapter is preliminary in nature, the analysis of results provides insights into modelling procedures and device behaviour that could be useful to others looking to develop similar array systems.

The structure of this chapter is as follows:

- The context of the modelling work is set out in **Section 6.1**
- Tank testing activities carried out on the 1:18 scale physical model are discussed in **Section 6.2**.
- An overview of the numerical modelling work is provided in **Section 6.3**.
- The model results are presented in **Section 6.4**, with the aim of highlighting the most appropriate data to be carried forward for ongoing design work. Particular focus is given to comparing time and frequency domain fatigue analysis methods, using the results from the two models to identify which are the most suitable for the design of multi-body, floating WECs.
- A discussion of the work is presented in **Section 6.5**, together with conclusions that can be drawn from the work.

6.1 Modelling Context

Numerical models provide the main tool for deriving design loads for wave energy converters (WECs), particularly for operational sea states, as they allow a large number of conditions to be covered that would not be feasible in a physical model or at full scale. However, to have confidence in the results it is important to validate the models using real data extracted from either tank testing at scale or full size prototypes.

To gain an initial insight into the overall performance and behaviour of the 12S array, the following preliminary modelling activities were carried out during the concept design phase:

1. Physical modelling of an 1:18 Froude scale array model, carried out at the FloWave Ocean Energy Research Facility at the University of Edinburgh (FloWave). The 1:18th scale was chosen as this was the largest scale that could realistically be modelled in the tank;
2. Preliminary numerical modelling in ANSYS Aqwa (Ansys AQWA, 2013) set up with the same properties as the physical model.

The intention was to use the conclusions from the preliminary models as inputs for more detailed modelling work. However, as the 12S development was halted this was not carried out, therefore there is a number of limitations with the available load data. Carrying out further validation activities to improve the data quality is beyond the scope of this IDCORE project and therefore the model results are used as is to develop relevant load cases for the ongoing design work.

Completion of the modelling activities required a wide range of skills, and therefore included input from a number of Albatern team members. Full descriptions of the methods used are included in this chapter for completeness; where work has been carried out by others this is clearly indicated and acknowledged within the relevant section.

6.2 Tank testing methodology

Tank testing for the 12S array was funded by Wave Energy Scotland (WES) as part of the Novel Wave Energy Converter (NWEC) programme (Wave Energy Scotland, 2016*b*). The WES project requirement was to characterise the device power absorption capabilities based on a specified set of design waves; this was the primary focus for the experimental design. The secondary focus was to gather enough data to allow for validation of the numerical models which could be then refined and used to derive detailed design load cases. Testing was carried out on a 1:18th Froude scale model at Flowave, as shown in Figure 6.1.

The model consists of Node and Link elements connected via a ball joint. Each link arm has five degrees of freedom (pitch and yaw rotation at each end, and torsion rotation at the centre as shown on Figure 6.2), with motions controlled through the use of electric motors.

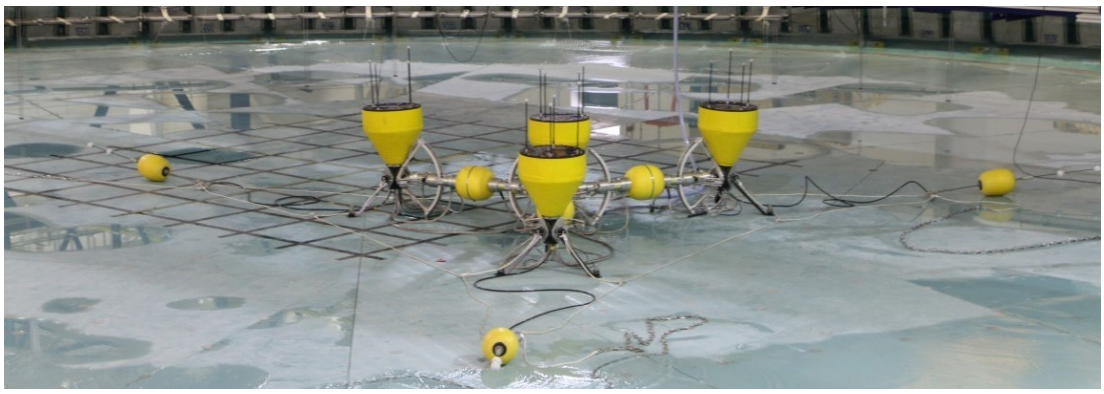

Figure 6.1: Squid configuration on tank floor at Flowave

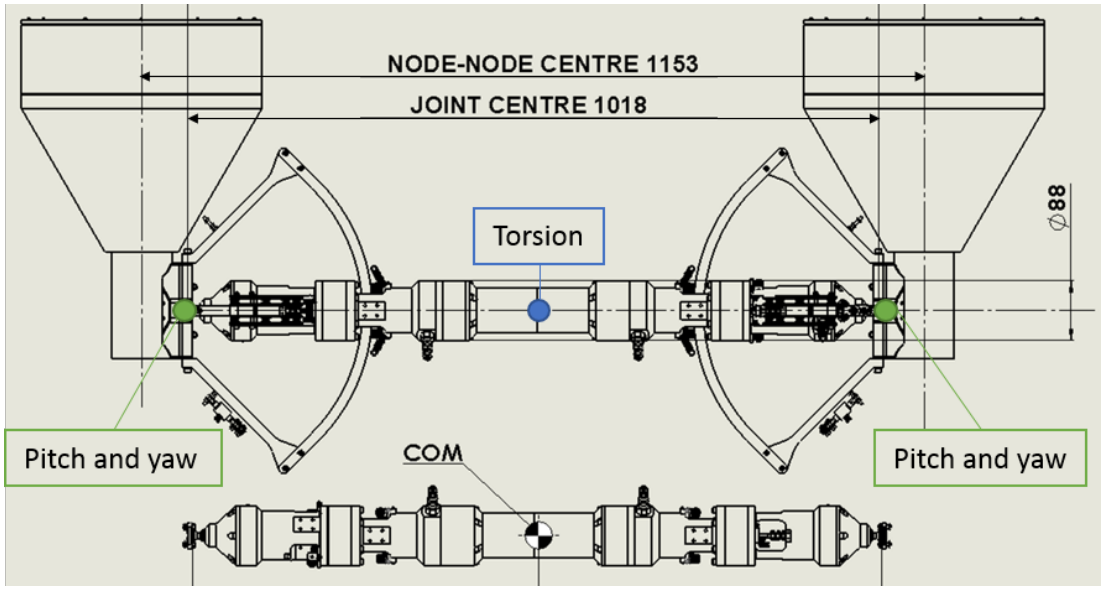

Figure 6.2: Node and link configuration, showing link arm degrees of freedom. Dimensions in mm *Drawing credit : Graham Terry*

Two sets of test were conducted: the first with a single Squid configuration (4 nodes and 3 links as seen in Figure 6.1), and the second with a full 1 Hex array (9 nodes and 9 links, as shown in the schematic in Figure 6.3). The purpose of the first set of tests was to get an idea of the behaviour and control of the model, and to troubleshoot any issues before carrying out tests on the full 1 Hex array. All analysis in this chapter uses results from the 1 Hex array system as this gives the most complete set of loading information. The naming convention is shown in Figure 6.3.

The link arms and articulations aligned with the wave direction (LA2, LA5 and LA8) are classed as “In-line”. Each node is categorised as a either “Singler” (S) with one attached link arm, a “Doubler” (D) with two attached links, or a “Central” node (C) with three attached links. Both the Squid and 1 Hex array were moored using a scaled mooring grid, with three

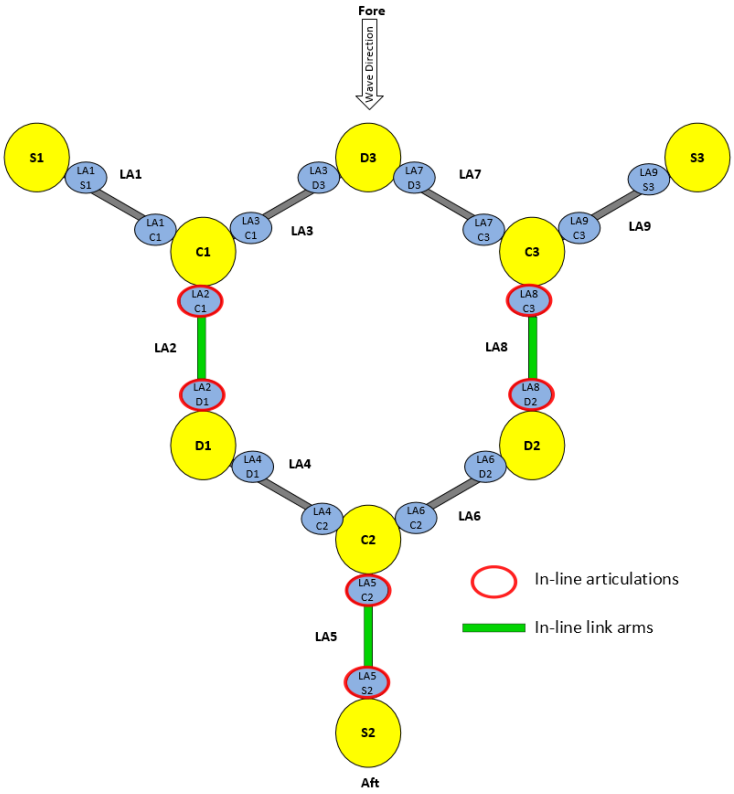

Figure 6.3: 1 Hex model naming conventions

catenary mooring legs attached to the tank floor. A mooring grid schematic for the 1 Hex array is shown in Figure 6.4.

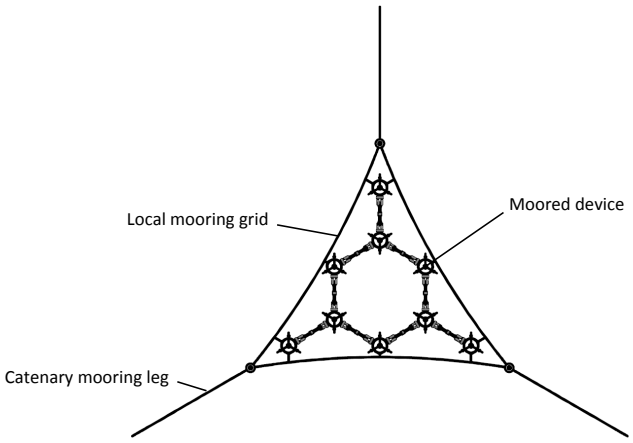

Figure 6.4: Mooring grid schematic

The design, set up and running of the testing involved a large number of the Albatern team, as listed below:

Overall technical lead David Findlay (Albatern CTO)
PTO design Alex McMillan (MSc Student) with Gregory Payne (external consultant)
Control system design Bin Li (Electrical Engineer) and Calum Kenny (IDCORE student)
Model design and build Graham Terry (Mechanical Engineer), Yan Gunawardena (Operations Manager), Hector Fleck (Workshop Manager)
Running of tests, and data processing Vivien Mavel (Hydrodynamic Modeller) and Anthony McDonald (IDCORE student)

The contribution of this research project included the selection of appropriate test sea states (discussed in Section 6.2.2), and design of the load measurement system (discussed in Section 6.2.3). In addition, all data analysis work included in this thesis relating to the tank testing is the author's own work.

6.2.1 Power take off simulation

Note: PTO design (including control and instrumentation) was carried out by others

The PTO mechanism at each joint damps the relative motion of the node and link around three degrees of freedom. This is achieved in the model using multiple high torque DC brushless Maxon motors. Each link arm contains five motors: two at each end resisting the motion in the pitch and yaw axis, and one in the centre resisting motion around the torsion axis. The motors were controlled to provide linear damping at each articulation, and wire drive mechanisms were included at the pitch and yaw axis to provide the relevant gearing, as can be seen in Figure 6.5.

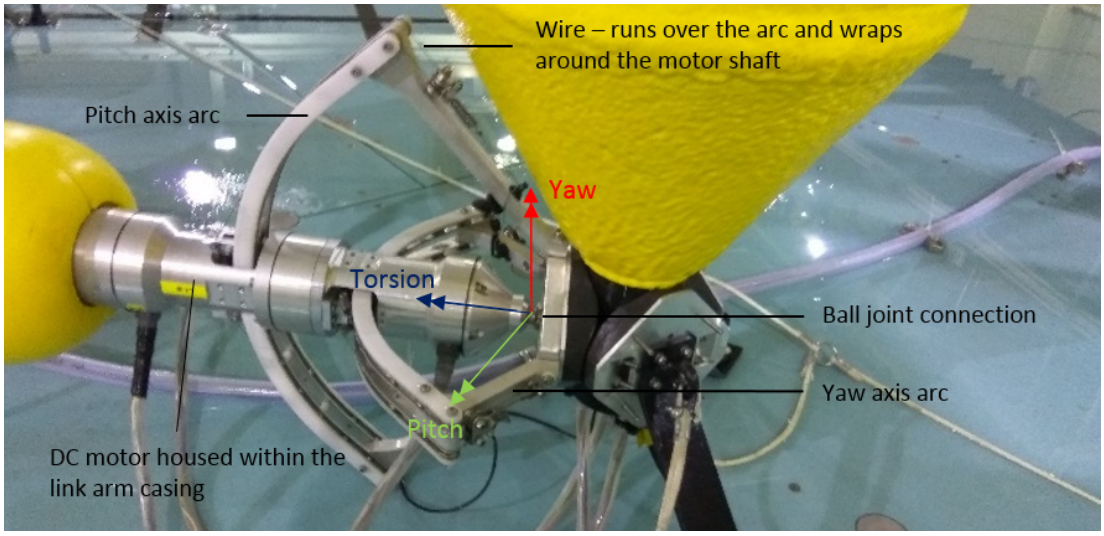

Figure 6.5: Wire drive mechanisms for tank testing model (for simulation of the PTO system)

6.2.2 Test Sea States

Note: Selection of relevant sea states and input into the test programme was carried out by the author as part of this research project.

Array behaviour and power output varies depending on the characteristics of the deployment site. A location off the west coast of the Isle of Harris (referred to as West Harris) was used as the reference site for the modelling.

Figure 6.6: West Harris commercial site location for the 12S array

The device was tested in 11 regular sea states and 21 irregular sea states as show in Tables 6.1 and 6.2. These were chosen to cover the operational range of the device, and also to fit in with the standard sea states specified by WES (highlighted in bold).

Table 6.1: Regular test sea states

H (m) / T(s)	5.5	6.5	7.5	8.5	9.5	10.5
4.5			**X**			
3.5		**X**	**X**	**X**		
2.5			**X**			
1.5	**X**	**X**	**X**	**X**	**X**	**X**

Table 6.2: Irregular sea states (Jonswap, gamma = 1)

H_s (m) / T_p (s)	7.7	9.1	9.9	10.5	11.9	12.6	13.3	14.7
4.5			**X**	**X**				
4								
3.5		X		**X**			**X**	
3			X			X		
2.5	**X**		**X**			X		
2	X	X		X		**X**		
1.5	**X**	X		**X**			**X**	**X**
1	X		X					

(a) Regular waves

The purpose of the regular wave tests was to:

- obtain information on behaviour of the device under regular excitation forces;
- provide a comparison against irregular wave runs in the numerical model simulations.

The regular tests were specified by WES; no additional tests were included as these covered enough sea states to obtain Response Amplitude Operators (RAOs) for the joint motions and to develop an initial power matrix based on the assumptions of linearity.

(b) Irregular waves

The purpose of the irregular wave tests was to:

- to obtain more detail on behaviour and performance of the device in real sea states;
- to validate extension of frequency domain model to time domain.

Sea states were chosen to cover the range of likely productive seas. A number of tests were specified at each wave height and period, to allow extrapolation of the results across the occurrence matrix (as recommended in Holmes, 2009). All tests were run with a general Jonswap spectra for a minimum of 200 waves, as this is sufficient to give an indication of power production capabilities (Ingram et al., 2011), while still allowing time for a number of tests to be carried out. The test sea states are overlain on the West Harris wave occurrence matrix in Figure 6.7, which shows the number of waves likely to occur in a single year for each sea state.

Hs / Tp	3	4	5	6	7	8	9	10	11	12	13	14	15	16	17	18	19	20	21
12.0	0	0	0	0	0	0	0	0	0	0	0	0	0	0	0	0	0	0	0
11.5	0	0	0	0	0	0	0	0	0	0	0	0	0	0	0	0	0	0	0
11.0	0	0	0	0	0	0	0	0	0	0	0	0	0	0	0	0	0	0	0
10.5	0	0	0	0	0	0	0	0	0	0	0	0	0	0	1	0	0	0	0
10.0	0	0	0	0	0	0	0	0	0	0	0	2	0	1	0	0	0	0	0
9.5	0	0	0	0	0	0	0	0	0	0	0	5	3	2	4	0	0	0	0
9.0	0	0	0	0	0	0	0	0	0	0	1	3	9	9	4	0	0	0	0
8.5	0	0	0	0	0	0	0	0	0	0	1	10	9	14	3	1	0	0	0
8.0	0	0	0	0	0	0	0	0	0	0	2	18	22	21	7	0	0	0	0
7.5	0	0	0	0	0	0	0	0	1	7	8	39	31	25	2	0	0	0	0
7.0	0	0	0	0	0	0	0	0	1	7	25	67	44	20	3	0	0	0	0
6.5	0	0	0	0	0	0	0	0	2	36	33	78	54	21	15	3	0	0	0
6.0	0	0	0	0	0	0	0	2	9	57	66	83	55	30	8	1	0	0	0
5.5	0	0	0	0	0	0	0	5	30	127	129	155	62	17	8	0	0	0	0
5.0	0	0	0	0	0	0	2	8	76	244	194	168	73	23	4	0	0	0	0
4.5	0	0	0	0	0	0	9	50	203	381	255	198	48	14	8	2	0	0	0
4.0	0	0	0	0	0	6	53	160	450	454	223	211	76	21	6	3	0	0	0
3.5	0	0	0	0	1	35	94	352	656	564	255	192	64	19	17	2	0	0	0
3.0	0	0	0	1	13	115	302	790	755	603	249	113	58	21	11	2	0	1	0
2.5	0	0	0	4	33	256	637	1083	860	558	175	109	47	15	13	5	0	2	0
2.0	0	0	0	36	179	640	1271	1175	699	401	117	101	42	26	6	3	0	0	0
1.5	0	0	38	111	429	1319	1251	1077	639	276	83	63	29	14	12	3	0	0	0
1.0	0	13	102	273	764	1220	879	442	274	74	42	17	24	11	5	2	0	0	0
0.5	1	37	73	104	264	183	128	91	38	25	6	6	2	1	1	0	0	1	0

Figure 6.7: West Harris occurence matrix. Tank test runs carried out with regular waves are shown in blue, irregular wave tests are highlighted in purple.

The primary purpose of the testing was to verify the power production capability of the device, and therefore the tests were limited to operational sea states: no extreme seas were tested, as the scale of the device was too large to generate storm conditions within the tank.

Further information about extreme loads could be gained from carrying out additional testing at a smaller scale, but this has not been undertaken as part of this thesis.

6.2.3 Sensor measurement design

Note: Sensor design was carried out by the author as part of this research project

This section discusses the design of the sensor system for the tank test model. The following parameters were required to be measured during tank testing:

- Mechanical power output: product of articulation torque and joint velocity[1];
- Mooring forces
- Link arm cross sectional forces

Options for each of these requirements are discussed below.

(a) Output power

Power measurement was an essential part of the tank testing programme, as assessing device performance was the primary aim of the tests. The motor output at each articulation gave an initial measure of the power output. However, the relationship of joint torque to motor torque was dependent on the location of the link arm and the effectiveness of the gearing system. Deriving the exact joint power output would require derivation from the motor characteristics, with careful consideration of any potential non-linearities.

It was therefore important to provide a secondary measure of power based on the actual torques and angular velocity of the joint to verify the motor power. In addition, the articulation torque gives a more accurate picture of the structural loads and is a parameter that can be easily compared to the outputs of the numerical models.

A discussion of the torque measurement options is included in Table 6.3. The final decision was driven primarily by cost, as the model required a lot of sensors, but the overall build had to come within a specified budget. Single degree of freedom sensors are significantly cheaper than multi-axial ones, and therefore the preferred option was to use in-line tension sensors on the wire drives (see Table 6.3 Option 2).

For accurate load measurement it would have been preferable to include two loads cells at each axis, one at each end of the wire, however it was not possible to do this at every joint and keep within budget. The maximum torques occur in pitch at the in-line link arms (LA2, LA8 and LA5 in Figure 6.3). Therefore, two load cells were included at the articulation points on these links, to allow accurate measurement of the maximum loads. A single cell was included to allow estimated torques to be calculated at the other articulations. This gave enough

1. The joint velocity was derived from the 6 DoF position of each node, which was measured using the Qualysis system designed and implemented by Flowave staff.

information to assess the power output to a significant degree of accuracy without an unreasonable amount of cost. Figure 6.8 shows a schematic of the joint mechanism, showing the location of the tension load cells.

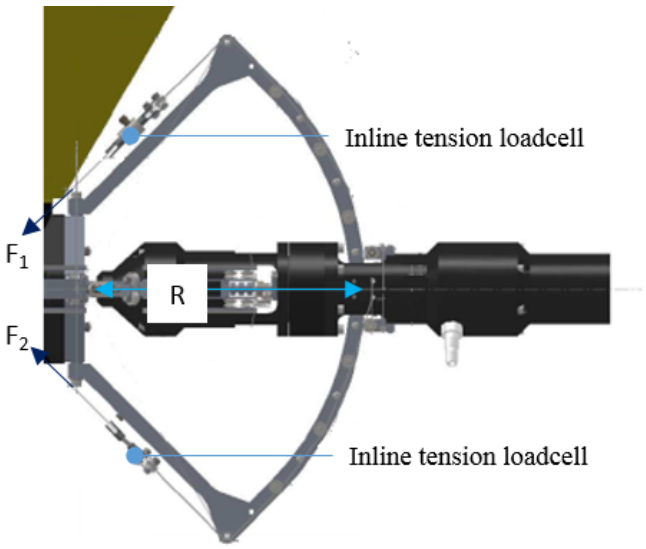

Figure 6.8: Link arm end torque measurement

The specification for the inline sensors required at the joints were based on the work done to design the wire drive gearing system (carried out by others) which gave the following requirements:

- Required measurement: In-line Tension
- Maximum constant pre-load: 35N
- Max variable tension range: +- 12N
- Size constraints: Needs to be as small as possible to fit into model

(b) Mooring forces

The tension of each catenary mooring leg was also measured, to allow the correct pre-tension to be set, provide further understanding of the device behaviour, and to give information for numerical model validation. The required range for the mooring load cells was derived from the numerical models of the full-scale device which have the preload set at 220kN, with +/- 150kN variation in the worst-case waves (H_{max} = 14 m). At an 1:18 model scale this gave the following specification:

- Required measurement: In-line Tension
- Maximum constant pre-load: 37.7 N
- Max variable tension range: +- 25.7N
- Size constraints: Needs to be as small as possible to fit into model
- No required (one per catenary mooring line): 3

Table 6.3: Options for end articulation torque measurements

				Squid		1Hex				
ID	Description	Measurements	No / joint	No joints	Total	No joints	Total	Advantages	Disadvantages	Typical sensor cost
1	Directly measure torques at ball joint	Mx, My, Mz	3	6	18	18	54	Direct measurement, minimal uncertainty	Did not find a way to directly measure torque at the ball joint	N/A
2	Calculate torques from tension in the wire drive gearing system. Measurement at both ends of wire	Fx on each wire end, (two per joint in each of pitch and yaw direction)	4	6	24	18	72	Single dof sensors significantly cheaper than multiple axis solution. - Some derivation of forces required from position of joint, but less uncertainty than from motor characteristics	Need careful consideration about where to locate sensors so as not to hinder movement of joint -Many sensors required	£215 per tension sensor £15480 in total
2a	Calculate torques from line tensions and position. Measurements at only one end of wire	Fx on each wire end, (one per joint in each of pitch and yaw direction)	2	6	12	18	36	-Fewer sensors required. Can use all the sensors when testing the individual squid model in order to fully characterise the behaviour of the joints, then use this information to derive the torques on the 1 Hex model when only using 1 sensor per joint	-Wire tension will not be the same on either side of the motor due to losses in the system. Will need to derive full torque measurements from overall joint behaviour	£215 per tension sensor £7740 in total
3	Derived from min 4 dof measurement at link arm centre	My, Mz, Fy, Fz	4	3	12	9	36	Only requires single sensor at centre of link arm	-Derivation of torques at a particular point based on forces at centre of link arm based on the assumption of static equilibrium; not directly valid - ignores dynamic effects which are likely to be significant -V. Expensive to get 4 dof sensors	Submersible multi-axis sensor - £2500 each (minimum) up to £6000 for full 6 dof measurement. Total cost - £18000 to £54000
4	Derived from torque at link arm centre, and shear at joint	Fy, Fz, @ joint	2	6	12	18	36	More measurements used in derivation of torque than for option 3, therefore uncertainty reduced	Increased amount of sensors required. 3 dof torque sensors v. expensive	£3795 for 3 dof submersible torque sensor -
		Mx,My, Mz @ link arm centre	3	3	21	9	63		Still get some uncertainty due to dynamic effects	£34155 in total

(c) Link arm cross sectional forces

In addition to torque measurements at the link ends, it is also advantageous to measure the loads at the link arm centres. Different options for this are included in Table 6.4; on the basis of this information, a reaction torque sensor was included to measure the torsion load within the link, and to provide a check against the output from the torsion motor.

Table 6.4: Link arm for measurement options

Measurements	Cost	Comment
Full 6 dof sensor (M_x, M_y, M_z, F_x, F_y, F_z)	£6000 per unit	Prohibitively expensive
3dof torque sensor (M_x, M_y, M_z)	£3965 per unit	Cheaper than 6 dof, but still very expensive
Submersible tension / compression cells (F_x)	£685	Cheaper than multi-axis, but axial force only is not that interesting
Torsion only reaction torque sensor	£346.50	Can be directly compared with torsion motor ouptput
Use of individual strain gauges	~£100 for pack of 10	Cheap, but complicated fixing, cabling and processing requirements.

(d) Final load measurement instrumentation

The final instrumentation used for load measurement is detailed in the Table 6.5. Locations of the sensors are shown in Figure 6.9.

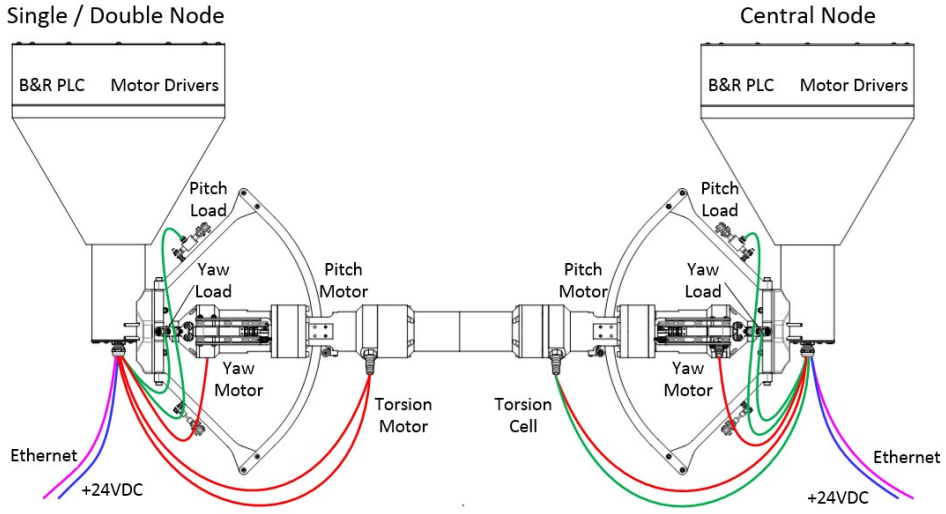

Figure 6.9: Sensor Location (*Drawing credit: Graham Terry*)

Table 6.5: Details of instrumentation used for load measurement

Parameter	Specifications	
PTO Torque (Pitch, Yaw axis)	**Inline Load Cell** • 0-50N measurement capacity • Full bridge strain gauge output, requires excitation, calibration voltage 10VDC • IP68 sealing to 10m	Applied Measurements: DDEANA4H-50N-005-000 
PTO Torque (Torsion axis)	**Torsion Cell** • 0-5.65Nm measurement capacity • Full bridge strain gauge output, requires excitation, calibration voltage 10VDC • Clockwise and Anticlockwise output, aluminium construction, shaft mountable	Futek: FSH00608-TFF325 
Mooring tension	**Submersible Load Cell** • 0-200N measurement capacity • 4-20mA conditioned output • IP68 sealing to 10m	Applied Measurements: DDEAT-200N-002-000 

6.2.4 Power capture

The measurement system discussed in Section 6.2.3 gives two different methods for measuring the power captured in the array. The electrical was calculated from direct measurements of the motor current and angular velocity, as shown below:

$$Torque_{motor} = C_t.I_m \qquad Power_{elec} = Torque_{motor}.\omega_{link} \tag{6.1}$$

where C_t = motor torque constant, I_m = current, ω_m = angular velocity of the motor. The mechanical power was calculated using the direct measurements of torque using the in-line load cells ($Torque_{link}$), together with the angular velocity of the motor;

$$Power_{mech} = Torque_{link}.\omega_m \tag{6.2}$$

An accurate measurement of the mechanical power is only possible at the articulations with two load cells, therefore the total reported power capture is:

$$= \Sigma(Power_{mech})_{in-line} + \Sigma(Power_{elec})_{all-other}$$

. $Power_{mech} > Power_{elec}$ due to losses in the system associated with the PTO model set up, therefore this method gives a conservative estimate of the potential power capture.

6.2.5 Damping Optimisation

During testing, different values of linear damping were applied at each sea state to identify the optimum value for power output. The torsion damping was held at a constant value, and the pitch and yaw damping was varied between 500-6000 kNms/rad (full-scale). The optimum damping levels for each test sea state are shown in Table 6.6.

Table 6.6: Optimum damping values for compulsory irregular sea states (kNms/rad full-scale)

H_s (m) / T_p (s)	7.7	9.1	9.9	10.5	11.9	12.6	13.3	14.7
4.5			5000	5000				
4								
3.5		5000		5000			3000	
3								
2.5	4000		3000					
2	4000	3000		3000		2000		
1.5	2000	2000		1000			500	500
1	1000		1000					

6.2.6 Model limitations

While every effort was made to create a realistic scaled replica of the full-scale device there were several limitations with the model set up. In particular:

- The wire drive arcs add hydrodynamic drag and damping that will not be present on the full-scale device. While they were designed to be hydrodynamically transparent, it is clear from decay tests carried out (by others in the Albatern design team) with and without the arcs that they have a significant impact on the node properties. The additional damping dissipates the incoming wave energy and therefore is likely to reduce the articulation loading compared to a full-scale device.
- The wire drive adds friction into the system that would not be present in the full-scale device, and results in large losses between the mechanical torque measured by the load cells, and the electrical motor torque. The additional friction adds to the overall damping of the joint, and acts to increase the articulation loading.

Unfortunately, it is not possible to quantify exactly how this effects the model results compared with the full scale device, and it is outside the scope of this project to refine the models. This thesis therefore assumes that the data provided is accurate enough to allow preliminary design work to be carried out, which can then be used as a starting point for further development as and when more accurate load data becomes available.

In addition to the model limitations, there are also limitations imposed by the chosen damping strategy for the motors. For simplicity, the applied PTO damping was linear (proportional to the angular velocity) and unlimited in magnitude. For the full-scale device the damping characteristics will be more complicated; even if perfect linear damping was achievable, the amount of torque that could be generated would be limited to avoid damaging the PTOs.

6.2.7 Data limitations

As discussed above, the main purpose of the tank testing was to prove the power generation capabilities, and load data acquisition was limited due to budget and practical constraints. As discussed in Section 6.2.3, most articulation joints only had one in-tension sensor. The intention had been to be derive torque estimates at these locations using information from the double load cells, and further dry tests to investigate motion characteristics of the wire drive systems. However, these dry tests were never carried out, and efforts to determine an estimate based on the tank test data alone (carried out by others) were unsuccessful. Power calculations were therefore carried out based on information primarily obtained from the motor output. This was deemed appropriate for the main purpose of the testing, but does mean that there is not enough tank test data to provide a full set of design loads. A summary of the available load data is shown in Table 6.7.

Table 6.7: Summary of load data from tank tests

Load action	Measurement locations	Comment
Pitch torque	In-linear articulations	Single load cell included on all other articulations, but data from these has not been used.
Yaw torque	N/A	Measured at all locations using single sensor, but required analysis to derive moment from the measurements has not been carried out.
Torsion	Link arm centre	Measured directly from torque sensors
Link arm axial force	N/A	Not measured in tank test model - to be taken from numerical model
Link arm shear force	N/A	
Node hull pressures	N/A	Not measured in tank test - to be calculated by hand.
Mooring loads	Top connection point of each mooring leg	

6.3 Numerical modelling methodology

Note: Numerical modelling work was carried out by others as part of the Albatern development work; a description is included here to provide context for the project, but full credit for the work in this section is given to Vivien Mavel and Anthony MacDonald.

A numerical model was set up to represent the physical model, which could be used as a tool for ongoing design work and parametrisation studies.

6.3.1 Model set up

An overview of the numerical model as set up in Ansys AQWA (Ansys AQWA, 2013) is shown Figure 6.10.

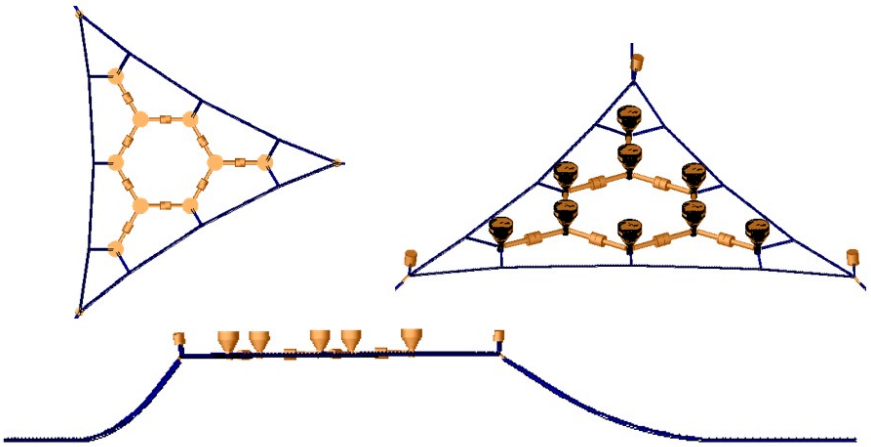

Figure 6.10: Snapshots of the 1Hex model with mooring system

The nodes are modelled as diffracting bodies with the geometry mass distribution and inertia equivalent to the tank test model nodes (at full scale). The wire drive arcs weight and inertia were included as part of the overall definition of the node, and a concentrated buoyancy force was applied at the articulations to accounted for the arc displaced volume. This modelling method does not include any viscous effects for the node, or the drag of the arc assemblies. To capture these effects additional linear damping terms were applied in heave, pitch and roll, using values established from decay tests on the individual node elements during physical testing.

The cylindrial link arms have a small diameter relative to the wave length and were therefore modelled as Morison tubes which account for the inertia and viscous forces from the waves but not for diffracting and radiating forces. The link arms are modelled with a torsion articulation at the centre. The mooring system has been defined using linear elastic

components with a given cross sectional area, mass per length, breaking strength and an axial stiffness.

6.3.2 Articulation characterisation

(a) Articulation set up

The model motion is controlled by the articulations between the Node and Link Arm bodies. In Aqwa, motion about an axis can be fixed, or free to move with specified stiffness and damping characteristics. For the WaveNET model the articulation at the link arm centre is defined with one degree of freedom along the link arm axis. The articulation between the link arms and the node is defined as a universal joint with two degrees of freedoms around the pitch and yaw axis. Articulation axis are defined in Figure 6.11.

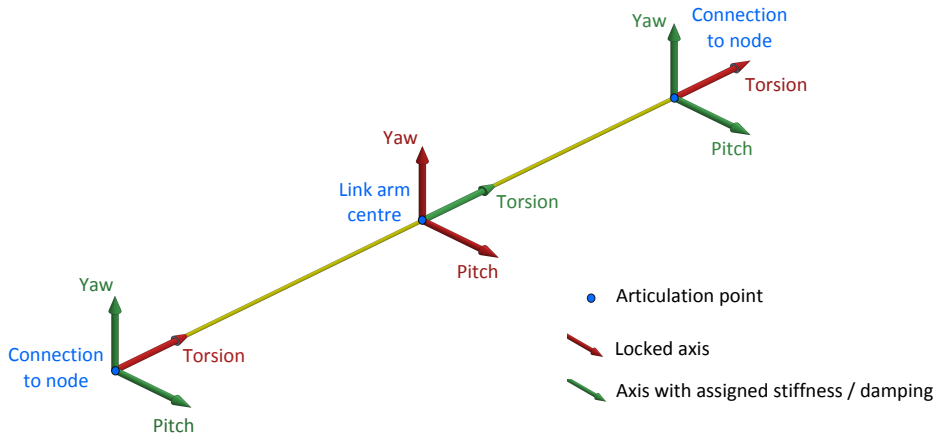

Figure 6.11: Numerical model articulation axis

Each axis of rotation is given a linear damping coefficient (in Nms/rad) to replicate the electrical damping applied in the physical model, and a friction coefficient (constant moment Nm, opposing the direction of rotation) to try and replicate the effect of the wire drives.

(b) Friction damping characterisation

To assess the friction at each articulation the physical model was run with a set of regular waves with no electrical damping applied. The graphs in Figure 6.12 show joint velocity vs mechanical torque for articulations LA2D and LA2C for illustration, and show that the behaviour is dominated by a friction effect, characterised by zero torque at zero velocity and a constant torque opposing the velocity at all other times.

The constant torque has been estimated as 2.7 Nm (283 kNm full scale) for articulation LA2C, LA5S, LA8C, and L8D; and 4 Nm (420 kNm full scale) for articulation LA2D. The difference at LA2D indicates that the wires were probably tighter than for the other articulations, resulting in a higher level of friction.

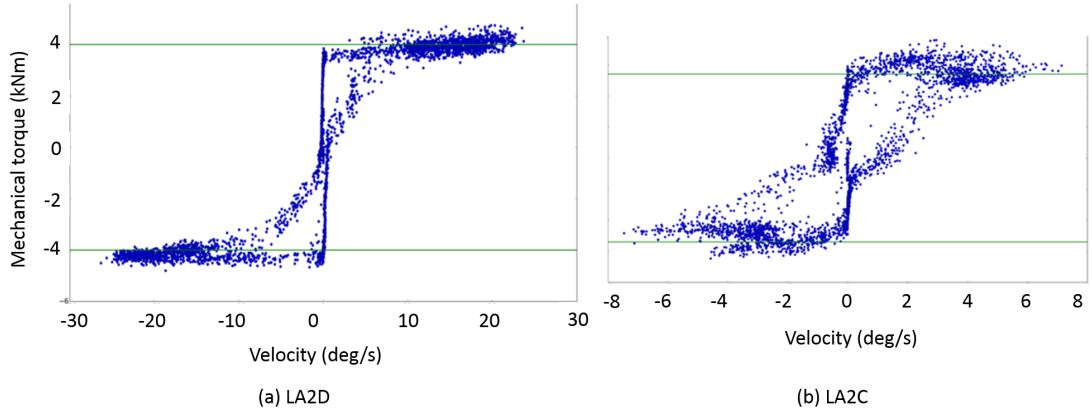

Figure 6.12: Velocity vs mechanical torque at pitch articulation

6.3.3 Model limitations

The following bullets list and discuss the main limitations with the Aqwa model:

Articulation set up: The pitch axis of rotation moves rigidly with the link arm and the yaw axis of rotation travels with the node; in the tank test model both axes move with the link arm, therefore the numerical model does not accurately represent the the physical model, particularly when there is a combination of pitch and yaw motion.

Articulation characterisation: The method of applying a pure friction characteristic plus linear damping to the articulation is a very simplistic. Further work to properly characterise the articulations had been planned, but not carried out.

Complex interactions: While not detailed in this document for space reasons, work carried out by others on comparing the node positions in the physical and numerical model show reasonable correlation for the singler and doubler nodes, with a much less satisfying comparison for the central nodes, indicating the link arms affect the response of the node in a way that is not captured by the set-up of the numerical model.

Node hydrodynamic coefficients: Additional linear damping characteristics are based on decay tests carried out for a single degree of freedom (when the response of the pitch and yaw axis will be coupled) with all three wire drive arcs attached (while not all the nodes have three arcs), therefore are not representative of all articulations.

PTO linear damping: As for the tank testing model, PTO damping is linear and unlimited, whereas in for the full-scale device will be an upper limit on the PTO torque. This will lead to the model predicting larger articulation forces than could actually occur, particularly in larger sea states.

While these limitations are acknowledged, data from the numerical model for is required deriving preliminary design loads due to limitations on the amount of available tank test data. It is therefore proposed to use the data as is from the numerical model, adjusted where comparison with the tank test results suggests that this is necessary.

6.4 Modelling activities - results

Note: While the tank testing and numerical modelling work included input from other members of the Albatern team as acknowledged in the previous sections, the analysis work carried out here is solely the work of the author.

The purpose of this section is to extract the relevant data from the models, provide a comparison between the numerical and physical modelling results, and determine the most appropriate data for deriving design load cases. Data extraction focusses on articulation loads (i.e. forces and moments); while articulation motions are important for the mechanical design, they are less important for structural design, and are not discussed here.

Section 6.4.1 compares the results of the regular wave tests, with the irregular wave tests presented in Section 6.4.2. Section 6.4.3 discusses fatigue loading; fatigue is often the driver for the design of dynamic WECs, and therefore a significant amount of research effort has been focussed on this topic. A comparison of fatigue damage calculated using the results from the two different models is presented, alongside a discussion on fatigue analysis procedures, investigating both time and frequency domain methods.

Throughout this section, the numerical model is referred to with the acronym NM, and the physical tank test model is referred to as TT.

6.4.1 Regular wave comparison

Array behaviour was investigated in both models by running a set of tests in regular waves, with $H = 1.5\,\text{m}$ and $5.5 < T < 10.5\,\text{s}$. Each sea state was run with three different values of PTO damping.

Results from the two models are shown in Table 6.8, which shows the pitch moment recorded at each of the in-line articulations. Data from the numerical model (NM) is shown in blue, with the tank test data (TT) shown in orange. Wave period is shown on the X axis, with pitch torque (at full scale) on the Y axis. There were some data collection issues in some of the physical model runs, and this is the cause of the missing data points.

These figures show the trends in the physical model are replicated in the numerical model, particularly for articulation LA5S (which occurs at a “Singler” node, with only one link arm attached), which gives confidence that the array behaviour is captured with reasonable accuracy. LA5S and LA8D show the best correlation, LA5C and LA2C show the worst correlation. This is to be expected as the additional link arms at the “Central” nodes introduce complex behavioural interactions which are not captured accurately in the numerical model. LA2D also shows poor correlation; this is possibly due to an issue with the physical modelling, as the wire drive kept failing during testing.

Table 6.8: Comparison of numerical models vs tank test results for regular wave tests. Graphs show wave period (s) vs articulation pitch torque (kNm). Tank test results are in orange, and numerical model results are in blue. All tests carried out with H = 1.5 m

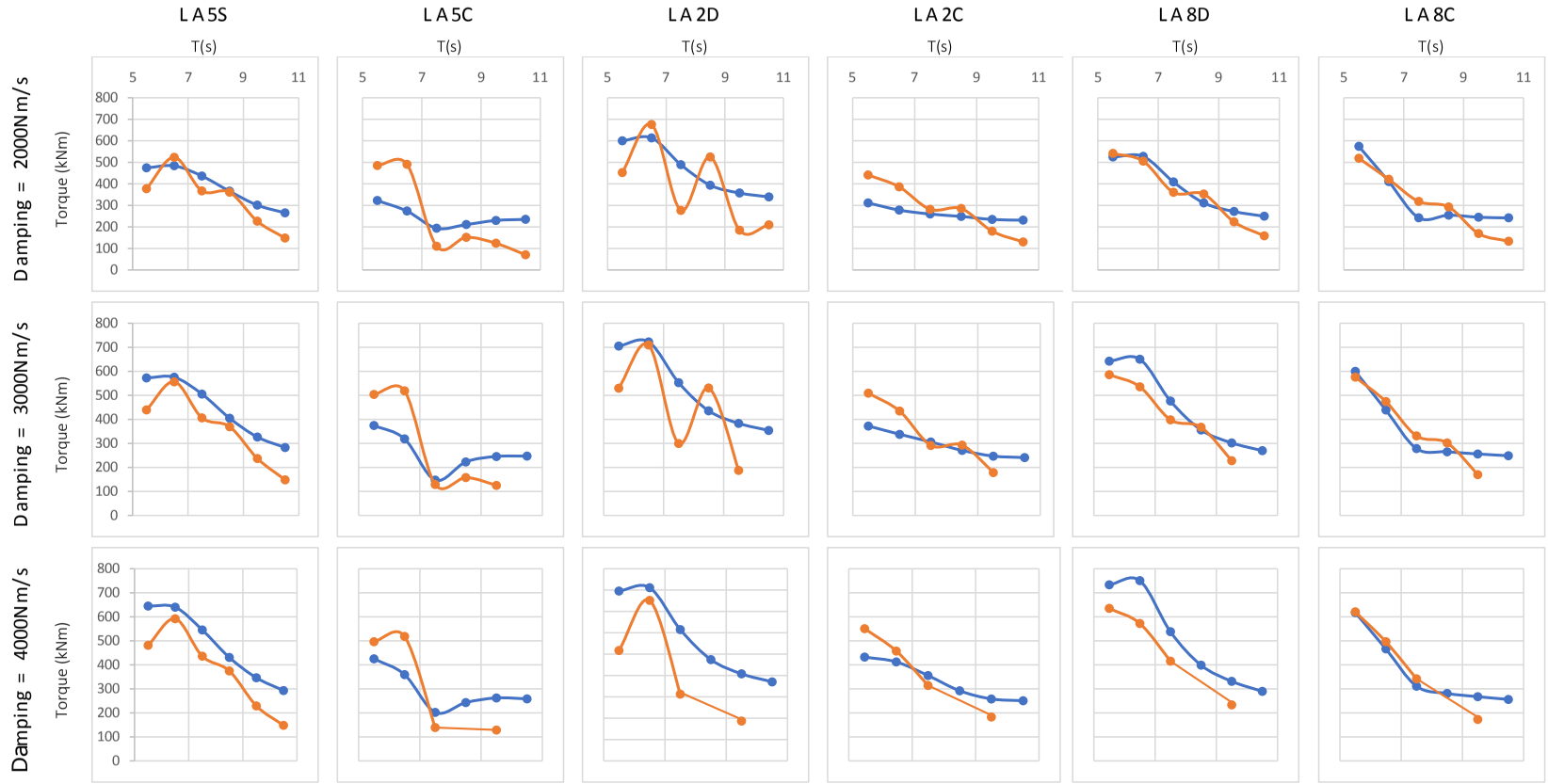

6.4.2 Irregular wave comparison

In addition to the regular wave tests, both models were also run with the same set of irregular sea states (as presented in Table 6.2), with the "optimum" level of electrical damping applied. Results from these tests are shown in Tables 6.9 and 6.10 which again show values of pitch torque for the in-line articulations. The absolute TT torque value is given in the left hand column, with the NM / TT ratio at the right. Table 6.9 shows this data for the average torque calculated from the time histories, and Table 6.10 gives the peak recorded torque.

For the average torque, Table 6.9 shows that the NM values are similar or larger than the TT values for all sea states, with the exception being at LA8C. At this articulation, $TT > NM$ for steeper seas. In general however, there is good correlation between the average torque values, especially for the more frequently occurring sea states ($1.5 < H_s < 2\,\text{m}$ and $T_p < 13\,\text{s}$) particularly for LA5S, where the largest NM / TT ratio in this range is 1.08.

When considering the peak torques, Table 6.10 shows that at LA2D, LA2C, and LA8D, $NM > TT$ for larger, steeper waves (which relate to more extreme waves), and $NM < TT$ for shallower, smaller waves (relating to operational waves). At LA5S, $TT > NM$ across all sea states, however the pattern is similar to other articulations, in that the ratio of NM / TT is greater in the larger, steeper waves.

This suggests that the method for dealing with viscous effects in the numerical model through the application of an additional linear damping term is not strictly accurate. As the tank test model gives proportionally lower peak loads for steeper waves (with higher velocities), and higher peak loads for shallower lower waves (with lower velocities), this would indicate a non-linear relationship between the damping and the body velocities. This results in the physical model having a more damped response in larger seas than the numerical model, with lower peak loads, and a less damped response in smaller seas, with higher peak loads.

The exceptions to this are at LA5C where the ratio of NM / TT is more similar for all sea states; and LA8C, where the trend appears to be reversed, with $NM > TT$ for smaller waves, and $TT > NM$ in steeper seas. It is difficult to explain exactly why this should be the case, although these articulations are located at "Central" nodes, indicating that the number of link arms significantly affects the behaviour of a particular articulation. This highlights that the simplified method of modelling articulation friction and the additional damping effects in the numerical model is not sufficient to capture the full behaviour of the device (as indeed would be expected).

Table 6.9: Irregular waves - average pitch articulation torques, for in-line articulations. Shows absolute values from tank testing (LH column) together with comparison of numerical model and tank testing results (RH column). H_s in m, T_p in s.

	Average pitch torque values from tank testing (TT) kNm								Comparison of average absolute values (NM / TT)							
	Hs/ Tp	7.7	9.1	9.9	10.5	11.9	12.6	13.3	14.7	Hs/ Tp	7.7	9.1	9.9	10.5	11.9	12.6	13.3	14.7
LA5S	1	153		121						1	1.13		1.18					
	1.5	223	204		184			138	122	1.5	1.05	1.02		1.00			1.07	1.11
	2	284	267		232		193			2	1.08	1.05		1.02		1.00		
	2.5	365		315			229			2.5	1.06		0.97			0.99		
	3			365			283			3			1.07			1.01		
	3.5		430		396			306		3.5		1.12		1.07			0.98	
	4									4								
	4.5				431	385				4.5				1.21	1.19			
LA5C	1	132		88						1	1.19		1.51					
	1.5	180	166		122			79	62	1.5	1.07	1.03		1.26			1.70	2.13
	2	246	220		168		119			2	0.92	0.93		1.07		1.26		
	2.5	287		209			161			2.5	0.91		1.03			1.04		
	3			279			193			3			0.90			1.00		
	3.5		293		286			206		3.5		0.97		0.89			0.96	
	4									4								
	4.5				317	236				4.5				0.91	1.10			
LA2D	1	242		190						1	1.07		1.19					
	1.5	323	296		241			192	172	1.5	0.99	1.00		1.13			1.22	1.24
	2	388	282		320		245			2	0.97	1.25		0.98		1.14		
	2.5	210		353			305			2.5	2.09		1.05			1.01		
	3			226			349			3			1.94			1.00		
	3.5		482		214			298		3.5		1.06		2.14			1.19	
	4									4								
	4.5				455	449				4.5				1.16	1.06			
LA2C	1	145		120						1	1.28		1.31					
	1.5	183	176		145			118	108	1.5	1.24	1.19		1.31			1.37	1.38
	2	231	200		186		149			2	1.16	1.25		1.19		1.30		
	2.5	231		209			181			2.5	1.34		1.25			1.19		
	3			227			209			3			1.38			1.18		
	3.5		298		205			193		3.5		1.18		1.58			1.31	
	4									4								
	4.5				239	241				4.5				1.52	1.38			
LA8D	1	145		123						1	1.40		1.42					
	1.5	210	185		170			132	114	1.5	1.18	1.21		1.20			1.36	1.49
	2	253	242		205		172			2	1.19	1.15		1.17		1.21		
	2.5	330		273			195			2.5	1.10		1.07			1.16		
	3			324			236			3			1.13			1.14		
	3.5		415		340			250		3.5		1.05		1.13			1.11	
	4									4								
	4.5				383	380				4.5				1.18	1.07			
LA8C	1	140		114						1	1.09		1.15					
	1.5	190	167		151			118	105	1.5	0.96	0.99		1.01			1.16	1.25
	2	230	218		179		152			2	0.93	0.87		0.96		1.02		
	2.5	278		228			170			2.5	0.88		0.85			1.00		
	3			213			207			3			1.06			0.89		
	3.5		361		285			214		3.5		0.73		0.83			0.87	
	4									4								
	4.5				307	285				4.5				0.87	0.86			

Table 6.10: Irregular waves - Peak pitch articulation torques, for in-line articulations. Shows absolute values from tank testing (LH column) together with comparison of numerical model and tank testing results (RH column). H_s in m, T_p in s.

	Peak pitch torque values from tank testing (TT) kNm								Peak torque value (NM / TT)							
LA5S	Hs/ Tp	7.7	9.1	9.9	10.5	11.9	12.6	13.3	14.7	Hs/ Tp	7.7	9.1	9.9	10.5	11.9	12.6	13.3	14.7
	1	746		555						1	0.58		0.52					
	1.5	1031	966		843			694	514	1.5	0.65	0.55		0.51			0.42	0.53
	2	1347	1337		1183		895			2	0.79	0.70		0.60		0.49		
	2.5	1621		1453			983			2.5	0.89		0.73			0.62		
	3			1638			1344			3			0.95			0.74		
	3.5		2217		1842			1283		3.5		0.91		0.93			0.86	
	4									4								
	4.5				2175	1815				4.5				0.99	1.07			
LA5C	Hs/ Tp	7.7	9.1	9.9	10.5	11.9	12.6	13.3	14.7	Hs/ Tp	7.7	9.1	9.9	10.5	11.9	12.6	13.3	14.7
	1	567		502						1	0.59		0.58					
	1.5	719	642		556			414	410	1.5	0.59	0.55		0.58			0.71	0.71
	2	908	950		604		476			2	0.60	0.51		0.66		0.64		
	2.5	995		720			641			2.5	0.70		0.72			0.52		
	3			1111			718			3			0.57			0.54		
	3.5		995		1172			673		3.5		0.85		0.56			0.60	
	4									4								
	4.5				1713	1100				4.5				0.46	0.59			
LA2D	Hs/ Tp	7.7	9.1	9.9	10.5	11.9	12.6	13.3	14.7	Hs/ Tp	7.7	9.1	9.9	10.5	11.9	12.6	13.3	14.7
	1	836		617						1	0.62		0.73					
	1.5	1082	1084		660			515	467	1.5	0.62	0.57		0.78			0.85	0.93
	2	1214	1168		1059		633			2	0.76	0.80		0.66		0.79		
	2.5	1432		1339			848			2.5	0.86		0.76			0.69		
	3			2227			1218			3			0.67			0.67		
	3.5		1615		1649			1178		3.5		1.16		0.92			0.71	
	4									4								
	4.5				1444	1534				4.5				1.29	0.98			
LA2C	Hs/ Tp	7.7	9.1	9.9	10.5	11.9	12.6	13.3	14.7	Hs/ Tp	7.7	9.1	9.9	10.5	11.9	12.6	13.3	14.7
	1	502		429						1	0.73		0.72					
	1.5	579	574		479			363	351	1.5	0.79	0.71		0.73			0.84	0.85
	2	748	705		586		469			2	0.82	0.85		0.76		0.74		
	2.5	908		705			601			2.5	0.89		0.88			0.66		
	3			890			735			3			1.03			0.75		
	3.5		964		885			593		3.5		1.18		1.06			0.98	
	4									4								
	4.5				936	961				4.5				1.22	1.04			
LA8D	Hs/ Tp	7.7	9.1	9.9	10.5	11.9	12.6	13.3	14.7	Hs/ Tp	7.7	9.1	9.9	10.5	11.9	12.6	13.3	14.7
	1	501		414						1	0.77		0.77					
	1.5	763	681		512			405	370	1.5	0.71	0.71		0.76			0.76	0.82
	2	978	1043		694		494			2	0.84	0.79		0.84		0.76		
	2.5	1299		1132			626			2.5	0.88		0.80			0.75		
	3			1527			920			3			0.90			0.76		
	3.5		1520		1582			906		3.5		1.17		0.90			0.81	
	4									4								
	4.5				1466	1637				4.5				1.22	0.87			
LA8C	Hs/ Tp	7.7	9.1	9.9	10.5	11.9	12.6	13.3	14.7	Hs/ Tp	7.7	9.1	9.9	10.5	11.9	12.6	13.3	14.7
	1	414		316						1	1.18		1.32					
	1.5	536	481		386			317	328	1.5	1.10	1.06		1.17			1.18	1.09
	2	722	694		505		389			2	0.96	0.88		1.03		1.11		
	2.5	812		686			436			2.5	1.00		0.88			1.07		
	3			806			613			3			0.91			0.85		
	3.5		1070		962			629		3.5		0.84		0.80			0.84	
	4									4								
	4.5				1012	939				4.5				0.90	0.80			

6.4.3 Fatigue comparison

Fatigue limit state (FLS) is often the driver for wave energy converters due to the highly dynamic nature of the loading regime. This section carries out high level fatigue analysis using data from both the numerical and physical models, to carry out comparison work with emphasis on three different aspects:

1. Data from the two different models are compared, to assess which is the more appropriate for use in fatigue design. Time domain fatigue methods are used for this comparison.
2. Results from the time domain analysis are used to compare the behaviour of different articulation points.
3. Results from fatigue analysis in both the time and frequency domain are compared to help make judgements on the most suitable methods for floating WECs.

This section starts by setting out the methodology for carrying out fatigue analysis, including time and frequency domain methods in (a). Results of the time domain and frequency domain analyses are presented in (b) and (c), and a discussion of the results follows in (d).

(a) Fatigue analysis methodology

To carry out the comparison work in this section, fatigue analysis has been carried out taking the link arm as a representative component for design, in a similar manner as for the concept design work in Chapter 5. Fatigue checks have been carried out assuming that the link arm is fabricated with a steel tube (diameter = 1.219 m, thickness = 12 mm). A separate check is included for each of the in-line articulations; at these locations the pitch torque is dominant, and so is assumed to be the only load acting on the arm.

Fatigue damage has been calculated assuming linear cumulative damage in accordance with the Palmgren-Miner hypothesis give in Equation 2.1 (given in the literature review). The stress in the steel is calculated as follows:

$$\begin{aligned} \sigma &= M_y/Z \\ Z &= \frac{(D^3 - (D - 2.t)^3)\pi}{32} \end{aligned} \tag{6.3}$$

Where Z = elastic section modulus, for a tube with diameter D and wall thickness t.

To calculate N_i for each stress cycle, the link arm has been classified as a "C" fatigue detail, in accordance with Table A.1 of DNV GL (2014), (a rolled steel tube subject to potential rust pitting). For a member in seawater with cathodic protection this gives the following data for the S-N curve (see DNV GL, 2014, Table2-2):

- For N < 106 cycles: $m_1 = 3.0$, $log(a_1) = 12.192$
- For N > 106 cycles: $m_2 = 5.0$, $log(a_2) = 16.320$

It is noted the fatigue category of the end connection details will be significantly more onerous than a “C”, however the design of the end connection is beyond the scope of this research. Using a reference link arm steel section allows a comparison of the fatigue effect at different connection points, and is therefore acceptable for this level of analysis.

The number of stress cycles (n_i) can be calculated using either time domain or frequency domain methods. Both methods have been carried out in this report; the methodology for each is discussed below.

(i) Time domain fatigue process

For analysis in the time domain, n_i is taken as being equal to the number of torque cycles present within the recorded time histories from the models. The torque cycle histogram has been determined by using the rainflow counting method (Schijve, 2001) to determine the number of cycles of each torque range within the time histories.

The rainflow counting method is a way of accounting for all stress reversals within a varying time history in a way that simple range counting does not, as illustrated in the Figures 6.13 and 6.14 (taken from Schijve, 2001).

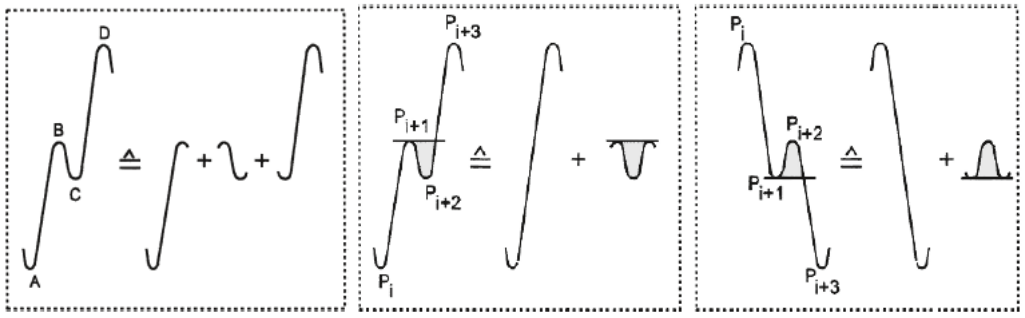

Figure 6.13: Intermediate load reversal as part of a larger range (Schijve, 2001, Fig 9.12)

Figure 6.13 (a) indicates the stress cycles (with ranges AB, BC and CD), that would be counted if only the sequential stress ranges were considered. This method does not however take into account the larger overall stress range AD, which would have a significant impact on the fatigue loading. To overcome this issue, the rainflow method first counts the small cycle BC, then removes it from the larger range AD, which is considered as a seperate cycle (Figure 6.13 (b)). This process is further illustrated in Figure 6.14.

For this thesis, rainflow counting to determine the number of torque cycles within the model load time histories has been carried out in Matlab, using the Rainflow Counting Algorithm function [2].

2. Created by Adam Nieslony, and accessed from https://uk.mathworks.com/matlabcentral/fileexchange/3026-rainflow-counting-algorithm?focused=5148889&tab=function

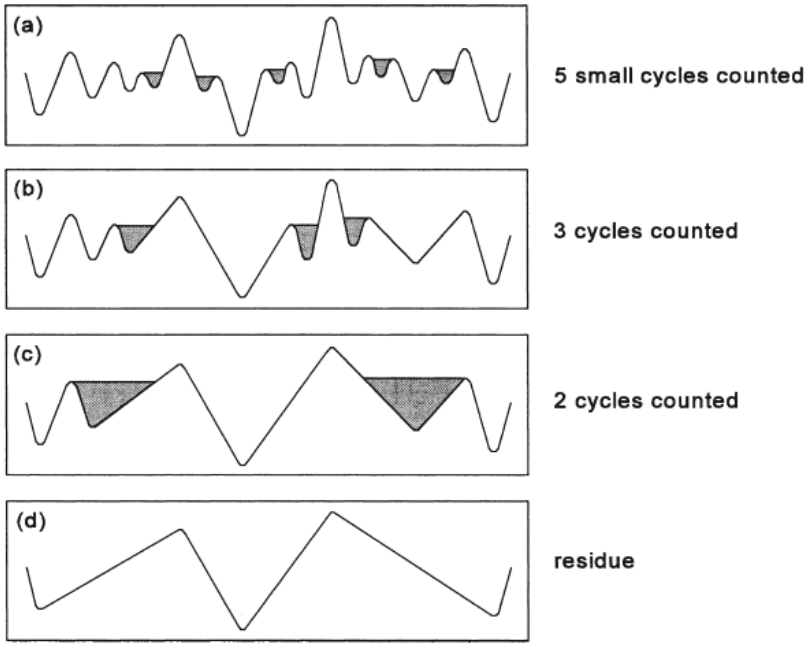

Figure 6.14: Successive rainflow counts (Schijve, 2001, Fig 9.13)

This algorithm consists of three steps:

1. The first step locates the local maxima and minima in the time history (using the function sig2ext.m) as shown in Figure 6.15 for a sample of the tank testing time history for LA5S, for the irregular sea state H_s = 1.5 m and T_p = 9s;
2. The second step counts the number of cycles present based on the located maxima and minima (using the function rainflow.m);
3. Finally the rainflow data is presented as a histogram using the function rfhist. Figure 6.16 shows this histogram for LA5 for the irregular sea state H_s = 1.5 m and T_p = 9s, which clearly shows that the majority of the cycles in this time history have a torque range of less the 10 kNm.

The output of this process is the total torque cycle count for each of the 21 irregular test sea states, which account for 42% of all the occurring sea states at the West Harris site in a given year. To account for the fatigue damage encountered over the whole design life, the number of cycles in each test time history has been multiplied by a factor (λ) derived from splitting up the full occurrence matrix into 21 separate sections, each containing one of test sea states. It is then assumed that results for a single test sea state also apply to all the other sea states within that section. The assumed matrix split is shown in Figure 6.17.

The multiplication factors have been determined based on the actual length of the time histories (T_{NM} for the numerical model, and T_{TT} for the tank testing), compared to the length of time each sea state would be expected to occur in a single year (T_{SS}).

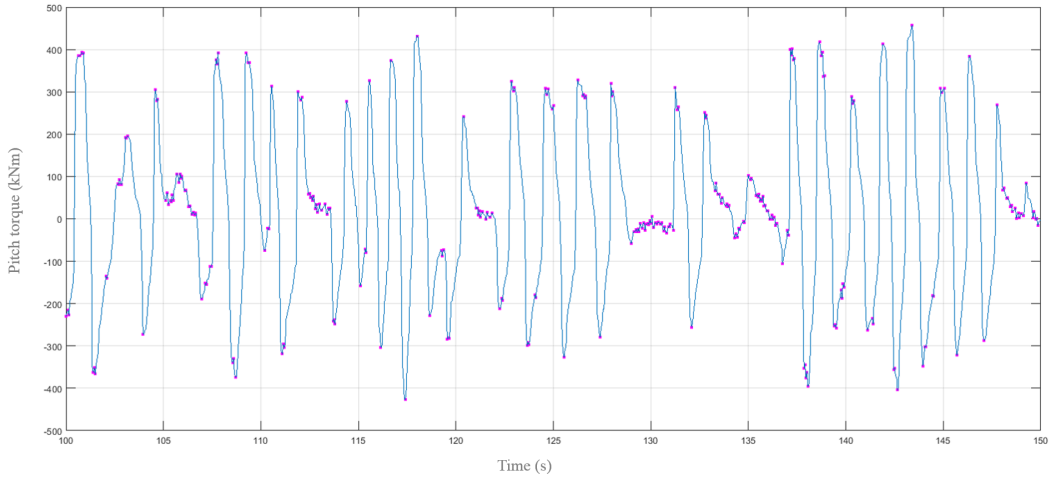

Figure 6.15: Local maxima and minima in tank testing time history for LA5S, (shown in pink), as identified using the sig2ext.m function in Matlab, H_s = 1.5 m and T_p = 9s.

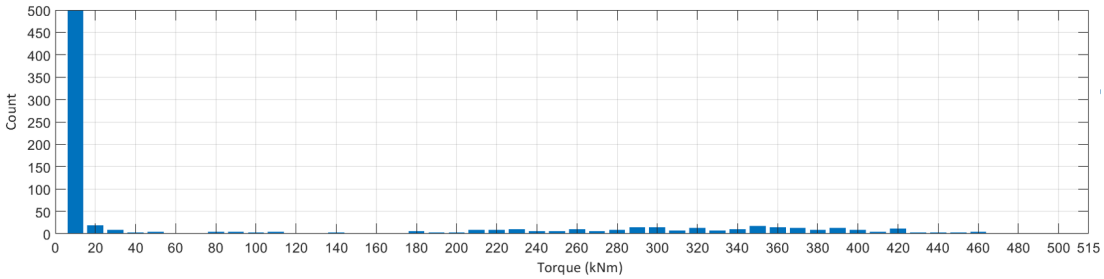

Figure 6.16: Torque cycle count histogram for LA5S, (shown in pink), H_s = 1.5 m and T_p = 9s.

The tank test time histories consist of 10902 readings, with a sampling rate of 20Hz. For the rainflow counting, the first 500 and last 902 reading have been ignored (to allow for warm up and settling time of the tank). Each time history is therefore 475 s long at model scale, which results in a value of $T_{TT} = 2015\,\text{s}\ (0.56\,\text{hrs})$ at full scale, for an 18th scale model. For the numerical model each sea state is run for 2600 s, giving $T_{NM} = 0.72\,\text{hrs}$. T_{SS} for each sea state as calculated from the scatter diagram split shown in Figure 6.17, is shown in Table 6.11, along with the calculated multiplication factor λ_{NM} and λ_{TT}.

The final torque histogram as calculated from the physical and numerical model results for LA5S are shown in Figure 6.18. The final step in the time domain fatigue is to transform this torque loading histogram to a stress histogram using Equation 6.3 - this gives n_i for use in Equation 2.1

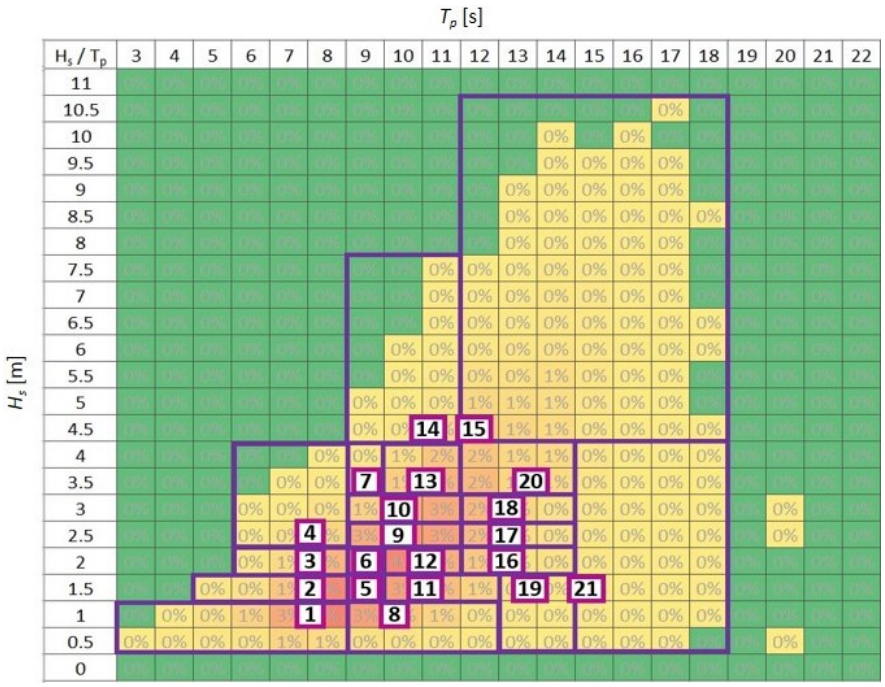

Figure 6.17: West Harris wave occurrence matrix, showing the test sea states (numbered), together with the portion of the matrix to which they are assumed to apply

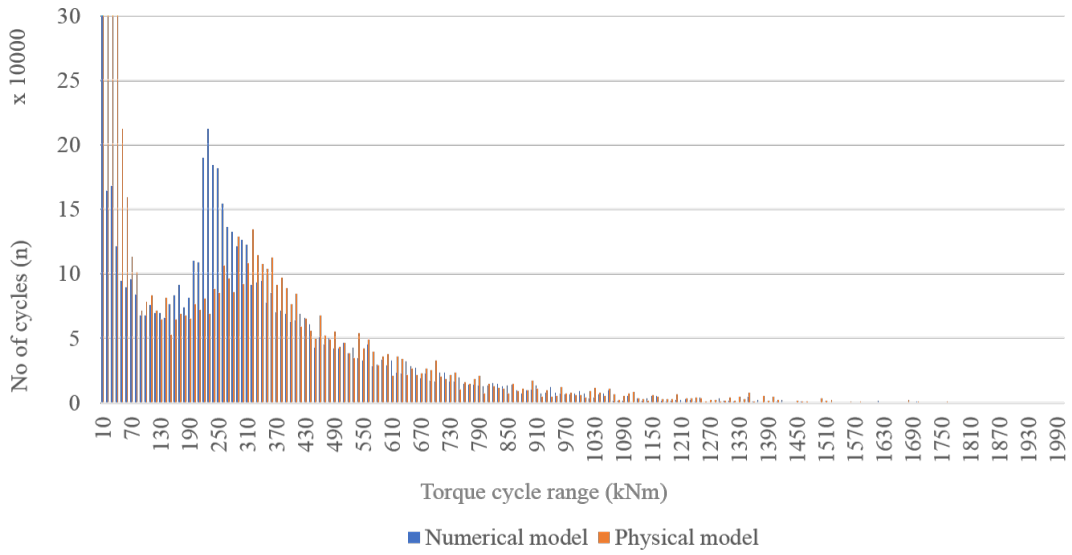

Figure 6.18: Torque cycle histogram, showing time domain cycle counts based on rainflow counting methods, for LA5S

Table 6.11: Calculation of weighting factors to be applied to rainflow cycle counts for each sea state time history

Sea state	H_s m	T_p s	Proportion of scatter diagram	T_{SS} hrs	λ_{NM}	λ_{TT}
1	1	7.7	10.4%	910.2	1260.3	1625.9
2	1.5	7.7	5.9%	514.2	712.0	918.6
3	2	7.7	2.9%	256.2	354.8	457.7
4	2.5	7.7	1.8%	154.0	213.3	275.1
5	1.5	9.1	5.2%	457.0	632.8	816.3
6	2	9.1	4.3%	380.9	527.4	680.4
7	3.5	9.1	0.5%	44.1	61.0	78.7
8	1	9.9	6.7%	584.3	809.1	1043.8
9	2.5	9.9	8.9%	780.6	1080.9	1394.4
10	3	9.9	6.3%	553.5	766.4	988.7
11	1.5	10.5	5.8%	507.3	702.5	906.2
12	2	10.5	6.4%	561.6	777.6	1003.1
13	3.5	10.5	5.5%	484.8	671.4	866.1
14	4.5	10.5	1.4%	119.3	165.1	213.0
15	4.5	11.9	10.5%	922.9	1278.0	1648.7
16	2	12.6	2.1%	185.5	256.8	331.3
17	2.5	12.6	2.9%	252.3	349.4	450.7
18	3	12.6	3.3%	289.2	400.4	516.6
19	1.5	13.3	0.7%	65.0	90.0	116.2
20	3.5	13.3	6.5%	569.0	788.0	1016.5
21	1.5	14.7	1.9%	168.1	232.8	300.3
	Total	100%	8760			

(ii) Spectral fatigue analysis process

As noted in the literature review, it is not always possible to carry out a full time history analysis, and spectral fatigue methods may be more appropriate. These predict the load cycle distribution based on the spectral properties of the structural loading response (referred to as the structural response spectrum, $S_R(f)$) which can be calculated using Equation 6.4;

$$S_R(f) = S_W(f).RAO^2 \tag{6.4}$$

where $S_W(f)$ is the wave energy spectral density, and the *RAO* (the Response Amplitude Operator, also described in some texts as the Transfer Function) gives the magnitude of the structural response to a sinusoidal wave of unit amplitude across a range of frequencies. The relevant structural response for this analysis is the articulation pitch bending moment; this allows a direct comparison with the time domain rainflow cycle counting method described above.

The steps taken in the spectral fatigue analysis are as follows:

1. Determine the articulation pitch bending moment RAO using the output from the numerical model runs with regular wave inputs and a unit amplitude wave height;
2. Calculate the pitch bending moment structural reponse spectrum ($S_R(f)$) using Equation 6.4, for each sea state in the wave occurrence matrix;
3. Predict the loading histogram for each sea state, based on the properties of $S_R(f)$ the assumed probability density function, and the length of time each sea state is expected to occur in a particular year. The total loading histogram for a given year is the sum of the histograms for each sea state;
4. Transform the articulation loading histogram to a stress histogram.

Further details of each of these steps are included below:

1. Estimation of the pitch bending moment RAO

RAOs are determined from either physical or numerical model tests by running a number of regular waves with a unit wave amplitude across a relevant range of frequencies (as recommended in Holmes 2009). In this case, the numerical model has been run for wider range of frequencies than the tank tests, and therefore the NM values have been used to obtain the RAOs for analysis (shown in Figure 6.19).

2. Calculation of loading response spectrum $S_R(f)$

As discussed in Section 6.2.2, the numerical and physical model tests have been run with a Jonswap wave spectra with $\gamma = 1$, and therefore this has been used to calculate $S_R(f)$. A plot of the wave spectra ($S_W(f)$) for H_s = 1.5 m and T_p = 9 s (which is the most common sea state for the West Harris deployment site) together with the square of the RAO for LA5S and the resulting response spectra ($S_R(f)$) is shown in Figure 6.20.

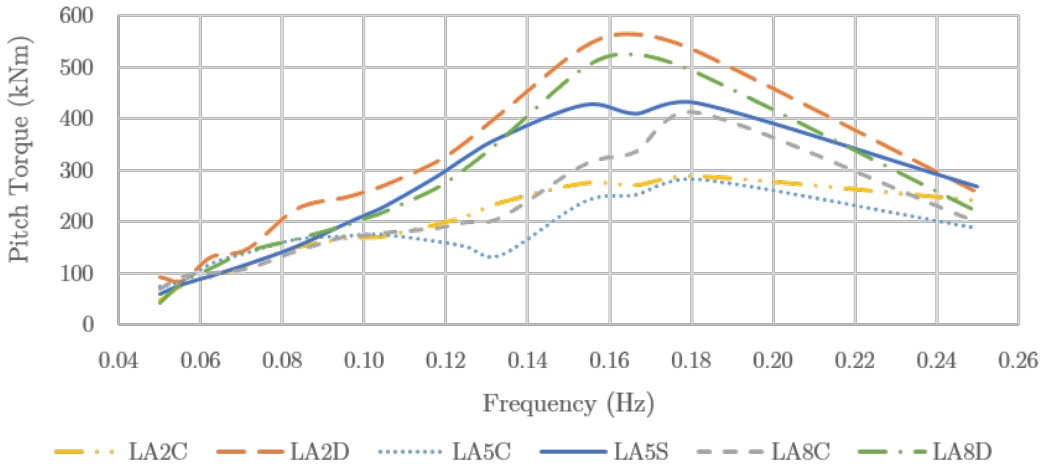

Figure 6.19: Articulation pitch torque RAOs, obtained from numerical model runs

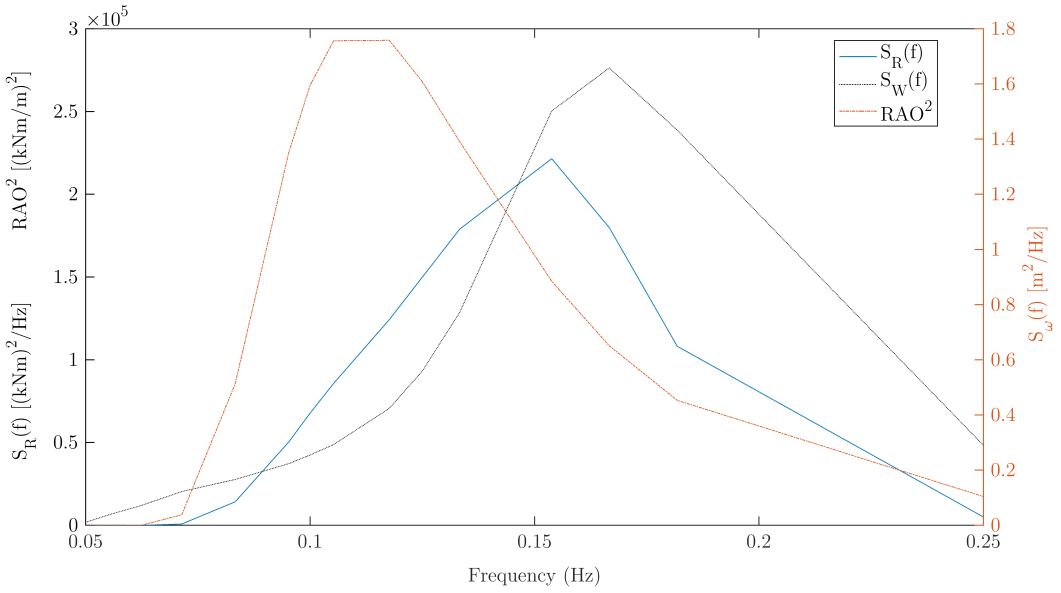

Figure 6.20: Calculation of $S_R(f)$ for H_s = 1.5 m and T_p = 9 s

3. Prediction of loading histogram

The loading range histogram is predicted using Equation 6.5 (Halfpenny, 1999).

$$N(S) = E[P].T.p(S) \tag{6.5}$$

Where N is the number of cycles of loading range S occurring in T seconds, $E[P]$ is the expected number of peaks obtained by equation 6.6, and $p(S)$ is the probability of S occurring, calculated using a particular probability density function (pdf). Note that in all the following equations, m_i is the i^{th} moment of area of $S_R(f)$, calculated as $m_n = \int f^n.S_R(f).df$.

$$E[p] = \sqrt{\frac{m_4}{m_2}} \tag{6.6}$$

Section 2.2 of the literature review provides a discussion of different pdf functions. For this exercise, both the Rayleigh and Dirlik pdfs have been used for comparison. The Rayleigh pdf (appropriate for narrowband loading) is given by Equation 6.7.

$$p(S)_R = \frac{S}{4.m_0}.e^{-\frac{S^2}{8.m_0}} \tag{6.7}$$

The Dirlik pdf (more appropriate for wideband loading) is given by Equation 6.8, with the relevant coefficients given in Equation 6.9.

$$p(S)_D = \frac{\frac{D_1}{Q}.e^{-\frac{Z}{Q}} + \frac{D_2.Z}{R^2}.e^{\frac{-Z^2}{2.R^2}} + D^3.Z.e^{\frac{-Z^2}{2}}}{2.\sqrt{(m_0)}} \tag{6.8}$$

$$\begin{aligned} D_1 &= \frac{2.(x_m - \gamma^2)}{1+\gamma^2} & D_2 &= \frac{1-\gamma-D_1+D_1^2}{1-R} & D_3 &= 1-D_1-D_2 \\ Z &= \frac{S}{2.\sqrt{m_0}} & Q &= \frac{1.25.(\gamma-D_3-D_2.R)}{d_1} & R &= \frac{\gamma-x_m-D_1^2}{1-\gamma-D_1+D_1^2} \\ \gamma &= \frac{m_2}{\sqrt{(m_0.m_4)}} & x_m &= \frac{m_1}{m_0}.\sqrt{(\frac{m_2}{m_4})} \end{aligned} \tag{6.9}$$

A Matlab script has been used to calculate and sum together the loading range histogram for each sea state in the occurrence matrix. Figure 6.21 shows the resulting histogram for the Dirlik and Rayleigh distributions for LA5S. It can be seen from this figure that the Rayleigh pdf predicts a lower number of cycles at the lower moment ranges ($< 250\,\text{kNm}$) and a higher number of cycles at high moment ranges.

4. Calculation of stress histogram

The final step in the Spectral fatigue analysis is to transform the loading histogram to a stress histogram using Equation 6.3 - this gives n_i for use in Equation 2.1

(b) Time domain fatigue calculation results

This section uses the time domain fatigue analysis results for two comparisons:

1. comparison of the behaviour of the different in-line articulations;
2. comparison of the behaviour of the two models;

The annual fatigue damage with n_i calculated in the time domain is shown in Table 6.12, together with the % of total array power generated at each articulation for the most frequently occurring sea state ($H_s = 1.5\,\text{m}$ and $T_p = 9\,\text{s}$). It is noted that the annual damage values are

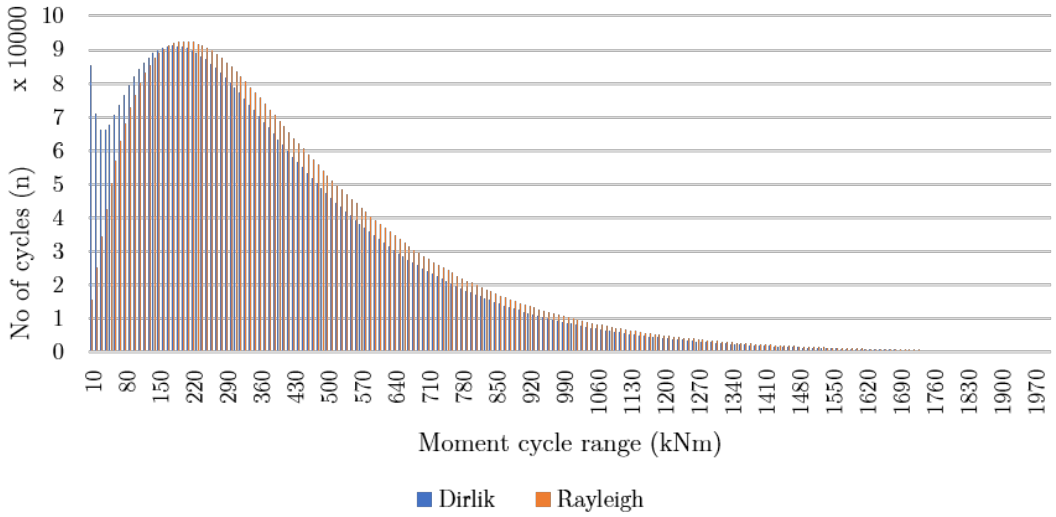

Figure 6.21: Loading range histogram calculated using the Dirlik and Rayleigh pdfs, for LA5S

very high, and would not be acceptable for a 20 year design life; this would need to be investigated further during detailed design.

Table 6.12: Annual fatigue damage based on numerical model and tank testing results

Articulation	Numerical model NM_{FD}	Tank testing TT_{FD}	TT_{FD}/NM_{FD}	% contribution to power
LA5S	0.731	0.965	1.32	18
LA2D	0.701	0.782	1.12	21
LA8D	0.379	0.435	1.15	25
LA5C	0.046	0.173	3.76	0
LA2C	0.132	0.09	0.68	3
LA8C	0.089	0.138	1.55	12

(i) Behaviour of different articulation points

Table 6.12 shows that the worst fatigue occurs at articulations at the doubler and singler nodes, with significantly lower damage at the central nodes. Interestingly the articulations which contribute the most to the array power (LA2D and LA8D) do not have the largest fatigue damage; this is a result that could be interesting to explore further as it appears that the addition of the additional link arm at these nodes improves fatigue behaviour, without compromising on power output.

(ii) Behaviour of the different models

Table 6.12 shows the same trends for both the NM and TT data which gives confidence that the general behaviour of the physical model is being adequately captured. With the exception of LA2C, $TT_{FD} > NM_{FD}$, with the difference varying between 12 and 32% for the most heavily loaded articulations. The reason for this is illustrated in Figure 6.22 which show the

cycle count (top), and annual fatigue damage (bottom) for each torque cycle range for LA5S. NM values are shown in blue, with TT values in orange.

The torque cycle counts trends are roughly similar for the two models, with high cycle counts at very low torque ranges, a secondary peak in the cycle count at torque ranges of around 220 kNm (NM) and 300 kNm (TT), and the cycle count tailing off towards the higher torque ranges. However, the TT histogram has a lower number of smaller torque cycles, and a higher number of larger torque cycles, which results in a greater amount of overall damage, therefore gives a more conservative result.

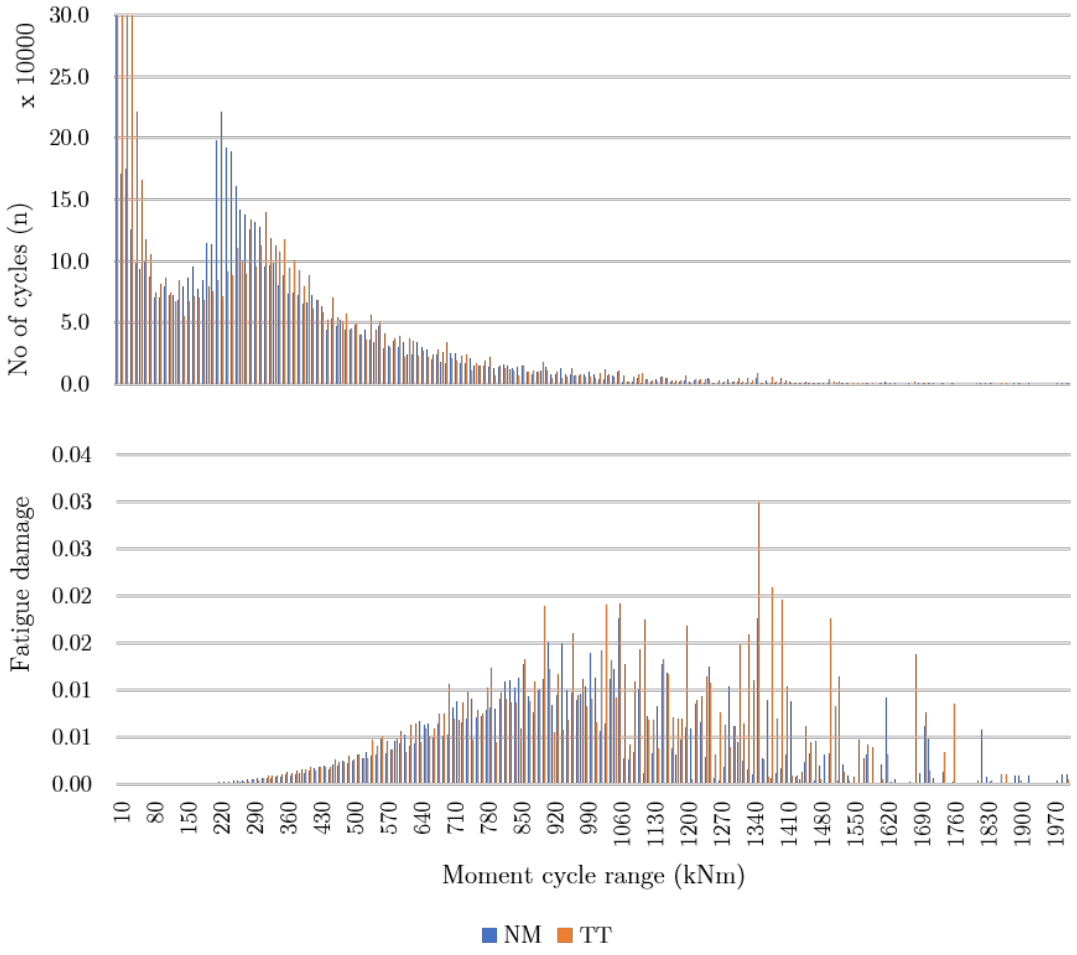

Figure 6.22: Comparison of fatigue cycles and damage for LA5. Comparison between tank testing and numerical model

This difference is most likely caused by method of applying only linear damping terms in the numerical model, leading to overdamping of the NM response (resulting in lower peak / average torque ratio) when compared to the TT response in the most frequently occurring sea states.

(c) Frequency domain results

The fatigue damage has been calculated for articulations LA5S, LA2D, LA8D, LA2C and LA8C using the output of the stress range histograms from both the Dirlik and Rayleigh distributions as described in the previous section; these are shown in Table 6.13, together with the damage calculated from the tank testing time histories, using the rainflow counting method.

Table 6.13: Annual fatigue damage calculated using spectral methods, compared with damage calculated using tank test time histories

Articulation	Tank test (TT)	Dirlik (D)	Rayleigh (R)	D/ R	Dirlik / TT
LA5S	0.965	1.16	1.37	1.18	1.20
LA2D	0.782	2.08	2.45	1.18	2.66
LA8D	0.435	1.44	1.69	1.17	3.32
LA5C	0.173	0.27	0.36	1.31	1.59
LA2C	0.09	0.34	0.45	1.32	3.75
LA8C	0.138	0.50	0.61	1.23	3.59

It can be seen from this table, that the Rayleigh method results in damage calculations that are consistently in the region of 20% higher than the Dirlik method, which in itself predicts higher levels of damage than the time domain counting method using the tank test time histories. The closest correlation between the Spectral and Time domain method occurs at articulation LA5S, where there is only one link arm attached to the node. The difference between the Spectral and Time domain methods increases as the number of link arms attached to the node increases, with the largest variation being for LA2C, although the absolute damage for the Central nodes are significantly lower than for the Singler and Doubler nodes.

Figure 6.21 shows the Dirlik moment histogram compared with the rainflow counting from the tank testing and numerical models for articulation LA5S, which shows that the peak of the Dirlik histogram occurs at a lower stress range than either the tank testing or numerical model, and while the tank test results has some individual count peaks at the higher stress ranges, in general the Dirlik distribution predicts larger numbers of cycles in the tail of the distribution, which leads to higher overall damage levels.

(d) Fatigue comparison - discussion

The Dirlik spectral fatigue method is based on two assumptions:

1. that the structural response spectrum is widebanded;
2. that the response can be modelled with a Gaussian distribution.

To investigate possible reasons for the difference between the spectral and time domain fatigue analysis methods shown in Figures 6.23 and Table 6.13, the properties of the structural

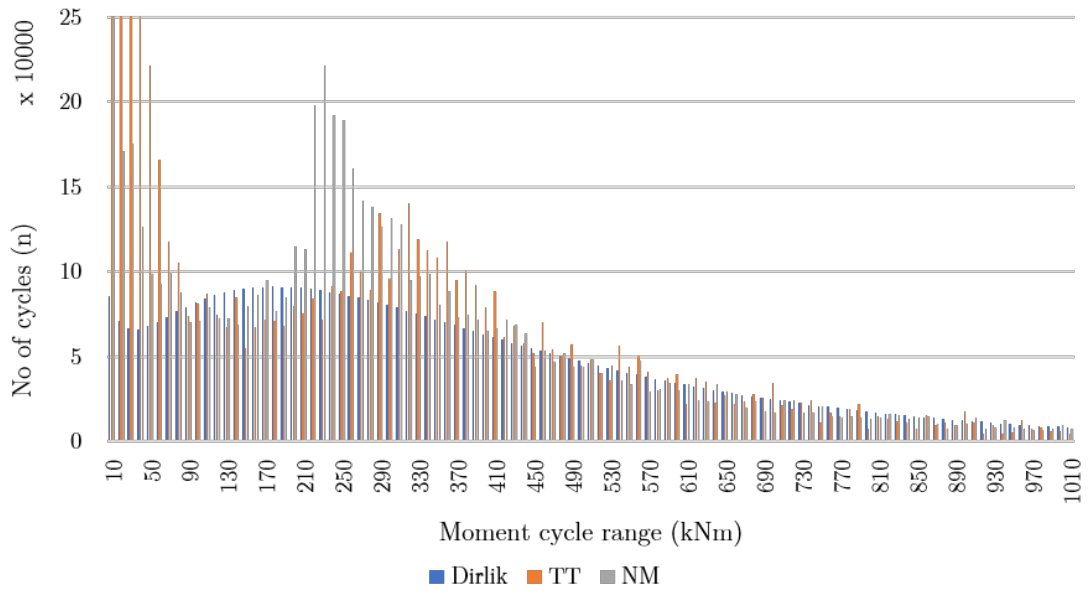

Figure 6.23: Comparison of torque histogram using Dirklik spectral fatigue methods, with TT and NM time domain methods, for articulation LA5S

response spectra from the results of the models irregular sea states have been examined to check the validity of these assumptions, by carrying out the followings steps:

i Determine structural response spectrum, using time histories from numerical and physical models;
ii Calculate spectral bandwidth to check "Widebanded" assumption;
iii Calculate statistical distribution of time history, to check the assumption that the input random loading follows a Gaussian distribution.

(i) Determining structural response spectrum from model time histories

In order to determine the structural response spectrum from the time history, a Fast Fourier Transform has been performed, using the dat2spec function in the WAFO matlab toolbox (Brodtkorb et al., 2011). The spectrum obtained from the raw data is highly irregular, with multiple peaks, so smoothing has been carried out to produce a representative spectrum. This has been done by specifying the maximum lag size (L_{max}) for the window function in the dat2spec function. Figure 6.24 (a) shows the response spectrum for articulation LA5S, for the tank test run with H_s = 1.5 m and T_p = 9 s, comparing the spectrum from the raw data, and with L_{max} = 400, and L_{max} = 80. Figure 6.24 (b) and (c) shows the Auto Covariance Function (ACF) for each of the smoothed spectra compared with the ACF for the raw data. This shows that the case where L_{max} = 400 shows good agreement with the estimated function for the raw data and therefore is an appropriate level of smoothing, whereas the case where L_{max} = 80 differs fairly significantly.

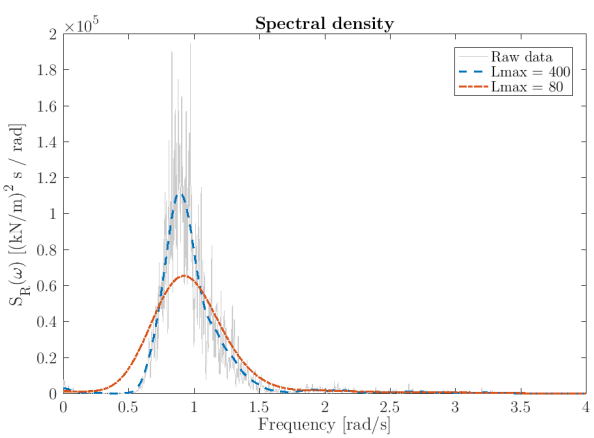

(a) Structural response

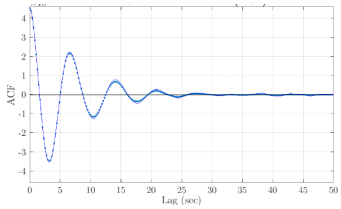

(b) ACF comparison with $L_{max} = 400$

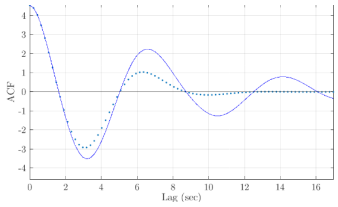

(c) ACF comparison with $L_{max} = 80$

Figure 6.24: Reponse spectrum for LA5S, from tank test run with irregular sea, H_s = 1.5 m and T_p = 9 s, Jonswap wave, γ = 1

(ii) Spectral bandwidth

The bandwidth of the response spectra has been calculated using Equation 6.10. This has been compared against the bandwidth of the Jonswap wave to examine the difference between the structural response and the incoming wave spectra, and to check the wideband assumption. (Zurkinden et al. (2013) notes that the response of WECs can be significantly damped by the PTO system, which in some cases can result in a structural reponse with a narrower band width than the incoming wave).

$$\Omega = \sqrt{1 - \frac{m_2^2}{m_0 m_4}} \tag{6.10}$$

The bandwidth has been for each of the in-line pitch articulations for the case where H_s = 1.5 m and T_p = 9 s. The results are shown in Table 6.14, compared with the bandwidth of the wave (Ω_w = 0.79).

Table 6.14: Bandwidth Ω of the structural response compared with the bandwidth of the incoming wave: H_s = 1.5 m, T_p = 9 s, Ω_w = 0.79

	Ω_{TT}	Ω_{TT}/Ω_w	Ω_{NM}	Ω_{NM}/Ω_w
LA5S	0.82	1.04	0.86	1.09
LA2D	0.80	1.01	0.86	1.09
LA2C	0.75	0.95	0.85	1.07
LA8D	0.89	1.12	0.85	1.08
LA8C	0.76	0.96	0.79	1.00

Table 6.14 shows that Ω_{TT} is similar to, or slightly higher than Ω_w for articulations at the Singler and Doubler nodes, but slightly lower at the Central nodes, indicating that there is a greater level of structural damping at these points. Ω_{NM} is slightly larger than Ω_w for all articulations except for LA8C, indicating again that the method of applying damping in the numerical model does not fully represent the true damping effects.

However, in general, as all the bandwidths calculated would be classed as "wide", and the response bandwidth is not significantly changed from the incoming wave bandwidth, the assumption of using a Dirlik pdf should be appropriate, as it was specifically developed for the type of wideband spectra typically associated with ocean waves.

(iii) Check on Gaussian distribution function

In order to check the assumption that the structural loading follows a Gaussian distribution, the “crossing spectrum” has been determined, using the dat2lc function in the WAFO toolbox, which calculates the average number of upcrossings in the time history per unit time. This is compared with the crossing spectrum estimated assuming that the response is Gaussian in nature. Plots for the tank test runs at H_s = 1.5 m and T_p = 9 s are shown in Figure 6.25.

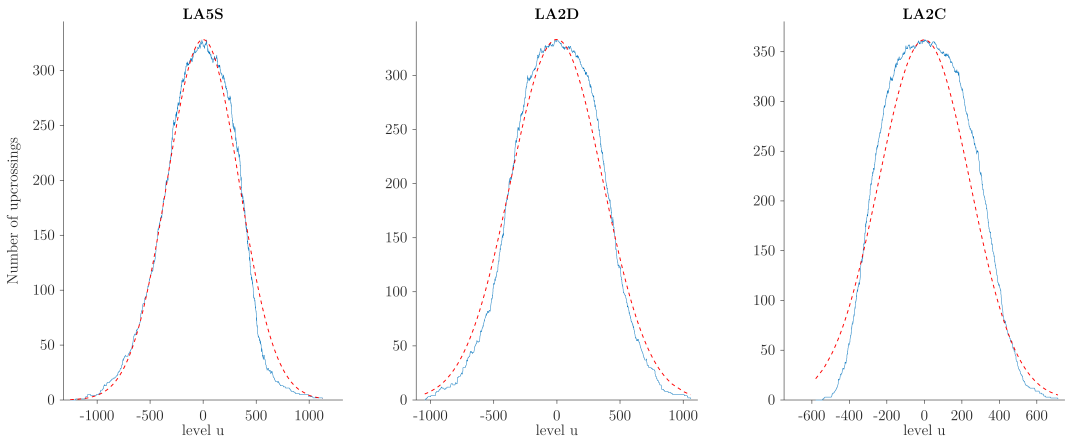

Figure 6.25: Upcrossing spectrum for LA5S, LA2D, LA2C, for H_s = 1.5 m and T_p = 9 s, compared with expected Gaussian response, indicated with a red dashed line

These figures show that while the time history for LA5S shows a good fit with the Gaussian distribution, LA2D (a Doubler node), and LA2C (a Central node) are increasingly deviant, therefore the assumption of the random loading being normally distributed is not valid. This is a possible explanation as to why spectral fatigue analysis using the Dirlik distribution gives greater levels of damage than the time domain methods for these articulations. Herve et al. (2015) notes that non-Gaussian processes are associated with structures that exhibit non-linear behaviour; this analysis indicates that increasing the number of link arms at a point increases the non-linearities of the structural response. There are methods for transforming non-Gaussian processes into Gaussian ones in order to allow Spectral fatigue analysis to be

applied (see Herve et al., 2015) and this would be interesting to explore further. However, for the rest of this work, as the Spectral methods appear to give more conservative estimates of fatigue damage, they are appropriate for preliminary design purposes, where the main aim is to show that different design options are achievable, and allow for comparison between options.

6.5 Summary and conclusions

The aim of this chapter has been to extract the most relevant data from the physical and numerical modelling activities, in order to develop structural load cases. Through this process, a number of observations have been made about the general behaviour of the device, the numerical modelling methods, and the most appropriate loads and analysis methods to be used in ongoing design activities. These observations are summarised and discussed further in the sections below.

6.5.1 Modelling process and structural behaviour discussion

(a) Numerical modelling process

The numerical model is set up to replicate the behaviour of the tank test model, and uses a number of simplifying assumptions, particularly regarding the characteristics of the articulations, where a simple value of friction and linear damping has been applied, no matter where the articulation is located. In addition the effects of viscous damping are captured by use of an additional linear damping term, whereas viscous effects are actually non-linear. This results in an under-damped numerical model with compared to the physical model in higher, steeper seas, (giving greater peak loads) and an over-damped model in smaller seas, (with resulting lower peak loads).

However, despite these limitations, the numerical model shows the same general trends as the physical model, giving confidence that it provides a reasonable representation of the array. This justifies using simplified models for initial design development, which are simple to set up and relatively quick to run, and give results that are suitable for the purpose of preliminary design.

A comparison of the articulation behaviour in both models shows the best correlation for articulations at Singler nodes. A reasonable correlation is achieved for articulations at Doubler nodes, with the worst correlation occuring at Central nodes. This indicates that the model complexity increases with an increasing number of interacting bodies, and the simplifying assumptions no longer capture the full behaviour of the array.

Therefore, while the numerical models that have been developed are appropriate for preliminary design work; anyone carrying out further modelling work in the future, either on

the 12S array, or other multi-body array with similar levels of complexity should be aware of the limitations of using simplified inputs, and be prepared to undertake work to fully characterise the more complicated articulation points before using such models to develop detailed design loads.

(b) Peak torque values

A comparison of the results from the irregular wave model runs show that the numerical model tends to over-predict the peak torques in more extreme conditions, due to the nature of applying a linear damping term to cover non-linear viscous effects. While analysis was restricted to a comparison of the pitch torque, as this was the only component measured directly in the tank test model, is assumed that this also follows through to the other articulation torques, axial forces and shear loads. It is therefore appropriate to derive load cases in larger seas using the numerical model data (rather than the tank test data) as the trends suggest that these loads will, if anything, be overestimated.

It is noted that torque loading in extreme seas will be determined by the physical PTO torque limit (see Chapter 7 for further discussion), which is not captured in either the physical or numerical model. However the axial forces and shear loads that could be coincident with the peak torque can be taken from the numerical model results.

(c) Fatigue behaviour

A simple time domain fatigue check shows that the numerical model under-predicts the fatigue damage when compared to the physical model. Again, this is likely due to the simplistic nature of the applied linear damping, which results in a more damped response in more frequently occurring, smaller seas. This gives a lower peak-to-average torque ratio across the recorded time history, with smaller number of the cycles occurring at the higher torque ranges, which contribute most to the overall fatigue damage.

This shows that it would be more appropriate to use the data from the physical model to carry out fatigue analysis, however, as there is limited load data available from the tank test this is not practical. It is therefore proposed that where a full time domain fatigue analysis is required, results from the numerical model should be taken, as this will give a full range of data that can be used. In order to account for any inaccuracies in the way the numerical model captures the fatigue behaviour of the physical device a factor of 1.35 should be applied to the calculated cumulative fatigue damage.

Both the numerical model and the physical tank test model show that the greatest fatigue damage occurs at the LA5S, which is the articulation attached to the Singler node. Interestingly, the articulations at the Doubler nodes perform better in fatigue than LA5S, but also contribute more to the total array power. This indicates that the additional link arm

improves the fatigue behaviour of an articulation, while not adversely impacting its power generation capability which is a potentially beneficial result worth exploring further. While the articulations at Central nodes have a low fatigue damage, they also contribute the least to the overall power, which would be something to consider when looking at larger array configurations, which could have a greater proportion of Central nodes.

A comparison of spectral fatigue analysis methods shows that even using well established probability density functions (such as the Dirlik pdf, developed for use with ocean wave loading) predicts significantly higher levels of fatigue damage than time domain methods.

The difference between fatigue damage calculated in the time and frequency domain increases with the number of link arms attached to the node. This indicates that the additional link arms introduce greater non-linearities into the structure, meaning that spectral methods are less appropriate for these locations, as they assume a stationary, Gaussian process, while non-linear behaviour results in a non-Gaussian structural response.

This is an interesting result, and one worth investigating further, as fatigue limit state is often the main design driver for dynamic floating WECs, and spectral method are often more appropriate to use than full time history analysis. The analysis carried out in this report indicates that the current spectral methods may not be appropriate for interconnected, multi-body devices with complex interactions, and could lead to over-conservative, un-economic designs.

6.5.2 Conclusions on appropriate results to use for further design

The numerical model provides a more complete data set than the physical model, and can be extended to cover sea states that were not tested in the tank. It is therefore easier to use numerical modelling results to derive relevant load cases for design.

The comparison between the numerical and physical model results shows that as the NM data over-predicts peak loads in extreme sea states, it is appropriate to use the numerical modelling results to derive the more extreme loads associate with Ultimate Limit State load cases.

However, the opposite is true for fatigue loading, as fatigue damage levels calculated in the time-domain using numerical modelling results are lower than those calculated using the physical modelling results. Therefore, if full time-domain fatigue methods are to be used, the results suggest a factor of 1.35 should be applied to any fatigue damage, to compensate for the differences between the modelling techniques.

Where it is more appropriate to use spectral fatigue methods, the Dirlik probability density function should be used, using RAOs determined from the numerical modelling, without any further safety factors. Initial checks show that using this method will give conservative estimates of fatigue damage. This is acceptable for preliminary design, where the main aim is

to compare and contrast different options, but could result in un-economical structural details if used for detailed design. Therefore, there would be benefit to carrying out further investigations into the most appropriate spectral methods to be used for multi-body floating wave energy converters.

Chapter 7

PTO torque limitation

The modelling activities in Chapter 6 have been carried out assuming that there was no limit on the power take off (PTO) torque that could be produced. However, in reality, there will be a torque limit related to the physical characteristics of the full-scale PTO mechanism.

Torque limitation affects the array power output, the size (and therefore cost) of the PTO components, as well as the sizing of the structural components. Therefore, setting the target PTO torque is an important design decision that needs to be made at an early point in the design process.

This chapter investigates the effect of limiting the PTO torque on these different factors, with the aim of identifying the optimum torque limit, balancing power output and structural loading to give a minimum value of the Levelised Cost of Energy (LCoE). Work is carried out using the results from tank tests on the physical model as in general these give larger peak torques than the numerical model in the smaller operational seas.

Outputs from this work forms the basis of a conference paper by the author, presented at EWTEC 2017 (Barker Ewart et al., 2017), and included in Appendix A.

The structure of this chapter is as follows:

- The methodology adopted for selecting the optimum PTO torque limits is covered in **Section 7.1**, covering power output, PTO sizing, outline structural design and LCoE modelling.
- The results of the torque optimisation process are presented in Section **7.2**.
- A discussion of the results, including a sensitivity analysis, and overall recommendations for the PTO torque limit to be used for ongoing design work is included in **Section 7.3**.

7.1 PTO torque limitation methodology

This section sets out the methodology for assessing the most appropriate PTO torque, using LCoE as an assessment metric. The methodology steps are summarised below, and discussed in more detail in the following sections. Note that each step is carried out across a range of torque limits (TL), with $200 < TL < 2500$ kNm:

1. Determine overall power output based on model time histories
2. Carry out high level sizing of PTO rams.
3. Perform preliminary structural design tasks, assuming that fatigue loads are the driver for design.
4. Estimate costs of main component, and feed information into LCoE calculation.

7.1.1 Power output

The impact of torque limit on power production has been investigated by capping the measured torque history at the specified TL, and then using this capped time history to recalculated the mean power capture; this process has been carried out for each in-line articulation, for each test sea state. It is noted that this is not entirely accurate as a physical torque limit would alter the behaviour of the device, however this is acceptable for the purpose of TL optimisation.

The post-processed results have then been used to develop a full power matrix, with data interpolated and extrapolated across the full range of sea states, using the scatteredInterpolant data object in Matlab. This is combined with the West Harris occurrence matrix to give an estimate of the Annual Energy Production (AEP). An example of the post-processed torque limited time history compared with the measured torque is shown in Figure 7.1, where TL = 600 kNm (full scale).

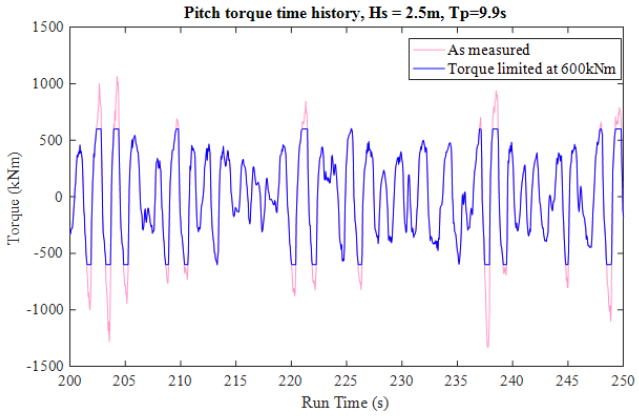

Figure 7.1: Extract from torque limited time history for LA5, for H_s =2.5 m, T_p = 9.9 s. Values reported at full scale

7.1.2 PTO Sizing

While the exact details of the full-scale PTO mechanism were not fully developed at the time of writing, the high-level concept is to have two hydraulic cylinders attached to the node and link using ball joints, allowing for movement and damping around three axes (left hand side of Figure 7.2). Assuming an operating pressure of 250bar for the cylinders (as recommended by the hydraulic engineer at Albatern), the required cylinder bore size has been calculated to give the appropriate ram force for a given torque limit as illustrated in right hand side of Figure 7.2.

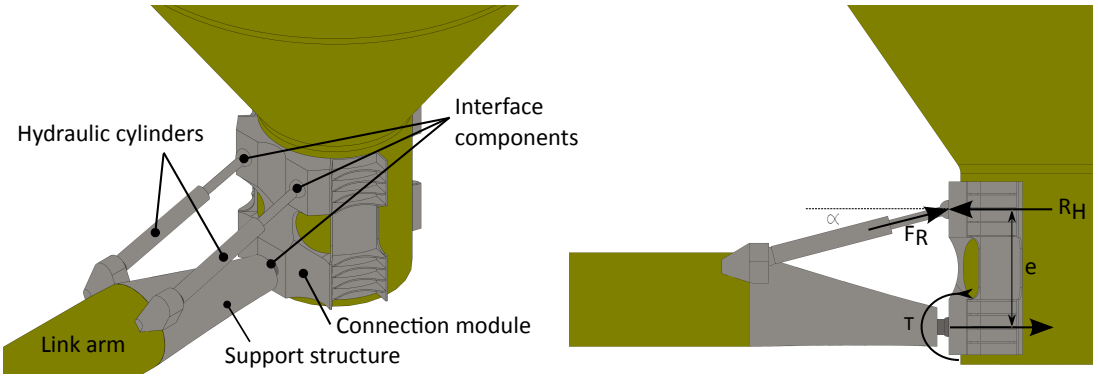

(a) PTO schematic (b) PTO force components

Figure 7.2: PTO mechanism schematic

Ram force is calculated as follows:

PTO torque:	T	Lever arm:	e
Reaction force:	$R_H = T/e$	Pressure:	$P = 250bar$
Bore:	B	Cross-section area:	$A = B^2\pi/4$
Angle:	$\alpha = 20^\circ$		

Ram force: $$F_R = PA = R_H/cos(\alpha)$$

7.1.3 Structural design

For identification purposes the device components are categorised into different systems and sub-systems as shown in Table 7.1.

As for previous work in Chapter 5 and 6, the link arm is taken as a representative component for design, as the loads can be directly derived from the PTO torque, independently of the PTO configuration. In contrast the Joint and Connection Module design is very dependent on the PTO mechanism; for these components it has been assumed that the steelwork weight varies in direct proportion to the change in required Link Arm weight.

Table 7.1: Systems, subsystems and components for the Albatern 12S array

SYSTEM / Subsystem/ *component*
STRUCTURAL SYSTEM
Node module
Link arm
Link arm steel tube
Fixtures and fittings
Joint module
Hydraulic cylinder
Support structure
Interface components
Connection module
MECHANICAL & ELECTRICAL SYSTEM
MOORING SYSTEM
TRANSMISSION AND GRID CONNECTION

The design of the Node structure will be driven by wave pressures on the hull (except for the connection to the steelwork), and therefore will not be greatly affected by the PTO torque. The design of this element is assumed to stay the same for all torque levels.

The link arm design is based on the required resistance to fatigue loads, calculated in the manner described in Section 6.4.3. The appropriate link arm cross sectional area has been determined to ensure that the fatigue usage factor $\mu \leq 1$, for a design life of 20 years, and a Design Fatigue Factor of 1 (assuming that the link arms can be inspected on a regular basis, see DNV GL, 2017, Table 1).

7.1.4 LCOE modelling

The aim of this work is to select the optimum PTO torque limit which gives the minimum LCoE; this has been estimated using a tool developed in-house at Albatern by Ciaran Frost.

The Levelised Cost of Energy (LCoE) is a measure of how much it costs to generate a unit of energy, taking into account whole lifetime cost. The basic equation for the LCoE calculation is given below:

$$LCOE = \frac{\sum_{t=1}^{n} \frac{CAPEX_t + OPEX_t}{(1+r)^t}}{\sum_{t=1}^{n} \frac{E_t}{(1+r)^t}} \tag{7.1}$$

Where:

- $CAPEX_t$ = capital expenditure in year t (assumed in this case to all occur in year 1; varies with PTO torque limit);
- $OPEX_t$ = operational expenditure in year t (calculated by others in the Albatern team, and assumed to be the same for all torque limits);
- n = design life, (taken as 20 years);
- r = discount rate (assumed in this case to be 8%);
- E_t = electrical energy produced in year t (calculated based on modelled power matrix (which varies with PTO torque limit), and expected wave conditions at the West Harris reference site (which remains the same for each scenario)).

The baseline scenario for the LCOE was taken when TL = 1 MNm. Captial costs for this scenario were estimated based on discussions with the Albatern design team, bringing together knowledge from production and manufacture of the Albatern prototype 6S device and quotes from suppliers. Estimated unit costs for the baseline scenario are included in Table C.1 in Appendix C.

The top level categories that have been considered in the cost estimate are shown in Table 7.2, together with the % contribution of each category to the total whole life cost for the baseline scenario.

Table 7.2: Categories and contribution to whole life cost, Baseline Scenario (Torque Limit = 1MNm)

Category	% contribution to cost
Structural system	43.8
Mechanical & electrical system	7.5
Mooring system	12.1
Transmission & grid connection	5.7
Installation	12.3
Operations & Maintenance	18.7

In this study, it is assumed that all costs remain constant except for the structural components listed in Table 7.2. This is a very simplified assumption, as the cost of other components such as hydraulic routing cables and accumulators will also vary with PTO torque. However, any additional increases and decreases are likely to exaggerate any variation in LCoE, and therefore this simplification is acceptable at this level of analysis. Table 7.3 shows the cost of each structural subsystem and component for the baseline scenario as a % of the Structural System cost.

To estimate the costs for each different torque limit, it is assumed that the cost of the steelwork items (which includes all components listed in Table 7.1, except for the hydraulic cylinders) vary in proportion with the variation in steel weight of the link arm.

Table 7.3: Systems, subsystems and components of array for cost purposes

Subsystem / *component*	% of structural system cost
Node module (assuming concrete)	44.5
Link element	16.2
Link arm steel tube	*14.7*
Fixtures and fittings	*4.7*
Joint module (PTO system)	39.2
Hydraulic cylinder	*7.6*
Support structure	*11.5*
Interface components	*7.1*
Fixtures and fittings	3.6
Connection module	9.6

Hydraulic cylinder costs have been estimated based on stock cylinder prices as published on the Interfluid website (Interfluid Hydraulics Ltd, 2017). A multiplier of 4 has been included in the pricing, to account for the increased cost associated with manufacturing bespoke cylinders; this is based on the difference between the quoted stock price and the actual price paid for the cylinders in the Albatern prototype 6S device. The Interfluid stock cylinders are smaller than those required for the 12S device, but prices increase linearly with bore size and stroke, and therefore the prices have been extrapolated as required.

7.2 PTO Torque limitation: Optimisation results

7.2.1 Power output results

Figure 7.3 shows the normalised power matrix extrapolated from the unlimited tank testing results over the full range of the West Harris occurrence sea states. Power output is based on the mechanical power capture, and values are given as a percentage of the maximum power output (which occurs when $H_s = 10\,\text{m}$, and $T_p = 11\,\text{s}$).

In comparison, as an example, the power matrix for the case where torque has been limited to 600kNm (full scale) is shown in 7.4. Values are given as a percentage of the maximum power output for the unlimited torque case shown in Figure 7.3.

Power matrices for different torque limits have been calculated, and then combined with the West Harris occurrence matrix to calculate the variation in annual mean energy production (AEP), as shown in Figure 7.5. It can be seen from this graph that the increase in AEP is significant between 0 and 0.6 MNm, but that there is little increase above 1 MNm. This is due to the fact that the larger sea states which would generate PTO torques of greater than this account only occur for a very small proportion of the design life of the array.

T_p [s]

H_s / T_p	3	4	5	6	7	8	9	10	11	12	13	14	15	16	17	18	19	20	21
10									100%	95%	92%	89%	86%	82%	71%	60%	58%	56%	54%
9.5									94%	89%	86%	83%	81%	74%	63%	56%	54%	52%	50%
9								92%	88%	83%	80%	78%	75%	66%	56%	52%	50%	48%	46%
8.5								86%	82%	77%	75%	72%	68%	59%	49%	47%	46%	44%	43%
8								80%	76%	72%	69%	66%	60%	51%	45%	43%	41%	40%	40%
7.5							78%	74%	70%	66%	63%	60%	53%	44%	41%	39%	37%	37%	37%
7							72%	68%	64%	60%	58%	54%	46%	39%	37%	35%	35%	34%	34%
6.5							67%	62%	59%	55%	52%	47%	40%	35%	33%	32%	32%	32%	32%
6							66%	56%	53%	49%	46%	40%	33%	31%	29%	29%	29%	29%	29%
5.5						84%	63%	50%	47%	43%	40%	34%	29%	27%	26%	26%	26%	26%	25%
5						79%	59%	45%	41%	37%	34%	28%	25%	24%	23%	23%	23%	23%	22%
4.5					58%	64%	54%	41%	35%	32%	28%	23%	21%	20%	20%	20%	20%	19%	18%
4					46%	52%	48%	35%	29%	26%	22%	19%	18%	17%	17%	17%	16%	16%	15%
3.5					36%	40%	39%	29%	23%	20%	17%	15%	15%	14%	14%	13%	13%	12%	11%
3				31%	30%	31%	30%	19%	18%	15%	12%	12%	11%	11%	10%	10%	9%	9%	8%
2.5				24%	23%	23%	21%	17%	13%	10%	9%	9%	8%	7%	7%	6%	6%	5%	5%
2			28%	24%	20%	16%	13%	11%	8%	6%	5%	5%	5%	4%	3%	3%	2%	2%	1%
1.5			13%	12%	11%	9%	8%	6%	5%	3%	2%	2%	1%	0%	0%	0%	0%	0%	0%
1		9%	8%	6%	5%	3%	2%	2%	1%	0%	0%	0%	0%	0%	0%	0%	0%	0%	0%
0.5	5%	3%	2%	0%	0%	0%	0%	0%	0%	0%	0%	0%	0%	0%	0%	0%	0%	0%	0%

H_s [s]

Figure 7.3: Extrapolated normalised power matrix based on mechanical power captured during tank testing, for unlimited torque case

T_p [s]

H_s / T_p	3	4	5	6	7	8	9	10	11	12	13	14	15	16	17	18	19	20	21
10									78%	76%	74%	72%	70%	67%	62%	56%	54%	53%	51%
9.5									74%	72%	70%	68%	66%	62%	56%	52%	51%	49%	48%
9								72%	70%	67%	65%	63%	61%	56%	51%	49%	47%	46%	44%
8.5								67%	65%	63%	61%	59%	56%	51%	46%	45%	43%	42%	41%
8								63%	61%	58%	56%	54%	51%	46%	43%	41%	40%	39%	38%
7.5							61%	58%	56%	54%	52%	50%	46%	41%	39%	38%	36%	36%	36%
7							56%	54%	52%	50%	47%	45%	41%	37%	35%	34%	33%	33%	33%
6.5							53%	49%	47%	45%	43%	40%	36%	33%	32%	31%	30%	30%	30%
6							52%	45%	43%	41%	38%	35%	31%	30%	28%	28%	27%	27%	27%
5.5						65%	50%	41%	38%	36%	34%	30%	27%	26%	25%	25%	24%	24%	24%
5						61%	47%	37%	34%	32%	29%	26%	24%	23%	22%	22%	21%	21%	21%
4.5					48%	51%	43%	34%	29%	27%	25%	22%	20%	20%	19%	19%	18%	18%	17%
4					39%	42%	38%	29%	25%	23%	20%	18%	17%	17%	16%	16%	15%	15%	14%
3.5					32%	34%	32%	25%	20%	18%	16%	15%	14%	13%	13%	12%	12%	11%	11%
3				28%	27%	27%	25%	17%	16%	14%	12%	11%	11%	10%	10%	9%	9%	8%	7%
2.5				23%	22%	20%	19%	16%	12%	10%	9%	8%	8%	7%	6%	6%	5%	5%	4%
2			27%	23%	19%	15%	13%	10%	8%	6%	5%	5%	4%	4%	3%	3%	2%	1%	1%
1.5			14%	13%	11%	9%	8%	6%	4%	3%	2%	2%	1%	0%	0%	0%	0%	0%	0%
1		9%	8%	6%	5%	3%	2%	2%	1%	0%	0%	0%	0%	0%	0%	0%	0%	0%	0%
0.5	5%	3%	2%	0%	0%	0%	0%	0%	0%	0%	0%	0%	0%	0%	0%	0%	0%	0%	0%

H_s [s]

Figure 7.4: Extraplated normalised power matrix based on mechanical power captured during tank testing, for PTO torque limit = 600kNm

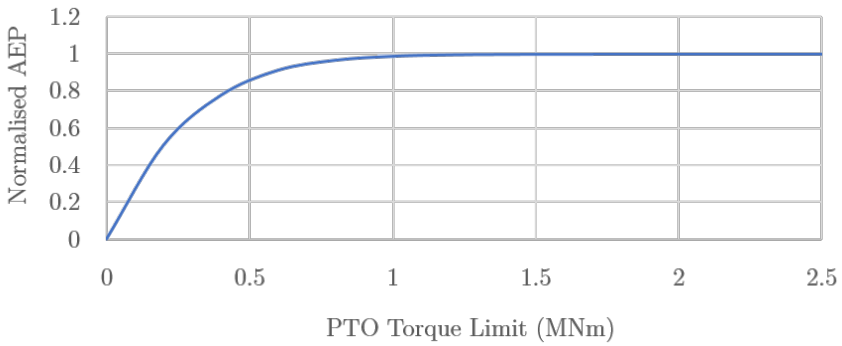

Figure 7.5: PTO torque limit (full scale) vs AEP

7.2.2 Component sizing & costing

Table 7.4 shows the required hydraulic cylinder bore size calculated for different PTO torque limits (TL) as described in Section 7.1.2, together with the estimated cylinder cost.

Table 7.4: Hydraulic cylinder estimated size and costs

TL (MNm)	0.2	0.4	0.6	0.8	1	1.2	1.5	2.5
Bore (mm)	70	100	120	140	160	180	200	250
Cost (£1000)	0.8	1.9	2.5	3	3.5	4.1	4.6	5.9

Table 7.5 shows the link arm cross-sectional area (CSA) required to keep fatigue damage accumulation levels below 1 for a life span of 20 years. The table also shows the % variation in required link arm steel weight, when compared to the baseline case.

Table 7.5: Required link arm cross sectional area (CSA)

TL (MNm)	0.2	0.4	0.6	0.8	1	1.2	1.5	2.5
CSA (cm2)	50	58	67	79	90	98	102	102
% difference	56	64	74	87	100	109	113	113

Costs have been estimated for each of the different torque limits based on the information given in Table 7.4 and 7.5. For the other steelwork items as listed in Table 7.3, it has been assumed that the costs vary in proportion to the required link arm weight.

Figure 7.6 shows the variation in costs with PTO torque limit. The Structural costs include all the subsystems as listed in Table 7.3. The total cost includes all systems listed in Table 7.2 (this value was subsequently used to calculate the LCoE) and values have been normalised against the maximum total cost.

These graphs show that generally the structural costs increase with torque limit, however the rate of change slows, with the greatest increase occurring between a torque limit of 0.2 and 1.2 MNm. This is because fatigue design is affected by the number of cycles at a particular stress range, not just the magnitude. In any given time period, there will be fewer cycles with larger magnitude loading, and therefore these have less of an impact on the overall design than the smaller magnitude loads, which contribute to a larger proportion of the overall damage. Lower torque limits therefore have a much greater impact on the number of cycles that the structure must endure than the larger torque limits, as they reduce the number of the low stress cycles applied to the device over its lifetime.

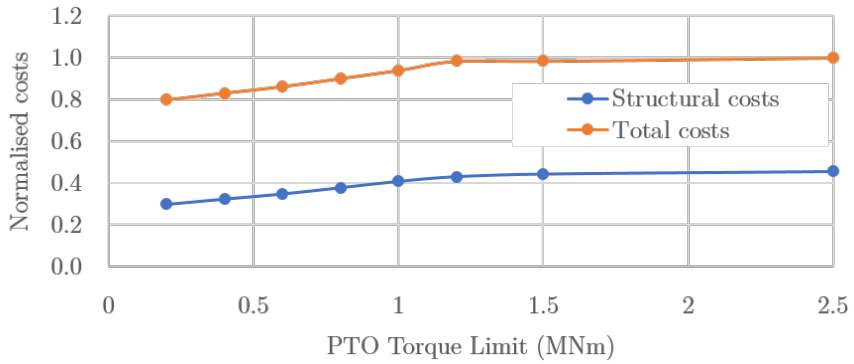

Figure 7.6: PTO torque limit (full scale) vs Normalised costs

7.2.3 LCoE

LCoE is a function of both device cost and total power production. Fig 7.7 shows the variation in cost, AEP and LCoE with PTO torque limit, normalised so that the maximum value of each is taken as 1. It can be seen from this figure that AEP increases rapidly between a torque limit of 0.2 and 0.6 but tends to a limit at around 1.2MNm. Costs continue to increase, but the rate of change slows above 1.2MNm. LCoE therefore shows a significant decrease up to the torque limit of 0.6MNm, and reaches a minimum at 0.8MNm. LCoE then starts to increase again, but at a slower rate than one might instinctively expect, because the rate of cost increase also slows. It should be noted however that this analysis only considers the variation in the cost of the structural items. As noted previously there are likely to be other components which vary in cost with PTO torque, however these differences would likely exaggerate the increase in LCoE for torque limits greater than 0.8kNm, and therefore would not change the overall outcome of the analysis. This work therefore shows that a torque limit of 0.8MNm would be beneficial, as it results in the lowest LCoE.

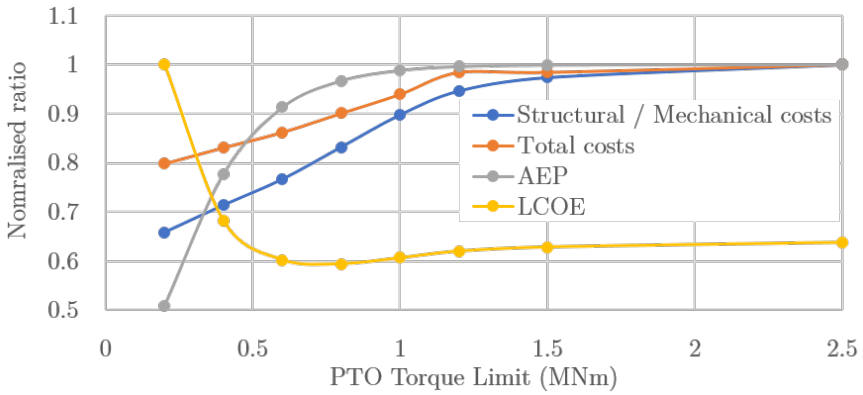

Figure 7.7: PTO torque limit (full scale) vs Costs, AEP and LCoE to satisfy fatigue design life of 20 years at West Harris stie

7.2.4 Sensitivity analysis

The results shown in Figure 7.7 are based on a number of assumptions regarding the variation in the cost of the structural elements with PTO torque limit; in particular, that the weight of all steelwork items varies in proportion to the variation in link arm weight. In order to assess the impact of this assumption on the overall results, a sensitivity study has been carried out.

Table 7.6 shows the normalised LCOE for two scenarios compared with the base case discussed in Section 7.2.3.

1. The variation in the weight of the additional steelwork items with PTO torque limit is double the variation in link arm weight,
2. The variation in the weight of the additional steelwork items with PTO torque limit is half the variation in link arm weight.

Table 7.6: Normalised LCoE values for different cost assumptions

TL (MNm)	0.2	0.4	0.6	0.8	1	1.2	1.5	2.5
Basecase	1.00	0.68	0.60	**0.59**	0.61	0.62	0.63	0.64
Scenario 1	1.00	0.68	0.59	0.58	**0.58**	0.59	0.60	0.60
Scenario 2	1.00	0.70	**0.63**	0.63	0.66	0.68	0.70	0.70

The minimum value of LCOE for each case is highlighted in bold. The values in Table 7.6 show that the optimum torque limit does vary slightly depending on the assumptions regarding the steelwork cost variation. For the Scenario 1, the minimum LCoE occurs 1 MNm. For the Scenario 2, the torque limit which gives the minimum LCoE value has shifted to 0.6 MNm. While this analysis does not consider the potential variation in all variables, it does indicate that the true value of the optimum LCoE is between 0.6 and 1 MNm.

7.3 PTO Torque limit - discussion and conclusion

7.3.1 Discussion

PTO torque limit has a significant impact on power output, structural design, and the cost of many of the components of a wave energy device, and therefore is it beneficial to highlight the optimum torque limit early in the design process. This chapter presents a simple method for this using high level concept design methods and early stage tank testing results. In principle, the method is applicable to other technologies, although would need to be adapted to drivers specific to the working principle of a given device.

However, there are certain limitations to the method presented here as this is a multi-objective and multi-parameter problem; for example, the results are very dependent on the chosen site and array configuration. There would be benefit in extending the analysis to check the

sensitivity of the results at other sites and array scales, as it would be advantageous to have a single device design suited to multiple sites and configurations. Also, the analysis only considers the effect of structural costs on LCoE, when other factors (such as the cost of hydraulic and electrical components) will also have an impact. At this stage, it is assumed that these other factors will follow the same trends as the structural costs, however it would be important to check that this is still valid if the design were to progress.

Despite these limitations, the method does provide an initial starting point for the PTO torque that can be taken forward to detailed design, using the limited information that is available at the early design stage. This is beneficial for the design process, as it allows for focussed design work to be carried out using a set PTO limit; while the exact limit might change with ongoing detailed design work, it is not likely to vary significantly from the value that has been determined here.

7.3.2 Conclusion

For the rest of the work in this thesis, the upper bound of the torque limit as suggested by the sensitivity analysis (1 MNm) will be taken as the PTO limit, applicable about each PTO axis. This PTO limit requires a hydraulic cylinder with a bore of 160 mm, and a link arm with a cross-sectional area of 90 cm^2 (diameter = 1.27 m, thickness = 23 mm)

Chapter 8

Summary of final load cases

The work carried out in the previous chapters of this part cover the concept design process from initial option selection, through the modelling work, and further results analysis to investigate appropriate design loads. This chapter brings together the results from this work to define a set of power take off (PTO) loads and design load cases that will be taken forward to the design activities discussed in Part III.

The structure of this Chapter is as follows:

- PTO articulations loads are discussed in **Section 8.1** bringing together results from the numerical and physical models, together with the analysis work on torque limitation to define a full set of articulation loads.
- Relevant sea states for design are considered in **Section 8.2**, and are then combined with appropriate articulation loads to define a set of limit state load cases.
- A summary of the relevant learning points from the whole of this part is included in **Section 8.3**.

8.1 PTO articulation loads for design

8.1.1 Discrete load cases (SLS, ULS and ALS)

The PTO articulation load components for different “Discrete” design limit states have been determined from the numerical modelling work discussed in Section 6.3 together with the work on PTO torque limitation discussed in this Chapter 7. Load cases associated with serviceability (SLS), ultimate (ULS) and accidental (ALS) limit states are referred to as “Discrete” load cases, as each load case is related to a specific sea state in the West Harris occurrence matrix.

The analysis in Section 6.4.2 concludes that the articulation loads obtained from the numerical model are suitable for preliminary design, particularly for steeper waves, where the peak torques are greater than the tank testing results.

As well as replicating the physical model test runs, the numerical model has also been run with the largest wave on the West Harris Occurrence matrix (H_s = 10 m and T_p = 14 s) to look at the behaviour in more extreme loads.

Table 8.1 shows the peak articulation loads extracted from the numerical model for the sea state where H_s = 4.5 m and T_p = 10.5 s (corresponding to one of the largest operational waves, taken to be representative of SLS loading), and Table 8.1 shows this for the sea state where H_s = 10 m and T_p = 14 s (corresponding to more extreme wave loading, taken as a ULS loadcase). The tables show the articulations at link arms 1 to 5; results for 7 to 9 are similar to 1 to 3 due to the symmetry of the model. Articulations labelled with an "F" relate to forces along an axis, with "M" referring to the bending moments about an axis. "X" is the torsion axis, "Y" is the pitch axis, and "Z" is the yaw axis.

These tables indicate that the increasing wave height has most impact on the pitch and yaw moments, as the other articulation reaction components are similar orders of magnitude between the two sea states. (Note that these tables present the unlimited torque values).

Table 8.1: Peak articulation actions from Numerical model, H_s = 4.5 m and T_p = 10.5 s, taken as an SLS loadcase

Link arm	F_X (kN)	F_Y (kN)	F_Z (kN)	M_X (kNm)	M_Y (kNm)	M_Z (kNm)
LA1S	549	64	176	383	1112	1171
LA1C	549	64	176	383	1110	1171
LA2D	1015	96	151	885	1864	715
LA2C	1015	93	151	885	1107	448
LA3D	589	162	173	740	1184	722
LA3C	589	162	173	736	1184	722
LA4D	852	129	159	558	1517	1485
LA4C	852	129	159	556	1517	1485
LA5S	936	32	207	136	1962	312
LA5D	936	29	207	136	930	312
Max	1015	162	207	885	1962	1485

Table 8.1 shows that the PTO torque around each of the Pitch and Yaw axis (M_y and M_z) exceeds the specified limit of 1 MNm value in the largest operational loads, with the Torsion nearly reaches 1 MNm (max of 885 kNm recorded). However, inspection of the time history shows that the peak loads around the three axis are out of phase, and therefore for the SLS loadcase, M_x and M_z have been set at 0.5MNm, combined with M_y = 1MNm. For the ULS load case it has been assumed that the maximum load can occur around all three axis simultaneously.

The connection point is one of the most critical components, and there is a risk of PTO mechanism lock up, that could result in articulation loads greater than the PTO torque limit. Therefore an ALS load case is also presented in Table 8.3, assuming that a pitch articulation

Table 8.2: Peak articulation actions from numerical model, H_s = 10 m and T_p = 14 s, taken as a ULS loadcase

Link arm	F_X (kN)	F_Y (kN)	F_Z (kN)	M_X (kNm)	M_Y (kNm)	M_Z (kNm)
LA1S	466	80	187	453	1672	297
LA1C	562	75	193	449	1189	1497
LA2D	961	199	146	889	2104	922
LA2C	1015	118	151	888	1107	662
LA3D	639	74	137	624	888	1002
LA3C	658	162	173	619	1184	820
LA4D	920	122	181	629	593	1360
LA4C	954	129	159	630	1517	1876
LA5S	990	35	274	136	3085	251
LA5D	1101	29	208	136	1046	312
Max	1101	199	274	889	3085	1876

of 5x the PTO torque limit could occur, simultaneously to a yaw and torsion articulation 2x the PTO torque limit. at this stage these factors have been chosen simply to ensure that the ALS articulation loads are greater than the maximum loads shown in Table 8.2; for detailed design further modelling work would be required to determine more accurate values.

Table 8.3 sets out the articulation load cases for the discrete load cases that will be taken forward for ongoing design work.

Table 8.3: PTO articulation load cases for ongoing design work

Limit state	F_X (kN)	F_Y (kN)	F_Z (kN)	M_X (kNm)	M_Y (kNm)	M_Z (kNm)
SLS	1000	250	250	500	1000	500
ULS	1100	250	250	1000	1000	1000
ALS	1500	500	500	2000	5000	2000

8.1.2 Fatigue loads

The study on fatigue analysis methods in Section 6.4.3 highlighted that using spectral analysis methods using response amplitude operators (RAOs) extracted from the numerical models gives conservative fatigue damage estimates, however are suitable for use in preliminary design calculations.

The numerical models have been run in regular waves with a unit wave height and for a range of wave periods, to determine the articulation load RAOs (as shown in Figure 6.19 on page 110); a selection of the articulation loads are presented in Table 8.4 for completeness.

Table 8.4: Articulation loads for spectral fatigue analysis, with varying T_p, and H_s = 1 m

T_p (s)	4	6	8	10	12	16	20
M_x (kNm)	171.0	184.8	200.8	136.8	69.2	56.1	43.3
M_y (kNm)	257.1	565.0	356.2	257.7	224.5	130.8	92.1
M_z (kNm)	229.6	238.9	219.2	185.3	178.1	191.1	214.0
F_x (kN)	56.3	133.4	106.1	63.0	49.4	56.9	58.6
F_y (kN)	19.3	20.3	20.1	19.1	19.8	21.2	14.9
F_z (kN)	45.8	49.2	15.1	11.1	7.3	5.5	3.2

8.2 Design sea states and limit state load cases

Figure 8.1 provides a summary of the different sea states that are of interest in design. The coloured fill indicates the operational sea states, where power is produced. At this stage this has been assumed to be any sea state which has more than 20 waves in a given year, with an upper limit to the operational H_s of 6 m.

Extreme sea states are based on the 1 in 100 year storm event (as recommended in DNV (2005)), which have been estimated from the West Harris scatter diagram data using extreme value analysis techniques by Johann Praeffe, (a mechanical engineer within Albatern). The resulting 1 in 100 year contour is shown on Figure 8.1.

In addition to the 1 in 100 year events specific to the reference site, two additional extreme sea states have also been considered related to the theoretical breaking limit of waves (H/L = 0.14[1]). These waves are considerably steeper than those that are predicted to occur, even in extreme conditions at the West Harris site; for this reason they have been designated as ALS sea states, to be combined with the ALS PTO loads.

These sea states are combined with the PTO loads given in Table 8.3 to give different limit state load cases as shown in Table 8.5.

Table 8.5: Limit state load case combinations

Limit State	H_s (m)	T_p (s)	Comment	Combined with:
SLS	1.5	9	Most common sea state at West Harris	SLS PTO load
SLS	4.5	10.5	Outer edge of operational sea states	SLS PTO load
SLS	6.0	12	Outer edge of operational sea states	SLS PTO load
ULS	9.4	10.1	1 in 100 yr event	ULS PTO load
ULS	14	12.2	1 in 100 yr event, and max H_s	ULS PTO load
ALS	10	7	Steep wave	ALS PTO load
ALS	14	8	Steep wave	ALS PTO load

1. It is noted that using T_p for the calculation of breaking waves is un-necessarily severe as breaking of larger waves dissipates energy, however as this gives an upper bound for preliminary design, and therefore is acceptable for this purpose

T_p [s]

H_s / T_p	3	4	5	6	7	8	9	10	11	12	13	14	15	16	17	18	19
14.0	0	0	0	0	0	0	0	0	0	0	0	0	0	0	0	0	0
13.5	0	0	0	0	0	0	0	0	0	0	0	0	0	0	0	0	0
13.0	0	0	0	0	0	0	0	0	0	0	0	0	0	0	0	0	0
12.5	0	0	0	0	0	0	0	0	0	0	0	0	0	0	0	0	0
12.0	0	0	0	0	0	0	0	0	0	0	0	0	0	0	0	0	0
11.5	0	0	0	0	0	0	0	0	0	0	0	0	0	0	0	0	0
11.0	0	0	0	0	0	0	0	0	0	0	0	0	0	0	0	0	0
10.5	0	0	0	0	0	0	0	0	0	0	0	0	0	0	0	0	0
10.0	0	0	0	0	0	0	0	0	0	0	0	1	0	0	0	0	0
9.5	0	0	0	0	0	0	0	0	0	0	0	2	1	1	1	0	0
9.0	0	0	0	0	0	0	0	0	0	0	0	1	3	3	1	0	0
8.5	0	0	0	0	0	0	0	0	0	0	0	3	3	4	1	0	0
8.0	0	0	0	0	0	0	0	0	0	0	1	6	7	7	2	0	0
7.5	0	0	0	0	0	0	0	0	0	2	2	12	10	8	1	0	0
7.0	0	0	0	0	0	0	0	0	0	2	8	21	14	6	1	0	0
6.5	0	0	0	0	0	0	0	0	1	11	10	24	17	7	5	1	0
6.0	0	0	0	0	0	0	0	1	3	0	21	26	17	9	2	0	0
5.5	0	0	0	0	0	0	0	2	9	40	40	48	19	5	2	0	0
5.0	0	0	0	0	0	0	1	2	24	76	61	52	23	7	1	0	0
4.5	0	0	0	0	0	0	3	16	63	119	80	62	15	4	2	1	0
4.0	0	0	0	0	0	2	17	0	140	142	70	66	24	7	2	1	0
3.5	0	0	0	0	0	11	29	110	205	176	80	60	20	6	5	1	0
3.0	0	0	0	0	4	36	94	247	236	188	78	35	18	7	3	1	0
2.5	0	0	0	1	26	80	230	315	268	174	55	34	15	5	4	2	0
2.0	0	0	0	11	56	200	397	367	218	125	37	32	13	8	2	1	0
1.5	0	0	12	34	134	356	406	274	168	86	26	20	9	4	4	1	0
1.0	0	4	32	85	238	381	274	138	86	23	13	5	7	3	2	1	0
0.5	0	12	23	32	82	57	40	28	12	8	2	2	1	0	0	0	0
0.0	0	0	0	0	0	0	0	0	0	0	0	0	0	0	0	0	0

H_s [m]

Figure 8.1: West Harris Occurrence Matrix, with design sea states highlighted. The blue contour line relates to the 1 in 100yr storm event. Red dots correspond to sea states at the wave breaking limit. Orange dots correspond to sea states at the edge of the power production zone, and the purple dot corresponds to the most common sea state at the West Harris site.

8.3 Final comments

The load cases detailed in this chapter will be taken forward to the ongoing design work for the Node structure as discussed in Part III. These load cases have been derived on the basis of the conceptual design work discussed in the preceeding chapters; a summary of the main discussion points and conclusions from this work is included below.

The concept selection work presented in Chapter 5 highlighted the importance of considering structural loading as well as power output when carrying out concept design, as in the 1st assessment stage, the option with the best power output, generated unreasonably high structural loads (option B1 in Table 5.8, page 78).

This trade-off between power generation and structural loading was explored further in Chapter 7, where an optimum torque limit of 1 MNm was identified as the best compromise between maximising power generation across the frequently occurring sea states, and minimising component costs, resulting in the lowest LCoE (taking into account sensitivity to uncertainties in the analysis process). This limit has been applied for both SLS and ULS load cases. The coincident load components have been taken from the numerical model, which, as

work in Section 6.4 shows, provides an adequate representation of the device behaviour at concept level, although would need to be further refined for detailed design work.

Fatigue limit state design will also be based on loads extracted from the numerical models as this provides the most complete set of information. Where it is possible to carry out analysis in the time domain, it will be necessary to include a factor of safety of 1.35 on the calculated damage, as using the numerical model time histories for fatigue analysis results in lower levels of damage than using the results of the tank test.

However, where spectral fatigue analysis is more appropriate, RAOs taken from the numerical model can be used without modification, as spectral methods appear to be more conservative than the equivalent time domain procedures.

PART III

Use of reinforced concrete for Wave Energy Converters

Part IV - Use of Reinforced Concrete

This part of the thesis investigates the potential for using reinforced concrete materials for floating wave energy converters, by carrying out design activities for the Node structure (see Chapter 9 and 10), and its connection to the power take off (PTO) system (see Chapter 11), using the design loads derived in Part II. This work contributes to the overall research objectives by highlighting optimal materials and structural details which offer low cost, but ultimately reliable design solutions.

The Node structure is an important component of the WaveNET system, as it is the main buoyancy element within the array. The Node accounts for 44.5% of the total array structural costs (see Table 7.3 on page 128), and therefore material choice and design of this component can have a significant impact on the cost and structural reliability for the overall array system. A techno-feasibility study of different materials is carried out in **Chapter 9**, which shows that reinforced concrete is the preferred option. The potential for advanced concrete technologies when compared with conventional materials is included in **Chapter 10.**

Design of the steel-concrete connection between the Node and the PTO Module is covered in **Chapter 11.** This joint is critical to the overall function of the device; however one of the main uncertainties associated with the use of concrete materials for WECs is the behaviour of steel-concrete joints subject to highly dynamic, multi-axial loads which create a set of design conditions beyond the application of typical steel-concrete connections. The aim of the work in Chapter11 is to reduce the overall risk by addressing some of the design uncertainties.

Chapter 9

Node material selection

One of the main concerns with wave power is the high levelised cost of energy (LCoE) that is currently being achieved. An important objective for design is therefore to minimise cost wherever possible; and optimal material selection is an important part of this.

This chapter details an initial techno-economic study of material options for the Node structure within the WaveNET array, (as shown in Figure 9.1). The aim of this work is to show that reinforced concrete is the preferred construction material, with the potential to significantly reduce overall costs when compared to other materials.

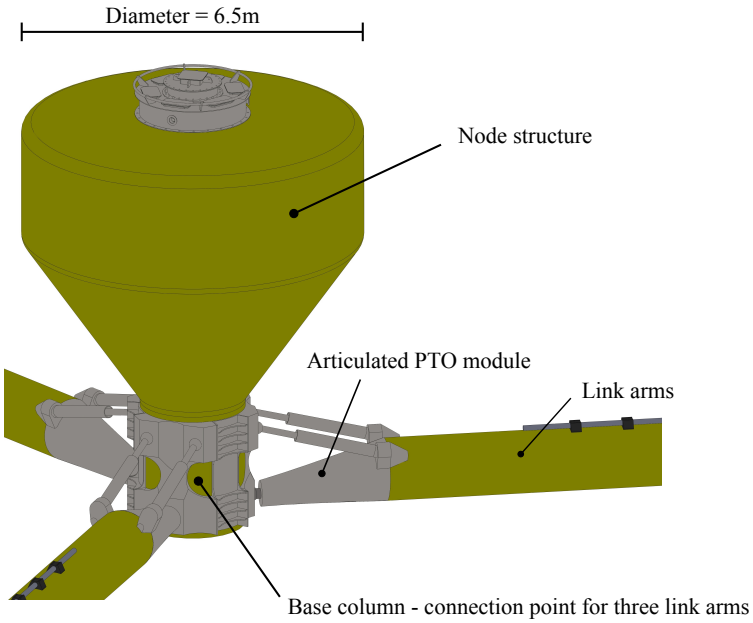

Figure 9.1: Overview of Node structure

The structure of this chapter is as follows:

- A high-level material screening exercise using the principles proposed by Ashby (2011) is discussed in **Section 9.1**;
- A conceptual design and costing exercise is presented in **Section 9.2**;

- A final summary of the chosen material to take forward in the design process is included in **Section 9.3**.

9.1 High level material selection

In order to carry out a high level appraisal of suitable materials, an initial screening process has been carried out following the formal material selection method proposed by Ashby (Ashby, 2011).

This process involves deriving material indices to compare the relative performance of materials against a specified design objective. The steps that have been followed in this process are as listed below:

1. Define the structural function of node;
2. Specify the design constriants;
3. Set out the objective (e.g minimise mass, or cost);
4. Derive material indices that allow a relative material comparison;
5. Select short list of materials as those that best meet the overall objective;
6. Further assess short list of materials on basis of design constraints.

9.1.1 Structural function of the node

The Node is a hollow structure, which is the main element in the array which interacts with the incoming waves. It is also the main buoyant element in the array, and is required to support its own self-weight, as well as the submerged weight of the attached link arms and PTO modules. The overall mass of the structure is therefore important and should be minimised where possible. However, it is not necessary to opt for the lightest material at all costs, providing that the buoyancy requirements are met. Whichever material is chosen must be able to withstand the conditions imposed by the marine environment, and resist the applied dynamic loading while offering a low cost solution.

Structurally, the node can be split into two sections: the base column, which which acts as a cantilever in bending to resist the applied PTO moments, and the node hull, which acts as a panel resisting the hydrodynamic loads from the passing waves, as illustrated in Figure 9.2.

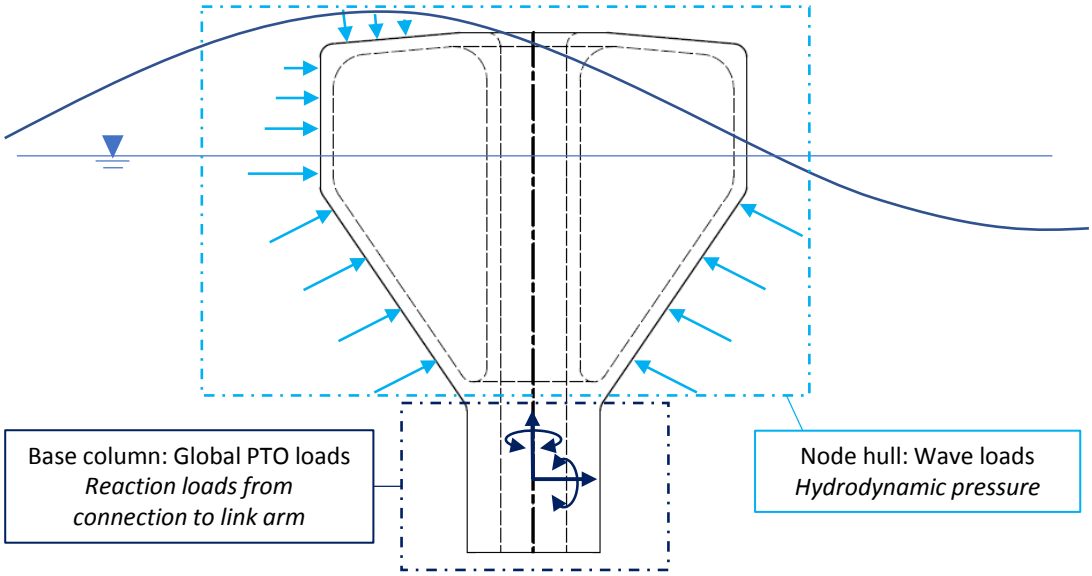

Figure 9.2: Typical loads experienced by node structure

9.1.2 Design constraints

The quantitative design constraints are the outer node dimensions, which have been set as part of the conceptual development work. Qualitative design constraints are shown in Table 9.1.

Table 9.1: Qualitative design constraints for the node

Type	Description
Structural constraints	• Correct fatigue properties to ensure structure can resist dynamic load regime • Adequate ductility to avoid brittle or sudden failure modes • Impact resistance • Ability to be formed into required shape for the node • Wide range of structural manufacturers • Ability to connect to link arms • Ease of repair
Environmental constraints	• Corrosion resistant • Watertight • Does not absorb water • Resistant to UV • Resistant to bio-fouling • Chemically inert (does not leach chemicals into water)

9.1.3 Objective function

As discussed in Chapter 1, Albatern were developing the array on two different scales; the 12S array which is the main focus of this thesis, and the 6S array, at half the physical scale. For the 6S array, weight is a dominating factor in order to get the correct buoyancy. For the 12S the dimensions (and therefore the available buoyancy) also increases, and heavier and potentially cheaper materials may be advantageous. For this exercise both minimum mass (Equation 9.1) and minimum cost objectives (Equation 9.2) will be considered, to compare the difference between the most suitable materials for each:

$$m = btL\rho \tag{9.1}$$

Where m is mass, b = component representative width, t = thickness, L = length, and ρ is the material density.

$$C = AL\rho C_m \tag{9.2}$$

Where C is cost, A is the cross sectional area, and C_m is the unit cost per mass of material.

9.1.4 Derivation of material indices

The structural design requirements of the base column and node walls can be used to derive material indices to aid with the high level material selection process.

(a) Node walls

The node walls can be modelled as a one-way spanning panel, resisting the wave pressures in bending. The panel will fail if the bending stress is greater than the failure strength of the material, with stress being calculated as follows:

$$M_b = Z.\sigma \tag{9.3}$$

Where M_b is the bending moment, Z is the elastic section modulus, which for a rectangular section of unit width = $t^2/6$, and t = wall thickness. Substituting for Z into equation 9.3, and rearranging for t (which is the only free variable in the equation) gives:

$$t = \sqrt{\frac{6M}{\sigma}} \tag{9.4}$$

Substituting equation 9.4 into the objective function (equation 9.1) gives:

$$m = \sqrt{6M_b}.bL.\frac{\rho}{\sqrt{\sigma}} \tag{9.5}$$

M_b, b and L are the same for all materials, therefore to minimise mass, we want to select the material with the smallest $\rho/\sqrt{\sigma}$ (or the maximum $\sqrt{\sigma}/\rho$). This gives the material index for strength at minimum weight as:

$$MI_{s,w} = \frac{\sqrt{\sigma}}{\rho} \tag{9.6}$$

To give strength at lowest cost instead, equation 9.6 can be divided by C_m where C_m is the cost per kg of the material to give the material index for strength at minimum cost.

$$MI_{sc,w} = \frac{\sqrt{\sigma}}{\rho.C_m} \tag{9.7}$$

9.1.5 Base cylinder

The base column can be represented by a cylindrical column, resisting the PTO loads in bending. In bending, the cylinder will fail either if the elastic material strength is reached, or if the cylinder buckles (which is driven by the stiffness of the material, E). These criteria can be used to derive further material indices in the same manner as the bending strength of the panel. Equation 9.8 gives the indices for bending strength (σ) at minimum weight, and cost. Equation 9.9 gives the indices for bending stiffness (E) at minimum weight and cost. Full derivations of these indices are included in Appendix D.1. It is noted that the PTO loading is very dynamic, and fatigue loading will also be a driver for design. However this is difficult to encompass in a single index, due to the varied nature of fatigue resistance for each material, and therefore will be considered during the qualitative assessment of the material short list.

$$MI_s = \frac{\sigma}{\rho} \qquad MI_s = \frac{\sigma}{\rho.C_m} \tag{9.8}$$

$$MI_s = \frac{\sqrt{E}}{\rho} \qquad MI_s = \frac{\sqrt{E}}{\rho.C_m} \tag{9.9}$$

9.1.6 Material selection graphs

This process gives multiple indices to aid with material selection, depending on whether the main criteria is to minimise weight (more of a driver for smaller scale floating devices) or minimise cost (which is the ultimate objective, when weight is not an issue).

Four material selection graphs are shown in Figure 9.3 which plot the 6 different index lines. The lines have been plotted through high yield carbon steel (f_y approximately 350MPa); this is a common material for use in wave energy converters, and is therefore used as a reference material. Materials which lie on the same line perform the same as steel for the given index. Materials above the line perform better, and below the line perform worse.

As the loads that need to be resisted are quite large, a minimum strength constraint of 10 MPa and a minimum stiffness constraint of 1 GPa have also been imposed, which automatically eliminates foams.

Table 9.2 and 9.3 lists the materials that perform better than carbon steel, with optimum material for each index at the top. For minimum mass design, a number of different materials appear to give better strength and stiffness properties per unit weight than steel, including composite (GFRP and CFRP), titanium, aluminium and magnesium alloys, various technical ceramics and wood. Some of these can be immediately discounted, such as ceramics which are very brittle, and magnesium alloys which are not currently produced in sufficient quantities for use as a large scale structural material, but this still leaves a few materials that would be worth considering further.

However, when the objective changes from minimum mass to minimum costs, the list of alternative materials reduces significantly, and shifts from lightweight, strong, but costly materials to more heavy duty materials more commonly used for structural purposes, including reinforced concrete (which performs the best for both strength and stiffness) and cast iron, alongside lighter materials such as wood and aluminium.

Table 9.2: Materials that perform better than steel when considering minimum weight

Strength	Stiffness
CFRP (best performance)	Various ceramics (best performance)
Various ceramics	CFRP
Titanium	Woods
Magnesium alloys	Magnesium alloys
Aluminium alloys	Titanium
GFRP	GFRP
Woods	Various polymers (similar performance)
Various polymers (similar performance)	

Table 9.3: Materials that perform better than steel when considering minimum cost

Strength	Stiffness
Reinforced concrete (best)	Reinforced concrete (best)
Cast iron	Cast iron
Wood	Wood
Aluminium (similar performance)	Aluminium (similar performance)

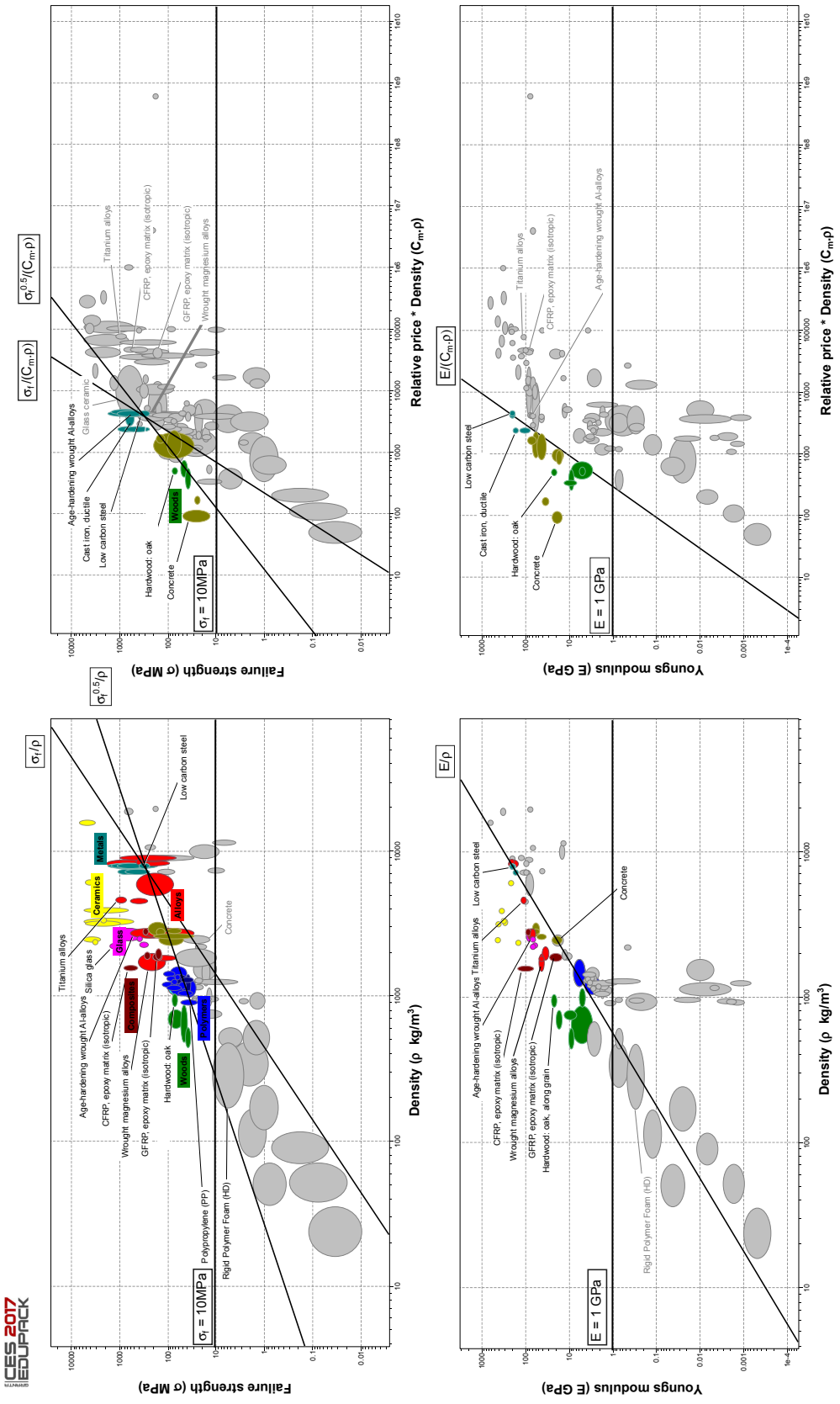

Figure 9.3: Material selection charts (created using CES2017 Edupack Granta Design Limited, 2017)

9.1.7 Short list materials

The screening process described in the previous sections highlights the following materials which offer good material properties per unit cost:

- Carbon steel
- Aluminium alloys
- Cast Iron
- Woods (parallel to the grain)
- Concrete (performs best in terms of both strength and stiffness)

This list can be narrowed down further by assessing the materials against the qualitative criteria listed in Table 9.1. A full assessment is included in Table D.1 in Appendix D.2, but in summary, the process highlights that concrete and steel are the materials which best meet the design requirements. Aluminium has poor fatigue properties and high potential for galvanic corrosion; wood is difficult to form into large, complex shapes and still remain watertight; and the size of the node is beyond the limits for ductile iron castings. On this basis steel and concrete will be the only materials considered further as part of the preliminary design assessment. The main advantages and disadvantages of these materials are summarised in the Table 9.4.

Table 9.4: Summary of potential node materials

Material	Advantages	Disadvantages
Steel	• Common structural material • Many different fabricators • Good strength per unit cost properties	• Needs additional corrosion protection in terms of galvanising, coatings or cathodic protection • Would have to be fabricated offsite, and then transported to location.
Concrete	• Common structural material. • Relatively easy to form into large complex structures • Very good strength properties per unit cost (out performs steel) • Good fatigue performance • Good corrosion resistance • Can be constructed on site with local materials • Can be cheap to provide non-structural mass, which is beneficial for devices which require ballast.	• Lack of tensile strength, but can be overcome with reinforcement or post-tensioning. • Practical minimum wall thicknesses can result in heavy structures, which can be issue for devices with limited available buoyancy.

9.2 Preliminary node design and costing

The selection process showed that concrete and steel are most suitable materials for the node construction, if minimising mass is not the required objective, as they are economic materials with good strength and stiffness properties. To further compare these two materials, a high level design and costing exercise has been carried out taking the hydrodynamic pressures on the hull as the preliminary design load case. Rather than carrying out a full design at this stage, it has been assumed that internal stiffeners and props will be used to keep the maximum free span within the hull to 1.5 m. At this stage wave slap and slam has not been considered, although would need to be taken into account during detailed design.

The maximum design pressure has been calculated as the pressure at the base of the node cone, taking the free water surface as 7 m above the still water level, which is the amplitude of the design wave, which has been taken as 14 m, as this is the maximum significant wave height (H_s) specified in Table 8.5 on page 138. This method assumes that the node is fully submerged by the passing wave - this gives the most conservative values of pressure but is a very unlikely scenario, as the node will to some extent follow the sea surface as the wave passes. For this reason the significant wave height (H_s) has been used for design rather than the maximum, as considering a node fully submerged by H_{max} would be over-conservative and lead to very onerous design conditions.

This gives a design wave pressure of $105\,\mathrm{kN/m^2}$, and a design bending moment (modelling the wall as a one way spanning panel, with fixed supports) of 20 kNm. This is conservative, as the three dimensional node shape will lead to a more complex distribution of stresses within the hull structure, but is adequate for this level of analysis, and allows the two materials to be compared. A more detailed consideration of the load distribution throughout the hull under dynamic wave loading is discussed in Chapter 10.

Details of the preliminary structural analysis for the concrete and steel hull are included in Appendix D.3, and the requirements are summarised here:

- For the concrete design, a 200 mm thick wall, with $200\,\mathrm{kg/m^2}$ of steel reinforcement is required to resist the design bending moment.
- For the steel design, a plate thickness of 15 mm with 100 mm stiffeners, 15 mm thick at 500 mm centres is required.

Schematics of the two outline designs are shown in Figure 9.4. Costs have been assessed based on industry estimates, and published construction indices (see Appendix E for further information on cost build ups). Table 9.5 show the quantities and overall costs for the two different options.

For the concrete option, the cost of the formwork is based on the fabrication of a robust steel structure that can be reused for at least five times (giving a total formwork cost of $\approx$ £85,000).

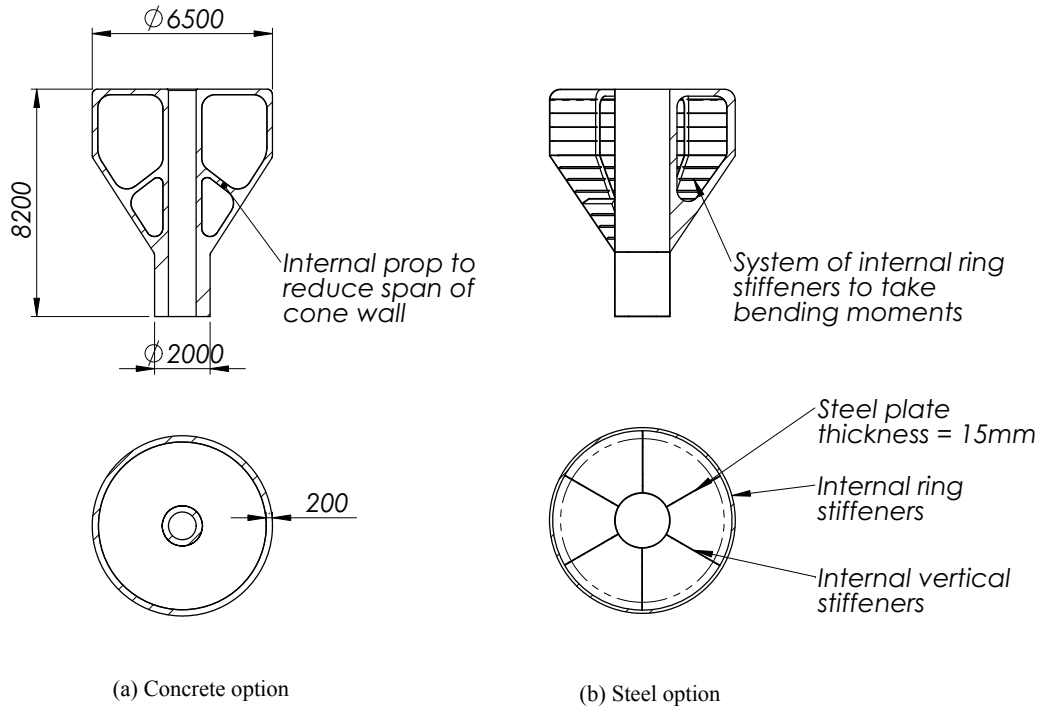

(a) Concrete option

(b) Steel option

Figure 9.4: Preliminary design options [units in mm]

An additional 20% cost has been included to cover any additional items that may be required, such as pre-stressing.

For the steel option, a cost for coating has been included to ensure that the steel has adequate protection against corrosion (which is not an issue for the concrete), and a nominal amount has been included for ballast, to ensure that the steel option sits at the same level in the water as the concrete option.

Table 9.5: Preliminary design concrete option; quantities and costs

Description	Quantity	Unit	Rate	Cost
Formwork	330	m^2	£51	£16,830
Provide and place 50MPa concrete	42	m^3	£200	£8,400
Provide and place steel reinforcement	8.5	t	£1,200	£10,200
Subtotal				£35,100
Additional items	20	%		£7,020
Total				£42,516

It can be seen from these tables that the steelwork option is over 60% more expensive than the concrete option which indicates that concrete is the preferable material for the node structure.

Table 9.6: Preliminary design steelwork option; quantities and costs

Description	Quantity	Unit	Rate	Cost
Steelwork fabrication	30	te	£2,000	£60,000
Coating area	240	m^2	£30	£7,200
Ballast	70	te	£20	£1,400
Total				£68,600

9.3 Summary

Table 9.7 summarises the benefits and disadvantages of both steel and concrete materials for the Node structure, on the basis of the preliminary design work, initial costing exercise, and the qualitative assessment of some of the design criteria highlighted in Table 9.1.

Concrete is significantly cheaper than steel, and also performs better in terms of fatigue and corrosion resistance which has implications for ongoing operations and maintenance. Concrete structures are also preferable for manufacture, as they can be constructed on site, therefore minimising transportation logistics. For these reasons concrete is considered to be the preferable material for the construction of the 12S Node structure.

There are, however, a number of uncertainties associated with the use of concrete, which performs worse than steel in the following categories:

- **Mass**: The required concrete structure is heavy, at the upper limits of the buoyancy requirements for the 12S array system;
- **Watertightness**: Concrete is a material that is designed to crack in tension, as this transfers the stress to the internal steelwork. This can cause issues for durability of the internal concrete, and also for floating structures which need to remain watertight;
- **Connection to steel link arm**: Connections between dynamic steel components are commonly formed and well understood. Dynamic connections between steel and concrete components are less common, and therefore required a greater level of consideration to ensure that connections are robust.

These areas are explored further in the rest of this thesis. Issues surrounding overall mass and the inherent tendency of concrete to crack under tension are explored in Chapter 10. The behaviour of the connection of the steel link arm to the concrete node is investigated in Chapter 11.

Table 9.7: Summary of material parameters Node structure made from steel or concrete

Criteria	Concrete	Steel
Cost	£42,120. Reinforcing steel, and formwork are main costs items	£68,600. Steel fabrication is expensive
Mass	100 t - heavy, at the upper limits of weight to maintain buoyancy.	30 t - lighter and easier to handle than concrete, but requires significant ballast to sit at correct level in the water
History of use in marine environment?	Yes- many offshore oil / gas platforms	Yes- main material in ship building
Fatigue properties	Good - better general fatigue performance than steel	Fair - can be an issue, but fatigue in steel is well understood
Ductility	Fair - Plain concrete is an inherently brittle material, but ductility is provided by adequate reinforcement detailing	Good
Manufacturability	Good - can be easily formed into complex shapes, although increased complexity increases costs for formwork and reinforcement.	Fair - can be fabricated into complex shapes, but fabrication is labour intensive (more expensive)
Availability of manufacturers	Very few limits on manufacturing location; can be made on site, reducing transportation requirements	Good, but will generally need transported from place of fabrication to location
Ease of repair	Generally ok - can repair cracks	Good
Ease of connection to steel link arm	Various methods of steel / concrete connection available, but would require careful detailing, to ensure robust section able to take multi-axial dynamic loads.	Good - welding / bolting and pin joints all well-established steel connection methods
Corrosion resistance	Good, providing suitable mix design is used, and good quality control	Poor - would require coating
Watertight	Yes - providing crack widths are adequately controlled; pre-stressing may be required to keep structure in compression	Yes

Chapter 10

Advanced concrete materials

The conclusion of the techno-economic study presented in Chapter 9 was that reinforced concrete is the preferred material for the construction of the Node structure for the 12S WaveNET array. However, the study also highlighted potential issues with using this in its conventional form for floating dynamic applications; in particular the overall mass of the material, and the fact that concrete cracks under tension, leading to reduction in durability and loss of watertightness.

This chapter considers the potential of advanced fibre reinforced concrete (FRC) materials, and using external carbon fibre wraps as an alternative to internal reinforcing bars to address these concerns. The aim of the chapter is to compare advanced FRC mixes against conventional materials to identify the circumstances where they can offer benefits and reduce overall costs. This work contributes to overall knowledge in the wave energy industry by improving the understanding of the use of concrete (both of conventional and advanced materials) for floating, dynamic wave energy converters.

This work has been carried out alongside Quoceant's "Advanced Concrete Engineering for Wave Energy Converter" project (ACE-WEC), funded by Wave Energy Scotland, which investigated the potential to use advanced concrete materials and production methods to reduce the capital costs of wave energy construction. The ACE-WEC project is a collaboration between Quoceant, The Concrete Technology Unit at the University of Dundee, Black & Veatch, and Innosea, and has studied the application of such materials and methods to a wide range of wave energy converters.

The work described in this chapter has been carried out solely by the author (unless explicitly specified) as part of the overall IDCORE project, looking in particular at the Albatern Node Structure; with the outcomes of this work feeding into the ACE-WEC reports. A discussion of the conclusions of the full ACE-WEC project is included in Section 10.7.1, in order to highlight the wider applications of the work.

Work presented in this chapter forms the basis for a conference paper and poster presented at ICOE2018, titled 'Advanced concrete materials for offshore floating structures' (Barker Ewart et al., 2018) which are included in Appendix A.

The chapter covers the following topics:

- The design and analysis process for the 12S node, specifying the design loads and loadcases, describing the finite element analysis used as a design aid, and defining different design sections within the Node structure is covered in **Section 10.1.**
- A derivation the material properties for use in design, with reference to the relevant documentation highlighted in the Literature Review is included in **Section 10.2.**
- The design requirements for a conventional reinforced concrete structure, which is then used as a reference design for comparison with further design options are set out in **Section 10.3.**
- Alternative designs using advanced FRC concrete options, and carbon-fibre wraps as an alternative to internal reinforcing bars are covered in Section **10.4,** followed by a comparison of all the different options, (including cost estimates) in Section **10.5**.
- The effect of scale on the choice of material is investigated in S**ection 10.6**, which looks at FRC designs for a node within the 6S array system (which is half the physical scale of the 12S). In this case, an RC design is not an option due to weight restrictions, and therefore the FRC option is compared against steel and GFRP alternatives.
- Finally a summary of the chapter, with further discussion on the wider application of the work, is included in **Section 10.7.**

10.1 Design and analysis process

In this chapter the Node element of the 12S array is considered as a standalone structure with design dominated by the PTO loads applied to the column base and the dynamic wave pressures on the hull as discussed in Section 9.1.1 (see Figure 9.2 on page 147).

The PTO load components at the articulation points were derived in Section 8. This work has been extended to give the global load actions in the base column in Section 10.1.1. The hydrodynamic wave pressures for the sea states of interest are derived in Section 10.1.2. The individual load components are then combined into SLS, ULS and ALS load cases which are are classed as “Discrete” limit states as each load case is related to a specific sea state. A separate FLS load case is also considered, covering loading across multiple sea states which occur over the full lifetime of the structure.

10.1.1 PTO loads

(a) Discrete limit states

The PTO articulation loads for the discrete limit states (SLS, ULS and ALS) were presented in Table 8.3, with the bending moments at SLS and ULS limited to the rated torque value of 1 MNm. These have been taken as the basis of the Global PTO loads acting on the base column, as shown in Table 10.1.

Each Node structure has three PTO connection points spaced at 120°, and there is the possibility that all PTOs could reach their rated torque simultaneously resulting in a global pitch torque of 2 MNm. However, this will not occur on a regular basis, and therefore has been taken as the ULS value. Values for F_x and F_z as given in Table 8.3 have also been doubled for the ULS load case in Table 10.1), however F_y has been kept the same, as components from the two leeward arms will cancel out. For the SLS load cases, all the values given in Table 8.3 have been kept the same for the global PTO load case.

Table 10.1: Global PTO loads (Environmental load Q)

ID	Limit state	F_X (kN)	F_Y (kN)	F_Z (kN)	M_X (kNm)	M_Y (kNm)	M_Z (kNm)
LP1	SLS	1000	250	250	500	1000	500
LP2	ULS	2000	250	500	1000	2000	1000
LP3	ALS	1500	500	500	2000	5000	2000

(b) Fatigue loads

Fatigue checks for the base column are to be carried out using the time history data for the articulation LA5S which was shown in Chapter 6 to have the worst case fatigue behaviour.

10.1.2 Hydrodynamic loads

In the absence of accurate hull pressure output from the hydrodynamic models, dynamic Froude-Krylov pressures have been calculated in accordance with linear wave theory, as shown in the Equation 10.1:

$$p = \rho g H . \frac{\cosh\left[2\pi(x+d)/L\right]}{\cosh(2\pi d/L)} \tag{10.1}$$

Pressures have been calculated at different points on the structure (indicated with red dots on Figure 10.1) to determine the distribution across the hull, and then added to the hydrostatic pressure (calculated from the still water level) to give the full pressure field for design.

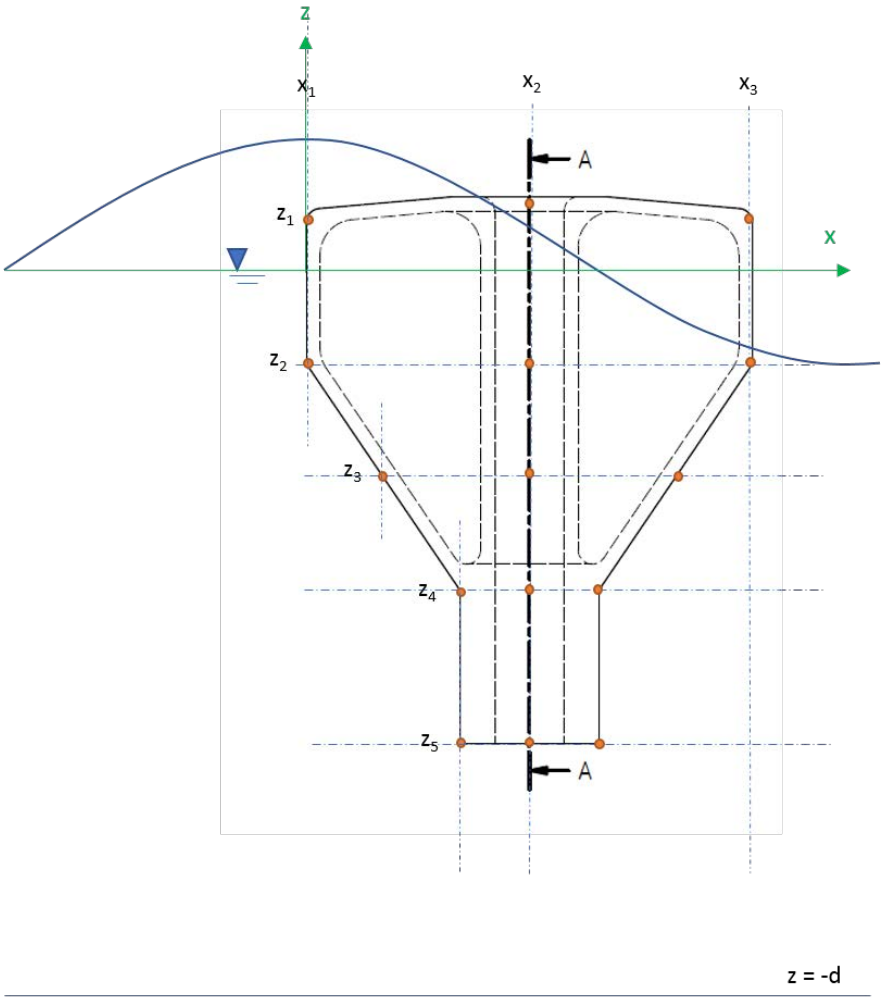

Figure 10.1: Locations for calculation of dynamic wave pressures *(Note: Wave dimensions and water depths are not to scale.)*

(a) Discrete limit states

Pressures for the discrete limit states have been calculated for the sea states presented previously in Table 8.5. As for the preliminary design carried out in Section 9.2, in most cases it is assumed that the node is fully submerged by the passing wave, combined with H_s.

While a fully submerged node gives the most critical local pressures at the base of the structure, the case where the node follows the wave crest could result in the greatest global moment, as the dynamic wave pressures are highest at the wave crest. Two load cases where the Node follows the wave crest have also been included to check this scenario.

It is noted that linear wave theory is not directly applicable to extreme sea states, but is acceptable at this stage of analysis considering the conservative nature of the load cases considered (very steep waves, with full submergence). While it would be important to check

the assumptions made regarding the wave pressures for a detailed design, there would be very little added value at this stage to spend the computational time and effort required to determine detailed non-linear solutions.

In addition to the wave loads, the structure has also been checked for the case where the structure is fully submerged with a hydrostatic load applied, to compare the difference between the dynamic wave pressure which varies with values of x, and the hydrostatic wave pressure which is uniform for a given z. The environmental loads included in the analysis are included in Table 10.2.

Table 10.2: Applied pressure forces (Environmental Load E)

Load name	Z (m)	H_s (m)	T_p (s)	Return period	Limit state	Max pressure (kPa)
LH1	9.2	-	-	hydrostatic	SLS	92.5
LH2	11.2	-	-	hydrostatic	SLS	112.6
LH3	14.2	-	-	hydrostatic	ULS	142.8
LE1	10.1	6	12	1 in 1yr	SLS	104.8
LE2	11.9	9.4	10.1	1 in 1yr	ULS	118.9
LE3 (f)	8.2	9.4	10.1	1 in 1yr	ULS	88.9
LE4	14.2	14	12.2	1 in 100yr	ULS	148.2
LE5	14.2	14	8.0	steep wave	ULS	130.4
LE6 (f)	8.2	14	8.0	steep wave	ULS	96.6

For loadcases noted with an (f), the Node is assumed to follow the wave crest

(b) Fatigue limit states

The design of the Node hull is dominated by the wave pressures. It is not easy to link these directly to the PTO articulation loads (which would allow time domain fatigue analysis methods to be carried out), so the spectral fatigue analysis method has been applied. A set of pressure loads have been applied in the finite element model (discussed in Section 10.1.4) covering a range of wave periods from 3.5 seconds to 11.5 s, with a unit wave height. These load cases have then been used to determine the section stress RAOs the spectral fatigue analysis following the method described in Section 6.4.3. Further details of this procedure are included in Appendix F.4 and the different applied pressures are shown in Table 10.3.

10.1.3 Node Loadcases

The individual loads derived in the previous sections are combined together in different load cases as shown in table 10.4. Partial load factors for the different limit states are shown in table 10.5.

Note: ULS partial load factor combinations (a) and (b) in Table 10.5 come from DNV (2012) Table D1. Combination (c) comes from DNV (2012), Sec 6, O602.

Table 10.3: Applied operational loads for fatigue analysis

Load name	T_p (m)	Max pressure (kPa)
LO0	3.5	72.9
LO1	4.5	73.8
LO2	5.5	74.8
LO3	6.5	75.6
LO4	7.5	76.3
LO5	8.5	76.8
LO6	9.5	77.1
LO7	10.5	77.4
LO8	11.5	77.7

Table 10.4: Load cases for design

Load case	Environmental load (E)	Variable function load (Q)
Serviceability limit state (SLS)		
SLS1	LE1	LP1
SLS2	LE2	LP1
SLS3	LE2	LP2
SLS4	LE3	LP1
SLS5	LH1	LP1
SLS6	LH2	LP1
SLS7	LH3	LP1
Ultimate limit state (ULS)		
ULS1	LE4	LP2
ULS2	LE5	LP2
ULS3	LE6	LP2
ULS4	LE7	LP2
Accidental limit state (ALS)		
ALS1	LE7	LP3

Table 10.5: Partial load factors

Load case	Environmental load (E)	Variable function load (Q)
SLS	1.0	1.0
ULS(a)	1.3	1.0
ULS(b)	0.7	1.3
ULS(c)	0.5	1.0
ALS	1.0	1.0

10.1.4 Finite Element Analysis Set-up

Structural analysis has been carried out using a finite element model to determine the stresses and strains in the node walls. A 3D solid model has been set up in Abaqus (DSS, 2014), using an initial wall thickness of 200mm. A section of the model is shown in Section 10.2. Wave forces are applied as a pressure load to the outer face of the model, and the PTO moments are applied as concentrated loads to a reference point at the centre of the base column, which is coupled to the base structure.

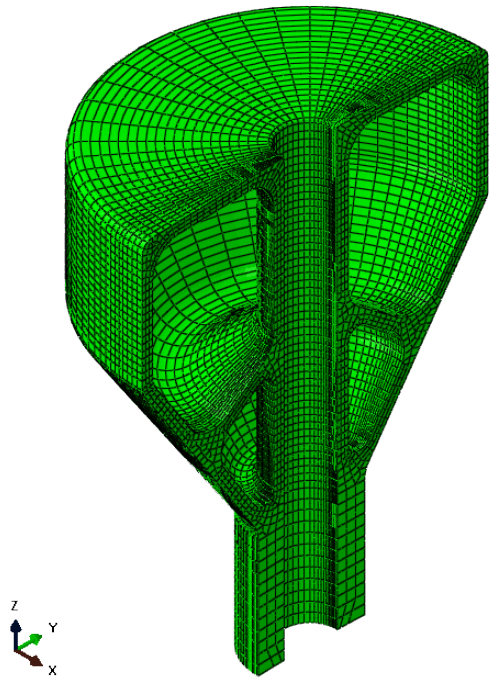

Figure 10.2: Section of node model in Abaqus

The model uses CD820R elements (a quadratic element, suitable for the analysis of bending problems), with a minimum of three elements through the thickness of each wall (determined through a convergence analysis included in Appendix F.1).

The model uses linear elastic material properties as shown in Table 10.6. While concrete materials (both conventional and advanced) are non-linear, use of linear elastic analysis is standard practice in concrete design, and including full non-linear plastic properties is too complex for this stage of development.

Table 10.6: Linear elastic concrete properties for model

Density kg/m^3	Modulus E GPa	Poisson's ratio
2500	37	0.2

10.1.5 Design sections

The Node structure is split into various characteristic design sections as shown in Figure 10.3. The black lines show the locations where stress results are extracted from the Finite Element model to determine bending moments and axial forces.

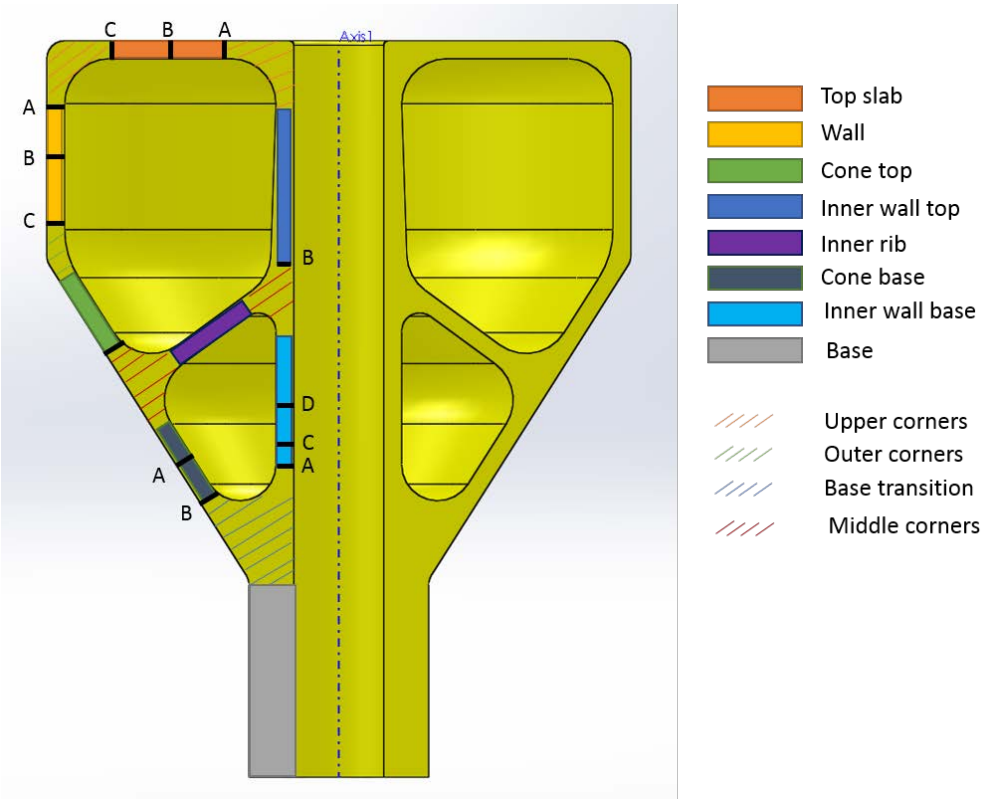

Figure 10.3: Design sections

The design sections fall into three different categories:

- A majority of the structure can be split into “slab" sections, which are designed to resist the applied bending moments and axial forces (with no significant shear forces) in accordance with standard methods as described in the codes.
- The varying thickness of the corner and transition sections result in more complex analysis requirements than for the “slab" sections. At this stage is it assumed that the reinforcement requirements for the slabs can be continued through the adjacent corners and transitions, rather than carrying out a separate rigorous analysis.
- The base section is considered as a stand alone structure, and is designed as a circular column to resist the applied PTO loads.

10.2 Material properties

The materials used in the development of the different design options include:

- Conventional reinforced concrete
- Fibre reinforced concretes with improved tensile properties
- Carbon-fibre wraps as an alternative to internal steel reinforcing bars

The preliminary design properties of these materials are included below.

10.2.1 Conventional Concrete

The mechanical properties of standard grade concrete are well documented, and for the purpose of design will be taken from DNV-OS-C502, with the relevant partial safety factors applied.

10.2.2 Fibre Reinforced Concrete

Fibre Reinforced Concrete (FRC) is a concrete mix containing dispersed fibres, generally < 50 mm in length. While many different materials can be used, this thesis uses carbon steel fibres. It is noted in the literature review that it is difficult to define theoretical design parameters for FRC as many different factors influence the material properties. However it is useful to provide a set of preliminary values as a basis for ongoing development; these have been derived using relationships identified in the literature review, dependant on the base concrete compressive strength, the fibre volumetric fraction and aspect ratio.

The first step is to define a set of tensile stress vs Crack Mouth Opening Displacement (σ-CMOD) values, similar to those that would be obtained from a standard bending test. The equations used for these are included in Table 10.7, and an example σ-CMOD plot is given in Figure 10.4 for f_{cck} = 100 MPa . As noted in Section 3.2.3, empirically derived theoretical relationships are only valid within the limits of the experiments on which they are based. The equation taken for the peak strength (see Thomas and Ramaswamy, 2007) is based on concretes with compressive strengths between 35 and 80 MPa, and therefore is reasonable at predicting material properties for concretes within this range, but tends to under-predict properties for mixes with high compressive strengths ($\geq$ 100MPa), giving conservative design values.

The flexural σ - CMOD values are then used to derive the uniaxial tension stress-strain curve and residual strength values for design, using the equations shown in Table 10.8, which have been taken from the fib Model Code (fib, 2013).

For preliminary design the following parameters have been assumed for a UHPFRC mix (compressive concrete strengths $\geq$ 100MPa):

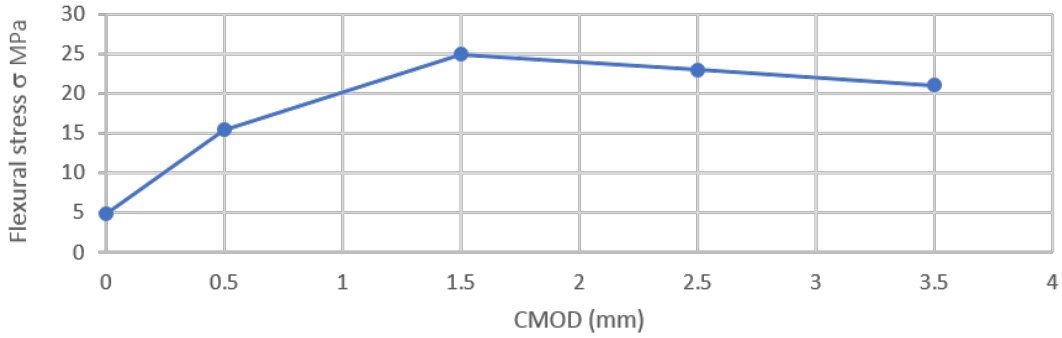

Figure 10.4: σ-CMOD values for concrete with compressive strength f_cck = 100 MPa

- Fibre volume fraction (%) $V_f = 5$
- Fibre length (mm) $L_f = 50$
- Aspect ratio $L_f/d_f = 80$

The selected fibre volumes and aspect ratios are those which appear to give the highest strengths as shown in literature (see Table B.1 in Appendix B). For cases where the use of fibres may be beneficial, but full strength UHPFRC is unecessary, (compressive strengths $\leq$ 100MPa) a fibre volume of 2.5% is assumed. The peak strength for these concrete mixes (SHCC) is assumed to occur at CMOD = 3.5mm rather than 1mm. Residual flexural strengths calculated in accordance with this method are shown in Table 10.9. Uniaxial strength values are shown in Table 10.10; design values in this table include a material partial safety factor of 1.5.

The purpose of the values that have been derived in this section is to allow preliminary design work to be carried out, in order to compare different design options. It is recognised that a significant amount of further testing would be required in order to validate and refine these values for further detailed design.

10.2.3 Carbon Fibre

While there are many different types of carbon fibre wraps, for the initial design a readily available commercial uni-directional woven carbon fibre wrap is used. Its properties are described in Table 10.11.

Table 10.7: Equations for assumed characteristic flexural stress-CMOD values for preliminary design (UHPFRC)

ID	CMOD (mm)	stress	State	Equation	Comment
L	0	f_{Lk}	Limit of proportionality (first crack)	$0.48\sqrt{f_{cck}}$	Assume that addition of fibres doesn't have an effect on underlying tensile cracking strength (DNV, 2012)
1	0.5	$f_{R1,k}$	SLS residual strength	$(f_{Lk} + f_{pk})/2$	Assume linear between f_{Lk} and f_{pk}
p	1	f_{pf}	Peak	$0.97\sqrt{f_{cck}} + 0.295\sqrt{f_{cck}}RI + 1.117RI$	Equation from Thomas and Ramaswamy (2007). Assumed to occur at CMOD=1 mm from results in Bencardino (2013).
2	1.5	$f_{R2,k}$	ULS residual strength	$f_p[1 - \frac{\delta}{kL/2}]^2$ $\delta = CMOD - 1$	Assume parabola distribution after Naaman (2008). k is a factor relating to the amount of damage of the fibres
3	2.5	$f_{R3,k}$			
4	3.5	$f_{R4,k}$			

Table 10.8: Equations for characteristic uniaxial tensile stress-strain values for design

Symbol	Description	Stress		Strain	
		Equation	Comment	Equation	Comment
f_{ct}	Crack strength	f_{Lk}	Assume tensile = flexural crack strength	$\varepsilon_{ct} = f_{ct}/E_c$	
f_{Fts}	SLS residual strength	$0.45 f_{R1}$	fib (2013) eq 5.6-5		Assume linear between f_{Lk} and f_{pk}
f_{pt}	Peak tensile strength	$0.7 f_{pk}$	Average ratio from published experimental values	$\varepsilon_{pc} = 0.5$	Peak strength for UHPFRC as recommended in Naaman (2008)
				$\varepsilon_{pc} = 4$	For SHCC
f_{Ftu}	ULS residual strength	$0.5 f_{R3} - 0.2 f_{R1}$	fib (2013) eq 5.6-6	$\varepsilon_{Fu} = 2$	As recommended in fib (2013)

Table 10.9: Residual flexural strength values for preliminary design (MPa)

ID	f_{cck}	f_{Lk}	f_{R1k}	f_{pk}	f_{R2k}	f_{R3k}	f_{R4k}
SHCC ($v_f = 2.5\%$)							
SH50	50	3.39	4.80	—	7.62	10.44	13.26
SH60	60	3.72	5.23	—	8.26	11.29	14.32
SH70	70	4.02	5.63	—	8.85	12.07	15.29
SH80	80	4.29	5.99	—	9.39	12.79	16.19
SH90	90	4.55	6.34	—	9.90	13.47	17.03
UHPFRC ($v_f = 5.0\%$)							
UH100	100	4.80	15.38	25.97	24.94	22.95	21.03
UH150	150	5.88	18.34	30.80	29.58	27.21	24.95

Table 10.10: Uniaxial tensile strength values for preliminary design (MPa)

		Characteristic				Design	
ID	f_{cck}	f_{ct}	f_{Fts}	f_{pt}	f_{Ftu}	$f_{Fts,d}$	$f_{Ftu,d}$
SHCC ($v_f = 2.5\%$)							
SH50	50	3.39	2.42	—	5.56	1.61	3.71
SH60	60	3.72	2.63	—	5.99	1.75	3.99
SH70	70	4.02	2.82	—	6.39	1.88	4.26
SH80	80	4.29	3.00	—	6.76	2.00	4.51
SH90	90	4.55	3.17	—	7.11	2.11	4.74
UHPFRC ($v_f = 5.0\%$)							
UH100	100	4.80	6.92	18.18	8.40	4.62	5.60
UH150	150	5.88	8.25	21.56	9.94	5.50	6.63

Table 10.11: Material properties for structural carbon fibre wrapping material

Orientation degrees	Areal weight g/m^2	Fibre Density g/cm^3	Fabric Thickness mm	Tensile strength MPa	Elastic modulus GPa	Strain at break %
0	300	1.8	0.17	3900	230	1.5

10.3 Conventional reinforced concrete design

The initial structural design has been carried out using conventional reinforced concrete. A standard weight C50 concrete has been assumed, and design has been carried out in accordance with DNV-OS-C502 (DNV, 2012) where appropriate. The initial design is driven by the following constraints:

(a) Overall geometry

The outer dimensions of the Node have been determined as part of the conceptual design work as discussed in Part II; these dimensions are shown in Figure 10.5.

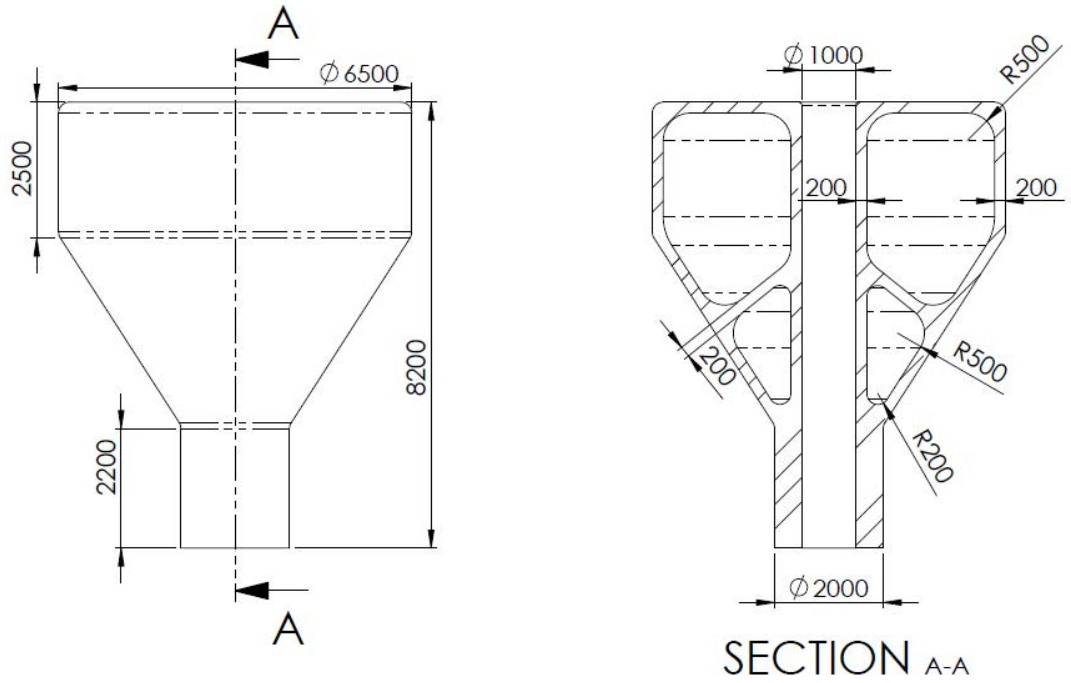

Figure 10.5: Generic Node Dimensions

(b) Minimum wall thickness

The minimum wall thickness is a practical constraint, driven by the need to fit in multiple layers of reinforcement, together with a suitable concrete cover to ensure the reinforcement durability. A schematic of the envisaged rebar requirements is shown in Figure 10.6 with the dimensional requirements as follows:

- 50mm of cover to inner and outer face + 5mm construction tolerance (reinforcement sensitive to corrosion, exposure class XS3, Table Q2 DNV-OS-C502. Reduced from the value of 60mm in the table to account for 20year rather than 50 years design life).
- 16mm radial reinforcement (two layers).
- 12mm hoop reinforcement (two layers).

- Min 35mm gap between layers of concrete (table Q1, free distance between each layer of reinforcement bars)

Minimum thickness = 199mm (Note this is based on the initial assumed reinforcement diameters as specified above – the minimum wall thickness will change depending on the final rebar requirements as discussed later in Section 10.3.4.)

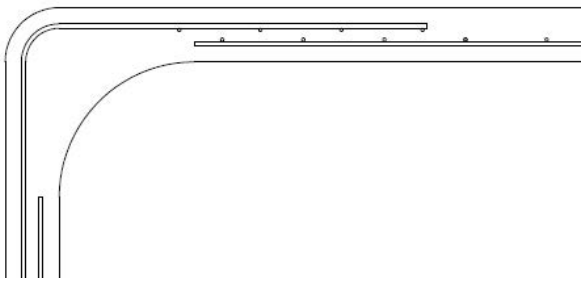

Figure 10.6: Conceptual reinforcement schematic

(c) Buoyancy

The Node structure needs to provide enough buoyancy to keep the array afloat. Assessment work (carried out by others as part of the 12S development project) indicates that a minimum reserve buoyancy of 20 t is required to support the weight of additional equipment and components not explicitly included in the overall buoyancy calculation. The mass and buoyancy properties for the node with a minimum wall thickness of 200mm are shown in Figure 10.7 and Figure 10.12.

The internal volume is split into two chambers: the top chamber is designed to be fully watertight, but it is very difficult to ensure that through thickness cracks won't form in the outer walls in the bottom chamber, and therefore some leakage is allowed in this section. F in Figure 10.7 shows the freeboard assuming no leakage into the bottom chamber. RF shows the reduced freeboard, assuming that bottom chamber is fully flooded.

Table 10.12: Node buoyancy and mass properties

Node mass (assuming concrete density = 2.5t/m^3)	104.0	t
Total overall displaced volume	136.7	m^3
Reserve buoyancy	36.1	t
Top chamber volume	83.3	m^3
Bottom chamber volume	11.2	m^3
Total displaced volume - flooded bottom chamber	125.5	m^3
Reserve buoyancy - flooded bottom chamber	24.6	t
Freeboard F	1.1	m
Reduced freeboard with flooded bottom chamber RF	0.7	m

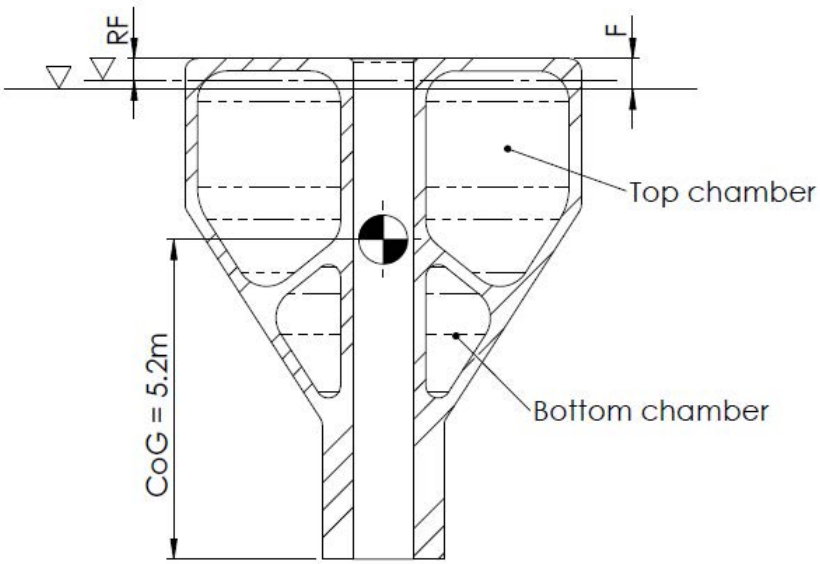

Figure 10.7: Node buoyancy schematic

(d) Crack widths

Conventional concrete design for offshore structures is often driven by crack width limits which are determined to ensure the durability of the structure throughout the design life. Cracking in concrete has two implications:

- Allows increased chloride penetration into the structure leading to corrosion of the internal reinforcement;
- Formation of through thickness cracks leading to leakage; which can cause issues for floating structures that need to remain watertight.

To ensure that the durability of the structure the following crack width constraints are imposed:

- Crack widths limited to 0.2mm (DNV, 2012, Section 6 Table O2, reinforcement sensitive to corrosion, with exposure class XS3 & XF4) ;
- Watertight sections are designed to have a permanent compression zone (DNV, 2012, section 6 O103) - this ensures that through thickness cracks cannot occur.

10.3.1 Slab sections

(a) Design actions

For each section the stress outputs taken from the FE model have been used to derive section bending moments and axial forces in two directions. This process is as described in full in Appendix F.2, and an example of the output is shown in Table 10.13 which gives the derived design actions for the Innerwall Base Section (refer to Figure 10.3 for the section definitions); this location has the most onerous design conditions. Stress outputs show that in-plane shear and torsion are negligible, and therefore can be neglected from the analysis.

Table 10.13: Design actions for the Innerwall Base location

Direction	Bending (kNm)	Axial (kN)	Load case
Hoop	5.0	118.0	SLS
Longitudinal	9.0	422.1	SLS
Hoop	2.2	237.0	ALS
Longitudinal	17.8	1057.1	ALS

(b) Section design

The required section thicknesses and steel reinforcement area has been based on the stress-strain relationships shown in Figure 10.8 and Figure 10.9; all tensile forces are assumed to be taken by the reinforcement. A full example calculation is shown included in Appendix F.3. For SLS checks the output stresses are used to calculate the crack width w_k using the equations set out in EC2 (BSI, 2004*a*, Clause 7.3.4) .

Table 10.14 shows the reinforcement requirements for each slab section, which is driven by one of the following criteria:

- Minimum reinforcement (Min): A code specified requirement to ensure that the reinforcement is well distributed to prevent the formation of large and harmful cracks;
- Crack width (SLS): A serviceability requirement to prevent ingress of water (limit of 0.2mm) and limit potential for reinforcement corrosion;
- Ultimate capacity (ULS): To resist the specified ultimate or accidental applied actions.

10.3.2 Post-tensioning requirements

Results from the FE model show that it necessary to provide post-tensioning to ensure that there is a permanent compression zone in the walls of the upper chamber. Figure 10.10 gives the maximum principal tensile stress in the node from the ULS(c) load combinations, showing that tensile stresses develop through the full thickness of the top of the inner wall, with a maximum tensile stress of approximately 1.0 MPa at this location. To ensure that there is a

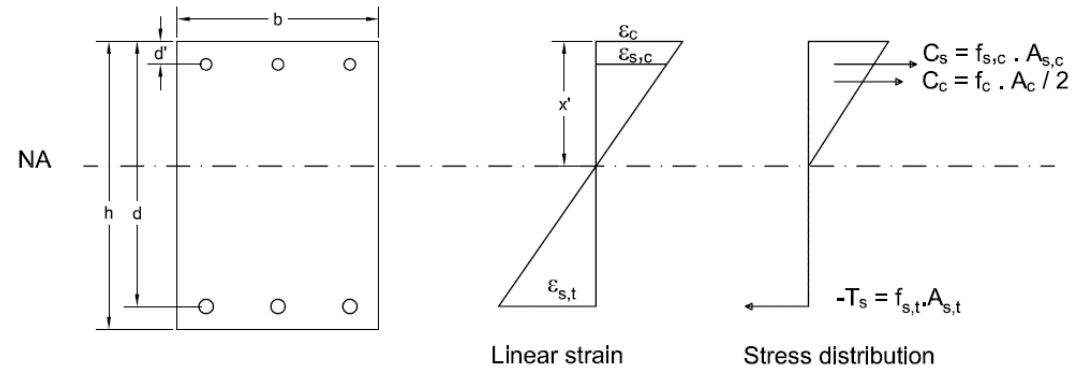

Figure 10.8: SLS stress distribution - linear elastic concrete compressive stress

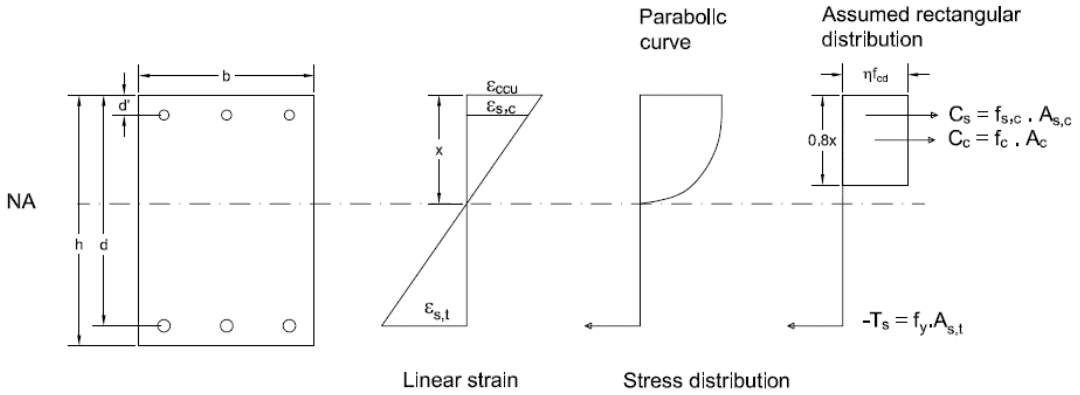

Figure 10.9: ULS and ALS stress distribution - assuming an equivalent rectangular concrete compressive stress distribution

Table 10.14: Reinforcement requirements for reference design

Rebar		Top slab (mm)	Wall (mm)	Cone top (mm)	Cone base (mm)	Innerwall top (mm)	Innerwall base (mm)
Long.	Diameter	12	12	12	20	12	20
	Spacing	300	300	300	125	250	125
Hoop	Diameter	12	12	12	16	12	16
	Spacing	300	300	300	300	250	200
Design driver		Min	Min	Min	SLS	SLS	SLS

permanent compression zone of at least 0.25 x h (= 50 mm) it will be necessary to apply a post-tensioning equal to 1.5 MPa, as shown in Figure 10.11. Note that the S_{max} values are given in Pa in the Abaqus output figures.

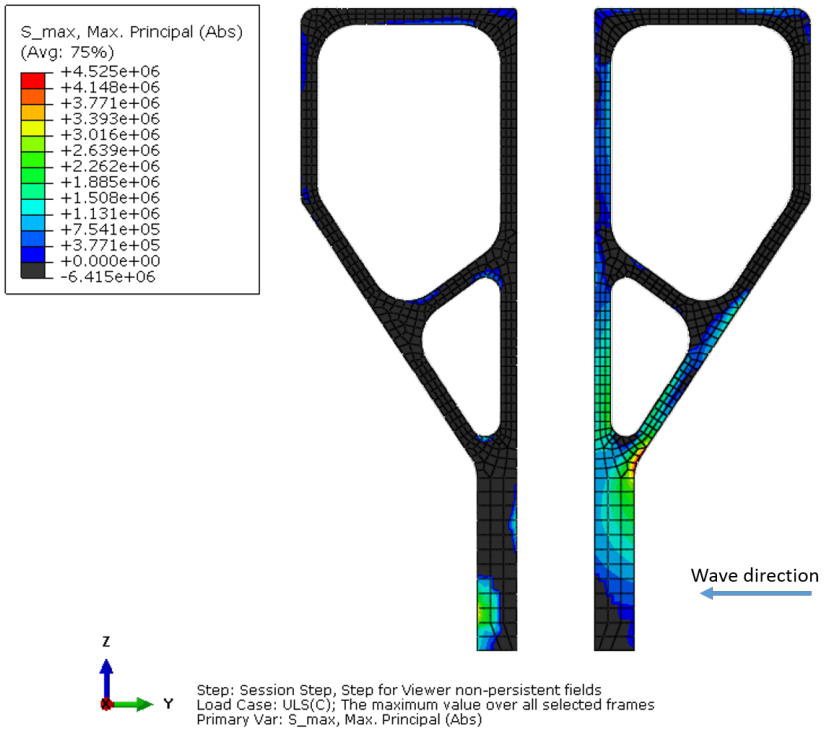

Figure 10.10: Maximum principal stress in node from ULS(c) load case - No post-tensioning

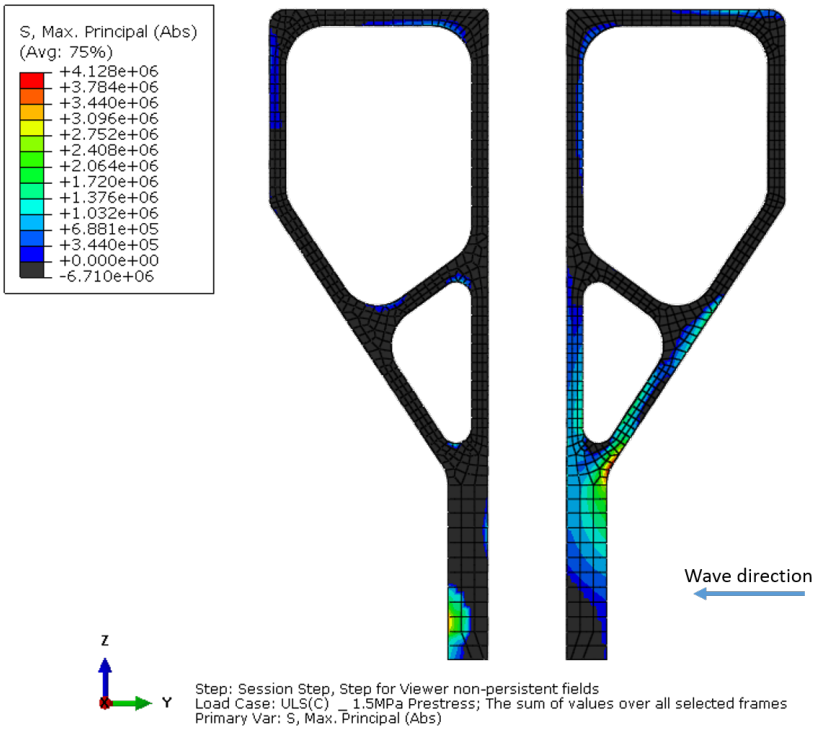

Figure 10.11: Maximum principal stress in node from ULS(c) load case - With 1.5MPa post-tensioning applied]

Applying the 1.5 MPa post-tensioning stress over the full area of the central column (0.59 m^2) results in a post-tensioning requirement of 884kN. Assuming 25% loss of post-tensioning over the long-term gives a total PT requirement of 1180kN.

In order to keep the walls as thin as possible, flat post-tensioning ducts can be used, similar to those manufactured by BBR (BBR VT International Ltd, 2017). The BBR VT CONA CMF-0205 post-tensioning tendons have a duct thickness of 20mm, and a characteristic ultimate resistance of 372kN, therefore a minimum of 4 tendons are required. However, to ensure that there is an even distribution of stress throughout the central column, 6no. tendons are included in the cost estimates.

10.3.3 Fatigue checks

Fatigue has been checked in accordance with DNV GL (2018). Fatigue in both the concrete and reinforcement has been checked against the relevant material S-N curves as specified in this code. Where the design life (N) for the largest acting stress amplitude corresponds to at least $2x10^6$ cycles, the fatigue capacity is assumed to be adequate with no further checks required (as allowed for in DNV GL, 2018, clause 6.13.1.13). Where this is not the case, detailed fatigue calculations have been carried out, in accordance with the Palgrem-Miner linear damage assumption as described in Section 6.4.3. For the base column the number of applied stress cycles have been calculated in the time domain, using the loading time histories from the tank test models. For the node hull structure, fatigue analysis has been carried out in the frequency domain using spectral methods as described in Section 6.4.3.

The worst case fatigue damage calculated in accordance with this methodology occurs in the steel reinforcement within the top slab. The calculated lifetime fatigue damage for this section is 0.133 (shown in Table F.7), which is considerably less than the damage limit of 0.33 specified in Table 6-7 in DNV GL (2018), which corresponds to sections which have no access for inspection and repair. This check shows that the fatigue limit state is not the driver for design for the concrete node structure.

10.3.4 Final reference design

Table 10.15 shows the requirements for the reference RC design, highlighting that the location where the base of the cone an inner wall meet the bottom cylinder is very heavily reinforced. The final cross section dimensions are shown in Figure 10.12, with an outline rebar layout shown in Figure 10.13. A check on the buoyancy requirements is shown in Table 10.16, indicating that the mass is at the very upper limits, as the reserve buoyancy in the flooded state (21.6 t) is very close to the specified limit of 20 t which does not leave much flexibility for ongoing design changes.

Table 10.15: Reference conventional RC design section requirements

	Unit	Top slab	Wall	Cone		Innerwall	
				Top	Base	Top	Base
Longitudinal rebar dia.	mm	12	12	12	20	12	20
Hoop rebar dia.	mm	12	12	12	16	12	16
Approx rebar fraction	kg/m^3	70	70	70	261	65	231
Cover	mm	50	50	50	50	50	50
Tolerance	mm	5	5	5	5	5	5
Spacing between layers	mm	35	35	35	35	35	35
Post-tensioning							
Pocket	mm	-	-	-	-	20	20
Additional spacing	mm	-	-	-	-	35	35
Total (nearest 5mm)		195	195	195	220	250	275

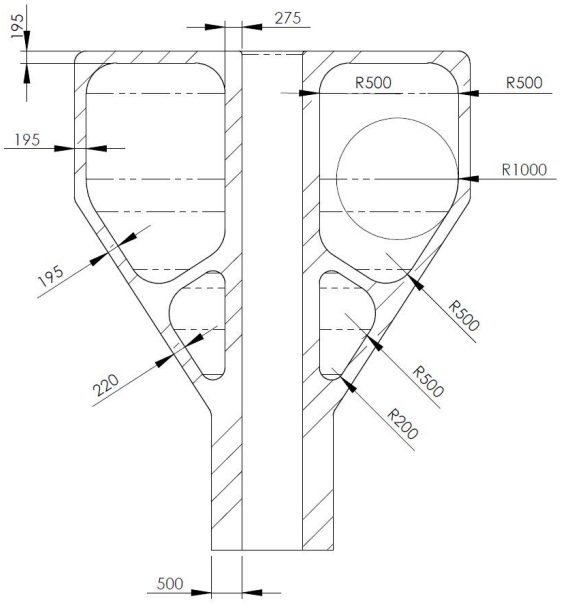

Figure 10.12: Reference design Cross section dimensions

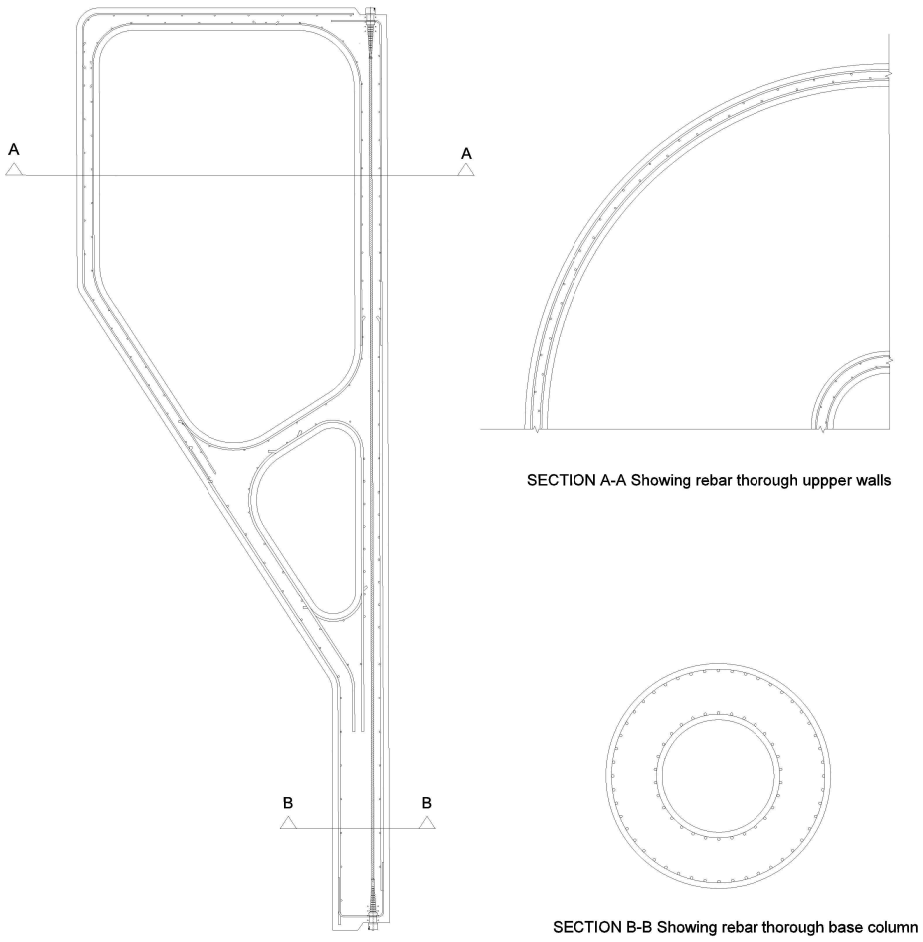

Figure 10.13: Outline rebar layout

Table 10.16: Final node buoyancy and mass properties

Node mass (assuming concrete density = 2.5t/m^3)	109	t
Total overall displaced volume	135.9	m^3
Reserve buoyancy	30.3	t
Top chamber volume	84.4	m^3
Bottom chamber volume	8.5	m^3
Total displaced volume - flooded bottom chamber	127.4	m^3
Reserve buoyancy - flooded bottom chamber	21.6	t
Freeboard F	0.9	m
Reduced freeboard with flooded bottom chamber RF	0.6	m

10.3.5 Potential areas for improvements

The design work carried out in Section 10.3.4 shows that while it is feasible to construct the 12S Node using conventional reinforced concrete there are areas where the use of advanced concrete materials may provide additional benefits. For example:

- There is the potential for using high strength fibre reinforced concrete, or external carbon fibre wraps in areas of high tensile stress to reduce or eliminate internal rebar requirements, and reduce wall thickness and overall structural mass.
- The use of advanced concrete mixes with enhanced post-cracking properties could eliminate the potential for development of through thickness cracks, eliminating the need for post-tensioning.

These points are discussed in more detail in the following sections. Modified designs that take these ideas into account are discussed in Section 10.4.

(a) Reducing rebar requirements

The RC reference design has some complex reinforcement requirements, particularly at the junction between the base column and the cone section. Figure 10.14 shows a close up of the reinforcement in this area, which is very congested (in excess of $250\,\mathrm{kg/m^3}$) increasing the difficulties for rebar fixing and placement of the concrete. The high stresses in this area also lead to the need for thicker wall sections (>200mm), which push the structure to the upper limits of buoyancy constraints. It may be possible to reduce or even eliminate the need for the internal reinforcement in this area through two different methods:

1. Using high performance concrete (UHPFRC), with increased tensile strength and ductility compared to conventional RC.
2. Using external carbon fibre wraps to take the tensile forces in the place of the internal reinforcement

(b) Reducing wall thicknesses

In areas where the imposed stresses are less onerous (for example the outer walls and top slab), the wall thickness are driven by space requirements and the need to fit in the minimum reinforcement with adequate cover. FRC mixes could be used in these locations to reduce the section thicknesses in these areas, decreasing the mass and giving more flexibility in term of overall buoyancy.

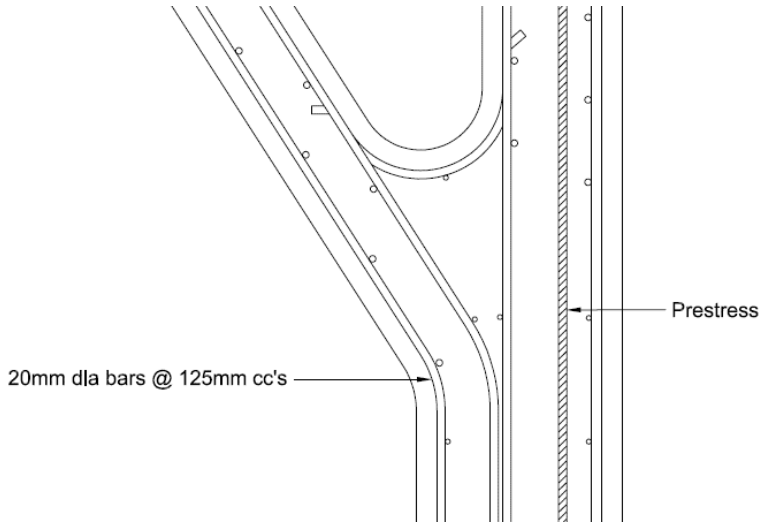

Figure 10.14: Reinforcement requirements at junction between base column and cone section

(c) Elimination of need for post-tensioning

For conventional concrete, the DNV code requires a permanent compression zone for a watertight structure, to ensure that there is no possibility for the formation of through thickness cracks which may lead to leakage. This leads to the requirement for post-tensioning as discussed in Section 10.3.2. However, the stresses that are actually induced in the structure in the watertight chamber are quite low (˜1MPa), and there is an argument to suggest that crack development in FRC materials at these stress levels (or even higher) is not a problem for permeability providing the mix design gives “strain-hardening” properties after initial cracking as discussed in the literature review.

10.4 Design modifications using advanced concrete materials

This section considers three design options which make use of advanced concrete materials, to assess whether they can offer any benefits over conventional RC, particularly with regard to the points highlighted in Section 10.3.5.

The three options are as follows:

1. **UHPFRC design**: This option looks at the potential for using Ultra High-Performance Fibre Reinforced Concrete (UHPFRC) throughout the whole Node structures with properties as given in Section 10.2. This option investigates whether it is possible to eliminate the internal reinforcement by using UHPFRC to resist the applied loads, and reduce the overall mass of the structure.
2. **SHCC / UHPFRC combination**: This option investigates using Strain Hardening Cement Composites (SHCC) materials in the upper chamber (where the stresses are

lower) to reduce or eliminate the need for post-tensioning (PT), combined with UHPFRC in the lower half of the structure (where stresses are higher). As discussed in the literature review, cracked SHCC concrete mixes have a similar permeability to uncracked concrete, due to the formation of multiple microcracks during the strain hardening phase, rather than crack localisation. If this behaviour can be exploited, post tensioning can be eliminated providing that the tensile stresses in the upper chamber are low enough to keep micro-cracks below the critical width for permeability.

3. **Carbon-fibre (CF) external wrap**: This option considers using external carbon fibre wrap reinforcement at the junction of the cone and base structure to reduce the amount of internal reinforcement that is required.

The design requirements for each of these options are discussed in detail in the following sections.

10.4.1 Option 1: UHPFRC design

(a) Discrete limit states

In this option, moment and axial force resistances have been calculated in accordance with stress-strain relationships similar to those shown in Figures 10.8 and 10.9, modified to account for the tensile capacity of the concrete (as shown in Appendix F.5.1). This follows the same methodology that is applied for conventional concrete design (see Section 10.3.1), but accounts for the tensile strength of the FRC.

The section resistances have been checked against the same design actions as for the reference design, to determine the required wall thicknesses. Following this process, the Abaqus model discussed in Section 10.1.4 has been modified to reflect the updated section thicknesses, and then used to check the principal stresses that occur across the whole structure, as shown in Table 10.17. This table shows the maximum principle stress for each limit state, together with the design limits for a UH150 concrete (as given in Table 10.8).

Table 10.17: Maximum principal stress for different limits for UHPFRC option

Limit state	Max principal stress (MPa)	Design limit (MPa)
SLS	4.4	5.50
ULS	6.6	6.63
ALS	9.4	6.63

Table 10.17 shows that for the SLS and ULS limit states, the maximum principle stress is below the design limit. At ALS the maximum stress is 40% higher than the design limit, but this is a stress at a concentrated point, calculated using linear analysis; in reality a degree of stress redistribution will occur due to material cracking, which is acceptable at ALS. The redistribution behaviour could be investigated further through more detailed non-linear

analysis, but this is not required at this stage in the design process. The stress plots from the FEA model are included in Figure F.7 in Appendix F for reference.

(b) Durability and crack widths

For conventional reinforced concrete, the long-term durability of the internal reinforcement is maintained through crack control. Crack widths are kept within specified limits to minimise water penetration and prevent corrosion of the internal reinforcement. However, this is not as much as an issue for sections without internal reinforcement. While internal fibres can corrode, the corrosion product deposited around the fibre is not sufficient to build up enough pressure to cause spalling of the concrete in the way that corrosion of conventional reinforcement can do (Eide and Hisdal, 2012) - therefore corrosion of individual fibres does not significantly affect the strength of the concrete. Crack widths have therefore not been explicitly calculated at this stage; however, this would need to be investigated further during detailed design development.

It is however necessary to limit the possibility of the formation of through thickness cracks in the same way as for the conventional design, particularly as the DNV code states that increasing the tensile strength of the concrete using fibres leads to increased crack width and crack spacing (DNV, 2012, Section 4, D118) . As for the reference design, post-tensioning of 1.5 MPa is specified to ensure that there is a permanent compressive zone in the upper chamber walls.

(c) Fatigue design

On the basis of the data published in the literature it is assumed that fibre reinforced concrete mixes perform the same as or better in fatigue than plain concrete for flexural and tensile loading. Therefore, fatigue damage has not been explicitly checked.

(d) Final design

The analysis in this section has shown that, providing the concrete design mix properties presented in Section 10.2.2 are achievable, it is possible to construct a node structure using a UHPFRC concrete with a fibre volume content of 5%, and a compressive strength of 150MPa.

The required section thicknesses are shown in Table 10.18, and a cross section schematic is shown in Figure 10.15. Final mass and buoyancy properties are shown in Table 10.19 showing that the overall mass is significantly reduced compared to the reference RC design, with a corresponding increase in reserve buoyancy.

Table 10.18: UHPFRC section thickness requirements

Top slab (mm)	Wall (mm)	Cone top (mm)	Cone base (mm)	Innerwall top (mm)	Innerwall base (mm)
100	100	100	175	100	200

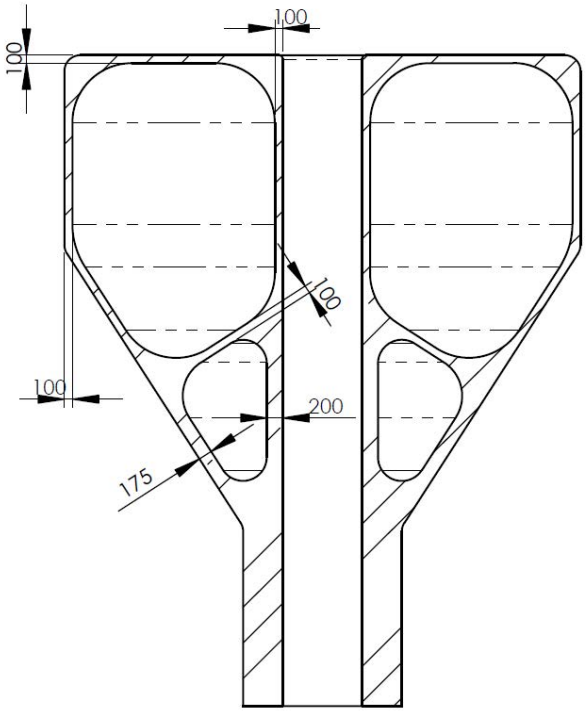

Figure 10.15: UHPFRC cross section requirements (dimensions in mm)

Table 10.19: UHPFRC section mass and buoyancy properties

Node mass (assuming concrete density = 2.5t/m^3)	78.4	t
Total overall displaced volume	135.9	m^3
Reserve buoyancy	60.9	t
Top chamber volume	94.8	m^3
Bottom chamber volume	8.5	m^3
Total displaced volume - flooded bottom chamber	127.4	m^3
Reserve buoyancy - flooded bottom chamber	52.2	t
Freeboard F	1.8	m
Reduced freeboard with flooded bottom chamber RF	1.5	m

10.4.2 Option 2: SHCC - UHPRFC combination

(a) Discrete limit states

In this option an SHCC material is used in the upper chamber. Cross sectional design at SLS, ULS and ALS has been carried out by applying the stress-strain curves developed for the UHPFRC design, together with the material properties for SHCC materials as given in Table 10.9. Different SHCC mixes will give different thickness requirements; for this design an SH80 has been selected, which gives a wall thickness of 150mm throughout the upper chamber (compared to 100m for the UHPFRC option).

UHPFRC is still to be used for the lower chamber and base, as the maximum ALS stress at the junction between the base and the cone is 9.42MPa. Therefore it would be difficult to use the lower tensile strength SHCC in this area without significantly increasing the cross-section area.

(b) Permeability criteria

As discussed previously, the DNV concrete code requires that watertight sections are designed to have a permanent compression zone, which leads to the requirement for post-tensioning for the conventional and UHPFRC options. However the tensile stresses that develop in this section are very low as can be seen in Figure 10.16; the shows that the maximum through thickness tensile stress across all the ULS(c) loadcases is 1.93MPa.

This stress is lower than the design SLS tensile strength for an SH80 mix and therefore it should be possible to rely on the improved permeability characteristics of the SHCC material to ensure that there is no leakage into the structure, without the need for post-tensioning.

(c) Final design

Figure 10.17 shows the cross-section requirements for the structure assuming the SHCC (with a fibre volume fraction v_f of 2.5%) is used for the walls and top slab of the upper chamber, with UHPFRC (with a v_f = 5%) used for lower section as highlighted on the figure. The exact location of the interface between the two materials would need to be investigated further with further design development. Mass and buoyancy properties for this design are shown in Table 10.20.

Figure 10.16: Max principal tensile stress ULS (c) combination 1.93MPa

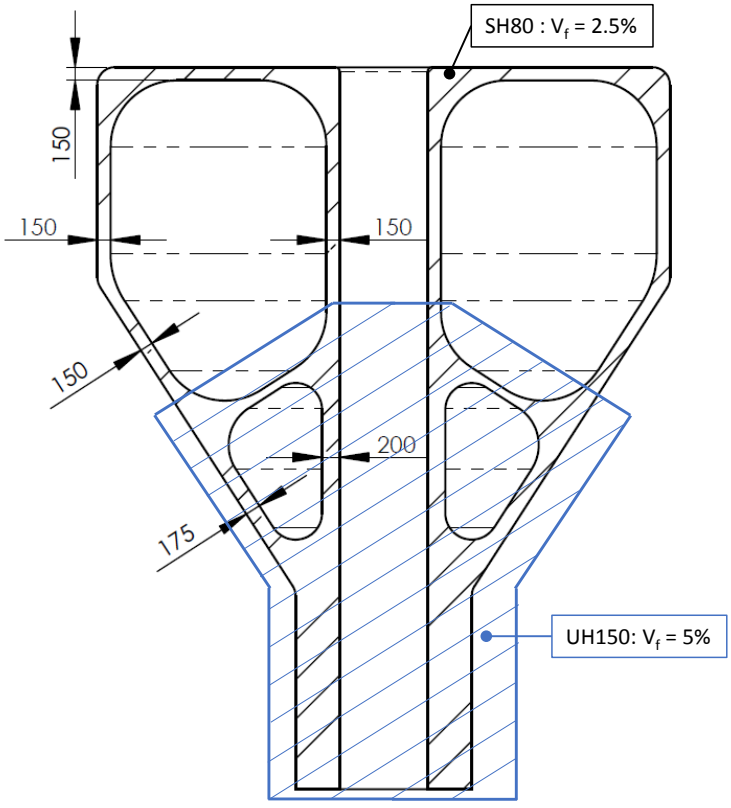

Figure 10.17: SHCC cross section requirements (dimensions in mm)

Table 10.20: SHCC section mass and buoyancy properties

Node mass (assuming concrete density = 2.5t/m^3)	93.3	t
Total overall displaced volume	135.9	m^3
Reserve buoyancy	46.4	t
Top chamber volume	91.9	m^3
Bottom chamber volume	10.1	m^3
Total displaced volume - flooded bottom chamber	125.9	m^3
Reserve buoyancy - flooded bottom chamber	43.2	t
Freeboard F	1.4	m
Reduced freeboard with flooded bottom chamber RF	1.1	m

10.4.3 Option 3: Use of carbon fibre external wrap

As an alternative to using fibre reinforced concrete, it may also be possible to reduce the amount of internal reinforcement by using external carbon fibre fabric reinforcement instead. As carbon fibre wraps are expensive compared to steel reinforcing bars, it is not cost efficient for global use, however it could possibly be used effectively in areas of congested rebar, such as at the junction between the base and the cone although it is noted that the shape of the Node at this location could add design challenges. However, reducing the internal reinforcement in this location by replacing it with external wrapping would simplify the rebar requirements and make construction easier.

For preliminary design, it is assumed that the required internal steel area calculated for the reference design can be directly replaced with the equivalent area of carbon fibre wrapping. The section width can also be reduced by the cover thickness to the rebar, to give the same lever. The wrap can be used to replace both the longitudinal and hoop rebar, providing that the fabric is orientated in the correct direction for each. The calculation for the equivalent required area is included in Appendix F.6, and shows that 4no. carbon fibre plys are required to replace the longitudinal reinforcement, with an additional ply to replace the hoop reinforcement.

A comparison of the solutions with and without carbon fibre external wrap is shown in Figure 10.18. It is only possible to use the carbon fibre wrap on the outer face of the node, as it would be too difficult to place the fibre on the inner face of the hull. Therefore, it is only possible to remove two layers of rebar with this solution. However, this does remove nearly 1200kg of internal rebar (˜30%), and improves the constructibility of the joint in terms rebar fixing and concrete placing. Table 10.21 shows the mass and buoyancy properties for this option.

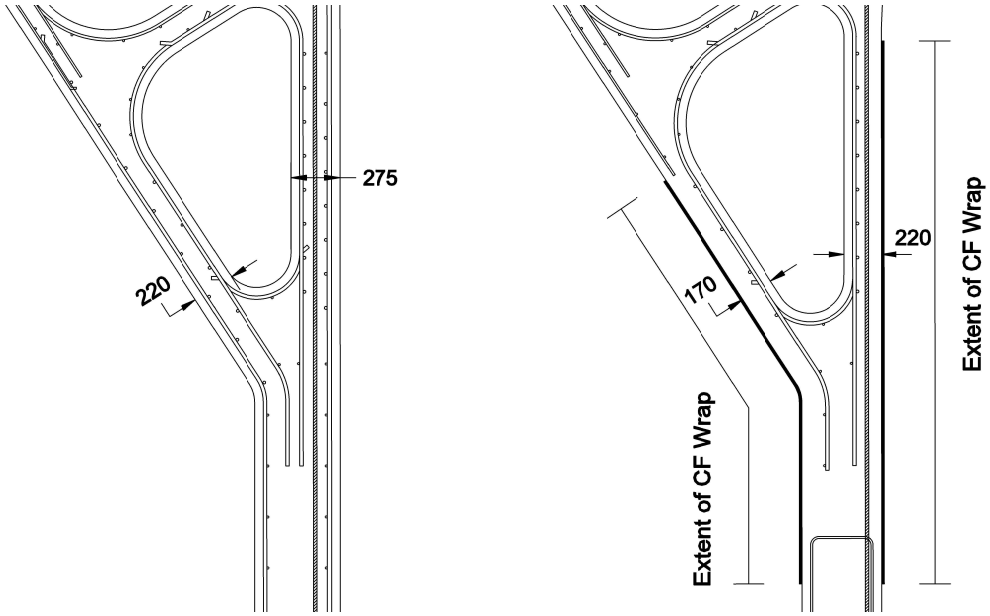

(a) Original design

(a) Alternative, including external carbon fibre wrapping

Figure 10.18: Carbon fibre wrap schematic

Table 10.21: Final node buoyancy and mass properties

Node mass (assuming concrete density = 2.5t/m^3)	104	t
Total overall displaced volume	135.9	m^3
Reserve buoyancy	35.3	t
Top chamber volume	84.8	m^3
Bottom chamber volume	10.1	m^3
Total displaced volume - flooded bottom chamber	125.8	m^3
Reserve buoyancy - flooded bottom chamber	25.0	t
Freeboard F	1.0	m
Reduced freeboard with flooded bottom chamber RF	0.7	m

10.5 Option comparison

10.5.1 Summary

Table 10.22 summarises the benefits the pros, cons and main risks associated with each option.

Table 10.22: Option comparison

Option	Pros	Cons	Main risks
Reference design	• Conventional design and materials • RC concrete is a proven material in the offshore environment	• Results in heavy structure due to minimum reinforcement and durability requirements - upper limits of buoyancy constraints • Complex rebar requirements in some areas • Requires post-tensioning	Further detailed design requirements (particularly regarding interactions with rest of the array) could result in increase in required cross section, pushing design further towards upper limits of buoyancy constraints
1: UHPFRC	• Eliminates need for internal reinforcement • Significantly reduces required concrete volume	• Requires a large volume of fibres, which is likely to be expensive. • Requires post-tensioning	Currently uncertainties regarding the exact material properties for structural design, therefore significant testing will be required before the material can be used in construction
2: SHCC	• Eliminates need for internal reinforcement • Significantly reduces required concrete volume • Eliminates need for post-tensioning • Slightly reduced fibre volume required compared to UHPFRC option	• Still requires a large volume of fibres, which is likely to be expensive.	Currently uncertainties regarding the exact material properties for structural design particularly in regard to the assumption that cracked SHCC has same permeability as uncracked plain concrete. Significant testing will be required before the material can be used in construction
3: Carbon-fibre wraps	• Reduces overall internal reinforcement volume • Simplifies rebar fixing and concrete placement at critical joint between base and column	• Likely to be expensive - increase in cost may not offset gains • Potential difficulties with application of material • Lack of knowledge and experience regarding the durability of the material and bond with the concrete in the offshore environment	Lack of knowledge and experience regarding the durability of the material and bond with the concrete in the offshore environment

10.5.2 Cost estimate

In order to carry out a quantitative comparison, capital costs have been calculated based on the material quantities shown in Table 10.23. The walls and base column are considered to be “simple" areas for fixing reinforcement and pouring concrete. All other parts of the structure have been classed as “complex" with a higher associated cost.

Table 10.23: Material quantities for different design options

Option	RC	UHPFRC	SHCC	CF wrap
Concrete mass [t]	109	78	93	104
% of reference	*100*	*72*	*85*	*95*
C50 simple pour [m^3]	14.8	-	-	14.6
C50 complex pour [m^3]	28.8	-	-	27.0
UH80 simple pour [m^3]	-	-	23.3	-
UH150 simple pour [m^3]	-	10.0	5.0	-
UH150 complex pour [m^3]		21.2	8.7	-
Steel reinforcement [kg]	4000	-	-	2830
Simple fix [kg]	700	-	-	700
Comple fix [kg]	3300	-	-	2130
Post-tensioning [MPa]	1.5	1.5	-	1.5
Fibre volume [kg]	-	12300	9480	-
Carbon fibre area [m^2]	-	-	-	30.8
No of CF plys	-	-	-	5

Rates have been built up based on industry quotations, costs quoted in the literature, and rates provided in construction handbooks such as Spon’s Civil Engineering Price Book (Langdon, 2016). The background information for the cost estimates are shown in Appendix E. To account for uncertainty in the estimates, optimistic and pessimistics cost have also been developed. Conventional concrete is the most well known, and therefore the cost estimates vary less than the FRC and carbon fibre wrap options. For the conventional concrete, the most uncertain item is the rate for the formwork, as this will vary significantly depending on the construction and the amount of times that it can be reused. It is assumed that the formwork will be fabricated from steel, with a total cost of £85k. For the baseline estimate it is assumed that the formwork can be reused 25 times. The optimistic estimate assumes that it can be reused 50 times, with the pessimitic estimate assuming only 5 reuses.

Full cost tables are shown in Appendix F.7, and the estimates for the baseline option are summarised in Tables 10.24 to 10.27. Figure 10.19 shows the costs for each option, presented as a multiplier of the baseline cost for the reference option. The cost estimates show that the baseline RC design is cheaper than the other options, which is in-line with what has been found in other studies, (as discussed in the Literature Review); that where there is a viable conventional RC design, it is likely to be cheaper than using more advanced materials. However it does very much depend on the assumptions made; for example the optimistic

estimate for the advanced concrete options are either very similar or less than the baseline reference estimate, showing that there would be benefit in exploring these options in more detail. In particular the optimistic cost for the SHCC option is significantly cheaper than the baseline cost for the reference design; driven mainly by the reduction in cost due to the elimination of the need for post-tensioning as well as the reduction in cost due to the elimination of the rebar. If further detailed design and material testing showed that the overall volume of fibres could be reduced, or the cheaper, lower strength SHCC could be used over a larger area of the structure this difference could be even more exaggerated.

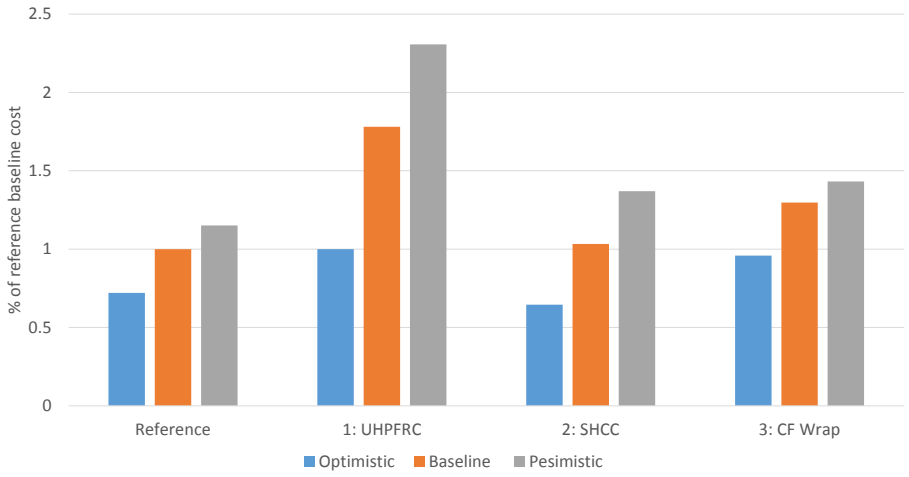

Figure 10.19: Option costs presented as a multiplier of the reference design baseline cost

Table 10.24: Reference RC option

Description	Quantity	Unit	Rate	Cost
Concrete and reinforcement				
Formwork	330	m^2	10	3395
50MPa concrete: provide and place, simple pour	14.8	m^3	170	2516
50MPa concrete: provide and place, complex pour	28.8	m^3	200	5760
Steel reinforcement: provide and fix, easy	0.7	t	1075	753
Steel reinforcement: provide and fix, complex	3.3	t	1160	3828
Prestressing				
Material and labour	1180	kN	7	8260
Hire of equipment	2	wks	515	1030
Formation of ducts	6	bar no.	7	42
Totals				**£25,583**

Table 10.25: Option 1: UHPFRC

Description	Quantity	Unit	Rate	Cost
Concrete and reinforcement				
Formwork	330	m^2	10	3395
UHPC concrete: provide and place, easy pour	10	m^3	575	5750
UHPC concrete: provide and place, complex pour	21.2	m^3	625	13250
Steel fibre	12.3	t	1018	12515
Prestressing				
Material and labour	1180	kN	7	8260
Hire of equipment	2	wks	515	1030
Formation of ducts	6	bar no.	7	42
Totals				**£44,242**

Table 10.26: Option 2: SHCC & UHPFRC

Description	Quantity	Unit	Rate	Cost
Concrete and reinforcement				
Formwork	330	m^2	10	3395
80MPa concrete: provide and place, easy pour	23.3	m^3	204	4753
UHPC concrete: provide and place, easy pour	5.0	m^3	575	2850
UHPC concrete: provide and place, complex pour	8.7	m^3	625	5415
Steel fibre	9.8	t	1018	9972
Totals				**£26,384**

Table 10.27: Option 3: Carbon fibre

Description	Quantity	Unit	Rate	Cost
Concrete and reinforcement				
Formwork	330	m^2	10	3395
C50 concrete: provide and place, simple pour	14.8	m^3	170	2516
C50 concrete: provide and place, complex pour	26.8	m^3	200	5360
Steel reinforcement: provide and fix, easy	0.7	t	1075	753
Steel reinforcement: provide and fix, complex	2.13	t	1160	2471
Carbon fibre wrap				
5 plys of wrap at 30.8m^2 per ply	154	m^2	58	8855
Prestressing				
Material and labour	1180	kN	7	8260
Hire of equipment	2	wks	515	1030
Formation of ducts	6	bar no.	7	42
Totals				**£32,681**

10.6 Scale Effect

The previous section showed that while advanced concrete mixes do offer some advantages over a conventional concrete design, a best estimate of costs shows that the conventional RC still appears to be the cheapest solution where there are no onerous design constraints. However, Albatern were hoping to develop their WaveNET floating array system on a number of different scales to meet the demands of different markets. For smaller scale devices conventional RC is not suitable due to buoyancy constraints, however fibre reinforced concrete is an option as it allows thinner wall sections to be used.

To assess the potential for FRC at a smaller scale a high level design exercise has been carried out for a node structure compatible with the WaveNET 6S array, which is a half the physical scale of the 12S array. A comparison of the parameters for the 6S and 12S are shown in Table 10.28.

Table 10.28: Characteristic parameters of different WaveNET array scales

Parameter	6S	12S
Rated power per unit	7.5kW	75kW
Design H_s	7m	14m
Characteristic distance between nodes	6m	12m

As the Ashby material selection process (presented in Chapter 9) showed, while conventional concrete was highlighted as the preferred material for the 12S Node (where the objective was to minimise the cost), for the 6S node, overall weight and buoyancy restrictions are more stringent, meaning that minimising weight (while still achieving an acceptable construction cost) is more important.

Referring back to Table 9.2 on page 151, when minimising weight was considered to be the overall objective, concrete did not perform favourably at all when compared to steel. Materials that showed an improvement over steel when providing strength and stiffness at a minimum weight include CFRP, titanium, woods and GFRP. Discounting CFRP and titanium due to the high price point, and woods due to the difficulty in making large watertight structures, leaves GFRP as a potential alternative. Therefore in this section, preliminary designs for the 6S node are carried out for a carbon steel reference design, together with a GFRP and an FRC structure for comparison.

Design loads are derived in Section 10.6.1, and material properties are given in Section 10.6.2. A brief discussion of the design methodology, together with schematics of the different options is included in Section 10.6.3, and finally cost estimates are presented in Section 10.6.4.

10.6.1 Design loads

Rather than carry out a separate analysis, actions for the 6S node structure have been scaled from the values derived for the 12S design. The design of sections in the upper chamber of the node (the Top slab, Wall, Cone top, Innerwall top, and Inner rib) are driven by the hydrodynamic wave pressures. For these sections the ULS and ALS design actions for the 12S array (see Table F.5) have been scaled down by a factor of 8. This accounts for the following factors:

1. 6S array design H_s = 0.5 x 12S array design H_s : wave pressures $\propto H_s$.
2. 6S array is half physical scale of 12S array: bending moment $\propto$ span^2.

The design of the Cone base, Inner wall base and Base Column are driven by the applied PTO moments. For these sections the design actions have been scaled down by a factor of 10, as the applied PTO torque is $\propto$ rated power). A full list of scaled design actions are included in Table F.12 in Appendix F.8, with the values for the Innerwall section shown in Table 10.29 for comparison with those presented in Table 10.13 on page 173.

Table 10.29: Scaled design actions for 6S design

Direction	Bending (kNm)	Axial (kN)
Hoop	0.2	3.7
Longitudinal	1.8	105.7

10.6.2 Materials

The properties of the different materials considered in this design exercise are as follows:

1. Carbon steel with f_y= 355MPa. Steel is one of the most commonly used materials for WECs, and therefore has been used as the reference design.
2. Glass fibre reinforced plastic (GFRP) sandwich construction with characteristic strength = 370MPa, and a configuration based on the construction method proposed in the materials study for main tubes of the Pelamis line attenuator device (Anderson, 2003, see). A schematic of the construction is shown in Figure 10.20.
3. SH80: A SHCC fibre reinforced concrete with a fibre volume fraction (v_f) = 2.5%, and material properties as presented in Table 10.9.

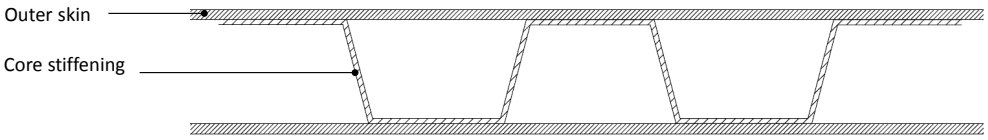

Figure 10.20: GFRP sandwich construction schematic

10.6.3 Design methodology

(a) Steel and GFRP options

For the steel and GFRP options a simple design check has been carried out based on the combined bending and axial resistance of a particular section, based on the following equations:

$$\text{Design moment resistance } M_R = Z.\sigma_d$$

Where Z is the section modulus, and σ_d is the design strength = σ_k/γ_m. γ_m is the material partial safety factor = 1.15 for steel.

$$\text{Design axial resistance } N_R = A.\sigma_d$$

Where A is the cross sectional area.

$$\text{Utilisation factor } U = \frac{M_d}{M_R} + \frac{N_d}{N_R} \leq 0.6$$

While there are many other factors that would need to be considered for a detailed design (e.g. fatigue loading, shear and buckling effects), this method is acceptable for preliminary sizing, and provides enough detail to be able to carry out a comparison between the options. The Utilisation Factor (U) has been kept below 0.6 in order to account for effects that have not been considered in detail at this stage.

(b) SHCC design

The SHCC design has been carried out using the same method as for the 12S device, using the stress-strain relationships presented in Figure F.5, and material properties as presented in Table 10.9.

Example calculations for the different options are included in Appendix F.9, and schematics of the final configurations are shown in Figure 10.21.

10.6.4 Cost estimates

Baseline cost estimates are shown in Table 10.30. As the steel and GFRP options are significantly lighter than the SHCC option, these include ballast to bring all options up to the same weight. The steel option includes a cost for coating as steel is susceptible to corrosion in the offshore environment. Again, an optimistic and pessimistic estimate have been included (shown in Figure 10.22, and in the Table F.13 in Appendix F.10).

All assumptions behind the build up of the unit rates are included in Appendix E.

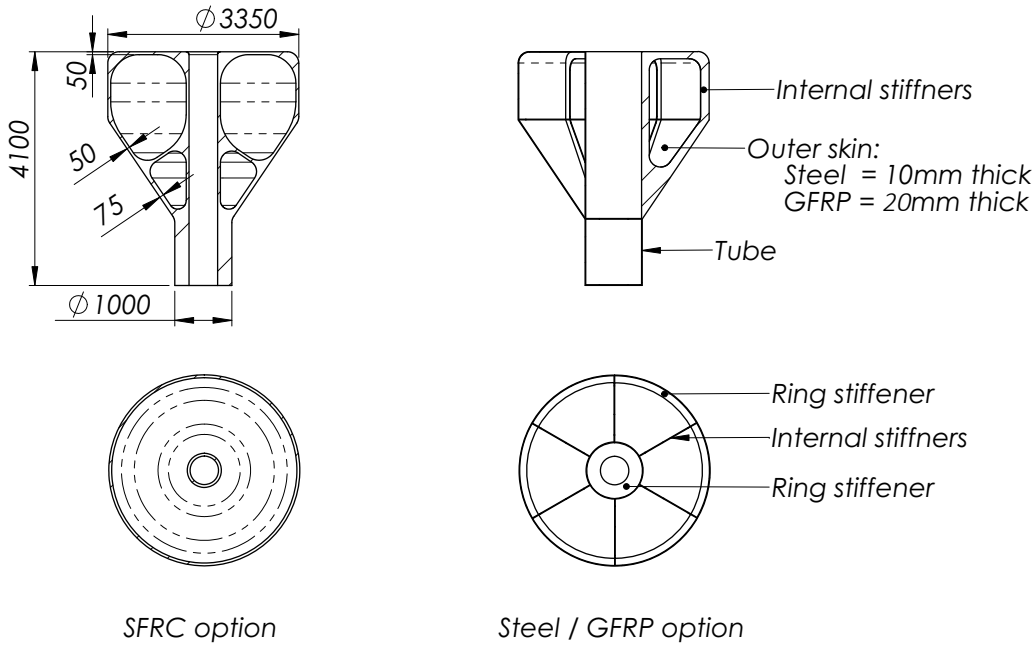

Figure 10.21: Schematics for different options for 6S scale node

The cost comparison in Figure 10.22 shows that the SHCC option is significantly cheaper than either the steel or GFRP option, even when the optimistic assumptions are taken into account. This shows that the use of SHCC could offer significant benefits in situations where additional constraints exist such as weight and buoyancy.

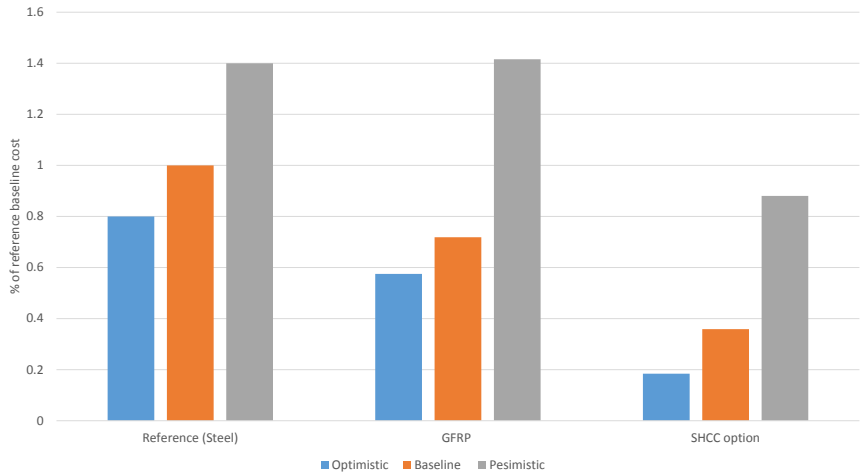

Figure 10.22: Option costs as a multiplier of the steel baseline cost

Note that the SHCC option is very sensitive to the cost of the formwork, which accounts for a larger proportion of the overall cost than the 12S Node, and therefore is the driver for the large variation between the baseline and the pessimistic estimates.

Table 10.30: 6S options cost comparison

Option	Item	Quantity	Unit	Rate	Cost
Steel option (reference design)					
	Tube	1	te	1800	1800
	Fabrication	3.2	te	2275	7280
	Coating	109	m^2	30	3270
	Ballast	5.8	te	50	290
	Total				**£12,640**
GFRP option					
	Tube	0.1	te	7500	750
	Fabrication	0.7	te	11250	7875
	Ballast	9.2	te	50	460
	Total				**£9,085**
SHCC option					
	Formwork	126	m^2	10	1296
	UHPFRC provide and place, complex	4	m^3	625	2500
	Steel fibre @ 2.5%	0.76	te	1018	778
	Ballast	0.20	te	50	10
	Total				**£4,584**

10.7 Discussion and conclusions

This chapter has investigated the potential of using advanced concrete materials for the Node structure within the WaveNET array system. These materials have been compared against different conventional reference materials depending on the physical scale of the Node.

For the 12S Node, the reference design is a conventional C50 reinforced concrete structure. The preliminary design work showed that it is possible to utilise this material, but highlighted areas where more advanced materials could offer benefits. For example the mass of the RC structure is on the upper limits of what is acceptable from a buoyancy perspective, and the reinforcement is very congested through the joint between the base column and the upper structure. In addition, post-tensioning is required in order to overcome through thickness tensile stresses in the inner column which are not acceptable for a watertight concrete structure.

Further design work illustrated that advanced concrete materials could overcome these issues in the following manner:

1. Using UHPFRC concrete with high tensile strength throughout the structure eliminates the need for internal reinforcement, and reduces the overall section mass;
2. Using SHCC concrete in areas with low tensile stresses enhances the permeability characteristics of the cracked concrete and removes the need for post-tensioning;

3. Using localised carbon fibre wraps can reduce the overall amount of internal reinforcement required.

The structural design work carried out in this study has shown that it is possible to develop a solution for all these options. However a cost comparison shows that reinforced concrete design is ultimately the cheapest solution when using best estimates for the costs.

Option 1 (UHPFRC) is the most expensive, coming in at nearly 180% of the reference cost. This is driven by the greater volume of steel required to provide a fibre volume fraction of 5% when compared with conventional reinforcing steel bars, and the increase in the cost of the underlying high performance concrete mix with a compressive strength of 150 MPa compared with a standard concrete mix with a compressive strength of 50 MPa. It is however possible that costs could be decreased through optimisation of the FRC mix, and by using lower strength mixes in areas with lower structural strength. This is illustrated in Option 2, which utilises lower strength (and therefore lower cost) SHCC for the upper section of the chamber. This material theoretically maintains the same permeability as uncracked plain concrete even in its cracked state, due to the formation of multiple micro-cracks under increasing strain rather than crack localisation. This removes the need for post-tensioning, which is a significant proportion of the reference design cost (40%). This option is only 3% more expensive than the reference, and therefore the actual relative cost between the two options depends very much on the assumptions behind the cost estimates. Indeed the optimistic estimate for Option 2 is significantly cheaper than the baseline estimate for the reference design (approximately 60%). This results shows that there is potential for using SHCC materials for wave energy devices, and therefore there would be benefits to carrying out further investigations of the properties of this type of material.

Option 3 (localised carbon-fibre wraps) is the second most expensive, coming in at 140% of the reference design cost, driven by the high cost of carbon fibre. While there may be certain circumstances which justify the use of this material for very localised structural strengthening applications, it does not appear to offer widespread benefits.

In addition to designs for the 12S node, preliminary designs have also been developed for a 6S node to investigate the effect of scale on material choice. This node is half the size of the 12S node, and it is not possible to use conventional RC at this scale due to weight and buoyancy restrictions. However unlike conventional RC, fibre reinforced concrete does not have a minimum thickness requirement, therefore it is possible to meet the weight restrictions with this material. An SHCC option has been compared with designs in steel and GFRP, and comes out very favourably in the cost estimates. The SHCC option is approximately 40% of the cost of the GFRP structure, and only 30% of the cost of the steel fabrication.

10.7.1 Wider applications of the work

This work has been carried out alongside Quoceant's ACE-WEC project which investigated the benefits of using advanced concrete materials and manufacturing methods for a wide range of wave energy converters, including floating line attenuators, fixed bottom surge oscillators, 2D of freedom surge and pitch buoys, floating inertial mass, and submerged pressure differential devices, (Quoceant and University of Dundee, 2018).

The project highlighted a number of benefits of using advanced FRC materials, similar to those discussed in this report for the Albatern Node, including being able to produce devices with thinner sections (and therefore lower mass) compared to conventional concrete, the ease of being able to use different mixes and fibre volumes in different locations to optimise design, simplification of construction and manufacturing compared with conventional RC with high levels of reinforcement, and offering good cost savings when compared against baseline designs from steel. In addition to advanced materials, the project also considered the possibility of advanced manufacturing techniques in the form of 3D printing (or additive manufacturing) of concrete structures. While this method is still in the early development states (and therefore not included in detail for the work on the Albatern Node structure discussed in this chapter), current research work indicates that this could significantly reduce manufacturing costs compared to conventional RC, due to the removal of the need for formwork, and the high rate of concrete pouring that is achievable. This could then bring the high costs of the high strength FRC materials as presented in this work so it is more in line with conventional concrete construction.

The LCoE analysis carried out as part of the ACE-WEC project indicated LCoE reductions of between 10-60% depending on the overall configuration of the device, and the reference baseline material, and the impact of the structural costs on the overall LCoE. These cost reductions include a reduction in manufacturing costs associated with 3D printed concrete, which results in cost reductions for FRC options, even when compared to conventional RC designs.

10.7.2 Conclusions

The main conclusions that can be drawn from the work carried out in this chapter are as follows:

- Where a conventional reinforced concrete design is possible, and there are no exceptional design constraints it is likely that this will be cheaper than using more advanced materials using currently available manufacturing methods.
- While very high strength UHPFRC materials are not able to compete in terms of outright cost with conventional reinforced concrete, in certain circumstances they could offer cost savings over materials like steel and fibre reinforced composites, particularly if mix

designs can be optimised for specific applications. UHPFRC could therefore be utilised for structures where a conventional RC option is not possible; for example where there are weight and buoyancy constraints.

- Lower strength SHCC materials are significantly cheaper than UHPFRC materials, as they have a lower volume of fibres, and a lower base concrete compressive strength, resulting in costs that are more comparable with conventional RC. Application of advanced manufacturing techniques could bring costs of these materials even further down, making them an attractive alternative.
- SHCC material show significant cost benefits over materials such as steel and GFRP, and therefore could offer benefits for smaller structures, where buoyancy is the design driver.
- The literature shows that permeability of SHCC materials in the cracked state is similar to that of uncracked plain concrete, providing that the widths of the micro-cracks remains below a certain threshold. Therefore there could be significant advantages to using these materials in structures that have low tensile stresses as this could eliminate the need for both the internal reinforcement and additional post-tensioning that is required for watertight conventional RC structures.
- The work carried out in this chapter is based on theoretical assumptions of the material properties. Significant testing would be required to validate these assumptions before such materials could be used for detailed design, construction and deployment of wave energy devices.

Chapter 11

Connection design

One of the uncertainties associated with the use of concrete for wave energy converters is the behaviour of connections between the concrete structure and the more dynamic components such as the PTO system. These connections are subject to highly dynamic, multi-axial loads, and are usually critical to the overall function of the device. They therefore need to maintain their structural integrity in the harsh offshore operating environment for the lifetime of the structure. This imposes a unique set of design conditions that are not seen in other common connection applications such as in the steel girder to concrete deck connection in composite bridges (which are highly dynamic but primarily loaded in shear) and connections between steel and concrete members in buildings (subject to multi-axial, but significantly less dynamic loads).

This chapter investigates some of the issues surrounding conventional reinforced concrete (RC) connections for floating wave energy converters, with particular reference to the effect of dynamic, multiaxial loading on the fatigue life of the components. The objective of this chapter is to review currently available methods of connecting steel and RC components, with the aim of being able to make general recommendations as to suitable connection configurations for floating WECs.

The structure of this chapter is as follows:

- An overview of the problem is included in **Section 11.1.**
- The methodology that has been followed for the high level connection design is presented in **Section 11.2.**
- Results of the preliminary option assessment is covered in **Section 11.3**; this section includes a high level evaluation of the different options available, hand calculations of the static resistance of the joint based on linear elastic material properties, and a preliminary fatigue analysis looking at fatigue damage of the steel connection elements.
- Results of a more detailed analysis of a sub-set of the connections is included in **Section 11.4**, which includes finite element analysis of the connections using non-linear material properties, and consideration of the fatigue behaviour and potential damage progression through the concrete.
- A discussion of the findings is included in **Section 11.5**.

11.1 Background and context

This chapter uses the Albatern 12S Node structure as a case study to assess the application and suitability of different connections options with particular emphasis on multi-axial dynamic load regimes.

Work carried out in Chapter 9 showed that concrete is the preferred construction material for the node, however, the durability of the critical joint between the Node structure and the articulated steel joint module is an area of uncertainty. This connection is the reaction point for the power take off system, and as such has to transfer large, dynamic loads about multiple degrees of freedom. An overview of the joint is shown in Figure 11.1, and the different loads acting on the connection are shown in Figure 11.2.

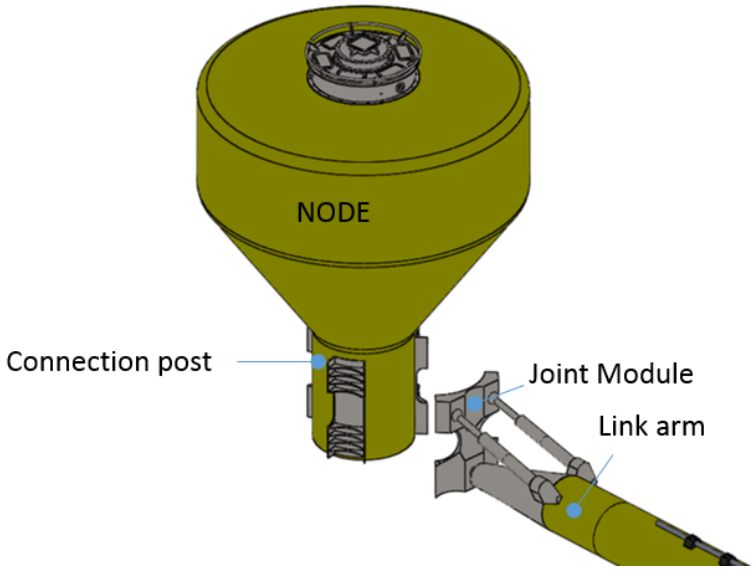

Figure 11.1: Joint overview

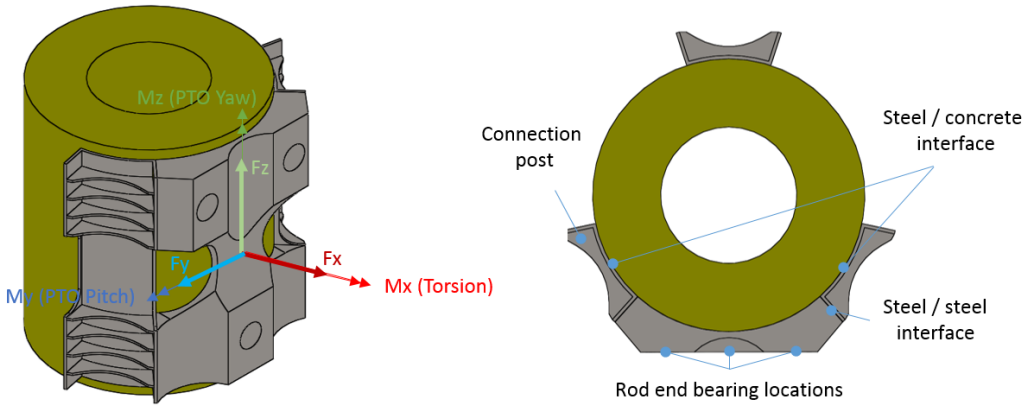

Figure 11.2: Connection loads

While the design work carried out is specific to the Albatern Node structure, the conditions that this device operates in are similar to many other wave energy converters, and therefore the knowledge gained from this work could be also be applied across the industry.

Early work on this topic formed the basis of a conference paper presented by the author at CORE 2016 (Barker Ewart et al., 2016). This paper is included in Appendix A and discusses the connection design for one of the preliminary concepts for the 12S Node structure.

11.2 Connection assessment methodology

The connection assessment process is split into two phases; a preliminary assessment covering a wide range of connections, and a more detailed analysis on a smaller subset of options. The steps taken in this assessment are summarised below, and discussed in more detail in the following sections:

1. Preliminary options assessment
   (a) Development of high level options, based on potential connection configurations as discussed in the literature review.
   (b) Derive local connection loads based on global PTO loads
   (c) Preliminary design based on static load cases, using linear elastic analysis and hand calculations.
   (d) Preliminary spectral fatigue analysis based on fatigue loads, focussing on the steel fatigue.
2. More detailed investigation of a sub-set of connection options
   (a) Detailed analysis of connection behaviour under static loads, using finite element models and non-linear material properites.
   (b) Evaluation of the behaviour of connections under fatigue loads, with particular focus on the behaviour of concrete.

11.2.1 Preliminary options assessment

(a) Connection options

This assessment focusses on cast-in, mechanical connection configurations. The literature review in Chapter 4 also discussed post-installed mechanical anchors and flat-faced adhesive joints, however there is little history of use of adhesive joints in the marine environment and post-installed anchors are most suitable to retrofitting applications or in-situ construction. Even within the category of cast-in mechanical anchors, there are a number of available options. This review focusses on widely used connection types, or those with a well documented development history, which leaves the following connection configurations (schematics are shown in Figure 11.3):

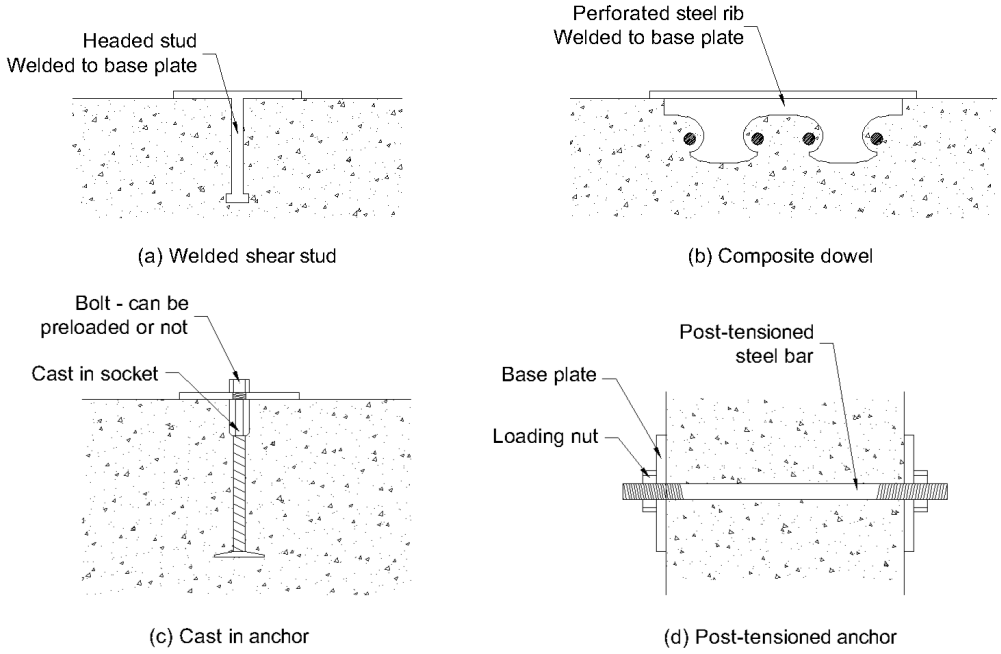

Figure 11.3: Connection schematics

- **Welded shear studs:** these are used widely in civil and offshore applications, and can be designed in accordance with standard design codes, including BS EN 1994-1-1:2004 (BSI, 2004*b*) and DNVGL-OS-C502 (DNV GL, 2018)
- **Composite dowel connectors:** these consist of profiled steel ribs which interact with the concrete under load and have been developed as an alternative to shear studs in composite bridge construction, where they have been shown to have superior static load capacity and resistance to fatigue under shear loads. They are included in this assessment to investigate whether the benefits also extend to multi-axial loading regimes.
- **Cast-in sockets with bolted fasteners:** these types of connections are commonly used in civil engineering applications, particularly in building construction. There are many types of proprietary systems available from manufacture such as Hilti and Halfen, which can be designed to take multi-axial loads, although generally at lower load levels than required for this purpose. Both pre-loaded and non-preloaded options for the fastening bolts will be considered.
- **Post-tensioned bars:** these types of connections are often used in the wind industry, both onshore and offshore to connect the steel towers to concrete foundations, typically in large diameter circular connections. This connection option is included to look at the benefits for using in smaller, more space confined connection details as are typically found in wave energy converters. The benefits of post-tensioned systems are that they can keep the concrete in compression (therefore reducing tension cracks) and reduce the impact of fatigue on steel components.

It is noted that limiting the scope of the review to this small sub-set of connection options could result in more novel options being overlooked. However, these carry more risk, and would require a large amount of analysis work that is beyond the scope of this current research project. Limiting the scope to currently available options allows solutions to be developed that would not require a great deal of further investigation in order to be made a reality.

(b) Connection loads

The connection has to resist the global PTO loads as derived in Section 8, and reproduced in Table 11.1. ULS loads are not considered, as the ALS loads are more critical.

Table 11.1: PTO articulation load cases for ongoing design work

Limit state	F_X (kN)	F_Y (kN)	F_Z (kN)	M_X (kNm)	M_Y (kNm)	M_Z (kNm)
SLS	1000	250	250	500	1000	500
ALS	1500	500	500	2000	5000	2000

These global articulation loads have been resolved into tension and shear loads at each of the four connection points as shown in Figure 11.4. This process results in the local connection load cases shown in Table 11.2. The global loads can act in either direction, therefore the ALS load combination results in two local connection combinations; one which givse the maximum shear load and one which gives the maximum tensile load.

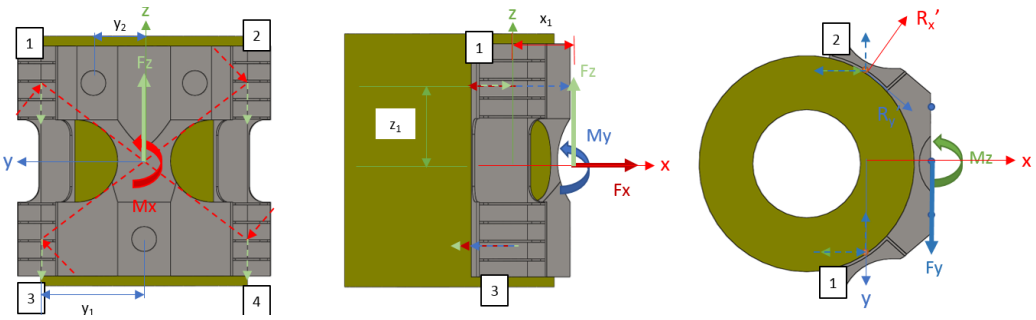

Figure 11.4: Local connection loads

Table 11.2: Connection loads

Loadcase	Tension (R'_x MN)	Shear (R'_y MN)	Shear (R'_z MN)
SLS	0.29	0.02	0.77
ALS (max tension)	1.67	2.12	0.46
ALS (max shear)	1.06	2.65	0.21

(c) Static load design

The baseline design of the connections has been carried out using the following codes and design guides;

- Shear studs have been designed in accordance with BS EN 1994-1-1:2004 (Eurocode for the Design of composite steel and concrete structures) (BSI, 2004*b*), which deals specifically with the design of welded shear studs. This code focusses on shear loading, but does not cover design of connections subject to tension loads. For this aspect of design, reference is made to the BS EN 1992-4 (Design of Fastenings for use in concrete) (BSI, 2013) .
- Design of the composite dowel connections is based on the recently developed German National Approval (Feldmann et al., 2016), which focusses solely on shear loading. Resistance to tensile loads is calculated in accordance with Classen and Hegger (2016).
- Cast in sockets and bolts have been designed in accordance with the principles in BS EN 1992-4 (BSI, 2013) with reference to additional technical guidance provided by Halfen (Halfen, 2014) which gives product specific guidance that is not included in the code.
- The post-tensioned bars are designed in accordance with Macalloy documentation (Macalloy, 2013); the design philosophy for the bars is that there is a "no-slip" condition for all loads up to the design SLS load case, taking account a potential 30% loss in pretension, and assuming a friction coefficient of 0.2 between the steel and the concrete. Up to this point the full shear load is transferred directly into the concrete. In addition, steel and concrete checks have been carried out in accordance with BSI (2004*b*) and BSI (2004*a*).

The initial design has been carried out assuming linear elastic connection behaviour and material properties.

(d) Fatigue limit state design

Preliminary fatigue checks have been carried out for the steel components, which are usually considered to be the critical element in the connection.

A spectral fatigue analysis method has been applied; full details of this method are included in Section 6.4.3, but in summary the output is a stress cycle count histogram which allows fatigue damage to be calculated in accordance with the Palmgren-Miner linear damage summation and published S-N data. The stress cycle histogram is calculated based on the statistical parameters of the structural response spectrum, which is a function of the input wave spectrum, and the local stress response amplitude operator RAO.

Steel stress RAOs have been determined using output from the Ansys Aqwa model described in Section 6.3. This model has been run in a series of regular wave conditions, each with a unit

wave height, for wave periods between 4 and 20 seconds. Articulation loads for each sea state have then been extracted from the model runs to give the load RAOs shown in Figure 11.5.

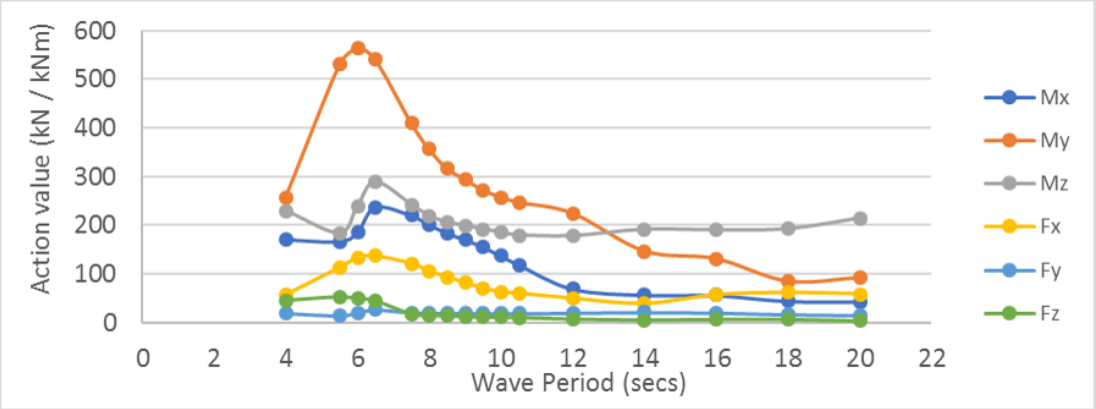

Figure 11.5: Articulation load RAOs

At each wave period, the 6 DoF articulation load is resolved into a set of local connections loads as shown in Figure 11.4, which are used to determine the stress RAO for each connection type, based on the maximum principal stress in the steel in order to capture effects of stresses about multiple axis (as suggested by Halfpenny, 1999).

S-N data has been taken from DNV GL (2014) (using data for steel in sea water, with cathodic protection) or taken from relevant literature, as shown in Table 11.3. Where S-N data varies depending on loading direction, the worst case values have been selected.

Table 11.3: S-N data for connection details

Detail	Fatigue category	m_1	$\log(a_1)$	m_2	$\log(a_2)$	Reference
Stud	E	3	11.610	5	15.35	DNV GL (2014) Table A-7(11)
Bolt	F1	3	11.299	5	14.832	DNV GL (2014) Table A-2(3)
Dowel	E/D	3	11.687	5	15.487	Berthellemy (2013) [1]
Bar	F1	3	11.299	5	14.832	DNV GL (2014) Table A-2(3)

For preloaded options, the cyclic stress in the bolt has been calculated taking into account the preload and connection geometry in accordance with UNBRAKO (2004).

1. Berthellemy (2013) derives the S-N data for Clothoidal shaped dowels in relation to the classes given in EN 1993-1-9, which has been used to provide the S-N data according to the DNV classes as provided in this table.

11.2.2 Detailed options assessment

A sub-set of the most promising connections will be analysed in more detail, making use of finite element models, and including non-linear material properties. The emphasis of this analysis will be the behaviour of the concrete within the connection, particularly under cyclic loads.

Concrete fatigue is often ignored in composite structures, as historically it has been shown that fatigue of the steel elements is dominant. However, as noted by Toth et al. (2016) the interaction between the steel and concrete in connections subject to multiaxial loads is complex, and therefore the impact of concrete fatigue on the overall connection behaviour should not be overlooked when considering suitable steel-concrete connection types for WECs.

(a) Behaviour under static loads

To investigate the connection behaviour under static loads, 3D solid finite element models have been set up in Abaqus. The purpose of the analysis is to compare the modelled behaviour with that predicted using the code based hand calculations, and to provide some information on the likely levels and location of concrete damage and cracking. An example of one the models is shown in Figure 11.6 , with concrete elements in grey, steel elements in maroon, and loads and boundary conditions shown with orange arrows.

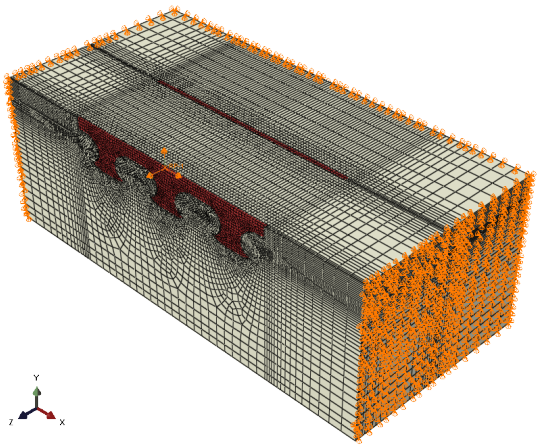

Figure 11.6: Section through FEA model for dowel connection

The concrete and steel connectors are modelled explicitly using C38DR solid elements. The reinforcement bars are modelled as stringers, using B31 beam elements, which are assumed to be perfectly bonded to the concrete. Steel components are modelled with perfectly plastic material properties. The concrete damaged plasticity material model has been used for the concrete sections, with parameters as specified in Jankowiak and Lodygowski (2005). It is noted that results of the model using this material model will be mesh-sensitive. However, a

mesh convergence study has not been carried out in this case, as the purpose of the design work is to provide a comparison between options which does not require accurate knowledge of the exact location and nature of the concrete damage.

Contact between the steel connectors and the surrounding concrete is modelled using the General Contact formulation, with "hard" contact in the normal direction and frictionless contact in the tangential direction. The exception to this is the contact face between the post-tensioned bar plates and the concrete, which have been assigned a tangential friction coefficient of 0.2, using the surface-to-surface penalty contact formulation. Loads are applied to a reference point which is rigidly tied to the top surface of the connector elements. The size of the modelled concrete section is selected in order to not introduce any boundary condition effects into the analysis. The outer vertical faces of the concrete are constrained in the vertical and horizontal directions.

(b) Assessment of fatigue load behaviour

It is noted in the literature (see Chapter 4) that concrete fatigue damage evolution is complex and not necessarily well described using standard S-N curves and the linear Palmgren-Miner summation method. However other proposed methods such as the fracture mechanics approach given in Toth et al. (2016) and the multi-stage process described in Grünberg and Göhlmann (2013) and Grünberg et al. (2005) require experimental input, or detailed knowledge of the full loading conditions, and are therefore not appropriate for preliminary design and option comparison. Therefore, simplified spectral fatigue analysis has been carried out, based on published S-N curves for concrete.

To determine the concrete stress RAOs, a set of finite element models have been run using the local articulation loads calculated across the range of wave periods. The models have been run with linear elastic material properties (as allowed for in DNV GL, 2018) in order to reduce computational time. Principal stresses for elements of interest have been extracted from the models to give the stress RAOs.

As noted in the literature review, fatigue damage in concrete is very dependant on the multi-axial loading state within the concrete. This has been accounted for by using a corrected S-N curve based on the method given in Grünberg and Göhlmann (2013), and described below.

The baseline S-N curve for concrete taken from DNV GL (2018) has been used as a starting point, with the multi-axial stress state accounted for by replacing f_{rd} (uniaxial failure strength) with f_3 (the failure strength dependant on the multi-axial stress state). This gives the following equation for the concrete S-N curve:

$$log_{10}N = C_1 . \frac{1 - \frac{\sigma_{max}}{f_3}}{1 - \frac{\sigma_{min}}{f_3}} \tag{11.1}$$

Where: N = Number of cycles to failure for given stress range

C_1 = 8 for stress ranges in the compression-tension range;

C_1 = 10 for stress ranges in the compression-compression range;

σ_{max} = the maximum compressive stress in the concrete;

σ_{min} = the minimum compressive stress

f_3 is calculated based on the 3 parameter William-Warnke failure criteria for a given tri-axial stress state (see Equation 11.2, taken from William and Warnke 1975). f_3 is taken as the value of σ_3 that lies on the failure surface for a given σ_1 and σ_2 (where $\sigma_{1,2,3}$ are the principal stresses).

$$\frac{1}{z}\frac{\sigma_a}{f_{cu}} + \frac{1}{r_q}\frac{\tau_a}{f_{cu}} = 0 \tag{11.2}$$

$$\sigma_a = \frac{1}{3}(\sigma_1 + \sigma_2 + \sigma_3) \tag{11.3}$$

$$\tau_a = \frac{1}{\sqrt{15}}.((\sigma_1 - \sigma_2)^2 + (\sigma_2 - \sigma_3)^2 + (\sigma_3 - \sigma_1)^2)^{0.5} \tag{11.4}$$

Where: f_{cu} is the uniaxial compressive strength of concrete;

z is a coefficient relating to the biaxial and tensile strength of the concrete; and

r_q describes the relevant point on the failure surface expressed in polar coordinates.

As discussed in Section 7.3, the PTO torque is limited to a maximum value of 1MNm, which is not captured in the hydrodynamic models, but has a significant impact on the fatigue damage. The damage calculation is therefore manually manipulated by taking the concrete stress developed under the SLS loads (as given in Table 11.2) as the upper limit for the σ_{max} in Equation 11.1. The number of cycles associated with values of σ_{max} greater than this are added on the cycle count for the limiting stress cycle, in order to give the same total count.

11.3 Results of preliminary options assessment

11.3.1 Connection options

Schematics and descriptions of the different connection options are shown in Figures 11.7 and 11.8.

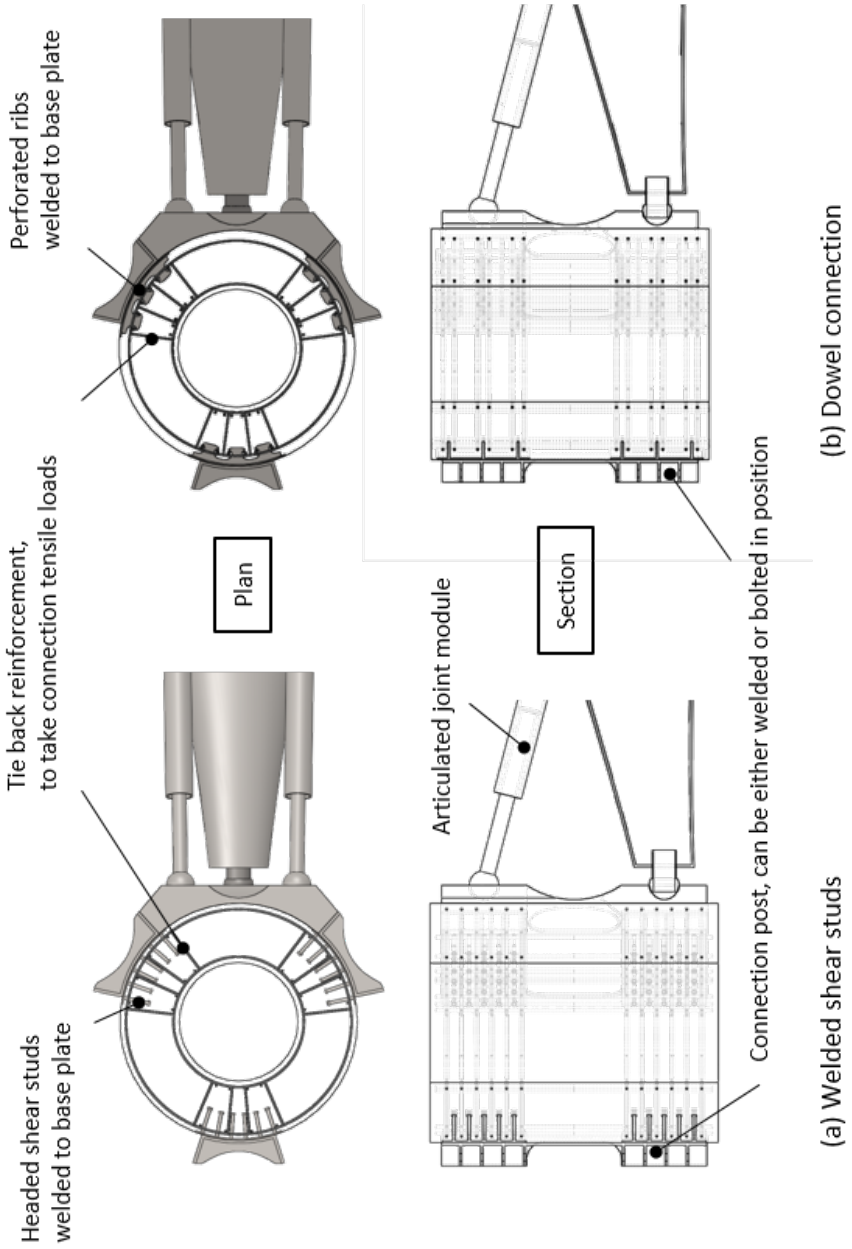

Figure 11.7: Connection option schematics (a) and (b)

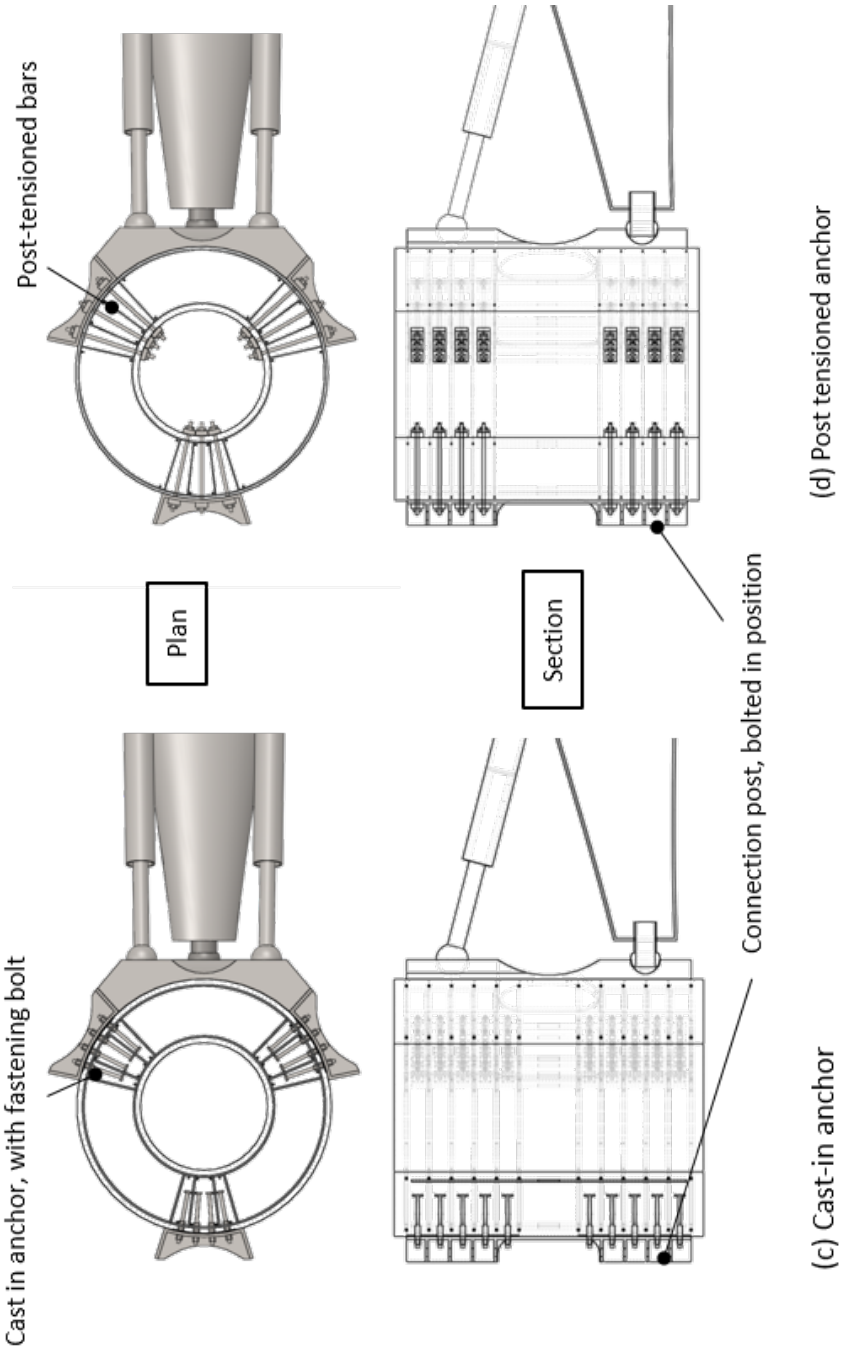

Figure 11.8: Connection option schematics (c) and (d)

11.3.2 Static design requirements

The static load resistance of each of the connections is discussed in the following sections. Full calculations are included in Appendix G.1.

(a) Shear studs

The static resistance design exercise shows that the shear studs connection requires 30no. 25mm diameter shear studs, with an embedment of 200mm to resist the ALS loads. The calculated ALS utilisation factors (design load / design resistance) for the relevant failure modes are shown in Figure 11.9, including:

- steel shear or tensile failure;
- localised concrete crushing at the stud root in shear loading, which in turn leads to greater bending stresses in the stud;
- pull-through of the individual fasteners under tensile loading, which is driven by crushing of the concrete under the stud head, and a tensile failure cone developing at the stud root;
- and global cone pull out failure of the bolt group, which is directly related to the tensile strength of the concrete.

This figure shows that the local individual failure modes are well within requirements, but the concrete strength alone is not sufficient to resist the global pull-out failure. This can however be mitigated through the use of reinforcement bars which take the tensile loads and tie the failure cone back into the overall structure.

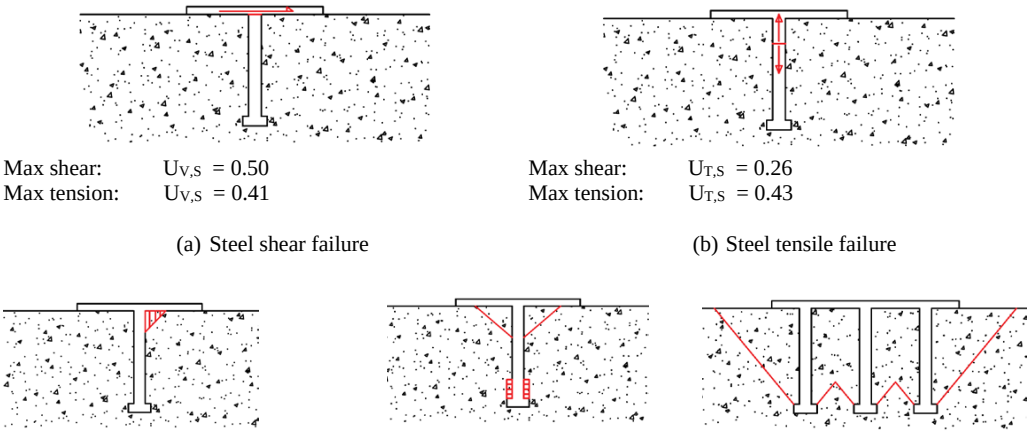

Figure 11.9: Shear stud failure modes

To verify the resistance to combined loads, the following equations also need to be satisfied (in accordance with BS EN 1992-4, table 7.3):

$$\left(\frac{N_{Ed}}{N_{Rd}}\right)^{1.5} + \left(\frac{V_{Ed}}{V_{Rd}}\right)^{1.5} < 1 \qquad \left(\frac{N_{Ed}}{N_{Rd}}\right) + \left(\frac{V_{Ed}}{V_{Rd}}\right) < 1.2 \qquad (11.5)$$

For the shear studs this gives: $U_{V,S}^{1.5} + U_{T,S}^{1.5} = 0.54$ and $U_{V,S} + U_{T,S} = 0.84$, therefore the connection has sufficient capacity at ALS.

(b) Composite dowel connection

The composite dowels design requires 3no. ribs, each with 3 no. dowels, with a dowel spacing of 250mm, and a rib thickness of 20mm to resist ALS loads. Utilisation factors for the relevant failure modes are shown in Figure 11.10, including:

- shear or tensile failure of the steel rib;
- double shear of the concrete dowel in shear loading;
- global cone pull out failure of the rib group;

The rib appears to perform better in terms of concrete shear resistance than the studs (with a utilisation factor of 0.34 compared to 0.50) but is more susceptible to global pull out failure, with a utilisation factor of 1.8 compared to 1.4 for the studs. While this failure mode can be mitigated through the use of supplementary rebar, is does indicate that as the connector is primarily designed to perform well in shear, it may not be the most appropriate to use in multi-axial loading conditions with significant tension loads.

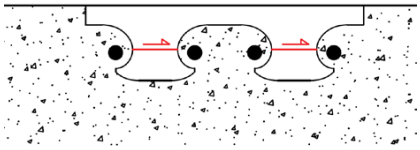

Max shear; $U_{T,S} = 0.83$
Max tension; $U_{T,S} = 0.67$

(a) Steel failure (shear)

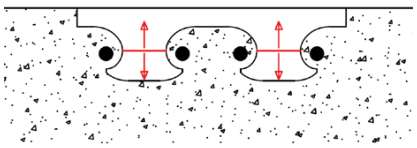

Max shear; $U_{T,S} = 0.19$
Max tension; $U_{T,S} = 0.30$

(b) Steel failure (tension)

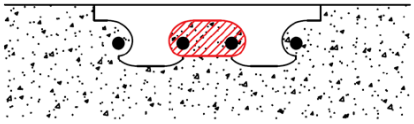

Max shear; $U_{V,CS} = 0.39$
Max tension; $U_{V,CS} = 0.31$

(a) Concrete dowel failure (shear)

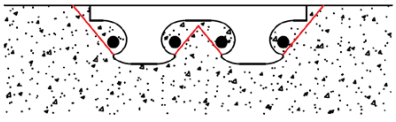

$U_{CF} = 1.8$; mitigated through use of supplementary reinforcement

(b) Global cone failure (tension)

Figure 11.10: Dowel connector failure modes

(c) Cast-in sockets

The cast-in socket design requires 20no. 25mm anchors, with an embedment of 300mm to resist ALS loads. The utilisation factors for the relevant failure modes are shown in 11.11 including: shear and tensile failure of the bolt fastener; localised crushing of the concrete, pull out failure of the fastener (tension); and global cone failure of the concrete.

In comparison with the shear studs connection, (where the failure is governed by the steel resistance to combined shear and tension), the failure of the cast in anchors is driven by the local concrete crushing at the anchor head, due to the higher shear load at each anchor (as fewer anchors overall are required).

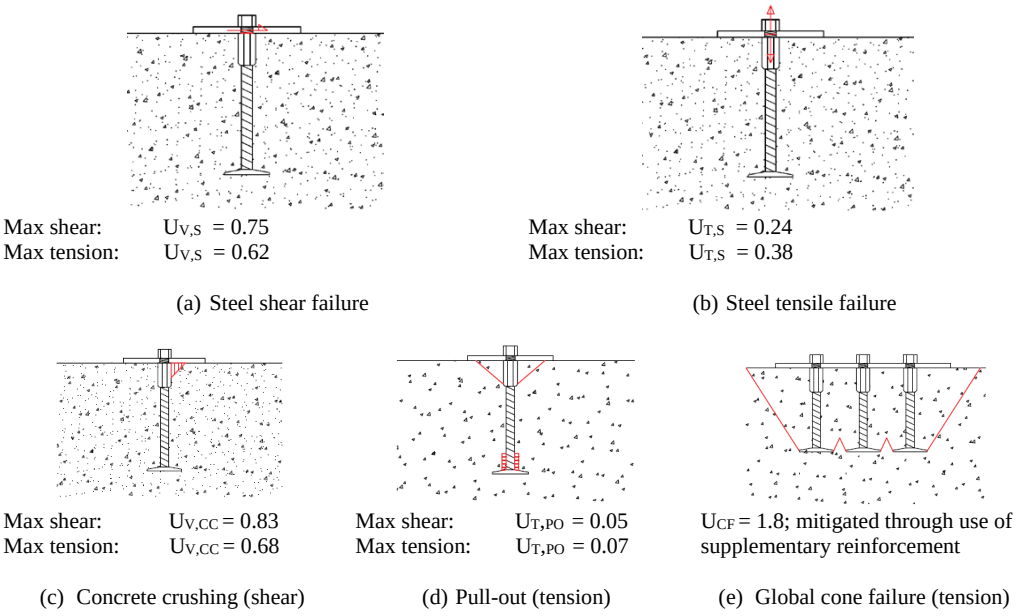

Figure 11.11: Cast in anchor failure modes

(d) Post-tensioned bar

The post-tensioned anchor design requires 12no. 32 bars, each designed to provide 330 kN of tension after allowing for a 30% pre-tension loss (resulting in 21 MPa prestress, applied over a 0.125 x 0.125 m plate). The design requirements for the anchors are slightly different to the other connections, as they are sized to provide the correct level of post-tensioning at SLS, so failure under ALS is not the design driver for the steel bars. However, there are two relevant failure modes at ALS, which are: bursting / splitting of the concrete under the anchor heads due to the prestress load; and global cone pull out failure of the anchor group, which is directly related to the tensile strength of the concrete.

The relevant failure modes are shown in Figure 11.12. Bursting and splitting loads occur with all post-tensioning systems due to the very large local stresses imposed from the anchor head - this is overcome through the use of spiral reinforcement around the anchor heads. This is the only connection of the three investigated where the concrete shear strength alone is enough to resist the global pull out loads - this is as the dimensions of the group of bars is greater than either for the studs or the ribs, and therefore the shear perimeter is greater. In addition, the transverse and link reinforcement will increase the concrete resistance to pull-out loads.

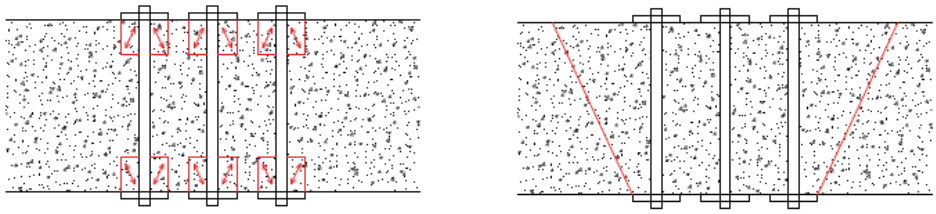

Mitigated through use of localised spiral rebar at anchor points

(a) Splitting / bursting failure under anchor heads, due to post-tension loads

$U_{T,PO}$ = 0.9 due to concrete shear strength alone. Further reduced through use of transverse and link rebar

(b) Global concrete pull-out

Figure 11.12: Post-tensioned bar failure modes

11.3.3 Fatigue life

Calculated fatigue damage for each of the connections is Table 11.4. The damage is based on a single year of operation; the table also gives the estimated design life in years (calculated as 1 / fatigue damage).

Table 11.4: Fatigue damage calculation for different options

Connection	Annual fatigue damage	Design life (yrs)
Shear stud	0.28	3.6
Composite dowel	0.02	43
Cast-in socket (no pre-load)	0.39	2.6
Cast-in socket (with pre-load)	<0.01	>100
Post-tensioned anchors	<0.01	>100

Calculations of the local stress RAOs for each of the connections, are shown in Appendix G.2.

11.3.4 Summary of design requirements

Table 11.5 summarises the connection requirements, including the required steel weight for resistance at ALS loads and the estimated fatigue life of the connection.

Table 11.5: Option design parameters

Option	Description	Steel weight	Fatigue life
Shear studs	30no. 25mm dia studs, 200mm embedment	88kg	3.6 yrs
Composite dowels	3no. ribs, 3no dowels, 250mm centres, 20mm thick plates	108kg	43yrs
Cast-in sockets, no preload	20 no. anchors, 300mm total embedment, 25mm diameter	95kg	2.6yrs
Cast-in sockets, with preload	As 3a, but with preloaded bolts	95kg	>100 yrs
Pre-tensioned bars	12 no. 32mm dia pre-tensioned Macalloy bars	158kg	>100 yrs

This shows that the design of the shear studs and the cast-in anchors with no pre-load is driven by fatigue loading, and therefore the specified steel weight would need to increase to improve the overall fatigue life. The composite dowel performs better than the shear studs in fatigue, with the pre-loaded options performing best overall.

11.3.5 Preliminary options discussion

As well as the behaviour under static and dynamic loads, other criteria that are important for the overall suitability of the connection include the corrosion potential, and ease of construction and maintainability. A discussion of the advantages and disadvantages of each option with regards to these criteria is included in table are shown in Table 11.6

Table 11.6: Connection advantages and disadvantage discussion

Sketch	Advantages	Disadvantages
Shear studs 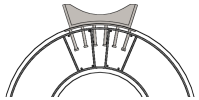	• Well known method of manufacture • Cheap and quick to install with access to correct machine	• Water ingress between plate and concrete could cause undetectable corrosion • Pathway for water ingress into the section; possibility of rebar corrosion • Cannot remove / replace any items if damage occurs.
Dowel 	• Improved fatigue detail	• Water ingress between plate and concrete could cause undetectable corrosion • Pathway for water ingress into the section; possibility of rebar corrosion • Cannot remove / replace any items if damage occurs
Cast-in sockets 	• Can remove and replace external steelwork • Possible to remove and replace fastening bolts	• Pathway for water ingress into the section; possibility of rebar corrosion • Potential corrosion issues with fastening bolts • Potential pre-loss in preloaded bolts
Tensioned anchors 	• Can remove and replace external steelwork • Easy to remove, inspect and replace steelwork • Sheathed bars could reduce ingress of water into conrete	• Potential loss of pre-tensioning • Need additional reinforcement to prevent rebar bursting • Through bolts give water path-way into structure; not an issue here but would be for water-tight connection

On the basis of the analysis carried out in this section, the options that will be considered in the more detailed analysis phase include:

1. Shear studs: while the shear studs are poor fatigue details, shear studs have historically been one of the most commonly used types of connections. Therefore they will be included for further analysis as a control case.
2. Composite dowels: These appear to perform well in terms of steel fatigue, and therefore will be included for further analysis, to look in more detail at the behaviour of the concrete.
3. Post-tensioned anchors: The preliminary analysis shows that post-tensioned connectors perform the best in fatigue. For the Albatern 12S configuration through section post-tensioned bars are better than pre-loaded bolts, as they are easier to replace, and are likely to be less of a corrosion risk. It is noted however that the Albatern connection does not need to be watertight, and therefore the fact that there is a pathway for sea water through the connection is not an issue. This could be more of a problem for other devices, where the connection does need to be watertight.

Further detailed analysis, particularly focussing on the behaviour of the concrete is discussed in the following section.

11.4 Results of detailed connection assessment

11.4.1 Behaviour under static loads

The behaviour of the connections under static load have been investigated with the use of 3D finite element models using Abaqus. Schematics of the models for the three connections are shown in Figure 11.13. Each model has been run under three different conditions, to compare single degree freedom shear and tension loading, with multi-axial loading:

1. Shear only: Single point load in the horizontal direction (model x direction) = 2.12 MN
2. Tension only: Single point load in the vertical direction (model y dirction) = 1.67 MN
3. Full connection load (ALS max tension condition): 3 DoF point load; x = 2.12 MN, y = 1.67 MN, z = 0.46 MN

For ease of modelling the curved wall has been neglected in the models, which is acceptable at this level of analysis as the purpose of the investigation is to provide a comparison between connections rather than develop a detailed design.

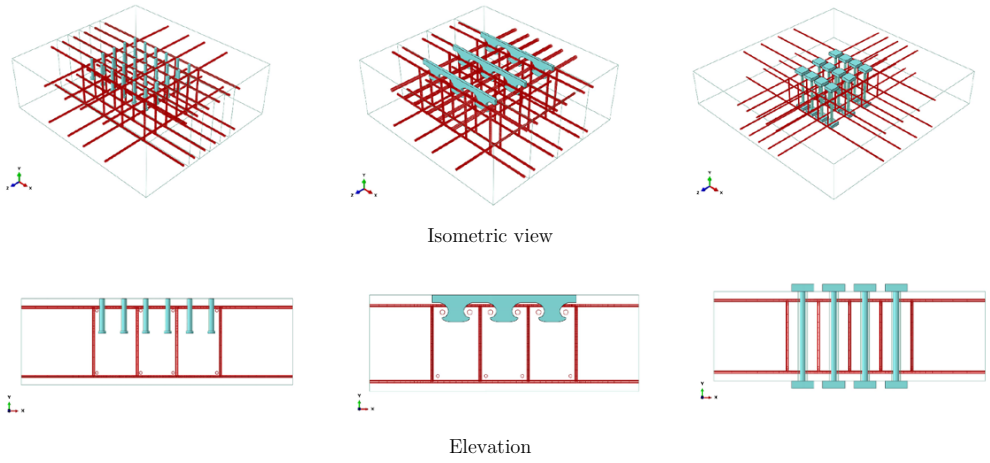

(a) Stud connection (b) Dowel connection (c) Anchor connection

Figure 11.13: Abaqus model schematics

(a) Shear studs

The FEA for the shear studs connection are shown in Figure 11.14, which shows the maximum principal stress for each load case (top figures) and the concrete tensile damage (bottom figure) through a section of the concrete. The top figures show that the maximum principal stress locations relate to the failure modes indicated by the hand calculations. The dominant failure mode in shear is localised crushing of the concrete at the stud root, which is indicated by the maximum compressive principal stress at the stud root. It is noted that stress (61MPa) is greater than the uniaxial compressive strength of the concrete (50MPa), due to the triaxial compressive stress states at this location, which increases the failure strength. The dominant failure mode in tension is pull out of the fastener, indicated by the maximum compressive stress under the shear head, and the zone of principal tensile stress at the stud roots. For the full load condition, the shear action appears more dominant, (as also shown in the hand calculations) with the maximum compressive stress at the stud root increasing from from 61MPa to 76MPa.

The bottom figures show the concrete tensile damage, which gives an indication of the potential crack locations. As RC is designed to crack in tension an individual crack does not automatically lead to global failure of the connection; however it does give an indication of the failure mode that may occur under increased load. Under shear load a transverse crack forms due to the tensile stress between the studs at the back row of the connection. Transverse reinforcement is therefore required to resist the shear loads at this location. There are also potential micro-crack locations in front of each of the studs due to local concrete crushing. Under tensile load there is only evidence of very localised damage occurring at each of the

stud heads. The combined loads result in more extensive damage, and the potential global cone failure location can clearly be seen at the rear of the stud group.

(b) Composite dowel connection

The FEA results for the concrete dowel are shown in Figure 11.15. Again, the top figures show the principal stress locations, which show that for both shear and tension loading the maximum compressive stresses occur within the concrete dowel, concentrated at the "heads" of the ribs. The maximum compressive stresses are greatly in excess of the uniaxial compressive strength (>100MPa in both shear and tension) due to the triaxial compressive stress state that occurs under the loading conditions. As the maximum stress occurs in the same location for both loadcases, the maximum compressive stress is significantly greater under full load conditions (275MPa compared to 120MPa due to shear alone).

Under shear loading, as was the case with the stud option, the damage plot shows the formation of a single crack running transversely across the connection, with more localised microcracks at the front contact point of the rib. Under tension load there is more extensive concrete damage under tension load than for the shear studs (as would be expected from the results of the hand calculations), with a possible initiation of a "splitting" crack (indicated by the transverse damage). It is noted that the stress results should be symmetrical, and the fact that this damage only occurs at one side indicates a potential inaccuracy in the model set up that would need to be investigated further for ongoing design work. However this does show that splitting failure should be considered when designing composite dowel sections under tensile load which is not currently encompassed in the design codes. The cracks do not indicate failure of the concrete as the stress can be carried by the reinforcement, however extensive concrete damage can lead to durability issues if large crack widths are allowed to form. The full load case shows more extensive damage than under shear or tension loading alone, and there is a clear initiation of the global cone failure at the back edge of the rib due to combined shear and tension loads.

(c) Post-tensioned anchor

The FEA results for the anchor connection are shown in Figure 11.16. As for the previous connections, the shear force results in a potential crack forming transversely across the connection at the back bars. Under tension load there is very minimal damage, with more extensive damage evident under the full load case, which shows the potential initiation of a cone pull-out failure occurring at the rear of the connection.

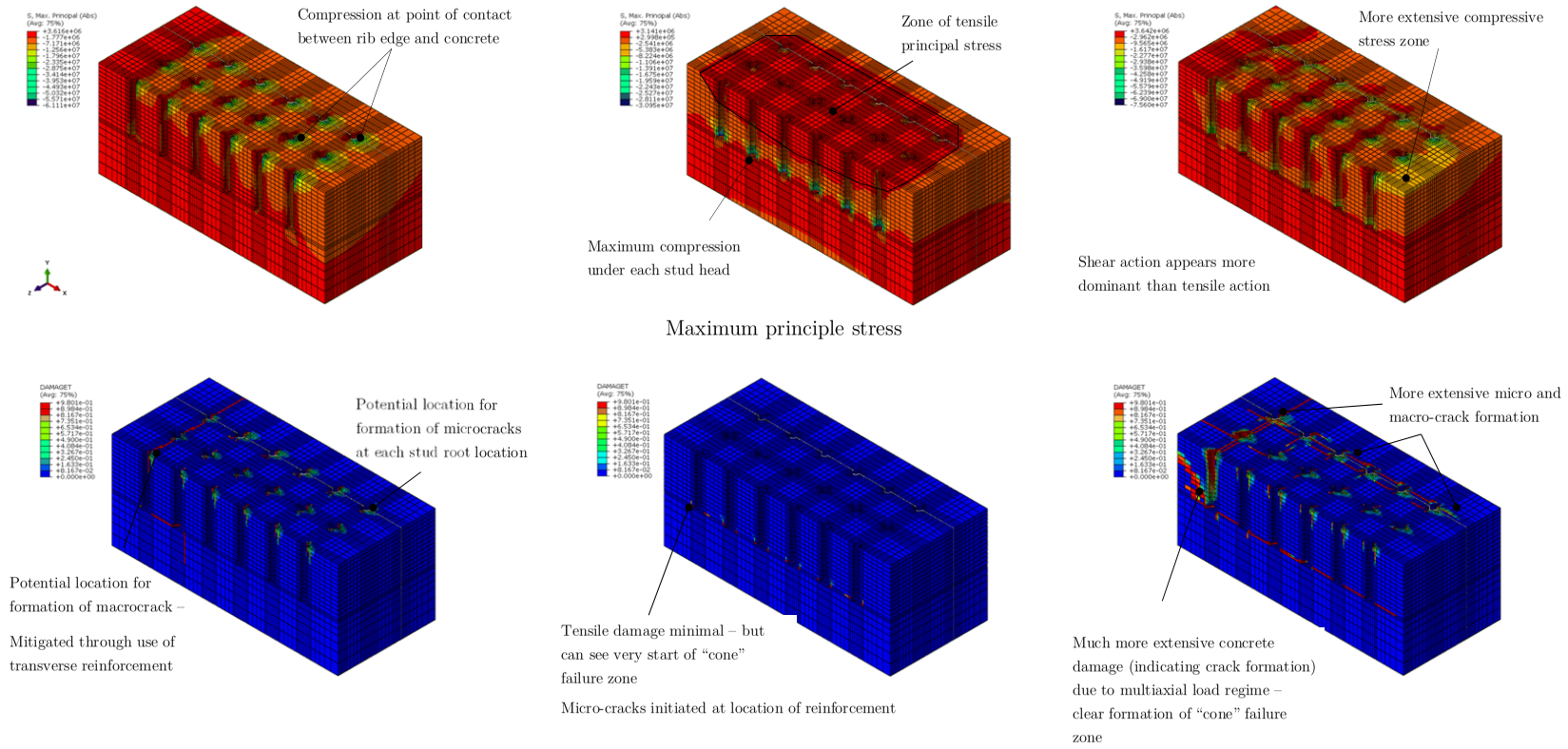

(a) Shear loading only (x direction)

(b) Tension loading only (y direction)

(c) Loading in 3 directions (x, y and z)

Figure 11.14: Finite element results - Stud static loads

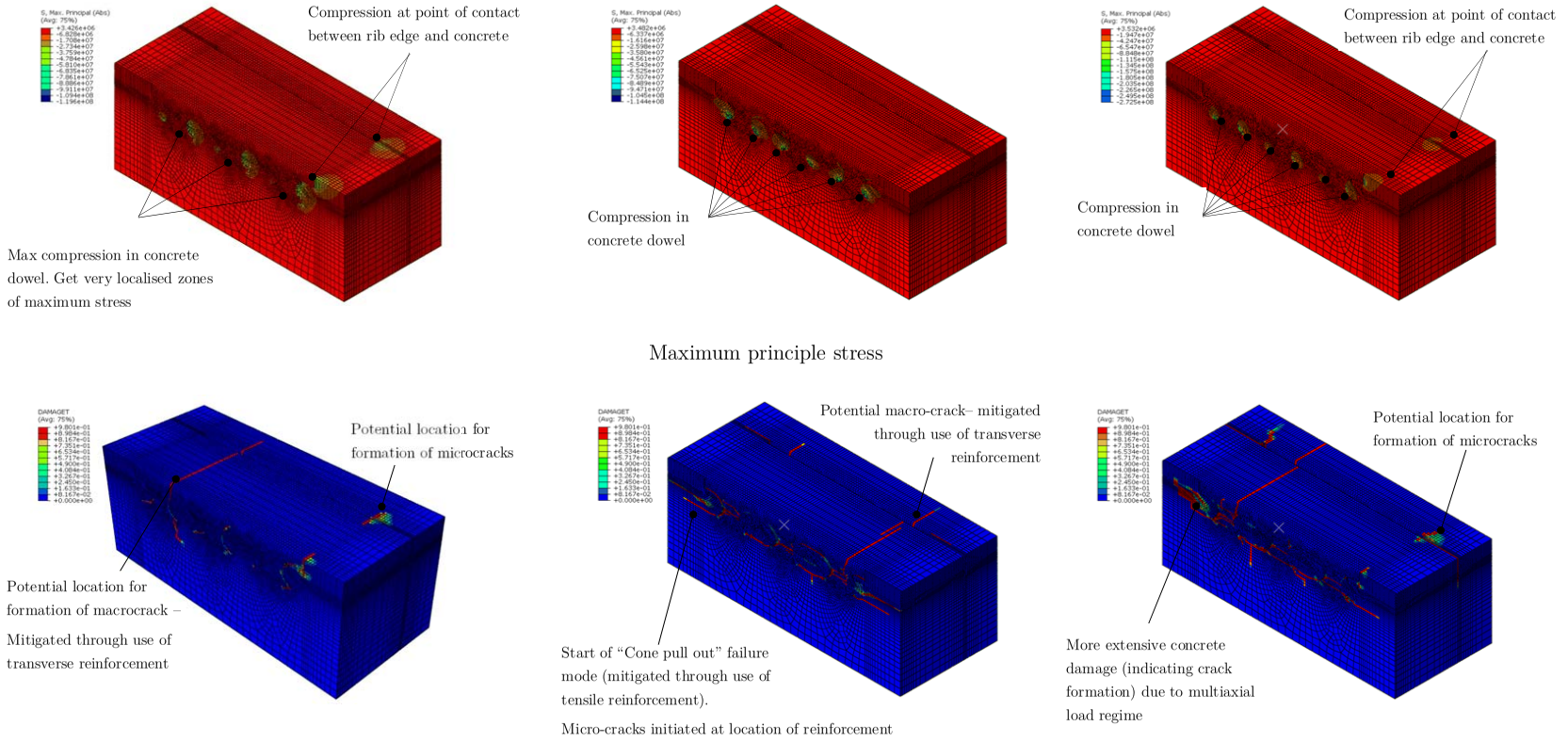

(a) Shear loading only (x direction)

(b) Tension loading only (y direction)

(c) Loading in 3 directions (x, y and z)

Figure 11.15: Finite element results - Dowel static loads

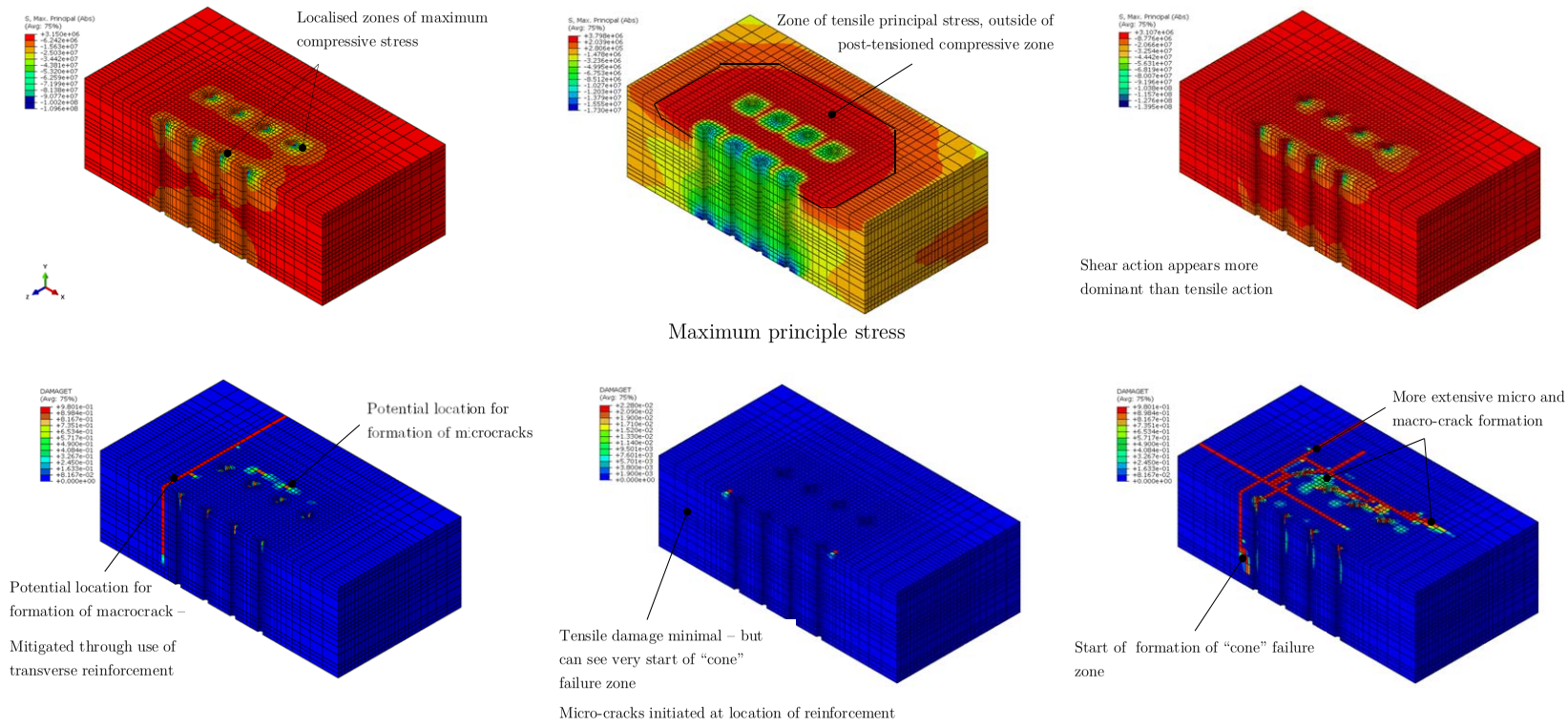

(a) Shear loading only (x direction)

(b) Tension loading only (y direction)

(c) Loading in 3 directions (x, y and z)

Figure 11.16: Finite element results - Post-tensioned bar static loads

(d) Summary of behaviour under static loads

To summarise, the results of the finite elements correspond well with the results of the hand calculations. The composite dowel option shows the potential for a splitting failure to occur under tensile loads, which is not covered by the current technical documentation. It is however noted that these connections are primarily designed to take shear loads, and therefore the design documentation has not been developed to deal with significant tension.

All connections show a certain level of concrete damage under the full ALS load condition (as would be expected); the table below shows the percentage of elements within the model where concrete tensile damage > 0.8:

Table 11.7: Percentage of concrete elements with tensile damage >0.8

Option	%
Shear studs	5.9
Dowel	9.6
Anchor	4.6

This table shows that the composite dowel connection develops the greatest level of damage under the ALS loadcase, with more than twice the level of damage as for the post-tensioned anchor which has the least extensive damage.

11.4.2 Fatigue

Following the investigation of the connections under static loads, the potential development of fatigue damage in the concrete has been calculated using the procedure set out in Section 11.2.2. Fatigue damage levels have been calculated based on the Palmgren-Miner summation for each element, including a correction to the S-N curve for concrete, based on the element triaxial stress state. It is noted that there are complex interactions between the steel and concrete is each of the connections which would need to be fully investigated in a detailed design situation, and that damage of an individual element, or even a wide range of elements does not necessarily indicate failure of the connection under fatigue loading. However, at a preliminary design level, this process provides a method for comparison between a range of details, which can indicate preferred options to take forward and investigate further.

(a) Shear studs

For the stud connection, the areas of investigation focus on the elements in front of the outer corner stud, (where the maximum compressive principal stress occurs), and the elements at the back face of the stud head, where there is evidence of tensile damage occurring in extreme loads. It can be seen from Figure 11.17 that fatigue damage of the concrete elements is very localised to the elements at the very root of the stud where it makes initial contact with the concrete under shear load. In these elements tensile principal stresses occur which reduces the compressive strength of the concrete at the very location where the compressive principal stress is highest, leading to localised damage. There is very little evidence of damage occurring away from this location.

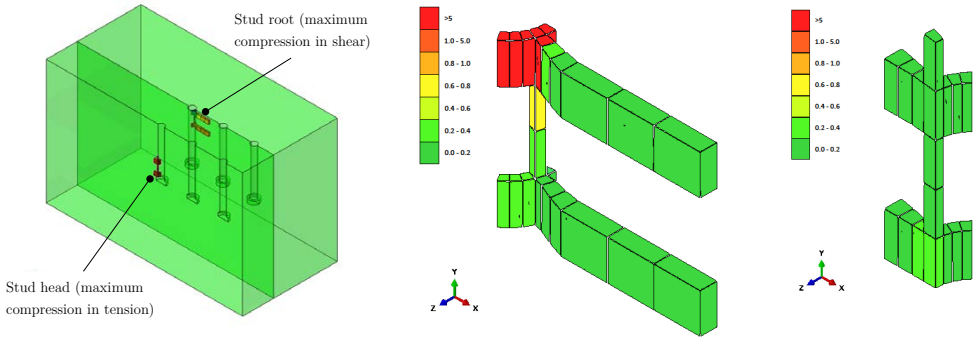

(a) Location of elements for fatigue calculations

(b) Damage levels in elements at stud root

(c) Damage levels in elements at stud head

Figure 11.17: Fatigue damage in the stud connection

(b) Composite dowel

For the composite dowel connection, the investigation has focussed on the elements within the concrete dowel itself. It can be see from Figure 11.18 that the fatigue damage of the concrete elements for this connection is much more widespread than for the stud, with damage occurring a significant distance across and through the dowel. The elements in the contact face show minimal damage, but this is where the maximum triaxial stress state occurs. Away from the point of direct contact the effective compressive strength decreases leading to increasing fatigue damage for decreasing principal stress.

While the extensive concrete damage may not necessarily lead to the ultimate failure of the connection, as noted in the literature review the damaged concrete dowel reduces the overall stiffness of the connection, and leads to increasing slip. When this occurs the assumption of a rigid, fully composite section is no longer valid, and this could lead to increasing stress levels and premature failure of the steel elements. In addition, as noted in the ULS section, damaged

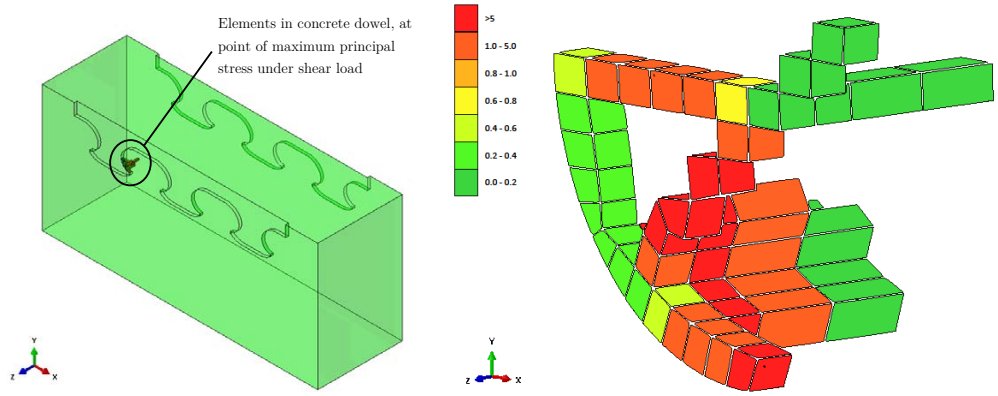

(a) Location of elements for fatigue calculations

(b) Damage levels in dowel elements

Figure 11.18: Fatigue damage in the composite dowel connection

concrete can lead to durability issues, if the formation of cracks increases the water penetration into the connection.

(c) Post-tensioned bar

For the anchor, the areas of investigation include the elements at the top of the bars, directly in front of the front bar which experiences the highest level of compressive stress in shear, and also elements at a 45 degree angle to one of the edge anchors, at a location where micro-cracks are shown to form under extreme loads. It can be seen from Figure 11.19 that this connection performs the best of the three configurations, with virtually non-existent damage, indicating that there are significant benefits to utilising post-tensioned connections.

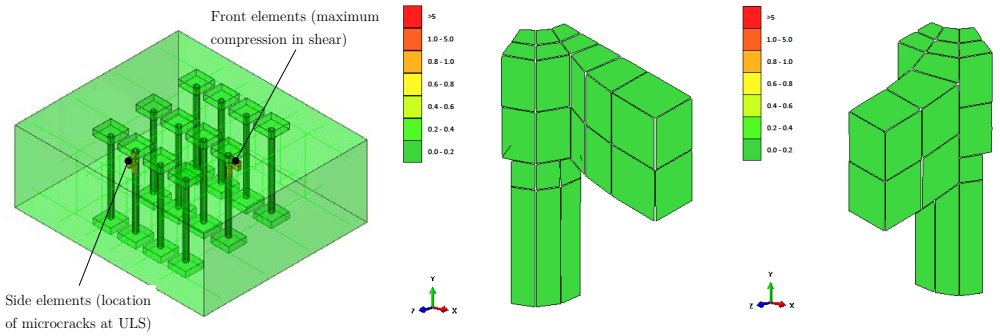

(a) Location of elements for fatigue calculations

(b) Damage levels in elements at stud root

(c) Damage levels in elements at stud head

Figure 11.19: Fatigue damage in the post-tensioned bar

11.5 Discussion and conclusions

11.5.1 Summary

To summarise, this chapter has investigated the application of a range of standard mechanical shear connections for use in the Albatern 12S WaveNET array to join the concrete Node structure to the steel articulated Joint Module. The aim of this work is to help make general recommendations as to suitable connection methods for floating WECs. The assessment has been carried out in two stages:

1. Preliminary assessment of the following connection options, calculating resistance to ALS and FLS loads, using hand calculation methods and linear elastic material properties:
   (a) Welded shear studs;
   (b) Composite dowel connectors;
   (c) Cast-in sockets with bolted fasteners (with pre-loaded and non-preloaded bolts);
   (d) Post-tensioned bars, through full depth of wall.
2. Further detailed investigation of sub-set of three connection options, using finite element models and non-linear material properties, to look in more detail at the behaviour of the different options, particularly with regards to the behaviour of the concrete. At this stage the following connections were assessed:
   (a) Welded shear studs;
   (b) Composite dowel connectors;
   (c) Post-tensioned bars, through the full wall thickness.

A brief discussion of the behaviour of each of the connection types is included in the following sections:

(a) Welded shear connectors

Welded shear studs are used extensively in a range of applications, including composite bridge construction, and in the offshore environment. The literature suggests that the detail performs poorly in fatigue due to the nature of the connection, which requires a certain amount of slip to occur before the full shear capacity is engaged. This is substantiated by the hand calculations, which show that the while the shear stud connection requires the least amount of steel work when only considering ALS loads, the option has a very short fatigue life.

While welded studs were primarily developed to resist shear loads, the head provides good resistance against uplift. Tensile and shear loads are resisted by different parts of the connection, which provides reasonable resistance against multi-axial loads. The finite element analysis shows that concrete damage under both static and fatigue loads is fairly localised, limited to locations immediately adjacent to the stud root, and under the head, which is

important in terms of the overall durability of the connection, as increase levels of damage allow a greater amount of water ingress, leading to potential for corrosion both of the shear studs and the internal rebar.

With regards to more qualitative assessment criteria, shear studs are commonly used, and are easy to use in the connection construction, providing there is access to an appropriate welding machine. However it is difficult to inspect, which could lead to undetected damage occurring (particularly corrosion if sea water gets in between the base plate and the concrete), and it is very difficult to remove and replace components if damage does occur.

(b) Composite dowel connectors

Composite dowel connectors, consisting of profiled steel ribs, which interact with the concrete under load, have been developed in recent years to overcome the fatigue issues with shear studs in composite bridge construction. While there is an infinite number of geometric possibilities for the profiled rib, a significant amount of research shows that a clothoidal profile performs well in fatigue, and this shape is encompassed in the recently published German National Approval (see Feldmann et al., 2016) covering the design of such connections.

The reported fatigue performance of the steel component in shear is validated by the hand calculations, which show a significant improvement in fatigue life of the steel compared to the shear studs. However the finite element analysis shows more extensive concrete damage under both static and dynamic loads. While this alone does not indicate connection failure, it can lead to greater levels of water ingress, and lower overall durability, and also results in a reduction in connection stiffness and increase in slip.

This connector was developed primarily to take shear loads, and these investigations show that they may not be the most suitable connection type to resist tensile or multi-axial loads. The tensile anchor resistance is less than for shear studs, and the greatest principal compressive stress occurs at the same point within the dowel under both shear and tensile loads. It is noted however that adopting a different steel profile could improve this behaviour - for example the earliest versions of perfobond connectors simply consisted of a circular opening within the steel rib, allowing for the full composite dowel to be developed from loading in both tensile and shear directions. However this does complicate construction, as it is more difficult to place the required reinforcement.

In terms of inspection, replacement and corrosion concerns, these are very similar to the issues for shear studs, as again it would be difficult to detect damage, or remove and replace components if necessary.

(c) Cast-in sockets with bolt fasteners

A variety of cast-in sockets and headed anchors are available from different manufacturers (e.g. Halfen and Hilti) for use in civil engineering applications and infrastructure, developed specifically to resist multi-axial loads. The hand analysis shows that providing the fastening bolts are pre-loaded, the connections perform well in fatigue, having a significantly improved fatigue life than both studs and dowels. The option requires more steel to resist ALS loads than the shear studs, but less than the dowels.

In terms of inspection, replacement and corrosion, this configuration has advantages over the studs and dowels as it is possible to inspect the bolts for corrosion, and to remove and replace components if necessary. There is however still a possibility of increased risk of corrosion of the internal rebar, as the cast in sockets could provide a pathway for water ingress into the structure. There is also the potential for loss of pre-load in the bolts.

This option was not considered in the detailed analysis, as while it has advantages over the shear studs and dowel connectors, for the Albatern configuration, post-tensioned bars (discussed in the following section) were more suitable, and therefore cast-in sockets were not considered further due to time limitations for analysis work.

(d) Post-tensioned bars

Post-tensioned bars are commonly used in the wind industry (both on and offshore) to connect steel turbine towers to concrete foundations. There is therefore precedence for using this type of connection to resist multi-axial dynamic loads.

Post-tensioning is used to keep components in compression which is useful to limit crack formation in concrete, and to minimise the effect of fatigue loading. This is evident in the hand calculations where the steel components have a very long fatigue life and the finite element models which show the lowest amount of concrete tensile damage under ALS loading, and virtually non-existent concrete fatigue damage. The connection is the heaviest of the options, however this disadvantage is counteracted by the option benefits, which extend to issues surrounding inspection, and ongoing maintenance, as is it possible to inspect, remove and replace all components within the connection.

It is noted that having full length bars results in a water path through the thickness of the wall. This is not a problem for this configuration of the Albatern 12S device, but could be an issue for connections that need to remain watertight. In this situation alternative configurations would need to be considered, such as embedding one end of the bar within the concrete, or reconsidering options such as the cast in sockets and bolts.

11.5.2 Conclusions

The main conclusions that can be drawn from this work are as follows:

- The option with post-tensioned bars appears to be the most suitable for floating WECs where the design requirements are to transfer dynamic multi-axial loads across critical joints. This connection performs well under both static and dynamic loads, shows the least amount of concrete damage, and has advantages in terms of ongoing maintenance, as it is possible to inspect, replace and repair all components within the connection.
- Where connections are required to be watertight, it may not be appropriate to use bars through the full wall section, and therefore further consideration could be given to cast-in sockets with pre-loaded bolts, or other such details where the connection remains in compression under serviceability loads.
- The steel components of welded shear studs do not perform well in fatigue, and therefore are not appropriate to use for critical connections with a high level of dynamic loads. However, they do appear to perform well under multi-axial loads, and therefore there could be used in locations that are less critical to the overall performance of the device.
- While research into composite dowels shows that they have many benefits for applications where the primary load is in shear they do not appear to be suitable for use under multi-axial loading conditions, and there appears to be significant degradation of the concrete within the dowel when subject to fatigue loads. Therefore it is not considered that these types of connections are suitable in this application.

11.5.3 Wider applications of the work

While the work carried out in this chapter uses the Albatern 12S array as a case study, the issues raised are common across the wave energy industry. As an example, early work carried out as part of this research project investigated potential connection options for the Pelamis devices for joining concrete structural long tubes to the steel PTO modules, as shown in the Figure 11.20.

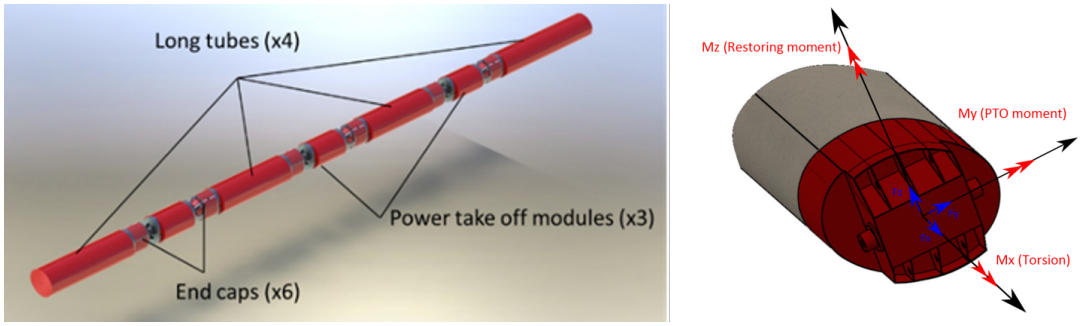

Figure 11.20: Pelamis connection schematics

While the physical scale and overall configuration of the Pelamis attenuator is very different to the Albatern array, the high level analysis work carried out at Pelamis highlighted very similar issues for the connection - namely the need to be able to transfer multi-axial, dynamic loads across a critical joint. Findings from this work could therefore be applied to Pelamis if further development was to occur, with a focus on the use of post-tensioned connections.

PART IV

Final remarks

Chapter 12

Concluding remarks

This thesis has focussed on the conceptual design of floating wave energy converters, and explored the potential for use of conventional and advanced concrete materials. The aim of this work is to take steps towards a reduction in LCoE by considering structural design and material selection aspects at an early stage in the development process. The objectives of this research were as follows:

1. To assess the trade off between power production and structural loading at an early stage in the design process, using LCoE as an assessment metric;
2. To determine best practice methods for using physical and numerical model output for preliminary structural design, with particular emphasis on fatigue loading;
3. To investigate the use of reinforced concrete as a low cost material for wave energy converters, highlighting potential issues with the material, and reducing associated risks and uncertainties;
4. To advance the knowledge of dynamic connections between concrete and steel components, which are often critical to the overall function of a floating WEC.

To fulfil these objectives, assessment methods for concept design have been developed, taking into account ultimate and fatigue loading alongside power production. In the option selection phase, decision matrix tools have been employed to select preferred concepts, including structural utilisation and power generation as assessment criteria. This theme has been extended for the preferred option, where the trade off between power production (a revenue generator) and structural loading (which heavily influences costs) has been explored to determine the optimum PTO torque limit, resulting in minimum LCoE.

Analysis of the results of numerical and physical model tests has given insights into the modelling process for complex multi-body arrays, and provided load cases for use in ongoing design work. This design work focusses on the potential for using conventional and advanced reinforced concrete mixes, and the behaviour of dynamic connections between concrete and steel components.

This chapter brings together the key results of the thesis, to highlight how the work has met the objectives and overall thesis aim. The structure of this chapter is as follows:

- A discussion of the outcomes of the work in relation to the aims and objectives is presented in **Section 12.1.**
- High level, key conclusions are included in **Section 12.2**.
- Potential for further work which could expand on the research carried out in this thesis is discussed in **Section 12.3.**

12.1 Discussion of research outcomes in relation to objectives

12.1.1 Trade off between power production and structural loading

Early WEC development often focusses on overall power generation capabilities, with little consideration given to structural loading until further into the development process, when it is more difficult to make design changes. In this thesis, assessment methods have been developed to take account of the influence of structural loads right from the outset, which highlight the importance of considering these factors at an early stage.

For example, in the options selection process, the Decision Matrix in Table 5.7 (in Chapter 5 on page 78) shows that Option B1, with a single axis PTO with high stiffness around the yaw axis, performs the best of all the 1^{st} stage assessment options in terms of power performance. However this option generated the highest structural loads, and therefore was not taken further in the assessment process. If structural loads had not been considered at this stage, then B1 would have been selected as the preferred option to take forward; the issues with high structural loads would then have been discovered later, when it would have been much more difficult to make design changes. This would most likely have increased the overall costs, and the resulting LCoE.

The influence of structural loads on overall costs is also highlighted by the PTO torque selection process (in Chapter 7), which shows that a 4% increase in Annual Energy Production (AEP) results in a 20% increase in structural costs; these factors together result in a increase in LCoE of approaching 8%, when comparing a torque limit of 2.5MNm to the optimum torque limit of 1MNm (see Figure 7.7 on page 131). This results shows that taking structural design issues and resulting costs is vital when making development decisions, as they have a significant impact on the final LCoE.

12.1.2 Outcomes from analysis of physical and numerical model results

Work in this thesis has been carried out with the aid of results from physical and numerical models, therefore a significant amount of research effort was applied to analyse and compare the model outputs to determine the most appropriate design loads.

The Albatern WaveNET array is a complex system, with multiple interacting bodies, and multi-degree of freedom articulations. While analysis of the model results does not have a direct impact on the LCoE reduction, it does provide insight into the challenges associated with modelling such systems. This has an indirect impact on LCoE, as determining accurate structural loads from physical and numerical models is an important factor when it comes to designing reliable and economic structures.

The analysis work discussed in Chapter 6 had three main aims:

1. To gain a deeper understanding of the numerical modelling process, and overall array behaviour;
2. To determine appropriate loads for preliminary design work;
3. To make judgements about the most suitable methods for fatigue analysis.

With regards to the first aim; results from both models show the same trends, giving confidence that the numerical model provides a reasonable representation of the physical array behaviour. The results increasingly diverge as the number of bodies at a particular articulation increase. This indicates that the array behaviour becomes more complex due to the multi-body interactions, and this effect is not fully captured by the simplified numerical model. Therefore, while the numerical model is appropriate for determining loads for preliminary design, further development and validation work would be required to give confidence in results to be used for detailed design.

For the second aim; the numerical model deals with non-linear viscous damping effects through the use of a linear damping term. This leads to an under-prediction of peak loads during the more frequent smaller sea states and an over-prediction in larger waves. Therefore, while it is appropriate to use the numerical model to determine load cases associated with more extreme events, care needs to be taken when using the results for fatigue loading. Analysis work shows that an additional factor of 1.35 should be applied to fatigue damage calculated in the time domain using the numerical model results, to account for the differences in the two models.

In relation to the third aim; investigation of the fatigue analysis process showed that spectral fatigue methods based on the Dirlik probability density function (pdf) over-predict fatigue damage compared to time domain methods, with the difference increasing as the number of interacting bodies increased. The Dirlik pdf assumes that the load spectrum has a Gaussian distribution, which generally occurs in a system with a linear structural response. However, time history analysis shows that the correlation with a Gaussian distribution decreases as the

number of interacting bodies increases, indicating an increasing level of non-linearity, leading to an over-prediction of fatigue damage when using standard spectral methods. This is an important result, particularly for dynamic floating wave energy converters, where fatigue is often the main design driver. Spectral fatigue methods are often more appropriate to use than time domain methods, however, over-prediction of fatigue damage can lead to over-conservative, and un-economic structural designs.

In addition, the fatigue analysis showed that damage decreases with an increasing number of interacting bodies. Articulations at central nodes have very limited fatigue damage (although also produce very little power), with the articulation at the singler node exhibiting the highest level of damage. The most interesting result showed that the articulations at doubler nodes contributed the highest proportion of array power, but exhibit a lower fatigue damage than the singler node. While the analysis is limited by the small number of articulations under consideration, this is a result that would be worth exploring further, as it appears that the addition of the additional link at the doubler node improves fatigue behaviour without compromising on power output. This would be of particular interest to Albatern when considering optimal configurations for larger arrays.

12.1.3 Use of reinforced concrete as a lower cost material

Reinforced concrete (RC) has a proven history of use in the offshore environment, predominantly in the oil and gas industry. However, to date the material has not been successfully utilised for a floating wave energy converter.

The techno-economic study in Chapter 9 showed that there are many benefits to using concrete, as it offers good strength and stiffness parameters at a low unit cost. The preliminary design exercise for the 12S Node structure showed that an RC option is 60% of the cost of an equivalent steel design. In addition, concrete has additional benefits over steel, including inherent corrosion resistance, and good fatigue properties, which lead to further cost benefits in terms of reduction in ongoing maintenance requirements. While these benefits have not been explicitly assessed they would contribute to even greater LCoE reductions.

However, there are a number of disadvantages of concrete; namely that it is heavy, therefore only suitable for large floating structures with sufficient buoyancy, and it is designed to crack under tensile loads, which can lead to durability issues, and a reduction in watertightness.

In order to overcome these issues, the potential for advanced fibre reinforced materials was investigated, looking at ultra high performance fibre reinforced concrete (UHPFRC) to reduce internal reinforcement requirements and overall section thickness, and strain hardening cementitious composites (SHCC), to ensure the watertightness of the structure and eliminate the need for post-tensioning.

In addition, carbon fibre wraps were considered as a method of reducing the internal reinforcement requirements, however the high-cost of such material means that the benefits of this are limited to very localised strengthening applications.

The benefits of fibre reinforced concrete materials (FRC) were assessed by comparing design details and costs against more conventional materials, including standard reinforced concrete (RC), and also steel and Glass Fibre Reinforced Plastic (GFRP) for situations where RC could not be used due to buoyancy restrictions, such as for the smaller scale 6S Node.

Cost estimates for the different options showed that where a conventional reinforced concrete solution is possible, this is likely to be the cheapest option. For the 12S Node, the SHCC option was 3% greater than the cost of the baseline RC option. For the option where UHPFRC was used throughout the node, the cost increased further, being 80% greater than the RC baseline.

However the cost estimates are very sensitive to the underlying assumptions. For example the optimistic estimate for the SHCC option is only 62% of the baseline RC option, indicating that this material could offer an economic solution with further mix design, structural optimisation and investigation of the manufacturing process. The potential benefit of SHCC is enhanced even further when scale effects are taken into account, and conventional RC is not an option; for example for the 6S Node the SHCC option is only 36% of the cost of the equivalent steel design, and only 50% of the cost of the GFRP option.

Therefore, this study concludes where a conventional reinforced concrete solution is possible, this is likely to be cheaper than using more advanced materials. However, in situations with exceptional design constraints which push the limits of conventional concrete design, FRC materials can offer significant economic as well as technical benefits, particularly when compared to other materials such as steel or GFRP. The cost of FRC materials increases with increasing fibre volume and base concrete compressive strength. Therefore, they offer the greatest cost benefit in situations with low tensile stress, where lower fibre volumes can be used to improve the post-cracking behaviour and permeability, without needing a significant improvement in tensile strength.

Overall, the work carried out in this thesis show that both conventional and advanced concrete materials offer potential benefits for wave energy converters, and could help towards the overall aim of reducing LCoE.

12.1.4 Behaviour of dynamic concrete-steel connections

An additional area of uncertainty with the use of concrete structural sections in wave energy converters, is how best to connect them to more dynamic mechanical steel components. These connections need to resist highly dynamic loads about multiple axis, and are often critical to the function of the device. For example, in the WaveNET array, the connection between the concrete Node, and the steel articulated joint module is the point of transfer for the PTO loads, and therefore failure of the connection would result in reduced power production.

A literature review of standard steel-concrete connection types indicated that cast-in mechanical connectors as being the most appropriate for use for dynamic floating WECs. Analysis work was then carried out on four well documented connection types, including welded shear studs, composite dowels with profiled steel ribs, cast-in anchors with bolted fasteners, and post-tensioned bars.

The analysis work highlighted that post-tensioned bars are the most suitable option for floating WECs where the design requirements are to transfer dynamic multi-axial loads across critical joints, as they perform well under both static and dynamic loads, show the least amount of concrete damage, and have advantages in terms of ongoing maintenance, as it is possible to inspect, replace and repair all components within the connection. However the disadvantage of this option is that the bars provide a path for water, which could be a problem for connections which need to remain watertight if the bars pass all the way through the section. In this situation, cast-in anchors with pre-loaded bolts may be a more suitable solution.

Shear studs have historically been shown to have poor fatigue resistance under dynamic loading which was shown to be true in this analysis. They are therefore not considered appropriate to use for critical connections with a high level of dynamic loads. However, they do appear to perform well under multi-axial loads, and therefore there could be used in locations that are less critical to the overall performance of the device.

Composite dowels using cast-in profiled steel ribs which interact with the concrete under shear loads have been developed to overcome some of the issues with shear studs in composite bridge construction - namely the poor fatigue resistance. While these benefits are proven under pure shear loading, it does not appear that they translate to dynamic multi-axial loads. The analysis in this thesis shows that they perform worse than the shear studs in this condition, with significant degradation of the concrete under fatigue loading. They are therefore not considered to be suitable for this application.

With reference to the overall thesis aim of reducing LCoE; while the choice of connection type does not have a significant impact on overall cost, being able to identify appropriate connection solutions facilitates the use of low cost reinforced concrete materials which does contribute to a lower overall LCoE.

12.2 Key conclusions

This thesis shows that taking account of structural design and material selection issues at an early point in development is essential, to ensure that the final design is robust, reliable, and ultimately achieves the lowest possible Levelised Cost of Energy. The conclusions of this work are as follows:

1. It is essential to consider the impact of both power production and structural loading when making conceptual design decisions, as concepts which generate the most power often result in the highest structural loads. This could lead to increased costs if not identified at an early stage.
2. It is not always the most economic solution to maximise power generation. The trade-off between power output and structural loading needs to be considered to identify the minimum value of LCoE.
3. Multi-body array systems behave in a very complex manner, which can be difficult to capture using simplified numerical modelling techniques. This is important when developing load cases and highlighting potential failure modes, as identifying appropriate design loads is a crucial step in developing a reliable and economic structure.
4. Structural non-linearities caused by multi-body interactions could mean that standard spectral fatigue analysis over-predict fatigue damage. This is likely due to the non-Gaussian structural reponse of the multi-body system, and is an important consideration for floating, dynamic wave energy converters where fatigue is the main design driver. Over-prediction of fatigue damage levels can lead to over-conservative, and un-economic structural designs.
5. There is significant potential for reducing costs through the use of reinforced concrete (RC) materials. For example, in the specific case of the Albatern 12S Node structure, an RC solution is 60% of the cost of an equivalent steel design.
6. For situations where design conditions push the limits of conventional RC materials, there is potential for using more advanced fibre reinforced concrete (FRC) materials. In particular, some FRC mixes can limit crack formation, increasing durability and permeability of structures with low tensile stresses, eliminating the need for post-tensioning.
7. FRC materials can also be used economically in situations where buoyancy limits prevent the use of heavier conventional RC. FRC eliminates the need for internal reinforcement, meaning thinner, lighter sections can be used. These materials are significantly cheaper than alternatives such as steel or GFRP. For example, for the 6S node the FRC solution is only 36% of the cost of the steel option, and 50% of the cost of the GFRP option.
8. The preferred solution for dynamic steel-concrete connections is the use of post-tensioned bars, as these perform well under static and dynamic loads, with minimal

concrete damage. They also have advantages in terms of ongoing maintenance, as it is possible to inspect, replace and repair all components within the connection.

It is noted that some of the analysis reported in this thesis is based on work done by others within the Albatern design team (as stated throughout the document). For clarity, conclusions 5 - 8 were derived entirely by the author, based solely on the author's own work. Conclusions 2 - 4 were derived entirely by the author, but building on numerical and physical modelling work carried out by others. Conclusion 1 was derived jointly with other members of the Albatern design team as part of the internal conceptual development process.

The work presented in this thesis has contributed to the knowledge in the industry, particularly with regards to appropriate fatigue analysis methods, potential benefits of conventional and advance concrete materials, and knowledge of the design of dynamic steel-concrete connections. These advances in knowledge could aid the decision making process for companies or developers looking to carrying out similar development work in the future.

This work has also contributed to academic knowledge through the publication of four conference papers (reproduced in Appendix A), three as a lead author, and one as a contributing author.

12.3 Further work

The research carried out in this thesis has highlighted a number of avenues for further work that would build on the conclusions made here. These are discussed further below.

12.3.1 Fatigue analysis

The fatigue analysis and comparison work in Chapter 6 revealed a number of interesting results that would be worth investigating further. In particular, work could focus on determining best practice methods for carrying out spectral fatigue analysis for complex arrays with interacting bodies, with non-linear structural responses. This research suggests that the standard methods which assume a Gaussian response over-predict fatigue damage, which could result in un-economic designs.

In addition, it would be worth investigating the impact of increasing the number of connected bodies on fatigue damage and power production, in particular for the 12S WaveNET array, as high-level analysis seems to suggest that Nodes with two link arms attached results in higher power output, but lower fatigue damage than Nodes with one link arm attached. While this result may be specific to the Albatern array, there may be wider implications for other device developers looking to exploit responses from multiple bodies.

12.3.2 Advanced concrete materials

The design work for the fibre reinforced concretes detailed in Chapter 10 have been based on assumptions regarding the mechanical properties of UHPFRC and SHCC concrete mixes. Extensive testing would be required to determine the exact properties of different mixes. Of particular interest would be the permeability of cracked SHCC under cyclic loads, as this could offer the most benefits for watertight floating wave energy devices with low tensile stresses.

In addition, research carried out elsewhere highlights the potential for 3D printed concrete to significantly decrease manufacturing costs of FRC, due to the elimination of the need for external formwork, and the ability to automate the casting process for volume manufacture. This is an area that is worth exploring further, as this could further enhance the economic benefits of FRC that have been highlighted in this thesis.

12.3.3 Steel-concrete connections

The analysis carried out in Chapter 11 has been based on finite element calculations, using conventional reinforced concrete. To take this work further it would beneficial to extend the FEA analysis to explicitly include dynamic loads, and carry out physical testing on connections under multi-axial and dynamic loads in order to validate the models. It would also be interesting to investigate whether using the advance fibre-reinforced concrete mixes considered in Chapter 10 would offer any potential benefits, particularly in regards to minimising concrete damage and crack formation under cyclic loads.

It is also noted that the analysis has been limited to commonly used, cast-in mechanical anchors; however as noted in the literature review there are a multitude of different connection options available, with novel options constantly being developed. It is possible that the scope of this review has overlooked potentially advantageous solutions that warrant further investigation. There is therefore a great deal of further research that could be carried out on this topic.

Appendix A

Publications

The following conference papers have been published as part of this thesis:

Title	Conference	Comment
Use of concrete as a primary construction material for the Pelamis wave energy converter	RENEW2014: 1st International Conference on Renewable Energies Offshore, 24-6 November 2014, Lisbon, Portugal	Contributing author. Paper covers preliminary work carried out at Pelamis.
Steel-concrete connections for floating wave energy converters	CORE2016: International Conference on Offshore Renewable Energy, 12-14 September 2016, Glasgow, UK.	Lead author. Papers covers preliminary work on steel-concrete connections, carried out using an early Albatern 12S concept as a case-study
Optimising structural loading and power production for floating wave energy converters	EWTEC2017: 12th European Wave and Tidal Energy Conference, 28-31 August 2017, Cork, Ireland	Lead author. Paper covers investigation into trade-off between power and load, using tank test results
Advanced concrete materials for offshore floating structures	ICOE2018: International Conference on Ocean Energy, 12-14 June 2018, Cherbourg, France.	Lead author. Paper and poster covering work on advanced concrete materials.

Use of Concrete as the Primary Construction Material for the Pelamis Wave Energy Converter

N.Khosravi
University of Dundee, Dundee, Scotland

L.Barker
Industrial Doctorate Centre for Offshore Renewable Energy,, Edinburgh, Scotland

V.O'Donoghue
Pelamis Wave Power ltd., Edinburgh, Scotland

J.Benzie
Pelamis Wave Power ltd., Edinburgh, Scotland

M. Newlands
University of Dundee, Dundee, Scotland

R. Jones
University of Dundee, Dundee, Scotland

ABSTRACT: This paper describes the program of research aimed to investigate the best approach for using concrete as the primary material for Pelamis Wave Energy Converter (WEC). One of the most concentrated renewable energy sources is wave power; but using this valuable source of energy needs further development of technology, as well as cost effective and fast manufacturing processes with flexibility of design for ongoing changes and improvements. Previous feasibility studies have proven that concrete can be considered as one of the main options for achieving this goal however the main challenge in this regard will be ensuring the durability of the proposed concrete structure, irrespective of manufacturing method. This paper introduces the program of research for investigating the use of concrete as the primary material for Pelamis and presents preliminary results of the durability property tests for the concrete mix designs and adhesive joints.

1. INTRODUCTION

1.1 *Wave energy*

The production of renewable energy has become one of the most important political, economic, environmental and technical issues around the globe and especially Scotland. Renewable energy can be generated from various sources, such as wind, tidal, wave and solar, and there are significant programs of research and investment being carried out across the whole of the renewable energy sector. Wave energy is currently one of the least developed of the offshore renewable technologies, but has significant potential if a cost effective method for exploiting the resource can be developed. Some of the benefits of wave energy can be described as follows:

- Environmentally friendly and clean
- High potential resource all across the globe in different countries.
- Highly predictable; it can be easily forecast one or two days in advance
- High demand in winter for electricity which can be balanced by higher wave energy in winter

1.2 *Pelamis Wave Energy Converter (WEC)*

The Pelamis wave energy converter (WEC) is a floating offshore device that converts ocean wave energy into electricity. It is a semi-submerged, articulated structure composed of multiple cylindrical sections linked by hinged joints. Motion of the hinged joints is restrained by hydraulic cylinders that pump fluid into high-pressure accumulators, which smooth out the irregular wave-by-wave absorbed energy.

Control of this pumping action allows the response of the device to be tuned to maximize absorption in small waves and minimize machine response in large storm conditions. All generation systems are housed within the machine, and power is transmitted to the shore using standard sub-sea cables and equipment.

The current P2 machine is a second generation design and is the result of over 13 years of development and operational experience. The machine consists of five tube sections linked by 4 universal joints. Each tube section has a diameter of 4m and an approximate length of 36m. The overall machine length is 180m and displaces approximately 1300 tonnes. The P2 machine is currently rated at 750kW and the target capacity factor is 25 – 40% depending on the chosen wave site. There are two P2 machines currently in operation at the European Marine Energy Centre (EMEC) in Orkney.

1.3 *Pelamis long term plans*

Reducing the cost of energy production is vitally important to enable Pelamis to complete with other renewable sources such as offshore wind energy. In order to become competitive there are several areas that Pelamis are developing:

1. Further design and optimization of device geometry and control methods to increase power capture capability.
2. Reduction in capital costs through use of alternative primary structural materials.
3. Development of structure and systems suitable for volume production to reduce costs through economies of scale.

1.4 *Preliminary studies on using concrete*

As mentioned above, one of the key areas of development for Pelamis is the investigation into the use of alternative structural materials. Currently the tubes are made of steel but initial studies carried out by Pelamis Wave Power (PWP) and some external third parties have highlighted the potential for using concrete as the primary structural material. Preliminary designs have predicted that changing from steel to concrete could result in around a 50% cost reduction for the main tube element, representing a10% reduction in total cost of producing each machine. Moreover, the next generation machine will have a greater power capture as it will be larger and makes use of a non-circular cross section. It is anticipated that this cross section will be easier to volume manufacture in concrete than in steel.

These factors will contribute to the reduction of capital costs for the machine, which will in turn help build a strong business case for the company and secure the long term growth of PWP within the renewable energy sector. However, the feasibility studies into the use of concrete have highlighted several areas in which further design and investigation are required in order to prove the potential of the material.

Over all, it can be summarized that Pelamis Wave Power Ltd wish to investigate concrete use for the following reasons:

1. Cost: Replacement of high-value steel fabrication with cheaper materials
2. Manufacturing: Faster production of sections for assembly.
3. Flexibility: Design of non-uniform section shapes and increase in machine scale (Pleamis Wave Power , 2003).

2. BRIEF HISTORY AND APPLICATION OF OFFSHORE CONCRETE STRUCTURES

Concrete offshore structures can be categorized into two main types:

1. Gravity based structures (GBS)
2. Floating structures

Within these major classifications there are various application and subdivisions; (Pérez Fernández & Lamas Pardo, 2013), for example ACI Committee 357 (2010) list the following examples of floating structures:

1. Ships and barges
2. Industrial plant ships
3. Floating piers and docks
4. Floating bridges
5. Immersed tunnels
6. Navigation structures

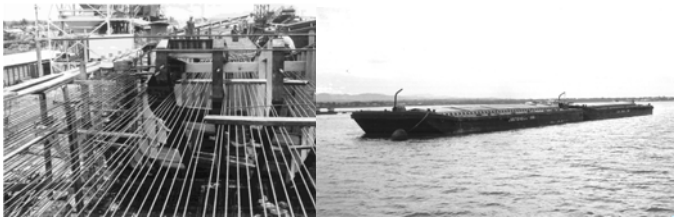

Figure 1. One of The world's first prestressed concrete barges launched in 1964 (Pérez Fernández & Lamas Pardo, 2013).

Historically, the use of concrete as structural material in the marine environment goes back to Roman and Greeks, but the first recorded floating reinforced concrete vessel was built by Lambot in 1848 .This boat was simply made by using sand-cement mortar on an iron mesh framework, and the remains of the vessels are now in a museum in France (Nawy, 2008).

The first self-propelled reinforced concrete vessel was M.S. Namsenfjord was built by N.K. Fougner in Norway in 1917. Following this, a shortage of steel during World War I and II resulted in continuing construction and development of concrete ships. For example, the U.S.A manufactured 12 reinforced concrete ships in 1918: these vessels were built with light-weight concrete using expanded clay and shale

aggregates, with a density of 1760kg/m^3 and 28 MPa strength. The vessels had a dead weight of up to 7500 tonnes. Construction of concrete vessels, barges and large floating dry docks continued throughout World War II with two further prestressed concrete ships being constructed during this period (ACI Committee 357, 2010).

The first concrete oil platform was installed in the Gulf of Mexico in 1950 and thousands of similar small concrete structures were subsequently constructed. However, construction of the gravity base structure named The Ekofisk tank in 1973 in the North Sea is considered a significant milestone in concrete offshore structure history, and this led to more than 40 such offshore structures being sited in the North Sea. Finally, one of the more recent large offshore concrete structures to be constructed was the Liquefied Natural Gas terminal (LNG) Adriatic. This was built in Algeciras in 2007, and was the world's first offshore gas terminal. (Pérez Fernández & Lamas Pardo, 2013)

3. ADVANTAGES OF CONCRETE TO STEEL FOR OFFSHORE STRUCTURES

As discussed in the previous section, the use of concrete in the marine environment has a long history, and the material is considered to have the following advantages:

- Concrete exhibits good corrosion properties especially when compared to steel, providing that the mix design and detailing takes into account the specific challenges of the marine environment. This eliminates the need for surface coatings, and reduces maintenance requirements over the life cycle of the structure.
- Concrete is a high rigidity material and is well suited to resisting hydrostatic and bending compression forces.
- The cost of concrete is less reliant on global markets compared to steel, as concrete can be easily produced locally and does not need to be imported. This also has the added benefit of producing local jobs.

Specific advantages for the Pelamis are as follows:

- The weight of the concrete reduces the need for ballast in the structure.
- Reinforced concrete is generally considered to have good fatigue properties which are important in a structure subject to dynamic loading such as the Pelamis.
- Cost reviews highlight that concrete tubes are likely to offer cost savings over steel, especially when looking at volume manufacture of intricate non-circular cross sections.

4. ASPECTS OF INVESTIGATION FOR A FLOATING MARINE CONCRETE STRUCTURES

Using concrete as primary material for PWP as a floating structure needs to bring together knowledge from a variety of different disciplines. The main aspects for investigation are discussed in the following paragraphs.

4.1 *Material and durability*

The mix design for offshore concrete has to be carefully considered. Marine concrete typically has a low water cement (W/C) ratio and high range water reducing admixtures are used to enhance workability. Supplementary cementitious materials such as fly ash, silica fume and ground-granulated blast-furnace slag (GGBS) are normally used to enhance durability and strength.

Both lightweight and normal weight aggregate have been known to be used for floating concrete structures. Lightweight aggregate can offer higher resistance to micro cracking, lower modulus of elasticity which leads to reduction of stress by shrinkage and creep, lower thermal conductivity and expansion and etc. However, there are not many precedents for high strength lightweight aggregate with high durability and it is more costly than normal aggregate. Therefore, as weight is not an issue for the Pelamis, for the preliminary studies, properties for normal aggregate will be assumed in design (ACI Committee 357, 2010).

Durability design should be based on standard specifications to prevent any degradation of the structural performance in harsh marine environment.

4.2 *Evaluation of loads*

Identification, definition and determination of the various loads which affect the floating structure in a marine environment are essential for design purposes. For each steel design, PWP conducts a thorough load evaluation, which is directly applicable to the design of the concrete machine. The load evaluation process determines the value of the live loads, accidental loads and environmental loads which are applied to the machine during the life of the structure. These loads include, amongst others, the hydrostatic, axial, moment, and torsional loads that the machine needs to resist. Further studies are required however to assess the construction loads, deformation loads and towing and installation loads for the specific concrete Pelamis machine.

4.3 *Design approaches*

The established design codes such as the DNV Offshore Codes will be used a starting point for identifying the appropriate design philosophy. These codes consider different limit states that are applicable over the service life of the structure such as:

- Ultimate limit state : related maximum load capacity of the structure
- Fatigue limit state : considering the effect of cyclic and repeated loading
- Accident limit state: relating to damage to components due to accidental events, or operational failure.
- Serviceability limit state: ensures acceptable performance of structure during normal use.

It should be noted that while the codes provide a starting point for design, they were primarily developed for the oil and gas industry and are applicable for structures which are subject to very different forces than the dynamic Pelamis machine. Therefore there may be areas in the design where it is appropriate to deviate from the current code specifications. The formulation of a robust design basis will therefore form one of the areas of investigation for the project.

4.4 *Construction*

There are many different construction methods used for offshore concrete structures. The most common approach is the use of post-tensioned precast segmental construction similar to the method used for constructing large bridges; but there are alternative methods such as slip or jump forming, where the structure is cast as a continuous member. These types of construction method reduce the amount of joints throughout the structure which can be beneficial, as it is the joints which tend to be the point of weakness. These different precast construction methods may be accompanied by some cast insitu components. For example, Figure 2 shows the precast construction for the internal hull of N'Kossa FPSO - Liquid Petroleum Gas (LPG), where the exterior walls were all cast in place.

As well as conventional mixes and designs, steel fibre concrete mixes are sometimes used to reduce the tensile cracking, and self-consolidating concrete (SCC) also has potential when there is congested steel reinforcement. (Gerwick, 1999)

4.5 *Towing and installation*

Stability, maneuverability and strength of the machine during towing will need to be evaluated as part of the design process, and a suitable technique which will ensure the safe and economical movement of the Pelamis will be developed. The tow route, water depth and environmental and weather conditions are the most important factors to consider in this regard.

Figure 2. The curved bottom of the vessel for LPG by match cast segmental construction (Gerwick, 1999).

4.6 *Maintenance*

Surveys, periodic inspections and proper installation of sensors are required to ensure the performance of structure during its service life. Causes of deterioration should be identified in order to plan for assessment of the amount and possible location of the damage. Finally a plan for repair approach following the inspection will be required.

5. PELAMIS CONCRETE PROJECT FORMATION

A Knowledge Transfer Partnership (KTP) has been formed between the University of Dundee and PWP in order to undertake the investigation into the application of concrete design and construction techniques for the Pelamis. KTP is a UK-wide programme with the aim of transferring the knowledge, technology and skills from the UK knowledge base to businesses in order to improve productivity and competitiveness of the company. (Knowledge Transfer Partnership, 2014).

There are two principle players within the partnership:

- Company partner: Pelamis Wave Power ltd which needs to identify innovative ideas and investigate the challenges for using concrete as a structural material.
- Knowledge-based partner : the Concrete Technology Unit (CTU) at the University of Dundee, which was established in 1989 and provides knowledge and expertise in cement science, concrete mix design, performance testing, long term durability, condition monitoring, construction methods and environmental aspects of concrete materials and construction.

Within the KTP there are two graduate associates who have been employed specifically for the project. These associates transfer knowledge between the company and the knowledge-base partner and work towards finding the solution for areas that company is seeking.

Outside of the KPT, PWP is also an industrial partner of the Industrial Doctoral Center for Offshore Renewable Energy (IDCORE). As part of this partnership, there is a Research Engineer working on the project as part of an engineering doctoral programme. The IDCORE Engineering Doctorate programme brings together expertise from the Universities of Edinburgh, Strathclyde and Exeter.

6. DETAILED AREAS OF INVESTIGATION

As mentioned above, there are three main employees from different partnerships investigating different aspects of the project as follows:

6.1 *Material and durability*

Helland, Aarstein, and Maage (2010) explain that the North Sea environment is considered as a harsh climate due to the following: 35 g/l salinity, surface temperature of 5-17ºC; wave heights of 25-30m and wind velocity in excess of 45m/s. Mehta (2002) categorizes deterioration factors in the marine environment firstly as physical deterioration such as cracking due to cyclic loading, and surface wear due to abrasion and secondly as chemical deterioration such as exchange reactions between aggressive fluid and components of hardened concrete. For durability design, mutual interdependence and the synergetic effects of these factors should be considered.

All of the potential deterioration parameters should be checked in the context of the specific conditions of the North Sea, but most durability studies focus on chloride induced corrosion as the main cause of damage. Ahn and Reddy (2001) claim that corrosion of reinforcing steel should be considered as the most important parameter in assessing durability of concrete because corrosion causes expansion, cracking and spalling of cover along with structural failure due to loss of bond between concrete and steel. Zhao, Ren, Dai, and Jin (2011) also note that tensile stresses are gradually produced by expansive corrosion products. Once the tensile stress is greater than the concrete tensile capacity, cracks at concrete surface initiate and propagate. These cracks can provide a suitable path for ingress of more chloride and other harmful agents. Therefore concrete cracking is usually considered as the serviceability limit for design.

Considering the importance of chloride movement through concrete and especially joints in segmental construction, the preliminary testing program is designed to evaluate the chloride diffusion coefficient in the proposed mix design and through the epoxy jointed construction. The following section describes the chosen mix design, and some of the durability tests that will be, and have already been carried out.

6.1.1.Proposed mix design

It is proven that supplementary cementitious materials positively affect the durability of concrete because they improve the microstructure of the cement matrix and decrease the porosity of the cement paste. When Portland cement reacts with water it forms Calcium Hydroxide Crystals (CSH) which are surrounded by large pores. If an additive such as GGBS is added to the concrete mix, reactions take place between the cement additive and the calcium hydroxide and leads to production of more CSH gel. This gel allows for a denser packing within the matrix, and fills the large pores, therefore decreasing the porosity, permeability and sorptivity of the concrete (The Concrete Society, 2011). Moreover the effect of the cement type influences the chloride binding effect due to the varying quantities of C_3A available. It is known that fly ash (FA), Mata Kaolin (MK) and GGBS have a naturally high C_3A content and therefore results in a lower diffusion coefficient due to their chloride binding capacity(Dhir & Jones, 1999). Considering the advantages of cement additions, availability and cost effectiveness of normal aggregate and precedents of using GGBS in offshore concrete structures, the mix design in Table 1 was suggested for initial studies. All the laboratory mixing is conducted based on BS 1881: Part 125: 1983.

Table 1. Initial proposed mix design for PWP

	Mix design (kg/m^3)
Water	170
Portland cement	225
GGBS	225
Sand	680
Course Aggregate	1090
Superplasticiser	0.4 % of cementitious material
Total	2390

6.1.2.Immersion test CEN TS-12390-11:2010

This test is used to find the unidirectional non-steady state chloride penetration parameters of hardened concrete. After 90 days of exposure in sea water salt solution, the exposed surface is ground in 8 layers to identify the acid soluble chloride content of powdered concrete for each layer by acid soluble. Finally, the non-steady state chloride diffusion coefficient

is calculated by curve fitting to this chloride profile. Figure 3 shows the equipment for the acid soluble and chloride profiling.

Figure 3. Chloride titration device -Metrohm 716 DMS Titrino Auto Titrator.

6.1.3.Migration test-NT Build 492

NT Build 492 is a standard test in Nordic countries. It is a non-steady state migration test for determining chloride migration coefficient in concrete, mortar other cement based materials.

Non steady state diffusion coefficient is related to the process of transport and binding of chloride in concrete. The electro migration principles are used in this experiment for driving chloride ion through the specimen. Figure 4 shows the schematic set up of the test with a cylindrical concrete sample.

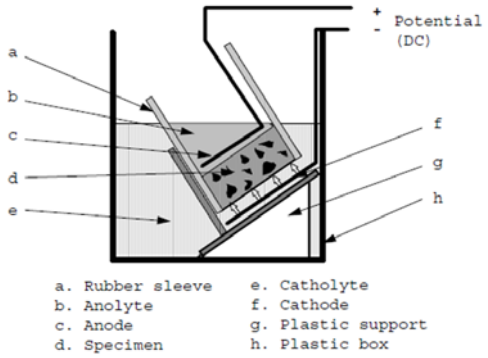

Figure 4. Schematic set up of NT Build 492 test

6.1.4.Migration test- Multi-regime method

This test consists of two compartments. One of them contains chloride solution and the other one is distilled water (

Figure 5). A voltage is applied between the compartments. By measuring the conductivity, the amount of chloride migrated to the downstream cell (anolyte) can be measured. The empirical correlation between chloride concentration and conductivity is used to measure the concentration of chlorides. The time lag for chloride ions to make a constant flux is used to calculate the non-steady state diffusion coefficient.

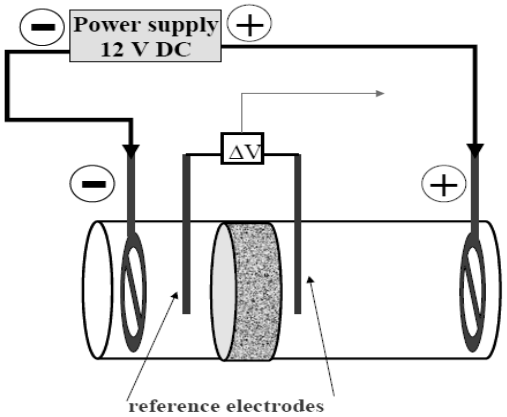

Figure 5. Schematic and laboratory set up of Multi regime method

The accelerated tests have been conducted with epoxy joints in two directions as can be seen in Figure 6 .

Figure 6. Joint vertical and horizontal to cut surface

6.1.5.Discussion and result of the preliminary durability testing

The average results for diffusion coefficient are shown in Table 2 and Figure 7. . There is no specific correlation between the diffusion coefficients of the full concrete samples, other than the fact that the chloride migration tests, NT Build 492 and Multi Regime MR have resulted in much lower diffusion coefficients than the CEN TS 12390-11 natural diffusion test. When a test is accelerated through use of electrical potential, it causes the ions within the seawater to compete for space, and also for driving

charge as they move through the concrete. Therefore when a test is accelerated and the chloride source is seawater, the resulting diffusion coefficient may be unrealistically small, compared to the natural diffusion tests in which such phenomena doesn't occur. Therefore the more realistic value of diffusion would be that of the CEN TS 12390-11 test, however a higher molarity was used on this test due to the lack of time, and also the test duration was only 45 days and so the diffusion coefficient obtained using this method would not be the expected result when concrete exposed to a marine environment.

Table 2. Average diffusion coefficient obtained from Table 2. Average diffusion coefficient obtained from various test methods

	NT Build 492	Multi Regime	CEN TS
	10^{-12} m^2/s	10^{-12} m^2/s	10^{-12} m^2/s
Full concrete	1.68	0.41	7.00
Horizontally Jointed	0.14	0.10	-
Vertically Jointed	1.94	0.18	-

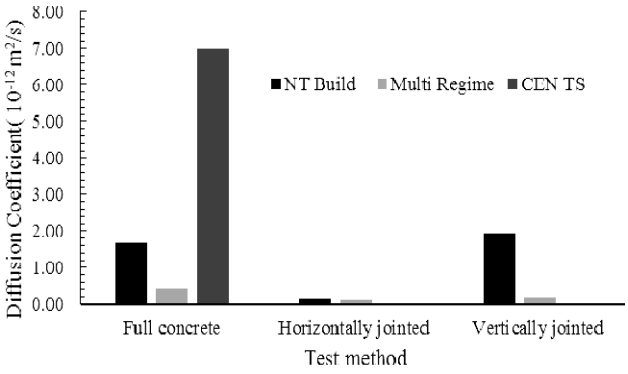

Figure 7. Average diffusion coefficient

The horizontal and the vertical specimens were both tested using the chloride migration tests NT Build 492 and the Multi Regime MR. The horizontal epoxy jointed specimens seem to show a high correlation between test methods, with the resulting diffusion coefficients being very similar. Although there are differences between the values obtained for the full concrete and epoxy jointed samples, because all of the diffusion coefficients are below 1 x10^{-12} m^2/s, it could be suggested that in regards to Pelamis, the addition of an epoxy joint will not cause a problem in term of durability.

6.2 *Design*

While the feasibility studies that have been carried out to date have indicated that the use of concrete offers benefits over steel, they have also highlighted areas of concern that need to be investigated further. These areas are discussed in the following section.

6.2.1 *Joint design*

Due to the overall arrangement of the machine there will be joints between different sections of the structure;

- The power take-off modules will continue to be constructed out of steel, and therefore there will be a steel / concrete interface between the module, and the concrete tube.
- If segmental pre-cast construction is chosen as the preferred manufacturing method there will also be concrete / concrete joints throughout the length of the tube structure.

The behavior of the joints requires careful consideration to ensure that they are capable of transmitting the required loads through the structure while remaining watertight.

Different joint configurations will be assessed in order to identify which is the most appropriate for transferring the dynamic loads from the power take-off modules through the main tube. For the steel to concrete joints, options include epoxy bonded flat faced joints with post-tensioning to increase the shear capacity, or fully composite sections where the concrete is cast directly against the steel, with shear connectors welded to the steel plate and embedded into the concrete to transfer the loads. Similarly for the concrete-concrete joints, the choice will be between flat-faced bonded joints, or joints which incorporate mechanical connections to transfer loads between different segments.

The simplest and therefore cheapest option would be flat face bonded joints without mechanical connections; however for this joint configuration load transfer depends on the strength of the epoxy bond, and hence the durability of this bond is a prime concern. The results from the durability tests as described in Section 6.1 will therefore have a significant impact on the final chosen joint design.

Joint design will be carried out with the aid of the finite element analysis (FEA) package Abaqus. In order to give confidence in the designs, FEA models will be validated against the results of laboratory load tests.

6.2.2 *Watertightness and durability of concrete*

Concrete does not have good tensile properties and will crack when subject to tensile strain. Excessive cracking can cause corrosion of the rebar as mentioned previously, and could result in leaking of the structure if through thickness cracks are allowed

to form. Therefore it is important to keep crack formation within acceptable limits.

In this case the intention is to use longitudinal post-tensioning steel to ensure that the structure is always in compression due to longitudinal bending, and hoop reinforcement to resist the tendency of the cross section to deform under external hydrostatic pressures. However it will not be possible to eliminate tensile stresses entirely in the circumferential direction, and therefore careful reinforcement detailing will be required to ensure that crack formation is be kept to a minimum.

Preliminary costing studies have shown that supplying and fixing the required reinforcement is a significant proportion of the manufacturing cost. Therefore one of the main focusses for the design work will be how to optimize the tube cross section so that the minimal amount of rebar is required while still keeping overall crack widths within the specified design limits. Options that could be considered for reducing the reinforcement include the potential addition of fibres within the concrete mix to reduce non-structural cracking, or the provision of waterproof linings in order to reduce the risk associated with water leakage via through-thickness cracks.

6.2.3 *Fatigue loading*

Pelamis is a dynamic structure, designed to move and respond when subject to wave loading. As such it is different to most of the other offshore concrete structures such as floating oil and gas platforms, which are designed as large, mostly static structures which do not respond to the passing waves.

Because of this, the structure will be subject to significant cyclic loading throughout the design life (20yrs), and the effect of this on the concrete, epoxy joints and post-tensioning system needs careful consideration.

Reinforced concrete itself has good fatigue properties, which is one of the benefits when compared to steel, but the behavior of the joint systems is less well understood. In order to address this issue, fatigue needs to be carefully considered when assessing the different joint options as described in Section 6.2.1. Details which are known to have poor fatigue behavior (such as some shear connector systems) will be avoided. In addition fatigue load testing will be carried out on the different proposed joint configurations, to investigate how the physical performance of components such as the epoxy bond, and the mechanical shear connectors change when subject to cyclic loading.

The results of these tests will be used to inform the design process, eliminate joint configurations that do not respond well to cyclic loading, and reduce the uncertainty associated with different design options.

6.3 *Manufacturing and cost*

The success of manufacturing concrete Pelamis WECs will depend on producing a concrete structure fit for purpose while also reducing the Cost of Energy (CoE). The following process is proposed and advantages of using concrete are briefly outlined.

6.3.1 *Manufacturing options*

A matrix of the various manufacturing options will be used to decide the most suitable methods of manufacture. The least suitable materials and techniques will be eliminated and the most suitable construction materials and techniques examined in greater detail for their use in the manufacturing of Pelamis WECs. Suitability will be determined based on the design, testing, cost and risk. Refinement of each of these processes will be carried out in conjunction with supply companies to minimize the cost and risk.

6.3.2 *Cost modelling*

Supply companies will be involved in costing the design and construction of the concrete WECs. As in LEAN supply chains the manufacturer (Pelamis) will work closely with suppliers to reduce the cost of the various elements of construction to find cost effective solutions to many of the technical issues faced in producing a concrete WEC. By generating a number of cost models based on the various manufacturing options the most suitable option can be chosen for the construction and any unforeseen costs and problems identified.

7. CONCLUSION

This paper has reviewed the overall program of research into the use of concrete as the primary construction material for the Pelamis wave energy converter. Through the use of concrete in the place of steel, there is the potential to reduce the Cost of Energy (CoE) of wave power and produce a competitive alternative form of renewable energy. The flexibility of the tube shape and faster manufacturing of concrete may lead to better energy capture and faster deployment respectively. However, the correct design and construction methods are needed to overcome the highlighted technological and durability issues. Therefore, the ongoing research considering the main aspects of durability, design and construction will be continued.

8. REFERENCES

ACI Committee 357. (2010). Report on Floating and Float-In Concrete Structures (M. Concrete, Trans.) (pp. 41): American Concrete Institute.

Ahn, W., & Reddy, D. (2001). Galvanostatic testing for the durability of marine concrete under fatigue loading. *Cement and Concrete Research, 31*(3), 343-349.

British Standards Institution, 1986. *BS 1881-125:1986 Testing concrete. Methods for mixing and sampling fresh concrete in the laboratory*.: British Standards Institution.

Castellote, M. A. C. &. A. C., 2001. Measurement of the steady and non-steady state chloride diffusion coefficients in a migration test by means of monitoring the conductivity in the anolyte chamber. *Cement and Concrete Research,* 31(10), pp. 1411-1420.

CEN/TC 104, 2010. CEN TS 12390-11*:* (2010) *Testing Hardened Concrete: Determination of the chloride resistance of concrete, unidirectional diffusion,* s.l.: British Standards Institution.

Dhir, R., & Jones, M. (1999). Development of chloride-resisting concrete using fly ash. *fuel, 78*(2), 137-142.

Gerwick, C. (1999). *Construction of marine and offshore structures*: CRC Press.

Helland, S., Aarstein, R., & Maage, M. (2010). In-field performance of North Sea offshore platforms with regard to chloride resistance. *Structural Concrete, 11*(1), 15-24.

Knowledge Transfer Partnership. (2014). 2014, from http://www.ktponline.org.uk/

Mehta, P. K. (2002). *Concrete in the marine environment*: CRC Press.

Nawy, E. G. (2008). *Concrete construction engineering handbook*: CRC press.

NT Build 492. (1995). Chloride migration coefficient from non-steady state migration experiments. NORDTEST, Espoo

Pelamis Wave Power, (2003). WEC-main body structural design and materilas selection, (V/06/00197/00/00/REP - DTI URN 03/1439.

Pérez Fernández, R., & Lamas Pardo, M. (2013). Offshore concrete structures. *Ocean Engineering, 58*, 304-316.

The Concrete Society. (2011). Cementitious Materials: The effect of ggbs, fly ash, silica fume and limestone fines on the properties of concrete.

Zhao, Y., Ren, H., Dai, H., & Jin, W. (2011). Composition and expansion coefficient of rust based on X-ray diffraction and thermal analysis. *Corrosion Science, 53*(5), 1646-1658.

STEEL-CONCRETE CONNECTIONS FOR FLOATING WAVE ENERGY CONVERTERS

L. Barker Ewart, *Industrial Doctorate Centre for Offshore Renewable Energy, University of Strathclyde, UK*
N. Barltrop, *University of Strathclyde, UK*
D. Findlay, *Albatern Ltd, UK,*
P. R. Thies, *University of Exeter, UK*
T. Stratford, *University of Edinburgh, UK*

ABSTRACT

In order to make wave power technologies competitive within the overall energy market, there needs to be significant reductions in the levelised cost of energy (LCoE). One area for potential cost reduction is the use of cheaper materials that are suitable for use in the harsh marine environment, such as reinforced concrete, which gives good corrosion and fatigue properties while providing excellent strength and stiffness at low unit cost. Concrete has the potential to be used for a wide range of wave energy device configurations, however in general use has been limited to nearshore fixed bottom wave energy converters. To date, no dynamic floating wave energy devices have successfully utilised reinforced concrete as structural material, mainly due to the uncertainty surrounding the behaviour of critical dynamic connections between concrete sections and other materials. This paper explores the main issues surrounding steel-concrete connections for floating wave energy converters, providing a review of available design options and standards and assessing the applicability of these to WECs. A methodology is proposed for the evaluation of connection options, and a case study of the Squid 12S floating WEC (developed by Albatern) is presented.

NOMENCLATURE

CAPEX	Capital expenditure
DNV-OS	Det Norske Veritas, Offshore Standard
EC	Eurocode
FLS	Fatigue limit state
LCoE	Levelised Cost of Energy
PTO	Power take off
ULS	Ultimate limit state
WEC	Wave Energy Converter

1. INTRODUCTION

While a significant amount of research has been carried out into wave energy generation, much of the focus to date has been on the development of the energy capture technology and proof of concept; material selection has therefore been a secondary concern. However, in order to progress towards commercialisation there need to be significant reductions in the LCoE and a potential avenue for this is the use of cheaper materials that are suitable for use in the harsh marine environment. A number of studies and reports (e.g. [1], [2], and [3]), have highlighted the benefits of reinforced concrete as an alternative to the more commonly used steel for marine structures and renewable energy devices, and the material has a long history of use in the marine environment (a history of offshore concrete structures can be found in [4] and [5]). The benefits of concrete include:

- High resistance to corrosion, especially when compared to steel, eliminating the need for additional coatings, and reducing through life maintenance costs;
- Low susceptibility to fatigue failure, which is very important for dynamic structures such as WECs;
- Ideal for volume manufacture of nonstandard shapes;
- Provides good strength and stiffness properties at a low unit cost: the raw material for reinforced concrete is approximately an order of magnitude cheaper per tonne than steel [6] ;
- Concrete is locally produced, and therefore less reliant on global markets when compared to steel.

Despite the economic and technical benefits of concrete, within the marine renewable industry use has mainly been restricted to foundations of offshore wind turbines, and nearshore fixed bottom wave energy converters, such as the Limpet. To date there are no dynamic floating wave energy devices that have managed to make the most of the

advantages that reinforced concrete has to offer. The main reason for this is the uncertainty surrounding the behaviour of joints and connections between concrete sections and other materials. This is a particular issue when connections are required between large non-moving parts of the structure (particularly suited for concrete), and articulated power take off systems (generally made from steel or other metallic materials). These joints are usually critical to the overall function of the device, and have to be capable of transferring very large dynamic forces and moments around multiple degrees of freedom, and therefore it is important to ensure that their integrity is maintained throughout the lifetime of the structure.

Although there are a number of existing applications that make use of steel to concrete connections: such as shear connectors in composite bridges; holding down anchors in concrete foundations; and connection of steel topside infrastructure to offshore concrete oil and gas platforms; none of these applications have the same particular design constraints as floating wave energy devices: namely the requirement to transmit dynamic, cyclic loading about multiple axes, in a harsh offshore environment, while ensuring that the connections remain watertight.

This paper investigates some of the issues surrounding concrete connections for floating WECs. The paper provides a review and evaluation of typical connection details (section 2) and standard design codes (section 3); sets out a proposed methodology for the evaluation of connection options (section 4); and provides a case study of the Squid 12S floating WEC (developed by Albatern Ltd) in section 5 and ends with conclusions (section 6).

2. OVERVIEW OF STEEL TO CONCRETE CONNECTION METHODS

There are many different methods for connection of steel sections to concrete structures, which can be generally categorised as follows, (each of which is discussed in the following section):

- Cast-in fully composite solutions;
- Cast-in removable solutions;
- Post-installed anchors; and
- Adhesive connections.

2.1 CAST IN FULLY COMPOSITE SOLUTIONS

One of the most common uses for mechanical shear connectors is in the design and construction of composite bridge structures, where welded headed shear studs are often used to transfer longitudinal shear between steel support beams and concrete decks. These studs are very easy to install, providing the contractor has access to a specifically designed stud welding machine. Because of the commonality of use of this type of connection their behaviour in shear is well understood, and designs can be carried out in accordance with standard design codes, such as EC4-1-1 [7].

One of the main issues with this type of connection is the amount of slippage that has to occur before the full shear capacity is mobilised, resulting in stress concentrations and crushing of the surrounding concrete (see Figure 1) which results in poor fatigue behaviour if subject to high cyclic loading. In addition, the individual shear capacity is quite low, and therefore many connectors are required to provide a full shear connection, which can be labour intensive. There can also be issues with corrosion if there is water ingress between the concrete and the face plate; this is very difficult to inspect and therefore could result in an unpredicted failure of the connection.

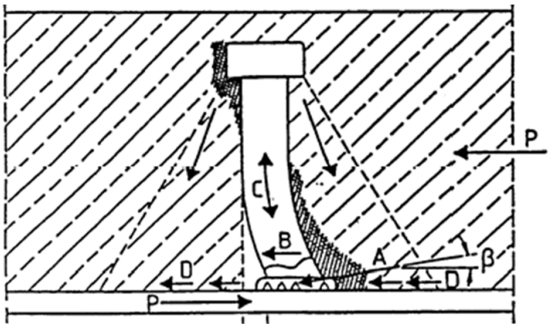

Figure 1: Load transfer from welded shear stud [8]

To overcome the potential fatigue issues with arc welded studs, the bridge designers Leonhardt, Andra and Partners developed the Perfobond shear connector in the 1980s as an alternative for shear connection in composite bridges [8]. The connector itself has a high shear capacity, and the composite shear resistance is developed through concrete compression dowels that form in the holes of the shear connector (see Figure 2). Reinforcing bars

can be placed through the holes to improve the overall ductility of the connection and increase the overall shear resistance. Fatigue behaviour is improved, as less slip is required to mobilise the shear connection, resulting in more elastic behaviour than for shear heads.

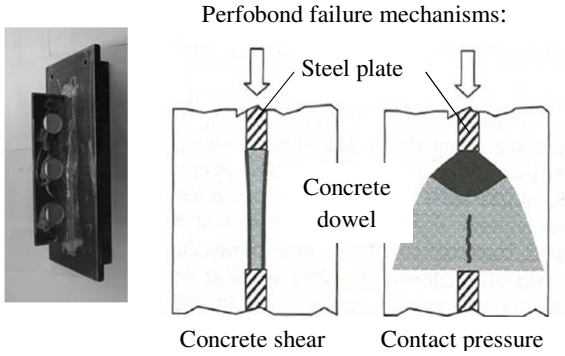

Figure 2: Perfobond shear connectors [8]

The disadvantage of this type of connector is that it more difficult to place the reinforcing bar within the concrete.

2.2 CAST IN REMOVABLE SOLUTIONS

The connection solutions discussed above are fully composite solutions, where the connection is cast into the concrete, requiring that the steel is incorporated into the formwork and permanently connected to the concrete structure. However, this may not always be feasible or practical, and there are a wide variety of proprietary cast-in socket and anchor solutions that allow sections to be bolted on after the casting process, such as those developed by Halfen (see Figure 3).

Failure mechanisms of cast-in anchor systems include failure of the steel connector in tension or shear, pull out of the fastener (caused by crushing of the concrete under the fastener head), concrete cone failure in tension, or edge failure in shear (governed by the concrete shear strength). Providing that these different failure modes are addressed, these types of connections are well suited to resisting loading around multiple axis.

The anchor bolts can also be pre-loaded, which improves fatigue resistance in tension as the pre-load reduces the stress fluctuations in the bolt due to cyclic loading. Pre-loading also improves behaviour in shear, as providing the frictional resistance is greater than the applied shear force, this results in a non-slip connection and the shear force is transmitted directly into the concrete, rather than taken by the steel fastener.

An extension of pre-loaded bolts is the use of pre-tensioned reinforcing bar. This is often used in situations where it is advantageous to keep the concrete in compression to reduce the potential for cracking under bending loads. Extending pre-tensioning systems across a joint keeps the joint in compression, and has therefore the same advantages for connection fatigue as pre-loaded bolts.

A disadvantage of this type of connection is that the connectors provide a potential path for water ingress into the concrete leading to durability issues, especially if they are cast all the way through a section. This is possible to overcome through provision of protective coatings for bolt ends, and any problems with corrosion will also be evident during inspections.

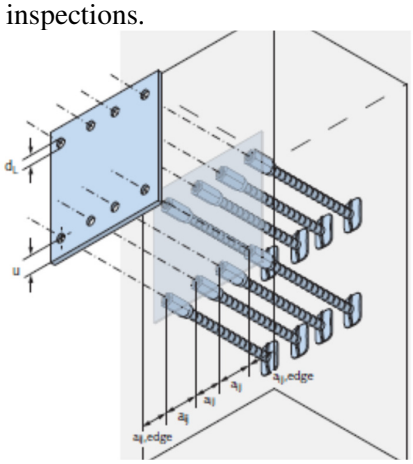

Figure 3: Cast in connections [9]

2.3 POST INSTALLED ANCHORS

Post-installed anchors (such as chemically bonded anchors placed in holes drilled in the concrete) are generally used for retrofitting applications, or for in-situ installations where accurate placing of cast in connections is not possible. Cast-in solutions are preferable for precast units as they can be fully integrated and tied into the steel reinforcement.

2.3 ADHESIVE CONNECTIONS

Externally bonded plates (either steel or FRP) have been successfully used to upgrade ageing concrete bridges in order to improve bending and shear resistance, and have the potential to replace traditional mechanical shear connections in

composite construction [10]. This would overcome some of the issues associated with mechanical shear connection including fatigue and stress concentrations. However, there has been very little investigation to date into the durability of such connections under fatigue loading in the marine environment; this is a very large area of potential research, but as such is outside the scope of this current study.

3. AVAILABLE CODES AND STANDARDS

Structural design is carried out in accordance with internationally recognised codes of practice which ensure that the structure will meet a specified target safety level over its design life. However, WECs are novel devices that can fall outside the scope of the available codes and standards. This section provides a brief review of design codes applicable for steel-concrete connections in wave energy applications.

Some of the most commonly used standards within Europe include the Eurocodes, and the DNV Offshore Standards (DNV-OS). The Eurocode suite covers the design of buildings and civil engineering works, but specifically state that they do not cover particular aspects of special types of civil engineering works such as offshore platforms, and therefore may not be entirely applicable to the design of wave energy converters. Eurocode 4 [7] covers composite buildings and bridges constructed from steel and concrete, and as discussed in Section 2 specifically details the design of arc welded shear studs. However, the scope of design for these connectors is limited to the transfer of longitudinal shear in composite beams, and therefore is not directly applicable to connections subject to loads around multiple degrees of freedom.

In addition to the Eurocodes, there is also a European Technical Specification in development (DD CEN/TS 1992-4) [11] which covers the design of many types of fasteners in concrete and includes fasteners subject to tension as well as shear. It therefore has a wider range of application than the design methods for shear studs in EC4; however, the scope of this document is the same as for the Eurocodes, and therefore similarly it is not necessarily directly applicable to offshore structures.

In comparison to the Eurocodes, the DNV-OSs were specifically written for offshore structures, but were developed primarily for the oil and gas industry and therefore deal with large static structures, in direct contrast to most WECs which are highly dynamic structures. They may therefore not always be suitable for design, particularly when it comes to safety philosophy for fatigue loads, as noted by Ambuhl et al. [13] who carried out work to calibrate the fatigue design factors presented in the DNV-OSs for steel connection details, and found that the published factors resulted in lower target levels of reliability than required. In addition to the concerns surrounding the applicability of the documents there are no specific guidelines for the design of concrete fastening systems within the DNV codes, although DNV-OS-C502 [14] does include a brief section on composite design with studs, which follows the same design philosophy as the Eurocodes.

The lack of applicable codes and standards for the design of connections for WECs highlights the issues and uncertainty surrounding this type of detail, and indicates that this is an area where further research would be beneficial in order to determine whether it is possible to exploit the benefits of concrete for the application of floating WECs.

The following section proposes a methodology for screening and evaluation of different connection options in absence of suitable design guidelines and standards.

4. PROPOSED METHODS FOR EVALUATION OF CONNECTIONS

While the connection design details for WECs will be heavily dependent on the configuration of the individual device, many of the issues and concerns are similar between devices. Therefore, a generic preliminary evaluation and assessment process has been developed with the following steps:

- Development of high level options, based on potential connection configurations as discussed in Section 2.
- Qualitative assessment of advantages and disadvantages of each option. At this stage, it may be apparent that some connection options are not suitable for a particular application, and

therefore these can be discounted, leading to a reduced short list that can then be assessed in further detail.

- Preliminary quantitative design based on outline design loads. This step should take place early in the design phase, and therefore it is likely that final design loads will not be available. However, this step allows for a comparison between options, to allow preferred options to be identified and taken forwards for further development.
- Preliminary spectral fatigue analysis based on outline fatigue loads. Again, this step allows for a comparison between designs, and gives an indication of whether fatigue is an issue for a particular configuration.
- Following the preliminary design, options can then be evaluated based on the following criteria:
  - Overall weight of steel within the connection which gives an indication of cost;
  - Fatigue resistance;
  - Corrosion potential;
  - Ease of construction; the easier the construction, the cheaper the connection will be;
  - Maintainability; the easier a detail is to inspect and maintain, the cheaper and more reliable it is likely to be.

In this paper, a quantitative evaluation process is recommended, whereby each criterion is given a score of between 1 and 5, where 1 is the most positive, and 5 is the least positive. The different criteria can then be summed together, and the preferred options will be those with the lowest overall scores. In the following section, this methodology has been applied to the Squid 12S floating WEC.

5. CASE STUDY- ALBATERN MULTINODE FLOATING WAVE DEVICE

Albatern are currently considering the use of reinforced concrete as a main structural material for the next generation of Squid device (the 12S), but one of the main areas of concern for design is the articulated interface between the concrete node structure and the steel link arm, which provides the connection point for the power take off mechanism.

5.1 OPTIONS

An overview of a potential configuration for the 12S Squid unit is shown in Figure 4. Initial techno-economic feasibility studies have shown that concrete is one of the preferred materials for the node structure, whereas the link arm and joints will be manufactured from steel.

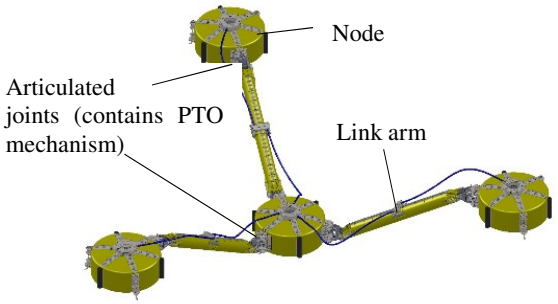

Figure 4: Overview of proposed configuration for 12S Squid

The critical component for structural design of the concrete node in this configuration is the articulated connection between the link arm and the node, which is the point of transfer of the dynamic PTO loads into the main structure, and needs to be robust and remain watertight through the design life. The load components that are transferred through the connections are shown in Figure 5. An overview of the options that are being considered for the connection are shown in Table 1 together with an overview of the advantages and disadvantages of each option (initial qualitative assessment), and the results of the preliminary quantitative design assessment (discussed in Section 5.1).

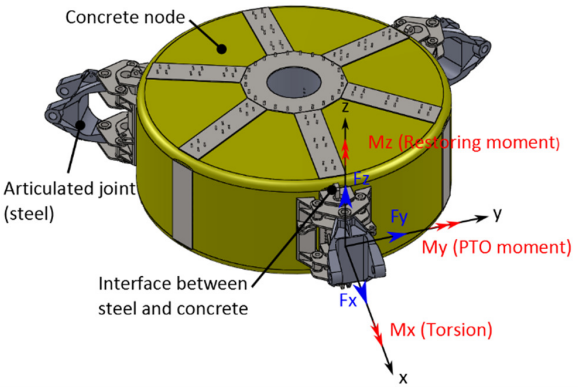

Figure 5: Load actions at connection between link arm and node

Table 1: Steel – concrete connection option assessment for the Squid 12S device

Option development		Qualitative assessment		Preliminary quantitative design	
Option	Sketch	Advantages	Disadvantages	Required ULS design	Fatigue
1	Composite welded shear studs 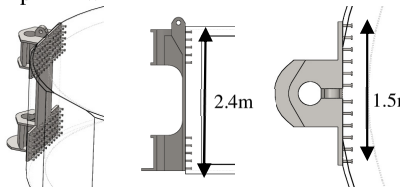	• Fully composite system- concrete and steel act together. Commonly used shear connection • Cheap and quick to install studs (providing there is access to correct machine)	• Not designed to take shear and tension • Poor fatigue detail • Need to incorporate steel section into concrete formwork and can't remove / replace steelwork • Potential corrosion issues if there is water ingress between the plate and the concrete which wouldn't be visible during inspections	25dia x 150 shear studs, total no. 96. Total steel weight: 244kg	2.4yrs
2	Cast-in plates (perfobond) 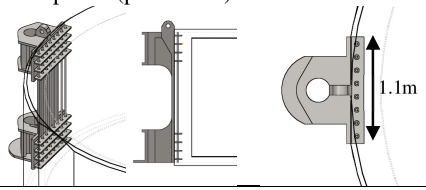	• Fully composite system – concrete and steel act together • Improved fatigue detail • Suited to taking shear and tension	• Need to incorporate steel section into concrete formwork • Can't remove / replace steelwork • Potential difficulties with placing rebar • Potential pathway for water ingress, increasing the possibility of corrosion of the reinforcement.	8 no. ribs, 1100x150x20mm dimensions. 8no. 50mm dia holes, with 25mm dia rebar in each Total steel weight: 250kg	18.3yrs
3a	Cast-in anchor sockets 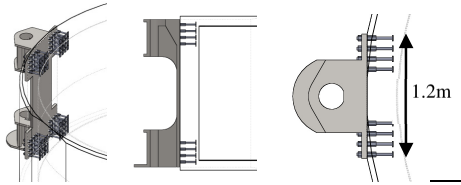	• Easy to cast in bolts • Steel work is separate from concrete – can be removed / replaced • Provides good resistance to loads around multiple axis • No welding required	• Non-preloaded bolts are poor in fatigue • Bolts may provide a pathway for water into the concrete, increasing the possibility of corrosion of the reinforcement. • May be corrosion issues for bolt heads. • Potential difficulties with rebar placement around bolts.	64 no. anchors, 240mm total embedment, 25mm diameter Total steel weight: 256kg	0.3yrs
3b	Cast-in anchor sockets with pre-loaded bolts (potentially long bolts to reduce loss of preload)	• As per 3a, but improved fatigue detail due to preload in bolts	• Potential loss of preload through the lifetime of the structure	As 3a, but with preloaded bolts Total steel weight: 256kg	19.5yrs
4	External concrete connection, with bolts in shear 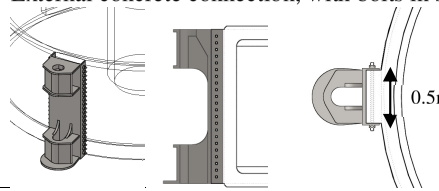	• No water path through into the node • Steel work separate to concrete • Easy to remove and replace steel work – including bolts	• Would need careful consideration of the rebar connection and strength of the concrete attachment 'nib'. • Reduced number of larger bolts, meaning each bolt takes a large amount of shear force – not particularly good for fatigue.	23 no. M30 bolts, clamping connection on to 500x200mm concrete outstand Total steel weight: 291kg	1.9yrs
5	External concrete connection, pre-tensioned bars 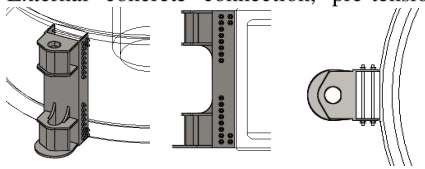	• Pre-load improves fatigue detail	• Bars have to have large pretension in order to ensure no slip of bolts in shear. • Potential preload loss through life time. • Careful detailing of rebar connection and concrete attachment 'nib' required. • Bars should not corrode or stress corrosion crack	20 no. 32mm dia pre-tensioned Macalloy bars Total steel weight: 291kg	>20yrs

5.1 PRELIMINARY QUANTITATIVE DESIGN

In order to quantify some of the advantages and disadvantages of different options for the Albatern device, an initial feasibility design had been carried out, based on preliminary design loads from hydrodynamic modelling of the full Squid unit. Although at this stage in the development process it is not possible to carry out a full detailed connection design, this feasibility study allows the different options to be compared on a like for like basis, and can therefore be used as a tool to inform the ongoing design process of this or other WECs.

5.1 (a) Ultimate limit state design (ULS)

While it is noted in Section 3 that the available codes and standards are not always directly applicable to wave energy devices, and do not have a large enough scope to cover the wide range of connection options that are available, they do however provide a good starting point for design. Therefore, where code based design methods are available they have been followed for the purpose of this initial study.

The connection configurations shown in Table 1 are based on the requirements for ULS design, looking at the extreme loads developed during the 1 in 100-year storm event. The connection has to transmit torsion (M_x), the PTO torque (M_y), vertical and horizontal shear (F_z and F_y), as well as axial tension and compression (F_x) into the concrete. The largest preliminary load actions are M_x and M_y (each >2MN.m), with $M_x = 1.6M_y$. For the purpose of this design study, it has been assumed that the worst case of all forces can act simultaneously. Partial factors have been applied to the loads and material resistances in accordance with recognised design codes or guidelines where available.

Headed shear studs (Option 1) have been designed in accordance with the guidance in BS EN 1994-4-2 [7] and also DNV-OS-C502 [14]. While it is noted that the equations presented in these standards are not directly applicable for connectors loaded in combined tension and shear, the Designers Guide to EC4 [14] provides a formula to check shear connectors for this load case.

The perfobond connector (Option 2) is not covered in any of the standard codes, however there are a number of different empirically derived design equations presented in the literature. For the purpose of this design, the equations proposed by Valente [8] have been used which are considered to result in a conservative design solution.

The bolted connection (Option 3) has been designed in accordance with the principles in DD CEN/TS 1994-4-1 and 2 [11], which deal with the general design of fastenings for use in concrete (Part 1), and headed fasteners in particular (Part 2). Reference is also made to the Halfen Technical documentation [9], which provides guidance on the design of these types of connections.

Bolts and pre-tensioned bars in shear have been checked in accordance with BS EN 1991-1-8 [15], with the shear resistance of the concrete checked in accordance with DNV-OS-C502 [13].

5.1 (b) Fatigue limit state design (FLS)

Due to the dynamic nature of floating wave energy devices, fatigue due to the operational loads is often the driving design criteria, rather than ultimate limit states which ensure survival during extreme events. To evaluate the fatigue behaviour of each of the connection options, an assessment of fatigue life has been carried out based on the required ULS.

Fatigue assessment is most commonly carried out in the time domain, with the number of stress cycles that a detail has to endure calculated from the stress time history using the rainflow cycle counting method [16]. However, the level of modelling and analysis that is required for this is not appropriate at this stage in design, and therefore a frequency domain approach has been followed in this case.

Rapid fatigue analysis methods, based in the frequency domain, were developed in the 1980s for the offshore oil industry [18], which allow the expected stress range and number of cycles to be determined for each sea state included in the wave scatter diagram for a particular site.

The current design is based on the North Atlantic Scatter Diagram (NASD), as given in [19]. This spectrum encompasses the worst case sea states

encountered throughout the North Atlantic, and therefore gives a conservative spectrum for structural design. The scatter diagram gives the number of occurrences expected for each sea state (defined by significant wave height H_s, and peak period T_p) in a given year. The process that has been followed for this fatigue analysis is presented below.

- For each action which contributes to fatigue loading, a load transfer function per unit wave amplitude has been determined from the hydrodynamic model of the device. This gives the magnitude of a particular action (for example the torsion moment at the connection Mx), for the full range of wave frequencies.
- For each connection detail, the magnitude of stress that occurs due to a unit load has been calculated, based on linear elastic analysis. This is multiplied by the load transfer function per unit wave amplitude in order to give the frequency domain stress transfer function per unit wave amplitude.
- The stress spectrum for a particular sea state is determined by multiplying the wave spectra for a particular sea state (assumed at this stage to be a Jonswap spectra defined in accordance with [19]) by the square of the stress transfer function.
- The long term stress range is calculated using the properties of the stress spectrum, assuming that the stress range is distributed in accordance with the Dirlik probability density function – this is an empirically derived function suitable for narrow band spectra, which gives better correlation with the time history rainflow counting method than other distributions such as the Rayleigh distribution [18].
- The number of cycles expected at each stress range can then be calculated for each sea state (this has been carried out using Matlab), depending on the expected duration of each sea state based on the NASD. This can then be summed together to give a full stress cycle histogram.
- Fatigue life has been estimated using published S-N curves, and the Palmgren-Minor summation rule for damage to different magnitude stress cycles.

As concrete generally performs better than steel under fatigue loading, this fatigue assessment has only considered the steel components. It is noted however that for a full detailed analysis, the fatigue life of the concrete components would also need to be considered.

S-N curves for different steel details have been taken from [20]. There is no specific S-N curve published for the perfobond connector as a whole, however it is assumed that fatigue failure would be a result of failure of either the weld between the rib and the faceplate, or stress concentrations due to bearing across the rib hole, and therefore each of these details have been checked individually.

The expected fatigue damage of each connection has been determined based on a single year duration; the fatigue life has then been calculated based on the number of years it would take for the damage level to be greater than 1 (no safety factors are included in this value). The fatigue life due to the torsion moment (M_x), and PTO induced moment (M_y), have been calculated separately and the worst case has been presented in the results section.

5.1(c) Results

Results from the ULS and FLS outline designs are included in columns 5 and 6 of Table 1.

5.2 DISCUSSION

Following on from the preliminary qualitative and quantitative assessment presented in Table 1 each option has been assessed on the basis of the criteria set out in Section 4. For each criterion, options have been given a score between 1 and 5, with 1 being the best and 5 being the worst.

The results of this assessment are presented in Table 2, which provides the score and a brief explanation for each option and criterion.

Table 2: Option assessment

Option	Weight	Fatigue	Ease of construction	Corrosion potential	Maintainability	Total
1	**1** *Lowest weight overall*	**5** *Very poor*	**4** *Complicated to incorporate steelwork into formwork*	**4** *Any corrosion of shear studs won't be visible*	**5** *Can't remove / replace steelwork*	19
2	**2** *Ribs slightly heavier than studs*	**2** *Much improved, but still less than required*	**4** *Difficulty placing rebar around ribs*	**4** *Any corrosion of ribs won't be visible*	**5** *Can't remove / replace steelwork*	17
3a	**3** *Cast in anchors slightly heavier*	**5** *Very poor*	**2** *Anchors are easy to incorporate into formwork.*	**3** *Corrosion potential – but can be inspected*	**2** *Most steelwork parts can be replaced*	15
3b	**3** *Cast in anchors slightly heavier*	**2** *Fatigue improved with preload, but still less than required*	**2** *Anchors are easy to incorporate into formwork.*	**3** *Corrosion potential – but can be inspected*	**2** *Most steelwork parts can be replaced*	12
4	**4** *High weight of steel due to additional plates*	**5** *Very poor*	**2** *Slight increased complexity with additional concrete nib*	**3** *Corrosion potential – but can be inspected*	**1** *Easy to replace bolts and connection if required*	15
5	**4** *High weight of steel due to additional plates*	**1** *Fatigue improved with preload*	**2** *Slight increased complexity with additional concrete nib*	**3** *Corrosion potential – but can be inspected*	**1** *Easy to replace bolts and connection if required*	12

Table 2 attempts to quantify the benefits and disadvantages of each option and shows that the preferred options are option 3b (Cast-in anchor sockets with preloaded bolts), and 5 (External concrete connection with pre-tensioned bars). The advantages of these configurations include the good fatigue behaviour provided by pre-tensioned connections, the ease of construction, and the improved inspection and maintainability characteristics, when compared to the other options.

Worst performing options are the composite connections, due to the increased complexity in construction and the lack of ability to inspect and maintain the connections. Option 1 (shear studs) is the least favoured option, due to the very poor fatigue behaviour.

An important point that the quantitative assessment has highlighted is the necessity to consider fatigue in design. Whilst some details performed significantly better than others, none of the calculated fatigue lives are as long as the required design life (which is around 20yrs) and an economic analysis would probably show that a safety factor on fatigue life should be included. This shows that fatigue is the dominant failure mode for the connection design and the presented connection details would have to strengthened to take this into account.

6. CONCLUSIONS

This study has looked into the issues surrounding steel-concrete connections for floating wave energy devices and has concluded the following:

- Current design codes do not adequately cover the design of steel-concrete connections for floating wave energy converters. These connections tend to be critical details transferring large dynamic loads from the power take off system into the main structure.The uncertainty surrounding the behaviour needs to be reduced in order to be able to make use of reinforced concrete in the design of these types of structures.
- Fatigue loading is an area of concern, and is very likely to drive design. Details which reduce fatigue loading, such as pre-loaded bolts or pre-tensioned reinforcement bars, are therefore preferable.
- Corrosion of connections needs to be considered carefully; details which allow water ingress should be avoided as this could exacerbate corrosion both of the connection steel work and also internal steel reinforcement within the concrete.
- Connections details which allow for easy inspection and maintenance are preferred, as this allows parts to be replaced in case of greater amounts of degradation or damage than expected during the lifetime of the structure.
- If a suitable system for steel-concrete connections can be identified, this will allow reinforced concrete to be used for the main structural components of floating wave energy converters, helping to minimise the overall CAPEX, and reduce the LCoE for WECs.

The assessments carried out within this study provide a high level overview of the issues, but further work is required in order to gain more knowledge and reduce the uncertainty surrounding the behaviour of these types of details, including dry laboratory tests to investigate behaviour under static and cyclic loads, and ultimately large scale sea trials to get a fuller idea of the behaviour in real sea conditions.

ACKNOWLEDGEMENTS

This work has been carried out as part of the IDCORE programme, funded by the Energy Technology Institute and RCUK Energy programme (grant no. EP/J500847/1)

REFERENCES

1. K. SANDVIK, R. EIE, J.-D. ADVOCAAT, A. GODEJORD, K. O.HÆREID, K. HØYLAND AND TOR OLE OLSEN, "Offshore Structures - A new challenge," in *XIV National Conference on Structural Engineering*, 2004.
2. HI-CON A/S, "FLOAT - development of new flexible UHPC," ForskEL, Hjallerup, Denmark, 2012.
3. OCEAN POWER DELIVERY LTD, "Pelamis WEC - Main body structural design and materials selection," DTI, 2003.
4. G. C. HOFF, "Concrete for Offshore structures," in *Concrete Construction Engineering Handbook, 2nd Edition*, E. G. Nawy, Ed., CRC Press, 2008, pp. 13-1 to 13-32.
5. R. P. FERNANDEZ AND M. L. PARDO, "Offshore concrete structures," *Ocean Engineering* , vol. 58, pp. 304-316, 2013.
6. M. F. ASHBY, "Appendix A: Data for Engineering Materials," in *Material Selection in Mechanical Design, 4th Edition*, Oxford, Butterworth-Heinemann, 2011, p. 218.
7. BSI, "BS EN 1994 Eurocode 4: Design of composite steel and concrete structures," 2004.
8. I. VALENTE, "Experimental studies on shear connection systems in steel and lightweight concrete composite bridges," 2007.
9. HALFEN, "Halfen HUC Universal Connection Technical Product Information," 2014.
10. A. SI LARBI, E. FERRIER, B. JURKIEWIEZ AND P. HAMELIn, "Static behaviour of steel concrete beam connected by bonding," *Engineering structures,* vol. 29, pp. 1034-1042, 2007.
11. BSI, "DD CEN/TS 1992 Design of fastenings for use in concrete," 2009.
12. S. AMBÜHL, F. FERRI, J. P. KOFOED AND J. D. SØRENSEN, "Fatigue Reliability and Calibration of Fatigue Design Factors of Wave Energy Converters," *International Journal of Marine Energy,* pp. 17-38, 2015.
13. DNV, "DNV-OS-C502 Offshore Concrete Structures," 2012.
14. R. P. JOHNSON, Designers' Guide to Eurocode 4: Design of composite steel and concete structures, 2nd edition, ICE Publishing, 2011.
15. BSI, BS EN 1993-1-8:2005 Eurocode 3 Design of steel structures. Design of joints.
16. J. SCHIJVE, Fatigue of structures and materials, Springer, 2009.
17. A. HALFPENNY, "A frequency domain approach for fatigue life estimation from finte element analysis," *Key Engineering Materials,* vol. 167, pp. 401-410, 1999.
18. DNV, "DNV-RP-C205 - Environmental Conditions and Environmental Loads," DNV, April 2014.
19. DNV, "DNV-RP-C203 fatigue design of offshore steel structures".

Optimising structural loading and power production for floating wave energy converters

Leah Barker Ewart[#1], Philipp R. Thies[2], Tim Stratford[3], Nigel Barltrop[4]

[#]*Industrial Doctorate Centre for Offshore Renewable Energy (IDCORE), University of Strathclyde*
[1]l.ewart@ed.ac.uk

[2]*University of Exeter*
[3]*University of Edinburgh*
[4]*University of Strathclyde*

Abstract— **This paper investigates the design trade-off between power production and structural loading for Wave Energy Converters (WECs), based on tank test results for the Albatern 12S floating wave energy array. This work feeds into the design development process, which is currently in the concept design and testing phase. The paper focuses on two methods for reducing structural loading: limiting the power take off (PTO) torque generation capacity (for operational loads), and controlling the PTO damping (for extreme loads).**

The torque that can be generated by the primary PTO mechanism affects the size (and cost) of the structural components within the device. Increased torque results in a potentially greater power capture, but also greater structural loading. It is therefore important to highlight the target torque limit early in the design process. The aim of this work is to identify the optimum torque limit to refine the design towards the lowest overall Levelised Cost of Energy (LCoE). In addition, a high-level investigation of the impact of PTO damping on extreme loading has been carried out, to help to identify appropriate "operational" and "survival" sea states for the device.

The paper calculates an optimum torque limit for the device at the West Harris site and quantifies the trade-off between Annual Energy Production and structural cost, using the LCoE as an optimisation criteria. The approach is in principle applicable to other technologies, if the design drivers are adjusted to the technology's working principle.

Keywords— **Wave energy, structural loading, tank testing, power production, LCoE.**

I. Introduction

During the early developmental stages of a wave energy converter (WEC), the primary research focus is the power production potential of the device, with optimisation of the structural design being a secondary concern. However, to progress beyond the development phase and move towards commercialisation, a more holistic view is required, with greater consideration of all factors that contribute the overall levelised cost of energy (LCoE).

Maximising power production across all sea states can increase the overall opportunities for revenue generation. However greater power production results in larger loads applied to the structure and the power take off (PTO) system, which in turn increases the cost of the device components. It is therefore important to consider the trade-off between maximising power production and minimising structural loading at an early developmental stage to ensure that it is possible to design a reliable and robust WEC structure, while achieving an acceptable LCoE.

This paper investigates this design trade-off for the Albatern 12S WEC, using results from tank testing carried out in the Flowave Ocean Energy Research Facility. The tank test set up is covered in Section II.

Two approaches to load limitation are covered in this study:

1) *PTO Torque Limitation:* The power generation capability of a device is limited by the amount of torque that can be generated by the power take off (PTO) mechanism. The effect of limiting the PTO torque on operational loads is investigated to identify the optimum torque limit which results in the lowest LCoE. The methodology is discussed in section III, with the results presented in sections IV.
2) *PTO damping control:* During operation, power output and structural loads will vary depending on the level of PTO damping. Damping can be controlled throughout operation to maximise power output in frequently occurring seas, and shed load in storm conditions. The effect of PTO damping control is considered in Section V, and the potential impact on extreme loads is discussed.

II. Tank Testing Set Up

The Albatern 12S device is a multi-body floating wave energy converter, consisting of node and link elements which can be configured in different numbers to form an array (Fig 1).

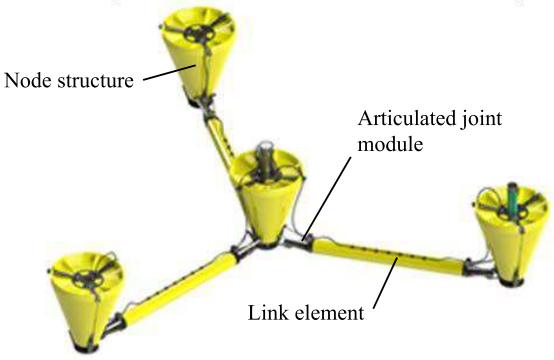

Fig. 1 Albatern 12S multi-body floating wave energy converter schematic

Fig. 1 shows the schematic of a system of 4 nodes and three link arms. Testing was carried out on a "1 Hex" array, consisting of 9 nodes, and 18 link elements (Fig. 2 and 3).

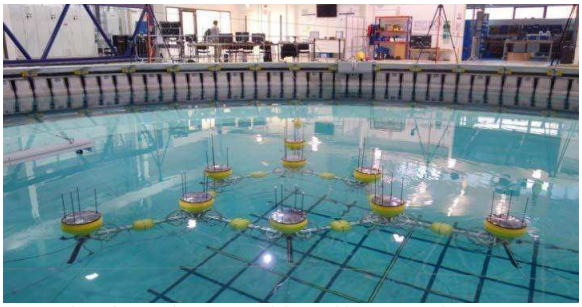

Fig. 2 Tank testing at Flowave. Model tested is a 1:18 scale "1 Hex" array, with 9 node and 18 link elements.

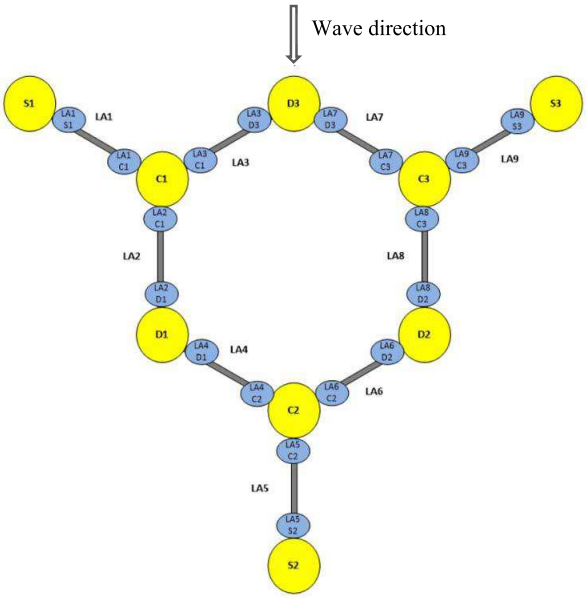

Fig. 3 Test array schematic and naming convention

A. PTO simulation

The Albatern device converts the incoming wave energy into mechanical power via the PTO mechanism at each joint which damps the relative motion of the node and link. Mechanical power capture is equal to the PTO torque (T) multiplied by the joint angular velocity (ϖ), and the generated torque is directly related to the PTO damping characteristics.

Details of the full-scale PTO mechanism are still in development; however, the main design criterion is to provide damping (and therefore power take off) around three degrees of freedom at each joint (as shown in Fig 4). This behaviour has been replicated at model scale using multiple high torque DC brushless Maxon motors. Each link arm contains five motors – two at each end resisting the motion in the pitch and yaw axis, and one in the centre resisting motion around the torsion axis. Each motor is controlled by an Escon drive, allowing for individual control of five degrees of freedom per link arm (45 in total for the whole model). The drive allows the PTO damping to be actively controlled using a feedback control loop, which provides an appropriate current to the motor based on the instantaneous measured angular velocity. Output motor torque is directly proportional to the motor current, and therefore it is possible to provide a specified torque for a given articulation velocity. Linear damping was applied during testing, whereby the output torque (T) was linearly proportional to the measured angular velocity (ϖ), however it would be possible with this system to test much more complex control strategies.

To provide the required torque at the pitch and yaw axis, wire drive gearing mechanisms are used, with sector arcs to ensure linearity between the motor and axis responses, (Fig. 4). The wire lies along the arcs and is wrapped around the motor shaft to drive the motor. A mechanical gearbox is used in conjunction with the torsion motor to provide the required torque in this axis.

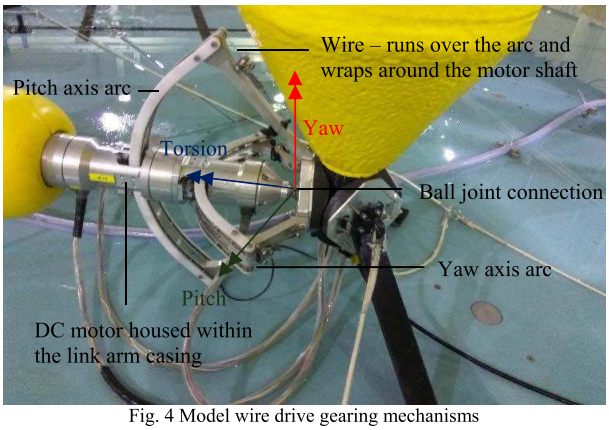

Fig. 4 Model wire drive gearing mechanisms

B. Load measurement

During testing, articulation torques were measured at the pitch and yaw axis using submersible inline tension load cells (manufactured by Applied Measurements, with a 0-50N measurement range) attached to the wire drive gear mechanism (Fig. 5).

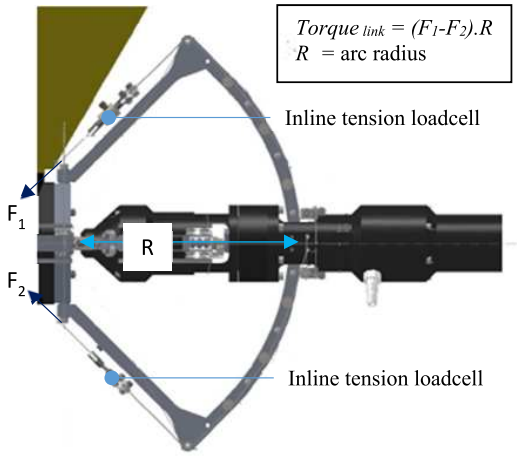

Fig. 5 Link arm end torque measurement

Unfortunately, due to budgetary constraints, it was not possible to include two load cells at each articulation axis. The maximum torques occur on the pitch axis on link arms that are in line with the direction of the oncoming waves (LA2, LA8 and LA5 in Fig. 3). Therefore, two load cells were included at the articulation points on these links, to allow accurate measurement of the maximum loads. A single cell was included on each of the other articulation locations, allowing an estimation of the torques to be calculated at these points, to be derived using information about the joint behaviour based on the articulations with the double load cells.

Link arm torsion moments were measured using a torsion load cell, placed in the centre of the link, manufactured by Futek, with a 0-5.65Nm measurement range.

C. Power capture

Two different methods have been used to measure the electrical and mechanical power captured in the array. The electrical power of the motors is calculated from direct measurements of the motor current and angular velocity, as shown in the following equations:

$$Torque_{motor} = C_t . I_m \qquad Power_{motor} = Torque_{motor} . \omega_m$$

(C_t =torque constant, I_m = current, ω_m = angular velocity).

Mechanical power has been calculated using the direct measurements of torque using the inline load cells, together with the angular velocity of the motor:

$$Power_{mech} = Torque_{link} . \omega_m$$

As an accurate measurement of the mechanical power is only possible at the articulations with two load cells, the total power capture by the array reported here is the sum of the measured mechanical power for the inline pitch articulations, and the electrical power of all other articulation locations.

Mechanical power capture is greater than the electrical power capture due to losses in the system associated with the PTO model set up, therefore this method for calculating total power capture is conservative in terms of mechanical power capture and optimistic regarding electrical power capture. While it would be possible to make a more accurate assessment of the mechanical power using data from the single load cells, at the time of writing this analysis had not been done. However, this is acceptable for this study as power output values are used for comparison only, and therefore accurate assessment of the absolute values is not necessary.

D. Test Sea States

The device was tested in 11 regular sea states (Table I), and 21 irregular sea states (Table II).

TABLE I
REGULAR TEST SEA STATES, REPORTED VALUES AT FULL SCALE

H(m) / T(s)	5.5	6.5	7.5	8.5	9.5	10.5
4.5			x			
3.5		x	x	x		
2.5			x			
1.5	x	x	x	x	X	X

TABLE II
IRREGULAR TEST SEA STATES (JONSWAP, GAMMA = 1)
REPORTED VALUES AT FULL SCALE

Hs (m) / Tp (s)	7.7	9.1	9.9	10.5	11.9	12.6	13.3	14.7
4.5				x	x			
4								
3.5		x		x			x	
3			x			x		
2.5	x		x			x		
5	x	x		x		x		
1.5	x	x		x			x	X
1	x		x					

Following guidance in [1], lines of constant significant wave height and peak period are included, as this allows the results to be extrapolated with some degree of confidence to give power output for all elements of the bivariate H_s / T_p wave occurrence matrix.

E. Damping Optimisation

As discussed in II.A, the motors were controlled to provide linear damping during testing. Tests were carried out with different applied damping levels to identify the optimum damping value for power output. The torsion damping was held at a constant value, and the pitch and yaw damping was varied between 500-6000 kNms/rad (full-scale). The full power matrix was then built up using the damping value which gave the highest power output at each sea state. In general, higher damping values were optimum for larger, steeper waves, with lower values giving higher power output for shallower, longer period waves. All power matrices discussed in this paper are based on the optimum damping levels for each sea state.

III. PTO Torque Limitation: Optimisation Methodology

This section investigates the impact of limiting the PTO torque generation capacity on power output, structural loading, and LCoE.

A. Power Output

In the scale model, the DC motors were sized to ensure that there were no constraints on the torque generated during testing. However in reality, there will be a limitation on the torque that can produced by the full-scale PTO mechanism. The amount of torque that can be achieved affects both the sizing and cost of the PTO components, as well as the sizing of the structural components, as this is one of the primary loads acting on the device. Therefore, setting the target PTO torque is an important design decision that needs to be made at an early point in the design process.

The effect of limiting the torque on overall power production has been investigated by post-processing the tank testing results. For each test sea state, the measured torque has been capped at the specified torque limit; this capped torque has then been used to recalculate the mean power capture (see Section II.C). It is noted that this is not entirely accurate as a physical torque limit would alter the behaviour of the device. However, at this stage this estimation is used to indicate the potential optimum torque limit, as including multiple torque limits within the physical testing would significantly increase the required testing time.

An example of the post-processed torque limited time history compared with the actual measured torque is shown in Fig. 6, for the case where torque is limited at 600kNm (full scale).

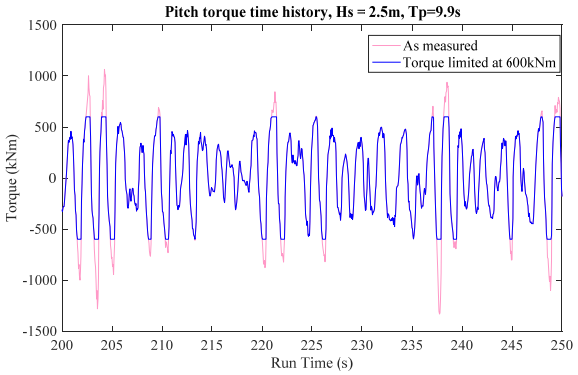

Fig. 6 Torque limited time history (Torque reported at Full Scale)

The post-processed results have then been used to develop a full power matrix for each specified torque limit. Data has been interpolated and extrapolated using the scatteredInterpolant data object in Matlab. There is some uncertainty associated with the results using this method, however as the tests cover the most commonly occurring sea states, the level of uncertainty is acceptable for comparison between different torque limits.

The power matrix has been combined with the occurrence matrix for a location to the west of the Isle of Harris to give an estimate of the Annual Energy Production (AEP). The West Harris site is a potential location for commercial deployment of the device, and occurrence data has been provided by MetOcean Solutions

B. PTO Sizing

While the exact details of the full-scale PTO mechanism are still in development, the high-level concept is to have two hydraulic cylinders attached to the node and link using ball joints, allowing for movement and damping around three axes (Fig. 7).

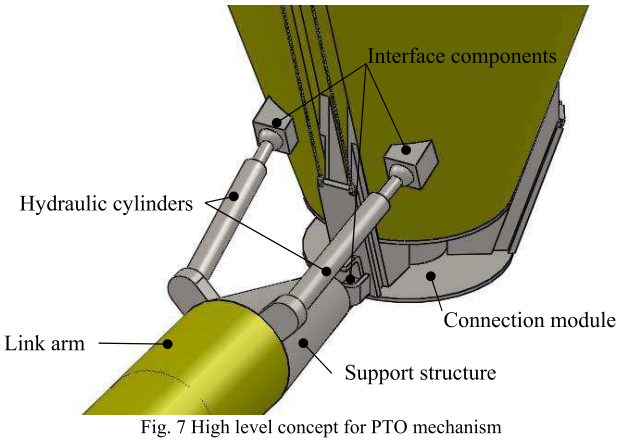

Fig. 7 High level concept for PTO mechanism

Assuming an operating pressure of 250bar for the cylinders, the required cylinder bore size has been calculated to give the appropriate ram force for a given torque limit as shown in Fig. 8.

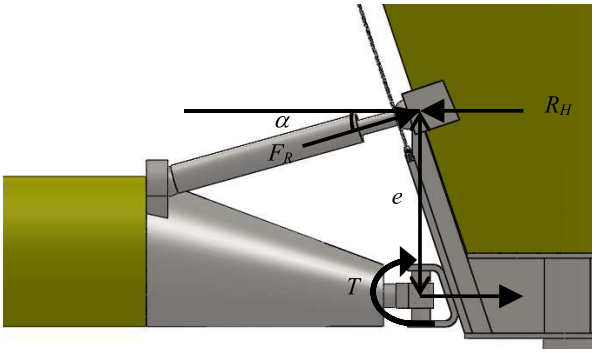

Fig. 8 Calculation of required cylinder bore for given PTO torque

PTO torque:	T	
Eccentricity:	e	$= 1.5m$
Angle:	a	$= 20^o$
Reaction force:	R_H	$= T/e$
Cylinder pressure:	P	$= 250bar$
Bore:	B	
Cross sectional area:	A	$= B^2\pi/4$
Ram force:	F_R	$= PA = R_H/cos\alpha$

C. Structural Design

For identification purposes, the device components are categorised into different systems and sub-systems as shown in Table III. This table also lists the components that are relevant to the structural design; these are shown in Fig.7.

TABLE III
SYSTEMS, SUBSYSTEMS AND COMPONENTS OF ALBATERN 12S ARRAY

SYSTEM / subsystem / *component*
STRUCTURAL SYSTEM
Node module
Link element
Link arm steel tube
Fixtures and fittings
Joint module
Hydraulic cylinder
Support structure
Interface components
Fixtures and fittings
Connection module
MECHANICAL & ELECTRICAL
MOORING SYSTEM
TRANSMISSION AND GRID CONNECTION

For this study, it has been assumed that the overall structural requirements can be characterised by the design requirements of the Link arm. This component is to be constructed from a steel tube, and the applied load actions can be directly derived

from the applied PTO torque, independent of the actual configuration of the PTO mechanism.

In contrast the details of the Joint and Connection Module will be very dependent on the PTO mechanism, and therefore outside the scope of this study. At this conceptual stage, it has been assumed that the weight of the steelwork in these components varies in direct proportion to the change in required Link arm weight.

The design of the Node structure will be for the most part driven by wave pressures on the hull (except for the connection to the steelwork), and therefore will not be greatly affected by the PTO torque. It has therefore been assumed that the design of this element is the same for all torque levels.

Structural design of the elements of a WEC should, as far as appropriate, be carried out in accordance with relevant codes and guidelines, such as [2]. This reference sets out the following limit states for design:

- Ultimate Limit State (ULS): corresponding to the ultimate resistance for carrying loads;
- Fatigue Limit State (FLS): related to the possibility of failure due to the effect of cyclic loading;
- Accidental limit states (ALS) corresponding to damage to an accidental event of operational failure;
- Serviceability limit states (SLS) corresponding to the criteria applicable to normal use or durability.

The main purpose of the tank testing was to verify the power output capabilities of the device in operational sea states, and did not include any testing in extreme sea states. It is therefore not possible to derive any ULS or ALS loadcases from the testing results. However, as noted in [3], for dynamic devices such as WECs, fatigue aspects are likely to govern the design. As the 21 irregular test sea states cover 42% of the sea states encountered in each year at the West Harris site, it is possible to estimate the fatigue loading on link arm for a 20-year design life based on the tank testing results.

Fatigue analysis has been carried out for the most heavily loaded link arm at the back of the array (LA5/S2). As this link is in-line with the waves, pitch loading is dominant and yaw and torsion loading are negligible.

Fatigue design has been carried out in accordance with [4], with analysis based on S-N data as set out in this reference. Fatigue damage has been calculated assuming linear cumulative damage (Palmgren-Miner rule), with the accumulated fatigue damage calculated in accordance with the following equation:

$$D = \sum_{i=1}^{k} \frac{n_i}{N_i} = \frac{1}{\bar{a}} \sum_{i=1}^{k} n_i . (\Delta\sigma_i)^m \leq \eta$$

D = accumulated fatigue damage
k = number of stress blocks
n_i = number of stress cycles in stress block i
N_i = number of cycles to failure at constant stress range $\Delta\sigma_i$
a = intercept of the S-N curve with the log N axis
m = negative inverse slope of the S-N curve
η = usage factor =1/DFF
DFF = Design Fatigue Factor

The number of stress cycles (n_i) has been calculated using the post-processed torque time histories from tank testing in irregular waves. Torque cycles have been counted using the rainflow counting method [5], [6], split into blocks with a range of 50kNm. Torque (T) is related to stress in the link arm by the following equation:

$$\sigma = \frac{T}{Z}$$

Z = elastic section modulus = $\frac{(D^4-(D-2.t)^4)}{64}\pi$ for a tube with diameter D and wall thickness t.

Each test time history consists of 10902 readings, with a sampling rate of 20Hz. For the rainflow counting, the first 500 and last 902 reading have been ignored (to allow for warm up and settling time of the tank). Each time history is therefore 475 seconds long at model scale, which relates to a length of 1840s full scale (for an 18th scale model).

To account for the stress cycles encountered over the whole design life of the structure, the number of stress cycles counted within each of the test time histories has been multiplied by an appropriate factor, derived from splitting up the full occurrence matrix. This has been done by assuming that the test sea state results also apply to adjacent sea states. The assumed split applied to the scatter diagram is shown in Fig. 9.

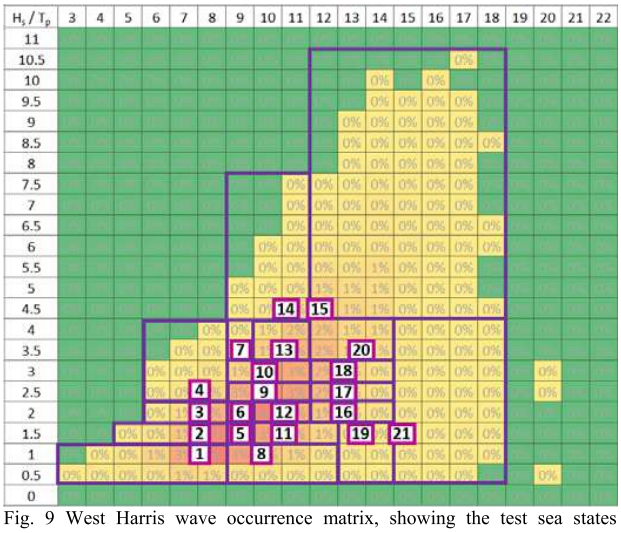

Fig. 9 West Harris wave occurrence matrix, showing the test sea states (numbered), together with the portion of the matrix to which they are assumed to apply.

To calculate N_i for each stress cycle, the link arm has been classified as a "C" fatigue detail, in accordance with Table A.1 of [4], (a rolled steel tube subject to potential rust pitting). For a member in seawater with cathodic protection this gives the following data for the S-N curve (Table 2-2 from [4]):

For $N \leq 10^6$ cycles: $m_1 = 3.0$, $\log a_1 = 12.192$

For $N \geq 10^6$ cycles: $m_2 = 5.0$, $\log a_2 = 16.320$

The Design Fatigue Factor has been taken as 1 (from table 5-1 of [2]), as it is assumed that the link arm will be inspected on a regular basis.

D. Levelised Cost of Energy (LCoE)

The main aim of this section of work is to select the optimum PTO torque limit which gives the minimum LCoE when considering overall power output and structural costs.

LCoE has been estimated using a tool developed in-house at Albatern. A torque limit of 1MNm has been taken as the baseline scenario. Costs for this scenario were estimated based on discussions with the Albatern design team, bringing together knowledge from production and manufacture of the Albatern prototype 6S device and quotes from suppliers.

The different top level categories that have been considered in the cost estimate are shown in Table IV, together with the % contribution to the total whole life cost.

TABLE IV
CATEGORIES AND CONTRIBUTION TO WHOLE LIFE COST

Category	**% contribution to cost**
Structural system	43.8
Mechanical & electrical system	7.5
Mooring system	12.1
Transmission & grid connection	5.7
Installation	12.3
Operations & Maintenance	18.7

For this paper, it is assumed that all costs remain constant except for the structural components listed in Table III. This is a very simplified assumption, as it is likely that the cost of other components such as hydraulic routing cables and accumulators will also vary with PTO torque. However, any additional increases and decreases are likely to exaggerate any variation in LCoE, and therefore this simplification is acceptable at this level of analysis.

Table V shows the cost of each structural subsystem and component for the baseline scenario as a % of the Structural System cost.

TABLE V
SYSTEMS, SUBSYSTEMS AND COMPONENTS OF ARRAY FOR COST PURPOSES

Subsystem / *component*	**% of structural system cost**
Node	44.5
Link element	16.2
Link arm	*14.7*
Fixtures and fittings	*4.7*
Joint module	39.2
Hydraulic cylinder	*7.6*
Support structure	*11.5*
Interface components	*7.1*
Fixtures and fittings	*3.6*
Connection module	9.6

To estimate the costs for each different torque limit, it is assumed that the cost of the steelwork items (which includes all components listed in Table V, except for the hydraulic rams) vary in proportion with the variation in steel weight of the link arm.

Hydraulic cylinder costs have been estimated based on stock cylinder prices as published on the Interfluid website [7]. A multiplier of 4 has been included in the pricing, to account for the increased cost associated with manufacturing bespoke cylinders; this is based on the difference between the quoted stock price and the actual price paid for the cylinders in the Albatern prototype 6S device. The Interfluid stock cylinders are smaller than those required for the 12S device, but prices increase linearly with bore size and stroke, and therefore the prices have been extrapolated as required.

IV. PTO TORQUE LIMITATION: OPTIMISATION RESULTS

A. Power Output Results

Fig. 10 shows the normalised power matrix extrapolated from the unlimited tank testing results over the full range of the West Harris occurrence sea states. Power output is based on the mechanical power capture, and values are given as a percentage of the maximum power output (which occurs when H_s = 10m, and T_p = 11sec).

H_s/T_p	3	4	5	6	7	8	9	10	11	12	13	14	15	16	17	18	19	20	21
10									100%	95%	92%	89%	86%	82%	71%	60%	58%	56%	54%
9.5									94%	89%	86%	83%	81%	74%	63%	56%	54%	52%	50%
9								92%	88%	83%	80%	78%	75%	66%	56%	52%	50%	48%	46%
8.5								86%	82%	77%	75%	72%	68%	59%	49%	47%	46%	44%	43%
8								80%	76%	72%	69%	66%	60%	51%	45%	43%	41%	40%	40%
7.5							78%	74%	70%	66%	63%	60%	53%	44%	41%	39%	37%	37%	37%
7							72%	68%	64%	60%	58%	54%	46%	39%	37%	35%	35%	34%	34%
6.5							67%	62%	59%	55%	52%	47%	40%	35%	33%	32%	32%	32%	32%
6							66%	56%	53%	49%	46%	40%	33%	31%	29%	29%	29%	29%	29%
5.5						84%	63%	50%	47%	43%	40%	34%	29%	27%	26%	26%	26%	26%	25%
5						79%	59%	45%	41%	37%	34%	28%	25%	24%	23%	23%	23%	23%	22%
4.5					58%	64%	54%	41%	35%	32%	28%	23%	21%	20%	20%	20%	20%	19%	18%
4					46%	52%	48%	35%	29%	26%	22%	19%	18%	17%	17%	17%	16%	16%	15%
3.5					36%	40%	39%	29%	23%	20%	17%	15%	15%	14%	14%	13%	13%	12%	11%
3				31%	30%	31%	30%	19%	18%	15%	12%	12%	11%	11%	10%	10%	9%	9%	8%
2.5				24%	23%	23%	21%	17%	13%	10%	9%	9%	8%	7%	7%	6%	6%	5%	5%
2			28%	24%	20%	16%	13%	11%	8%	6%	5%	5%	5%	4%	3%	3%	2%	2%	1%
1.5			13%	12%	11%	9%	8%	6%	5%	3%	2%	2%	1%	0%	0%	0%	0%	0%	0%
1		9%	8%	6%	5%	3%	2%	2%	1%	0%	0%	0%	0%	0%	0%	0%	0%	0%	0%
0.5	5%	3%	2%	0%	0%	0%	0%	0%	0%	0%	0%	0%	0%	0%	0%	0%	0%	0%	0%

Fig. 10 Extrapolated normalised power matrix based on mechanical power captured during tank testing, for unlimited torque case.

In comparison, as an example, the power matrix for the case where torque has been limited to 600kNm (full scale) is shown in Fig. 11. Values are given as a percentage of the maximum power output for the unlimited torque case shown in Fig. 10.

H_s/T_p	3	4	5	6	7	8	9	10	11	12	13	14	15	16	17	18	19	20	21
10									78%	76%	74%	72%	70%	67%	62%	56%	54%	53%	51%
9.5									74%	72%	70%	68%	66%	62%	56%	52%	51%	49%	48%
9								72%	70%	67%	65%	63%	61%	56%	51%	49%	47%	46%	44%
8.5								67%	65%	63%	61%	59%	56%	51%	46%	45%	43%	42%	41%
8								63%	61%	58%	56%	54%	51%	46%	43%	41%	40%	39%	38%
7.5							61%	58%	56%	54%	52%	50%	46%	41%	39%	38%	36%	36%	36%
7							56%	54%	52%	50%	47%	45%	41%	37%	35%	34%	33%	33%	33%
6.5							53%	49%	47%	45%	43%	40%	36%	33%	32%	31%	30%	30%	30%
6							52%	45%	43%	41%	38%	35%	31%	30%	28%	28%	27%	27%	27%
5.5						65%	50%	41%	38%	36%	34%	30%	27%	26%	25%	25%	24%	24%	24%
5						61%	47%	37%	34%	32%	29%	26%	24%	23%	22%	22%	21%	21%	21%
4.5					48%	51%	43%	34%	29%	27%	25%	22%	20%	20%	19%	19%	18%	18%	17%
4					39%	42%	38%	29%	25%	23%	20%	18%	17%	17%	16%	16%	15%	15%	14%
3.5					32%	34%	32%	25%	20%	18%	16%	15%	14%	13%	13%	12%	12%	11%	11%
3				28%	27%	27%	25%	17%	16%	14%	12%	11%	11%	10%	10%	9%	9%	8%	7%
2.5				23%	22%	20%	19%	16%	12%	10%	9%	8%	8%	7%	6%	6%	5%	5%	4%
2			27%	23%	19%	15%	13%	10%	8%	6%	5%	5%	4%	4%	3%	3%	2%	1%	1%
1.5			14%	13%	11%	9%	8%	6%	4%	3%	2%	2%	1%	0%	0%	0%	0%	0%	0%
1		9%	8%	6%	5%	3%	2%	2%	1%	0%	0%	0%	0%	0%	0%	0%	0%	0%	0%
0.5	5%	3%	2%	0%	0%	0%	0%	0%	0%	0%	0%	0%	0%	0%	0%	0%	0%	0%	0%

Fig. 11 Extrapolated normalised power matrix based on mechanical power captured during tank testing, for PTO torque limit = 600kNm

Power matrices as shown in Fig. 10 & 11 have been calculated for several different torque limits, and then combined with the West Harris occurrence matrix to calculate the variation in annual mean energy production (AEP), as shown in Fig. 12. It can be seen from this graph that the increase in AEP is significant between 0 and 0.6MNm, but that there is little increase above 1MNm.

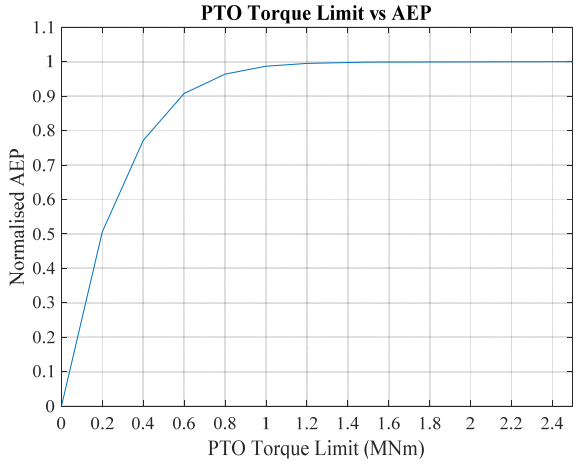

Fig. 12 PTO torque limit (full scale) vs AEP

B. Component Sizing & Costing

1) Hydraulic rams: Table VI shows the required hydraulic cylinder bore size calculated for different PTO torques limits (TL), as described in III.B, together with the estimated cylinder cost.

TABLE VI
HYDRAULIC CYLINDER ESTIMATED SIZE AND COSTS

TL (MNm)	**0.2**	**0.4**	**0.6**	**0.8**	**1**	**1.2**	**1.5**	**2.5**
Bore (mm)	70	100	120	140	160	180	200	250
Cost (1000£)	0.8	1.9	2.5	3	3.5	4.1	4.6	5.9

2) Link Arm: Table VII shows the link arm cross-sectional area (CSA) required to keep fatigue damage accumulation levels below 1 for a life span of 20 years. The table also shows the % variation in required link arm steel weight, when compared to the baseline case.

TABLE VII
REQUIRED LINK ARM CROSS SECTIONAL AREA (CSA)

TL (MNm)	**0.2**	**0.4**	**0.6**	**0.8**	**1**	**1.2**	**1.5**	**2.5**
CSA (cm^2)	50	58	67	79	90	98	102	102
% difference	56	64	74	87	100	109	113	113

3) Device Costs: Cost have been estimated for each of the different torque limits based on the information given in Table VI and VII. For the steelwork items as listed in Table V, it has been assumed that the costs vary in proportion to the required link arm weight.

Fig. 13 shows the variation in costs with PTO torque limit. The Structural costs include all the subsystem as listed in Table V. The total cost includes all systems listed in Table IV (this value was subsequently used to calculate the LCoE) and values have been normalised against the maximum total cost.

These graphs show that generally the structural costs increase with torque limit, however the rate of change slows, with the greatest increase occurring between a torque limit of 0.2 and 1.2MNm. This is because fatigue design is affected by the number of cycles at a particular stress range, not just the magnitude. In any given time period, there will be fewer cycles with larger magnitude loading, and therefore these have less of an impact on the overall design than the smaller magnitude loads, which contribute to a larger proportion of the overall damage. Lower torque limits therefore have a much greater impact on the number of cycles that the structure must endure than the larger torque limits, as they reduce the number of the low stress cycles applied to the device over its lifetime.

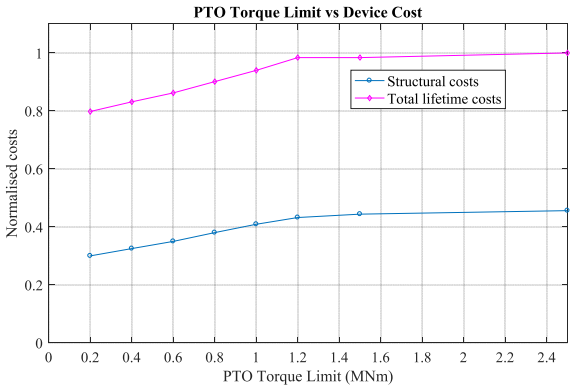

Fig. 13 PTO torque limit (full scale) vs Device Cost to satisfy fatigue design life of 20 years at West Harris site

C. LCoE

LCoE is a function of both device cost and total power production. Fig. 14 shows the variation in cost, AEP and LCoE with PTO torque limit– normalised so that the maximum value of each is taken as 1. It can be seen from this figure that AEP increases rapidly between a torque limit of 0.2 and 0.6 but tends to a limit at around 1.2MNm. Costs continue to increase, but the rate of change slows above 1.2MNm. LCoE therefore shows a significant decrease up to the torque limit of 0.6MNm, and reaches a minimum at 0.8MNm. LCoE then starts to increase again, but at a slower rate than one might instinctively expect, because the rate of cost increase also slows. It should be noted however that this analysis only considers the variation in the cost of the structural items. As noted previously there are likely to be other components which vary in cost with PTO torque, however these differences would likely exaggerate the increase in LCoE for torque limits greater than 0.8kNm, and therefore would not change the overall outcome of the analysis.

This work therefore shows that a torque limit of 0.8MNm would be beneficial, as it results in the lowest LCoE.

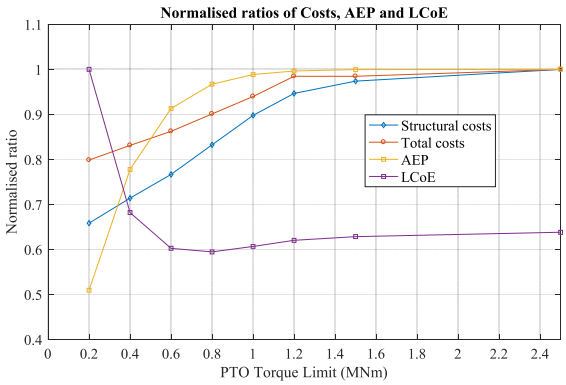

Fig. 14 PTO torque limit (full scale) vs Costs, AEP, and LCoE to satisfy fatigue design life of 20 years at West Harris site

D. *Sensitivity*

The results shown in Fig. 14 are based on a number of assumptions regarding the variation in the cost of the structural elements with PTO torque limit; in particular, that the weight of all steelwork items varies in proportion to the variation in link arm weight. In order to assess the impact of this assumption on the overall results, a sensitivity study has been carried out.

Table VIII below shows the normalised LCOE for two scenarios compared with the base case in Section IV.C

1) the variation in the weight of the additional steelwork items with PTO torque limit is double the variation in link arm weight,
2) The variation in the weight of the additional steelwork items with PTO torque limit is half the variation in link arm weight.

The minimum value of LCOE for each case is highlighted in blue.

TABLE VIII
NORMALISED LCOE VALUES FOR DIFFERENT COST ASSUMPTIONS

TL (MNm)	0.2	0.4	0.6	0.8	1	1.2	1.5	2.5
Basecase	1.00	0.68	0.60	0.59	0.61	0.62	0.63	0.64
Scen. 1	1.00	0.68	0.59	0.58	0.58	0.59	0.60	0.60
Scen. 2	1.00	0.70	0.63	0.63	0.66	0.68	0.70	0.70

The values in table VIII show that the torque limit does vary slightly depending on the assumptions regarding the steelwork cost variation. For the 1st scenario, the minimum LCoE value still occurs at 0.8MNm, but the LCoE at 1MNm is also very similar. For the 2nd scenario, the LCoE which gives the minimum value has shifted to 0.6MNm. While this analysis does not consider the potential variation in all variables, it does indicate that the true value of the optimum LCoE is between 0.6 and 1MNm. This should therefore be taken as the starting point for further detailed PTO design.

V. PTO DAMPING CONTROL IN EXTREME SEA STATES

While the PTO torque limit is a physical constraint that cannot be changed once the device is built, the PTO damping can be varied throughout the life of the device. During the most frequently occurring sea states the damping should be controlled to give the maximum power output. Higher damping levels however result in greater loads, and therefore it may be possible to reduce the damping in more extreme seas to limit the impact on the structure.

While it is not possible at this stage to determine a detailed PTO damping control strategy, the test results do show that reducing damping levels has a significant effect on the peak bending moment experienced by the link arm as shown in Fig. 15. This shows the pitch moment response for a unit wave height across a range of frequencies for different PTO damping levels as measured during the regular wave tests. It can be seen from this figure that the peak load response for a damping level of 500kNms/rad is nearly 40% less than the peak load response for a damping level of 6000kNms/rad, indicating that it should be possible to use damping controls to limit loading in larger seas.

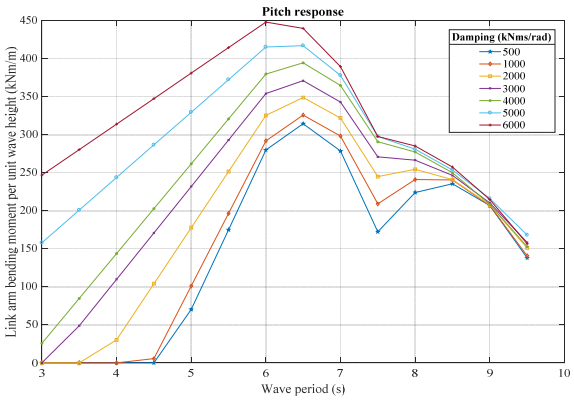

Fig. 15 Pitch response for articulation LA5/S2

The first step in defining a PTO control strategy is to identify appropriate "operational" and "survival" sea states for the device. In the operational state, the machine will be optimised for power extraction. In the survival state, controls will be implemented to facilitate load shedding – no power would be extracted during these sea states.

While the tank testing program was not focussed on extreme storm events it is possible to infer some details about the behaviour of the device in extreme seas from the results, which can then be used as a starting point for design.

Table IX shows the peak pitch bending moment at the LA5/S2 articulation as measured during the tank tests (with unlimited PTO torque, and damping optimised for maximum power output).

TABLE IX
PEAK PITCH BENDING MOMENT (MNM, FULL SCALE)– LA5 / S2

H(m) / T(s)	7.7	9.1	9.9	10.5	11.9	12.6	13.3	14.7
4.5				2.17	1.82			
4								
3.5		2.21		1.84			1.28	
3			1.64			1.34		
2.5	1.62		1.45			0.99		
2	1.34	1.33		1.19		0.89		
1.5	1.03	0.97		0.84			0.69	0.51
1	0.75		0.56					

These results have then been interpolated across the H_s /T_p matrix, up to Hs = 4.5m, which was the highest full scale wave tested in the tank. For larger wave heights and waves close to the breaking limit, the load behaviour will become highly non-linear and therefore a linear extrapolation cannot be applied.

H_s/T_p	3	4	5	6	7	8	9	10	11	12	13	14	15	16	17	18	19	20	21
4.5			2.7	2.7	2.9	3.1	2.7	2.3	2.0	1.8	1.6	1.4	1.2	1.0	0.9	0.9	0.8	0.7	0.6
4			2.4	2.4	2.5	2.6	2.5	2.1	1.9	1.7	1.5	1.2	1.1	0.9	0.9	0.8	0.7	0.6	0.4
3.5		2.1	2.1	2.1	2.2	2.3	2.2	2.0	1.7	1.6	1.4	1.1	1.0	0.9	0.8	0.7	0.6	0.4	0.3
3		1.9	1.9	1.9	1.9	1.9	1.9	1.6	1.6	1.4	1.1	1.0	0.9	0.7	0.7	0.5	0.4	0.3	0.2
2.5		1.6	1.6	1.6	1.6	1.6	1.6	1.4	1.3	1.1	1.0	0.9	0.7	0.6	0.5	0.4	0.3	0.1	0.0
2	1.6	1.6	1.5	1.4	1.4	1.3	1.3	1.2	1.1	1.0	0.8	0.8	0.6	0.5	0.4	0.2	0.1	0.0	0.0
1.5	1.0	1.0	1.0	1.0	1.0	1.0	1.0	0.9	0.8	0.8	0.7	0.6	0.5	0.3	0.2	0.1	0.0	0.0	0.0
1	1.0	0.9	0.9	0.8	0.8	0.7	0.6	0.5	0.5	0.4	0.4	0.4	0.3	0.2	0.1	0.0	0.0	0.0	0.0
0.5	0.7	0.6	0.6	0.5	0.5	0.4	0.3	0.2	0.2	0.2	0.2	0.2	0.2	0.1	0.0	0.0	0.0	0.0	0.0

Fig. 16 Peak pitch bending moment (MNm, Full Scale) – LA5

The matrix in Fig. 16 shows that loading increases with increasing wave height and steepness. It is expected that this trend would be further exaggerated above Hs = 4.5m due to the non-linear behaviour in steeper seas.

As an initial starting point for definition of the "operational" and "survival" sea states, the link arm steel section required to resist the FLS loading (as calculated in Section III.C) has been checked against different applied extreme link arm bending moments. ULS code based checks have been carried out in accordance with Norsok N-004 [8]. The ULS partial load factor has been taken as 2.6. [4] recommends a load factor of 1.3 for environmental loading, but this has been doubled here to account for the significant amount of uncertainties surrounding the analysis method. The graph in Fig. 17 shows the resulting variation in the utilisation factor (U) with applied bending moment.

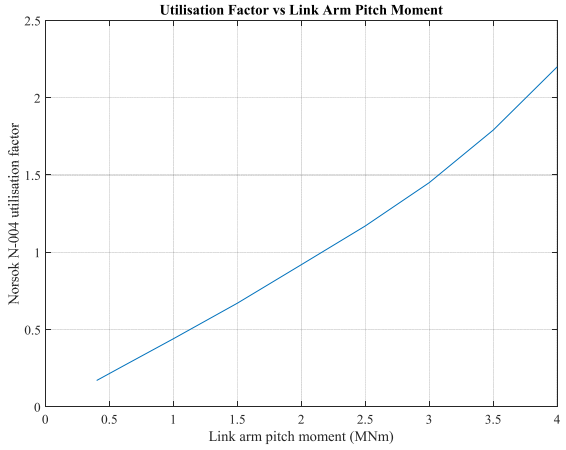

Fig. 17 Utilisation factor vs Link arm Pitch Moment (Full Scale)

This shows that U > 1 for bending moments greater than 2.2MNm. If power production were to take place in sea states where bending moments greater than this value could occur, ULS loading would dominate the design, and the link arm cross sectional area would have to be increased over that required for FLS loading, increasing the overall structural costs and reducing the LCoE.

This criterion has been applied to the bending moments presented in Fig. 16; the sea states where bending moments are greater than 2.2MNm are shown superimposed on the West Harris occurrence matrix shown in Fig. 18, highlighting that they do not occur on a regular basis. If the device was set to be in survival mode during these events to reduce structural loading, this would have a minimal impact on the overall power production capabilities of the device. Using a truncated power matrix, ignoring power generated in the sea states as shown in Fig. 18 reduces the AEP by just 1.5%.

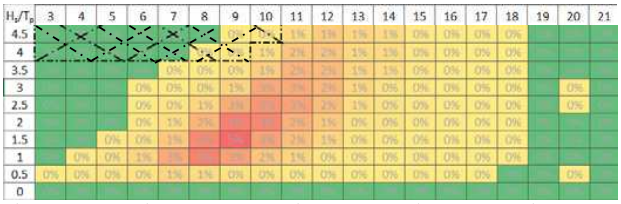

Fig. 18 West Harris Occurrence Matrix. Sea states where ULS requirements > FLS requirements for the design of the link arm are shown in the hatched area.

While the value of this analysis is currently limited by the fact that it is only being carried out for sea states up to Hs = 4.5m, when pitch bending moments are available for higher sea states, the same methodology can then be used to extend the analysis across the full power spectrum, and the actual sea states where ULS loading dominates over FLS loading will be revisited.

At this early stage, the analysis indicates that selecting sea states where ULS loading would dominate over FLS loading as a criterion for defining "survival" and "operational" sea states is an appropriate strategy, as it appears to minimise the loss of power production, while reducing the need for larger, more expensive structural components.

VI. Discussion

A. PTO torque limitation

PTO torque limit has a significant impact on power output, structural design, and the cost of many of the components of a wave energy device, and therefore is it beneficial to highlight the optimum torque limit early in the design process. This paper presents a simple method for this using high level concept design methods and early stage tank testing results. In principle, the method is applicable to other technologies, although would need to be adapted to drivers specific to the working principle of a given device.

However, there are certain limitations to the method presented here; for example, the results are very dependent on the chosen site and array configuration. There would be benefit in extending the analysis to check the sensitivity of the results at other sites and array scales, as it would be advantageous to have a single device design suited to multiple sites and configurations. Also, the analysis only considers the effect of structural costs on LCoE, when other factors (such as the cost of hydraulic and electrical components) will also have an

impact. At this stage, it is assumed that these other factors will follow the same trends as the structural costs, however it will be important to check that this is still valid as the design progresses.

B. PTO damping control and machine state definition

As the tank testing focussed on the behaviour of the device during operational sea states, the validity of the analysis carried out for the ULS loading is limited as it is currently only applied up to Hs = 4.5m. However, the benefit of the work presented here is that it sets out an approach to determine ULS and FLS dominated regions, which can be used to define appropriate "operational" and "survival" sea states. It is valuable to carry this out at an early stage, as it feeds into the development of the PTO design and control strategy, which will need to define appropriate damping settings to allow for maximum power generation in the smaller "operational" seas, and load shedding in larger "survival" seas.

VII. Conclusions

This paper has investigated the relationship between power output and structural loading, looking at the effect of the PTO torque limit on operational loads, and PTO damping controls on extreme loads.

From this work the following conclusions can be drawn:

- The selected PTO torque limit has a significant effect on the fatigue damage accumulated during the lifetime of the device.
- While structural costs continuously increase with increasing PTO torque, the rate of change slows with increasing torque limit. This is because lower torque limits have a greater impact on the amount of fatigue cycles that the device is subject to than higher limits.
- While the optimum torque limit varies depending on the assumptions made during analysis, this study shows that it most likely falls between 0.6 and 1MNm and this should be taken forward as a starting point for the detailed design of the PTO mechanism for the identified site.
- Reduction in PTO damping reduces structural loading, and therefore it can inform a "survival" control strategy to limit structural loading during extreme sea states
- Defining "survival" sea states as those where ULS loading would dominate over FLS loading (which is driven by the "operational" sea states) appears to have a minimal effect on power output, while reducing the need for larger, more expensive structural components. Therefore, this could be an appropriate strategy to adopt for defining the different machine states.

VIII. Further Work

This work uses results from tank testing, which provides detailed information about the behaviour of the device during a limited amount of sea states. The next step in this work is to use the tank testing results to validate the numerical models used for design. These models can then be used to give detailed information about the behaviour in sea states that were not tested, to reduce the uncertainties associated with the interpolation and extrapolation of the tank testing results.

Further testing programmes would also be beneficial to focus on the behaviour of the device during extreme events, and to study the impact of different damping control strategies and torque limitation.

Acknowledgment

This work has been carried out using tank test data with the permission of Albatern Wave Energy. The analysis presented in this paper builds on work carried out by other members of the Albatern team, in particular Vivien Mavel and Anthony McDonald who ran the testing programme and carried out the initial data processing and analysis, and Ciaran Frost who developed the LCoE modelling tool.

Tank testing was funded by Wave Energy Scotland (WES) as part of the Novel Wave Energy Converter Stage 1 (NWEC1) programme.

This work has been carried out as part of the IDCORE programme, funded by the Energy Technology Institute and RCUK Energy programme (grant no. EP/J500847/1)

References

[1] B. Holmes, *Tank Testing of Wave Energy Conversion Systems*, Marine Renewable Energy Guides, EMEC, 2009

[2] *Design of Offshore Steel Structures, General (LRFD Method)*, DNV Offshore Standard, DNV-OS-C101, 2014.

[3] DNV, *Guidelines on Design and Operations of Wave Energy Converters,* Carbon Trust, 2005.

[4] *Fatigue Design of Offshore Steel Structures*, DNV Recommended Practice, DNV-RP-C203, 2011.

[5] J. Schijve, *Fatigue of Structures and Materials,* Springer, 2009.

[6] A. Nieslony, *rainflow.m,* matlab function, Available: http://uk.mathworks.com/matlabcentral/fileexchange/3026-rainflow-counting-algorithm

[7] (2017) Interfluid Hydraulics Ltd website. [Online] Available: https://interfluid.co.uk/store/

[8] *Design of Steel Structures*, NORSOK Standard N-004, rev 3, 2013.

ICOE 2018 12 / 14 JUNE CHERBOURG FRANCE

Advanced concrete materials for offshore floating structures

Leah Barker Ewart[*], Nigel Barltrop[**], Philipp R. Thies[***], Tim Stratford [+]

[*] Industrial Doctorate Centre for Offshore Renewable Energy (IDCORE)
[**] University of Strathclyde
[***] University of Exeter
+ University of Edinburgh

Abstract- Reinforced concrete (RC) is particularly suited for use in the offshore environment and can be more cost effective than using materials such as steel. However, the demands of wave energy converters (WECs) can be difficult to overcome using conventional RC techniques, for example: the minimum wall thickness requirement can make RC structures too heavy for floating WECs with tight buoyancy constraints; post-tensioning is required to prevent concrete cracking which can significantly increase costs; and large, multi-axial dynamic loading regimes can lead to complex reinforcement requirements. This paper investigates the potential for advanced fibre reinforced concretes to overcome these issues, by reducing the need for internal reinforcement; reducing the wall thickness and overall structural mass; and increasing the permeability of the material in the cracked state, which could remove the need for post-tensioning. If advanced concrete mixes can be successfully exploited they offer a significant benefit for floating wave energy converters and other offshore structures. The potential for the use of these materials is investigated through a case study, looking at the design of a Node structure, which is the main buoyancy element of the WaveNET array developed by Albatern. The paper compares the benefits of fibre reinforced concrete designs against baseline designs using conventional materials using finite element models, and shows that fibre reinforced concrete materials can be used to eliminate the requirement for internal reinforcement and post-tensioning required for conventional RC structures, reduce overall structural mass, and lower CAPEX costs.

Keywords- Offshore floating structures, reinforced concrete, fibre-reinforced concrete, CAPEX costs

I. INTRODUCTION

The levelized cost of energy (LCoE) for wave energy needs to reduce to make wave power technologies competitive within the overall energy market. One potential area for cost reduction is the use of cheaper materials such as reinforced concrete (RC) which is particularly suited for offshore structures, as the material has a high resistance to corrosion, a low susceptibility to fatigue failure and offers good strength and stiffness properties at a low unit cost. However, use of the material in the wave industry has currently been limited to nearshore bottom fixed structures such as the Limpet due in part to the demands of wave energy devices which can be difficult to overcome using conventional concrete techniques. In particular:

- Concrete structures tend to be large, with minimum section thicknesses dictated by construction practicalities and durability concerns. This can be an issue for floating structures which need to remain buoyant;
- Concrete is designed to crack under tension to transfer the tensile forces to the internal reinforcement, which can lead to durability issues and leakage. Offshore structures often require post-tensioning to keep the structure in compression, which can significantly increase the capital costs.
- Many wave energy devices need to resist large multi-axial dynamic forces which can lead to complex reinforcement requirements, which is a high cost item for reinforced concrete structures.

This paper investigates the potential for advanced steel fibre reinforced concretes to overcome these issues. Two different types of concrete mix are considered. The first is an Ultra-High-Performance Fibre Reinforced Concrete (UHPFRC) mix with up to 10 times the tensile capacity of plain concrete, which could be used to eliminate the need for internal reinforcement, thereby reducing the wall thickness and overall structural mass. The second is a lower strength Strain Hardening Cement Composite (SHCC) material which exhibits post-cracking strain hardening behaviour, with peak tensile strengths approximately double that of plain concrete. For this type of material, the strain hardening phase is characterised by the formation of multiple micro-cracks before crack localisation. Theoretically the permeability of cracked SHCC materials is the same as the un-cracked material providing that the width of the micro-cracks is kept below

a critical value. If this behaviour can be successfully exploited it could have significant benefit for floating wave energy structures and other offshore structures subject to low tensile stresses, as this could remove the requirement for post-tensioning.

The potential for the use of these materials is investigated through a case study, looking at the design of a Node structure, which is the main buoyancy element of the WaveNET array developed by Albatern. The paper compares the benefits of fibre reinforced concrete designs against baseline designs using conventional materials using results from finite element models and code based structural design methods, and shows that UHPFRC and SHCC materials could successfully be used to eliminate the requirement for internal reinforcement and post-tensioning, and reduce overall structural mass.

II. CASE STUDY OVERVIEW

A schematic of the 12S WaveNET array developed by Albatern is shown in Figure 1. This is a multibody array, made up of Node elements and interconnecting Link Arms, connected with articulated joints which house the Power Take Off (PTO) systems.

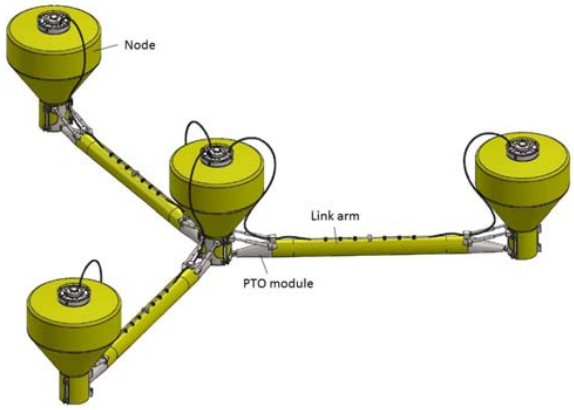

Figure 1 : Schematic overview of 12S WaveNET array

Initial internal studies have shown that reinforced concrete is the preferred material for use for the Node structure, as it offers many techno-economic advantages over other materials such as steel. However, the preliminary design process has highlighted areas where the use of advanced concrete may provide additional benefits, for example:

- UHPFRC could be used in areas of high tensile stress to reduce or eliminate the need for internal reinforcement, and reduce wall thickness and overall structural mass.
- SHCC concrete mixes with enhanced post-cracking properties could eliminate the potential for the development of through thickness cracks, and hence remove the need for post-tensioning

To investigate the potential for these materials, design options have been developed and compared against a baseline reinforced concrete design to see the impact on overall weight, material quantities and cost. These designs are discussed in section IV.

A. Scale effect

In addition to the 12S array as shown in Figure 1, Albatern's growth plan was to develop the WaveNET system on different scales to meet the requirements of different energy markets [1]. This paper also investigates the benefits of using advanced concrete materials at different scales, by looking at design options for a node structure in a "6S" array, which is half the physical size of the 12S, and is developed for off-grid markets such as aquaculture. A comparison of the 12S and 6S array parameters is shown Table 1.

Table 1: Characteristic parameters of WaveNET array scales

Parameter	12S	6S
Rated power per unit	75kW	7.5kW
Design Hs	14m	7m
Distance between nodes	12m	6m

At the 6S scale, it is not possible to use conventional RC for the Node structure due to overall weight and buoyancy constraints. However, fibre reinforced concretes can be used, as thinner wall sections can be achieved. At this scale, advanced concrete materials are therefore compared to steel and Glass Fibre Reinforced Plastic (GFRP) designs. These design options are discussed in Section V.

III. MATERIAL PROPERITES

A. Baseline materials

Depending on the scale, baseline designs are based on a C50 concrete mix with properties as given in DNV-OS-C502 [2], S355-J2 mild carbon steel [3], or a GFRP sandwich construction as described in [4].

B. Advanced concrete materials

Fibre reinforced concretes (FRC) include discrete fibres within the concrete mix to improve the material behaviour, particularly in the post-cracking phase under tensile loads. FRC has increased ductility compared to conventional concrete due to the capacity of the fibres to bridge crack faces. The mechanical characteristics of FRCs vary depending on multiple factors, including (amongst others) fibre volume fraction (v_f), fibre shape, length and aspect ratio, as well as the exact nature of the underlying concrete mix. In general, FRC mixes can be classified as either Steel Fibre Reinforced Concrete (SFRC); Strain Hardening Cement Composites (SHCC) and Ultra High Performance Fibre Reinforced Concrete (UHPFRC). The properties for each are summarised in Table 2.

Table 2: Fibre Reinforced Concrete (FRC) classifications

Type	Typ. v_f	Description
SFRC	<2%	Mix characterised by post-cracking strain softening behaviour, with peak tensile strengths the same as plain concrete. Typical compressive strengths ≤ 50MPa.
SHCC	1.5-2.5%	Mix characterised by post-cracking strain hardening behaviour, with moderate residual tensile strengths up to 2x that of normal strength concrete. Peak strength achieved at high strain levels (4-5%). Typical compressive strengths 50 - 100 MPa
UHPFRC	up to 5%	Mix characterised by immediate post-cracking strain hardening behaviour, with high residual tensile strengths up to 10x that of normal strength concrete. Peak strength achieved at low strain levels (0.5-1%). Typical compressive strengths ≥ 100MPa.

This paper focusses on SHCC and UHPFRC mixes with strain-hardening behaviour, which have increased tensile strength compared with conventional RC. Typical stress-strain curves for these materials are shown in Figure 2. SHCC1 and SHCC2 relate to two different mixes, giving an indication of the range of mechanical properties that can be achieved

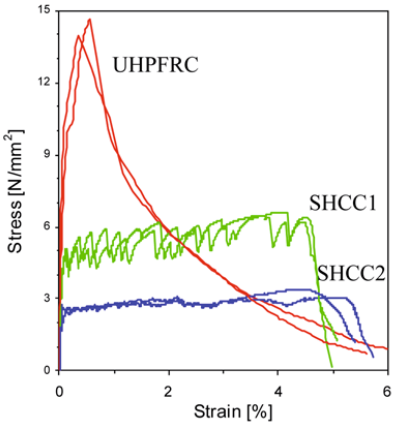

Figure 2 : Typical uniaxial tensile behaviour of different fibre reinforced concrete types [5]

As well as increased peak strengths, one of the major advantages of FRC over conventional RC is the improved cracking behaviour; as steel fibre transfer tensile stresses across cracks, this leads to a reduction in crack widths, therefore improving durability. In addition, SHCC materials are characterised by the formation of micro-cracks before crack localisation, keeping the material permeability low even at relatively high strain levels. The permeability of SHCCs has been investigated by several authors, with the general conclusion being that cracked SHCC has the same permeability as the un-cracked material providing that micro-cracks remain below approximately 60μm [6, 7, 8]. The benefits of using SHCC as a method of seepage control has been recognised by various authors for structures such as tunnels [9], dams [10] and buildings [11], but there is limited research relating to its use in watertight offshore structures, which are subject to more dynamic loading regimes. Low permeability in the cracked state is a particularly useful property and could provide significant benefits for floating wave energy converters and other offshore structures. Thus, the use of SHCC in watertight dynamic structures is an area which warrants further research. For this paper it is assumed that SHCC materials do indeed remain watertight through the strain-hardening phase and can therefore tolerate low levels of tensile stress without the risk of developing through thickness cracks.

The fib Model Code [12] categorises FRC mixes in terms of compressive strength f_{ck}, and residual strength values f_{Fts} (for serviceability loading), and f_{Ftu} (for ultimate loading). In addition, UHPFRC mixes are defined by the peak strength f_{Pt}. These values are typically determined from standard bending tests for design purposes, but in this paper mechanical design properties as shown in Table 3 have been assumed based on typical properties defined in the literature. While there are many different materials that can be used for fibres, the properties for steel fibres are used in this paper, as this is the most common.

Table 3: FRC mix design mechanical properties

Mix	v_f	f_{ck}	f_{Rts}	f_{Pt}	f_{Rtu}
	%	MPa	MPa	MPa	MPa
SHCC	2.5	80	2.0	-	4.5
UHPFRC	5	150	5.5	21.6	6.6

IV. 12S DESIGN

A. Overview

The node structure is designed to take the load components as shown in Figure 3. Pressure loads are calculated based on dynamic Froude-Krylov pressures in accordance with linear wave theory. The PTO loads come from hydrodynamic and physical modelling carried out by Albatern discussed in more detail in [13]. A number of load cases have been assessed covering Serviceability, Ultimate and Accidental limit states (SLS, ULS and ALS) in accordance with [2], with the appropriate factors of safety applied.

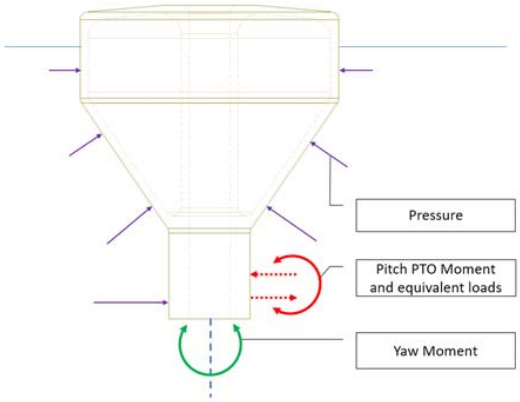

Figure 3 : Node dimensions

Overall dimensions for the node structure and a general schematic of the internal layout are shown in Figure 4. The internal volume is split into two chambers: the top chamber is designed to be fully watertight using post-tensioning of the central column if required to keep the section in compression. Some leakage is allowed in the bottom chamber as it is very difficult to ensure that through thickness cracks will not form in the outer walls in the bottom chamber.

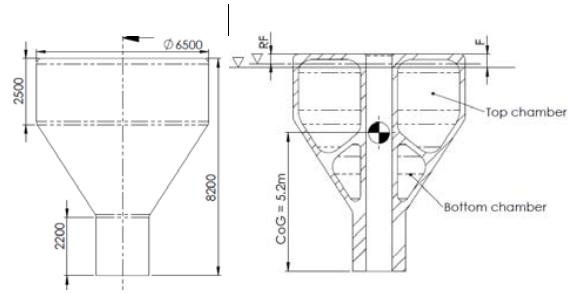

Figure 4 : Node dimensions and internal layout

For design purposes, the section has been split into different sections as shown in Figure 5.

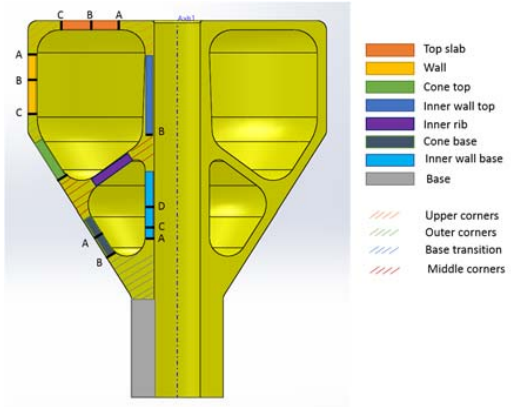

Figure 5 : Node dimensions and internal layout

The design sections fall into three different categories:

- A majority of the structure can be classified as “slab" sections, and designed to resist the applied bending moments and axial forces (with no significant shear forces) in accordance with standard methods as described in design codes such as [2], modified as necessary to allow for FRC materials.
- The varying thickness of the corner and transition sections result in more complex analysis requirements than for the “slab" sections. At this stage it is assumed that the reinforcement requirements for the slabs can be continued through the adjacent corners and transitions, rather than carrying out a separate rigorous analysis, which could lead to less conservative requirements
- The base section is considered as a stand-alone structure, and is designed as a circular column to directly resist the applied PTO bending moments.

Designs have been carried out with the aid of a 3D solid finite element model set up in Abaqus 6.14. A section of the model is shown in Figure 6. The model uses CD820R elements, and assumes linear elastic material properties. While concrete materials (both conventional and advanced) are non-linear, use of linear elastic analysis is standard practice in concrete design, and including full non-linear plastic properties is too complex for this stage of development. Linear elastic analysis gives an upper design solution, as plastic deformations and stress redistribution are not allowed to occur. While this is appropriate at this level of design, the use further non-linear analysis could lead to more economic designs at a later stage.

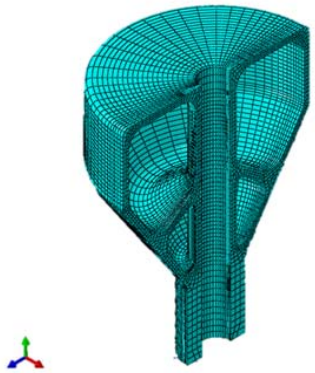

Figure 6 : Abaqus model section

A. Reference concrete design

The conventional concrete design is driven by the following constraints:

- **Minimum wall thickness:** this is a practical constraint, driven by the need to fit in multiple layers of reinforcement, with a suitable concrete cover to ensure reinforcement durability. The minimum wall thickness is taken as 195mm.
- **Crack widths:** cracking in concrete can increase chloride penetration into the structures, leading to corrosion of the internal reinforcement, and can result in leaks, if through thickness cracks develop. The following crack width constraints are imposed (based on the requirements given in [2]) to ensure the durability of the structure:
  - Crack widths are limited to 0.2mm.
  - Watertight sections are designed to have a permanent compression zone to eliminate the possibility of through thickness crack formation.
- **Ultimate capacity:** the structure must be able to resist the ultimate limit state design loads (with a suitable material partial safety factor) without failure.

The final design section thicknesses are shown in Figure 7. 1.5MPa of post-tensioning is required through the central column to keep the walls of the upper chamber in compression.

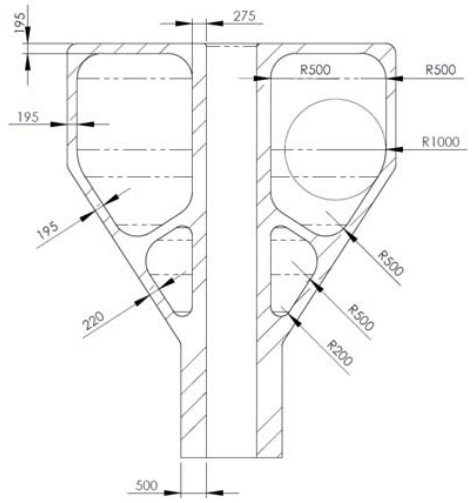

Figure 7 : Reference design dimensions

The reference design highlights the following areas where use of advanced concrete materials may provide additional benefits:

- **Reducing rebar requirements:** There is an area of high stresses at the junction between the base column and the cone section, which results in complex, congested reinforcement (>250kg/m^3) and thicker wall sections which push the structure to the upper limits of buoyancy constraints. This could be improved using UHPRC to increase the tensile strength and ductility of the base concrete material.
- **Reducing wall thickness**: In areas of low stress, the minimum wall thicknesses are the design driver. If FRC mixes were used, it may be possible to reduce the wall thicknesses in these areas, reducing the overall mass.
- **Elimination of the need for post-tensioning**: the tensile stresses that are induced in the watertight chamber are relatively low (~2MPa), therefore it may be possible to use SHCC mixes to increase the permeability of the concrete, and therefore eliminate the need for post-tensioning.

B. Option 1 – UHPFRC

The first design option looks at the potential for using UHPFC with design properties as given in Table 3, to eliminate the need for internal reinforcement. This is possible if the tensile stresses developed in the structure are less than the design strengths of the material. This has been checked by looking at the maximum principal tensile stress (σ_1) in the Abaqus model, with reduced section thicknesses where possible. Table 4 compares this stress with the design limit for both serviceability (SLS) and ultimate loads (ULS). The results show that the principal tensile stress is indeed less than the design limit. These results provide an indication that UHPFRC materials may be used without the use of internal reinforcement, and with reduced section thicknesses as shown in Figure 8.

Table 4: FRC mix design mechanical properties

Limit state	σ_1 MPa	Design limit MPa
SLS	4.4	5.5
ULS	6.6	6.63

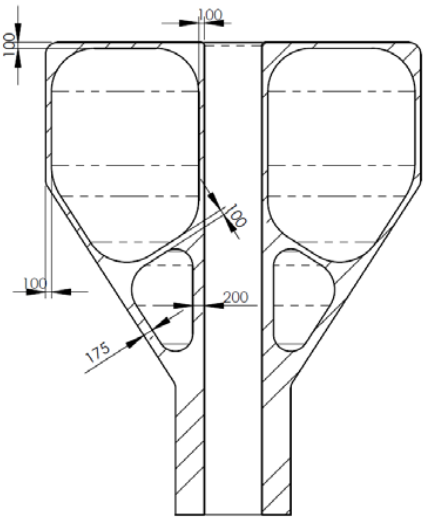

Figure 8 : UHPFRC design dimensions

As for the reference design, post-tensioning is still required to ensure that there is a permanent compressive zone in the upper chamber walls.

C. Option 2 – SHCC

The second design option explores the use of SHCC to eliminate the need for post-tensioning within the structure. It is assumed that this would be possible providing that the principle tensile stress in the upper chamber under the relevant load case is less than the serviceability residual tensile strength for the SHCC material (as given in Table 3). The results from the Abaqus model show that the maximum principal tensile design stress at ULS is 1.9MPa, which is marginally less than the design f_{Rts} for SHCC (2.0MPa), and therefore SHCC can be used without the need for post-tensioning, or internal reinforcement in the upper chamber.

The stresses that occur at the junction between the base column and the cone remain high for this option, and it would be difficult to use SHCC without internal rebar, unless the wall thickness was significantly increased. Therefore, it is preferable to use UHPFRC in this location. This solution gives the final design dimensions as shown in Figure 9. The hatched area shows the approximate extent of the UHPFRC – the exact location of the interface between this and the SHCC would need to be investigated further as part of future design developments.

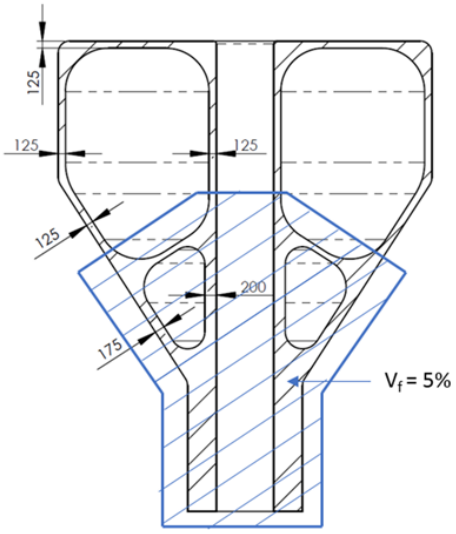

Figure 9 : SHCC + UHPFRC (blue shaded lower area) design dimensions

D. 12S Option comparison

Table 4 shows the material quantities for each of the options. This shows that the reference design is the heaviest, at the upper limits of the buoyancy constraints. Both the UHPFRC and the SHCC option result in lighter sections, and eliminate the need for internal reinforcement, which can reduce overall labour costs and construction time associated with fixing rebar cages. However, the overall steel volume is still greater in both options, compared to the conventional steel option, as a higher volume of fibres is required, compared to the overall volume of steel reinforcement.

Table 5: 12 S Design options material quantities

Quantity	Reference	UHPRFC	SHCC
Concrete mass (te)	109	78	93
Steel rebar (te)	4	-	-
Post-tensioning (MPa)	1.5	1.5	-
Fibre volume (te)	-	12.3	9.5

E. 12S - Cost Estimates

To carry out a quantitative comparison capital costs have been estimated based on the material quantities shown in Table 4. Cost rates are based on industry quotations, literature values and rates provided in construction handbooks such as Spon's [14]. At this level of design there are significant levels of uncertainty associated with the estimates, therefore optimistic and pessimistic costs are shown included. The cost estimates provided in Figure 10 are presented as a multiplier of the baseline cost for the reference option. Conventional concrete is the most well-known material, and therefore the cost for the reference options varies less than for the FRC options.

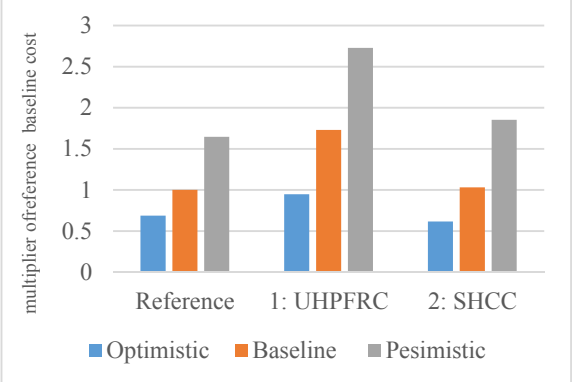

Figure 10 : 12S Option costs as a multiplier of the reference baseline cost

Figure 10 shows that for the baseline cost estimate, the reference design is cheaper than the other options, indicating that where there is a viable conventional concrete design, it is likely to be cheaper than using more advanced materials. However, this does depend on the assumptions made; for example, the optimistic estimate for both the UHPFRC and the SHCC option are cheaper than the reference design baseline cost, with the SHCC option showing a significant reduction, driven primarily by the elimination of the post-tensioning, and to a lesser extent

the reduction in labour cost and construction time associated with the removal of the internal reinforcement. Further design refinements may show that the overall volume of fibres can be reduced, or cheaper, lower strength SHCC can be used over a larger area of the structure, making this option more attractive.

V. 6S DESIGN

A. Overview

As discussed in Section II.A, the 6S design is a half scale version of the 12S array. It is not possible to use conventional RC at this smaller scale due to overall weight and buoyancy restrictions; however, it is possible to use an FRC mix. To look at the potential advantage of this against other materials, three designs have been considered:

1. SHCC mix with fibre volume fraction = 2.5%
2. Carbon steel with characteristic yield strength = 355MPa
3. Glass fibre reinforced plastic (GFRP) sandwich construction with characteristic strength = 370MPa, as shown in Figure 11.

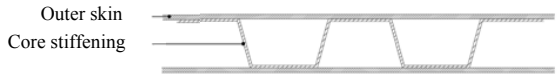

Figure 11 : 12S Option costs as a % of the reference baseline cost

The 6S is ½ the physical dimensions of the of the 12S array (with a length scale L), designed to resist a design wave (Hs) that is ½ the height of the design wave for the 12S structure. Therefore, design actions have been multiplied by a factor of 8 (as the design actions are proportional to □(H. L^2)).

B. SHCC design

The SHCC design has been carried out using the same methodology for the 12S device. The final design dimensions for this option are shown in Figure 12. It can be seen that the use of FRC material allows a much thinner wall thickness than could be achieved using conventional concrete.

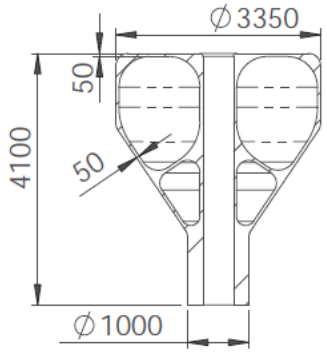

Figure 12 : 6S SHCC design dimensions

C. GFRP and Steel design

For the steel and GFRP options a simple design check has been carried out, based on the combined bending and axial resistance of a particular section. While there are other factors that would need to be considered for a detailed design (e.g. fatigue loading, shear and buckling effects), this gives sufficient information for the preliminary sizing and to allow a comparison between design options. A schematic for an optional design is shown in Figure 13.

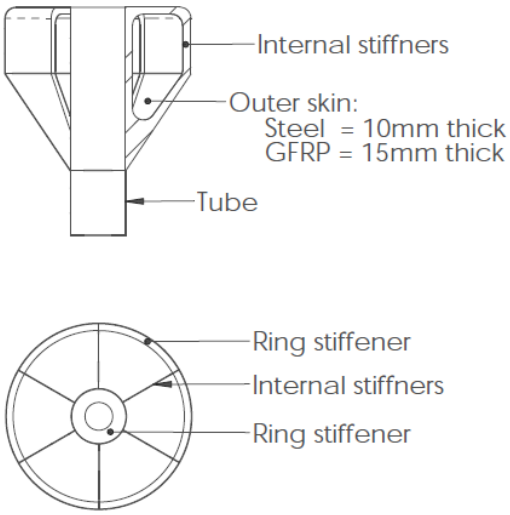

Figure 13 : Steel / GFRP option schematic

D. Option comparison

Cost estimates have been developed based on the quantities given in Table 6. The steel and GFRP options are significantly lighter than the SHCC section, therefore ballast is included to bring all options up to the same weight. The steel option includes a cost for coating as steel is susceptible to corrosion in the marine environment. The cost comparison is shown in Figure 14, with costs presented as a multiplier of the SHCC baseline cost.

Table 6: 6S Design options material quantities

Item	Quantity
SHCC	
Formwork	126 m^2
SHCC	3.9 m^3
Steel fibre @ 2.5%	0.76 te
Steel	
Base tube	1 te
Steel fabrication	3.2 te
Coating	109 m^2
Ballast	5.8 te
GFRP	
Base tube	0.1 te
GFRP fabrication	0.7 te
Ballast	9.2 te

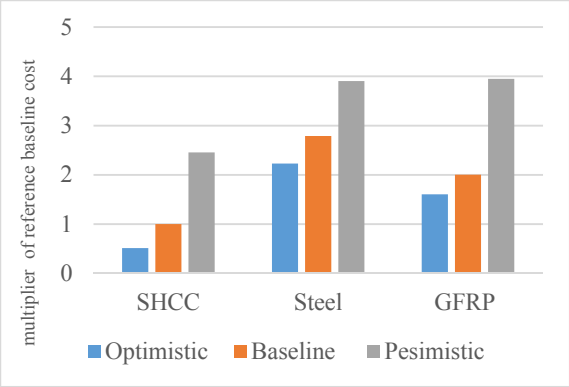

Figure 14 : 6S Option costs as a multiplier of the SFRC baseline cost

Figure 14 shows that the SHCC option is significantly cheaper than either the steel of the GFRP options, even considering the optimistic assumptions. This shows that the use of advanced FRC materials could offer significant benefits in situations where additional constraints exist such as weight and buoyancy restrictions.

VI. DISCUSSION AND CONCLUSIONS

This paper has shown that advanced fibre reinforced concrete materials with increased tensile strength and improved post-cracking behaviour can theoretically be used in place of conventional concrete to reduce structural mass and reduce the need for internal reinforcement. It may also be possible to exploit the superior permeability characteristics of strain hardening mixes to eliminate the need for post-tensioning.

In normal design conditions, where a conventional reinforced concrete solution is possible, this conventional design is likely to be cheaper than using more advanced materials. However, in situations with exceptional design constraints which push the limits of conventional concrete design, FRP materials can offer significant economic as well as technical benefits, particularly when compared to other materials such as steel or GFRP. The cost of FRC materials increases with increasing fibre volume and base concrete compressive strength. Therefore, they offer the greatest cost benefit in situations with low tensile stress, where lower fibre volumes can be used to improve the post-cracking behaviour and permeability, without needing a significant improvement in tensile strength.

The findings of this paper are based on assumptions surrounding the behaviour of FRC materials which would need to be proved through a material testing programme. The paper provide justification for such a programme to be carried out, as if FRC can be successfully exploited for dynamic, floating, watertight structures this could have significant benefits both for wave energy converters and other structures in the wider offshore industry.

ACKNOWLEDGMENT

Work has been carried out as part of the IDCORE programme, funded by the ETI and RCUK Energy programme (grant no. EP/J500847/1) Work has been carried out alongside the “Advanced Concrete Engineering for Wave Energy Converters” project (ACE-WEC), funded by Wave Energy Scotland, led by Quoceant.

REFERENCES

[1] Albatern Ltd “Technology Development” http://albatern.co.uk/wavenet/technology-development/
[2] DNV, “DNV-OS-C502 Offshore Concrete Structures,” 2012.
[3] BSI, “BS EN 10025-1 Hot rolled products of structural steels, General technical conditions”, 2004
[4] Pelamis Wave Power, “WEC-main body structural design and materials selection”, (V/06/00197/00/00/REP - DTI URN 03/1439). 2003.
[5] G.P.A.G van Zijl, W.P Boshoff, “Mechanisms of creep in fibre-reinforced Strain-Hardening Cement Composites (SHCC)” in Crrep, Shrinkage and Durability Mechanics of Concrete and Concrete Structures, Tanabe Ed. London: Taylor & Francis, 2009.
[6] Michael D Lepech and Victor C Li. “Water permeability of engineered cementitious composites”. Cement and Concrete Composites, 31(10):744-753, 2009.
[7] C-M Aldea, Surendra P Shah, and A Karr. “Permeability of cracked concrete. Materials and structures”, 32(5):370-376, 1999.
[8] Gideon PAG van Zijl. “Durability under mechanical load - micro-crack formation (ductility)”.In Durability of Strain-Hardening Fibre-Reinforced Cement-Based Composites (SHCC)”, pages 9-39. Springer, 2011.
[9] B Maidl and J Dietrich. “Verification of serviceability for SFRC in tunnelling”. Structural Engineering International, 2(2):114{117, 1992.
[10] H. Liu, Q. Zhang, C. Gu, H. Su, and V. C Li. “Influence of microcracking on the permeability of engineered cementitious composites”. Cement & Concrete Composites, 72:104-113, 2016.
[11] J Yu, H Li, C KY Leung, X Lin, J YK Lam, I ML Sham, and K Shih. “Matrix design for waterproof engineered cementitious composites (ECCS)”. Construction and Building Materials, 139:438-446, 2017.
[12] Federation Internationale du Beton. “fib Model Code for concrete structures 2010”. Berlin, Germany, 2013.
[13] L Barker Ewart, P T Theis, T Stratford, N Barltrop “Optimising structural loading and power production for floating wave energy converters” in proceeding of EWTEC 2017.
[14] Spon’s “Civil Engineering and Highway Works Price Book” 2018

AUTHORS

Correspondence Author – Leah Barker Ewart, l.ewart@ed.ac.uk.

Appendix B

FRC material properties from the literature

Section 3.2.3 in the literature review discusses different theoretical equations derived to predict the mechanical properties of FRC material based on different mix characteristics. Table B.1 summarises results of various experiments carried out to determine the mechanical properties of different mixes, and compares the measured values against those predicted using three different equations presented in the literature for determining the peak flexural strength of FRC materials.

The three different equations used for comparison are as follows:

[1] $\sigma_{bf} = \sigma_{bf0}(1 - v_f) + 0.307 v_f (l_f/d_f)$ (Kang et al., 2010)

[2] $f_{fl} = 0.97(f_{cu})^{0.5} + 0.295(f'_{cu})^{0.5} RI + 1.117 RI$ (Thomas and Ramaswamy, 2007)

[3] $f_{tk} = (0.48 + 0.1v)(f_{cck})^{0.5}$ (DNV, 2012)

Notation used in the table is defined as follows:

f_{cu}	compressive strength of plain concrete
l	fibre length
l/d	fibre length to diameter aspect ratio
v_f	volume fraction
RI	ratio index = $v_f.l/d$
$f_{cu,f}$	compressive strength of fibre
f_{st}	splitting strength
$f_{f,fc}$	flexural strength (first crack)
$f_{f,l0}$	flexural strength - base concrete
f_{fl}	flexural strength (modulus of rupture)

Table B.1: Summary of experimentally derived mechanical properties of FRC from literature, and comparison with theoretical predictions

					Reported values from literature [Mpa]					f_{fl} predictions			Predicted / measured f_{fl}			Reference
f_{cu}	l	l/d	v_f	RI	$f_{cu,f}$	$f_{f,fc}$	f_{st}	$f_{f,l0}$	f_{fl}	eq [1]	eq [2]	eq [3]	[1] / f_{fl}	[2] / f_{fl}	[3] / f_{fl}	
50	30	0	0		50.0		4.06	5.94	5.9	5.94	6.86	3.39	1.0	1.2	0.6	Yazici *et al* (2007)
50	30	45	0.5	0.225	50.8		4.50	5.94	6.1	9.88	7.58	3.75	1.6	1.2	0.6	
50	30	45	1	0.45	53.7		4.69	5.94	6.3	13.82	8.30	4.10	2.2	1.3	0.6	
50	30	45	1.5	0.675	57.7		5.69	5.94	7.8	17.75	9.02	4.45	2.3	1.2	0.6	
50	60	65	0.5	0.325	53.5		4.51	6.24	6.2	13.10	7.90	3.75	2.1	1.3	0.6	
50	60	65	1	0.65	58.3		4.77	6.24	8.1	19.96	8.94	4.10	2.5	1.1	0.5	
50	60	65	1.5	0.975	56.4		6.26	6.24	9.3	26.81	9.98	4.45	2.9	1.1	0.5	
50	60	80	0.5	0.4	56.0		4.58	6.42	6.4	15.49	8.14	3.75	2.4	1.3	0.6	
50	60	80	1	0.8	58.3		5.18	6.42	9.7	24.56	9.42	4.10	2.5	1.0	0.4	
50	60	80	1.5	1.2	52.1		5.90	6.42	10.8	33.63	10.70	4.45	3.1	1.0	0.4	
80	50	80	0	0	80.1	5.7		5.7	5.7	5.70	8.68	4.29	1.0	1.5	0.8	Bencardino (2013)
80	50	80	1	0.8	80.5	7.6		5.7	12.5	24.56	11.68	5.19	2.0	0.9	0.4	
80	50	80	2	1.6	78.2	7.7		5.7	15.3	43.42	14.68	6.08	2.8	1.0	0.4	
100	13	65	0	0	100			18	18.0	18.00	9.70	4.80	1.0	0.5	0.3	Yu *et al* (2014)
100	13	65	0.5	0.325	115			18	19.8	18.98	11.02	5.30	1.0	0.6	0.3	
100	13	65	1	0.65	125			18	21.7	19.96	12.34	5.80	0.9	0.6	0.3	
100	13	65	1.5	0.975	135			18	24.1	20.93	13.67	6.30	0.9	0.6	0.3	
100	13	65	2	1.3	145			18	27.0	21.91	14.99	6.80	0.8	0.6	0.3	
100	13	65	2.5	1.625	155			18	33.5	22.89	16.31	7.30	0.7	0.5	0.2	

Table B.1 Continued

					Reported values from literature [Mpa]					f_{fl} predictions			Predicted / measured f_{fl}			Reference
f_{cu}	l	l/d	v_f	RI	$f_{cu,f}$	$f_{f,fc}$	f_{st}	$f_{f,l0}$	f_{fl}	eq [1]	eq [2]	eq [3]	[1] / f_{fl}	[2] / f_{fl}	[3] / f_{fl}	
125	35	0	0	0	124	14.0	11.50	16	16.0	16.00	10.84	5.37	1.0	0.7	0.3	Eldin *et al* (2014)
125	35	30	1	0.3	137	12.8	12.73	16	16.8	9.21	12.17	6.48	0.5	0.7	0.4	
125	35	30	2	0.6	145	12.8	15.59	16	19.2	2.42	13.49	7.60	0.1	0.7	0.4	
125	35	30	3	0.9	151	13.4	17.82	16	21.6	-4.37	14.82	8.72	-0.2	0.7	0.4	
125	35	50	1	0.5	141	12.0	15.40	16	18.0	15.35	13.05	6.48	0.9	0.7	0.4	
125	35	50	2	1	147	13.2	17.45	16	20.0	14.70	15.26	7.60	0.7	0.8	0.4	
125	35	50	3	1.5	154	13.6	19.10	16	22.4	14.05	17.47	8.72	0.6	0.8	0.4	
35	30	55	0	0	36.6		3.93	5.20	5.2	5.20	5.27	2.84	1.0	1.0	0.5	Thomas and
35	30	55	0.5	0.275	37.0		4.37	5.2	6.0	11.04	6.07	3.14	1.8	1.0	0.5	Ramaswamy (2007)
35	30	55	1	0.55	37.5		4.87	5.2	6.8	16.89	6.86	3.43	2.5	1.0	0.5	
35	30	55	1.5	0.825	37.9		5.43	5.2	7.6	22.73	7.66	3.73	3.0	1.0	0.5	
65	30	55	*0*	0	66.6		5.19	7.2	7.2	7.20	7.11	3.87	1.0	1.0	0.5	
65	30	55	0.5	0.275	67.1		5.81	7.2	8.0	12.04	8.08	4.27	1.5	1.0	0.5	
65	30	55	1	0.55	67.5		6.49	7.2	9.2	16.89	9.05	4.68	1.8	1.0	0.5	
65	30	55	1.5	0.825	68.4		7.33	7.2	10.0	21.73	10.01	5.08	2.2	1.0	0.5	
85	30	55	*0*	0	86.1		5.76	8	8.0	8.00	8.08	4.43	1.0	1.0	0.6	
85	30	55	0.5	0.275	86.5		6.48	8	9.2	12.44	9.14	4.89	1.4	1.0	0.5	
85	30	55	1	0.55	87.0		7.20	8	10.4	16.89	10.20	5.35	1.6	1.0	0.5	
85	30	55	1.5	0.825	88.3		7.98	8	11.2	21.33	11.26	5.81	1.9	1.0	0.5	
150	13	65	1	0.65				8.88	20.0	19.96	14.95	7.10	1.0	0.7	0.4	Kang *et al* (2010)
150	13	65	2	1.3				8.88	31.0	31.03	18.03	8.33	1.0	0.6	0.3	
150	13	65	3	1.95				8.88	42.1	42.11	21.10	9.55	1.0	0.5	0.2	
150	13	65	4	2.6				8.88	53.2	53.18	24.18	10.78	1.0	0.5	0.2	
150	13	65	5	3.25				8.88	64.3	64.26	27.25	12.00	1.0	0.4	0.2	

Appendix C

Unit costs for LCoE calculation

Chapter 7 calculates the optimum torque limit based on minimising Levelised Cost of Energy LCoE. The LCoE is based on assumptions of costs for the various components, which have been determined based on discussions with the Albatern design team, bringing together knowledge from production and manufacture of the Albatern prototype 6S device, and quotes from suppliers. These baseline costs (for an assumed torque limit of 1 MNm) are shown in Table C.1.

Table C.1: Assumed unit costs for LCoE calculation, for a torque limit of $1\,\mathrm{MNm}$

Project Area	Component	Sub-component	Unit Cost	Unit	Parent	Overall	Multiplier	Per Parent	Total System
Structural					1		1		£572,220
	Sunken Node	Sunken Node			3	3	1	£34,980	£104,940
		Sunken Node	£15,000	Unit	1	3		£15,000	£45,000
		Hitch Post	£5,600	Unit	3	9		£16,800	£50,400
		Fixtures and Fittings	£3,180	Set / Skn Node	1	3		£3,180	£9,540
	Top Node	Top Node			9	9	1	£34,980	£314,820
		Top Node	£15,000	Unit	1	9		£15,000	£135,000
		Hitch Post	£5,600	One off item	3	27		£16,800	£151,200
		Fixtures and Fittings	£3,180	Set / Top Node	1	9		£3,180	£28,620
	Link Arm	Link Arm			9	9	1	£169,400	£152,460
		Link Arm	£12,000	Unit	1	9		£12,000	£108,000
		M Boss	£850	Unit	4	36		£3,400	£30,600
		Fixtures and Fittings	£1,540	Set / Link Arm	1	9		£1,540	£13,860
Mechanical & Electrical					1		1		£523,318
	Pumping Module (PM)	Pumping Module (PM)			18	18	1	£20,060	£361,073
		Hydraulic Cylinder	£3,536	Unit	1	18		£3,536	£63,648
		Node Wing	£6,000	Unit	1	18		£6,000	£108,000
		Spherical Bearing	£350	Unit	2	36		£700	£12,600
		Pins	£200	Unit	6	108		£1,200	£21,600
		Bushes	£450	Unit	4	72		£1,800	£32,400
		Hitch Clamp	£5,000	Unit	1	18		£5,000	£90,000
		Fixtures and Fittings	£1,824	Set / PM	1	18		£1,824	£32,825
	Hydraulic Routing Module (HRM)	Hydraulic Routing Module (HRM)			3	3	1	£11,000	£33,000
		Hydraulic Routing Module	£10,000	Unit	1	3		£10,000	£30,000
		Fixtures and Fittings	£1,000	Set / HRM	1	3		£1,000	£3,000

Table C.1 Continued

Project Area	Component	Sub-component	Unit Cost	Unit	Parent	Overall	Multiplier	Per Parent	Total System
	PTO Module	PTO Module			3	3	1	£8,965	£26,895
		Hydraulic Motor	£1,250	Unit	1	3		£1,250	£3,750
		Generator (PM)	£600	Unit	1	3		£600	£1,800
		Hydraulic Manifold Block	£1,000	Unit	1	3		£1,000	£3,000
		Cooling	£300	Unit	1	3		£300	£900
		Casing	£5,000	Unit	1	3		£5,000	£15,000
		Fixtures and Fittings	£815	Set / PTO	1	3		£815	£2,445
Mechanical & Electrical (cont.)	Electric Routing Module (ERM)	Electric Routing Module (ERM)			3	3	1	£8,250	£24,750
		Switchgear	£2,000	Unit	1	3		£2,000	£6,000
		Casing	£5,500	Unit	1	3		£5,500	£16,500
		Fixtures and Fittings	£750	Set / ERM	1	3		£750	£2,250
	Data Monitoring Systems	Data Monitoring Systems			3	3	1	£4,000	£11,000
		Labjack T7 Pro	£500	Unit / Skn Node	1	3		£500	£1,500
		Monitoring Systems & Sensors	£3,000	Set / Skn Node	1	3		£3,000	£9,000
		Data Monitoring Station	£500	Unit	1	1		£500	£500
	Dynamic Umbilical	Dynamic Umbilical			3	3	1	£9,000	£27,000
		Intra-Array with plugs	£9,000	Set / Skn Node	1	3		£9,000	£27,000
	Buoyancy Control Module (BCM)	Buoyancy Control Module(BCM)			12	12	1	£3,300	£39,600
		Buoyancy Control Module	£3,000	Unit	1	12		£3,000	£36,000
		Fixtures and Fittings	£300	Set / ERM	1	12		£300	£3,600
Mooring System						1	1		£261,220
	Mooring Leg	Mooring Leg			3	3	1	£46,770	£140,311
		Anchor (10t)	£15,000	Unit	1	3		£15,000	£45,000
		Anchor shackles	£276	Unit	2	6		£552	£1,656
		Chain	£4,223	Shot (27.5m)	7	21		£29,561	£88,683
		Joining shackles	£276	Unit	6	18		£1,657	£4,972
	Mooring Grid	Mooring Grid			1	1	1	£120,909	£120,908.55
		Mooring Buoys (10T)	£37,308	Unit	3	3		£111,924	£111,924
		Mooring line	£2,995	Unit	3	3		£8,985	£8,985
Transmission & Grid						1	1		£121,944
	Seabed Cable	Seabed Cable			2	2	1	£60,000	£120,000
		20kV Single core cable	£20,000	Km	3	6		£60,000	£120,000
	Onshore Works/Equipment	Onshore Works/Equipment			1	1	1	£3,888	£1,944
		Cable Landfall Civils	£264	Unit	1	1		£264	£264
		Inverter & Electrical systems	£1,680	Set	1	1		£1,680	£1,680

Appendix D

Material selection

D.1 Material index derivation for base cylinder

Section 9.1.5 presents the material selection indices for the node cylinder. This section provides the derivation for these indices. Again the objective functions are to minimise mass (Equation D.1) or minimise cost (Equation D.2).

$$m = \pi DtL\rho \tag{D.1}$$

Where D = diamater, t = wall thickness, L = length, and ρ = material density.

$$m = \pi DtL\rho C_m \tag{D.2}$$

Where C_m is the unit cost / mass of material.

D.1.1 Strength

For a thin walled cylinder, we want to keep the wall stress due to bending less than the material yield (or failure) stress, based on the bending theorum: .

$$\frac{M_b}{I} = \frac{\sigma}{y} \tag{D.3}$$

Where: M_b = bending moment

I = Second moment of area, for a thin walled cylinder: $(D^3 t\pi)/8$

y = distance to outer fibre: $y = D/2$

σ = maximum stress in cylinder

Equating these equations gives:

$$M_b < \frac{(D^2 t\pi)}{4}\sigma_f \tag{D.4}$$

Where σ_f is the failure stress of the material. Diameter D is a fixed quantity, but we can vary thickness t. Arranging Equation D.4 to be in terms of wall thickness t gives:

$$t = \frac{4M}{D^2\pi}.\frac{1}{\sigma_f} \tag{D.5}$$

Replace t in Equation D.1, with Equation D.5, to give first constraint equation:

$$m_1 = 4M_b.\frac{L}{D}.\frac{\rho}{\sigma_f} \tag{D.6}$$

M_b, L, and D are fixed quantities, therefore to minimise mass, we want a minimum value of ρ/σ_f. In general for the material indices we look for values we can maximise, therefore the material index for strength at minimum mass is as follows:

$$MI_s = \frac{\sigma_f}{\rho} \tag{D.7}$$

If we want strength at lowest cost, we can divide Equation D.7 by C_m, to give:

$$MI_s = \frac{\sigma_f}{\rho.Cm} \tag{D.8}$$

D.1.2 Buckling stiffness

As the cylinder bends there is the potential for it to fail in buckling, rather than yield, which is governed the stiffness of the material. For a long elastic cylinder, the critical buckling moment is given by the following equation:

$$M_{crit} = K.\frac{E}{1-\nu^2}.\frac{D}{2.t^2} \tag{D.9}$$

Where K is a constant related to the applied loading conditions, (0.99 for pure bending, and 0.72 as minimum), E is the modulus, ν is the Poisson's ratio.

Rearranging for t gives the following equation:

$$t = \sqrt{\frac{2M_{crit}}{K}.(1-\nu^2).\frac{1}{D}.\frac{1}{E}} \tag{D.10}$$

Replacing t in Equation D.1 with Equation D.10 gives the second constraint equation:

$$m_2 = \sqrt{\frac{2M_{crit}}{K}/K.(1-\nu^2)}.(\pi D^{0.5}L).\frac{\rho}{\sqrt{E}} \tag{D.11}$$

Note that the formulation of the equation in this way assumes that the Poisson's ratio for each of the materials we are likely to consider is roughly similar, and therefore is considered to be a constant. If we want to minimise m_2, we want to maximise the following index (for a given diameter and length):

$$MI_b = \frac{\sqrt{E}}{\rho} \tag{D.12}$$

If we want stiffness at lowest cost, we can divide by Cm in the same way as before.

$$MI_b = \frac{\sqrt{E}}{\rho.C_m} \tag{D.13}$$

D.2 Material assessment

Table D.1 gives an assessment of the different short listed materials presented in Section 9.1.7 against the qualitative design requirements set out in Table 9.1.

Table D.1: Summary of material parameters

Criteria	Concrete	Steel	Aluminium	Wood	Cast Iron
History of use in marine environment?	Yes- many offshore oil / gas platforms	Yes- main material in ship building	Yes- ships, leisure crafts, lightweight topsides for offshore structures, Seatricity wave energy device	Yes- historical use for ships / boats/ marine jetties / piers. Modern uses in boats for wood epoxy laminates	Yes
Fatigue properties	Good - better general fatigue performance than steel	Fair - Can be poor depending on details, but well understood	Poor - Lower fatigue strength than steel	Poor	Fair - providing areas of stress concentration are limited
Ductility	Fair - Ductility is provided by adequate reinforcement detailing	Good	Good	Fair	Fair - but lower ductility than structural steel
Impact resistance	Poor - but can be improved through appropriate steel detailing	Good	Good	Fair	Fair

Continued on next page

Table D.1 – continued from previous page

Criteria	Concrete	Steel	Aluminium	Wood	Cast Iron
Manufacturability	Good - can be easily formed into complex shapes	Fair - can be fabricated into complex shapes, fabrication is labour intensive (more expensive)	Fair - similar to steel.	Ok - reasonably flexible, but labour intensive to form into complex shapes	Can be made into any shape, but limits on size of casting. Size of node would be well beyond limits
Availability of manufacturers	Very few limits on manufacturing location; can be made on site, reducing transportation requirements	Good, but will generally need transported from place of fabrication to location	Fair	Limited for complex shapes	Very limited for large scale structures
Ease of repair	Generally ok - can repair cracks	Good	Good	Ok	Ok

Continued on next page

Table D.1 – continued from previous page

Criteria	Concrete	Steel	Aluminium	Wood	Cast Iron
Ease of connection to steel link arm	Various methods of steel / concrete connection available, but would require careful detailing, to ensure robust section able to take multi-axial dynamic loads.	Good - welding / bolting and pin joints all well-established steel connection methods	Have to be very careful with dissimilar metals - due to galvanic corrosion issues	Various methods of wood/ steel connection available, but would require careful detailing	Good - bolting and pin joints well established methods of connection
Corrosion resistance	Good, providing suitable mix design is used, and good quality control	Poor - would require coating	Very susceptible to galvanic corrosion	Doesn't corrode but does have other issues in sea water	Poor - would require coating
Watertight	Yes - providing crack widths are adequately controlled	Yes	Yes	Lots of joints required for wood structures - potential for leaks	Yes
Water absorption	Very little	None	None	Requires treatment	None
Resistant to UV	Yes	Yes	Yes	Yes	Yes

Continued on next page

Table D.1 – continued from previous page

Criteria	Concrete	Steel	Aluminium	Wood	Cast Iron
Resistant to bio-fouling	No, but no worse than other materials	No, but no worse than other materials	No, but no worse than other materials	Susceptible to marine borers if not treated correctly	No, but no worse than other materials
Chemically inert	Yes	Yes	Yes	Yes	Yes
Consider further?	**Yes**	**Yes**	No - Has potential, but difficulties with fatigues and galvanic corrosion are concerns.	No - difficulties with forming into watertight large complex shapes	No - due to size limitations

D.3 Techno-economic study, preliminary design

Section 9.2 presents the preliminary design options for the 12S node, looking at reinforced concrete and steel options. The following sheets set out the preliminary structural analysis for these options.

D.3 Preliminary design RC concrete option, page 1 of 2

Section definition

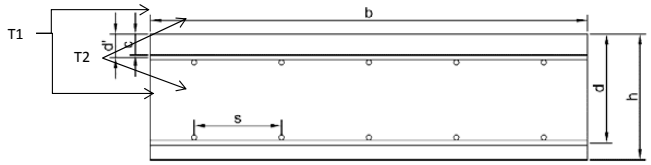

User input values are in blue
Values from code are in purple

Section overview			Ref
Description	Units	Hoop	
Section loads			
Ultimate Moment per meter width (M_{Ed})	kN.m	30	
Serviceability Moment per meter width ($M_{Ed'}$)	kN.m	20.00	
Shear force due to ultimate loads (V_{Ed})	kN		
Axial force due to ultimate load (N_{Ed})	kN	0	Ignore compressive stress (reduces overall crack widths)
Axial force due to servicability load ($N_{Ed'}$)	kN	0	
Section geometry			
Breadth of concrete section (b)	mm	1000	
Overall depth of concrete section (h)	mm	200	
Diameter of tension bars (dia_t)	mm	16	
Spacing of tension bars (s_t)	mm	175	
Area of tension steel provided ($A_{s,Bot}$)	mm^2	1149	
Diameter of the horizontal tension bars (dia_{ht})	mm	16	
Spacing of horizontal tension bars ($spac_h$)	mm	175	
Area of horizontal tension steel provided ($A_{s,2Bot}$)	mm^2	1149	
Diameter of compression bars (diac)	mm	16	
Spacing of compression bars (spacc)	mm	175	
Area of compression steel provided ($A_{s,Top}$)	mm^2	1149	
Diameter of the horizontal compression bars (dia_{hc})	mm	16	
Spacing of horizontal compression bars ($spac_{ch}$)	mm	175	
Area of horizontal compression steel provided ($A_{s,2top}$)	mm^2	1149	
Flag to identify reinforcement run (T1 or T2)		2	
Effective depth of section (d)	mm	126.00	
Depth to compression bars (d')	mm	74.0	
Material properties			
Characteristic concrete strength at 28 days (f_{cck})	MPa	50	
Normalised concrete strength at 28 days (f_{cn})	MPa	45.8	Sec 4. C302
Mean compressive strength at 28 days (f_{cm})	*MPa*	*58.0*	*Not used in DNV*
Tensile strength of concrete at 28 days (f_{ctm})	MPa	3.39	Sec 4. C304
Normalised in-situ strength f_{tn}	MPa	2.37	Sec 4. C304
Young modulus of concrete at 28 days (E_{cm})	MPa	34736	Sec 4. C314
Characteristic steel strength (f_{yk})	MPa	500	
Young modulus of steel (E_s)	MPa	200000	

Section check summary

Minimum reinforment area (SLS)	mm^2	308.1	In both directions top and bottom
Max allowed crack width	mm	0.15	
Miniimum reinforcement area (ULS) for bending	mm^2	565.69	
Compression steel area required	mm^2	0.00	
Additional extra steel requirement for axial tensile force	mm^2	0.00	

Provided tensile reinforcement	mm^2	1148.9
Additional over requirement for bending	mm^2	583.2
Provided compression reinforcement	mm^2	1148.9
Additional over requirement for compression	mm^2	1148.9
Provided for axial tensile foce		1732.2
Crack width	mm	0.13

D.3 Preliminary design RC concrete option, page 2 of 2

DETAILED CALCULATIONS

Stress state of the section (SLS)			
Description	Units	Value	
Creep coefficient (φ(∞,t0))		1.21	(note - the creep coefficient makes very little difference to any of the answers)
Effective Modulus $E_{c,eff}$	MPa	15707.75	Sec 6 - 701 (not specifically the equation - but the graph
B		10000000.00	
C		585150747.25	
D		-5.85E+10	
DELTA		2.6830E+18	
Stress in compression concrete (σ_c)	MPa	7.856	
Strain in compression concrete (ε_2)		0.0005001	
Force in compression steel	kN	-46.625	
Stress in compression steel (σ_{cs})	MPa	-40.582	
Strain in compression steel		-0.00020291	
Strain in tensile concrete lower effective area (ε1)		0.001400	

Assumes triangular stress distribution in compressed concrete

Minimum reinforcement areas (SLS) DNV_OS-C502 Sec 6 Q704		
Description	Units	Value
Coefficient considerding depth of section (k_w)	ratio	1.3
Concrete cross sectional area Ac	mm2	200000.00
concrete tensile strength (ftk)	MPa	2.369881404
fsk	MPa	500
Minimum reinforcement areas (As)	**mm2**	**308**

Limiting calculated crack width	mm	0.15	Read from table O32
Effective depth of concrete in tension surrounding the lower reinforcement (hc,ef)	mm	49.12	EC2 7.3.2 (3) and DNV-OS-V502 App E A202
Effective area of concrete in tension surrounding the lower reinforcement (Ac,eff)	mm2	49119.38	
ρp,eff		0.023390	eq 7.10
Factor dependent on the duration of the load (kt)		0.4	
Modular ratio (αe)		5.76	
Average strain in flexure (εsm-εcm) [Eq. 7.9 (a)]		0.000466996	
Average strain in flexure (εsm-εcm) [Eq. 7.9 (b)]		0.000418154	
Average strain in flexure (εsm-εcm)		4.670E-04	eq 7.9
Coefficient which takes into account the bond properties of the bonded reinforcement (k1)		0.8	
Coefficient which takes into account of the distribution of strain (k2)		0.50	
k3		3.4	DNV actually recommend 1.36 as a minimum for this value - therefore use EC2 recommendation of 3.4 (more conservative than minimum recommended value)
k4		0.425	
Maximum crack spacing (sr,max)		286.2867	
Crack width (wk) [Eq. 7.8]		**0.1337**	

Stress state of the section (ULS)			
Description	Units	Value	
Coefficient taking account of long term effects on the compressive strength (αcc)		0.85	From NA (overides recommended value of 1.0)
Partial safety factor for concrete (γc)		1.50	
Design value of concrete compressive strength (fcd)	MPa	30.56	
Factor to define the effective height of the compression zone (λ)		0.8	eq 3.19 & 3.20
Factor to define the effective strength (η)		1.00	
Partial factor for steel for ultimate limit state (γs)		1.15	
Design yield strength of shear reinforcement (fywd)	MPa	434.78	
A		9777.777778	
B		-3080000	
C		30000000	
DELTA		8.3131E+12	
Neutral axis (x)	mm	10.062	
x/d		0.080	
Lever arm (z)	mm	121.975	
Is compression reinforcement required		NO	
Force in compression concrete (Fc)	kN	245.95	
Stress in compression concrete (σc)	MPa	30.56	
Strain in compression concrete (εc)		0.0009	
Force in compression steel (Fcs)	kN	0.00	
Stress in compression steel (σcs)	MPa	0.00	
Strain in compression steel (εcs)		0.0000	
Limit of neutral axis (xlim)	mm	0.000	

Assuming rectangular stress distribution as given in BS-EN-1992 Figure 3.5

DNV clause Sec 6 - C120 states that different stress distributions may be used, therefore assume that rectangular stress distribution as given in EC2 is acceptable

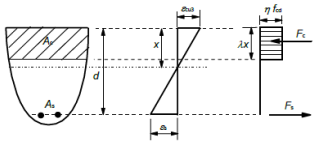

Figure 3.5: Rectangular stress distribution

STEEL				
Section properties				
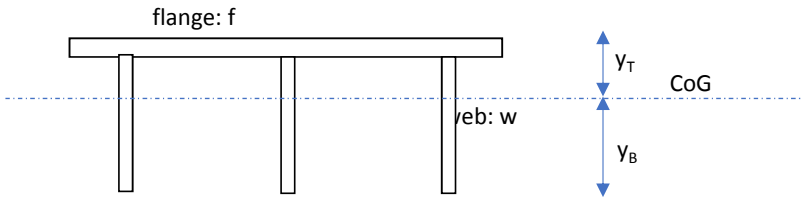				
d_w	web depth	mm	100	
t_w	web thickness	mm	15	
b_f	flange width	mm	1000	
t_f	flange thickness	mm	15	
w_s	web spacing	mm	500	
n_w	No of webs	unit	2	
	no	area mm^2	centroid mm	ax mm^3
flange	1	15000	7.5	1.13E+05
web	2	1500	65	1.95E+05
Total		18000		3.08E+05
CoG	=Σ(ax)/Σa		mm	17.08
	no	I mm^4	y mm	Ay^2 mm4
flange	1	281250	-9.58	1.38E+06
web	2	1250000	47.92	3.44E+06
Itot	=Σ(I+Ay^2)			1.10E+07
y_T	distance to extreeme fibre	mm	17.08	
y_B		mm	97.92	
$Z_{xx(T)}$	Section modulus	mm^3	6.47E+05	I/y
$Z_{xx(B)}$		mm^3	1.13E+05	
r_{xx}=	radius of gyration	mm	24.77	$(I/A)^{0.5}$
Material and resistance properties				
M	Design ULS moment	kNm	20	
σ_k	characteristic strength	MPa	355	
γ_m	material factor		1.2	
σ_d	design strength	MPa	308.70	= σ_k/γ_m
$F_{R,d}$	Design axial force resistance	kN	5556.52	= $A\sigma_d$
$M_{R,d}$	Design moment resistance	kNm	34.83	= $Z\sigma_d$
ULS Utilisation checks				
	Moment utilisation	unit	0.57	

Appendix E

Rates and cost build ups

Sections 9.2 and 10.6.4 present cost estimates for different design options. Tables E.1 to E.3 show the build up of the rates used for these estimates, for a baseline, optimistic and pessimistic scenario.

The tables makes reference to the following sources of information:

1. **2018 Spons** refers to Spon's Civil Engineering and Highway Works Price Book 2018 Langdon (2016)
2. **Morison 2017** refers to cost estimates provided by Morison's to Pelamis in 2013 for the construction of the Pelamis P2e machine, inflated to 2017 prices.
3. **Dundee estimate** refers to cost estimates put together by the University of Dundee Concrete Technology Unit as part of the WES funded ACE-WEC project.
4. **Albatern quote for steel tube** refers to costs provided to Albatern by various steel fabricators as part of the 12S development project.
5. **DTI pelamis report** refers to the materials study carried out by Pelamis in 2003 Anderson (2003), inflated to today's prices.

Table E.1: Unit rates for cost estimates - baseline

BASELINE ESTIMATES

Category	Description	Unit	Labour	Plant	Materials	Total	Comment
Concrete & ancilliaries							
	Formwork	m^2				10	Use rate for fabricated steel, assuming 12mm thick plates + 20% extra for stiffeners etc, but assume that can be used for 25 units
	C50 concrete: provide and place, Easy pour	m^3	45		125	170	Using 2018 Spons[1] rates as basis
	C50 concrete: provide and place, Complex pour		75		125	200	Using 2018 Spons rate as baseline - but also ties in with Morisons 2017[2] costs
	UHPC concrete: provide and place, Easy pour	m^3	75		500	575	Assuming 4x material cost, and same labour cost as per complex pour (more skill to place UHPC correctly)
	UHPC concrete: provide and place, complex pour	m^3	125		500	625	Assuming 4x material cost, and same easy / complex ratio for labour as C50 concrete
	Steel reinforcement: provide and fix, straight bars	t	425		650	1075	Using Morison 2017 costs; slightly lower than Spons 2018 rates
	Steel reinforcement: provide and fix, complex		510		650	1160	Assume fixing cost is 20% over straight bars
	Steel fibre	t	42.5		975	1017.5	Assume cost of steel fibres is 50% greater than baseline cost of rebar, and labour cost is 10% of rebar fixing (accounts for requirement to mix fibre into mix)
	Carbon wrap, provide and install, simple locations	m^2 / Ply	25		20	45	Take material cost from Dundee estimate[3]. Assume minimum of 1 man hour to apply $1m^2$
	Carbon wrap, provide and install, complex locations		37.5		20	57.5	Allow for 50% increase in labour cost
Pre-stressing							
	Materials and labour per bar	no. bar	1350		1100	2450	From Morison 2017 sheet, allowing 20% of material cost to be attributed the bar (not accounting for bar strength)
	Additional material cost per kN	kN			5	5	
	Hire of equipment	wks		515		515	
	Formation of ducts	no. bar				7	From Morrison sheet
Steel & ancilliaries							
	Steel tubes	t				1800	Using Albatern quote for steel tube[4], including 2% increase per year for inflation (then rounding up)
	Fabricated steel	t				2275	From Spons 2018 for fabricated steelwork. Ties in with quote from AG fabrications for fabricated pipe for 12S (as provided to Albatern)
	Coating	m^2				30	From spons 2018 for painting
GFRP							
	Tubes	t				7500	Corresponds to quote for filament wound tube provided to Albatern, and also price used in DTI Pelamis[5] report if increased for inflation
	Fabricated / complex shapes/ hand layup	t				11250	Allow for 50% of price of tube, corresponds to cost quoted in DTI Pelamis report for large wind turbine blades if increased for inflation.

Table E.2: Unit rates for cost estimates - optimistic

OPTIMISTIC ESTIMATES

Category	Description	Unit	Labour	Plant	Materials	Total	Comment
Concrete & ancilliaries							
	Formwork	m^2				5	Assume can be used for 50 units
	C50 concrete: provide and place, Easy pour	m^3	36		100	136	20% decrease
	C50 concrete: provide and place, Complex pour		60		100	160	20% decrease
	UHPC concrete: provide and place, Easy pour	m^3	60		200	260	Assuming 2x material cost, and same labour cost as per complex pour (more skill to place UHPC correctly)
	UHPC concrete: provide and place, complex pour	m^3	100		200	300	Assuming 2x material cost, and same easy / complex ratio for labour as C50 concrete
	Steel reinforcement: provide and fix, straight bars	t	340		520	860	20% decrease
	Steel reinforcement: provide and fix, complex		408		520	928	Assume fixing cost is 20% over straight bars
	Steel fibre	t			650	650	Assume cost of steel fibres is same as baseline rebar cost, and no additional labour cost required
	Carbon wrap, provide and install, simple locations	m^2 / Ply	20		16	36	20% decrease in costs
	Carbon wrap, provide and install, complex locations		30		16	46	20% decrease in costs
Pre-stressing							
	Materials and labour per bar	no. bar	1080		880	1960	20% decrease
	Additional material cost per kN	kN			4	4	20% decrease
	Hire of equipment	wks		412		412	20% decrease
	Formation of ducts	no. bar				5.6	20% decrease
Steel & ancilliaries							
	Steel tubes	t				1440	20% decrease
	Fabricated steel	t				1820	20% decrease
	Coating	m^2				24	20% decrease
GFRP							
	Tubes	t				6000	20% decrease
	Fabricated, hand layup	t				9000	20% decrease

Table E.3: Unit rates for cost estimates - pessimistic

PESSIMISTIC ESTIMATES

Category	Description	Unit	Labour	Plant	Materials	Total	Comment
Concrete & ancilliaries							
	Formwork	m^2				51	Assume can only be used for 5 units
	C50 concrete: provide and place, Easy pour	m^3	54		150	204	20% increase in costs
	C50 concrete: provide and place, Complex pour		90		150	240	20% increase in costs
	UHPC concrete: provide and place, Easy pour	m^3	90		750	840	Assuming 5x material cost of C50
	UHPC concrete: provide and place, complex pour	m^3	150		750	900	Assuming 5x material cost, and same easy / complex ratio for labour as C50 concrete
	Steel reinforcement: provide and fix, straight bars	t	600	100	650	1350	Using spons 2018 rates for 20mm diameter deformed high yield steel bars
	Steel reinforcement: provide and fix, complex		720	120	650	1490	Assume cost for fixing and plant is 20% over
	Steel fibre	t	150		1300	1450	Assume cost of steel fibres is 100% greater than baseline cost of rebar, and labour cost is 25% of rebar fixing (accounts for requirement to mix fibre into mix)
	Carbon wrap, provide and install, simple locations	m^2 / Ply	35		28	63	40% increase in costs
	Carbon wrap, provide and install, complex locations		52.5		28	80.5	40% increase in costs
Pre-stressing							
	Materials and labour per bar	no. bar	1890		1540	3430	40% increase
	Additional material cost per kN	kN			7.5	7.5	40% increase
	Hire of equipment	wks		721		721	40% increase
	Formation of ducts	no. bar				9.8	40% increase
Steel & ancilliaries							
	Steel tubes	t				2520	40% increase
	Fabricated steel	t				3185	40% increase
	Coating	m^2				42	40% increase
GFRP							
	Tubes	t				15000	100% increase
	Fabricated, hand layup	t				22500	100% increase

Appendix F

Node design appendix

Chapter 10 presents design work for different options using reinforced concrete materials. This Appendix provides details of the design calculations which back up that work.

F.1 Finite element convergence study

A convergence study has been carried out to determine the appropriate number of through thickness elements for the model, based a strip from the top face of the model, as shown in Figure F.1.

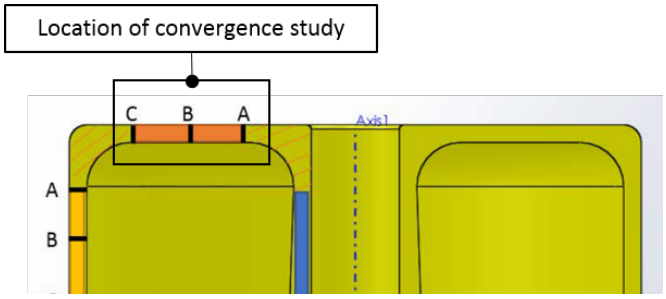

Figure F.1: Location of convergence study

For this study, a uniform pressure has been applied to the model, and the number of model elements increased within the strip until the principal stress (which is the most important value for design) converges. The number of elements considered for each run are shown in Table F.1 with the stress variation with number of elements is shown in Figure F.2.

It can be seen from Figure F.2 that there is minimal variation in the stress from 3 to 4 elements through width, therefore 3 elements have been used in the model. Due to the symmetry of the node and the loading, the design can be based on a single cross section strip through the model. The load results away from this location are not important for design, and therefore the size of the element mesh is increased in order to reduce the overall computational time.

Due to the nature of the applied loading, for each loadcase there is an imbalance between the wave pressures and the PTO articulation loads. This is due to the simplified nature of the loads

Table F.1: Convergence study values

No. of elements			
Through	Width	Along	Stress (MPa)
1	1	5	1.144
2	2	10	1.109
3	3	15	1.105
4	4	20	1.104

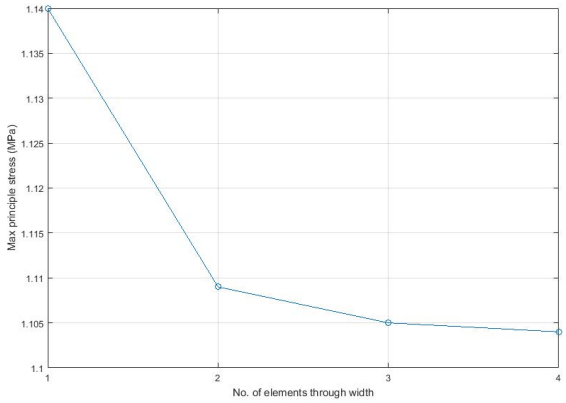

Figure F.2: Variation in principle stress with no. of through thickness elements)

which do not capture the complex dynamic interactions between the Node structure, the PTO system and the surrounding body of water. In order to balance the finite element model during the analysis the Node structure is unrestrained (with no external boundary conditions) and an Inertia Relief constraint is applied, which applies inertia (body acceleration) forces to the Node structure during the static analysis procedure to balance the external forces.

F.2 Deriviation of design moments and forces

Applied bending moments and axial forces have been derived from the cross-sectional nodal stress outputs (as discussed in Section 10.3.1). The method for deriving these actions from the through section stresses is shown in Figure F.3.

An example of this process is described below. The nodes highlighted in Figure F.4 show the design cross section for the top slab at the point of the maximum hogging moment. The applied load case in this particular example is ULS1(a), and stress component shown is s11, which is the stress in the radial direction.

The nodal stresses are shown in Table F.2, and the derived design moment and force using the equations in Figure F.3 are shown in Table F.3

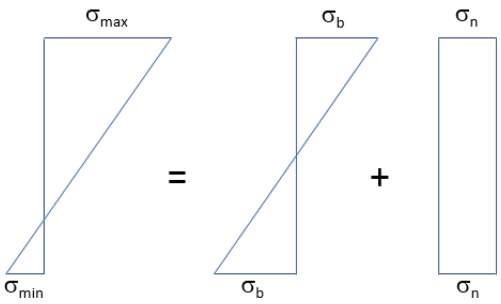

$$\sigma_{max} = \sigma_b + \sigma_n \qquad \sigma_b = \frac{M}{Z}$$

$$\sigma_{min} = -\sigma_b + \sigma_n \qquad Z = \frac{1}{6}bt^2$$

$$2\sigma_n = \sigma_{max} + \sigma_{min} \qquad M = \frac{1}{6}bt^2.\sigma_b$$

$$\sigma_n = \frac{\sigma_{max} + \sigma_{min}}{2} \qquad \sigma_n = FA$$

$$\sigma_b = \sigma_{max} - \sigma_n$$

Figure F.3: Derivation of design moments and axial force from through section stresses

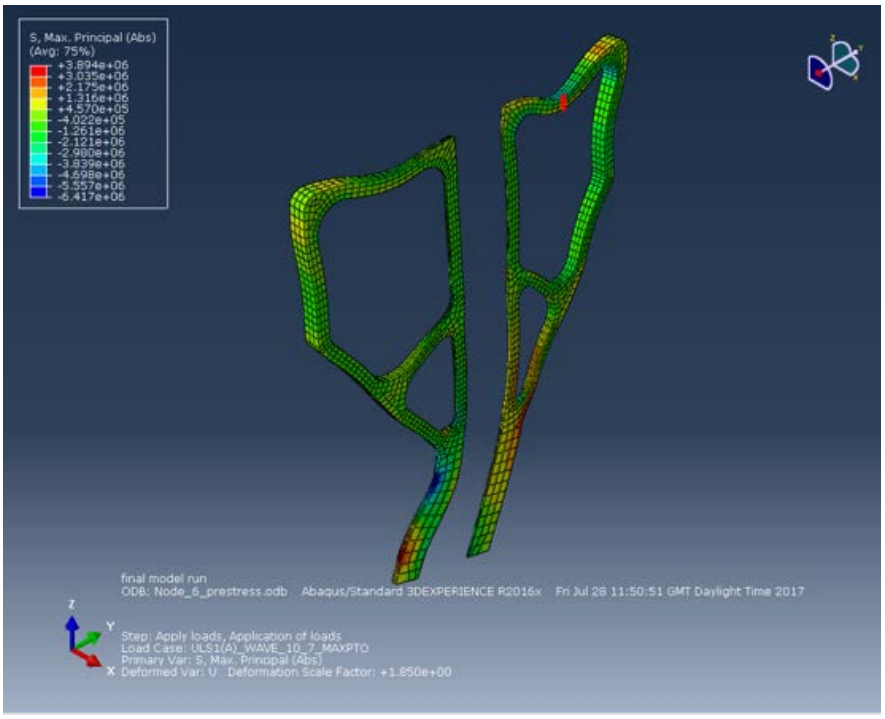

Figure F.4: Cross sectional stress values (s11) for the top slab, section B, for ULS1(a)

Table F.2: Top slab design section through section stresses

Node	5680	146594	23325	146599	23326	146602	5667
s11 stress (MPa)	-0.84	-0.64	-0.45	-0.25	-0.06	0.14	0.34

Table F.3: Top slab design section bending and axial force derivation

σ_{max} (MPa)	σ_{min} (MPa)	σ_n (MPa)	σ_b (MPa)	M (kNm)	F (kN)
0.34	-0.84	-0.25	0.59	3.9	50.1

This procedure has been carried out for all design cross sections and loadcases. The results show that the output shear and through thickness stresses are less than 1MPa in all cases, and therefore are considered to be negligible.

A summary of the design values for each section and direction shown in Tables F.4 (for the SLS load cases) and F.5 (for the ULS and ALS load cases). The table also indicates the critical cross-section and load case for each design section. Positive figures represent tension forces, which are more critical for design than compressive forces. In all cases the compressive stresses are below the compression strength of the concrete.

Table F.4: SLS design actions

Section	Direction	Bending (kNm)	Axial (kN)	Location	LC
Top slab	Circumferential	4.26	−18.77	Topslab2 A	SLS2
(max moment)	Radial	6.41	−103.29	Topslab2 C	SLS3
Top slab	Cicumferential	0.37	19.80	Topslab2 C	SLS4
(max tension)	Radial	2.31	6.78	Topslab1 A	SLS4
Walls	Hoop	1.77	38.76	Wall1 A	SLS2
	Longitudinal	8.02	−67.24	Wall1 A	SLS2
Cone top	Hoop	2.02	−81.83	Conetop2	SLS2
	Longitudinal	3.43	16.35	Conetop2	SLS4
Cone base	Hoop	4.58	80.11	Conebase2 B	SLS2
	Longitudinal	5.42	346.35	Conebase2 B	SLS4
Innerwall top	Hoop	1.60	3.10	Innerwall2 B	SLS2
	Longitudinal	9.85	36.55	Innerwall2 B	SLS4
Innerwall base	Hoop	5.04	118.00	Innerwall2 A	SLS2
	Longitudinal	9.04	422.13	Innerwall2 A	SLS2

Table F.5: ULS and ALS design actions for slab sections

Section	Direction	Bending (kNm)	Axial (kN)	Location	LC
Top slab	Circumferential	12.64	−129.26	Topslab2 C	ULS4(a)
(max moment)	Radial	7.16	−24.88	Topslab2 A	ULS3(a)
Top slab	Cicumferential	5.25	14.28	Topslab1 A	ALS
(max tension)	Radial	4.44	46.91	Topslab2 C	ULS4(a)
Walls	Hoop	0.65	62.24	Wall1 C	ALS
	Longitudinal	13.41	−224.82	Wall2 A	ULS2(a)
Cone top	Hoop	2.61	−47.09	Conetop2	ALS
	Longitudinal	7.21	87.04	Conetop2	ALS
Cone base	Hoop	5.54	244.28	Conebase2 B	ALS
	Longitudinal	12.14	862.84	Conebase2 B	ALS
Innerwall top	Hoop	0.15	59.84	Innerwall2	ALS
	Longitudinal	2.39	143.56	Innerwall2 B	ALS
Innerwall base	Hoop	2.17	237.04	Innerwall2 A	ALS
	Longitudinal	17.84	1057.05	Innerwall2 A	ALS

F.3 Conventional RC section design

Node wall section design as described in section 10.3.1 are based on standard stress-strain relationships and code based design procedures. The following sheets provide an example calculation carried out for the Innerwall Base location.

F.3 RC Section design

Calculation for Innerwall Base section, page 1 of 3

Section definition

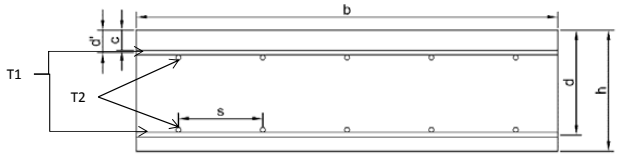

User input values are in blue
Values from code are in purple

Section overview				Ref
Description	Units	Hoop	Membrane	
Section loads				
Ultimate Moment per meter width (M_{Ed})	kN.m	2.2	18	
Serviceability Moment per meter width ($M_{Ed'}$)	kN.m	5.04	9.00	
Shear force due to ultimate loads (V_{Ed})	kN			
Axial force due to ultimate load (N_{Ed})	kN	-237	-1057	Ignore compressive stress (reduces overall crack widths)
Axial force due to servicability load ($N_{Ed'}$)	kN	-118	-422	
Section geometry				
Breadth of concrete section (b)	mm	1000	1000	
Overall depth of concrete section (h)	mm	275	220	
Nominal concrete cover (c)	mm	50	50	
Reinforcing steel				
Diameter of tension bars (dia_t)	mm	16	20	
Spacing of tension bars (s_t)	mm	200	125	
Area of tension steel provided ($A_{s,Bot}$)	mm^2	1005	2513	
Diameter of the horizontal tension bars (dia_{ht})	mm	20	16	
Spacing of horizontal tension bars ($spac_h$)	mm	150	200	
Area of horizontal tension steel provided ($A_{s,2Bot}$)	mm^2	2094	1005	
Diameter of compression bars (diac)	mm	16	20	
Spacing of compression bars (spacc)	mm	200	125	
Area of compression steel provided ($A_{s,Top}$)	mm^2	1005	2513	
Diameter of the horizontal compression bars (dia_{hc})	mm	20	16	
Spacing of horizontal compression bars ($spac_{ch}$)	mm	150	200	
Area of horizontal compression steel provided ($A_{s,2top}$)	mm^2	2094	1005	
Flag to identify reinforcement run (T1 or T2)		2	1	
Effective depth of section (d)	mm	197.00	160.00	
Depth to compression bars (d')	mm	78.0	60.0	
Material properties				
Characteristic concrete strength at 28 days (f_{cck})	MPa	50	50	
Normalised concrete strength at 28 days (f_{cn})	MPa	45.8	45.8	Sec 4. C302
Mean compressive strength at 28 days (f_{cm})	*MPa*	*58.0*	*58.0*	*Not used in DNV*
Tensile strength of concrete at 28 days (f_{ctm})	MPa	3.39	3.39	Sec 4. C304
Normalised in-situ strength f_{tn}	MPa	2.37	2.37	Sec 4. C304
Young modulus of concrete at 28 days (E_{cm})	MPa	34736	34736	Sec 4. C314
Characteristic steel strength (f_{yk})	MPa	500	500	
Young modulus of steel (E_s)	MPa	200000	200000	

Section check summary				
Minimum reinforment area (SLS)	mm^2	399.2	333.7	In both directions top and bottom
Max allowed crack width	mm	0.20	0.20	
Miniimum reinforcement area (ULS) for bending	mm^2	25.71	261.80	
Compression steel area required	mm^2	0.00	0.00	
Additional extra steel requirement for axial tensile force	mm^2	545.10	2431.10	
Provided tensile reinforcement	mm^2	1005.3	2513.3	
Additional over requirement for bending	mm^2	979.6	2251.5	
Provided compression reinforcement	mm^2	1005.3	2513.3	
Additional over requirement for compression	mm^2	1005.3	2513.3	
Provided for axial tensile foce	mm^2	1984.9	4764.8	
Crack width	mm	0.16	0.19	

DETAILED CALCULATIONS

Stress state of the section (SLS)				
Description	Units	Value	Value	
Creep coefficient (φ(∞,t0))		1.19	1.19	Assumes triangular stress distribution in (note - the creep coefficient makes very little difference to any of the answers)
Effective Modulus $E_{c,eff}$	MPa	15868.08	15868.08	Sec 6 - 701 (not specifically the equation - but the graph indicates that this is the correct method of taking creep into account)
Modular ratio (αe)		12.60	12.60	
A		-39333.33	-140666.67	
B		-470318.13	-22235471.38	
C		950059546.90	6451991481.47	
D		-1.76E+10	-6.27E+10	
f		-2.42E+04	-5.42E+04	
g		5.43E+05	3.16E+06	
h		-4.51E+11	-3.41E+12	
I		7.25E+05	2.43E+06	
J		89.82	134.41	
K		1.95	2.28	
L		-89.82	-134.41	
M		0.80	0.73	
N		1.05	1.19	
P		-3.99	-52.69	
x1		138.85	142.28	
x2		-169.75	-310.45	
x3		18.94	10.09	
Neutral axis (x)	mm	18.94	10.09	
Inertia Moment (I_{zz})	m4	4.482E-04	7.911E-04	
Equivalent area of the section	mm2	4.429E+04	7.345E+04	
Force in tension steel	kN	131.14	433.76	
Stress in tension steel (σ_s)	MPa	130.45	172.59	
Strain in tension steel		0.0006522	0.0008629	
Force in compression concrete	kN	56.64	156.16	
Stress in compression concrete (σ_c)	MPa	1.101	0.922	
Strain in compression concrete (ε_2)		0.0000694	0.0000581	
Force in compression steel	kN	-43.495	-144.402	
Stress in compression steel (σ_{cs})	MPa	-43.266	-57.456	
Strain in compression steel		-0.00021633	-0.00028728	
Strain in tensile concrete lower effective area (ε1)		0.000938	0.001208	

Minimum reinforcement areas (SLS) DNV_OS-C502 Sec 6 Q704			
Description	Units	Value	Value
Coefficient considerding depth of section (k_w)	ratio	1.225	1.28
Concrete cross sectional area Ac	mm2	275000.00	220000.00
concrete tensile strength (ftk)	MPa	2.369881404	2.369881404
fsk	MPa	500	500
Minimum reinforcement areas (As)	**mm2**	**399**	**334**

Calculation of crack widths (SLS) [EN 1992-1-1:2004 - Section 7.3.4]				Note - these calculations are carried out in accordance with the equations given in EC2, but with coefficients as recommended by DNV-OS-J101_2011
Description	Units	Value	Value	
Limiting calculated crack width	mm	0.20	0.20	Read from table O32
Effective depth of concrete in tension surrounding the lower reinforcement (hc,ef)	mm	85.35	69.97	EC2 7.3.2 (3) and DNV-OS-V502 App E A202
Effective area of concrete in tension surrounding the lower reinforcement (Ac,eff)	mm2	85351.98	69968.42	
pp,eff		0.011778	0.035920	eq 7.10
Factor dependent on the duration of the load (kt)		0.4	0.4	
Modular ratio (αe)		5.76	5.76	
Average strain in flexure (εsm-εcm) [Eq. 7.9 (a)]		0.000222534	0.000703686	
Average strain in flexure (εsm-εcm) [Eq. 7.9 (b)]		0.000391342	0.000517758	
Average strain in flexure (εsm-εcm)		3.913E-04	7.037E-04	eq 7.9
Coefficient which takes into account the bond properties of the bonded reinforcement (k1)		0.8	0.8	
Coefficient which takes into account of the distribution of strain (k2)		0.50	0.50	
k3		3.4	3.4	DNV actually recommend 1.36 as a minimum for this value - therefore use EC2 recommendation of 3.4 (more conservative than minimum recommended value)
k4		0.425	0.425	
Maximum crack spacing (sr,max)		400.9312	264.6545	
Crack width (wk) [Eq. 7.8]		**0.1569**	**0.1862**	

F.3 RC Section design

Calculation for Innerwall Base section, page 3 of 3

Stress state of the section (ULS)			
Description	Units	Value	Value
Coefficient taking account of long term effects on the compressive strength (αcc)		0.85	0.85
Partial safety factor for concrete (γc)		1.50	1.50
Design value of concrete compressive strength (fcd)	MPa	30.56	30.56
Factor to define the effective height of the compression zone (λ)		0.8	0.8
Factor to define the effective strength (η)		1.00	1.00
Partial factor for steel for ultimate limit state (γs)		1.15	1.15
Design yield strength of shear reinforcement (fywd)	MPa	434.78	434.78
A		9777.777778	9777.777778
B		-4815555.556	-3911111.111
C		2200000	18000000
DELTA		2.3104E+13	1.4593E+13
Neutral axis (x)	mm	0.457	4.656
x/d		0.002	0.029
Lever arm (z)	mm	196.817	158.137
Is compression reinforcement required		NO	NO

Assuming rectangular stress distribution as given in BS-EN-1992 Figure 3.5

DNV clause Sec 6 - C120 states that different stress distributions may be used, therefore assume that rectangular stress distribution as given in EC2 is acceptable

From NA (overides recommended value of 1.0)

eq 3.19 & 3.20

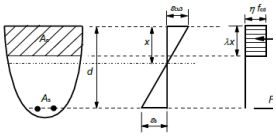

Figure 3.5: Rectangular stress distribution

Ultimate moment of resistance zone 2 (MRd)	kNm	220.25	145.29
Ultimate moment of resistance zone 3 (MRd)	kNm	350.06	230.91
Area of compression reinforcement required (Acsreq)	**mm2**	**0**	**0**
Area of tensile reinforcement required (Atsreq) for bending	**mm2**	**26**	**262**
Additional area of steel due to axial forces (As*)	**mm2**	**545.1**	**2431.1**
Flag to identify zone		**TWO**	**TWO**
Force in tension steel (Fs)	kN	11.18	113.83
Stress in tension steel (σs)	MPa	434.78	434.78
Strain in tension steel (εs)		0.01000	0.01000
Force in compression concrete (Fc)	kN	11.18	113.83
Stress in compression concrete (σc)	MPa	30.56	30.56
Strain in compression concrete (εc)		0.0000	0.0003
Force in compression steel (Fcs)	kN	0.00	0.00
Stress in compression steel (σcs)	MPa	0.00	0.00
Strain in compression steel (εcs)		0.0000	0.0000
Limit of neutral axis (xlim)	mm	0.000	0.000

F.4 Fatigue analysis

Section 10.3.3 discusses the fatigue calculations for the node structure. This appendix section presents more detailed calculations to back up that work. For each section, a two stage fatigue analysis has been carried out. The first stage is a simplistic assessment of the number of cycles to failure (N) calculated taking the largest stress amplitude that the section is subject to. If $N > 2x10^6$, then no further checks are required (as allowed for in DNV GL, 2018, clause 6.13.1.13).

The number of cycles to failure of concrete subject to cyclic stresses has been calculated from the following equation (DNV GL, 2018, clause 6.13.2.1):

$$\log_{10} N = C_1 \frac{\left(1 - \frac{\sigma_{max}}{C_5 . f_{rd}}\right)}{\left(1 - \frac{\sigma_{min}}{C_5 . f_{rd}}\right)}$$

Where f_{rd} is the compression strength for the type of failure in question, σ_{max} is the numerically largest compressive stress, calculated as the average value within each stress-block, σ_{min} the numerically least compressive stress, calculated as the average value within each stress-block (= 0 for tension), C_5 is fatigue strength parameter = 1.0 for concrete, and $C_1 = 8.0$ (corresponding to structures in water for stress blocks in the compression-tension range).

The design life of reinforcement has been calculated in accordance with the following equation (DNV GL, 2018, clause 6.13.2.2):

$$\log_{10} N = C_3 - C_4 \log_{10} \Delta\sigma$$

Table F.6: S-N curve constants

	Level of Stress Variations (MPa)		
	$\Delta\sigma > 235$	$235 > \Delta\sigma > 65$	$65 > \Delta\sigma > 40$
C_3	15.7	13.35	16.97
C_4	4.5	3.5	5.5

Where N calculated by this process is greater than $2x10^6$, a spectral fatigue analysis has then been carried out, with the following steps:

1. A series of wave loads covering periods between 3.5 and 11.5 seconds have been applied to the full Node structure finite element model. For each sea state the wave height has been selected to give the same wave steepness (0.02) for all sea states.

2. For each applied wave load, the nodal stresses for each design section has been taken from the FEA model. These have been used to derive the section bending moment and axial forces using the method described in section 10.3.1.
3. Maximum tensile stress in the concrete and reinforcing steel for each wave load has been calculated using the stress distribution shown in fig. 10.8, and then divided by the appropriate wave height to give a frequency domain stress transfer function per unit wave amplitude (STF).
4. The stress spectrum (SS) for a particular sea state is determined by multiplying the wave spectra for a particular sea state (assumed at this stage to be a Jonswap spectra), by the square of the STF.
5. The short term stress range distributions are determined from each of the stress spectra. These short term distributions are combined together to determine the long term distributions, assuming that the stress range is distributed in accordance with the Dirlik probability density function .
6. The number of cycles expected at each stress range can then be calculated for each sea state (this has been carried out using Matlab), depending on the expected duration of each sea state based on the West Harris Occurrence Matrix and then summed together to give a stress cycle histogram.

Calculated fatigue lifes and damage values following this process are shown in Table F.7.

Table F.7: Fatigue checks

Design section		Cycles to failure N$^{(1)}$		Damage D$^{(2)}$
		Concrete	Steel	n/N
Top slab	Radial	1.56E+07	**6.26E+05**	0.093
	Circumferential	2.47E+07	**1.68E+06**	0.133
Wall	Hoop	4.63E+07	**3.81E+05**	1.42×10^{-5}
	Longitudinal	1.08E+07	**3.30E+05**	0.0139
Conetop	Hoop	4.85E+07	2.25E+07	-
Conetop	Longitudinal	1.02e07	2.09e05	8.87×10^{-4}
Innerwall (top)	Hoop	7.45E+07	1.20E+09	-
	Longitudinal	5.13E+07	**1.09E+06**	1.97×10^{-7}
Conebase	Hoop	2.85E+07	**1.73E+05**	2.10×10^{-7}
	Longitudinal	6.89E+07	**1.55E+05**	0.000 37
Innerwall (base)	Hoop	5.15E+07	**3.24E+05**	3.20×10^{-7}
	Longitudinal	5.74E+07	**1.21E+05**	0.022

(1) *calculated using the maximum stress amplitude*
(2) *calculated using the full stress histogram, over 20 years*

The damage limit has been taken as 0.33 in accordance with Table M1 in DNV (2012), which corresponds to sections which have no access for inspection and repair, and is the strictest limit that can be imposed. The values in Table 10 show that the for all sections the calculated

design life for the concrete using the maximum stress amplitude is well above the specified limit of $2x10^6$, therefore no detailed checks are required. For the steel reinforcement, where detailed damage checks have been carried out, the damage value D is always less than 0.33 over the 20 year period, therefore the structure is adequate in fatigue throughout the design life.

F.5 UHPFRC design

F.5.1 Stress-strain relationships for FRC sections

Stress-strain relationships for fibre reinforced concrete have been developed assuming that the concrete takes tensile as well as compressive forces (as discussed in Section 10.4.1). In this particular case the design is driven by tensile forces, so the calculation of ULS capacity assumes that the section fails in tension rather than compression (i.e. the section reaches the ultimate tensile strain of 2% before it reaches the ultimate compressive strain of 0.35%). UHPFRC is assumed to act the same as plain concrete in compression, with linear behaviour up to 0.175% strain. The ULS section is simplified as it assumes linear behaviour in tension up to the peak stress, ignoring the behaviour up to the first crack.

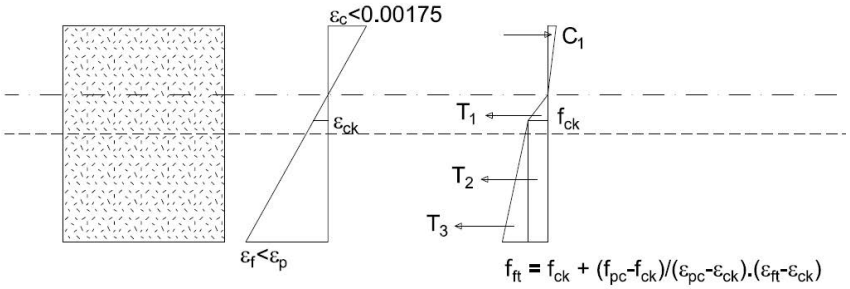

Figure F.5: SLS stress-strain relationship for UHPFRC sections

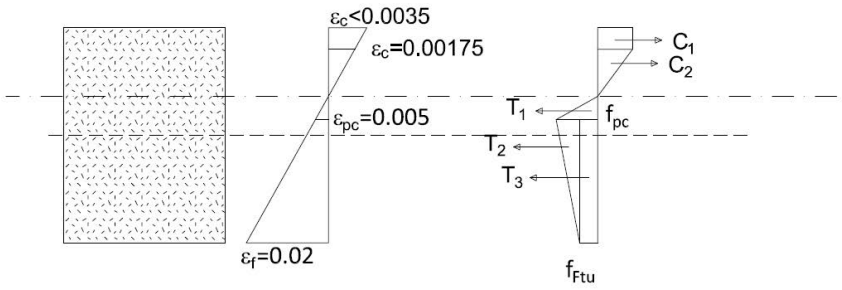

Figure F.6: ULS stress-strain relationship for UHPFRC sections

F.5.2 FEA modelling results

Table 10.17 in Section 10.4.1 presents the maximum principle stress in the UHPFRC node from the Abaqus model. Figure F.7 shows the Abaqus outputs that back up these figures.

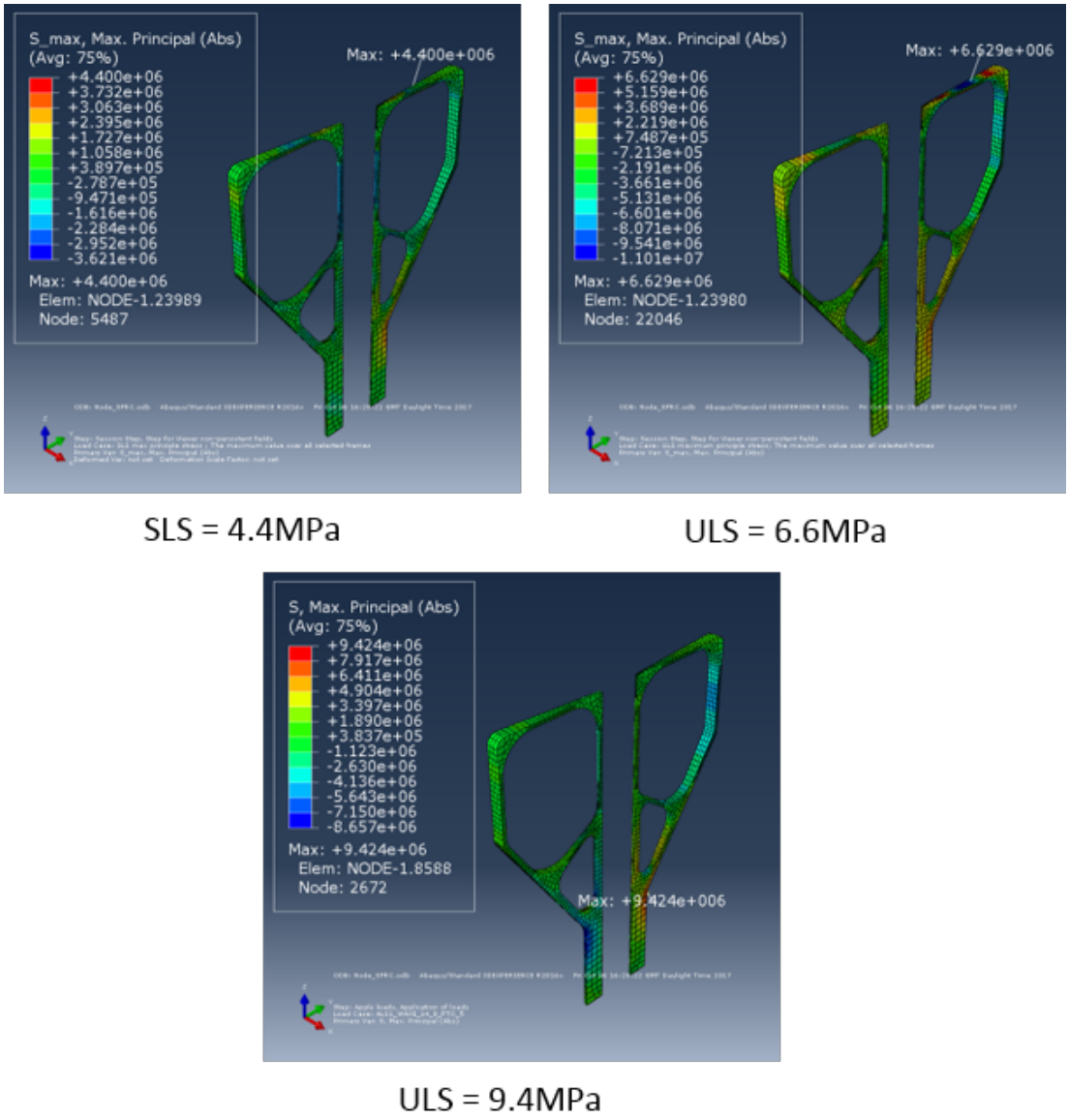

Figure F.7: Maximum principle stress in UHPFRC Node Structure

F.6 Carbon fibre external wrap

For preliminary design, it is assumed that the required steel area can be directly replaced with the equivalent area of carbon fibre wrapping (as discussed in Section 10.4.3). The calculation for the equivalent required area of carbon fibre is as follows:

Characteristic yield strength of steel reinforcement	= 435 MPa
Characteristic strength of carbon fibre wrap	= 1742 MPa
Thickness of single ply	= 0.17 mm
Longitudinal reinforcement - requirement = T20s @ 125cc	= 2513 mm^2/m
Equivalent required area of carbon fibre wrap = 2513 x 435 / 1742	= 628 mm^2/m
No of plys required = 628 / 170 = 3.7 - round up to	= 4 no.
Hoop reinforcement - requirement = T16s @ 300cc	= 670mm^2/m
Equivalent required area of carbon fibre wrap = 670 x 435 / 1742	= 167mm^2/m
No of plys required = 167 / 170 = 0.98 - round up to	= 1 no.

F.7 Cost estimates

Work in Section 10.5.2 shows the cost estimates for the different options based on the baseline unit rates. Tables F.8 to F.11 show the breakdown of costs for the different options, including the pessimistic and optimistic options.

Table F.8: Reference option

			Baseline		Optimistic		Pessimistic	
Description	Quantity	Unit	Rate	Cost	Rate	Cost	Rate	Cost
Concrete and reinforcement								
Formwork	330	m^2	10	3395	5	1697	51	16973
50MPa concrete: provide and place, simple pour	14.8	m^3	170	2516	136	2013	204	3019
50MPa concrete: provide and place, complex pour	28.8	m^3	200	5760	160	4608	240	6912
Steel reinforcement: provide and fix, easy	0.7	t	1075	753	860	602	1350	945
Steel reinforcement: provide and fix, complex	3.3	t	1160	3828	928	3062	1490	4917
Prestressing								
Material and labour	1180	kN	7	8260	4	4720	7.5	8850
Hire of equipment	2	wks	515	1030	412	824	206	721
Formation of ducts	6	bar no.	7	42	6	34	10	59
Totals				**£25,583**		**£17,560**		**£43,117**

Table F.9: Option 1: UHPFRC

			Baseline		Optimistic		Pessimistic	
Description	Quantity	Unit	Rate	Cost	Rate	Cost	Rate	Cost
Concrete and reinforcement								
Formwork	330	m^2	10	3395	5	1697	51	16973
UHPC concrete: provide and place, easy pour	10	m^3	575	5750	260	2600	840	8400
UHPC concrete: provide and place, complex pour	21.2	m^3	625	13250	300	6360	900	19080
Steel fibre	12.3	t	1018	12515	650	7995	1300	15990
Prestressing								
Material and labour	1180	kN	7	8260	4	4720	7.5	8850
Hire of equipment	2	wks	515	1030	721	824	206	412
Formation of ducts	6	bar no.	7	42	6	34	10	59
Totals				**£44,242**		**£24,230**		**£70,794**

Table F.10: Option 1: SHCC & UHPFRC

			Baseline		Optimistic		Pessimistic	
Description	Quantity	Unit	Rate	Cost	Rate	Cost	Rate	Cost
Concrete and reinforcement								
Formwork	330	m^2	10	3395	5	1697	51	16973
80MPa concrete: provide and place, easy pour	23.3	m^3	204	4753	163	3803	245	5704
UHPC concrete: provide and place, easy pour	5.0	m^3	575	2850	260	1289	800	4163
UHPC concrete: provide and place, complex pour	8.7	m^3	625	5415	300	2599	900	7798
Steel fibre	9.8	t	1018	9972	650	6370	1300	12740
Prestressing	None in this option							
Totals				**£26,384**		**£15,758**		**£47,377**

Table F.11: Option 3: Carbon fibre

Description	Quantity	Unit	Baseline Rate	Baseline Cost	Optimistic Rate	Optimistic Cost	Pessimistic Rate	Pessimistic Cost
Concrete and reinforcement								
Formwork	330	m^2	10	3395	5	1697	51	16973
C50 concrete: provide and place, simple pour	14.8	m^3	170	2516	136	2013	204	3019
C50 concrete: provide and place, complex pour	26.8	m^3	200	5360	160	4288	240	6432
Steel reinforcement: provide and fix, easy	0.7	t	1075	753	860	602	1350	945
Steel reinforcement: provide and fix, complex	2.13	t	1160	2471	928	1977	1490	3174
Carbon fibre wrap								
5 plys of wrap at 30.8m^2 per ply	154	m^2	58	8855	46	7084	58	8932
Prestressing								
Material and labour	1180	kN	7	8260	4	4720	7.5	8850
Hire of equipment	2	wks	515	1030	721	824	206	412
Formation of ducts	6	bar no.	7	42	6	34	10	59
Totals				**£32,681**		**£23,238**		**£49,826**

F.8 Scale effect design actions

Section 10.6.1 discusses the method for scaling the 12S design actions in order to provide design loads for the 6S device. Table F.12 presents the scaled actions for all the design sections.

Table F.12: Scaled design actions for 6S design

Section	Direction	Bending (kNm)	Axial (kN)
Top slab	Circumferential	1.58	−16.16
(max moment)	Radial	0.90	−3.11
Top slab	Cicumferential	0.66	1.79
(max tension)	Radial	0.56	5.86
Walls	Hoop	0.08	7.78
	Longitudinal	1.68	−28.10
Cone top	Hoop	0.33	−5.89
	Longitudinal	0.90	10.51
Cone base	Hoop	0.55	24.28
	Longitudinal	1.21	86.84
Innerwall top	Hoop	0.02	7.48
	Longitudinal	0.30	17.95
Innerwall base	Hoop	0.22	3.70
	Longitudinal	1.78	105.71

F.9 6S option design calcs

Section 10.6.3 presents the preliminary design methodology and solutions for the three different design options for 6S node. The full calculations for these design solutions are included here.

F.9 6S Design calcs

Steel and GFRP option

STEEL

Section properties

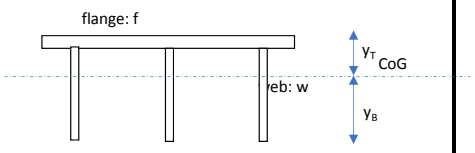

d_w	web depth	mm	0	
t_w	web thickness	mm	0	
b_f	flange width	mm	1000	
t_f	flange thickness	mm	10	
w_s	web spacing	mm	0	
n_w	No of webs	unit	0	

	no	area mm2	centroid mm	ax mm3
flange	1	10000	5	5.00E+04
web	0	0	10	0.00E+00
Total		10000		5.00E+04
CoG	=Σ(ax)/Σa		mm	5.00

	no	I mm^4	y mm	Ay^2 mm^4
flange	1	83333.33	0.00	0.00E+00
web	0	0	5.00	0.00E+00
Itot	=Σ(I+Ay^2)			8.33E+04

y_T	distance to extreme fibre	mm	5.00	
$Z_{xx(T)}$	Section modulus	mm3	1.67E+04	I/y
r_{xx}=	radius of gyration	mm	2.89	$(I/A)^{0.5}$

Material and resistance properties

M	Design ULS moment	kNm	1.8	
A	Axial force	kNm	106	
σ_k	characteristic strength	MPa	355	
γ_m	material factor		1.2	
σ_d	design strength	MPa	308.70	= σ_k/γ_m
$F_{R,d}$	Axial force resistance	kN	3086.96	= $A\sigma_d$
$M_{R,d}$	Moment resistance	kNm	5.14	= $Z\sigma_d$

ULS Utilisation checks

	Moment utilisation	unit	0.35	
	Axial force		0.03	
	Combined		0.38	

GFRP sandwich

Section properties

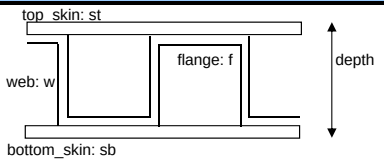

D	overall depth		20	mm
d_w	web depth		10	mm
t_w	web thickness		2	mm
t_f	flange thickness		2	mm
b_s	overall section width		1000	mm
t_s	skin thickness		3	mm
w_s	web spacing		300	mm
n_w	No of webs		3	mm

	no	area mm2	centroid mm	ax mm3
top skin	1	3000	1.5	4500
top flange	1	1000	4	4000
web	3	20	10	600
bot flange	1	1000	16	16000
bot skin	1	3000	18.5	55500
Total		8060		80600
CoG	=Σ(ax)/Σa			10

	no	I mm^4	y mm	Ay^2 mm^4
top skin	1	2250	-8.5	2.17E+05
top flange	1	333.3333	-6	3.60E+04
web	3	166.6667	0	0.00E+00
bot flange	1	333.3333	6	3.60E+04
bot skin	1	2250	8.5	2.17E+05
Itot	=Σ(I+Ay^2)			0.00E+00

y_T	distance to extreme fibre	mm	10.00	
$Z_{xx(T)}$	Section modulus	mm^3	2.56E+04	I/y
r_{xx}=	radius of gyration	mm	5.63	$(I/A)^{0.5}$

Material and resistance properties

M	Design ULS moment	kNm	1.8	
A	Axial force	kNm	106	
σ_k	characteristic strength	MPa	370	
γ_m	material factor		2.7	
σ_d	design strength	MPa	138.58	= σ_k/γ_m
$F_{R,d}$	Axial force resistance	kN	1116.93	= $A\sigma_d$
$M_{R,d}$	Moment resistance	kNm	3.55	= $Z\sigma_d$

ULS Utilisation checks

	Axial force utilistaion	unit	0.09	
	Moment utilisation	unit	0.51	
	Combined	unit	0.60	

F.9 6S Design calcs SHCC option page 1of4

Section Overview					
Symbol	Description	Unit	Value	Equation	Comment / ref
Section loads					
$M_{ED',SLS}$	Design serviceability moment	kN.m	0.9	Input	
$N_{ED',SLS}$	Design serviceability axial force	kN	-42	Input	-ve tensile
$M_{ED'ALS}$	Design ULS moment	kNm	1.8	Input	
$N_{ED',ALS}$	Design ULS axial force	kN	-106	Input	-ve tensile
Section properties					
b	Breadth of section	mm	1000	Input	
h	Overall depth of section	mm	75	Input	
c	Nominal cover	mm	50	Input	
Material properties					
Fibre					
V_f	Fibre volumetric fraction	%	2.5	input	
l_f	fibre length	mm	50	input	
l_f / d_f	fibre aspect ratio	ratio	80	input	
RI	reinforcing index	ratio	2	$RI = \frac{V_f l_f}{d_f}$	
k	damage factor	factor	1	input	assuming undamaged fibres
Concrete matrix					
f_{cck}	Characteristic cylinder compressive strength	MPa	80	input	
Concrete class:			**SHCC**		
f_{cn}	Normalised concrete strength at 28 days	MPa	69.3	$f_{cn} = f_{cck}(1 - f_{cck}/600)$	Sec 4. C302
γ_c	partial material safety factor for concrete	factor	1.5		
E_{cn}	Young modulus of concrete at 28 days	MPa	42933	$E_{cn} = 22000(f_{cck}/10)^{0.3}$ <65MPa $E_{cn} = 4800(f_{cck})^{0.5}$ >65MPa	Sec 4. C314
E_{cd}	Design youngs modulus of concrete	MPa	28622	$E_{cd} = E_{cn}/\gamma_c$	Sec 6. C111
ε_{cu}	ultimate compressive concrete strain	ratio	0.0035	input	
$\varepsilon_{fu,t}$	ultimate tensile fibre concrete strain, flexural	ratio	-0.02	input	Fib model code
SFRC Design strengths					
f_{cd}	Concrete compressive strength	MPa	46.22	$f_{cd} = f_{cck}(1 - f_{cck}/600)/\gamma_C$	DNV OSC502, Sec 4 C302
Flexural tensile properties - design					Defined as stress - CMOD, derived from bending tests
f_{1d}	First crack strength	MPa	-3.26	$f_{1d} = 0.48(f_{cd})^{0.5}$	Equal to tensile strength of matrix f_{td} as defined in DNV OS C502, Sec 4, C304
f_{R1d}	Residual strength @ CMOD = 0.5	MPa	-8.05	$f_{R1d} = (f_{LK}+f_p)/2$	peak
f_{pd}	Peak strength	MPa	-12.84	$f_{pd} = 0.97(f_{cd})^{0.5} + 0.295(f_{cd})^{0.5}\mathrm{RI} + 1.117\mathrm{RI}$	Thomas and Ramaswamy, 2007. Assume occurs @ CMOD = 1mm.
f_{R2d}	Residual strength @ CMOD = 1.5	MPa	-12.33	$f_{Rid} = f_p\left[1 - \frac{\delta_i}{kL/2}\right]^2$	Naaman, 2008. Assuming parabolic softening curve from peak strength
f_{R3d}	Residual strength @ CMOD = 2.5	MPa	-11.35		"
f_{R4d}	Residual strength @ CMOD = 3.5	MPa	-10.40	$\delta = CMOD - 1$	"
Uniaxial tensile properties					Defined as stress - strain, derived from bending test results using code recommendations
f_{ck}	First crack strength	Mpa	-3.26		Assume same as flexural
f_{Ftsd}	Serviceablity residual tensile strength	Mpa	-3.62	$f_{Ftsd} = 0.45 f_{r1}$	
f_{pt}	peak strength	Mpa	-3.78	$f_{pt} = 0.7 f_{pf}$	
f_{Ftud}	Ultimate residual tensile strength	MPa	-3.78	$f_{Ftud} = f_{R3d}/3$	FIB model code 2010, eq 5.6-4. Linear model
ε_{ck}	First crack strain	ratio	-0.00011	$\epsilon_{ck} = f_{ck}E_{cd}$	Assuming linear elastic behaviour up to first crack (with same E as for compression)
ε_{Sls}	serviceabilty strain	ratio	-0.01392		Assume linear between crack and peak
ε_{pc}	peak strain	ratio	-0.020		Assume at 0.5% after Naaman
ε_{uls}	ultimate strain	ratio	-0.020		distribution
TR34 ULS design properites					
σ_{r1}	SLS residual strength	MPa	-3.62	$\sigma_{r1} = 0.45 f_{r1}$ $\sigma_{r2} = 0.35 f_{r4}$	equivalent to f_{Ftsd}
σ_{r4}	ULS residual strength	MPa	-3.85		same purpose as f_{Ftud}, but uses f_{R4d} rather than f_{R3d}

F.9 6S Design calcs SHCC option page 2of4

SLS bending and axial force (pre-crack localisation)					
x	neutral axis	mm	15.63	Iterate to balance M	If negative - then all section is in tension
INITIAL CHECK ON CRACKED / UNCRACKED SECTION					Assume simplified stress distribution to check whether cracked / uncracked
f_b	bending stress	Mpa	-0.96	$f_b = 6M_{ED,SLS}/(bt^2)$	
f_n	normal stress	MPa	-0.56	$f_n = N_{ED,SLS}/(bh)$	
$f_{tot,c}$	total compressive fibre stress		0.4		
$f_{tot,t}$	total tensile fibre stress	Mpa	-1.52	$f_{tot} = f_b + f_n$	
Cracked / uncracked?			UNCRACKED		
f_{NA}	neutral axis stress	Mpa	0.00		
				Uncracked / Cracked	
A	Equation coefficients		0	0 / $A = f_{NA}b(h-x)$	
B			223648506	$B = 0.5bxE_{cd}$	
C			-3.228E+09	$= 0.5b(h-x)\left(\frac{(x-h)}{x}E_{cd}\right)$ / $= 0.5b(h-x)\frac{(x-h)}{x}\cdot\frac{1}{\epsilon_{pc}}(f_{pc}-f_{NA})$	
ϵ_c	concrete strain		1.398E-05	$\epsilon_c = \frac{N-A}{B+C+D}$	
ϵ_{ft}	steel fibre strain		-5.311E-05	$\epsilon_{ft} = \epsilon_c\frac{(x-h)}{x}$	
FINAL CHECK ON CRACKED / UNCRACKED SETION					
Cracked / uncracked?			UNCRACKED		
Initial assumption is:			TRUE		
f_{cd}	concrete compressive stress	Mpa	0.40	$f_{cd} = \epsilon_c E_{cd}$	
f_{ft}	fibre tensile stress	Mpa	-1.52	$f_{ft} = \epsilon_{ft}E_{cd}$ / $f_{ft} = f_{NA} + \frac{\epsilon_{ft}}{\epsilon_{pc}}(f_{pc}-f_{NA})$	
C_1	Concrete compressive force	kN	3.1265825	$N_1 = 0.5bxf_{cd}$	
T_1		kN	0	$T_1 = f_{NA}b(h-x)$	
T_2		kN	-45.126582	$T_2 = 0.5b(h-x)(f_{ft}-f_{NA})$	
N calc		kN	-42	$N = C_1 + T_1 + T_2$	
N check		kN	0		
M calc		kNm	0.90		
M check		kNm	0.00	$M = N_1\left(\frac{h}{2}-\frac{x}{3}\right) - T_1\left(\frac{h}{2}-\frac{h-x}{2}\right) - T_2\left(\frac{h}{2}-\frac{h-x}{3}\right)$	Iterate x to get this value = 0
SERVICEABILITY LIMIT STATE CHECK					
$f_{ft,sls}$	Maximum serviceabilty tensile stress	MPa	-1.52	OK	
$0.6f_{Ftsk}$	Allowable serviceability stress	MPa	-2.76		FIB model code 2010 7.7.4.1
ULS CAPACITY CHECKS					
FIB Rigid Plastic: ULS bending and axial force - post peak (crack localisation phase)					
η	factor defining effective strength	factor	0.85	$\eta = 1.0 - (f_{cck}-50)/200$	FIB model code, eq 7.2-19
λ	factor defining height of compressive zone	factor	0.725	$\lambda = 0.8 - (f_{cck}-50)/400$	FIB model code, eq 7.2-16
x	neutral axis	mm	5.51	$x = \frac{N/b - f_{Ftud}.h}{\eta f_{cd}.\lambda - f_{Ftud}}$	Determined to balance N
C_1	Compressive concrete force	kN	156.81	$C_1 = \eta f_{cd}.A_c = \eta f_{cd}.\lambda x.b$	
T_1	Tensile concrete force	kN	-262.81	$T_1 = f_{Ftud}.y.b = f_{Ftud}.(h-x).b$	
N	Axial force check	kN	-106	$N = C_1 + T_1$	
x_s	centroid of stressed section	mm	37.50	$x_s = h/2$	Point of action of axial force
Mult	Ultimate moment capacity for given N	kNm	6.29	$M_{ult} = C_1\left(x_p - \frac{\lambda x}{2}\right) - C_2\left((h-x_p) - \frac{y}{2}\right)$	
ϵ_f	fibre strain @ ultimate moment	ratio	-0.0441815		assume concrete has reached ultimate strain in compression: 1
ϵ_c	concrete strain @ ultimate moment	ratio	0.0015844		assume fibre has reached ultimate strain in tension: 0
				Failure in tension	

F.9 6S Design calcs SHCC option page 3of4

T34 Constant strain hardening: SHCC ULS capacity assuming concrete fails in tension					
ε_{ftu}	ultimate tensile strain	ratio	-0.02		
f_{ftud}	ultimate tensile stress	MPa	-3.78	$f_{Ftud} = \sigma_{r5}$	Extreme fibre tensile stress
x_{bal}	balanced neutral axis	mm	9.21		failure in compression & tension simultaneously
x	neutral axis (from compressive face)	mm	4.49		iterate this value to balance N
ε_{fc}	compressive strain		0.00127	Failure in tension	Failure check - if this value is greater than ultimate compressive strain, concrete would fail in compression before tension
d_1	depth of elastic compressive section	mm	9.21	$d_1 = x(0.00175/\epsilon_{fc})$ max = x	
d_2	depth of yielded compressive section	mm	0.00	$d_2 = x - d_1$	
h_c	depth of tensile section	mm	70.51		
f_{cd}	compressive stress	mm	33.67		
N_1	Concrete compressive force (elastic)	kN	155.05	$N_1 = 0.5d_1bf_{Cd}$	
N_2	Concrete compressive force (yeilded)	kN	0.00	$N_2 = d_2bf_{Cd}$	
T_1	Concrete tensile force 1	kN	-255.46	$T_1 = bh_c\sigma_{r1}$	
T_2	Concrete tensile force 2	kN	-5.59	$T_2 = 0.5bh_c(\sigma_{r5} - \sigma_{r1})$	
N	resultant force	kN	-106.00		
N_{calc}-N_d	force check	kN	0.00		Iterate neutral axis so = 0
x_s	Centroid of stressed section	mm	37.50	=h/2	take moments about centroid of stressed section
Mult	Ultimate moment capacity	kNm	5.99	$M_{ult} = N_1e_{n1} + N_2e_{n2} - T_1e_{t1} - T_2e_{t2}$	

T34 Constant strain hardening: SHCC ULS capacity assuming concrete fails in compression					
ε_{fcu}	compressive strain		0.00350		
x_{bal}	balanced neutral axis	mm	9.21		failure in compression & tension simultaneously
x	neutral axis (from compressive face)	mm	4.76		iterate this value to balance N
ε_{ft}	ultimate tensile strain	ratio	-0.0517	Failure in tension	tensile strain, concrete would fail in compression before tension
d_1	depth of elastic compressive section	mm	2.38	$d_1 = x(0.00175/\epsilon_{fc})$ max = x	
d_2	depth of yielded compressive section	mm	2.38	$d_2 = x - d_1$	
h_c	depth of tensile section	mm	70.24		
f_{cd}	compressive stress	mm	46.22		
σ_{r1}	Serviceabilty stress limit	MPa	-3.62	$\sigma_{r1} = 0.45f_{r1}$	Code assumes that this occurs at 0 tensile strain (see stress strain figure)
σ_{r4}	Ultimate stress limit	MPa	-3.85	$\sigma_{r5} = 0.35f_{r4}$	
σ_{r5}	Tensile fibre stress	MPa	-4.09	$\sigma_{r5} = \sigma_{r1} + (\epsilon_{ft}/0.025(\sigma_{r4} - \sigma_{r1}))$	
N_1	Concrete compressive force (elastic)	kN	54.95	$N_1 = 0.5d_1bf_{Cd}$	
N_2	Concrete compressive force (yielded)	kN	109.90	$N_2 = d_2bf_{Cd}$	
T_1	Concrete tensile force 1	kN	-254.51	$T_1 = bh_c\sigma_{r1}$	
T_2	Concrete tensile force 2	kN	-16.33	$T_2 = 0.5bh_c(\sigma_{r5} - \sigma_{r1})$	
N	resultant force	kN	-106.00		
N_{calc}-N_d	force check	kN	0.00		Iterate neutral axis so = 0
x_s	Centroid of stressed section	mm	37.50	=h/2	take moments about centroid of stressed section
Mult	Ultimate moment capacity	kNm	6.71	$M_{ult} = N_1e_{n1} + N_2e_{n2} - T_1e_{t1} - T_2e_{t2}$	

Calculate ULS capacity assuming concrete fails in tension (using strain hardening / softening with peak @ 0.5%)					Codes do not currently cover UHPFRC - stress strain relationship derived from literature
ϵ_{ftu}	ultimate tensile strain	ratio	-0.02		
f_{FTU}	ultimate tensile stress	MPa	-3.78		
ϵ_{pc}	peak tensile strain	ratio	-0.020		
f_{pc}	peak tensile stress	MPa	-3.78		
x_{bal}	balanced neutral axis	mm	9.21		failure in compression & tension simultaneously
x	neutral axis (from compressive face)	mm	1.03		iterate this value to balance N
ϵ_{fc}	compressive strain		0.00028	Failure in tension	TRUE
d_1	depth of elastic compressive section	mm	9.21	$d_1 = x(0.00175/\epsilon_{fc})$ max = x	
d_2	depth of yielded compressive section	mm	0.00	$d_2 = x - d_1$	
h_c	depth of tensile section	mm	73.97		
h_1	depth to peak	mm	73.97		
h_2	depth from peak	mm	0.00		
f_{cd}	compressive stress	mm	7.35		
N_1	Concrete compressive force (elastic)	kN	33.87	$N_1 = 0.5 d_1 b f_{cd}$	
N_2	Concrete compressive force (yeilded)	kN	0.00	$N_2 = d_2 b f_{cd}$	
T_1	Concrete tensile force 1	kN	0.00	$T_1 = b h_2 f_{ftu}$	
T_2	Concrete tensile force 2	kN	0.00	$T_2 = 0.5 b h_2 (f_{pc} - f_{ftu})$	
T_3	Concrete tensile force 3	kN	-139.87		
N	resultant force	kN	-106.00		
N_{calc}-N_d	force check	kN	0.00		Iterate neutral axis so = 0
x_s	Centroid of stressed section	mm	37.50	=h/2	take moments about centroid of stressed section
$M_{ult\ comps}$	Ultimate moment capacity calc	Nm	1166.14	$N_1 e_{n1} = N_1 (x_s - (d_2 + d_1/3))$	
		Nm	0	$N_2 e_{n2} = N_1 (x_s - (d_2/2))$	
		Nm	0	$T_1 e_{t1} = T_1 ((h - x_s) - h_2/2)$	
		Nm	0	$T_2 e_{t2} = T_1 ((h - x_s) - h_2/3)$	
		Nm	1796.3904	$T_3 e_{t3} = T_3 (x_s - (x + 2h_1/3))$	
Mult	Ultimate moment capacity	kNm	2.96	$M_{ult} = N_1 e_{n1} + N_2 e_{n2} - T_1 e_{t1} - T_2 e_{t2} + T_3 e_{t3}$	

ULTIMATE LIMIT STATE CHECK			
Concrete class		SHCC	
Failure mechanism		Failure in tension	
Ultimate moment capacity		5.99	
Design ultimate moment		1.8	OK

F.10 6S design option cost estimates

Section 10.6.4 presents cost estimates for the 6S design options, based on the baseline costs. Table F.13 presents costs for all options, including the pessimistic and optimistic options.

Table F.13: 6S options cost comparison

Option	Item	Quantity	Unit	Baseline Rate	Baseline Cost	Optimistic Rate	Optimistic Cost	Pesimistic Rate	Pesimistic Cost
Concrete and reinforcement									
	Formwork	126	m^2	10	1296	5	648	51	6481
	UHPFRC provide and place, complex	3.92	m^3	625	2450	300	1176	900	3528
	Steel fibre @ 2.5%	0.76	t	1018	778	650	497	1450	1108
	Ballast	0.20	t	50	10	40	8	70	14
	Total				**£4,534**		**£2,329**		**£11,131**
Steel option									
	Tube	1	t	1800	1800	1440	1440	2520	2520
	Fabrication	3.2	t	2275	7280	1820	5824	3185	10192
	Coating	109	m^2	30	3270	24	2616	42	4578
	Ballast	5.8	t	50	290	40	232	70	406
	Total				**£12,640**		**£10,112**		**£17,696**
GFRP option									
	Tube	0.1	t	7500	750	6000	600	15000	1500
	Fabrication	0.7	t	11250	7875	9000	6300	22500	15750
	Ballast	9.2	t	50	460	40	368	70	644
	Total				**£9,085**		**£7,268**		**£17,894**

Appendix G

Connection design calculations

G.1 Preliminary design calcs

Section 11.3.2 presents the results of the preminary design calculations for the static load cases for the different connection options. Full design calculations are included here.

STEEL TO CONCRETE CONNECTION CALCS

Outline design shear stud connectors

1.0 INTRODUCTION

The purpose of these calculations is to determine the required number of shear studs to transfer dynamic loads from link arm into concrete node.

This is a preliminary design, for the purpose of comparison between connection types.
Calculations are based on outline design loads only.

1.1 Schematic

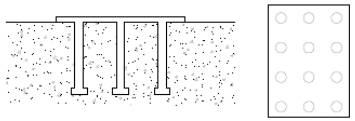

1.2 Reference documents

BS EN 1994-1-2:2004 Euorcode 4: Design of composite steel and concrete structures - Part 1-1: General rules and rules for buildings (referred to as EC4-1 through document)

Designers guide to EN 1994-2 C.R Hendy, and R.P Johnson, Thomas Telford Publishing, 2006

Draft BS EN 1992-4 Eurocode 2: Design of concrete structures - Part 4: Design of Fastenings for use in concrete (referred to as EC2-4 through document)

DNV-OS-C502 2012-09 Offshore concrete structures (referred to as DNV C502 through document)

2.0 DESIGN LOADS

2.1 Ultimate design loads

Node / PTO joint connection transmits 6 dof loads - which are resisted by steel/ concrete connections.

Force components on individual connection group determined in spreadsheet "Global Connection Loads", based on assumed ALS loads. Gives two design load cases:

Maximum tension:

Connection shear load $V_{cT} := 2.17MN$

Connection tension load $N_{cT} := 1.67MN$

Maximum shear:

Connection shear load $V_{cS} := 2.65MN$

Connection tension load $N_{cS} := 1.06MN$

2.2 Bolt group design philosophy

Assume a linear elastic connection, and determine stresses on each shear stud assuming the shear and tension loads are distributed evenly across studs.

Note that this is only valid if the following assumptions are correct (EN 1992-4) sec 6.2:

- Fixture is sufficiently rigid
- Axial stiffness of all fasteners is equal
- In zone of compression, fasteners do not take forces

2.3 Shear stud properties

Ultimate tensile strength of stud $f_u := 450MPa$

diameter of shear stud $d \equiv 25mm$

diameter of shear stud head $h := 41mm$

overall nominal height of stud $h_{sc} := 200mm$

effective embedment depth $h_{ef} := h_{sc} = 200 \cdot mm$

Area of stud $A_s := \pi \cdot \frac{d^2}{4} = 490.874 \cdot mm^2$

Area under head $A_h := \pi \frac{\left(h^2 - d^2\right)}{4} = 829.38 \cdot mm^2$

Dimensional checks:

Minimum spacing $l_s := 5 \cdot d = 0.125\,m$ EC 4 6.6.5.7 (4)

Minimum height $h_m := 3 \cdot d = 0.075\,m$ EC4 6.6.5.7 (1)

Spacing $s_1 := l_s = 0.125\,m$

Edge distance $c_e := 0.2m$

No of rows $n_r := 5$

No of columns $n_c := 6$

No of shear studs $N_s := n_r \cdot n_c = 30$

Fastener spacing factor $s_{crN} := 2 \cdot h_{ef} = 0.4\,m$ *[EC2-4 7.2.1.6]*

Edge spacing factor $c_{crN} := 3 \cdot h_{ef} = 0.6\,m$

2.4 Design loads Load factor $\gamma_f := 1.0$ ALS loadcase

2.4.1 Max tension

Maximum shear load $P_{kdT} := \frac{V_{cT}}{N_s} = 72.333 \cdot kN$

Maximum tensile load $F_{TkdT} := \frac{N_{cT}}{N_s} = 55.667 \cdot kN$

Ultimate design loads

Shear load $V_{EdT} := P_{kdT} \cdot \gamma_f = 72.333 \cdot kN$

Tensile load $N_{EdT} := F_{TkdT} \cdot \gamma_f = 55.667 \cdot kN$

2.4.2 Max shear

Maximum shear load $P_{kdS} := \frac{V_{cS}}{N_s} = 88.333 \cdot kN$

Maximum tensile load $F_{TkdS} := \frac{N_{cS}}{N_s} = 35.333 \cdot kN$

Ultimate design loads

Shear load $V_{EdS} := P_{kdS} \cdot \gamma_f = 88.333 \cdot kN$

Tensile load $N_{EdS} := F_{TkdS} \cdot \gamma_f = 35.333 \cdot kN$

3.0 SHEAR STUD CAPACITY

3.1 Shear capacity

Capacity of shear stud calculated in accordance with EC4, section 6.6.3.1:

$$P_{Rd} = \frac{0{,}8\, f_u\, \pi\, d^2/4}{\gamma_V} \qquad (6.18)$$

or:

$$P_{Rd} = \frac{0{,}29\, \alpha d^2 \sqrt{f_{ck} E_{cm}}}{\gamma_V} \qquad (6.19)$$

whichever is smaller, with:

$$\alpha = 0{,}2\left(\frac{h_{sc}}{d} + 1\right) \quad \text{for } 3 \le h_{sc}/d \le 4 \qquad (6.20)$$

$$\alpha = 1 \quad \text{for } h_{sc}/d > 4 \qquad (6.21)$$

where:

γ_V is the partial factor;

d is the diameter of the shank of the stud, 16 mm ≤ d ≤ 25 mm;

f_u is the specified ultimate tensile strength of the material of the stud but not greater than 500 N/mm²;

[AC1] f_{ck} [AC1] is the characteristic cylinder compressive strength of the concrete at the age considered, of density not less than 1750 kg/m³;

h_{sc} is the overall nominal height of the stud.

Note: The value for γ_V may be given in the National Annex. The recommended value for γ_V is 1,25.

Ultimate tensile strength of stud $f_u := 4.5 \times 10^8\,\text{Pa}$

Yeild strenght of stud $f_y := 355\text{MPa}$

partial factor in shear $\gamma_v := 1$

partial factor in tension $\gamma_{Mst} := 1.2 \cdot \frac{f_u}{f_y} = 1.521$ *[EC2-4-1 4.4.3]*

characteristic cylinder compressive strength of concrete $f_{ck} := 50\,\frac{N}{mm^2}$

Youngs modulus of concrete $E_{cm} := 35\text{GPa} = 3.5 \times 10^{10}\,\text{Pa}$

overall nominal height of the stud $h_{sc} = 0.2\,\text{m}$ $\frac{h_{sc}}{d} = 8$

$\alpha_1 := 0.2 \cdot \left(\frac{h_{sc}}{d} + 1\right) = 1.8$ $\alpha_2 := 1$ $\alpha := \text{if}\left(\frac{h_{sc}}{d} > 4, \alpha_2, \alpha_1\right) = 1$

$P_{rd.1} := \frac{0.8 \cdot f_u \cdot \pi \cdot \frac{d^2}{4}}{\gamma_v} = 176.715 \cdot \text{kN}$ shear strength of stud

$P_{rd.2} := \frac{0.29 \cdot \alpha \cdot d^2 \cdot (f_{ck} \cdot E_{cm})^{0.5}}{\gamma_v} = 239.771 \cdot \text{kN}$ concrete crushing strength

$P_{rd} := \min(P_{rd.1}, P_{rd.2}) = 176.715 \cdot \text{kN}$

3.2 Tensile capacity

EC4 doesn't give tensile capacity for shear studs, therefore design according to EC2-4

Tension resistance $N_{Rds} := 0.9 \cdot \frac{f_u}{\gamma_{Mst}} \cdot A_s = 130.695 \cdot \text{kN}$

4.2.3 Concrete resistance - tension loads

(a) Pull-out failure of fastener *[EC2-4 7.2.1.4]*

Limited by concrete pressure under head of fastener

Factor for cracked concrete $k_1 := 7.5$

$N_{Rkp} := k_1 \cdot A_h \cdot f_{ck} = 311.018 \cdot \text{kN}$

(b) Concrete cone failure *[EC2-4 7.2.1.6]*

Characteristic resistance of single fastener *[EC 2-4 eq (7.14)]*

load transfer factor $k_{cr} := 8.9 \sqrt{\frac{N}{mm}}$ as recommended in standard note for headed fasteners for cracked concrete

$k_{cm} := 12.7 \sqrt{\frac{N}{mm}}$

$N_{Rk0} := k_{cr} \cdot \sqrt{f_{ck}} \cdot h_{ef}^{1.5} = 178 \cdot \text{kN}$

$N_{Rk0} := k_{crn} \cdot \sqrt{f_{ck}} \cdot h_{ef}^{1.5} = 254 \cdot \text{kN}$

Reference projected area of single fastener $A_{cN0} := s_{crN}^2 = 0.16\,\text{m}^2$

Actual projected area limited by overlapping cones of adjacent fasteners

$A_{cN} := \left[(n_c - 1) \cdot s_1 + s_{crN}\right] \cdot \left[(n_r - 1) \cdot s_1 + c_e + 0.5 s_{crN}\right] = 0.922\,\text{m}^2$

Concrete edge factor $\varphi_{sN} := \min\left[\left(0.7 + 0.3 \cdot \frac{c_e}{c_{crN}}\right), 1\right] = 0.8$

Shell spalling factor $\varphi_{reN} := \min\left[\left(0.5 + \frac{h_{ef}}{200\text{mm}}\right), 1\right] = 1$

Eccentricty factor $\varphi_{ecN} := 1$ Loads applied at centroid

Compression factor $\varphi_{MN} := 1$ No bending applied

Fastener positioning factor $\varphi_{ucrN} := 1$ cracked concrete

Concrete cone resistance $N_{Rkc} := N_{Rk0} \cdot \frac{A_{cN}}{A_{cN0}} \cdot \varphi_{sN} \cdot \varphi_{reN} \cdot \varphi_{ecN} \cdot \varphi_{ucrN} = 1.172 \times 10^3 \cdot \text{kN}$

Cone resistance < total tension load, therefore supplementary reinforcement will be needed to take tensile loads

(c) Splitting failure *[EC2-4-2 6.2.6.2]*

Reinforcment will be included to prevent splitting, therefore no explicit check is required

(d) Blow out failure *[EC2-4-2 6.2.7]*

critical edge distance $c_{crb} := 0.5h_{ef} = 0.1\,m$

Edge distance $c_e = 0.2\,m$ which is greater than critical therefore verification not required

Maximum spacing of stud to prevent plate buckling in compression (6.6.5.5 (2))

Plate thickness $t_h := 12mm$

Yield strength of plate $f_{yk\_p} := 275MPa$

$$l_{smax} := 22 \cdot t_h \cdot \left(\frac{235MPa}{f_{yk\_p}}\right)^{0.5} = 0.244\,m$$

Tension resistance $N_{Rd} := \min\left(N_{Rds}, N_{Rkp}\right) = 130.695 \cdot kN$

4.0 DESIGN CHECKS

4.1 Maximum tension

Steel shear usage factor $U_{TvS} := \frac{V_{EdT}}{P_{rd.1}} = 0.409$

Steel tension usage factor $U_{TT} := \frac{N_{EdT}}{N_{Rds}} = 0.426$

Concrete crushing usage factor $U_{TvCC} := \frac{V_{EdT}}{P_{rd.2}} = 0.302$

Concrete pull out usage factor $U_{TTPO} := \frac{N_{EdT}}{N_{Rkp}} = 0.179$

Cone concrete failure $U_{CF} := \frac{N_{cT}}{N_{Rkc}} = 1.425$

Combined tension / shear interaction $U_{TvS}^{1.5} + U_{TT}^{1.5} = 0.54$

$U_{TvS} + U_{TT} = 0.835$

4.2 Maximum shear

Steel shear usage factor $U_{SvS} := \frac{V_{EdS}}{P_{rd.1}} = 0.5$

Steel tension usage factor $U_{ST} := \frac{N_{EdS}}{N_{Rds}} = 0.27$

Concrete crushing usage factor $U_{SvCC} := \frac{V_{EdS}}{P_{rd.2}} = 0.368$

Concrete pull out usage factor $U_{STPO} := \frac{N_{EdS}}{N_{Rkp}} = 0.114$

Combined tension / shear interaction $U_{SvS}^{1.5} + U_{ST}^{1.5} = 0.494$

$U_{SvS} + U_{ST} = 0.77$

G.1 Preliminary connection calculations

COMPOSITE DOWEL DESIGN

Based on German technical approval as described in "Composite dowels as shear connectors for composite beams - background to the German technical approval" Feldmann et. al 2016

Clothoid (CL) shape - schematic

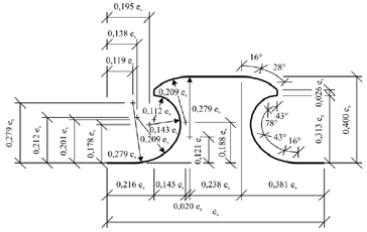

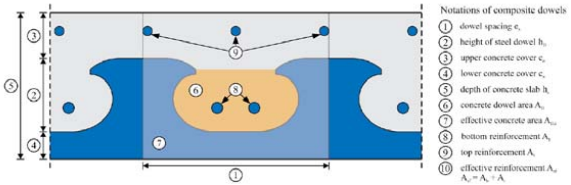

1.0 DOWEL DIMENSIONS and DESIGN PROPS

1.1 Steel dimensions

Dowel spacing	$e_x \equiv 250mm$
Height of steel dowel	$h_D := 0.4e_x = 100 \cdot mm$
Web thickness	$t_w \equiv 20mm$
Overall concrete thickness	$h_c := 500mm$
Lower concrete cover	$c_u := 90mm$
Upper concrete cover	$c_o := h_c - h_D - c_u = 310 \cdot mm$
No of dowels in rib	$n_D \equiv 3$
No of ribs	$n_R \equiv 3$
Rib spacing	$s_R := 0.3m$
Youngs modulus of steel	$E_s := 200GPa$
Yield strength of steel	$f_y := 355MPa$

1.2 Reinforcement

(a) Top reinforcement

No of bars	$n_{st} := 2$
Diameter of bars	$d_{st} := 20mm$

G.1 Preliminary connection calculations

Total area of top steel	$A_t := n_{st} \cdot \pi \cdot \frac{d_{st}^2}{4} = 628.319 \cdot mm^2$

(b) Bottom reinforcement

No of bars	$n_{sb} := 3$
Diameter of bars	$d_{sb} := 16mm$
Total area of bottom steel	$A_b := n_{sb} \cdot \pi \cdot \frac{d_{sb}^2}{4} = 603.186 \cdot mm^2$

1.3 Concrete

Characteristic concrete strength	$f_{ck} := 50MPa$
Youngs modulus of concrete	$E_{cm} := 30GPa$

3.0 DESIGN LOADS

3.1 Ultimate design loads

Node / PTO joint connection transmits 6 dof loads - which are resisted by steel/ concrete connections.
Force components on individual connection group determined in spreadsheet "Global Connection Loads", based on assumed ALS loads. Gives two design load cases:

Maximum tension:

Connection vertical shear load	$V_{vT} := 0.45MN$
Connection horizontal shear load	$V_{hT} := 2.13MN$
Connection tension load	$N_{cT} := 1.67MN$

Maximum shear:

Connection vertical shear load	$V_{vS} := 0.21MN$
Connection horizontal shear load	$V_{hS} := 2.65MN$
Connection tension load	$N_{cS} := 1.06MN$

3.2 Individual rib load

(a) Maximum tension

Longitudinal shear	$P_{RdT} := \frac{V_{hT}}{n_R} = 710 \cdot kN$
Vertical bearing	$V_{RdT} := \frac{V_{vT}}{n_R} = 150 \cdot kN$
Axial tension	$N_{RdT} := \frac{N_{cT}}{n_R} = 556.667 \cdot kN$

(b) Maximum shear

Longitudinal shear	$P_{RdS} := \frac{V_{hS}}{n_R} = 883.333 \cdot kN$
Vertical bearing	$V_{RdS} := \frac{V_{vS}}{n_R} = 70 \cdot kN$
Axial tension	$N_{RdS} := \frac{N_{cS}}{n_R} = 353.333 \cdot kN$

G.1 Preliminary connection calculations

4.0 DOWEL RESISTANCE

4.1 Longitudinal shear capacity

(a) Concrete shearing

Concrete dowel area $A_D := 0.2 \cdot e_x^{\,2} = 0.013\ m^2$

Geometry reduction factor $\eta_D := \left(3 - \frac{e_x}{180mm}\right) \cdot \sqrt{MPa} = 1.611 \times 10^3 \frac{kg^{0.5}}{m^{0.5} \cdot s}$

Reinforcement ratio $\rho_D := \frac{E_s \cdot A_b}{E_{cm} \cdot A_D} = 0.322$

Concrete shearing resistance per dowel $P_{shk} := \eta_D \cdot e_x^{\,2} \cdot \sqrt{f_{ck}} \cdot (1 + \rho_D) = 941.073 \cdot kN$

Total concrete shear resistance $P_{shktot} := P_{shk} \cdot n_D = 2.823 \times 10^3 \cdot kN$

(b) Steel failure

Steel shear capacity per dowel $P_{plk} := 0.25 \cdot e_x \cdot t_w \cdot f_y = 443.75 \cdot kN$

Total steel shear capacity $P_{plkt} := P_{plk} \cdot n_D = 1.331 \times 10^3 \cdot kN$

4.2 Pull out capacity

Note that the German Technical Approval does not deal with pullout loads. These have been estimated using the equations in "Anchorage of composite dowels" (Classen & Hegger, 2016). These equations have been developed for "Puzzle" shaped dowels, but assume that they can be applied to clothoidal dowels.

(a) Concrete cone resistance

Embedment depth to top of rebar $h := c_u + 0.313 \cdot e_x = 0.168\ m$

Length of cone $l_0 := 3 \cdot h + 7.5 \cdot \frac{d_{sb}}{2} = 0.565\ m$

Length of dowel $l_{dowel} := 3 \cdot h + 7.5 \cdot d_{sb} + \min\left(3 \cdot h, \frac{e_x}{e}\right) = 0.717\ m$

Width of cone $b_0 := 3 \cdot h = 0.505\ m$

Width of dowel $b_{dowel} := 3 \cdot h + 7.5 \cdot d_{sb} = 0.625\ m$

Longitudinal stress factor $\Psi := 0.9$ Assume longitudinal stress acting

Anchorage capacity of a single dowel $F_{Rdowel} := 8 \cdot \sqrt{f_{ck}} \cdot h^{1.5} \cdot \Psi \cdot \frac{b_{dowel}}{b_0} \cdot \frac{N^{0.5}}{mm^{0.5}}$

Length of dowel group $l_{group} := e_x \cdot 2 \cdot (2 \cdot n_D - 1) + 3 \cdot h + 2 \cdot 7.5 \cdot \frac{d_{sb}}{2}$

Anchorage capacity of dowel group $F_{Rgroup} := F_{Rdowel} \cdot \frac{l_{group}}{l_{dowel}} = 599.578 \cdot kN$

By same logic can work out anchorage capacity of rib group

Width of rib group $b_{group} := s_R \cdot (n_R - 1) + 3 \cdot h + 7.5 \cdot d_{sb} = 1.225\ m$

Anchorage capacity of rib group $F_{RRgroup} := F_{Rgroup} \cdot \frac{b_{group}}{b_{dowel}} = 1.175 \times 10^3 \cdot kN$

G.1 Preliminary connection calculations

(b) Steel failure of rib

Width of narrowest section of dowel $b_{re} := e_x - 2 \cdot (0.138 \cdot e_x + 0.143 \cdot e_x) = 109.5 \cdot mm$

Effective area in tension $A_{re} := b_{re} \cdot t_w = 2.19 \times 10^3 \cdot mm^2$

Total steel area in rib $A_{reTot} := A_{re} \cdot n_D = 6.57 \times 10^3 \cdot mm^2$

Steel resistance to tension per rib $N_{sTk} := A_{reTot} \cdot f_y = 2.332 \times 10^3 \cdot kN$

5.0 CONNECTION VERIFICATION Load factor $\gamma_v := 1.25$

(a) Design shear resistances

Concrete shearing resistance $P_{shdtot} := \frac{P_{shktot}}{\gamma_v} = 2.259 \times 10^3 \cdot kN$

Steel shear failure $P_{pldt} := \frac{P_{plkt}}{\gamma_v} = 1.065 \times 10^3 \cdot kN$

(b) Design tension resistance

Concrete cone failure (for all ribs) $F_{RRD} := \frac{F_{RRgroup}}{\gamma_v} = 940.323 \cdot kN$

Steel failure per rib $N_{std} := \frac{N_{sTk}}{\gamma_v} = 1.866 \times 10^3 \cdot kN$

5.1 Maximum tension

Concrete shearing $U_{shT} := \frac{P_{RdT}}{P_{shdtot}} = 0.314$

Steel shear failure $U_{plT} := \frac{P_{RdT}}{P_{pldt}} = 0.667$

Concrete cone failure $U_{RRT} := \frac{N_{cT}}{F_{RRD}} = 1.776$

Steel tension failure $U_{stT} := \frac{N_{RdT}}{N_{std}} = 0.298$

5.2 Maximum shear

Concrete shearing $U_{shS} := \frac{P_{RdS}}{P_{shdtot}} = 0.391$

Steel shear failure $U_{plS} := \frac{P_{RdS}}{P_{pldt}} = 0.829$

Concrete cone failure $U_{RRS} := \frac{N_{cS}}{F_{RRD}} = 1.127$

Steel tension failure $U_{stS} := \frac{N_{RdS}}{N_{std}} = 0.189$

STEEL TO CONCRETE CONNECTION CALCS
Cast in bolted connection

1.0 INTRODUCTION

Preliminary calcs for link arm to node connection - for connection made with cast in bolts/studs/ anchors or similar

Check forces on individual connectors as per a bolted connection calcs:

1.1 Schematic

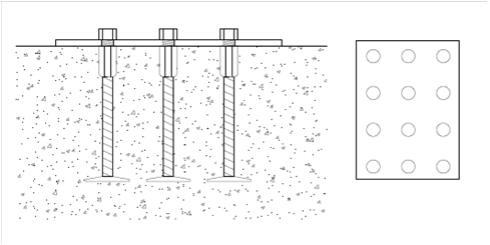

1.2 References

Draft BS EN 1992-4 Eurocode 2: Design of concrete structures - Part 4: Design of Fastenings for use in concrete (referred to as EC2-4 through document)
Halfen HUC Universal Connection Technical Product Information (HUC)
Halfen HSC Stud Connector Technical Product Information (HSC)

2.0 DESIGN LOADS

2.1 Ultimate design loads

Node / PTO joint connection transmits 6 dof loads - which are resisted by steel/ concrete connections.
Force components on individual connection group determined in spreadsheet "Global Connection Loads", based on assumed ALS loads. Gives two design load cases:

Maximum tension:

Connection shear load $V_{cT} := 2.17MN$
Connection tension load $N_{cT} := 1.67MN$

Maximum shear:

Connection shear load $V_{cS} := 2.65MN$
Connection tension load $N_{cS} := 1.06MN$

2.2 Bolt group design philosophy

Assume a linear elastic connection, and determine stresses on each fastener assuming the shear and tension loads are distributed evenly across studs.

Note that this is only valid if the following assumptions are correct (EN 1992-4) sec 6.2:

- Fixture is sufficiently rigid
- Axial stiffness of all fasteners is equal
- In zone of compression, fasteners do not take forces

Dimensions of bolt group

No of bolt columns $N_c := 4$
No of bolt rows $N_r := 5$
No of bolts $N_b := N_c \cdot N_r = 20$
Minimum bolt spacing $a_{ij} := 66mm$ *[HUC pg 9]*
Bolt spacing $s_1 := 125mm$ $s_2 := 175mm$
Edge distance $c_e := 300mm$

2.3 Design loads Load factor $\gamma_f := 1.0$ ALS loadcase

2.4.1 Max tension

Maximum shear load $P_{kdT} := \frac{V_{cT}}{N_b} = 108.5 \cdot kN$
Maximum tensile load $F_{TkdT} := \frac{N_{cT}}{N_b} = 83.5 \cdot kN$

Ultimate design loads

Shear load $V_{EdT} := P_{kdT} \cdot \gamma_f = 108.5 \cdot kN$
Tensile load $N_{EdT} := F_{TkdT} \cdot \gamma_f = 83.5 \cdot kN$

2.4.2 Max shear

Maximum shear load $P_{kdS} := \frac{V_{cS}}{N_b} = 132.5 \cdot kN$
Maximum tensile load $F_{TkdS} := \frac{N_{cS}}{N_b} = 53 \cdot kN$

Ultimate design loads

Shear load $V_{EdS} := P_{kdS} \cdot \gamma_f = 132.5 \cdot kN$
Tensile load $N_{EdS} := F_{TkdS} \cdot \gamma_f = 53 \cdot kN$

4.0 ANCHORAGE DESIGN

Calculation to be based on Halfen Universal Connection System, consisting of cast in HSC-B socket bars, for connections with standard bolts.

Check capacity of bolts and socket bar system: HSC-B 25 preselection graph *[HUC pg 12]*

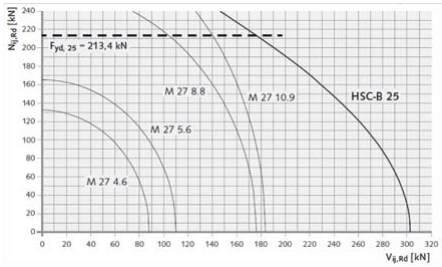

From graph - HSC-B 25 with M27 8.8 bolts will be acceptable. For steel failure - bolt will be critical rather than HSC socket bar.

4.1 Connection properties

4.1.1 Material properties of bolt

Ultimate strength $f_{ubk} := 800MPa$ *[HUC pg 11]*

Yield strength $f_{ybk} := 640MPa$

Area of bolt $A_{sp} := 4.59cm^2$

Shear factor $\alpha_v := 0.6$

Yield strength of socket $R_{p0.2} := 440MPa$

4.1.2 Dimensions of socket

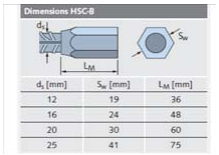

d_s [mm]	S_w [mm]	L_M [mm]
12	19	36
16	24	48
20	30	60
25	41	75

$d_s := 25mm$ *[HUC pg 13]*

$S_w := 41mm$

$L_M := 75mm$

4.1.3 Dimensions of head

[HSC pg 8]

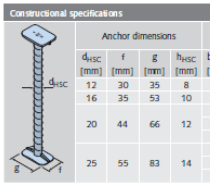

d_{HSC} [mm]	f [mm]	g [mm]	h_{HSC} [mm]
12	30	35	8
16	35	53	10
20	44	66	12
25	55	83	14

$f_s := 55mm$

$g_s := 83mm$

Area of head $A_h := f_s \cdot g_s = 4.565 \times 10^3 \cdot mm^2$

Embedment depth $h_{ef} := 300mm$

Fastener spacing factor $s_{crN} := 2 \cdot h_{ef} = 0.6\,m$ *[EC2-4 7.2.1.6]*

Edge spacing factor $c_{crN} := 3 \cdot h_{ef} = 0.9\,m$

4.1.4 Concrete properties

Concrete cube strength $f_{ck} := 50MPa$

4.2 Calculation of resistances

4.2.1 Partial factors for material resistance ULS *[EC2-4-1 4.4.3]*

Tension loading steel bolt $\gamma_{Mst} := 1.2 \cdot \frac{f_{ubk}}{f_{ybk}} = 1.5$

Shear loading steel bolt $\gamma_{Mss} := 1.0 \cdot \frac{f_{ubk}}{f_{ybk}} = 1.25$

Concrete $\gamma_{Mc} := 1.5$

For pull out failure $\gamma_{Mp} := \gamma_{Mc}$ as recommended in the note in the standard

Reinforcement in tension $\gamma_{MSre} := 1.15$

4.2.2 Bolt resistance *[HUC pg11]*

Tension resistance $N_{Rds} := 0.9 \cdot \frac{f_{ubk}}{\gamma_{Mst}} \cdot A_{sp} = 220.32 \cdot kN$

Shear resistance $V_{Rds} := \alpha_v \cdot \frac{f_{ubk}}{\gamma_{Mss}} \cdot A_{sp} = 176.256 \cdot kN$

4.2.3 Concrete resistance - tension loads

(a) Pull-out failure of fastener *[EC2-4 7.2.1.4]*

Limited by concrete pressure under head of fastener

Factor for cracked concrete $k_1 := 7.5$ $N_{Rkp} := k_1 \cdot A_h \cdot f_{ck} = 1.712 \times 10^3 \cdot kN$

(b) Concrete cone failure *[EC2-4 7.2.1.6]*

Characteristic resistance of single fastener *[EC 2-4 eq (7.14)]*

load transfer factor $k_{cr} := 8.9 \sqrt{\frac{N}{mm}}$ as recommended in standard note for headed fasteners

$N_{Rk0} := k_{cr} \cdot \sqrt{f_{ck}} \cdot h_{ef}^{1.5} = 327.007 \cdot kN$

Reference projected area of single fastener $A_{cN0} := s_{crN}^2 = 0.36\,m^2$

Actual projected area limited by overlapping cones of adjacent fasteners

$A_{cN} := \left[\left(N_c - 1\right) \cdot s_1 + s_{crN}\right] \cdot \left[\left(N_r - 1\right) \cdot s_2 + c_e + 0.5 s_{crN}\right] = 1.268\,m^2$

Concrete edge factor $\varphi_{sN} := \min\left[\left(0.7 + 0.3 \cdot \frac{c_e}{c_{crN}}\right), 1\right] = 0.8$

Shell spalling factor $\varphi_{reN} := \min\left[\left(0.5 + \frac{h_{ef}}{200mm}\right), 1\right] = 1$

Eccentricity factor $\varphi_{ecN} := 1$ Loads applied at centroid

Compression factor $\varphi_{MN} := 1$ No bending applied

Fastener positioning factor $\varphi_{ucrN} := 1$ cracked concrete

Concrete cone resistance $N_{Rkc} := N_{Rk0} \cdot \frac{A_{cN}}{A_{cN0}} \cdot \varphi_{sN} \cdot \varphi_{reN} \cdot \varphi_{ecN} \cdot \varphi_{ucrN} = 921.069 \cdot kN$

Cone resistance < total tension load, therefore supplementary reinforcement will be needed to take tensile loads

(c) Splitting failure *[EC2-4-2 6.2.6.2]*

Reinforcment will be included to prevent splitting, therefore no explicit check is required

(d) Blow out failure *[EC2-4-2 6.2.7]*

critical edge distance $c_{crb} := 0.5h_{ef} = 0.15\,m$

Edge distance $c_e = 0.3\,m$ which is greater than critical therefore verification not required

4.2.4 Concrete resistance - shear loads

(a) Local concrete crushing *[HUC pg 13]*

$$V_{c.loc.Rd} := \frac{1.44}{\gamma_{Mc}} S_w^{\,2} \cdot \left(f_{ck} \cdot R_{p0.2}\right)^{0.5} = 239.359 \cdot kN$$

(b) Concrete edge failure *[EC2-4-2 6.3.5]*

Verification not required, as supplementary reinforcement will be included to take tensile loads

4.2.5 Supplementary reinforcement - tension

Diameter of reinfrocement bars $d_{re} := 16mm$

(a) Steel failure of reinforcement *[EC2-4 7.2.1.9]*

Area of reinforcement bars $A_{sre} := \pi \cdot \frac{d_{re}^{\,2}}{4} = 201.062 \cdot mm^2$

Yeild strength of reinforcement $f_{ykre} := 450 \frac{N}{mm^2}$

Steel reinforcement resistance per bar $N_{Rkre} := A_{sre} \cdot f_{ykre} = 90.478 \cdot kN$

(b) Anchorage failure in concrete cone

Length of anchorage $l_1 := 500mm$

Bar influencing factor $\alpha := 0.7$ Hooked bars

Ultimate bond stress *[EC2 - 1 8.4.2]*

Tensile strength of concrete $f_{ctd} := 2.9MPa$

Bond condition coefficient $\eta_1 := 1$

Bar diameter coefficient $\eta_2 := 1$

Bond stress $f_{bd} := \eta_1 \cdot \eta_2 \cdot f_{ctd} = 2.9 \cdot MPa$

Anchorage resistance per bar $N_{Rda} := l_1 \cdot \pi \cdot d_{re} \cdot \frac{f_{bd}}{\alpha} = 104.121 \cdot kN$

5 CONNECTION VERIFICATION

5.1 Max Tension

Tension design action on single bolt: $N_{EdT} = 83.5 \cdot kN$

Steel failure of fastener: $N_{Rds} = 220.32 \cdot kN$ $UT_{RdsT} := \frac{N_{EdT}}{N_{Rds}} = 0.379$

Pull out failure of fastener: $N_{Rdp} := \frac{N_{Rkp}}{\gamma_{Mp}} = 1.141 \times 10^3 \cdot kN$ $UT_{RdpT} := \frac{N_{EdT}}{N_{Rdp}} = 0.073$

Concrete cone failure, and splitting failure not required as supplementary reinforcement will be included to take the tension resulting from these failure modes.

Blow out failure not required as edge distance is greater than half embedment depth

Supplementary reinforcement

Steel failure of reinforcement per bar $N_{Rdre} := \frac{N_{Rkre}}{\gamma_{MSre}} = 78.676 \cdot kN$

Anchorage failure of reinforcement per bar $N_{Rda} = 104.121 \cdot kN$

Reinforcment resistance $N_{Rr} := \min\left(N_{Rdre}, N_{Rda}\right) = 78.676 \cdot kN$

Total no. of bars required to take tension $n_{sr} := \frac{N_{cT}}{N_{Rr}} = 21.226$

Shear design action on single bolt: $V_{EdT} = 108.5 \cdot kN$

Steel failure of fastener (no lever arm): $V_{Rds} = 176.256 \cdot kN$ $UV_{RdsT} := \frac{V_{EdT}}{V_{Rds}} = 0.616$

Local concrete crushing $V_{Rdcp} := \frac{V_{c.loc.Rd}}{\gamma_{Mc}} = 159.573 \cdot kN$ $UV_{RdcpT} := \frac{V_{EdT}}{V_{Rdcp}} = 0.68$

Tension shear interaction verification for steel $\left(\frac{N_{EdT}}{N_{Rds}}\right)^2 + \left(\frac{V_{EdT}}{V_{Rds}}\right)^2 = 0.523$

Tension shear interation for other failure modes

$$\left(UT_{RdpT}\right)^{1.5} + UV_{RdcpT}^{\,1.5} = 0.58$$

$$\left(UT_{RdpT}\right) + UV_{RdcpT} = 0.753$$

Concrete cone failure

$$\frac{N_{cT}}{N_{Rkc}} = 1.813$$

5.1 Max Shear

Tension design action on single bolt: $N_{EdS} = 53 \cdot kN$

Steel failure of fastener: $N_{Rds} = 220.32 \cdot kN$ $UT_{RdsS} := \frac{N_{EdS}}{N_{Rds}} = 0.241$

Pull out failure of fastener: $UT_{RdpS} := \frac{N_{EdS}}{N_{Rdp}} = 0.046$

Concrete cone failure, and splitting failure not required as supplementary reinforcement will be included to take the tension resulting from these failure modes.

Blow out failure not required as edge distance is greater than half embedment depth

Shear design action on single bolt: $V_{EdS} = 132.5 \cdot kN$

Steel failure of fastener (no lever arm): $V_{Rds} = 176.256 \cdot kN$ $UV_{RdsS} := \frac{V_{EdS}}{V_{Rds}} = 0.752$

Concrete crushing failure $UV_{RdcpS} := \frac{V_{EdS}}{V_{Rdcp}} = 0.83$

Tension shear interaction verification for steel $\left(\frac{N_{EdS}}{N_{Rds}}\right)^2 + \left(\frac{V_{EdS}}{V_{Rds}}\right)^2 = 0.623$

Tension shear interation for other failure modes

$\left(\left(UT_{RdpS}\right)\right)^{1.5} + UV_{RdcpS}{}^{1.5} = 0.767$

$\left(\left(UT_{RdpS}\right)\right) + UV_{RdcpS} = 0.877$

6 PRELOADED BOLTS

The calculations in the previous sections have been determined on the basis of un-preloaded bolts. However preloading bolts increases the fatigue life of a connection as it reduces the magnitude of stress fluctuations, and reduces slip under shear, and therefore is recommended for dynamic connections.

The effect of externally applied loads on a preloaded bolt depends on the relative stiffness of the bolt (in tension), and the joint (in compression) can be determined using a joint diagram as shown in the figure below:

6.1 Determine stiffness of bolt and anchor

Axial spring stiffness K=EA/l, and for combination of different areas 1/K = 1/K1+1/K2 .... +1/Kn.

Assume bolt and stud anchor act as composite section.

Youngs modulus of steel $E_s := 200GPa$

M27 Bolt $A_{sp} = 459 \cdot mm^2$ $l_{sp} := 25mm$ thickness of bearing plate

Socket head $S_w = 41 \cdot mm$ $A_{sh} := \frac{2 \cdot 3}{\sqrt{3}} \cdot \left(\frac{S_w}{2}\right)^2 = 1.456 \times 10^3 \cdot mm^2$ $L_M = 0.075\,m$

Anchor $A_a := d_s^2 \cdot \frac{\pi}{4} = 490.874 \cdot mm^2$ $l_a := h_{ef} - L_M$

Stiffness of bolt

$$K_b := \frac{1}{\left[\frac{1}{E_s} \cdot \left(\frac{l_{sp}}{A_{sp}} + \frac{L_M}{A_{sh}} + \frac{l_a}{A_a}\right)\right]} = 3.544 \times 10^5 \cdot \frac{kN}{m}$$

6.2 Determine stiffness of joint

Take cross section of concrete from Unbrako paper on Joint Diagrams, for case where joint diameter is greater than 3x the diameter of the loaded area. Assume that preload spreads through base plate at 45º, and washer is used to transfer loads, with 1.5x diameter of head. therefore diameter of loaded area of concrete = 1.5*Sw + l.sp

Diameter of loaded area = $d_l := 1.5S_w + l_{sp} = 0.087\,m$

Effective area of concrete $A_{sc} := \frac{\pi}{4}\left[\left(d_l + 0.1 \cdot h_{ef}\right)^2 - d_s^2\right] = 1.017 \times 10^4 \cdot mm^2$

Youngs modulus of concrete $E_c := 30GPa$

Stiffness of joint concrete $K_{jc} := \frac{E_c \cdot A_{sc}}{h_{ef}} = 1.017 \times 10^6 \cdot \frac{kN}{m}$

6.3 Joint diagram

Set preload as maximum allowable $F_{pI} := 173.3kN$ *[HUC pg 9]*

Assume loss of preload over life = $p_{loss} := 30\%$

Therefore final preload $F_p := F_{pI} \cdot \left(1 - p_{loss}\right) = 121.31 \cdot kN$

Bolt extension under preload $\delta_b := \frac{F_p}{K_b} = 0.342 \cdot mm$

Joint compression under preload $\delta_j := \frac{F_p}{K_{jc}} = 0.119 \cdot mm$

$$\delta l := \begin{pmatrix} 0 \\ \delta_b \\ \delta_j + \delta_b \end{pmatrix} \qquad Fe := \begin{pmatrix} 0 \\ F_p \\ 0 \end{pmatrix}$$

STEEL TO CONCRETE CONNECTION CALCS
Post-tensioned bars

1.0 INTRODUCTION

Preliminary calcs for link arm to node connection - for connection made with post-tensioned anchorage

Check forces on individual connectors as per a bolted connection calcs:

1.2 References

BS EN 1994-1-2:2004 Euorcode 4: Design of composite steel and concrete structures - Part 1-1: General rules and rules for buildings (referred to as EC4-1 through document)

BS EN 1992-4-2:2009 Design of fastenings for use in concrete, part 4-2 Headed fasteners (ref EN2-4-2)

BS EN 1991-1 Design of cocnrete structures, part 1-1: General rules and rules for buildings

Macalloy Post Tensioning System Product Brochure January 2018 [ref MPTB]

2.0 DESIGN LOADS

2.1 Ultimate design loads

Node / PTO joint connection transmits 6 dof loads - which are resisted by steel/ concrete connections.
Force components on individual connection group determined in spreadsheet "Global Connection Loads", based on assumed ALS loads. Gives two design load cases:

Maximum tension:

Connection shear load $V_{cT} := 2.12MN$

Connection tension load $N_{cT} := 1.67MN$

Maximum shear:

Connection shear load $V_{cS} := 2.65MN$

Connection tension load $N_{cS} := 1.06MN$

2.2 Bolt group design philosophy

Assume a linear elastic connection, and determine stresses on each bolt assuming the shear and tension loads are distributed evenly across studs.

Note that this is only valid if the following assumptions are correct (EN 1992-4) sec 6.2:

- Fixture is sufficiently rigid
- Axial stiffness of all fasteners is equal
- In zone of compression, fasteners do not take forces

Dimensions of bolt group

No of bar columns $N_c := 4$

No of bar rows $N_r := 3$

No of bar $N_b := N_c \cdot N_r = 12$

Bar spacing $s_1 := 300mm$

Edge distance $c_e := 200mm$

Bar diameter $d_b := 32mm$

2.3 Design loads

2.4.1 Max tension

Maximum shear load $P_{kdT} := \frac{V_{cT}}{N_b} = 176.667 \cdot kN$

Maximum tensile load $F_{TkdT} := \frac{N_{cT}}{N_b} = 139.167 \cdot kN$

Load factor $\gamma_f := 1.0$ ALS loadcase

Ultimate design loads

Shear load $V_{EdT} := P_{kdT} \cdot \gamma_f = 176.667 \cdot kN$

Tensile load $N_{EdT} := F_{TkdT} \cdot \gamma_f = 139.167 \cdot kN$

2.4.2 Max shear

Maximum shear load $P_{kdS} := \frac{V_{cS}}{N_b} = 220.833 \cdot kN$

Maximum tensile load $F_{TkdS} := \frac{N_{cT}}{N_b} = 139.167 \cdot kN$

Ultimate design loads

Shear load $V_{EdS} := P_{kdS} \cdot \gamma_f = 220.833 \cdot kN$

Tensile load $N_{EdS} := F_{TkdS} \cdot \gamma_f = 139.167 \cdot kN$

4.0 ANCHORAGE DESIGN

Calculation to be based on Macalloy S1030 post-tensioning bars

Bars to be tensioned through full thickness of wall, therefore embedment depth equal to wall thickness

$h_{ef} := 500mm$

length of end plate $p_l := 100mm$

Area of end plate $A_h := p_l^2 = 1 \times 10^4 \cdot mm^2$

Fastener spacing factor $s_{crN} := 2 \cdot h_{ef} = 1\,m$ *[EC2-4 7.2.1.6]*

Edge spacing factor $c_{crN} := 3 \cdot h_{ef} = 1.5\,m$

4.1 Connection properties

4.1.1 Material properties of bar

Ultimate strength $f_{ubk} := 1030MPa$ *[MPTB Table 2]*

Yield strength $f_{ybk} := 835MPa$

Diameter of bar $d_s := 32mm^2$

Area of bolt $A_{sp} := 847mm^2$

Shear factor $\alpha_v := 0.6$

4.1.4 Concrete properties

Concrete cube strength $f_{ck} := 50MPa$

Elastic modulus $E_{cm} := 35 \cdot 10^{9} Pa = 3.5 \times 10^{10} Pa$

4.2 Calculation of resistances

4.2.1 Partial factors for material resistance ULS *[EC2-4-1 4.4.3]*

Tension loading steel bolt $\gamma_{Mst} := 1.2 \cdot \frac{f_{ubk}}{f_{ybk}} = 1.48$

Shear loading steel bolt $\gamma_{Mss} := 1.0 \cdot \frac{f_{ubk}}{f_{ybk}} = 1.234$

Concrete $\gamma_{Mc} := 1.5$ For pull out failure $\gamma_{Mp} := \gamma_{Mc}$

Reinforcement in tension $\gamma_{MSre} := 1.15$

4.2.2 Bolt resistance ***[MPTB Table 3]***

0.1 % proof load $N_p := 670kN$

Tension resistance $N_{Rds} := \frac{N_p}{\gamma_{Mst}} = 452.629 \cdot kN$

Shear resistance $V_{Rds} := \alpha_v \cdot \frac{f_{ybk}}{\gamma_{Mss}} \cdot A_{sp} = 344.009 \cdot kN$

$A_{sp} = 8.47 \times 10^{-4} m^2$

4.2.3 Concrete resistance - tension loads

(a) Pull-out failure of fastener *[EC2-4 7.2.1.4]*

Limited by concrete pressure under head of fastener

Factor for cracked concrete $k_1 := 7.5$ $N_{Rkp} := k_1 \cdot A_h \cdot f_{ck} = 3.75 \times 10^{3} \cdot kN$

(b) Punching shear calc *[EC2-1 6.4]*

Concrete will act as full block for pull out - so will need to be checked for punching shear around perimeter

Control perimeter is taken as 2d from centre line of bars.

$d := h_{ef} = 0.5 m$ $2d = 1 m$

This can't really occur in radial direction, so assume a 45 deg shear line, and take perimeter as central point on that line

$d_r := 800mm$

distance from centre to edge = $d_e := 450mm$

vertical spacing $s_v := 200mm$

Total perimeter $u_1 := 2 \cdot 2 \cdot d + 2 \cdot d_e + 2.s_v + d_r = 4.1 m$

Total shear area $A_v := u_1 \cdot d = 4.6 m^2$

shear stress $v := \frac{N_{cT}}{A_v} = 0.363 \cdot MPa$ $v_{min} := 0.4MPa$ $\frac{v}{v_{min}} = 0.908$

(c) Splitting failure *[EC2-4-2 6.2.6.2]*

Reinforcment will be included to prevent splitting, therefore no explicit check is required

(d) Blow out failure *[EC2-4-2 6.2.7]*

critical edge distance $c_{crb} := 0.5 h_{ef} = 0.25 m$

Edge distance $c_e = 0.2 m$ which is greater than critical therefore verification not required

4.2.4 Concrete resistance - shear loads

(a) Concrete crushing (as per shear studs) *[EC2-4-2 6.3.4]*

$P_{rd.2} := \frac{0.29 \cdot d_b^{2} \cdot (f_{ck} \cdot E_{cm})^{0.5}}{\gamma_{Mc}} = 261.894 \cdot kN$

(b) Concrete edge failure *[EC2-4-2 6.3.5]*

Verification not required, as supplementary reinforcement will be included to take tensile loads

5 CONNECTION VERIFICATION

5.1 Max Tension

Tension design action on single bolt: $N_{EdT} = 139.167 \cdot kN$

Steel failure of fastener: $N_{Rds} = 452.629 \cdot kN$ $UT_{RdsT} := \frac{N_{EdT}}{N_{Rds}} = 0.307$

Pull out failure of fastener: $N_{Rdp} := \frac{N_{Rkp}}{\gamma_{Mp}} = 2.5 \times 10^{3} \cdot kN$ $UT_{RdpT} := \frac{N_{EdT}}{N_{Rdp}} = 0.056$

Concrete crushing in shear

Shear design action on single bolt: $V_{EdT} = 176.667 \cdot kN$

Steel failure of fastener (no lever arm): $V_{Rds} = 344.009 \cdot kN$ $UV_{RdsT} := \frac{V_{EdT}}{V_{Rds}} = 0.514$

Tension shear interaction verification for steel $\left(\frac{N_{EdT}}{N_{Rds}}\right)^2 + \left(\frac{V_{EdT}}{V_{Rds}}\right)^2 = 0.358$

5.1 Max Shear

Tension design action on single bolt: $N_{EdS} = 139.167 \cdot kN$

Steel failure of fastener: $N_{Rds} = 452.629 \cdot kN$ $UT_{RdsS} := \frac{N_{EdS}}{N_{Rds}} = 0.307$

Pull out failure of fastener: $UT_{RdpS} := \frac{N_{EdS}}{N_{Rdp}} = 0.056$

Concrete cone failure, and splitting failure not required as supplementary reinforcement will be included to take the tension resulting from these failure modes.

Blow out failure not required as edge distance is greater than half embedment depth

Shear design action on single bolt: $V_{EdS} = 220.833 \cdot kN$

Steel failure of fastener (no lever arm): $V_{Rds} = 344.009 \cdot kN$ $UV_{RdsS} := \frac{V_{EdS}}{V_{Rds}} = 0.642$

$U_{Vc} := \frac{V_{EdS}}{P_{rd.2}} = 0.843$

Tension shear interaction verification for steel $\left(\frac{N_{EdS}}{N_{Rds}}\right)^2 + \left(\frac{V_{EdS}}{V_{Rds}}\right)^2 = 0.507$

6 PRELOADED BAR

The calculations in the previous sections have been determined on the basis of un-preloaded bolts. However preloading bolts increases the fatigue life of a connection as it reduces the magnitude of stress fluctuations, and reduces slip under shear, and therefore is recommended for dynamic connections.

The effect of externally applied loads on a preloaded bolt depends on the relative stiffness of the bolt (in tension), and the joint (in compression) can be determined using a joint diagram.

6.1 Determine stiffness of bolt and anchor

Axial spring stiffness K=EA/l, and for combination of different areas 1/K = 1/K1+1/K2 .... +1/Kn.

Assume bolt and stud anchor act as composite section.

Youngs modulus of steel $E_s := 200GPa$

M32 Bar $A_{sp} = 847 \cdot mm^2$ $l_b := h_{ef} = 0.5\,m$ thickness of bearing plate

Socket head $S_w := 75mm = 0.075\,m$ $A_{sh} := \frac{2 \cdot 3}{\sqrt{3}} \cdot \left(\frac{S_w}{2}\right)^2 = 4.871 \times 10^3 \cdot mm^2$ $L_M := 40mm$

Anchor $A_a := d_b^2 \cdot \frac{\pi}{4} = 804.248 \cdot mm^2$ $l_a := h_{ef}$

Stiffness of bolt

$$K_b := \frac{1}{\left[\frac{1}{E_s} \cdot \left(\frac{l_b}{A_{sp}}\right)\right]} = 3.388 \times 10^5 \cdot \frac{kN}{m}$$

6.2 Determine stiffness of joint

Take cross section of concrete from Unbrako paper on Joint Diagrams, for case where joint diameter is greater than 3x the diameter of the loaded area. Assume that preload spreads through base plate at 45º, and washer is used to transfer loads, with 1.5x diameter of head. therefore diameter of loaded area of concrete = 1.5*Sw + l.sp

Diameter of loaded area = $d_l := 1.5S_w = 0.113\,m$

Effective area of concrete $A_{sc} := 100mm \cdot 100mm - \left(\frac{\pi}{4}\right) \cdot \left(d_b^2\right) = 9.196 \times 10^3 \cdot mm^2$

Youngs modulus of concrete $E_c := 30GPa$

Stiffness of joint concrete $K_{jc} := \frac{E_c \cdot A_{sc}}{h_{ef}} = 5.517 \times 10^5 \cdot \frac{kN}{m}$

G.2 Preliminary fatigue calcs

Section 11.3.3 presents the results of the preliminary fatigue analysis for the different connection options. This appendix presents the local stress RAOs that have been used in the spectral fatigue analysis for each connection.

Calculation of stress RAOs for connections - for use in preliminary fatigue analysis

1.0 CALCULATION OF LOCAL ARTICULATION LOADS

Period	s	4	5.5	6	6.5	7.5	8	8.5	9	9.5	10	10.5	12	14	16	18	20
6 dof articulation loading for 1m wave height - extracted from Aqwa																	
MX	kNm	171.0	166.8	184.8	237.6	220.2	200.8	184.2	170.1	155.9	136.8	118.8	69.2	56.7	56.1	44.1	43.3
MY	kNm	257.1	530.5	565.0	541.0	410.1	356.2	316.4	294.1	271.9	257.7	246.8	224.5	146.6	130.8	84.6	92.1
MZ	kNm	229.6	183.6	238.9	288.9	242.3	219.2	205.9	199.0	192.1	185.3	179.6	178.1	191.1	189.9	192.3	214.0
Fx	kN	56.3	112.9	133.4	136.9	121.5	106.1	93.1	81.9	70.8	63.0	59.9	49.4	38.7	56.9	61.6	58.6
Fy	kN	19.3	14.2	20.3	26.8	20.7	20.1	19.6	19.2	18.7	19.1	18.7	19.8	21.2	20.3	16.5	14.9
Fz	kN	45.8	52.9	49.2	44.6	17.7	15.1	13.5	12.5	11.4	11.1	10.4	7.3	5.5	6.4	6.4	3.2
Local loads - calculated in accordance with Figure 11.4																	
Rx'	kN	-57.8	-95.8	-111.4	-111.4	-87.6	-76.7	-76.7	-65.4	-61.5	-59.8	-59.1	-61.0	-52.5	-52.1	-47.5	-52.1
Ry'	kN	-23.4	-24.0	-25.4	-32.5	-31.2	-28.1	-28.1	-23.3	-21.0	-17.8	-14.9	-6.5	-4.0	-4.2	-3.2	-3.4
Rz'	kN	171.8	240.0	270.5	283.3	223.6	197.9	197.9	168.1	156.8	148.2	141.6	129.0	109.9	109.5	98.1	104.3
Absolute values																	
Rz'(abs)	kN	171.8	240.0	270.5	283.3	223.6	197.9	197.9	168.1	156.8	148.2	141.6	129.0	109.9	109.5	98.1	104.3
Rx'(abs)	kN	57.8	95.8	111.4	111.4	87.6	76.7	76.7	65.4	61.5	59.8	59.1	61.0	52.5	52.1	47.5	52.1
Ry'(abs)	kN	23.4	24.0	25.4	32.5	31.2	28.1	28.1	23.3	21.0	17.8	14.9	6.5	4.0	4.2	3.2	3.4
Shear Rv'	sqrt(Rz^2+Rx^2)	173.4	241.2	271.6	285.2	225.8	199.8	199.8	169.7	158.2	149.3	142.4	129.2	109.9	109.6	98.2	104.4

2.0 CALCULATION OF LOCAL STRESES IN ARTICULATIONS

(a) Shear studs		no of rows		5.0		no of columns			6.0	Total no. of shear studs			30.0		diameter		25.0
															Area		490.9
Tension per stud (kN)	Rx' / No of shear studs	1.9	3.2	3.7	3.7	2.9	2.6	2.6	2.2	2.0	2.0	2.0	2.0	1.7	1.7	1.6	1.7
Tensile stress (MPa)	Tension / Area σ	3.9	6.5	7.6	7.6	6.0	5.2	5.2	4.4	4.2	4.1	4.0	4.1	3.6	3.5	3.2	3.5
Shear per stud (kN)	Rv' / No of shear studs	5.8	8.0	9.1	9.5	7.5	6.7	6.7	5.7	5.3	5.0	4.7	4.3	3.7	3.7	3.3	3.5
Shear stress (Mpa)	Shear / Area τ	11.8	16.4	18.4	19.4	15.3	13.6	13.6	11.5	10.7	10.1	9.7	8.8	7.5	7.4	6.7	7.1
Principal	σ/2 +sqrt(σ/2^2+ τ^2)	13.9	20.0	22.6	23.5	18.6	16.4	16.4	14.0	13.0	12.4	11.9	11.1	9.5	9.4	8.5	9.1
(b) Composite dowel		no of ribs		3.0		no of dowels		3.0		total no of dowels			9.0		thickness		20.0
															length		110.0
															area		2200.0
dowel height = 0.313ex						78.3 mm											
height to narrowest section = (0.313-0.118)ex						48.8 mm											
Tension per dowel (kN)	Rx' / No of shear studs	6.4	10.6	12.4	12.4	9.7	8.5	8.5	7.3	6.8	6.6	6.6	6.8	5.8	5.8	5.3	5.8
Tensile stress (Mpa)	Tension / Area σ	2.9	4.8	5.6	5.6	4.4	3.9	3.9	3.3	3.1	3.0	3.0	3.1	2.7	2.6	2.4	2.6
Shear per dowel (kN)	Rv' / No of shear studs	19.3	26.8	30.2	31.7	25.1	22.2	22.2	18.9	17.6	16.6	15.8	14.4	12.2	12.2	10.9	11.6
At narrowest part		12.0	16.7	18.8	19.7	15.6	13.8	13.8	11.8	10.9	10.3	9.9	8.9	7.6	7.6	6.8	7.2
Shear stress (Mpa)	Shear / Area τ	5.5	7.6	8.5	9.0	7.1	6.3	6.3	5.3	5.0	4.7	4.5	4.1	3.5	3.4	3.1	3.3
Principal	σ/2 +sqrt(σ/2^2+ τ^2)	7.1	10.4	11.8	12.2	9.7	8.5	8.5	7.2	6.8	6.4	6.2	5.9	5.0	5.0	4.5	4.9

(c) i Cast in sockets with no preload on bolts		no of rows		4.0		no of columns			5.0 Total no of studs				20.0	diameter			25.0
														Area			459.0
Tension per stud (kN)	Rx' / No of shear studs	2.9	4.8	5.6	5.6	4.4	3.8	3.8	3.3	3.1	3.0	3.0	3.0	2.6	2.6	2.4	2.6
Tensile stress (MPa)	Tension / Area σ	6.3	10.4	12.1	12.1	9.5	8.4	8.4	7.1	6.7	6.5	6.4	6.6	5.7	5.7	5.2	5.7
Shear per stud (kN)	Rv' / No of shear studs	8.7	12.1	13.6	14.3	11.3	10.0	10.0	8.5	7.9	7.5	7.1	6.5	5.5	5.5	4.9	5.2
Shear stress (Mpa)	Shear / Area τ	18.9	26.3	29.6	31.1	24.6	21.8	21.8	18.5	17.2	16.3	15.5	14.1	12.0	11.9	10.7	11.4
Principal	$\sigma/2 + \sqrt{(\sigma/2^2 + \tau^2)}$	22.3	32.0	36.3	37.7	29.8	26.3	26.3	22.4	20.9	19.8	19.1	17.8	15.2	15.1	13.6	14.6

(c) ii Cast in sockets with preloaded bolts		no of rows		4.0		no of columns			5.0 Total no of studs				20.0	diameter			25.0
														Area			459.0
Preload	F_p	121.31 kN			See calcs in Appendix G.3												
Coefficient of friction	μ																
Friction force	$F_p.\mu$	24.262															
Stiffness of bolt	K_B	3.54E+05 kN/m															
stiffness of joint	K_J	1.02E+06 kN/m															
Tension per stud (kN)		2.9	4.8	5.6	5.6	4.4	3.8	3.8	3.3	3.1	3.0	3.0	3.0	2.6	2.6	2.4	2.6
Additional bolt force	$T_{add} = T.K_B / (K_B + K_J)$	0.7	1.2	1.4	1.4	1.1	1.0	1.0	0.8	0.8	0.8	0.8	0.8	0.7	0.7	0.6	0.7
Tensile stress (MPa)	T_{add} / Area	1.6	2.7	3.1	3.1	2.5	2.2	2.2	1.8	1.7	1.7	1.7	1.7	1.5	1.5	1.3	1.5
Shear per stud (kN)		8.7	12.1	13.6	14.3	11.3	10.0	10.0	8.5	7.9	7.5	7.1	6.5	5.5	5.5	4.9	5.2
Shear stress (Mpa)	zero if shear stud < friction	0.0	0.0	0.0	0.0	0.0	0.0	0.0	0.0	0.0	0.0	0.0	0.0	0.0	0.0	0.0	0.0
Principal	$\sigma/2 + \sqrt{(\sigma/2^2 + \tau^2)}$	1.6	2.7	3.1	3.1	2.5	2.2	2.2	1.8	1.7	1.7	1.7	1.7	1.5	1.5	1.3	1.5

(d) Post-tensioned bars

No of bars		12.0															
Stiffness of bar		3.39E+05 kN/m															
Stiffness of joint		5.52E+05 kN/m															
Tension per bar	Rx' / No of shear studs	4.8	8.0	9.3	9.3	7.3	6.4	6.4	5.4	5.1	5.0	4.9	5.1	4.4	4.3	4.0	4.3
Additional tension	$T_{add} = T.K_B / (K_B + K_J)$	1.8	3.0	3.5	3.5	2.8	2.4	2.4	2.1	1.9	1.9	1.9	1.9	1.7	1.7	1.5	1.7

References

Aalborg University (2014), 'Structural design of wave energy devices (SDWED) 2010-2014', https://www.sdwed.civil.aau.dk. [Website - Accessed 13 July 2018].

ABS (2005), Spectral based fatigue analysis for floating offshore structures, Technical report, American Bureau of Shipping.

ACI (1996), State-of-the-art report on fiber reinforced concrete, Technical Report ACI 544.1 R-96, American Concrete Institute-ACI Committee and others.

Adam, F., Ritschel, U., Dahlhaus, F. and Großmann, J. (2016), Development of an economical and insured TLP substructure for a 6MW wind turbine–use of steel-concrete composite material, *in* '2nd International Conference on Offshore Renewable Energy. Glasgow', pp. 12–14.

Ahsan, R. (2016), Fatigue in concrete structures, *in* 'BSRM Seminar on fatigue properties of construction steel'.

Albatern (2017*a*), 'Array configurations - Albatern', http://albatern.co.uk/wavenet/array-configurations/. [Website - Accessed 12 July 2018].

Albatern (2017*b*), 'Grid scale - Albatern', http://albatern.co.uk/markets/grid-scale/. [Website - Accessed 12 July 2018].

Aldea, C.-M., Shah, S. P. and Karr, A. (1999), 'Permeability of cracked concrete', *Materials and structures* **32**(5), 370–376.

Anderson, C. (2003), Pelamis WEC - Main body structural design and materials selection, Technical Report V/06/00187/00/00/REP - DTI URN 03/1439, Ocean Power Delivery Ltd.

Ansys AQWA (2013), Theory manual, Release 15.0, Technical report, ANSYS Inc., USA.

Arup (2018), Concrete as a technology enabler (CREATE) - WES Structural materials and manufacturing processes Stage 1 public report, Technical Report MC11-ARP-WES Public report, Wave Energy Scotland.

Arup and Cruz Atcheson Consulting (2016), Structural forces and stresses for wave energy devices - landscaping study, Technical Report WES-LS02-ER Forces and Stresses, Wave Energy Scotland.

Arya, C., Clarke, J., Kay, E. and O'Regan, P. (2002), 'TR 55: Design guidance for strengthening concrete structures using fibre composite materials: a review', *Engineering Structures* **24**(7), 889–900.

Ashby, M. F. (2011), *Material Selection in Mechanical Design, 4th Edition*, Butterworth-Heinemann.

Barker Ewart, L., Barltrop, N., Findlay, D., Thies, P. R. and Stratford, T. (2016), Steel-concrete connections for floating wave energy converters, *in* '2nd International Conference on Offshore Renewable Energy. Glasgow'.

Barker Ewart, L., Barltrop, N., Findlay, D., Thies, P. R. and Stratford, T. (2018), Advanced concrete materials for offshore floating structures, *in* 'International Conference on Ocean Energy (ICOE)'.

Barker Ewart, L., Thies, P. R., Stratford, T. and Barltrop, N. (2017), Optimising structural loading and power production for floating wave energy converters, *in* '11th European Wave and Tidal Energy Conference (EWTEC), Cork'.

Barnes, R. A. and Mays, G. C. (2001), 'The transfer of stress through a steel to concrete adhesive bond', *International journal of adhesion and adhesives* **21**(6), 495–502.

Barstow, S., Mørk, G., Mollison, D. and Cruz, J. (2008), *The Wave Energy Resource*, Springer Berlin Heidelberg, Berlin, Heidelberg, pp. 93–132.

BBR VT International Ltd (2017), BBR CT CONA CMD BT European Technical Assessment, Technical Report ETA - 12/0076, BBR.

Benasciutti, D., Sherratt, F. and Cristofori, A. (2015), 'Basic principles of spectral multi-axial fatigue analysis', *Procedia Engineering* **101**, 34–42.

Benasciutti, D. and Tovo, R. (2006), 'Comparison of spectral methods for fatigue analysis of broad-band gaussian random processes', *Probabilistic Engineering Mechanics* **21**(4), 287–299.

Bencardino, F. (2013), 'Mechanical parameters and post-cracking behaviour of HPFRC according to three-point and four-point bending test', *Advances in Civil Engineering* **2013**.

Bendat, J. (1964), Probability functions for random responses NASA report on contract NAS-5-4590, Technical Report Report on Contract NAS-5-4590, NASA.

Berthellemy, J. (2013), 'Fatigue designed CL-cutting shape: A new economic steel-concrete connection system and some applications for bridges', *Procedia Engineering* **66**, 138–149.

Blanchette, J. L. (2012), Pullout strength of epoxy anchors installed underwater, Master's thesis, Faculty of California Polytechnic State University.

Brodtkorb, P. A., Johannesson, P., Lindgren, G. and Rychlik, I. (2011), WAFO–A Matlab toolbox for analysis of random waves and loads, Tutorial for wafo version 2.5, WAFO Group, Lund Institute of Technology. Lund, Sweden.

BSI (2004*a*), Eurocode 2: Design of concrete structures - Part 1-1: General rules and rules for buildings, Standard BS EN 1992-1-1, British Standards Institution.

BSI (2004*b*), Eurocode 4: Design of composite steel and concrete structures - Part 1-1: General rules and rules for buildings, Standard BS EN 1994-1-1, British Standards Institution.

BSI (2013), Eurocode 2: Design of concrete structures. Part 4: Design of fastenings for use in concrete, Standard BS EN 1992-4, British Standards Institution.

Buttignol, T. E. T., Sousa, J. and Bittencourt, T. (2017), 'Ultra high-performance fiber-reinforced concrete (UHPFRC): a review of material properties and design procedures', *Revista IBRACON de Estruturas e Materiais* **10**(4), 957–971.

Charron, J.-P., Denarié, E. and Brühwiler, E. (2007), 'Permeability of ultra high performance fiber reinforced concretes (UHPFRC) under high stresses', *Materials and structures* **40**(3), 269–277.

Chen, J. and Tao, Y. (2011), Finite element modelling of FRP-to-concrete bond behaviour using the concrete damage plasticity theory combined with a plastic degradation model, *in* 'Advances in FRP Composites in Civil Engineering', Springer, pp. 45–50.

Classen, M. and Gallwoszus, J. (2016), 'Concrete fatigue in composite dowels', *Structural Concrete* **17**(1), 63–73.

Classen, M. and Hegger, J. (2016), 'Anchorage of composite dowels', *Steel Construction* **9**(2), 138–150.

De Andres, A., Medina-Lopez, E., Crooks, D., Roberts, O. and Jeffrey, H. (2017), 'On the reversed LCOE calculation: Design constraints for wave energy commercialization', *International journal of marine energy* **18**, 88–108.

de Montaignac, R., Massicotte, B., Charron, J.-P. and Nour, A. (2012), 'Design of SFRC structural elements: post-cracking tensile strength measurement', *Materials and structures* **45**(4), 609–622.

Denarié, E. and Bruhwiler, E. (2011), 'Strain-hardening ultra-high performance fibre reinforced concrete: deformability versus strength optimization', *Restoration of Buildings and Monuments* **17**(6), 397–410.

DexaWave (2013), 'DexaWave - Converters', `http://www.dexawave.com/converters.html`. [Website - Accessed 15/12/2014].

di Prisco, M., Colombo, M. and Dozio, D. (2013), 'Fibre-reinforced concrete in fib model code 2010: principles, models and test validation', *Structural Concrete* **14**(4), 342–361.

Dirlik, T. (1985), Application of computers in fatigue analysis, PhD thesis, University of Warwick.

DNV (2005), Guidelines on design and operation of wave energy converters, Technical report, Carbon Trust/DNV.

DNV (2008), Certification of tidal and wave energy converters, Offshore Service Specification DNV-OSS-312, Det Norske Veritas.

DNV (2012), Offshore concrete structures, Offshore Standard DNV OS-C502, Det Norske Veritas.

DNV (2013), Qualification procedures for new technology, Recommended Practice DNV-RP-A203, Det Norske Veritas.

DNV GL (2014), Fatigue design of offshore steel structures, Recommended practice DVNGL-RP-C203, DNV GL.

DNV GL (2017), Design of offshore steel structures, general - LRFD method, Offshore standards DNVGL-OS-C101, DNV GL.

DNV GL (2018), Offshore concrete structures, Standard DNVGL-ST-C502, DNV GL.

DSS (2014), Abaqus analysis user's manual 6.14-2, Technical Report 6.14-2, Dassault Systèmes Simulia Corp.

Eide, M. B. and Hisdal, J.-M. (2012), Ultra high performance fibre reinforced concrete (uhpfrc), Technical Report 44-2012, SINTEF Building and Infrastructure.

Eldin, H. K. S., Mohamed, H. A., Khater, M. and Ahmed, S. (2014), 'Mechanical properties of Ultra-High Performance Fiber Reinforced Concrete', *International journal of engineering and innovative technology* **4**, 4–10.

Eligehausen, R. (2017), Fastening in concrete construction; past, present, future, *in* A. Sharma and J. Hofmann, eds, '3rd International Symposium on Connections between Steel and Concrete: Stuttgart, Germany, 27th-29th September 2017; proceedings', Institute of Construction Materials, pp. 1311–1330.

ENERCO (2013), 'Prefabricated concrete tower factory', `http://www.eneop.pt/en/subcanais_n1.asp?id_subcanal_n1=184&id_canal=105`. [Website - Accessed 22/12/2014].

Fam, A., Greene, R. and Rizkalla, S. (2003), Field applications of concrete-filled FRP tubes for marine piles, Technical Report SP.215-9.

Feldmann, M., Kopp, M. and Pak, D. (2016), 'Composite dowels as shear connectors for composite beams–background to the German Technical Approval', *Steel Construction* **9**(2), 80–88.

Fernandes, C. (2013), 'Oscillating Water Column - large scale oscillating water column design', `http://owc-wec.weebly.com/oscillating-water-columns.html`. [Website - Accessed 15/12/2014].

fib (2013), fib model code for concrete structures 2010, Technical report, Fédération Internationale Du Béton.

Frigione, M. and Lettieri, M. (2018), 'Durability issues and challenges for material advancements in FRP employed in the construction industry', *Polymers* **10**(3), 247.

Gooch, D. (2000), 'Material issues in renewable energy power generation', *International Materials Reviews* **45**(1), 1–14.

Göransson, F. and Nordenmark, A. (2011), Fatigue assessment of concrete foundations for wind power plants, Master's thesis, Chalmers University of Technology.

Granta Design Limited (2017), 'CES Edupack2017'.

Grünberg, J. and Göhlmann, J. (2013), *Concrete structures for wind turbines*, John Wiley & Sons.

Grünberg, J., Göhlmann, J. and Ertel, C. (2005), 'Concrete foundations for offshore wind energy converters subjected to fatigue loading', *Copenhagen Offshore Wind* .

Gunn, K. and Stock-Williams, C. (2012), 'Quantifying the global wave power resource', *Renewable Energy* **44**, 296–304.

Halfen (2014), HALFEN HUC universal connection - technical product information, Technical Report HUC 16-E, Halfen. [Downloaded from `https://downloads.halfen.com/catalogues/de/media/catalogues/reinforcementsystems/HUC_16-E.pdf`].

Halfpenny, A. (1999), A frequency domain approach for fatigue life estimation from finite element analysis, *in* 'Key Engineering Materials', Vol. 167, Trans Tech Publ, pp. 401–410.

Hamedni, B. and Ferreira, C. B. (2014), SDWED D5.2 Generic WEC risk ranking and failure mode anaylsis, Deliverable D5.2, SDWED/DNV-GL.

Hamedni, B., Mathieu, C. and Bittencourt Ferreira, C. (2014), Generic WEC system breakdown, Deliverable D5.1, SDWEC / DNV-GL.

Herve, R., Mohamed, B., Fabien, L. et al. (2015), 'Comparison of spectral methods for fatigue analysis in non-gaussian random processes –Application to elastic-plastic behaviour', *Procedia Engineering* **101**, 430–439.

Hi-Con A/S (2012), FLOAT - Development of new flexible UHPC–Final report, Technical Report NEI-DK-5747, Hjallerup, Denmark.

Hi-Con A/S (2016), FLOAT2 - New flexural UHPC application for wave converters 2, Technical Report 2012-1-10754.

Hilti AG (2010), 'Fastening technology manual - dynamic design for anchors'.

Hoff, G. (2008), Concrete for offshore structures, *in* E. G. Nawy, ed., 'Concrete Construction Engineering Handbook, Second Edition', CRC press.

Holmes, B. (2009), Tank testing of wave energy conversion systems, Technical report, EMEC. Marine Renewable Energy Guides.

Hover, E., Psomas, S. and Eddie, C. (2015), 'Estimating crack widths in steel fibre-reinforced concrete', *Proceedings of the Institution of Civil Engineers-Construction Materials* **170**(3), 141–152.

Hudson, J. A., Phillips, D. C. and Wilkins, N. J. M. (1980), 'Materials aspects of wave energy converters', *Journal of Materials Science* **6**(15), 1337–1363.

Ingram, D., Smith, G., Bittencourt-Ferreira, C. and Smith, H. (2011), Protocols for the equitable assessment of marine energy converters, Technical report, EquiMar.

Interfluid Hydraulics Ltd (2017), 'Interfluid store (website)', `https://interfluid.co.uk/store/`. [Website - Accessed February 2017].

IPCC (2012), *Renewable Energy Sources and Climate Change Mitigation: Special Report of Intergovernmental Panel on Climate Change*, Cambrige University Press. Intergovernmental Panel on Climate Change.

Jankowiak, T. and Lodygowski, T. (2005), 'Identification of parameters of concrete damage plasticity constitutive model', *Foundations of civil and environmental engineering* **6**, 53–69.

Johnston, C. D. and Zemp, R. W. (1991), 'Flexural fatigue performance of steel fiber reinforced concrete–influence of fiber content, aspect ratio, and type', *Materials Journal* **88**(4), 374–383.

Kang, S.-T., Lee, Y., Park, Y.-D. and Kim, J.-K. (2010), 'Tensile fracture properties of an ultra high performance fiber reinforced concrete (UHPFRC) with steel fiber', *Composite Structures* **92**(1), 61–71.

Khosravi, N., Barker, L., O'Donoghue, V., Benzie, J., Newlands, M. and Jones, R. (2015), Use of concrete as the primary construction material for the Pelamis wave energy converter, CRC Press, pp. 305–312.

Kleineidam, P., Schaumann, P. et al. (2005), Evaluation of different damage prediction methods for support structures of offshore wind energy converters, *in* 'The Fifteenth International Offshore and Polar Engineering Conference', International Society of Offshore and Polar Engineers.

Langdon, D. (2016), *Spon's Civil Engineering and Highway Works Price Book*, CRC Press.

Larsen, C. E. and Irvine, T. (2015), 'A review of spectral methods for variable amplitude fatigue prediction and new results', *Procedia Engineering* **101**, 243–250.

Lee, M. and Barr, B. (2004), 'An overview of the fatigue behaviour of plain and fibre reinforced concrete', *Cement and Concrete Composites* **26**(4), 299–305.

Lepech, M. D. and Li, V. C. (2009), 'Water permeability of engineered cementitious composites', *Cement and Concrete Composites* **31**(10), 744–753.

Liu, H., Zhang, Q., Gu, C., Su, H. and Li, V. C. (2016), 'Influence of micro-cracking on the permeability of engineered cementitious composites', *Cement and Concrete Composites* **72**, 104–113.

Long, M., Djelal, C., Kesteloot, S., Bigourdan, B., Le Gac, P. and Szulc, J. (2012), Durability of CFRP-concrete bonding in a marine environment, *in* 'Proceedings of ECCM15-15th European Conference on Composite Materials. Venice, Italy'.

López, J. Á., Serna, P., Navarro-Gregori, J. and Camacho, E. (2015), 'An inverse analysis method based on deflection to curvature transformation to determine the tensile properties of UHPFRC', *Materials and Structures* **48**(11), 3703–3718.

Lorenc, W., Kożuch, M. and Rowiński, S. (2014), 'The behaviour of puzzle-shaped composite dowels - Part i: Experimental study', *Journal of Constructional Steel Research* **101**, 482–499.

Low Carbon Innovation Coordination Group (2012), 'Technology innovation needs assessment (TINA): marine energy summary report', *Technical report, Low Carbon Innovation Coordination Group* .

Lu, X., Ye, L., Teng, J. and Jiang, J. (2005), 'Meso-scale finite element model for FRP sheets/plates bonded to concrete', *Engineering Structures* **27**(4), 564–575.

Ma, H., Qian, S. and Zhang, Z. (2014), 'Effect of self-healing on water permeability and mechanical property of medium-early-strength engineered cementitious composites', *Construction and Building Materials* **68**, 92–101.

Macalloy (2012), The foundation anchor solution for wind turbines, Company documentation, Macalloy Bar & Cable Systems. [Downloaded from http://www.srglimited.com.au/images/files/brochures/wind-turbine-anchor-solutions_srg.pdf].

Macalloy (2013), Macalloy 1030 post tensioing system design data, Company design documentation. [Downloaded from https://www.macalloy.com/application/files/8115/0046/3186/POST_TENSIONING_SYSTEM_July_2017.PDF].

Mahrenholtz, C. and Sharma, A. (2017), Comparison of design rules for anchor channels with channel bolts, *in* '3rd International Symposium on Connections between Steel and Concerte: Stuttgart, Germany 27th-29th September 2017; proceedings'.

Maidl, B. and Dietrich, J. (1992), 'Verification of serviceability for steel fibre reinforced concrete in tunnelling', *Structural Engineering International* **2**(2), 114–117.

Markeset, G., Rostam, S. and Klinghoffer, O. (2006), Guide for the use of stainless steel reinforcement in concrete structures, Technical Report 04118, Nordic Innovation Centre.

Mindess, S. (2007), Thirty years of fibre reinforced concrete research at the University of British Columbia, *in* 'International Conference on Sustainable Construction Materials and Technologies', pp. 259–268.

Morton Kramer, L. M. and Frigaard, P. (2011), Performance evaluation of the Wavestar prototype, *in* 'EWTEC 2011 conference'.

Naaman, A. E. (2008), *High performance fiber reinforced cement composites*, World Scientific Publishing, chapter 3, pp. 91–153.

Newlands, M. D. and Jones, R. (2017), State of the art literature review and supply chain study, Technical Report WEC-ACE-D-0001, University of Dundee. Confidential project report.

Newlands, M., Khosravi, N., Jones, R. and Chernin, L. (2018), 'Mechanical performance of statically loaded flat face epoxy bonded concrete joints', *Materials and Structures* **51**(2), 49.

Niesłony, A., Růžička, M., Papuga, J., Hodr, A., Balda, M. and Svoboda, J. (2012), 'Fatigue life prediction for broad-band multiaxial loading with various PSD curve shapes', *International Journal of Fatigue* **44**, 74–88.

Paepegem, W. V., Blommaert, C., Baere, I. D., Degrieck, J., Backer, G. D., Rouck, J. D., Degroote, J., Vierendeels, J., Matthys, S. and Taerwe, L. (2011), 'Slamming wave impact of a composite buoy for wave energy applications: Design and large-scale testing', *Polymer Composites* **32**(5), 700–713.

Park, S. H., Kim, D. J., Ryu, G. S. and Koh, K. T. (2012), 'Tensile behavior of ultra high performance hybrid fiber reinforced concrete', *Cement and Concrete Composites* **34**(2), 172–184.

Pérez Fernández, R. and Lamas Pardo, M. (2013), 'Offshore concrete structures', *Ocean Engineering* **58**, 304–316.

Pilakoutas, K., Guadagnini, M., Neocleous, K. and Matthys, S. (2009), 'The fib perspective on FRP reinforcement in RC', *FRPRCS-09, Sydney* .

Pitoiset, X., Preumont, A. and Kernilis, A. (1998), Tools for a multiaxial fatigue analysis of structures submitted to random vibrations, *in* 'Proc. European conference on spacecraft structures materials and mechanical testing'.

Pyo, S. (2014), Characteristics of ultra high performance concrete subjected to dynamic loading, PhD thesis, University of Michigan.

Quoceant and University of Dundee (2018), ACE-WEC public report, ACE-WEC Project report MC11-QUO-WES, Quoceant.

RILEM Technical Committee 36-RDL (1994), 'Long term random dynamic loading of concrete structures', *Materials and Structures - Research and Testing* **17**(98), 1–97.

Romualdi, J. P. and Batson, G. B. (1963), 'Mechanics of crack arrest in concrete', *Journal of the Engineering Mechanics Division* **89**(3), 147–168.

Salter, S. (2003), 'Research requirements for 4th generation wave energy devices', `http://www.see.ed.ac.uk/~shs/Wave%20Energy/`. [Website - Accessed February 2015].

Sandvik, K., Eie, R., Advocaat, J.-D., Godejord, A., O.H, K., H, K. and Olsen, T. O. (2004), Offshore structures - a new challenge, *in* 'XIV National Conference on Structural Engineering'.

Schijve, J. (2001), *Fatigue of structures and materials*, Springer Science & Business Media.

Shariati, A., RamliSulong, N., Shariati, M. et al. (2012), 'Various types of shear connectors in composite structures: A review', *International Journal of Physical Sciences* **7**(22), 2876–2890.

Sharma, A. and Hofmann, J. (2017), '3rd International symposium on connections between steel and concrete: Stuttgart, germany, 27th-29th september 2017; proceedings'.

Si Larbi, A., Ferrier, E., Jurkiewiez, B. and Hamelin, P. (2007), 'Static behaviour of steel concrete beam connected by bonding', *Engineering structures* **29**(6), 1034–1042.

Song, Y., Meng, X. et al. (2006), Fatigue failure criterion of concrete under multi-axial and variable-amplitude cyclic loading and its application in offshore engineering, *in* 'The Sixteenth International Offshore and Polar Engineering Conference', International Society of Offshore and Polar Engineers.

The Concrete Centre (2014), Concrete gravity foundations for offshore wind, Information leaflet.

Thomas, J. and Ramaswamy, A. (2007), 'Mechanical properties of steel fiber-reinforced concrete', *Journal of materials in civil engineering* **19**(5), 385–392.

Tom, N. M., Yu, Y.-H. and Wright, A. D. (2016), Balancing power absorption and structural loading for a novel fixed-bottom wave energy converter with nonideal power take-off in regular waves: Preprint, Technical report, National Renewable Energy Lab.(NREL), Golden, CO (United States).

Toth, M., Ovzbolt, J., Fuchs, W. and Hofmann, J. (2016), 'Fatigue behaviour of fasteners in case of concrete failure: Numerical and experimental investigations', *fib Symposium on Performance-based Approaches for Concrete Structures* .

Tricklebank, A. H., Halberstadr, P. H. and Magee, B. J. (2007), Concrete towers for onshore and offshore wind farms - Conceptual design studies, Technical report, Gifford & The Concrete Centre.

UNBRAKO (2004), Unbrako engineering guide - socket products, Technical report, Unbroko Group. [Downloaded from: `http://www.unbrako.com/images/downloads/engguide.pdf,November2015`].

Valente, I. (2007), Experimental studies on shear connection systems in steel and lightweight concrete composite bridges, PhD thesis, University of Minho, Portugal.

van Zijl, G. P. A. G. (2011), Durability under mechanical load–micro-crack formation (ductility), *in* G. van Zijl and F. Wittmann, eds, 'Durability of Strain-Hardening Fibre-Reinforced Cement-Based Composites (SHCC)', Springer, pp. 9–39.

van Zijl, G. P. A. G. and Boshoff, W. (2008), 'Mechanisms of creep in fibre-reinforced strain-hardening cement composites (SHCC)'.

Ventus, V. (2011), 'Offshore wind turbines: concrete foundations'. marketing publication.

Walraven, J. C. (2009), 'High performance fiber reinforced concrete: progress in knowledge and design codes', *Materials and Structures* **42**(9), 1247–1260.

Walsh, M. and Henderson, C. (2016), Alternative reinforcement for concrete in corrosive environments, Technical Report ST-2016-020-01, US Department of the Interior, Bureau of Reclamation.

Wang, Z., Zhao, X.-L., Xian, G., Wu, G., Raman, R. S., Al-Saadi, S. and Haque, A. (2017), 'Long-term durability of basalt-and glass-fibre reinforced polymer (BFRP/GFRP) bars in seawater and sea sand concrete environment', *Construction and Building Materials* **139**, 467–489.

Wave Energy Scotland (2016*a*), Materials landscaping study - final report, Technical Report WES-LS01-ER-Materials.

Wave Energy Scotland (2016*b*), 'Novel wave energy converter projects', `http://www.waveenergyscotland.co.uk/programmes/details/novel-wave-energy-converter/`. [Website - Accessed 12 July 2018].

Wave Energy Scotland (2017), 'Materials - wave energy scotland', `http://www.waveenergyscotland.co.uk/programmes/details/materials/`. [Website - Accessed 12 July 2018].

William, K. J. and Warnke, E. (1975), 'Constitutive model for the triaxial behavior of concrete', *International association of bridge and structural engineers, Seminar on concrete structures subjected to triaxial stresses*, .

Wittel, F. (2016), Constitutive models for steel reinforced concrete, lecture given in mechanics of building materials, Lecture notes, ETH Zurich. [Downloaded from `http://www.ifb.ethz.ch/education/msc-courses/msc-mechanics-building-materials.html`].

Xie, E. and Valente, I. (2011), Fatigue strength of shear connectors, Bridging the gap - research report, University of Minho, Guimaraes, Portugal.

Yazıcı, Ş., İnan, G. and Tabak, V. (2007), 'Effect of aspect ratio and volume fraction of steel fiber on the mechanical properties of SFRC', *Construction and Building Materials* **21**(6), 1250–1253.

Yeter, B., Garbatov, Y. and Soares, C. G. (2013), 'Spectral fatigue assessment of an offshore wind turbine structure under wave and wind loading', *Developments in maritime transportation and exploitation of sea resources* pp. 425–433.

Yu, J., Li, H., Leung, C. K., Lin, X., Lam, J. Y., Sham, I. M. and Shih, K. (2017), 'Matrix design for waterproof engineered cementitious composites (ECCs)', *Construction and Building Materials* **139**, 438–446.

Yu, R., Spiesz, P. and Brouwers, H. (2014), 'Mix design and properties assessment of ultra-high performance fibre reinforced concrete (UHPFRC)', *Cement and concrete research* **56**, 29–39.

Zhao, W. and Baker, M. J. (1992), 'On the probability density function of rainflow stress range for stationary gaussian processes', *International Journal of Fatigue* **14**(2), 121–135.

Zurkinden, A., Gao, Z., Moan, T., Lambertsen, S. and Damkilde, L. (2013), Spectral based fatigue analysis of the wavestar–arm taking into account different control strategies., *in* 'Proceedings of the ASME 2013 32nd International Conference on Ocean, Offshore and Arctic Engineering, OMAE2013, June 9-14, 2013, Nantes, France'.